NUMERICAL AND PHYSICAL MODELLING OF DAM-BREAK FLOOD WAVES IN X-T AND R-T SPACE

BY

ADNAN H. AL-SALIHI

B.Sc. (University of Baghdad) 1976

M.Sc. (University of Baghdad) 1978

A thesis submitted for the degree of

Doctor of Philosophy

October 1986

Department of Civil Engineering

University of Strathclyde

GLASGOW

UNITED KINGDOM

TO MY PARENTS

ACKNOWELDGEMENTS

The author would like to express his gratitude to Dr. J.M. Townson, Reader, for his kindly help and encouragement throughout this research. It was Dr. Townson who suggested this problem and supervised its progress.

The author wishes to express his grateful appreciation to Professor D.I.H. Barr, Department of Civil Engineering, for his comments, valuable suggestions and supervision for part of the work.

Thanks are due to the Technicians of the Hydraulics Laboratory for their help in building the physical models, and a special word of appreciation to Mr. D. Burgess for his help in this matter. Thanks should also go to the members of the Computer Advisory Service for their recommendations concerning the computational aspects.

The author is grateful to the Committee of Vice-Chancellors and Principals of the Universities of the United Kingdom for awarding him the Overseas Research Students Award, also to the University of Strathclyde for awarding him David Livingstone Bursary. Thanks are due to Mrs E. MacKinnon for typing the text.

Finally, the author expresses his sincere thanks to his parents, his wife and his son for their endless support and encouragement throughout this study.

Adnan Al-Salihi
Glasgow, U.K.
1986

ABSTRACT

The techniques for computing dam-break flood waves in prismatic channels are reviewed. Numerical models for cases with or without an initially dry downstream bed are developed. The models are based on the characteristic forms of the shallow water equations, both in (X-T) and (R-T) space, using specified time intervals and incorporating the Rankine-Hugoniot shock equations.

Three numerical models for rectangular section channels are studied, namely the parallel (X-T), the expanded (R-T) and the contracted (R-T) cases; any two of these are then linked to produce three further models, described as the Contracted-Plain (RT-XT), the Contracted-Expanded (RT-RT) and the Plain-Expanded (XT-RT) models.

Four physical models were tested and compared with results from the numerical models and with those from Barr and Das (1980), Marshall and Menendez (1981) and Katopodes and Schamber (1983). The numerical and experimental results are given in the form of comparative plots of front heights, surface profiles, front trajectories and depth hydrographs. Variations from the well-known solutions by Ritter (1892) and Stoker (1957), including those caused by radial flow effects are found to occur and are discussed.

INDEX

LIST OF FIGURES *

---

* All the figures are kept at the end of each chapter unless they are illustrated in the text.

Figure

Figure

Figures

LIST OF TABLES

Table

NOTATIONS

A	Index in transition control function
A_s	Area on which the side pressure force acts in the Radial Jump
B	Breadth of the channel
c	Wave celerity
C_r	Courant number
C_u	Units coefficient
d_e	Equivalent diameter of open channel
E	Constant of transition control function
F_g	Force due to gravity
F_p	Pressure force
g	Acceleration due to gravity
H	Constant of transition control function, Total water depth
H_o	Initial fluid depth downstream of the dam
H_1	Initial fluid depth upstream of the dam
H_2	Depth of the shock wave
H'	Distance measured from the free surface to the centre of the trapezoid in the Radial Jump
I	Integer, Grid number along x or r-direction
K	Constant in equation (3.59), Nikuradse's sand roughness size
n	Manning coefficient of roughness
N	Total number of grid points along the computational line
P	Hydrostatic pressure force
P_s	Channel side pressure force
q	Discharge per unit length
Q	Flow discharge
r	Radius along the channel bed

Δr	Distance step along r-direction
R	Reynold's number of flow, Channel Hydraulic radius
R_*	Roughness Reynold's number
R_{**}	Approximation for the roughness Reynold's number R_*
S_o	Channel slope along x-direction
S_f	Friction slope
t	Time
Δt	Time step along t-direction
u	Depth-mean velocity
w	Velocity of the shock wave
W	Index in transition control function
x	Distance along the channel bed
Δx	Distance step along x-direction
θ	Angle in the radial flow
λ	Friction factor
ν	Kinematic viscosity of liquid
ρ	Fluid density

CHAPTER ONE

INTRODUCTION

The use of dams for water impoundment goes back to the dawn of history. Reservoirs were constructed in the Middle East before man could read or write. Although most of these have collapsed because of old age, or lack of maintenance, their value to the communities they serve has been inestimable. Some historians even speculate that the deterioration of the Arab Empire was caused by inadequate maintenance of the reservoirs which were so vital to food production and life [Sowers (1974)]. Also, as Toran (1973) stated, 'Dams are large, noble; they are elephants needing an attendant to care for them'.

Flood waves caused or augmented by dam failures have been in the newspaper headlines in recent years. In the Daily Telegraph issued on Monday, 21st April 1986, '100 Dead as Dam Bursts', was the headline, and stated, 'At least 100 people were feared dead yesterday after a reservoir bank collapsed in eastern Sri Lanka and water engulfed a nearby town. Officials in the district capital of Trincomalee estimated that 18,000 people in the town of Kantalai had been left homeless. Officilas said the bank collapsed at a point where a crack had been noticed several weeks ago, but had been left unattended'.

According to the New Civil Engineer magazine issued on 1st May 1986, the force was tremendous since the reservoir is about 25km square and the water about 14m deep. The reservoir emptied in three hours whilst 7800 people had been made homeless by the flooding. The Sri Lankan government needed to know rapidly whether saboteurs had caused the breach or, if it was due to other factors, whether steps needed to be

taken to safeguard other reservoirs. Various facts were subsequently reported by that magazine issued on 29th May 1986. After a prompt but nevertheless thoroughly researched investigation the conclusion was reached that sabotage had played no part in the Kantalai disaster. Rather, Dr. P. Back and D. Knight then concluded, piping of water and consequential collapse of the upstream end of a sluice in the bund's left bank seem certain to have been the cause of failure. Averaging out the information available, the point of failure was located at the edge of a temporary excavation made by the Royal Engineers many years before when installing the sluice.

The sluice was thought to have been built by cut and cover techniques leaving a sloping interface between ancient compacted fill which was built 1300 years ago and the Royal Engineer's backfill when construction finished. Also an unwisely sited pumphouse was built by a French company in 1982 or 1983 during which construction the excavation process caused considerable vibrations and seems to have played a part in the collapse.

Flash floods resulting from dam failures have often claimed heavy casualties and property damage. The losses in such events can be categorized in the following way:

a. Human lives and injuries.

b. Property losses.

c. Environmental damage.

d. Loss of function of the reservoir.

In all cases, the financial cost is large and difficult to quantify.

The possibility of such an occurrence has caused many countries to impose regulations requiring the determination of the wave parameters likely to follow the collapse of every large dam. Such calculations for new dams are routinely made as a part of the dam design project, in order to organize the defence of inhabitants and structures in the valley downstream. In the United Kingdom, for example, the risk of such an incident is reduced by regular government inspections under the Reservoir Safety Act of 1975. Furthermore, the growing concern for the safety of nuclear power plants, where liable to be inundated, has contributed to questions about the effects of dam failures.

The mechanisms giving rise to dam failure are the result of one or more of the following:

a. Hydraulic conditions (overtopping, seepage, piping, uplift).
b. Type of structure and construction (inadequate design, seepage through poor materials).
c. Geological conditions (landslide).
d. Environmental conditions (frost, ice, earthquake).
e. Deliberate action (wartime).

One of the earliest records of a dam breach is given in the Koran '.... so we sent upon them the flood of Irem'. The scene of this disaster was the Mareb Dam situated in the Yemen, 300 km north of Aden, S.W. Arabia. The dam was built about 1700 B.C. by the Kingdom of Saba, from huge blocks of dressed and fitted stones held together by small rods of lead. It is believed to have been breached about 100 A.D. The dam was 3.2 km long and had a height of 37 m [Babb and Mermel (1968) and Thomas (1976)].

One of the most catastrophic examples of failed dams was the St. Francis Dam, U.S.A., built in 1926; it was a curved gravity dam 60 m high which failed without warning on 12th March, 1928. Five hundred lives were lost and the damage to property was then estimated as being in the range of $(12.5-15) million. The concrete structure suddenly broke up; a single piece remained standing whilst the rest slumped to the valley floor and was swept downstream. Blocks of concrete weighing thousands of tons were carried more than a kilometre down the canyon. The reservoir of 46.9 million m^3 was practically full at the time. The average discharge during the flood was 11,327 $m^3.sec^{-1}$, and the maximum was between 16,990 and 22,654 $m^3.sec^{-1}$. The average velocity of the flood wave was 15.68 $km.hr^{-1}$, and the maximum was 28.80 $km.hr^{-1}$, with minimum velocity 9.44 $km.hr^{-1}$. The structure had been well built and the prime cause of failure was the foundation rock's weakening on saturation [Outland (1963), Toran (1973) and Thomas (1976)].

A 'superflood' wave following a sudden release of water may occur which is not necessarily from a ruptured dam. This happened at the Vaiont Dam in Italy; in October 1963, a rock mass of approximately 250 million m^3 bordering the reservoir, changed from creeping into a sudden slide with a velocity of 25 $m.sec^{-1}$. It apparently displaced 40 million m^3 of water, which was reported to have reached a maximum elevation of 100 m above the reservoir level and overtopped the dam causing the deaths of 1900 people and completely destroying four villages. The arch dam itself was practically undamaged [Toran (1973) and Thomas (1976)].

Even small dams cause disasters when they fail. A 7.62 m high earthfilled dam burst and discharged 60,000 m^3 of water into the town of East Lee in the U.S.A. Two persons were killed, several homes

were destroyed and a manufacturing plant was damaged at a cost of $8 million [Reynolds (1975)].

The following are the known instances of dam failure in Scotland (where this research has been carried out) and in Iraq (the author's country). In Scotland two dams have failed; in 1859 at Baxter on the Angus river, north of Dundee and at Skelmorlie in April 1925, where the dam was overtopped by 26,600 m^3 water from a quarry filled by choked culvert which suddenly released [Babb and Mermel (1968)]. Recently a crack was discovered in the Mullardoch Dam owned by the North of Scotland Hydroelectric Board, necessitating drainage of the reservoir. Six dams have failed in Iraq which are tabulated in Table 1.1 below, after Babb and Mermel (1968):

Table 1.1 : Known Instances of Dam Failure in Iraq

Dam Name	Location	Date of Construction	Type	Cause of Flood
Abu Habba	North of Baghdad	600 B.C.	Masonry	Flood
Atheim	At Atheim River, tributary to Tigris	2500 B.C.	Masonry	Flood
Atrush	At Atrush River, tributary to Tigris, North of Mossul	700 B.C.	Masonry	Flood
Diyala	North East of Baghdad	completed 500 B.C.	Masonry	Flood
Sennacherib	At Tigris River, North of Nineveh	800 B.C.	Stone	unknown
Shuster	At Tigris River	250 A.D.	Masonry	Piping

In an emergency situation, which occurs when a dam fails upstream from a populated area, there is no way to stop the destructive force. The alternative is to evacuate the people as quickly as possible, and wait for the energy to be dissipated through natural flow downstream. To assess this possibility, certain information is clearly needed before the disaster:

a. The arrival time of the wave-front in order to locate a refuge which may be reached within a limited time.

b. The propagation velocity and profile of the wave-front for estimating the impulsive force on the local structures.

c. Inundation area and the distribution of water depth, etc.

Calculations of such quantities may be made by using computer programs which simulate the dam break mechanism. A review of the achievements hitherto by this approach is given in the next chapter. From the literature survey it appears that there is no one type of model completely satisfying the solution requirements of the dam-break problem.

It may be that the predominant features of water motion in the reservoir and the downstream channel can be simulated by connecting together any two from three geometrically simple forms of channel, as may be locally appropriate. The three sections are defined as follows:

a. Plain or parallel sides (X-T)

b. Expanded or divergent sides (R-T)

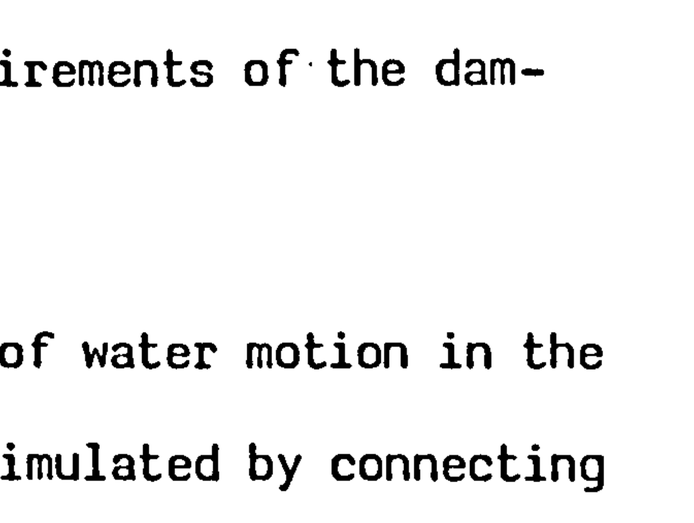

c. Contracted or convergent sides (R-T)

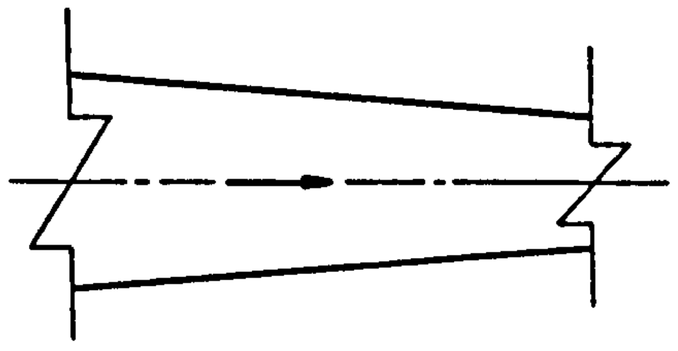

The present work describes three numerical models for rectangular section channels with a wet or dry bed downstream. These are the parallel, the expanded and the contracted models; two of these were then connected together to produce another three models, as follows:

a. Contracted - Plain (RT-XT)

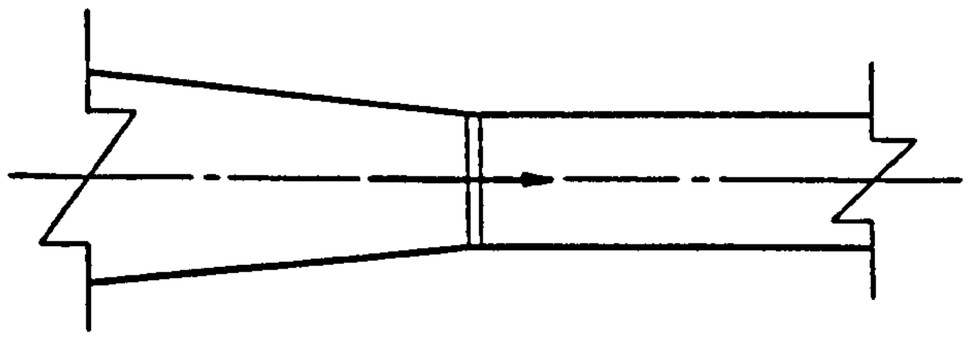

b. Contracted - Expanded (RT-RT)

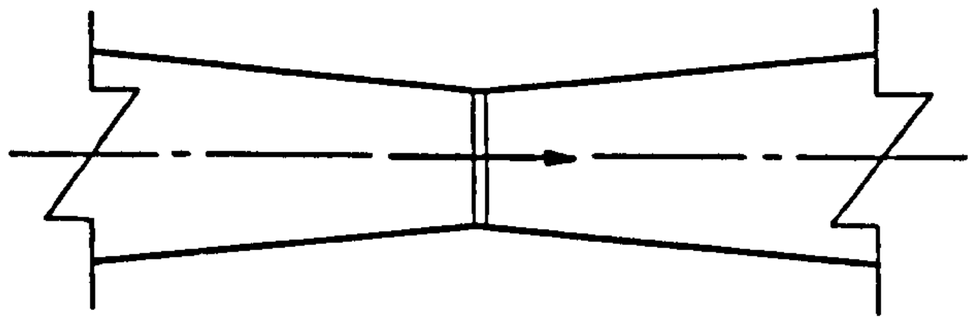

c. Plain-Expanded (XT-RT)

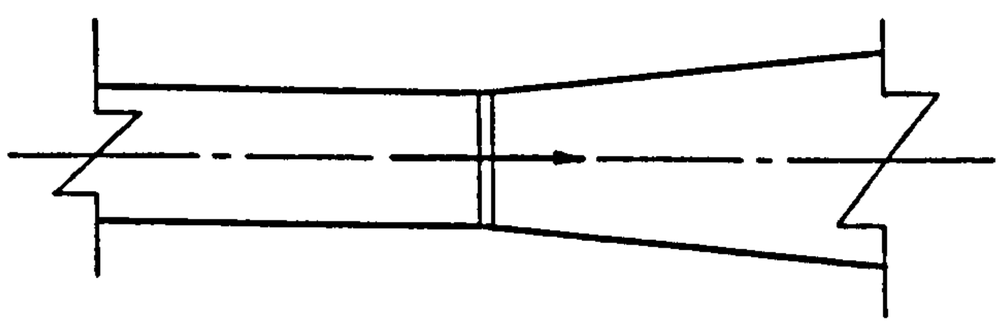

Four physical models were built, in the Hydraulics Laboratory at the University of Strathclyde, of the plain (X-T), the contracted-plain (RT-XT), the contracted-expanded (RT-RT), and the plain-expanded (XT-RT), all having a smooth, horizontal bed.

CHAPTER TWO

PREVIOUS SOLUTIONS FOR THE DAM-BREAK AND BORE WAVES

2.1 Introduction

It is the extreme rapidity of variation of water stages and velocities which makes simulation of unsteady flow due to dam failure a special case. When a dam collapses, the water retained behind it begins to move; the wall of water 'rotates' at the dam section, as shown in Figure 2.1. After the initial phase of acceleration, a negative wave is created upstream of the dam and propagates along the reservoir with a celerity depending upon the topography. The negative wave corresponds to the volume evacuated as a positive wave propagating downstream, advancing either on a dry bed, or in a water depth corresponding to the downstream flow before the failure. The downstream initial conditions are of decisive importance as to the character and behaviour of the positive wave. If the wave propagates on a dry bed, its front has very strong curvature near its tip as shown in Figure 2.1(a). The celerity of the front is then equal to the velocity of the water particles situated immediately behind it. If the wave propagates in some initial depth of water, its front is much more like a mobile hydraulic jump (bore) which may be most conveniently schematized as a sharp discontinuity with two different water stages at the same longitudinal point, as seen in Figure 2.1(b).

The dam-break flow can be schematised as four regions (see section 3.4.1); the horizontal motion, the negative wave, the

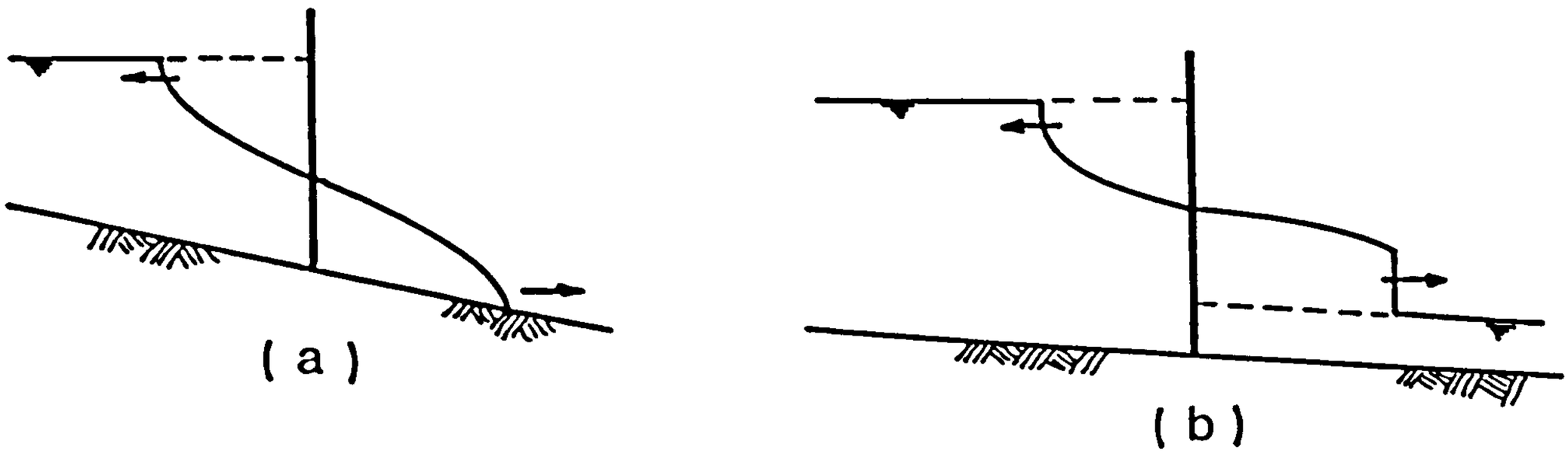

Figure 2.1 : Two Types of Dam Break Waves . (a) Propagation on a Dry Bed, (b) Propagation on an Initial Depth

gradually varied unsteady flow, and the positive wave. Generally the flow in the reservoir is subcritical, at least until the negative wave reaches the upstream limit of the reservoir. After that time, the motion depends upon the reservoir's topography (mainly the longitudinal slope) and upon the discharge entering it through the upstream section. As for the flow downstream, its character depends upon the topography of the valley and also upon the initial depth of water downstream of the dam. For a rectangular frictionless cross section, if the ratio of the initial downstream depth to the initial upstream (reservoir) depth is less than about 14% (the exact solution of the analytical case being 0.1384), the flow downstream of the dam after its failure will be supercritical [Stoker (1957)]. Otherwise it will be subcritical.

A considerable amount of effort has been spent in past years to obtain satisfactory solutions to the dam-break problem. There existed a number of hydrodynamic models ranging from very theoretical, which use the nonlinear shallow-water equations, to empirical models formulated only on the basis of the experimental results.

The practical importance of the dam-break problem is indicated by the fact that many engineers and mathematicians have obtained

approximate solutions to this problem since the first solution was offered by Ritter (1892) over 90 years ago. The Ritter solution was obtained for a reservoir of semi-infinite extent upon a horizontal bed with zero bed resistance. About 60 years later, Dressler (1952) and Whitham (1955) obtained approximate solutions that included resistance effects. In more recent years, the emphasis has shifted towards numerical solutions such as those given by Chen (1980), Chen and Armbruster (1980), Sakkas and Strelkoff (1973) and (1976) and Strelkoff, Schamber and Katopodes (1977). Most recently, however, Hunt (1982) and (1984) has shown how the kinematic-wave approximation can be used to obtain approximation for dam-break problem. In this chapter a survey of the previous work is presented.

2.2 Numerical Methods for Bores or Shock Waves

Waves approaching the shore steepen at the front, develop bores and run up the beach. The dam-break wave released into a wet channel develops a bore that changes in height and speed due to the bottom friction and the varying cross-sectional area. The dam-break wave released onto a dry channel behaves in a manner similar to the wave runup on the beach. Also it is the same for the shock waves in open channel, as is well known, shock waves are characterized by a steep front.

Conventional methods for determining the rate of propagation and depth of surge and shock fronts in open-channel flow are based on numerical integration techniques of the one-dimensional shallow-water equations, which allow either for discontinuous or a weak solution at the front [Terzidis and Strelkoff (1970)].

Stoker (1948), in his classic work on bores and breakers, proposed using the method of characteristics for predicting inception of a bore. Also within the framework of the frictionless, shallow-water theory the calculation of a non-steady open stream with a shock was performed by Keller, Levine and Witham (1960). The net method with Lax's (1954) explicit difference staggered scheme was used. In that case the shock was calculated by means of a special system of differential equations; the time and length intervals were related by the Courant-Friedrichs-Lewy condition within an iteration process.

Cunge (1970) devised an explicit diffusive scheme specifically for computing dam-break waves. A later implicit method, often referred to as the Preissmann implicit scheme [Cunge (1975)], uses a finite difference scheme with a weighting factor and has been applied successfully to the computation of shock waves. Numerical solutions of shock waves obtained either by using the explicit diffusive method or the implicit method are 'smeared' out or diffused over a certain length of the flow. This is in contrast to the clear-cut, sharp shock fronts (discontinuities) imposed by the Rankine-Hugoniot equations in the shock fitting method. The length of smear or diffusion as well as the numerical stability, or oscillation of computation, depends largely on the weighting coefficient introduced in the time derivative (for the explicit diffusive scheme) or in the space derivative (for the implicit scheme) to aid in the numerical solutions. Both explicit diffusive and implicit methods may collectively be called 'through' methods [Cunge, Holly, and Verwey (1980)]. The through methods and the shock fitting method are frequently used to simulate the front after dam-break. Non-dissipative schemes (such as the leap-frog method)

need artificial damping in the form of a pseudoviscosity term [Von Neumann and Richtmyer (1950)], and may thus be called Pseudoviscosity methods [Cunge, Holly, and Verwey (1980)].

Faure and Nahas (1961) employed Saint-Venant equations which are applied to portions where the flow can be regarded as slowly varying. The solution of Saint-Venant equations is obtained by means of deriving differential forms of the characteristic equations and integrating them by the finite-difference method. When using the method of characteristics, one should isolate the shock, and this is done with the aid of wave front equations.

The above-mentioned methods for numerical calculation of shock waves, i.e. the net method with the introduction of 'Pseudoviscosity' [Preissmann and Cunge (1961)], the method of characteristics with additional shock conditions [Faure and Nahas (1961a)],and the net method in accordance with the explicit staggered scheme with the isolation of the shock line [Keller, Levine, and Whitham (1960)] are all to some extent connected with application of numerical methods in gas dynamics [Gilmore, Plesset, and Crossley (1950), and Whitham (1958)].

Several successful attempts have been made towards the development of two-dimensional shallow-water-wave models. The method of bicharacteristics seems to be one of the most elegant and accurate solution techniques available for continuous flows [Katopodes (1984)].

In addition to the numerical models, there have been experimental studies [for example Haws (1954) and Sandover and Zienkiewicz (1957)].

2.3 Review of Dam-Break Wave Solutions

2.3.1 Analytical Solution

The simplest analytical solution is well-known as Ritter's solution [Ritter (1892)]. It was obtained by applying the shallow-water equations in the Euler form to a highly idealized dam-break surge in a horizontal, frictionless dry channel of infinite width. A function for the time-dependent position of the water surface was found which may be written in the following form:

$$H = \frac{1}{9g}\left(2\sqrt{gH_1} - \frac{x}{t}\right)^2 \qquad (2.1)$$

where H = the fluid depth, g = the acceleration due to gravity, H_1 = the initial fluid depth, x = the distance along the channel bed, and t = the time, as shown in Figure 2.2.

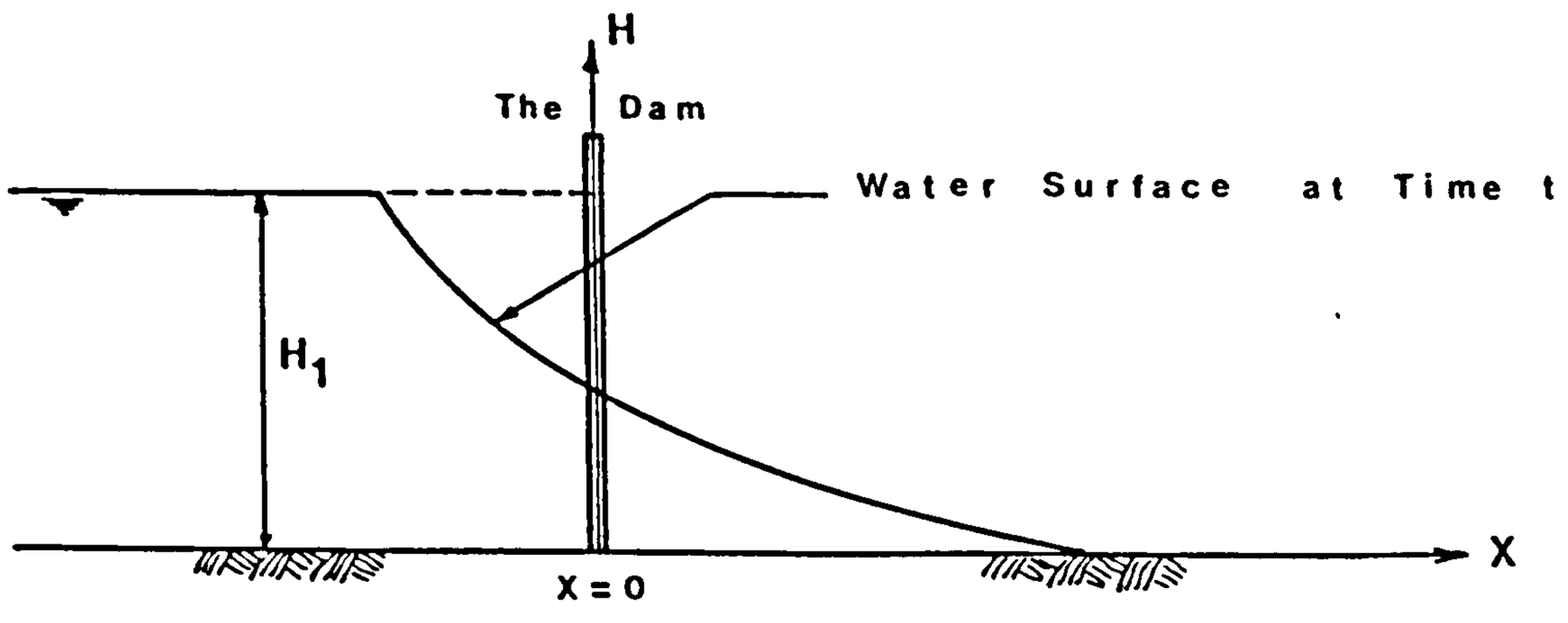

Figure 2.2 : Definition sketch for Ritter's solution

This parabolic water surface profile for given time (t) intersects the line (x=0) at the height $(4H_1/9)$, with a constant discharge rate $(8H_1\sqrt{gH_1}/27)$. From experimental investigations, it is known that Ritter's solution approaches the true positions of the water surface for time values $(t\sqrt{g/H_1} > 2)$ [Martin (1983)].

Unlike Ritter, Pohle (1952) used the Langrangian equations of hydrodynamics (instead of the Saint-Venant equations) to develop his model. The model can be used for a wide variety of problems of which the breaking of a dam is one.

Another investigator who solved the problem analytically was Dressler (1952). He added the Chezy resistance formula to the non-linear shallow-water equations to solve the dam-break with a dry but rough, horizontal bed downstream. Furthermore Whitham (1955) applied the Pohlhausen method (which is used in conventional boundary-layer problems) to a study of the effect of the resistance where the water surface meets the ground near the head of the wave. A retardation of the wave-front behind the position predicted by Ritter (1892) was found to occur.

Dressler (1958) also obtained an exact solution for the water wave in a sloping channel produced by the sudden release of a triangular wedge of water (the reservoir) initially at rest behind a vertical wall. The behaviour of the solution was exhibited for convenience in two level-line charts, and representative wave profiles and velocity distributions were presented.

Most recently an analytical solution was given by Hunt (1982) who used the kinematic wave approximation to obtain a simple, closed-form

solution for the catastrophic failure of a dam upon a dry, sloping channel. The results were compared with those from previous numerical solutions by Sakkas and Strelkoff (1976) and with experimental results. These comparisons suggested that the kinematic wave solution becomes asymptotically valid after the flood wave has advanced about four reservoir lengths downstream. The differences between theory and experiment were found to be well within experimental error, which might have been the result of surface tension, since the scale was small. Hunt's model demonstrated that valuable results can be obtained at sufficiently long distances downstream of the dam; evidently the kinematic-wave solution should be considered as an alternative method, under some circumstances, for simulating dam-break floods [Katopodes (1983)].

Hunt (1983) extended his model to obtain a solution for a sloping channel in which finite flow depths exist both upstream and downstream from the dam. The solution showed that increasing the initial water depths in the channel, both upstream from the reservoir and downstream from the dam, increases both the time and distance that are required for the resulting shock to approach any given depth downstream. Also it had been shown that the kinematic-wave solution becomes valid only after the shock travels a certain distance downstream and that increasing the initial water depth in the channel increases this distance. This seems intuitively obvious.

In another extension to his model, Hunt (1984a) obtained a closed-form solution for the more usual case when the reservoir, the dam breach and the downstream channel all have different widths. The reservoir outflow was calculated by using a quasi-steady-flow approximation; downstream flood depths were calculated by using the kinematic-wave

approximation. The maximum water depth in the reservoir was assumed to change slowly enough with time to allow the reservoir outflow to be treated as quasi-steady (distributed mass source). The kinematic-wave approximation downstream is equivalent to assuming that the free surface was nearly parallel to the channel bottom. A numerical example showed that maximum downstream flood depths decay relatively slowly because of storage contained within the upstream reservoir.

In order to enhance the validity of the kinematic-wave solutions, Hunt (1984b) used the method of matched asymptotic expansions to find a solution for the complete and instantaneous collapse of a dam in a prismatic and infinitely-long, sloping channel. In this solution, the formal outer solution was a kinematic-wave approximation whilst an inner solution, including a depth-gradient term in the momentum equation, was calculated for the region near the moving kinematic shock front. The reservoir was modelled as a point source of mass rather than the distributed mass source that was used earlier by Hunt (1982), (1983) and (1984a). This approach, like the earlier solutions, suggested that the solution becomes asymptotically valid after the wave front has advanced about four reservoir lengths downstream.

2.3.2 Graphical Solution

Earlier studies of the problem in France have been centered around various graphical techniques based on the method of characteristics for solving the Saint-Venant equations [for example Re (1946), Craya (1946), and Levin (1952)].

Faure and Nahas (1961) first programmed Craya's (1946) graphical solution procedures on the computer for the computation of shock waves,

whether resulting from powerhouse operations or from dam failures in either an initially dry or wet channel. Their method was also based on the Saint-Venant equations and the shock wave equations.

2.3.3 Solutions Depending on Characteristics Method Coupled with Moving Jump Equations

Stoker (1948) and (1957) used the method of characteristics and the theory of moving hydraulic jump to deal with the dam-break problem for a channel with constant depth downstream. He considered four different regions in the fluid at any time (t > 0), as shown in Figure 2.3:

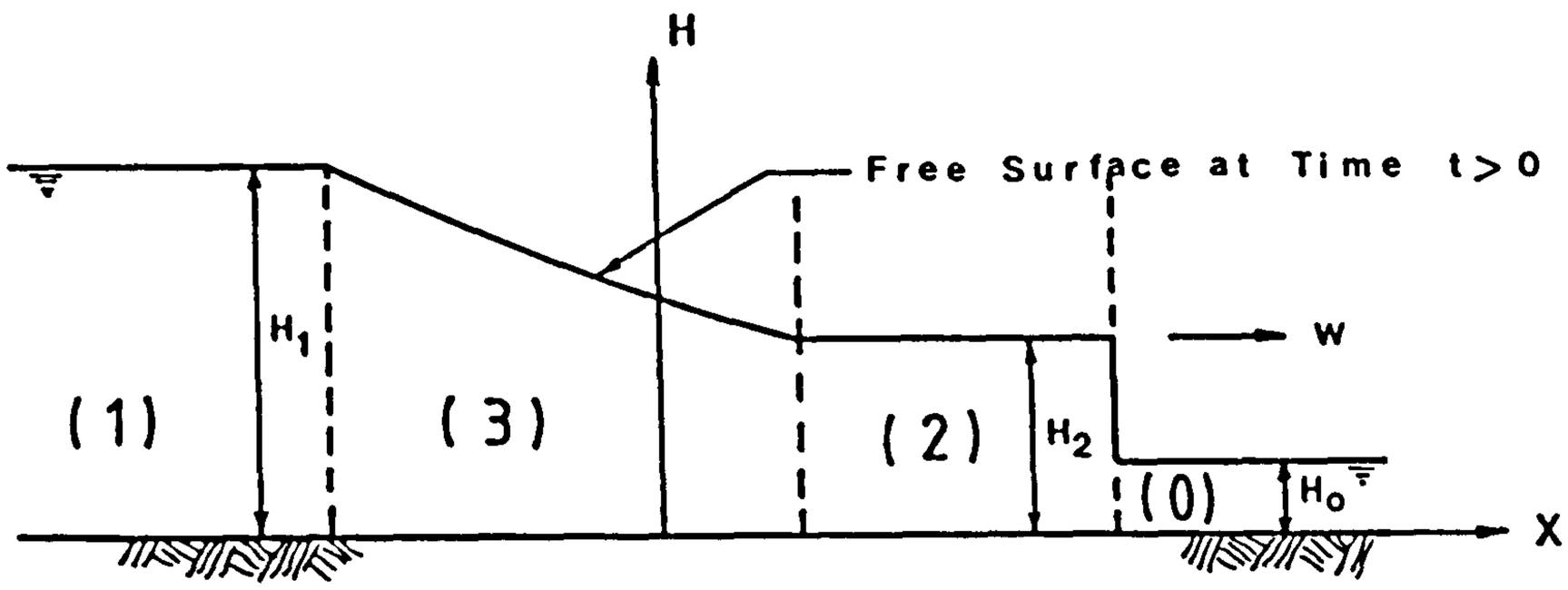

Figure 2.3 : Definition for the Four Zones - by Stoker

The zone (0) is the zone of quiet downstream which is terminated on the upstream side by the shock wave; the zone (2) is a zone of constant state in which the water, however, is not at rest; the zone (3) is a centered simple wave which connects the constant state (2) with the constant state (1) of the undisturbed water upstream. These zones were also utilised by Henderson (1966). If H_2 = the shock wave depth, w = the shock wave velocity, and H_o = the initial fluid depth

downstream, then using the conservation of mass and momentum in a moving hydraulic jump gives:

$$w = \frac{u_2H_2 - u_oH_o}{H_2-H_o} \tag{2.2}$$

$$w = u_o \pm \sqrt{\frac{gH_2}{2H_o}(H_2+H_o)} \tag{2.3}$$

By connecting the state (2) with the state (1) through the zone (3) along two curved characteristics from each, where the quantity u+2c is a constant:

$$u + 2c = 2c_1 = u_2 + 2c_2 \qquad \text{since } u_1=0 \tag{2.4}$$

where u = the fluid velocity and c = the celerity = $\sqrt{gH}$.

H_2 may be found for all values of the ratio H_o/H_1 between zero and one. Then a curve was fitted for $[(H_2-H_o)/H_1]$ versus (H_o/H_1). The curve rises very steeply to its maximum ($H_2-H_o = 0.32H_1$) for ($H_o/H_1 = 0.176$) and then falls to zero again when $H_o=H_1$, as shown in Figure 2.4.

Sakkas and Strelkoff (1973) used also the characteristic equations which they were derived from the Saint-Venant equations to solve the problem. Strelkoff (1969) and (1970) investigated the characteristics solution of Saint-Venant equations. The equations were transformed to dimensionless form.

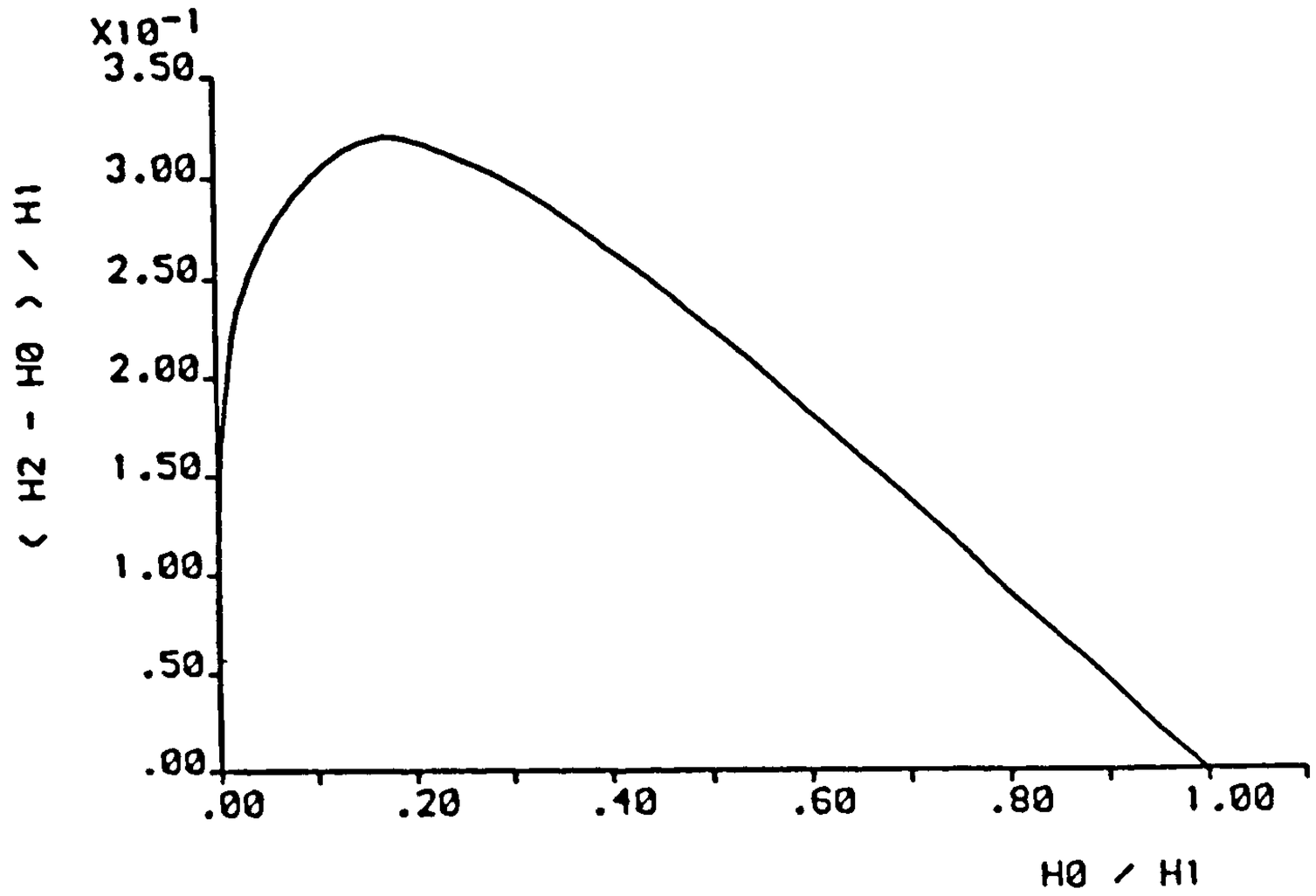

Figure 2.4 : The Height of the Shock Wave- by Stoker

Yevjevich (1975) used the shock fitting method as a numerical scheme for the solution of the Saint-Venant equations for computing rapidly varied flows resulting from sudden water release. In the method, the velocity and depth across the shock front were considered as discontinuities and were made to satisfy the shock conditions (the Rankine-Hugoniot equations). The waves upstream and downstream of the discontinuity were assumed to be gradually varying and were simulated by a solution of the Saint-Venant equations using the method of characteristics on specified time intervals.

Kordas and Witkowska (1976) presented a mathematical model of the dam break wave for a schematised natural valley having a nonprismatic, trapezoidal form of cross-section with different successive side

slopes, various roughness coefficients and bed slopes. The model was based on the numerical integration of the Saint-Venant equations and shock wave equations (moving hydraulic jump). The computations were performed by two explicit finite difference methods (Lax-Wendroff and leap-frog) [see for example Lax (1964), and Lax and Wendroff (1960) and (1964)].

Amein (1977) used the shallow water equations together with the jump conditions to solve both the dam break and the bore problem [Amein (1966b)]. The method of characteristics was applied to the dam-break wave both in a dry and in a wet channel. Using an explicit finite difference scheme, the characteristic differential equations were replaced by analogous finite difference algebraic equations. For irregular channels and cases where friction becomes important, it was thought necessary to use an implicit solution [Amein (1966a)]. The application of the method was illustrated by numerical examples restricted to infinitely wide horizontal channels.

2.3.4 Discontinuity at Time (t=0)

To initiate numerical solutions, prior specification of conditions of downstream flow are usually found to be essential. Water behind the dam is at rest before dam failure. The discontinuity in H at the dam position when (t=0) tends to inhibit smooth starting of the numerical solution. Therefore at the time of dam failure the steady state may be considered to be succeeded by a so-called simple wave in which neither bottom slope nor resistance plays a role. This intermediate state, if continuously connected to the general unsteady flow domain, thus constitutes an appropriate initial condition for the start of the computation. Subsequently the increasingly dominant resistance and

topographical terms cause the attenuation of any errors in the initial condition.

Initial conditions to be imposed prior to the numerical solution, at a small initial time, may be chosen from one of the following:

a. Ritter's (1892) solution for dry bed downstream.

b. Stoker's (1957) theory for wet bed downstream.

c. Dressler's (1952) perturbation solution modified by Su and Barnes (1970).

A generalized Ritter's solution for a prismatic channel of general parabolic cross section was obtained and used as the initial condition by Sakkas and Strelkoff (1973). Ritter's solution was also used by many others like Kordas and Witkowska (1976), Amein (1977), Katopodes and Strelkoff (1978) and Matsutomi (1983). For the case of an existing downstream water depth, Stoker's theory was used by Kordas and Witkowska (1976) for example. Das (1978) and Barr and Das (1980) used Dressler's (1952) perturbation solution modified by Su and Barnes (1970) to impose the initial conditions.

2.3.5 Shock Front Treatment and Negative Wave

The elementary theory of a moving hydraulic jump [Stoker (1957)] to deal with the discontinuity at the front cannot be used when the downstream channel is dry. Since the flow near the tip differs strongly from the flow in other regions, an alternative treatment is essential.

Dressler (1952) visualized the tip region to be moving somewhat like a separate entity pushed along by the water behind it, and within the tip, the velocity u to be changing (increasing) rather slowly

towards the front so that u_T could be taken as an approximation for the front velocity w, as shown in Figure 2.5:

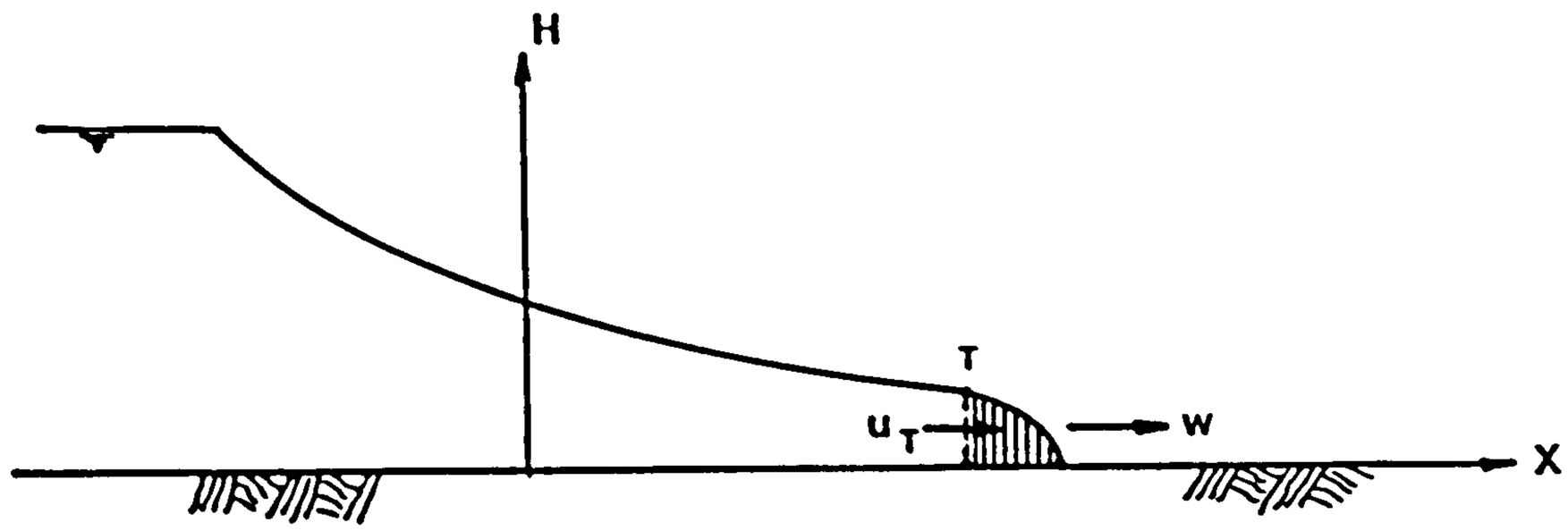

Figure 2.5 : Velocities in the wave tip-by Dressler (1952)

This theory was called 'Backwave' theory by Dressler (1954) since it uses results of resistive action in the full region behind the tip to give information for the entire wave without actually studying the tip region itself. In 1953 Whitham [according to Dressler (1954)] studied this tip and joined its solution to the solution given by Ritter (1892). The method required the solving of one highly non-linear ordinary differential equation to guarantee continuity at the unknown join position. This was called the 'Tip' theory, which was presented and used by Dressler (1954). Subsequently, Whitham (1955) applied the Pohlhausen method, as mentioned in section 2.3.1.

Montouri (1965) also assumed a small depth of water in the neighbourhood of the wave front moving along the dry bed. Utilizing the method of characteristics, he obtained a boundary condition at the

wave front simply by equating the velocity of propagation of the wave and the flow velocity at a section of some small depth near the wave front. Vasiliev (1970) and Katopodes and Strelkoff (1978) used Montouri's method to find the solution at the wave front with a dry bed downstream. The experimental corroboration of computed results was satisfactory.

Sachdev and Bhatnagar (1969) studied the progress of a bore, produced by the sudden break of a dam, when there is a flow of water over the downstream bed which also has a mild slope and offers resistance. They employed Whitham's (1958) method.

Su and Barnes (1970) extended Dressler's (1952) theoretical study to include the effects both of resistance and of channel cross-section on the waves following a sudden release. It was shown that the effect of channel cross-sectional shape and resistance was significant. The solutions for water surface profiles and velocity distributions, with and without resistance, for rectangular, parabolic and triangular shapes were presented. The retardation effect by the channel boundary roughnesses was apparent. Furthermore, the effect of variable cross-sectional geometry with a fixed resistance indicated that the narrowing of each cross-sectional shape increases the retarding effect on the positive wave front. Also Su (1970 and 1977) used the same technique and conditions with the additional effect of the bed slope. He obtained the trajectory of the positive wavefront from the mathematical model and compared the theoretical results with experimental data extracted from the literature. He found that the effect of channel slope becomes more significant in the region of the negative wave, as time and distance from the origin increases.

Furthermore, the experimental results demonstrated that the effect of channel resistance on the negative wavefront is insignificant. The trajectory of the positive wavefront, computed from the mathematical model, was in good agreement with the experimental data. As expected, for the case without resistance, the flow was subcritical upstream of the origin (the dam site), supercritical downstream, and critical at the origin. However, for the case with resistance, the critical section which separates the subcritical and supercritical no longer remained at the origin but moved downstream with respect to time. Finally a summary of the relative significance of the channel parameters was given and is reproduced in Table 2.1.

Table 2.1 - Relative Significance of Channel Parameters - after Su (1977)

	Negative wave		Positive wave	
	Front	Body	Body	Front
	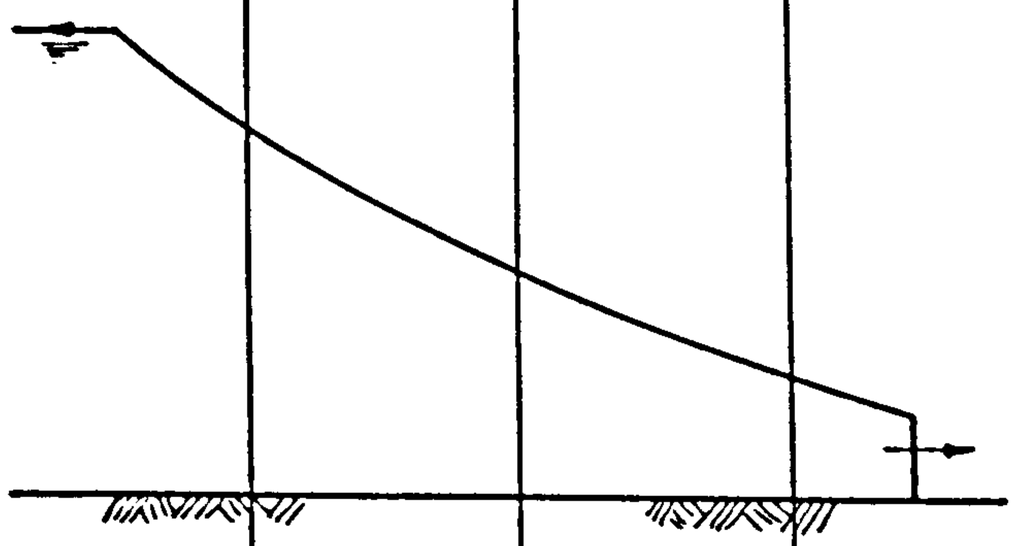			
Channel Boundary Resistance	3	2	2	1
Channel Cross-Sectional Geometry	3	2	2	1
Channel Slope	1	3	3	2

Symbols of Relative Significance:

1. Most Significant, 2. Less Significant, 3. Least Significant

Sakkas and Strelkoff (1973) used a simplified form of the equation of motion, derived from consideration of the physical situation existing in the tip region, after Whitham (1955). The computed results were compared with theoretical and experimental results obtained by Dressler (1952) and (1954). The agreement with experimental results was generally good. Kordas and Witkowska (1976) also used the Whitham (1955) method in the case of a dry bed in the front region. Das (1978) and Barr and Das (1980) used the method of Sakkas and Strelkoff (1973).

Marshall and Menendez (1981) solved the non-conservation forms of the equations of shallow water theory by an extension of the Random Choice Method (RCM). The non-conservation Riemann problem was analysed in terms of two non-linearly interacting waves and was solved by means of a numerical integration along characteristic curves. The advantages of the method are, firstly, that there is no need for a separate treatment of discontinuities and, secondly, that one can use a fixed rectangular mesh. The method automatically accounts for the spontaneous formation of shocks without introducing numerical diffusion and dispersion. Numerical solutions for the dam-failure problem in cartesian (x-t) were presented. The results were compared with the numerical results obtained by Sakkas and Strelkoff (1973) and Re (1946). These comparisons were shown to be satisfactory.

Kosorin (1983) observed that since the flow in both of the dam break singularities (the initial phase of the wave and the flow structure at the front) did not suit the assumptions of the shallow

water theory, it was necessary to treat those items outside the framework of this theory. He therefore used the 'theory of boundaries' which permits certain N-dimensional hydrodynamic problems to be transformed into (N-1) dimensions. This allowed him to obtain both a new relation for the wave front speed (which differed from Ritter's solution) and also a relation between the height and the velocity of the wave front. According to these ideal flow calculations, the vertical components of celerity and acceleration in the free surface, during the initial moments of sudden and total failure, attain substantial values (depending on the dam height). However, because of the presence in reality of damping in time and space, the shallow water equations were deemed still to be generally suitable for the wave as a whole.

Hunt (1984b) eliminated the discontinuity which appeared in his outer kinematic-wave solution by decreasing peak depths behind the shock and by placing a rounded nose in front of the kinematic shock. Mass was conserved during this process by making the volume of water contained between the new shock nose and the kinematic shock equal to the volume lost behind the kinematic shock when the kinematic-wave solution was replaced with the inner solution.

A simple treatment to circumvent the singularity problem at the front wave in the case of dry bed consists of assuming a fictitious base flow downstream. Chen (1980) assumed such a fictitious depth (very small) downstream in the case of dry bed. In general, agreement between the computed and the measured results was close. Katopodes and Schamber (1981) discussed Chen's (1980) work especially with reference to the fictitious flow and the negative wave profile approaching the horizontal tangentially.

In the subsequent discussion closure, Chen (1982) explained the validity and generality of the fictitious initial flow and also showed that computed results with the negative wave taken into account did not differ very much from those without it. Therefore, for simplicity and less time-consuming computation, the negative wave was not taken into account. Marshall and Menendez (1981) also assumed a fictitious depth since the Random Choice Method (RCM) cannot deal with a dry bed downstream.

Sakkas and Strelkoff (1976) extended the solution for the even more general problem of when the negative wave-front arrives at the upstream end of the reservoir. There, the depth of flow reduces to zero at the upper end of the moving water body. Because of poorly defined intersections of the characteristics at the very low depths near the trailing edge, the usual method of integration does not work well. Instead, the simple assumption was made that a fictitious stream enters the flow field at the upstream computational boundary, a little short of the end of the reservoir. The fictitious inflow amounted to less than 5% of the discharge at the flood crest. Comparison with experimental data was considered to be adequate.

2.3.6 Two-Dimensional Models

Abbott (1974 and 1979) provided a numerical analysis of flows with continuous and discontinuous parts, leading to numerical procedures for efficient simulation of these flows. One of these flows was the failure of a dam. He clarified both the one-dimensional and the two-dimensional flows then occurring, also with structures downstream intercepting the two-diemnsional flow.

Katopodes and Strelkoff (1978) and (1979), they also used a

mathematical model of the two-dimensional dambreak flood wave, based on the method of characteristics, to solve the problem involving three independent variables. The selection of the method was based on the fact that the curvilinear wave boundaries and irregular geometry associated with the dambreak problem in two space dimensions are poorly modelled by direct finite difference methods. In addition, the propagation of the wave boundaries, the transition from subcritical to supercritical flow inside the flow domain, and the finite speed of propagation of information had been found to lead to considerable difficulties when the finite element method was employed. Initial conditions were constructed at a small initial time out of the one-dimensional Ritter solution (as mentioned in section 2.3.4). The negative wave upstream was assumed one dimensional across the width of the breach. In quarter circles of plan area centered on each edge of the breach, the same profile was ascribed onto vertical planes radiating out from the breach edge. The short jet downstream was taken to be unidirectional and perpendicular to the dam axis. Its profile followed the Ritter solution except at the very tip where a short'nose'of uniform velocity was placed to account for the initial effects of bottom resistance. The mathematical model was tested for its effectiveness and stability. The qualitative similarity with a laboratory scale model was evident, although some disagreement was ascribed to the assumption of hydrostatic pressure distribution everywhere. Also, the computational cost was relatively high compared to those of one-dimensional models.

Katopodes (1977 and 1980) studied the wave emerging from a breached dam using both computational and experimental data. The

location of the wave front was determined by means of high speed photography in the laboratory, and the results were compared to the solution from a two dimensional mathematical model. The extent of the divergent flow downstream of the dam was determined and the two-dimensional computation was allowed to degenerate to a one-dimensional unsteady flow model. This was then used for the computation of the remaining part of the wave. The model, consisting of a two-dimensional part near the breach and the one-dimensional part used for the remainder of the wave, was found to produce satisfactory results with reasonably low cost and good resolution. Comparisons of the results obtained by the mathematical and physical models indicated the following: The depth of flow at the breach and the central area of the channel agreed quite well. The same was true within the angle of expansion. The height of the side wave was in error, but the discrepancy there was not in agreement with the theoretical prediction. For some runs the computed values were higher and for others lower than observed. The highly turbulent nature of the wave and the fluctuation of its peak were thought to have caused some lack of precision in the laboratory measurements.

Jovanovic and Radojkovic (1982) also developed a two-dimensional model for simulation of the unsteady flow caused by dam failure. The model was based on an explicit finite difference scheme with a dissipative weighting factor being used as an artificial damping term. The verification of the model was carried out using a small-scale laboratory model following which the numerical model was applied to a real-life situation. Computed results were compared with the experimental ones and also with the method of characteristics. It was found that finite difference results were only somewhat inferior in comparison to those from the method of characteristics.

Matsutomi (1983) also developed an explicit finite difference model of two-dimensional, rapidly-varied flow on a dry bed. Dam-break flows in one-dimensional channel were computed and the results were compared favourably with experimental results.

2.3.7 Experimental Investigations

The first reported experiments with waves produced by sudden water releases were those conducted by Schoklitsch (1917) [according to Yevjevich (1975)]. His results agreed with Ritter's solution for the negative wave. For the positive wave, his experimental data indicated a 40% slower velocity than did Ritter's theoretical velocity. Later experiments made by Egiazarov (1935) showed that:

a. The velocity with which a wave propagates over a dry channel was about 70% smaller than the theoretical velocity given by Ritter.

b. Roughness of the channel significantly influenced the propagation velocity of the positive wave front; the greater the roughness, the larger was the wave height, and consequently, the smaller the propagation velocity.

c. The front of a positive wave tended to steepen, and could be assumed to be approximately vertical.

Martin and Moyce (1952) used a very thin waxed paper diaphram, held in position in a horizontal flume, of 5 inches height (127mm) and 2.25 inches width (57.15mm), to simulate the sudden-release device. The major emphasis was on the phenomena related to the collapse of liquid column on to a rigid horizontal plane, rather than to the effects of other physical factors such as the channel roughness,

geometry and bed slope on the wave propagation.

To check his theoretical solutions, Dressler (1954) made experiments in a horizontal rectangular flume 65m long and 0.225m wide. An uplift gate with spring system was used to simulate the instantaneous release. Three different channel bottoms ranging from smooth to very rough were used. The experimental results deviated in a consistent way from the theoretical results, indicating more generally that the Chezy resistance function, normally used for steady flows, may be inadequate to describe either the highly unsteady flow or the nature of turbulent resistance in a tip region. Thus instead of using the Chezy or Manning formulae for resistance assessments, Das (1978) and Barr and Das (1980) used the Colebrook-White (C-W) turbulent transition function. Their experimental data was obtained from two horizontal rectangular flumes, the larger having a smooth painted bed and the smaller with both smooth and rough beds. There was good agreement between the numerical solution and the experimental data.

The U.S. Corps of Engineers (1960) conducted experiments in a sloped (0.005), rectangular flume 400 feet (121.92m) in length and 4 feet (1.2192m) in width with the dam located midway along its length. The dam was lifted upward by a pulley-weight system. Various test conditions, each representing a different breach pattern, were simulated with and without a base flow. The base flow was accomplished by water passing through a partial opening in the model dam. Experimental results showed that :

a. The propagation celerity of the negative wave front was independent of channel roughness.

b. The propagation celerity of the positive wave front varied inversely with the flume roughness expressed by Manning's coefficient.

Faure and Nahas (1961) conducted experiments for the propagation of a positive wave front both in a dry and wet channel. The time trajectory of the positive wavefront was in good agreement with the theoretical solutions, computed by the Whitham's method (1955).

That the wave patterns in dry and wet channels are substantially different was verified by Nakagawa et al.(1969) in experiments at Kyoto University, Japan. They showed four kinds of wave patterns, distinguished by different values of (H_o/H_1):

a. $H_o/H_1 = 0$ (the case of dry bed),a parabolic wave with rounded front.

b. $0 < H_o/H_1 < 0.4$, a uniformly progressive wave with a breaking front (moving hydraulic jump).

c. $0.4 < H_o/H_1 < 0.56$, unstable undular bore with a front partly broken.

d. $0.56 < H_o/H_1 < 1.0$, stable undular bore.

Memos et al.(1983) presented experimental results from a two-dimensional model where the breach, the reservoir and the channel each had different but finite widths.

2.3.8 Applications to Real Problems

Escande et al.(1961) obtained experimental results from a 1:300 scale model of the Truyere Valley below the Sarrans Dam in France. Different roughnesses were used, and the experimental results for

the height and velocity of the wave, indicated that the propagation celerity of positive wave was a function of the initial water depth behind the dam, the initial base flow and the river bed roughness.

Balloffet et al. (1974) studied the hypothetical collapse of the temporary works for the Bou Regreg dam (in Morocco). The dam was located so as to regulate flows in two rivers. Important precautions were thus called for in the design of the river diversion system during construction. Data was required for a flood warning and evacuation plan following collapse of the upstream cofferdam. Two sets of studies were made; an 'engineering' study in which a gradual collapse mechanism was simulated and the 'theoretical' case of the instantaneous removal of the cofferdam. The mathematical model techniques involved the finite difference solution of the one-dimensional equations. The results obtained appeared to be adequate, both for design purposes and so as to prepare an emergency plan for the anticipated failure (which, fortunately, did not occur).

Xanthopoulos and Koutitas (1976) investigated the propagation of a flood wave due to dam failure both on one and two dimensional dry plains by mathematical model. The velocity components, the water depth and the position of the water front for each time step were computed through an explicit finite difference scheme in Eulerian space. A series of numerical experiments validated the model for the case of unidirectional flow following its comparison with laboratory experiments. The model was then applied to the inundation of a plain in Northern Greece which might result from the failure of an existing earth dam. The forcing function consisted of a specified form of discharge hydrograph at a plain boundary point. The model exhibited

satisfactory descriptive properties for small water heights and velocities and negligible inertia terms.

The computed flood wave resulting from a hypothetical failure of MacKay Dam, which is located on the Big Lost River in south-central Idaho, U.S.A., was used to show the validity and the applicability of the coupling technique developed by Chen and Druffel (1977) (see section 2.3.9) . Chen (1980) later improved the explicit version of the characteristics method employed. Not only was the model applied to failure (full and partial) of the MacKay Dam but also, laboratory data on dam-break flood waves were used in the verification of the model. This data was collected in 1960-1961 at the United States Army Engineer Waterways Experiments Station, as mentioned in section 2.3.7. Chen and Armbruster (1980) further improved the same one-dimensional model. The flood wave resulting from the failure of Laurel Run Reservoir Dam (southwest Pennsylvania, U.S.A.) was first reconstructed by using the model and then compared with data from field surveys. The major improvement consisted of a large reduction in the inaccuracies and oscillations of computed flows at a rapid contraction or expansion, such as may occur at a partial dam breach. The model was deemed to be particularly suitable for routing in a nonprismatic channel because of the close agreement between observed and computed peak stages.

Matsutomi (1983) applied his model to the flood occurring after the Zenkoji Earthquake in 1847. This was thought to have been the biggest disaster, caused by landslide failure of an embankment, in Japan. The results indicated the same flow pattern as the old records.

2.3.9 Comparison Between Different Models

Vasiliev (1970), with others in the Institute of Hydrodynamics (Novosibirsk, USSR) applied three different numerical methods to solve the equations of unsteady, one-dimensional flow in an open channel. The methods were the use of characteristics, the 'continuous calculation', and the 'isolation of discontinuities' methods. They considered that the use of characteristics was not convenient for programming, while the continuous calculation, which was relatively simple to program, caused smoothing of the discontinuities. The third method allowed for the isolation of significant discontinuities, whilst on the other hand smoothing the insignificant ones.

Chen and Druffel (1977) investigated two numerical techniques for computing dam-break flood waves in nonprismatic channels, with or without a base flow. One technique was to formulate an explicit scheme based on the characteristics method with specified time intervals and use the Rankine-Hugoniot shock equations for the solution of the shock wave. The other technique was to formulate a linearized implicit finite-difference scheme for the solution of the Saint-Venant equations and compute a shock wave without resorting to the shock equations. The former technique gave a clear-cut, sharp shock front (or discontinuity), while the latter technique spread the wave-front over a certain length of the flow. Several dam-breaking problems under different hypothetical base-flow conditions and channel geometries were investigated using both techniques. The comparison indicated that a technique using the method of characteristics scheme works better soon after the dam break, and the other technique works better at later times. For attaining the best resolution of a practical

problem, both techniques were linked.

Katopodes and Schamber (1983) compared five dam-break flood wave models. These consisted of:

A. Saint-Venant Models

   a. Inverse Characteristic Scheme

   b. Predictor-Corrector, Finite-Difference Scheme

B. Approximate Routing Models

   a. Zero-Inertia Implicit Scheme

   b. Kinematic-Wave Characteristic Model

   c. Kinematic-Shock-Profile Model.

These models were compared with the experimental results obtained by the Waterways Experiment Station (U.S.A.). They were used in dimensionless form to establish general criteria for their applicability, in prismatic channels of rectangular cross section, to total failure on a dry bed. Saint-Venant models are able to compute surges advancing on a dry bed. They can also compute the propagation of a hydraulic bore on an existing stream. The models can also handle a number of other internal or external boundary conditions, such as partial breaches, recession, free overfall at critical conditions, and internal hydraulic jumps. By contrast, the approximate models are constructed with the aim of achieving relatively simple and inexpensive predictions of the flood waves. In approximate models, the absence of the inertia terms precludes computing flow conditions either in the negative wave region or at the failed structure itself, unless the discharge hydrograph at the breach is known a priori. The results of computational experiments

with the five models, indicated the following; for a prismatic channel, the characteristic and integrated finite-difference models gave results of similar accuracy and expense; the characteristic model was far more sensitive and aborted rather earlier in the presence of difficulties (It was, however, the easier of the two to interpret as regards identifying and eliminating sources of trouble); the zero-inertia model presented both a relatively inexpensive and a versatile model; the kinematic-wave model was both inexpensive and 'tolerant'; the kinematic-shock profile model yielded results almost identical to that of zero inertia; finally the combined kinematic-wave and shock-profile model seemed to be an attractive means for inexpensive dam-break flood prediction.

2.3.10 Partial Failure

Examination of the literature on historical failures indicates that concrete arch and gravity dams breach by the sudden collapse, overturning or sliding away of the structure due to overstresses. Correspondingly, the predominant mechanism for breaching of earthfill dams is the erosion of the embankment material by the flow of water either over or through the dam. In this type of dam failure, the breach size grows continuously as material is removed by outflows. Thus the size, shape, and time required for development of the breach are dependent on the erodability of the embankment material and the characteristics of the flow forming the breach. Breaches of this type can occur fairly rapidly or can take several hours to develop. Also, the size of the breach is often significantly less than the entire dam. Other than the brief review following,the studies presented in this thesis do not deal with this type of breaching mechanism.

A conceptual method for reproducing flood wave peaks due to overtopping failures of small homogeneous earthfill dams had been introduced by Fread and Harbaugh (1973). A mathematical model based on a numerical solution of the St. Venant unsteady flow equations was developed for predicting the transient reservoir flow produced by the gradual breach of an earthfill dam.

Rajar (1978) analysed total, partial, and gradual collapse of dams in prismatic and nonprismatic channels with wet and dry bed downstream. Two numerical methods were used, namely the diffusive scheme and the Lax-Wendroff scheme. Also a physical model was made of a dam in the form of a vertical plate, which was lifted in approximately 0.1 second to simulate total and instantaneous collapse. To simulate partial (instantaneous) collapse, a vertical plate was ejected downward through a slot in the bottom so that a part of the plate remained in the flow; to simulate a gradual collapse, the plate was moved down with a constant speed, the duration of collapse being from 0.1 to 10 seconds.

One limitation on the use of the numerical models for partial dam failures is the accuracy of the input data for the geometric and temporal characteristics of the dam breach. Data on a number of historical dam failures were collected by MacDonald and Langridge-Monopolis (1984). Both earthfill dams, in which breaches are formed by erosion of the embankment material, and non-earthfill dams, that may have failed partly due to erosion and partly due to sudden collapse caused by instabilities, were studied. These data were analyzed to develop relationships which would form the basis of a methodology for estimating the geometric and temporal characteristics of breaches.

Schamber and Katopodes (1984) compared three one-dimensional models, for partially breached dams, based on a characteristic model and on a difference scheme of the predictor-corrector type. The breach section was treated as an internal boundary condition which interrupted the continuous long wave occurring upstream and downstream of the dam. At the breach section, the basic equations of mass, momentum, and energy conservation were formulated in terms of depths and velocities occurring immediately upstream and downstream of the dam. These equations were then coupled with the long time solution of the unsteady flow equation via appropriate characteristic relations emanating from the breach.

2.3.11 Radial Flow

The radial flow condition is remarked as the simplest example of two-dimensional wave propagation [Abbott (1966)]. In practice the flow through an expanding or contracting channel section could be analysed as a radial flow. A few investigators of dam break have since used the radial flow theory whilst Abbott (1968) and Abbott and Lindeyer (1969) employed it elsewhere.

Marshall and Menendez (1981) used the Random Choice Method (RCM) to calculate the dam break wave through a contracting channel section in cylindrical coordinates (radial flow, R-T space).

Martin (1983) developed theoretical solutions on the basis of the shallow water theory for the dewatering flows caused by the sudden collapse of a dam in a horizontal rectangular channel (Plane dewatering) and in channels with divergent side walls (Radial dewatering). For the plane dewatering flows, the initial conditions were derived from

earlier work by Pohle (1952). For the radial case the boundary conditions were determined at the dam location with the initial conditions being derived from experimental investigations. The numerical results were compared with experimental investigations for models having both different radii and angles.

It was concluded that at a time [$t = (\sqrt{g/H_1})^{-1}$] the discharge per unit length of the dam ($q = 8\ H_1\ \sqrt{gH_1}/27$) is achieved, for all reservoir shapes, whilst for [$t > (\sqrt{g/H_1})^{-1}$] boundary conditions apply so long as no reflected waves from the reservoir boundary arrive at the location of the dam. The influences of friction and storage in the downstream regions were ignored.

To this Author's knowledge no other work has been carried out, using a radial application of the method of characteristics, for the various combinations of parallel, converging and diverging boundaries - both upstream and downstream of a dam break.

2.4 Conclusion

Franz (1977) discussed the various important points which must be taken into consideration to develop the ideal analysis method for dam break waves. His expectations were:

a. The procedure should be able to simulate both continuous and discontinuous flow without restriction as to the state of the flow (subcritical or supercritical). Dry bed conditions should also be simulated.

b. The procedure should be able to establish meaningful initial conditions once the flowrates at the initial time have been given. Comprehensive error detection and reporting were considered to be essential.

c. The procedure should be sufficiently robust that flow situations never tested should have a high probability of being successfully simulated. Moreover, the cost of performing an analysis should increase in a nearly linear fashion with the complexity of the system.

These are high expectations and no method seems, so far, to have come close to meeting them. Various models must continue to be developed with the above objectives if dam-break, flood-wave analysis is to become an established part of the set of tools used by civil engineers. It was with this in mind that the work which follows was carried out.

CHAPTER THREE
BASIC THEORY AND NUMERICAL INTEGRATION

3.1 Shallow Water Waves

Any change of discharge in an open channel causes a wave to be propagated from the point where the change is started. The wave is often said to be 'translatory' implying that all particles of water in any cross-section move together and may be assumed to remain in one plane. Open channel waves may also be classified depending on whether the vertical component of the acceleration of particles of water is negligible or not.

Both these general circumstances are contained by 'shallow water' theory, in which the mean vertical displacements experienced by the fluid particles are sufficiently small, compared with their mean horizontal displacements, for wave speeds to be depth dependent.

The dam-break flood wave is usually regarded as belonging to the shallow water class whose equations are the basic hydrodynamic equations of motion under the assumption of hydrostatic pressure distribution.

Liggett (1975) has shown that the hydrostatic assumption is indeed justified for problems characterized by scales which are much larger in the horizontal than in the vertical. Even if the vertical displacement is significant, still the flow can be well-characterized as 'shallow' as long as the vertical acceleration has a negligible effect on pressure distribution. This requires that surface curvature is small in the Boussinesq sense - as discussed by Abbott, Petersen and Skovgaard (1978).

The bore is a discontinuity in the fluid motion at the front of the dam-break and the bore motion is described by the integral momentum equation. When the jump conditions at the bore are coupled to the equations of the shallow water theory, a procedure for evaluating the entire motion is established (see Figure 3.8).

In order to present the problem completely, this chapter includes (a) derivations of the shallow water equations for one-diemnsional flow in (X-T) and (R-T) space; (b) application of the method of characteristics to these equations; (c) the discontinuous solution for the front and the resulting stability criteria for the overall solution.

3.2 Shallow Water Equations

3.2.1 Equations in X-T Space

There are a number of methods to derive the shallow water equations. Each has its advantages in that it displays some of the assumptions and approximations that go into the equations. Probably the most elegant of the derivations begins with the Navier-Stokes equations of hydrodynamics. However, the derivation provided in the following presentation is chosen for its simplicity.

The following derivation is for the (X-T) one-dimensional equations in which the dependent variables are the depth-mean velocity u, and total water depth H, and the independent variables are longitudinal distance x and time t.

The continuity equation represents conservation of mass for a control volume and requires that 'The net rate of flow into the volume = rate of storage change in the volume'.

The control volume Figure 3.1 is one unit wide in the horizontal direction normal to flow and, the position x is at the mid-point. The volume is of finite height, H, but the dimension in the x-direction, Δx, will be taken to zero. Thus the mass balance is

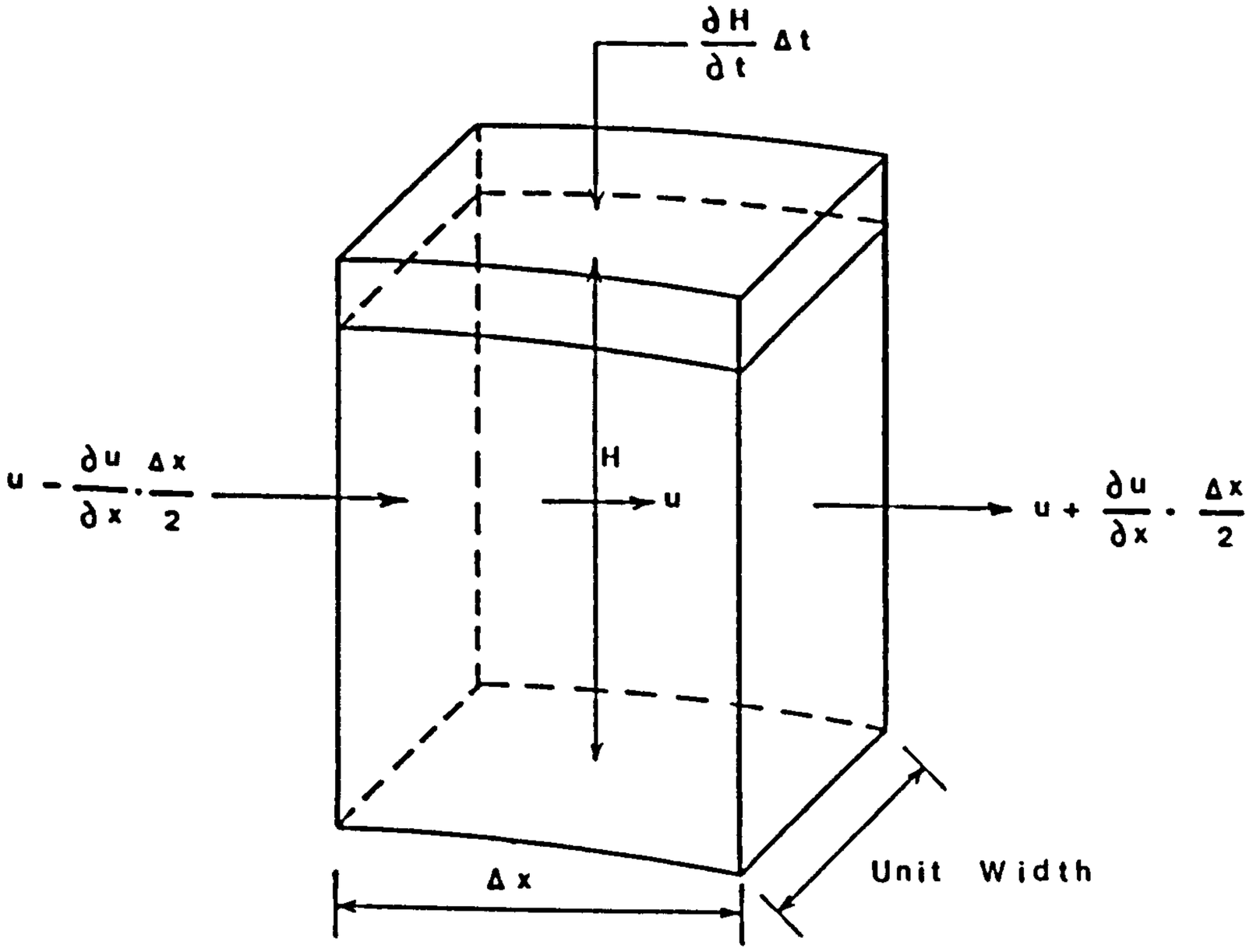

Figure 3.1 : Element employed in deriving the partial differential equations of shallow water wave motion in a homogeneous fluid in (X-T) space.

Inflow (Quantity entering the element) = $(u - \frac{\partial u}{\partial x} \cdot \frac{\Delta x}{2})(H - \frac{\partial H}{\partial x} \cdot \frac{\Delta x}{2})$

Outflow (Quantity leaving the element) = $(u + \frac{\partial u}{\partial x} \cdot \frac{\Delta x}{2})(H + \frac{\partial H}{\partial x} \cdot \frac{\Delta x}{2})$

Change of storage = $\frac{\partial H}{\partial t} \cdot \Delta x$

so,

$$(u - \frac{\partial u}{\partial x} \cdot \frac{\Delta x}{2})(H - \frac{\partial H}{\partial x} \cdot \frac{\Delta x}{2}) - (u + \frac{\partial u}{\partial x} \cdot \frac{\Delta x}{2})(H + \frac{\partial H}{\partial x} \cdot \frac{\Delta x}{2}) = \frac{\partial H}{\partial t} \cdot \Delta x \qquad (3.1)$$

After multiplying out the factors and taking Δx to zero, the continuity equation is:

$$\frac{\partial H}{\partial t} + \frac{\partial}{\partial x}(uH) = 0 \qquad (3.2)$$

The momentum equation requires conservation of momentum so that 'The net rate of momentum entering the element + the sum of the forces acting on the element = the rate of accumulation of momentum'. The rate of flow of momentum in a fluid is the product of the mass rate of flow and velocity.

$$\text{Momentum entering} = \rho \{u(uH) - \frac{\partial}{\partial x}[u(uH)] \cdot \frac{\Delta x}{2}\}$$

$$\text{Momentum leaving} = \rho \{u(uH) + \frac{\partial}{\partial x}[u(uH)] \cdot \frac{\Delta x}{2}\}$$

Three types of forces will be considered; gravity, pressure and frictional resistance.

The force due to gravity $F_g = \rho g H S_o \Delta x$

where ρ = fluid density, S_o = the channel slope along x-direction.

The pressure force $F_p = \frac{1}{2} \rho g [(H - \frac{\partial H}{\partial x} \cdot \frac{\Delta x}{2})^2 - (H + \frac{\partial H}{\partial x} \cdot \frac{\Delta x}{2})^2]$

The frictional resistance $F_s = \rho g H S_f \Delta x$

where S_f = the friction slope. Combining these elements into a single equation for conservation of momentum gives:

$$\rho[u^2 H - \frac{\partial}{\partial x}(u^2H).\frac{\Delta x}{2}] - \rho[u^2H + \frac{\partial}{\partial x}(u^2H).\frac{\Delta x}{2}] +$$

$$\rho g H S_o \Delta x + \frac{1}{2}\rho g[(H^2 - \frac{\partial H^2}{\partial x}.\frac{\Delta x}{2}) - (H^2 + \frac{\partial H^2}{\partial x}.\frac{\Delta x}{2})] -$$

$$\rho g H S_f \Delta x = \frac{\partial}{\partial t}(\rho u H)\Delta x \qquad (3.3)$$

After combining terms, dividing through by ρ and Δx, then taking Δx to zero,

$$\frac{\partial}{\partial t}(uH) + \frac{\partial}{\partial x}(u^2H) + \frac{g}{2}.\frac{\partial}{\partial x}(H^2) = gH(S_o - S_f) \qquad (3.4)$$

The derivatives are rearranged to give:

$$H.\frac{\partial u}{\partial t} + u.\frac{\partial H}{\partial t} + u.\frac{\partial}{\partial x}(uH) + uH.\frac{\partial u}{\partial x} + gH.\frac{\partial H}{\partial x} = gH(S_o - S_f) \qquad (3.5)$$

The second and third terms are eliminated by equation (3.2) and dividing through by H, the momentum equation is:

$$\frac{\partial u}{\partial t} + u.\frac{\partial u}{\partial x} + g.\frac{\partial H}{\partial x} = g(S_o - S_f) \qquad (3.6)$$

3.2.2 Equations in R-T Space

The simplest example of an expanding or a contracting flow is provided by purely radial flow [Marshall and Menendez (1981) and Martin (1983)]. Taken by itself , of course, purely radial flow is something of an abstraction. However it's consideration is important because it typifies the problems of restricted expansions and contractions in canals, rivers and estuaries in a continuous representation. Also it is the simplest example of two-dimensional wave propagation [Abbott (1966)].

To construct the corresponding equations of continuity and motion, the element shown in plan and in isometric in Figure 3.2 is referred to:

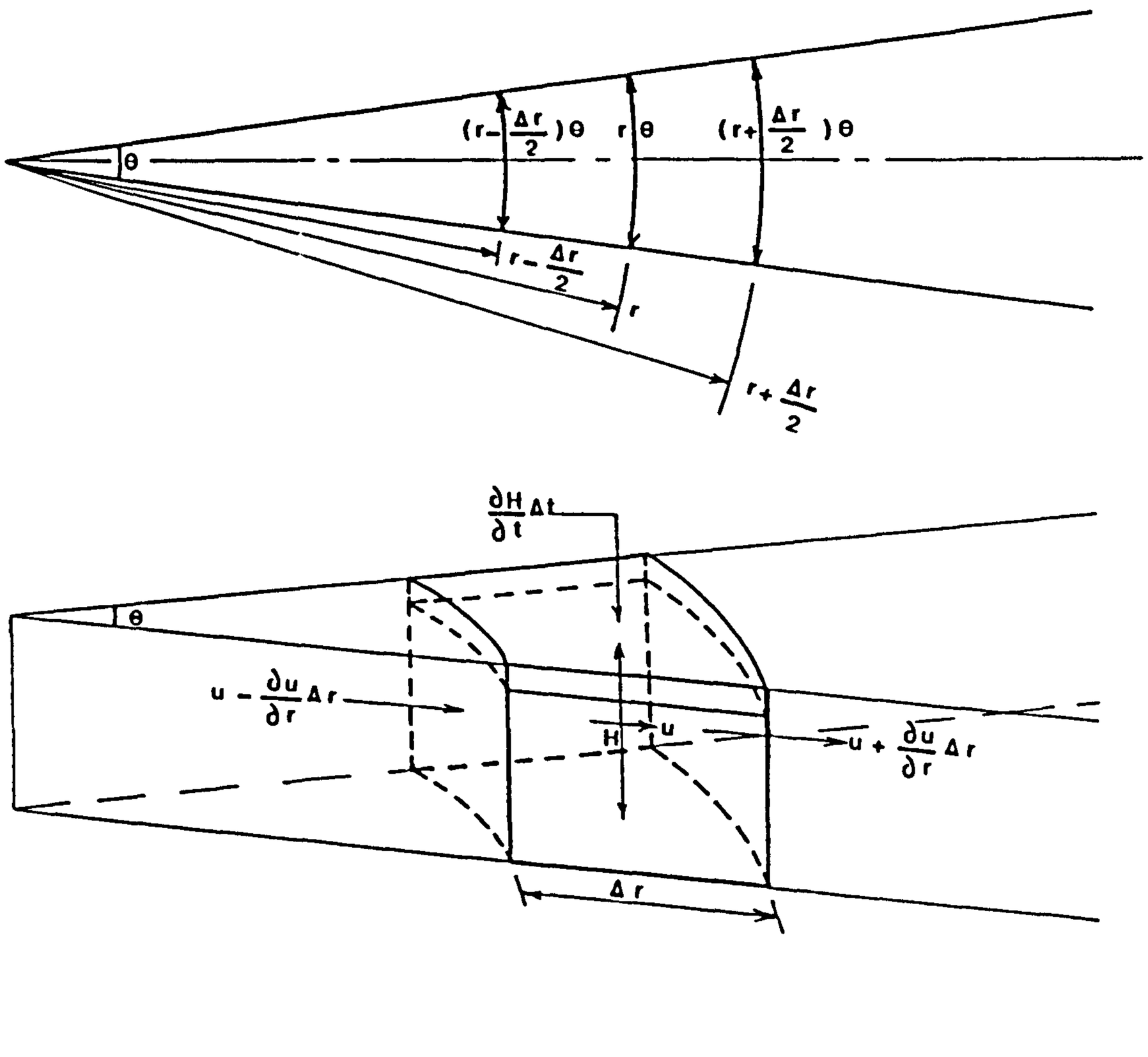

Figure 3.2 : Element employed in deriving the partial differential equations of radially symmetric shallow water wave motion in a homogeneous fluid in (R-T) space

On the same principles as in section 3.2.1 , the shallow water equations are derived herein.

The continuity equation;

$$\text{Inflow entering the element} = \left(u - \frac{\partial u}{\partial r} \cdot \frac{\Delta r}{2}\right)\left(H - \frac{\partial H}{\partial r} \cdot \frac{\Delta r}{2}\right)\left[\theta\left(r - \frac{\Delta r}{2}\right)\right]$$

Outflow leaving the element = $(u + \frac{\partial u}{\partial r}. \frac{\Delta r}{2})(H + \frac{\partial H}{\partial r} .\frac{\Delta r}{2})\ [\theta(r + \frac{\Delta r}{2}\ )\ ]$

Change of storage = $\frac{\partial H}{\partial t}\ .\ \Delta r\ (\theta r)$

According to the conservation of mass for a control volume,

$$(u - \frac{\partial u}{\partial r}\ .\ \frac{\Delta r}{2}\ )(H - \frac{\partial H}{\partial r}\ .\ \frac{\Delta r}{2}\ )\ [\theta(r- \frac{\Delta r}{2}\ )] - (u+ \frac{\partial u}{\partial r}\ .\ \frac{\Delta r}{2}).$$

$$(H + \frac{\partial H}{\partial r}\ .\ \frac{\Delta r}{2}\ )\ [\theta(r + \frac{\Delta r}{2}\ )] = \frac{\partial H}{\partial t}\ .\ \Delta r\ (\theta r) \qquad (3.7)$$

After multiplying out the factors and taking Δr to zero, the continuity equation is:

$$\frac{\partial H}{\partial t} + \frac{\partial}{\partial r}\ (uH) + \frac{uH}{r} = 0 \qquad (3.8)$$

The momentum equation :

Momentum entering = $\rho\{u(uH) - \frac{\partial}{\partial r}\ [u(uH)].\frac{\Delta r}{2}\ \}[\theta(r - \frac{\Delta r}{2}\ )\ ]$

Momentum leaving = $\rho\{u(uH) + \frac{\partial}{\partial r}\ [u(uH)].\frac{\Delta r}{2}\ \}[\theta(r + \frac{\Delta r}{2}\ )\ ]$

The force due to gravity $F_g = \rho g H S_o \Delta r\ (\theta r)$

The pressure force $F_p = \frac{1}{2}\ \rho g\{(H - \frac{\partial H}{\partial r}\ .\ \frac{\Delta r}{2})^2\ [\theta(r - \frac{\Delta r}{2}\ )] - (H +$

$\frac{\partial H}{\partial r}\ .\ \frac{\Delta r}{2})^2\ [\theta(r + \frac{\Delta r}{2}\ )] + 2\ H^2\ \Delta r.\ \frac{\theta}{2}\ \}$

The frictional resistance $F_s = \rho g H S_f\ \Delta r\ (\theta r)$

Combining these elements into a single equation for conservation of momentum gives:

$$\rho[u^2H - \frac{\partial}{\partial r}(u^2H).\frac{\Delta r}{2}][\theta(r - \frac{\Delta r}{2})] - \rho[u^2H + \frac{\partial}{\partial r}(u^2H).\frac{\Delta r}{2}][\theta(r+ \frac{\Delta r}{2})] + \rho gHS_o\,\Delta r(\theta r) + \frac{1}{2}\rho g\{(H - \frac{\partial H}{\partial r}.\frac{\Delta r}{2})^2[\theta(r - \frac{\Delta r}{2})] - (H + \frac{\partial H}{\partial r}.\frac{\Delta r}{2})^2[\theta(r + \frac{\Delta r}{2})] + 2H^2\,\Delta r.\frac{\theta}{2}\} - \rho gHS_f\,\Delta r(\theta r) = \frac{\partial}{\partial t}(\rho uH)\Delta r(\theta r) \quad (3.9)$$

After combining terms, dividing through by ρ, θ, r and Δr, then taking Δr to zero,

$$\frac{\partial}{\partial t}(uH) + \frac{u^2H}{r} + \frac{\partial}{\partial r}(u^2H) + \frac{g}{2}.\frac{\partial}{\partial r}(H^2) = gH(S_o - S_f) \quad (3.10)$$

The derivatives are rearranged to give:

$$H.\frac{\partial u}{\partial t} + u.\frac{\partial H}{\partial t} + u.\frac{\partial}{\partial r}(uH) + u(\frac{uH}{r}) + uH.\frac{\partial u}{\partial r} + gH.\frac{\partial H}{\partial r} = gH(S_o - S_f) \quad (3.11)$$

The second, third and fourth terms are eliminated by equation (3.8) and dividing through by H, the momentum equation is,

$$\frac{\partial u}{\partial t} + u.\frac{\partial u}{\partial r} + g.\frac{\partial H}{\partial r} = g(S_o - S_f) \quad (3.12)$$

Note that this is identical to the equation (3.6) of motion for one-dimensional (rectilinear) propagation in(X-T) space, as determined in section 3.2.1.

3.3 Numerical Integration

3.3.1 Integration in X-T Space

The equations (3.2) and (3.6) in section 3.2.1 are the continuity and the momentum equations for open channel of constant rectangular cross-sectional shape and constant longitudinal bottom slope (prismatic channel). These equations constitute a system of non-linear partial differential equations of the hyperbolic type. In other words they are two simultaneous quasi-linear partial differential equations of two dependent variables (u and H) and two independent variables (x and t) [Lister (1960)].

These equations are non-linear and no uniquely determined solutions can be obtained unless extensive simplification and linearisation are made. This difficulty in direct integration is dealt with by choosing one of various numerical integration techniques. There are two fundamental divisions of methods for the solution of hyperbolic partial differential equations. The method of characteristics is based upon the characteristic form of the equations whilst finite difference methods are based upon the partial differential equations as originally derived. It is difficult to make a comprehensive analysis of the available numerical methods used to solve the shallow water equations. However, Liggett and Woolhiser (1967), Price (1974) and Liggett and Cunge (1975) have studied a number of finite difference methods for the solution of shallow water equations. Their general conclusion was that the method of characteristics has some general advantages over other explicit schemes using finite differences. In fact Liggett and Woolhiser (1967) stated that 'The method of characteristics was found to be the most suitable general method in

that it gave good results over wide ranges of the parameters', and Price (1974) concluded that 'The fixed mesh characteristic method is most accurate when ($\Delta x/\Delta t$) is slightly smaller than the Courant speed'. Also, as is well known, the solution proceeds numerically along the paths followed by waves in the physical plane. This property has the advantage of leading to a clear understanding of the physical implications of the numerical procedures [Vardy (1976)].

Historically speaking one should remember that the first application of the characteristics method to hydraulics was made by Massau (1889) and its development to Craya (1946). The method of characteristics may be described as a technique whereby the problem of solving two simultaneous partial differential equations can be replaced by the problem of solving four ordinary differential equations. This description of the method implies a continuous situation, where derivatives are everywhere defined in almost all directions. Here, linear combinations of the differential equations are sought which contain derivatives of the two unknown functions in one direction only. For this type of equation there are two such directions, called characteristic directions.

Several procedures are available for transforming the equations into the characteristic form. One must first remove H from equation (3.6) by substitution (c^2=gH), where c is the speed of a long low wave in water of depth H; accordingly, c becomes the measurement of the depth. Note that [d(gH) = d(c^2)=2cdc], so the equation (3.6) will be:

$$\frac{\partial u}{\partial t} + u.\frac{\partial u}{\partial x} + 2c.\frac{\partial c}{\partial x} = g(S_o - S_f) \qquad (3.13)$$

Equation (3.2) is expanding into the following form:

$$\frac{\partial H}{\partial t} + u.\frac{\partial H}{\partial x} + H.\frac{\partial u}{\partial x} = 0 \qquad (3.14)$$

Multiplying throughout by g, and substituting (c^2=gH) as before, and dividing throughout by c, equation (3.14) will be:

$$2.\frac{\partial c}{\partial t} + 2u.\frac{\partial c}{\partial x} + c.\frac{\partial u}{\partial x} = 0 \qquad (3.15)$$

The two equations (3.13) and (3.15) after rearranged:

$$\frac{\partial u}{\partial t} + u.\frac{\partial u}{\partial x} + 2c.\frac{\partial c}{\partial x} = g(S_o - S_f) \qquad (3.16)$$

$$c.\frac{\partial u}{\partial x} + 2.\frac{\partial c}{\partial t} + 2u.\frac{\partial c}{\partial x} = 0 \qquad (3.17)$$

By writing first the sum, and then the difference, of equations (3.16) and (3.17), obtaining two further equations:

$$\frac{\partial u}{\partial t} + (u+c).\frac{\partial u}{\partial x} + 2.\frac{\partial c}{\partial t} + 2(u+c).\frac{\partial c}{\partial x} = g(S_o - S_f) \qquad (3.18)$$

$$\frac{\partial u}{\partial t} + (u-c).\frac{\partial u}{\partial x} - 2.\frac{\partial c}{\partial t} - 2(u-c).\frac{\partial c}{\partial x} = g(S_o - S_f) \qquad (3.19)$$

From equations (3.18) and (3.19), the so-called 'characteristic form' is:

$$\left\{\frac{\partial}{\partial t} + (u+c).\frac{\partial}{\partial x}\right\}(u+2c) = g(S_o - S_f) \qquad (3.20)$$

$$\left\{\frac{\partial}{\partial t} + (u-c).\frac{\partial}{\partial x}\right\}(u-2c) = g(S_o - S_f) \qquad (3.21)$$

According to equations (3.20) and (3.21) functions c and u are differentiated along curves in the (x,t) plane which satisfy the differential equations ($\frac{dx}{dt} = u \pm c$). The differentiation operators are nothing more than total derivatives along these curves:

$$\frac{D+}{Dt}(u+2c) = g(S_o - S_f) \qquad (3.22)$$

$$\frac{D-}{Dt}(u-2c) = g(S_o - S_f) \qquad (3.23)$$

Thus for any point moving through the fluid with the velocity ($u \pm c$), the relationship (3.22) is true along the positive characteristic curves, defined by ($\frac{dx}{dt} = u+c$) , while the relationship (3.23) is valid along the negative characteristic curves, defined by ($\frac{dx}{dt} = u-c$). If the channel is frictionless and horizontal (i.e. $S_f = S_o = 0$), equation (3.22) state (u+2c = constant) along the positive characteristic, while equation (3.23) state (u-2c = constant) along the negative characteristic, as shown in Figure 3.3.

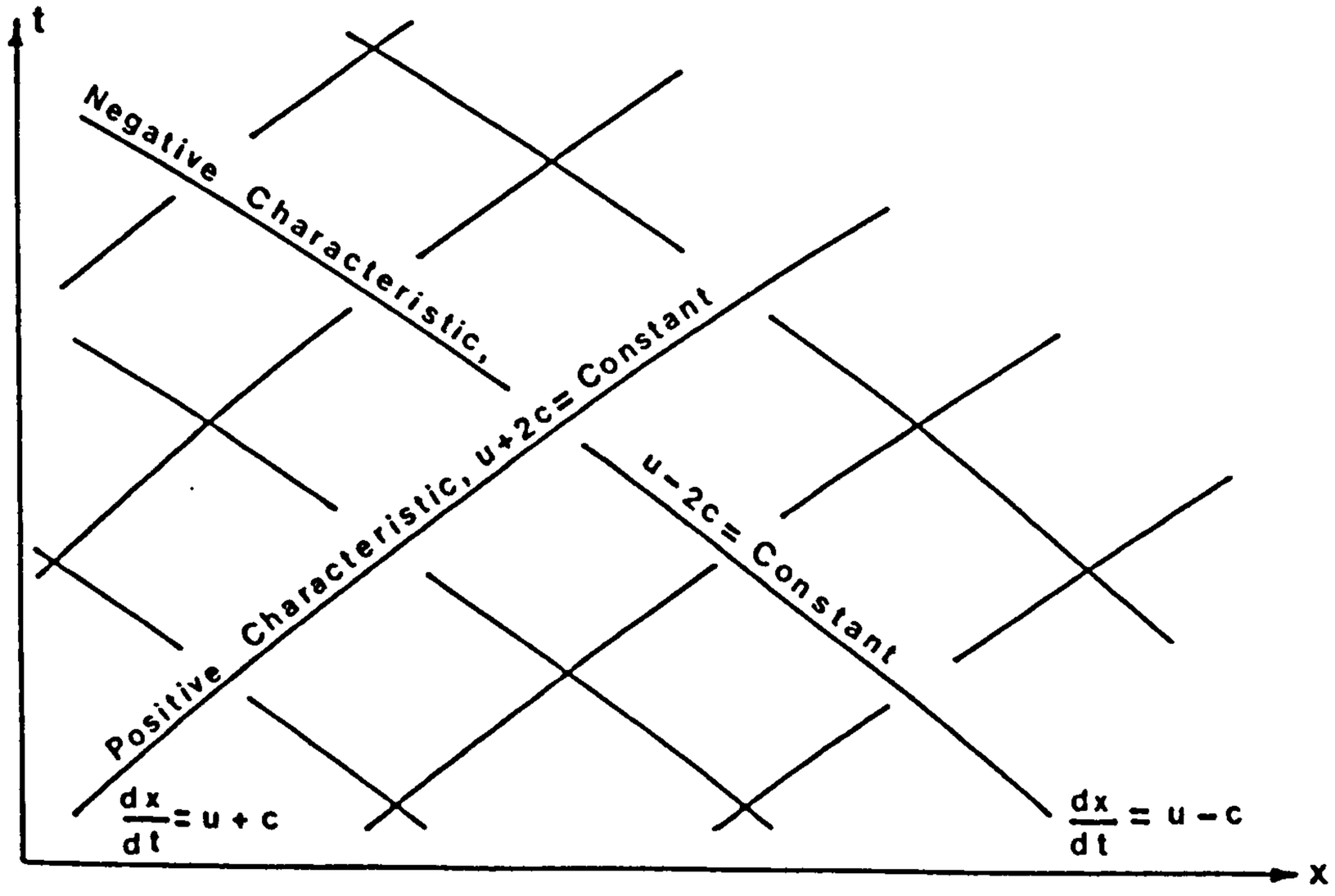

Figure 3.3 : Characteristic Lines in the (x,t) Plane

For a prismatic channel with $S_f \neq 0$ and $S_o \neq 0$, expressions between two points 1 and 2 along positive characteristic can be obtained from equation (3.22):

$$[u+2c]_1^2 = g \int_{t_1}^{t_2} (S_o - S_f)\ dt \qquad (3.24)$$

and along negative characteristic from equation (3.23)

$$[u-2c]_1^2 = g \int_{t_1}^{t_2} (S_o - S_f)\ dt \qquad (3.25)$$

So the characteristics are curves in (x-t) space and they are defined by:

$$\frac{dx}{dt} = u \pm c \qquad (3.26)$$

In Figure 3.4, two characteristic curves are passing through point M where solutions are required. The dependent variables at points L and R are assumed known and the solution is to be projected to point M. From equations (3.24) through (3.26):

$$(u_M + 2c_M) - (u_L + 2c_L) = g \int_{t_L}^{t_M} (S_o - S_f)\ dt \qquad (3.27)$$

$$x_M - x_L = \int_{t_L}^{t_M} (u+c)\ dt \qquad (3.28)$$

$$(u_M - 2c_M) - (u_R - 2c_R) = g \int_{t_R}^{t_M} (S_o - S_f)\ dt \qquad (3.29)$$

$$x_M - x_R = \int_{t_R}^{t_M} (u-c)\ dt \qquad (3.30)$$

Four equations,(3.27) through to (3.30), consist of four unknowns (u_M, c_M, x_M and t_M) for which solutions can be obtained. The integrals are line integrals along the characteristics. No approximations have been made. The numerical approximation enters in evaluating the integrals.

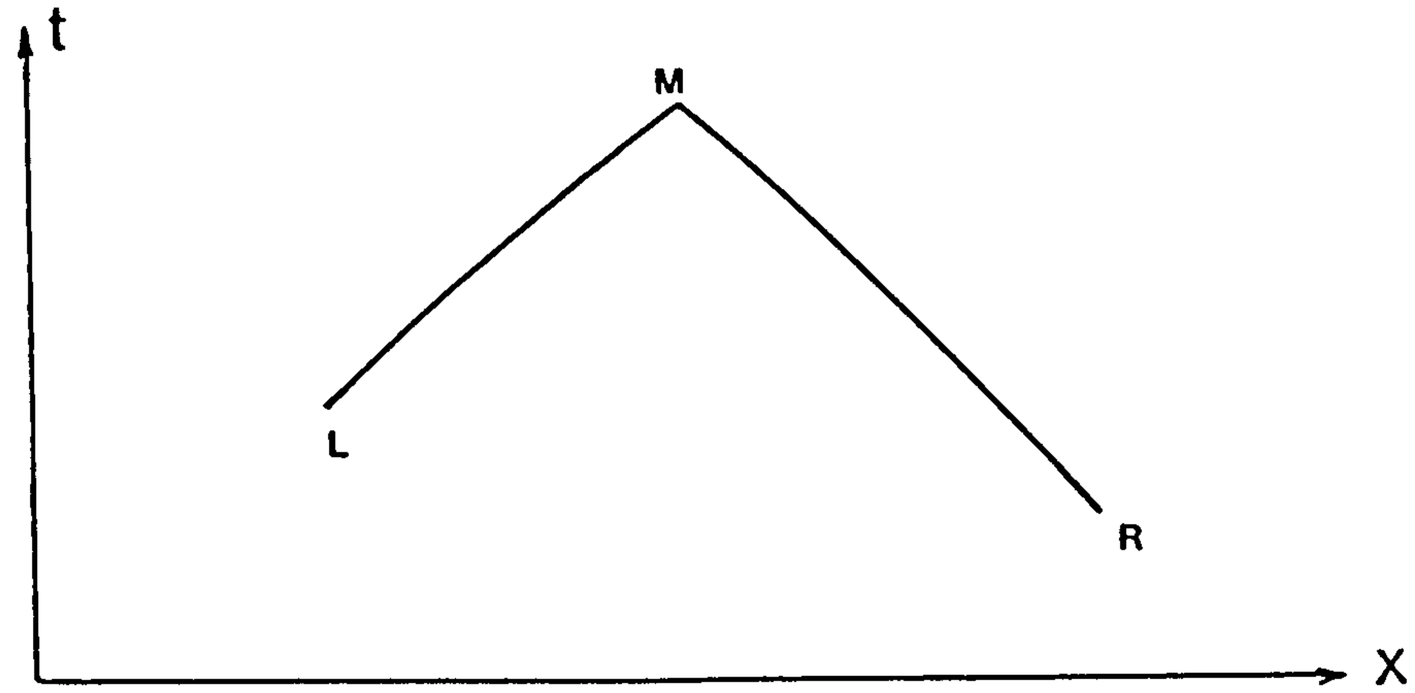

Figure 3.4 : Characteristic Solution for Point M

Liggett and Cunge (1975) stated that trapezoidal integration is the most accurate method that can be used without bringing in additional points. Thus equations (3.27) through to (3.30) can be approximated by:

$$(u_M + 2c_M) - (u_L + 2c_L) = g(S_o - \frac{S_{f_M} + S_{f_L}}{2}) (t_M - t_L) \quad (3.31)$$

$$x_M - x_L = (\frac{u_M + c_M + u_L + c_L}{2}) (t_M - t_L) \quad (3.32)$$

$$(u_M - 2c_M) - (u_R - 2c_R) = g(S_o - \frac{S_{f_M} + S_{f_R}}{2}) (t_M - t_R) \quad (3.33)$$

$$x_M - x_R = \left(\frac{u_M - c_M + u_R - c_R}{2} \right) (t_M - t_R) \qquad (3.34)$$

In this way the characteristic method forms a net of points spaced at uneven intervals. In practice, however, solutions at certain points at certain times are usually preferred. Therefore, a rectangular grid system in x and t can easily be formed, as shown in Figure 3.5. Where I is the grid number along x direction.

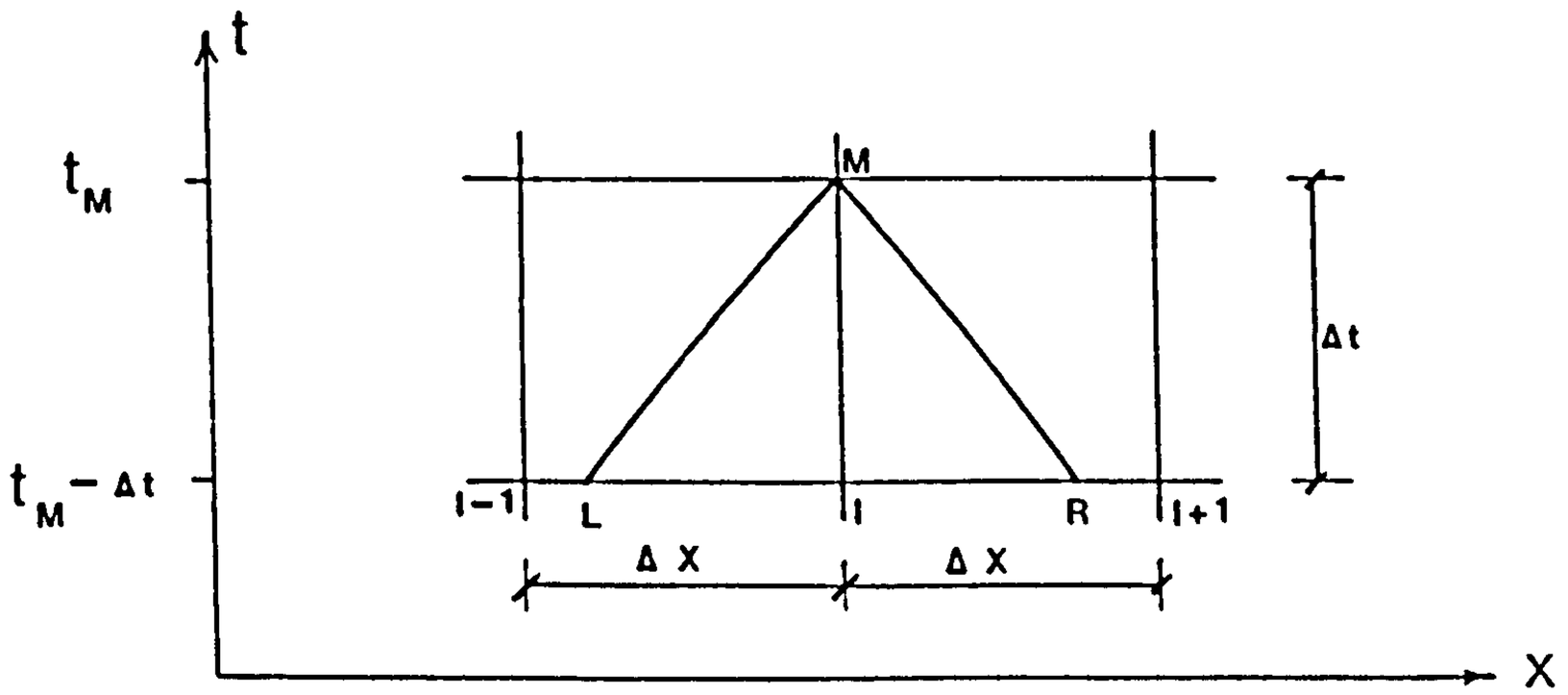

Figure 3.5 : Rectangular Grid in (x,t) Plane

Solution point M is located at a grid point on time level t_M and characteristic curves passing through M are extended backwards until they intersect the distance line at $(t_M - \Delta t)$,as shown in Figure 3.5. The dependent variables at grid points on time level $(t_M - \Delta t)$ are assumed known, and the solution needs to be advanced to time level t_M. Integration along characteristic curves ML and MR can be performed by an iterative method, as originally suggested by Hartree (1953). The various techniques employed depend on which

point is being used to find the slope of the characteristics, commonly by using point I, whilst some use of point M or points L and R has been made - as in equations (3.31) through to (3.34) [Courant and Friedrichs (1948)].

As shown in Figure 3.5, with a rectangular grid system, characteristic curves do not always pass through grid points. So, interpolation becomes necessary to locate the intersecting points of characteristics along the distance-line. In dam-break problems, since the water surface rapidly changes from one point to the other, the method of interpolation becomes more important than locating the slope of the characteristics; as will be shown in section 3.5. Alternatively, both Wylie (1980) and Kaya (1985) have suggested time-line interpolation schemes in order to reduce the numerical error. However, in dam-break the flow changes from subcritical flow to supercritical flow causing the method to fail at certain points, as shown in Figure 3.6, unless special treatment is given in advance to those points. This also makes the computer program more complicated and the distance-line interpolation scheme was used herein.

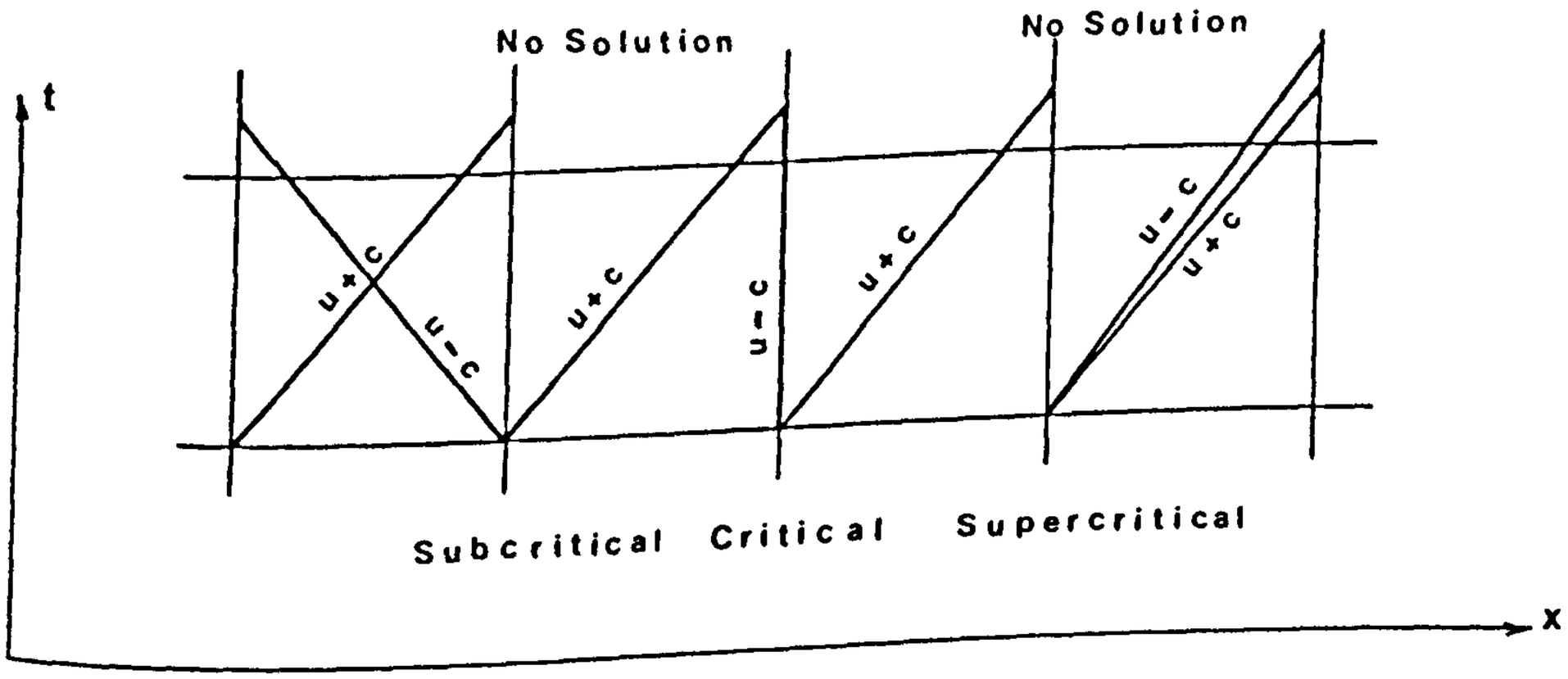

Figure 3.6 : Time-line interpolation in flow changing from subcritical to supercritical

3.3.2 Integration in R-T Space

On the same basis as in section 3.3.1, the shallow water equations (3.8) and (3.12) in (R-T) space may be transformed into their characteristic form. Removing H from the momentum equation (3.12) by the substitution (c^2=gH) gives:

$$\frac{\partial u}{\partial t} + u.\frac{\partial u}{\partial r} + 2c.\frac{\partial c}{\partial r} = g(S_o - S_f) \qquad (3.35)$$

The continuity equation (3.8) is expanding into the following form:

$$\frac{\partial H}{\partial t} + u.\frac{\partial H}{\partial r} + H.\frac{\partial u}{\partial r} + \frac{uH}{r} = 0 \qquad (3.36)$$

Multiplying throughout by g, and substituting (c^2=gH) as before, and dividing throughout by c, equation (3.36) will be:

$$2.\frac{\partial c}{\partial t} + 2u.\frac{\partial c}{\partial r} + c.\frac{\partial u}{\partial r} + \frac{uc}{r} = 0 \qquad (3.37)$$

The two equations (3.35) and (3.37) after being rearranged are:

$$\frac{\partial u}{\partial t} + u.\frac{\partial u}{\partial r} + 2c.\frac{\partial c}{\partial r} = g(S_o - S_f) \qquad (3.38)$$

and

$$c.\frac{\partial u}{\partial r} + 2.\frac{\partial c}{\partial t} + 2u.\frac{\partial c}{\partial r} = -\frac{uc}{r} \qquad (3.39)$$

First taking the sum, and then the difference, of equations (3.38) and (3.39), obtaining two further equations:

$$\frac{\partial u}{\partial t} + (u+c).\frac{\partial u}{\partial r} + 2.\frac{\partial c}{\partial t} + 2(u+c).\frac{\partial c}{\partial r} = -\frac{uc}{r} + g\ (S_o - S_f) \qquad (3.40)$$

$$\frac{\partial u}{\partial t} + (u-c).\frac{\partial u}{\partial r} - 2.\frac{\partial c}{\partial t} - 2(u-c).\frac{\partial c}{\partial r} = +\frac{uc}{r} + g\ (S_o - S_f) \qquad (3.41)$$

From equations (3.40) and (3.41), the characteristic form is:

$$\left\{\frac{\partial}{\partial t} + (u+c)\frac{\partial}{\partial r}\right\}(u+2c) = -\frac{uc}{r} + g\ (S_o - S_f) \qquad (3.42)$$

$$\left\{\frac{\partial}{\partial t} + (u-c)\frac{\partial}{\partial r}\right\}(u-2c) = +\frac{uc}{r} + g\ (S_o - S_f) \qquad (3.43)$$

According to equations (3.42) and (3.43) functions c and u are differentiated along curves in the (r,t) plane which satisfy the differential equations:

$$\frac{dr}{dt} = u \pm c \qquad (3.44)$$

The differentiation operators (total derivatives) along these curves:

$$\frac{D+}{Dt}(u+2c) = -\frac{uc}{r} + g\ (S_o - S_f) \qquad (3.45)$$

$$\frac{D-}{Dt}(u-2c) = +\frac{uc}{r} + g\ (S_o - S_f) \qquad (3.46)$$

Thus for any point moving through the fluid with the velocity $(u \pm c)$, the relationship (3.45) is true along the positive characteristic curves, defined by $\left(\frac{dr}{dt} = u+c\right)$, while the relationship

(3.46) is valid along the negative characteristic curves, defined by ($\frac{dr}{dt}$ = u-c). These equations differ from (3.22) and (3.23) by the terms ($\pm \frac{uc}{r}$) only.

Expressions between two points 1 and 2 along positive characteristic can be obtained from equation (3.45)

$$[u+2c]_1^2 = \int_{t_1}^{t_2} [- \frac{uc}{r} + g\ (S_o - S_f)\ ]\ dt \qquad (3.47)$$

and along negative characteristic from equation (3.46)

$$[u-2c]_1^2 = \int_{t_1}^{t_2} [+ \frac{uc}{r} + g\ (S_o - S_f)\ ]\ dt \qquad (3.48)$$

Solving for point M in r-t plane as in Figure 3.4 the equation (3.31) through to (3.34) will be:

$$(u_M+2c_M) - (u_L+2c_L) = [- \frac{(u_M+u_L)(c_M+c_L)}{2(r_M+r_L)} + g\ (S_o - \frac{S_{f_M}+S_{f_L}}{2})]\cdot$$

$$\cdot(t_M-t_L) \qquad (3.49)$$

$$x_M-x_L = (\ \frac{u_M+c_M+u_L+c_L}{2}\ )\ (t_M-t_L) \qquad (3.50)$$

$$(u_M-2c_M) - (u_R-2c_R) = [+ \frac{(u_M+u_R)(c_M+c_R)}{2(r_M+r_R)} + g\ (S_o - \frac{S_{f_M}+S_{f_R}}{2}\ )]\cdot$$

$$\cdot\ (t_M-t_R) \qquad (3.51)$$

$$x_M-x_R = (\ \frac{u_M-c_M+u_R-c_R}{2}\ )\ (t_M-t_R) \qquad (3.52)$$

The four equations, (3.49) through to (3.52), contain four unknowns, u_M, c_M, r_M and t_M, for which solutions can be obtained in

principle, but which in fact prove to be rather difficult. This is especially so at the front when they are coupled with the jump equations. For simplicity the equations are written as:

$$(u_M+2c_M) - (u_L+2c_L) = [- \frac{u_L c_L}{r_L} + g(S_o-S_{f_L})] (t_M-t_L) \quad (3.53)$$

$$x_M-x_L = (u_L+c_L) (t_M-t_L) \quad (3.54)$$

$$(u_M-2c_M) - (u_R-2c_R) = [+ \frac{u_R c_R}{r_R} + g(S_o-S_{f_R})] (t_M-t_R) \quad (3.55)$$

$$x_M-x_R = (u_R-c_R) (t_M-t_R) \quad (3.56)$$

So the main equations for radial flow in characteristic form are:

$$\frac{dr}{dt} = u \pm c \quad (3.57)$$

and

$$[u \pm 2c]_1^2 = \int_{t_1}^{t_2} [\mp \frac{uc}{r} + g(S_o-S_f)] dt \quad (3.58)$$

Thus, the case of radial flow leads to quasi-invariants, and since (3.58) must hold for all wave regions one supposes that there must be some energy exchange between the characteristic components. This is suported by the observation that any localised disturbance will spread, through the integrals in (3.58), so as to influence every point within the disturbance's region of influence, so that the disturbance is attenuated . This condition obtains in the application of equations (3.58) to the computation of flow over changes in canal section. The form of computation in this case is

schematized in Figure 3.7.

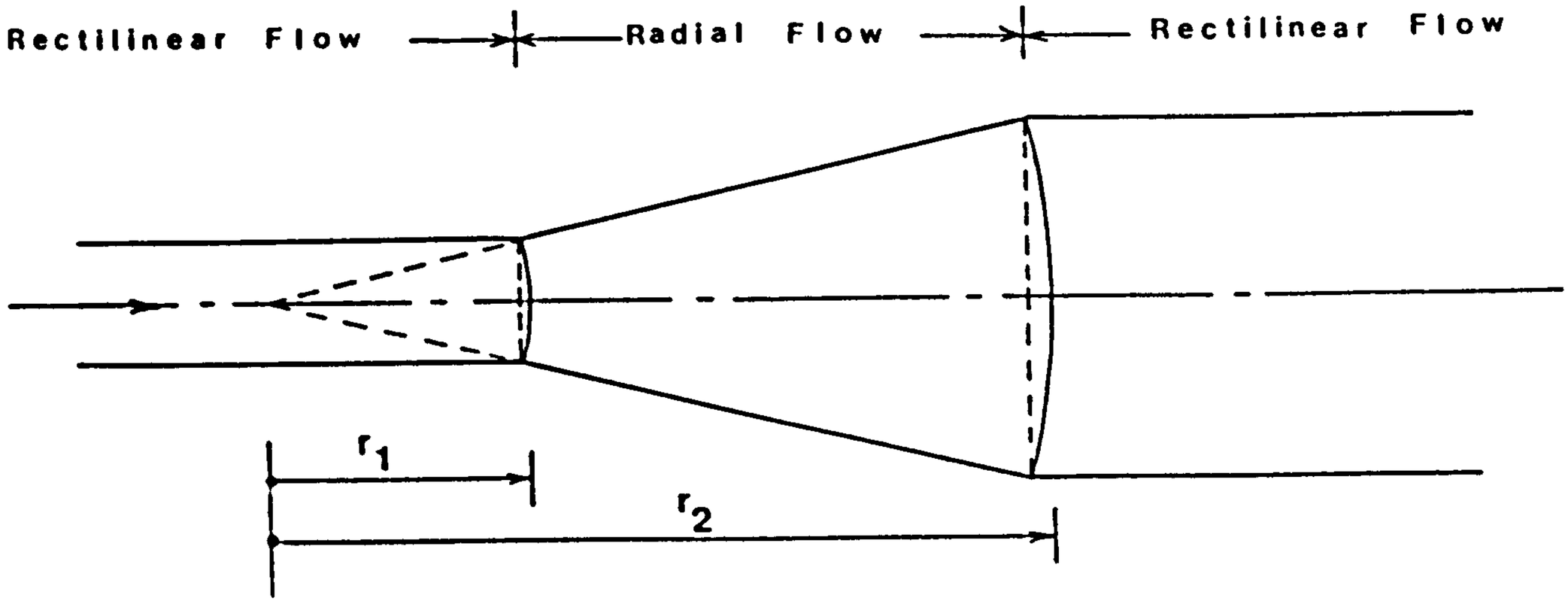

Figure 3.7 : Schematization of a change of canal section, regarded as an example of radial flow

In this respect, the change of section in Figure 3.7 corresponds to the equation [Abbott (1966)]:

$$B = K r \quad \text{and} \quad r_1 \leqslant r \leqslant r_2 \tag{3.59}$$

where B is the breadth of the canal, K is a constant, and r_1 and r_2 are the inception points of the change of section.

3.4 Discontinuous Solution for Bores

3.4.1 Discontinuity in Open Channel

As mentioned in section 3.1, open channel waves may be divided into two broad categories depending on whether the vertical component of the acceleration of particles of water is negligible or not. If the vertical component is small, there is said to be gradually-varied, unsteady flow; a large vertical component is

associated with rapidly-varied, unsteady flow.

Examples of gradually-varied, unsteady flow are flood waves in rivers and the change of flow resulting from slow operation of controlling structures such as gates and sluices.

With rapidly-varied, unsteady flow an abrupt change of surface level occurs as a 'surge' moves along the channel. Surges are of different types, depending on whether they move upstream or downstream and whether the water level behind them is higher than in front (a positive surge) or lower (a negative surge) [Pickford (1969)].

A positive surge moves downstream into the valley below a dam after the dam failure. Such a surge may also be caused by a sudden gate opening. A negative surge moves upstream into the reservoir after the dam failure, which becomes an attenuated wave.

Thus, the dam-break flow may be divided to four zones depending on the type of flow, as shown in Figure 3.8.

As indicated by Figure 3.8, the method of characteristics may be applied to zones (1), (2) and (3) and coupled with the jump equation in zone (4) - see later in this section (3.4). Since a proper numerical solution for the negative wave becomes time-consuming a separate treatment is employed as described in section 4.3.5.

The path of the bore on the (x-t) plane is represented as the discontinuity separating two regions of continuous flow as shown in Figure 3.9 [Cunge (1975) and Cunge, Holly and Verwey (1980)].

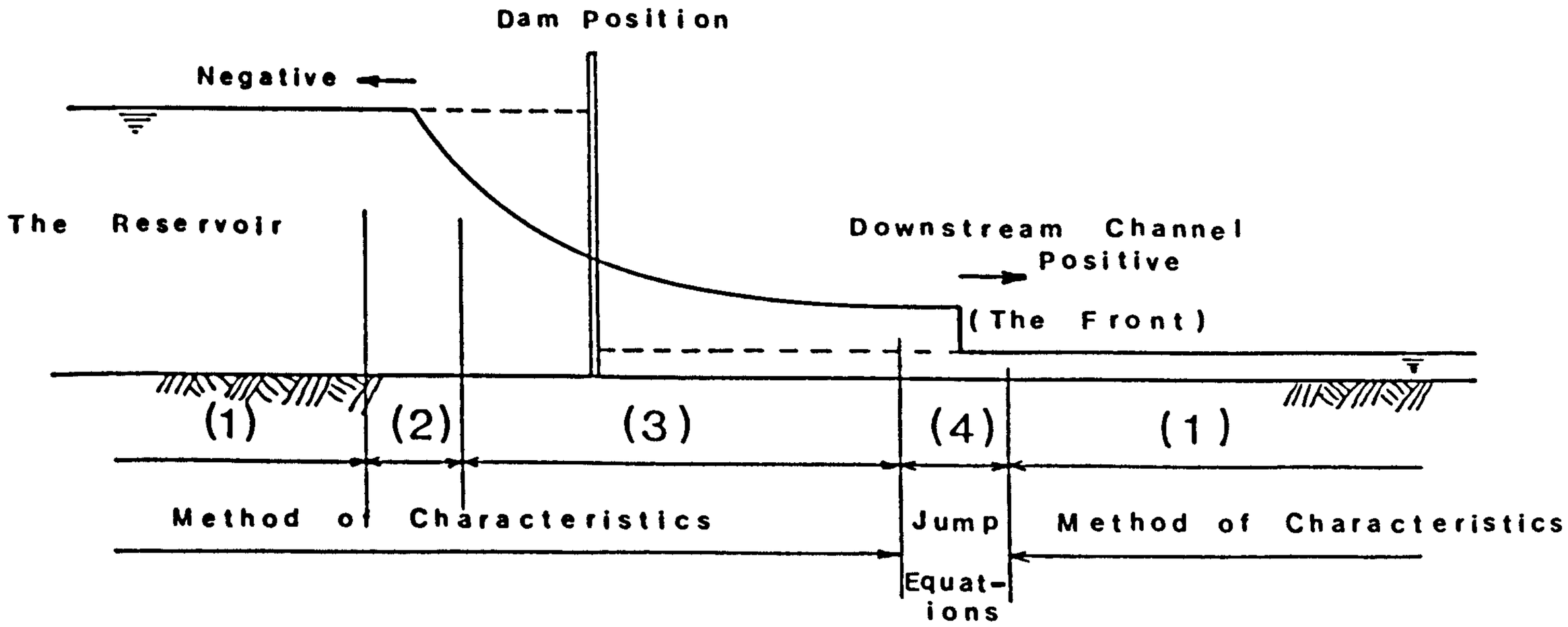

(1) Mainly Horizontal Motion, (2) Negative wave , (3) Gradually Varied Unsteady Flow, and (4) Positive Surge (considerable vertical motion)

Figure 3.8 : Schematization of the Dam-Break Flow

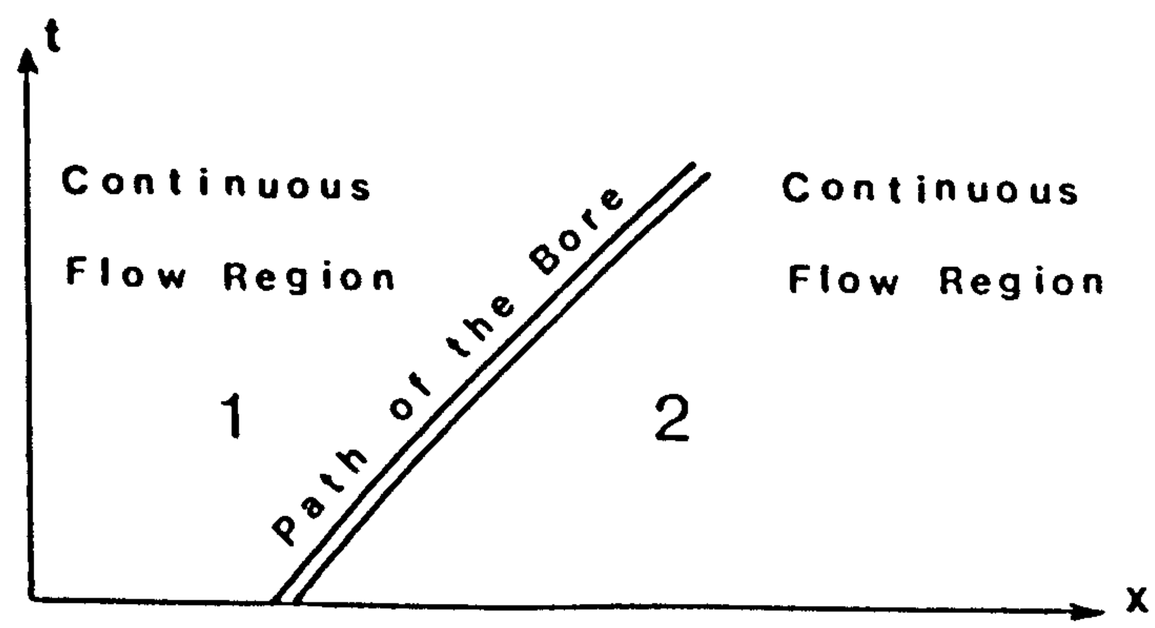

Figure 3.9 : Path of a Bore Separating Two Regions

Region 1 is situated on the side of greater depth than Region 2. The actual path of the bore is the solution of ordinary differential equation derived from the relationships valid across the front and the slope of this path is defined by the bore velocity.

$$\frac{dx}{dt} = w \tag{3.60}$$

The relationships are valid whatever happens inside the shock. They are the hydraulic equivalents of the Rankine-Hugoniot relationships for shocks in gases. For an observer moving with the velocity w, they reduce to the equation of the stationary hydraulic jump.

Thus a hydraulic bore is a moving jump. It is obvious that in the neighbourhood of the jump the basic shallow water hypotheses are violated; the streamline curvature is very strong, vertical accelerations are not negligible, and hydrostatic pressure distribution cannot be considered to be a valid assumption. However, by considering the bore to be a simple discontinuity in the water surfaces of infinitesimal length, the moving hydraulic jump relations may be used to link the regions upstream and downstream. In the following two sections the moving hydraulic jump relationships in (X-T) and (R-T) space are derived.

3.4.2 Unsteady Hydraulic Jump in X-T

The classical hydraulic jump in (X-T) space is shown in Figure 3.10 [following Henderson (1966)].

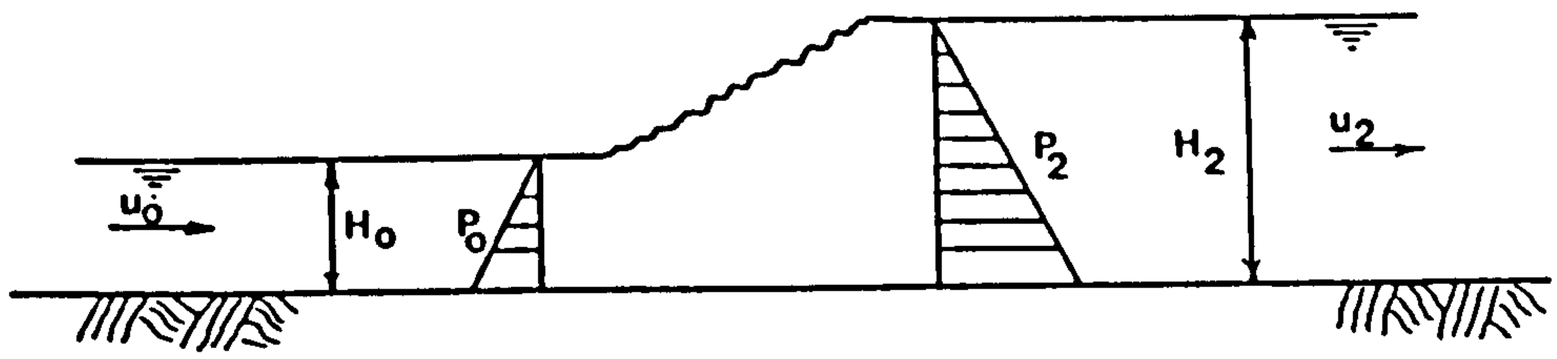

Figure 3.10 : Classical Hydraulic Jump in (X-T) space

The continuity equation for unit width of the channel:

$$u_o H_o = u_2 H_2 \tag{3.61}$$

The momentum equation is:

$$P_o - P_2 = \rho Q(u_2 - u_o) \tag{3.62}$$

where P is the hydrostatic pressure force. For unit width, equation (3.62) is:

$$\frac{\rho g H_o^2}{2} - \frac{\rho g H_2^2}{2} = \rho(u_2^2 H_2 - u_o^2 H_o) \tag{3.63}$$

Dividing throughout by (ρg) , and multiplying throughout by 2, equation (3.63) becomes:

$$H_o^2 - H_2^2 = \frac{2}{g}(u_2^2 H_2 - u_o^2 H_o) \tag{3.64}$$

Substituting for $(u_2 = \frac{u_o H_o}{H_2})$, from equation (3.61), and expanding the right hand side, equation (3.64) gives:

$$(H_o - H_2)(H_o + H_2) = \frac{2}{g}\left(\frac{u_o^2 H_o^2}{H_2^2} \cdot H_2 - u_o^2 H_o\right) \tag{3.65}$$

or,

$$(H_o-H_2)\ (H_o+H_2) = \frac{2}{g} \cdot \frac{u_o^2 H_o}{H_2} \cdot (H_o-H_2) \qquad (3.66)$$

Dividing throughout by (H_o-H_2), and rearranging equation (3.66):

$$u_o^2 = \frac{gH_2}{2H_o}\ (H_o+H_2) \qquad (3.67)$$

Equations (3.61) and (3.67) are the continuity and momentum equations for a steady hydraulic jump. These equations may be used for moving bores if the later are reduced to stationary bores as shown in Figure 3.11.

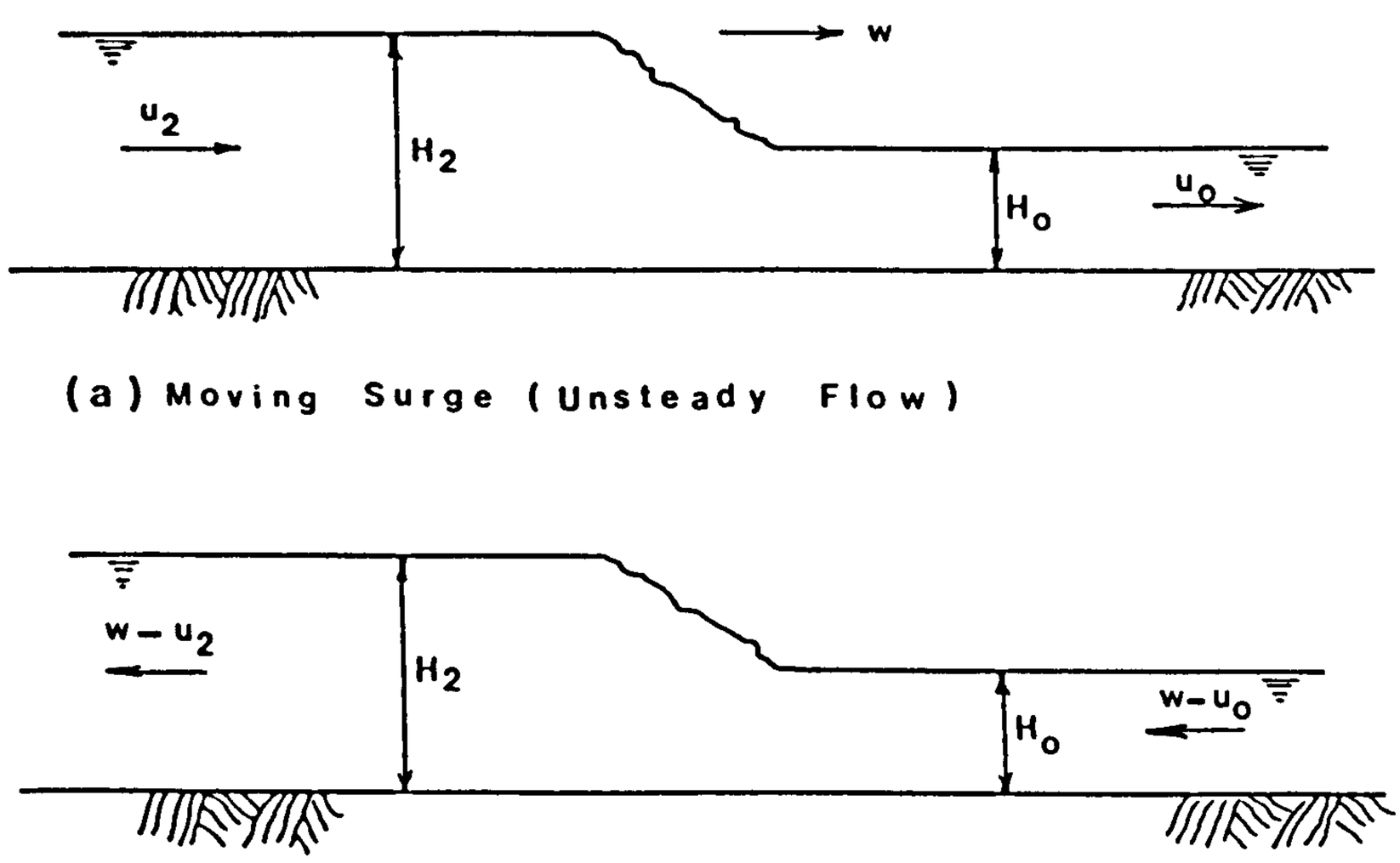

Figure 3.11 : Reduction of the Moving Bore to a Stationary Bore

Figure 3.11(a) shows the bore as seen by an observer on the bank, as unsteady flow; Figure 3.11(b) shows it as seen by an observer moving with the bore, as a steady-flow case, since the

surge is now stationary. The second picture is produced from the first by superimposing on the whole system a velocity equal and opposite to that of the bore w ; the stream velocities are therefore reduced to $(w-u_o)$ and $(w-u_2)$ as shown. The state of affairs shown in Figure 3.11(b) is simply like the hydraulic jump but with flow transfers from high water level in supercritical condition to low water level in subcritical condition through the bore itself.

In this case the continuity equation (3.61) is:

$$(w-u_2)\, H_2 = (w-u_o)\, H_o \tag{3.68}$$

Solving for w in equation (3.68),

$$w = \frac{u_2H_2 - u_oH_o}{H_2-H_o} \tag{3.69}$$

or substituting $(c^2=gH)$, equation (3.69) is:

$$w = \frac{u_2c_2^{\,2} - u_oc_o^{\,2}}{c_2^{\,2}-c_o^{\,2}} \tag{3.70}$$

and equation (3.67) becomes:

$$(w-u_o)^2 = \frac{gH_2}{2H_o}\ (H_o+H_2) \tag{3.71}$$

Again solving for w,

$$w = u_o \pm \sqrt{\frac{gH_2}{2H_o}\ (H_o+H_2)} \tag{3.72}$$

or substituting $(c^2=gH)$, equation (3.72) is:

$$w = u_o \pm \sqrt{\frac{c_2^2}{2c_o^2}(c_o^2 + c_2^2)} \qquad (3.73)$$

Equations (3.69) and (3.72) are used in section 3.4.4 for the discontinuity at the front.

3.4.3 Unsteady Hydraulic Jump in R-T

The steady radial hydraulic jump equation can be obtained by applying the momentum and continuity equations to the element shown in Figure 3.12 [See, for example, Koloseus and Ahmad (1969), Khalifa and McCorquodale (1979), France (1981), and Lawson and Phillips (1983)].

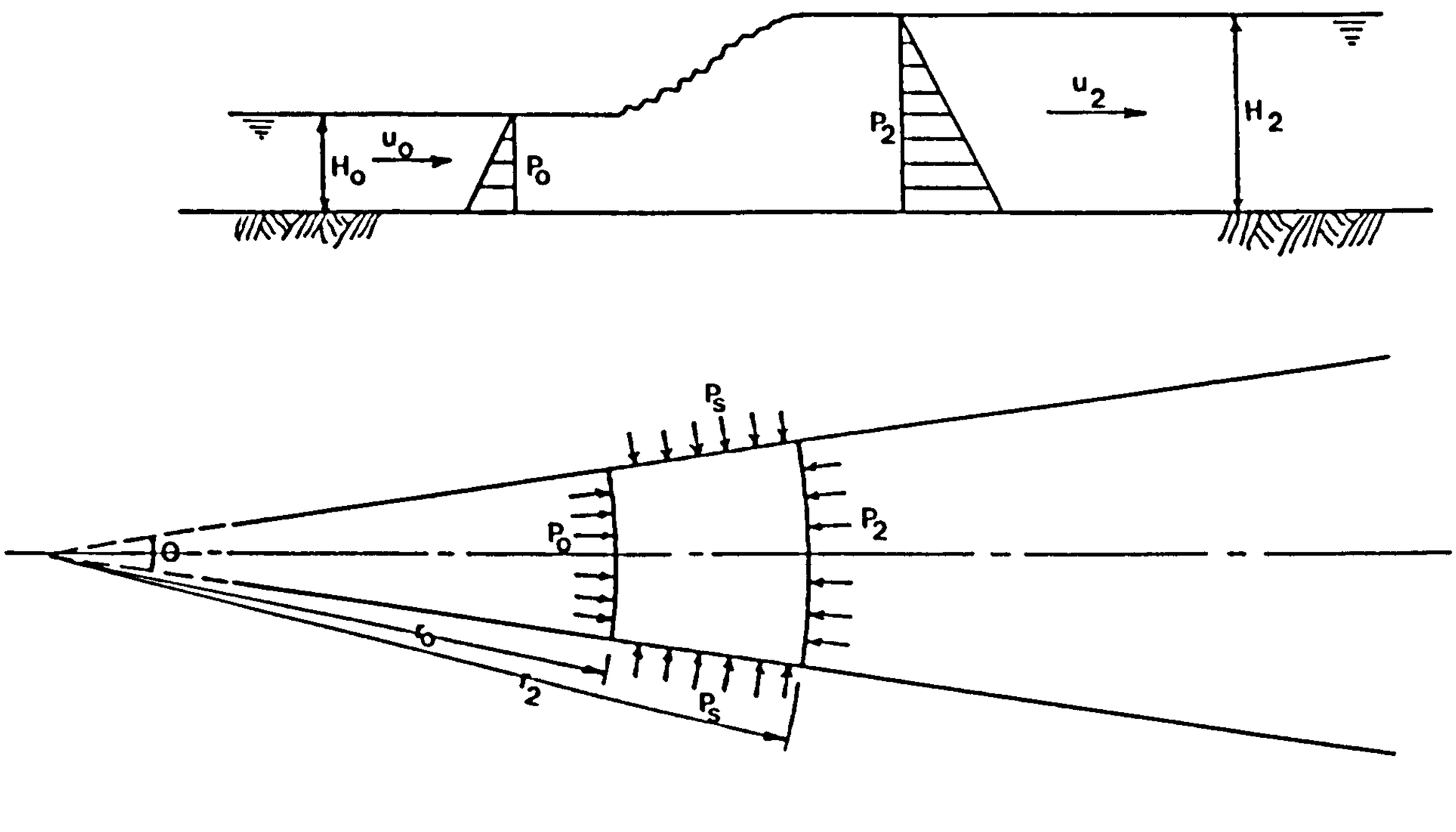

Figure 3.12 : Definition Sketch for Radial Hydraulic Jump

The continuity equation through the element in Figure 3.12 is:

$$u_o H_o (r_o \theta) = u_2 H_2 (r_2 \theta) \tag{3.74}$$

or

$$u_o H_o r_o = u_2 H_2 r_2 \tag{3.75}$$

The momentum equation is:

$$P_o + 2P_s \sin(\tfrac{\theta}{2}) - P_2 = \rho Q(u_2 - u_o) \tag{3.76}$$

where P_s is the channel side pressure force. Considering a wedge-shaped element of the jump and integrating all the component forces over the angle θ . This yields:

$$P_o = \frac{1}{2} \rho g H_o^2 (2r_o \sin \frac{\theta}{2}) \tag{3.77}$$

and

$$P_2 = \frac{1}{2} \rho g H_2^2 (2r_2 \sin \frac{\theta}{2}) \tag{3.78}$$

As the jump surface profile is a straight line, a longitudinal section is a trapezoid and the magnitude of the hydrostatic force acting on one side can be expressed as:

$$P_s = \rho g A_s H' \tag{3.79}$$

where H' is the distance measured from the free surface to the centre of the trapezoid and is given by:

$$H' = \frac{H_o^2 + H_2^2 + H_o H_2}{3(H_o + H_2)} \tag{3.80}$$

and the area A_s on which the side pressure force acts is given by:

$$A_s = \frac{H_o + H_2}{2} (r_2 - r_o) \tag{3.81}$$

Substituting for H' and A_s into equation (3.79) gives:

$$P_s = \frac{\rho g}{6}(r_2-r_o)(H_o^2+H_2^2+H_oH_2) \qquad (3.82)$$

Substituting for P_o, P_2, P_s and Q into equation (3.76) gives:

$$\rho g H_o^2 r_o \sin\frac{\theta}{2} + \frac{\rho g}{3}(r_2-r_o)(H_o^2+H_2^2+H_oH_2)\sin\frac{\theta}{2}$$

$$- \rho g H_2^2 r_2 \sin\frac{\theta}{2} = 2\rho(u_2^2 r_2 H_2 - u_o^2 r_o H_o)\sin\frac{\theta}{2} \qquad (3.83)$$

Dividing throughout by $(\rho g \sin\frac{\theta}{2})$, and solving for u_o after substituting for u_2 from equation (3.75):

$$u_o^2 = \frac{g}{2(r_o^2 H_o^2 - r_o r_2 H_o H_2}\ [r_o r_2 H_o^2 H_2$$

$$+ \frac{1}{3}(r_2^2 - r_o r_2)(H_o^2 H_2 + H_2^3 + H_o H_2^2) - r_2^2 H_2^3] \qquad (3.84)$$

On the same principle as in section 3.4.2 and Figure 3.11, the continuity equation for moving bore is obtained from equation (3.75):

$$(w-u_o)H_o r_o = (w-u_2)H_2 r_2 \qquad (3.85)$$

solving for w,

$$w = \frac{u_2 H_2 r_2 - u_o H_o r_o}{H_2 r_2 - H_o r_o} \qquad (3.86)$$

or substituting $(c^2=gH)$,

$$w = \frac{u_2 c_2^2 r_2 - u_o c_o^2 r_o}{c_2^2 r_2 - c_o^2 r_o} \qquad (3.87)$$

The momentum equation will be, from equation (3.84):

$$(w-u_o)^2 = \frac{g}{2(r_o^2 H_o^2 - r_o r_2 H_o H_2)} \left[r_o r_2 H_o^2 H_2 + \frac{1}{3}(r_2^2 - r_o r_2) \right.$$

$$\left. (H_o^2 H_2 + H_2^3 + H_o H_2^2) - r_2^2 H_2^3 \right] \qquad (3.88)$$

solving for w,

$$w = u_o \pm \sqrt{\frac{g}{2(r_o^2 H_o^2 - r_o r_2 H_o H_2} \left[r_o r_2 H_o^2 H_2 + \frac{1}{3}(r_2^2 - r_o r_2) \right.}$$

$$\left. (H_o^2 H_2 + H_2^3 + H_o H_2^2) - r_2^2 H_2^3 \right] \qquad (3.89)$$

Assuming that the front is always distinct, as shown in Figure 3.13, one may substitute r for r_o and r_2, and the continuity equation (3.86) becomes:

Figure 3.13 : A Front which is Distinct so that $r_o = r_2 = r$

$$w = \frac{u_2H_2 - u_oH_o}{H_2-H_o} \tag{3.90}$$

i.e. equation (3.87) is:

$$w = \frac{u_2c_2^{\,2} - u_oc_o^{\,2}}{c_2^{\,2} - c_o^{\,2}} \tag{3.91}$$

The momentum equation (3.89) is,

$$w = u_o \pm \sqrt{\frac{gH_2}{2H_o}(H_2+H_o)} \tag{3.92}$$

or substituting ($c^2=gH$),

$$w = u_o \pm \sqrt{\frac{c_2^{\,2}}{2c_o^{\,2}}(c_o^{\,2}+c_2^{\,2})} \tag{3.93}$$

Thus, the continuity and the momentum equations for a moving jump are exactly the same for both (X-T) and (R-T) space when assuming that the front is distinct in shape.

3.4.4 Solution of the Discontinuity

When the flow conditions are such that a steep front occurs, the basic equations founded upon the shallow water hypotheses are not valid in the neighbourhood of the discontinuity. As is described in section 3.4.1, this is mainly because of the existence of the vertical accelerations coinciding with strong streamline curvature. When the steep front forms as a roller, or mobile hydraulic jump, the zone it affects and in which the shallow water hypotheses are invalid is very narrow, most often narrower than the distance Δx(or Δr) between two computational points. In such cases it is possible to assume that the discontinuity is a boundary

between two separate regions in which the shallow water hypotheses are valid.

Three practical methods for the computation of steep fronts have been described by Cunge, Holly and Verwey (1980). These were the shock-fitting, the pseudoviscosity, and the 'through' methods. The shock-fitting method was used to compute dam break waves by Vasiliev, Temnoeva, and Shugrin (1965) as in this work.

In the shock-fitting approach, the propagation of the discontinuity is computed for one time step, independently of the computation in the two adjacent shallow-water equation regions. Depending upon the resulting motion, modifications are then made in the boundary conditions and in the extent of these regions. This schematization of a bore, which may appear at some time $t > 0$ in the solution plane (x,t) or (r,t), is physically justified only if the detailed structure of the discontinuity is of secondary importance.

The shock points are considered separately from points on the standard mesh and are allowed to move independently through the mesh. Referring to Figure 3.14 the shock wave is represented by the extra point pair S (at time t_o, say) which at the later time $(t_o+\Delta t)$ has moved to S'. Equations (3.69) and (3.72) imposed at the shock front (x_s and $x_{s'}$) are actually those for one of the two cases classified by Stoker (1957). With reference to Figure 3.14, the dam-break shock wave is a typical example of the case in which $w > u_2 > u_o$ and $H_2 > H_o$, and the shock celerity w satisfies the following inequality:

$$u_2 + \sqrt{gH_2} > w > u_o + \sqrt{gH_o} \tag{3.94}$$

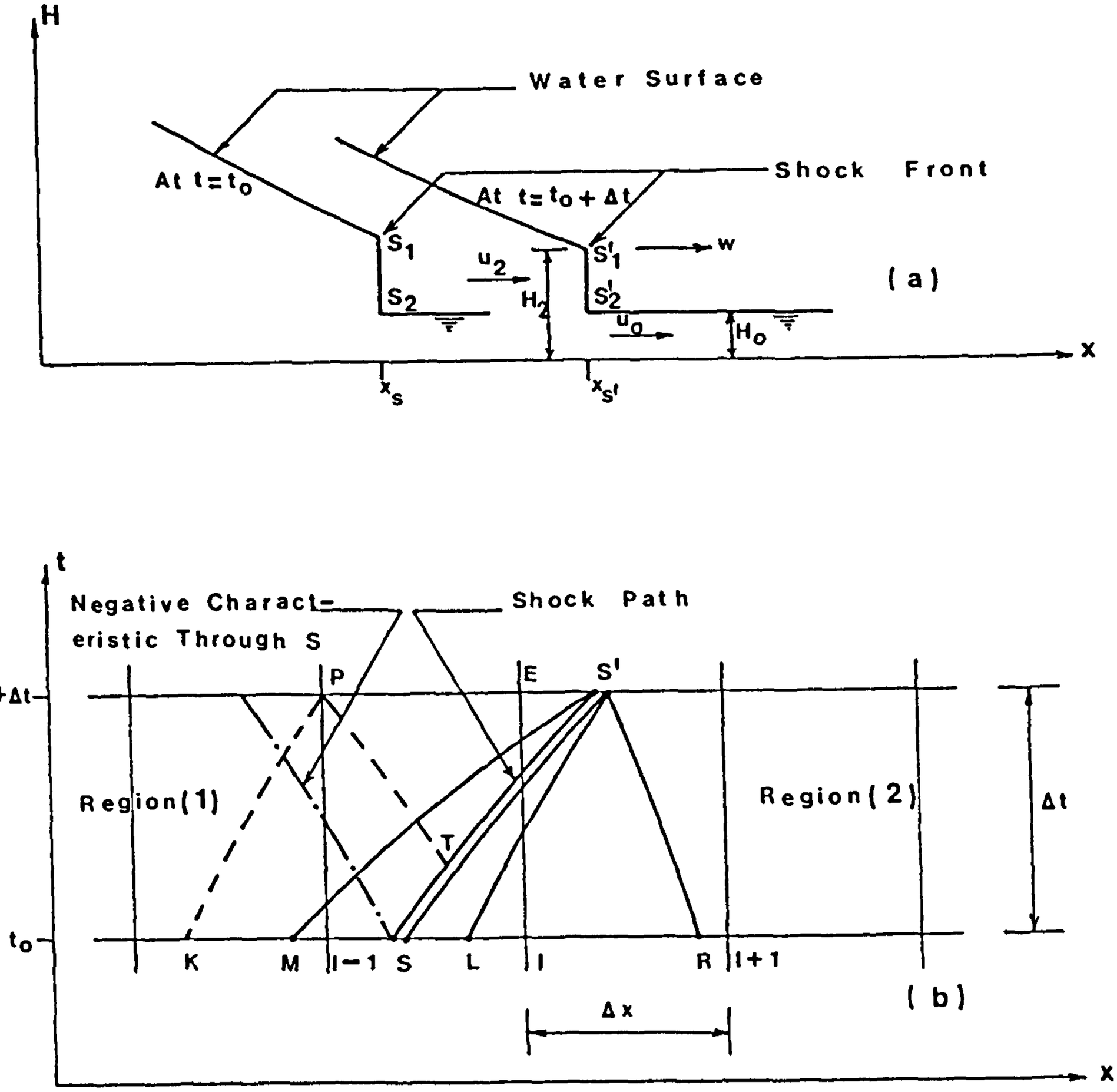

Figure 3.14 : Steep front calculation using the shock fitting method; (a) Physical situation; (b) Computational grid

This inequality states that the shock always travels faster than a gravity wave on the shallow side and slower than a gravity wave on the deep side. Also equation (3.94) states that there are two characteristics from region (2), S'L and S'R, in front of, but only one characteristic from region (1), S'M, behind the shock, as

shown in Figure 3.14(b). At time level to, the position of the discontinuity x_s corresponds to four flow variables as shown in Figure 3.14(a) : $(H_s,u_s)_1$ at the upstream side of the discontinuity, and $(H_s,u_s)_2$ at the downstream side. The new position of the front is $x_{s'}$ at time level $(t_o+\Delta t)$ and the flow variables on both sides are $(H_{s'},u_{s'})_1$ and $_2$ or, as shown in Figure 3.14(a), (u_2,H_2) and (u_0,H_0), and with shock velocity w. Therefore, at time $(t_o+\Delta t)$, there are six unknowns ; $x_{s'}$, $w_{s'}$, $H_{s'_1}$, $u_{s'_1}$, $H_{s'_2}$ and $u_{s'_2}$. It was found by trial that the most practical way in which to determine the unknowns at S' is (see the flow chart in Figure 3.15):

1. Obtain an estimate of the position of S' by assuming the value of the shock velocity along SS' to be that at S, from equation (3.60)

$$x_{s'} \simeq x_s + w_s . \Delta t \qquad (3.95)$$

2. Calculate the solution on the low depth side of S' by the characteristic equations (3.31) through (3.34):

$$(u_{s'_2} + 2c_{s'_2}) - (u_L+2c_L) = g(S_o-S_f)(t_o+\Delta t-t_o) \qquad (3.96)$$

$$x_{s'} - x_L = (u_L+c_L)\ (t_o+\Delta t-t_o) \qquad (3.97)$$

$$(u_{s'_2} - 2c_{s'_2}) - (u_R-2c_R) = g(S_o-S_f)(t_o+\Delta t-t_o) \qquad (3.98)$$

$$x_{s'} - x_R = (u_R-c_R)\ (t_o+\Delta t-t_o) \qquad (3.99)$$

where $(c^2=gH)$. Another four equations from the linear interpolation on the distance-line, at the time t_o, lead to u and c at the two

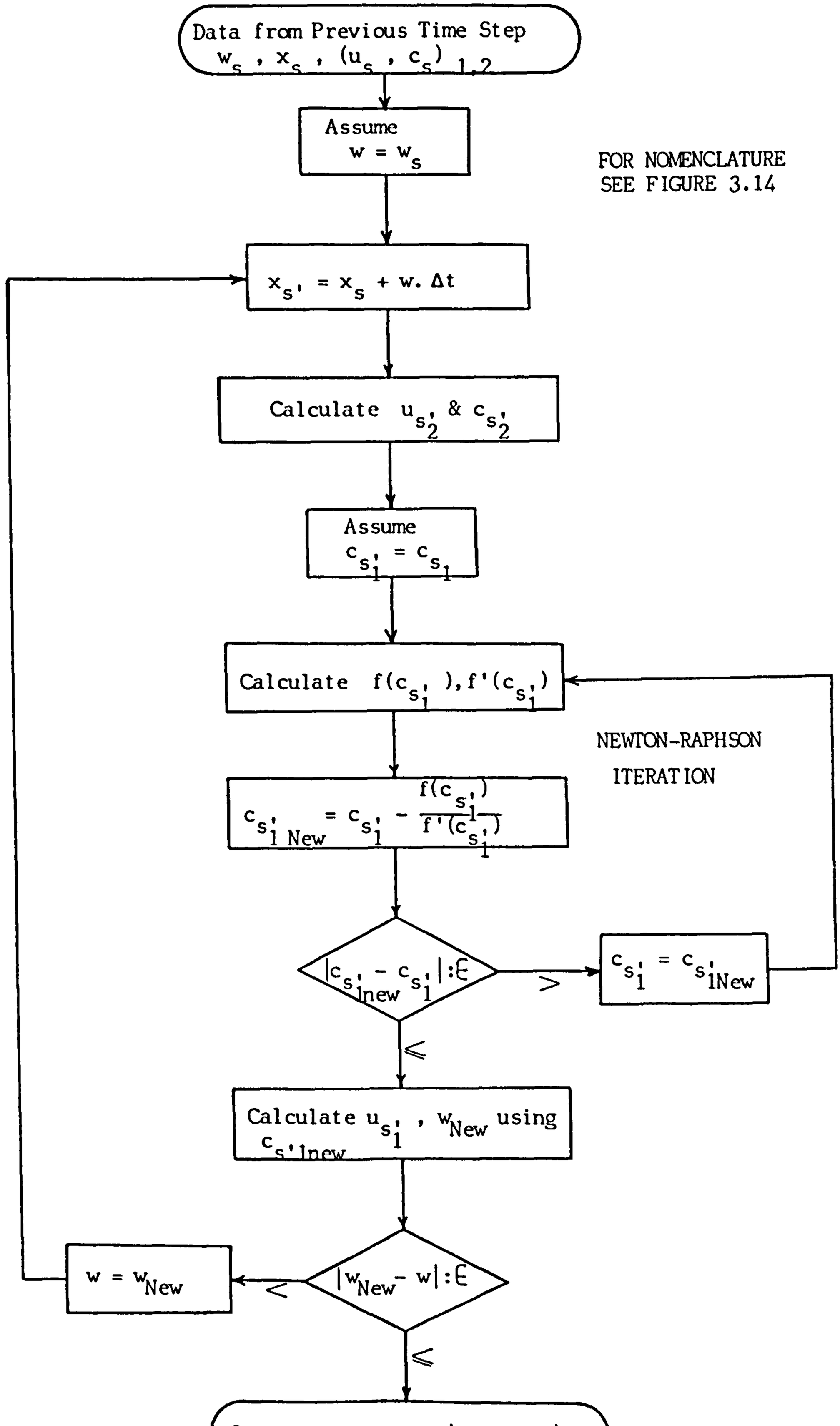

FOR NOMENCLATURE
SEE FIGURE 3.14

FIGURE 3.15 : FLOW CHART OF THE DISCONTINUITY SOLUTION .

points L and R while u, c and x at point S and all the grid points are known at time t_o. Hence the solution for $(u_{s'}, c_{s'})_2$ is obtained.

3. Use the characteristic relations along MS', equations (3.31) and (3.32):

$$(u_{s'_1} + 2c_{s'_1}) - (u_M + 2c_M) = g(S_o - S_f)(t_o + \Delta t - t_o) \qquad (3.100)$$

$$x_{s'} - x_M = (u_M + c_M)\ (t_o + \Delta t - t_o) \qquad (3.101)$$

Also, the flow variables u_M and c_M at the point M on the distance-line at time t_o, have to be determined by interpolation.

4. Use the shock equations (the jump equations) (3.70) and (3.73) at shock point S':

$$w = \frac{u_{s'_1} c_{s'_1}^{\ 2} - u_{s'_2} c_{s'_2}^{\ 2}}{c_{s'_1}^{\ 2} - c_{s'_2}^{\ 2}} \qquad (3.102)$$

and

$$w = u_{s'_2} + \sqrt{\frac{c_{s'_1}^{\ 2}}{2c_{s'_2}}^2 (c_{s'_1}^{\ 2} + c_{s'_2}^{\ 2})} \qquad (3.103)$$

So in the equations (3.100) through to (3.103),there are four unknowns in four equations. Because the unknowns are implicit in the equations, the Newton-Raphson method is used for solutions. The familiar Newton-Raphson iteration for z in f(z) is [see for example McCalla (1967)]:

$$z' = z - \frac{f(z)}{f'(z)} \qquad (3.104)$$

where z is the assumed value, z' is the new value, f(z) is the

function for assumed z, and f'(z) is its derivative. This gives the solution for w and $(u_{s'}, c_{s'})_1$.

5. Use the shock velocity w at S' to find an improved estimate of the position of S' and repeat from (2) until the whole process has converged. This scheme has always been found to converge.

When the values at S' have been determined the point E (or E and P, if P lies to the right of the negative characteristic through S) may be calculated. It could not be calculated previously since the point T lies on the shock path and not on the line $t=t_o$. So to find T, interpolation along the shock path is necessary.

The use of the Courant condition to limit the time step Δt to maintain stability also ensures that the shock will not cross more than one mesh point in a single time step, as will be shown in section 3.6.

The same general scheme is followed for the discontinuity in radial flow.

3.5 Distance-Line Interpolation

Referring to Figure 3.5 and section 3.3.1, the solution at point M, which is located at a forward grid point on time level t_M, arises from equations (3.31) through to (3.34). The Intersection points,L and R, do not generally coincide with the grid points on time level $(t_M-\Delta t)$, for which the dependent variables are known. In order to find the dependent variables at these points (L and R), linear interpolations between the grid points are required. Since

the water surface changes rapidly in the dam-break problem, the method of interpolation becomes critical.

Linear interpolation between grid points (I-1) and (I+1), as shown in Figure 3.16, is commonly adopted by many users of the characteristics method, and it is:

$$(u,c)_L = (u,c)_{I-1} + \frac{(u,c)_{I+1}-(u,c)_{I-1}}{2\Delta x}\ (x_L-x_{I-1}) \qquad (3.105)$$

$$(u,c)_R = (u,c)_{I+1} + \frac{(u,c)_{I+1}-(u,c)_{I-1}}{2\Delta x}\ (x_R-x_{I+1}) \qquad (3.106)$$

Equations (3.105) and (3.106) indicate that the dependent variables at points, L and R, are approximated by those along the line AC instead of along the curve ABC, as shown in Figure 3.16. This approximation tends to cause the water surface in the dam-break problem to exhibit saw-toothed variations [also noted by Liggett and Cunge (1975)], as shown in Figure 3.17. Here the dam break problem has been computed at t=0.725, 1.45 and 2.175 seconds, with the initial water depths upstream H_1 = 10.0m and downstream H_o=0.01m, in a rectangular, horizontal and frictionless channel.

The saw-toothed solution results from the method of interpolation and should not be confused with the Courant instability. It may be corrected by using the grid points, I-1 and I, to find L, and the grid points, I and I+1, to find R, through linear interpolation, as follows:

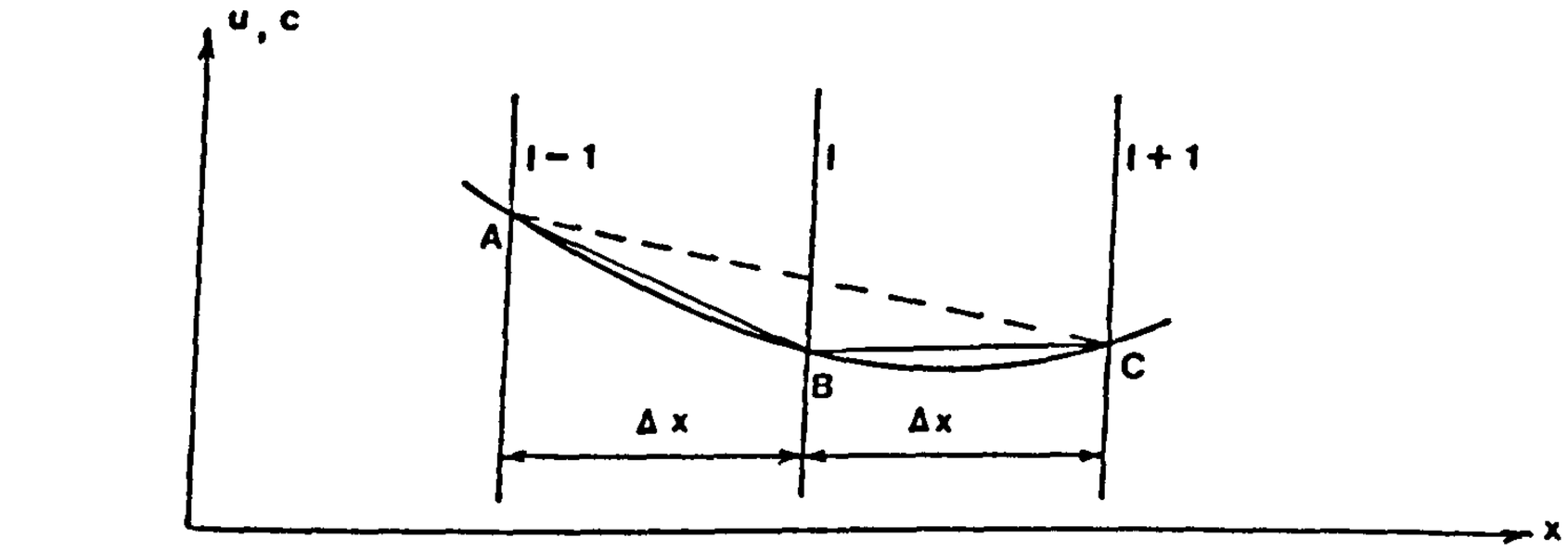

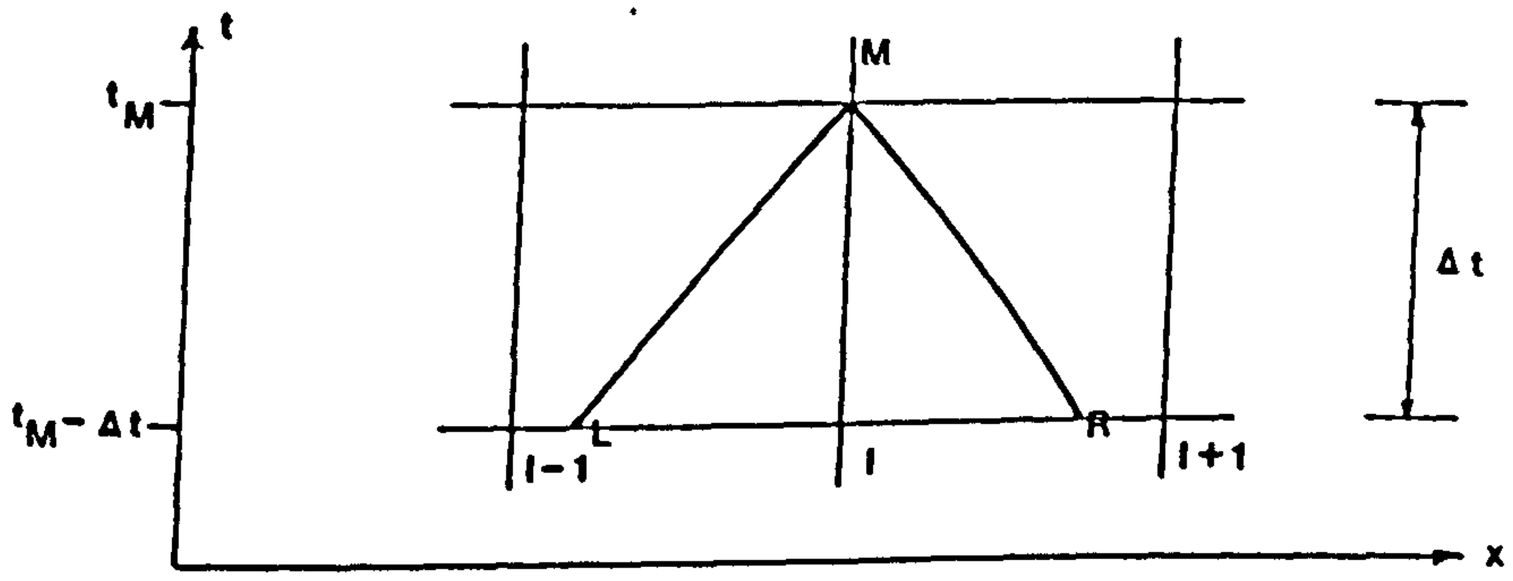

Figure 3.16 : Linear interpolation between the grid points on the distance-line

$$(u,c)_L = (u,c)_{I-1} + \frac{(u,c)_I - (u,c)_{I-1}}{\Delta x}(x_L - x_{I-1}) \qquad (3.107)$$

$$(u,c)_R = (u,c)_{I+1} + \frac{(u,c)_{I+1} - (u,c)_I}{\Delta x}(x_R - x_{I+1}) \qquad (3.108)$$

Equations (3.107) and (3.108) indicate that the dependent variables at points, L and R, are approximated along the lines AB and BC, as shown in Figure 3.16. This approximation is closer to the real values and is evidently sufficient to smooth the water surface as shown in Figure 3.18, where conditions are otherwise as for Figure 3.17.

In Figure 3.19 the saw-toothed surface is compared with the smooth surface (computed at time t=2.175 seconds) and indicates that the former is damped on the upstream side of the dam. Together with further improvements,presented in section 4.3.5, the above interpolation scheme based on the grid points, I-1 and I, to obtain point L and the grid points,I and I+1,to obtain point R, was used exclusively for both (X-T) and (R-T) space.

3.6 Stability Criteria

The time increment (Δt) in a numerical scheme is always subject to certain restrictions because of stability considerations. For explicit schemes, including those based on the method of characteristics, it has been shown that stability is assured when the domain of dependence of any forward point as given by the finite difference approximation to the characteristic equations is not less than the exact domain of dependence of the differential equation. In other words, with reference to Figure 3.5, the points L and R at the base of characteristic lines through point M are internal to the line (I+1)(I-1).

This is the so called Courant-Friedrichs-Lewy (CFL) condition, established by the three authors in 1928. For a fixed grid characteristics scheme, requires that:

$$\Delta t \leq \frac{\Delta x}{c+|u|} \tag{3.109}$$

Thus a Courant number C_r may be defined as:

$$C_r = \frac{(c+|u|)\Delta t}{\Delta x} \tag{3.110}$$

The time increment, Δt, is selected jointly on the basis of the Courant condition $C_r < 1$ and also on the basis of the shock velocity which is:

$$\Delta t \leq \frac{\Delta x}{W} \tag{3.111}$$

The latter ensures that the shock will travel less than the distance increment ; Δx or Δr, in one time step.

Δt is chosen as the lesser of the values determined from the Courant condition and the shock velocity condition at all grid points, multiplied by a Courant number of less than unity, the latter being chosen by trials.

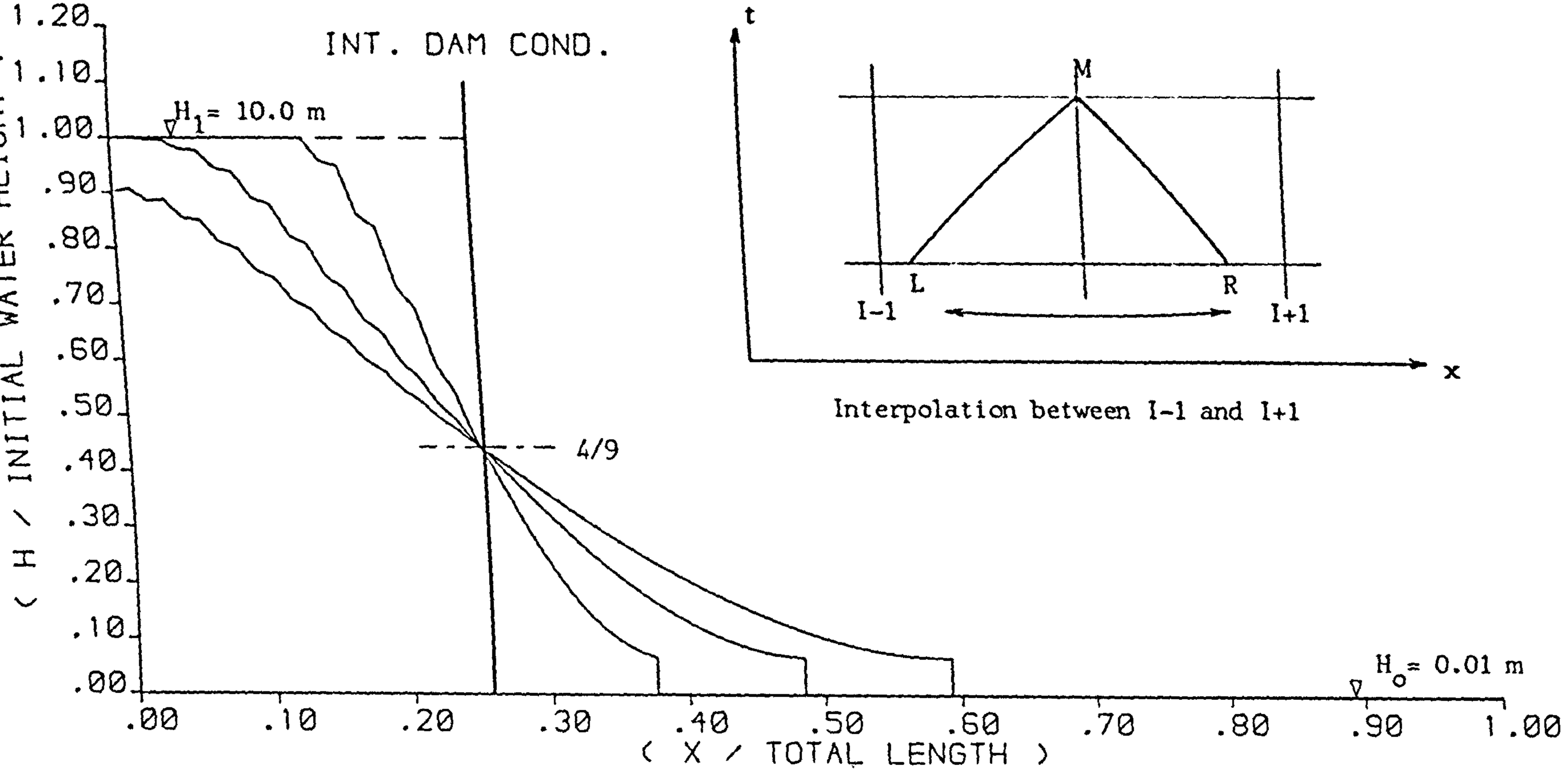

FIGURE 3.17 : DAM – BREAK PROBLEM WITH THE WATER SURFACE SHAPED AS THE SAW TEETH , AT TIME t = 0.725 , 1.45 AND 2.175 sec. , H_1/ TOTAL LENGTH = 10 .

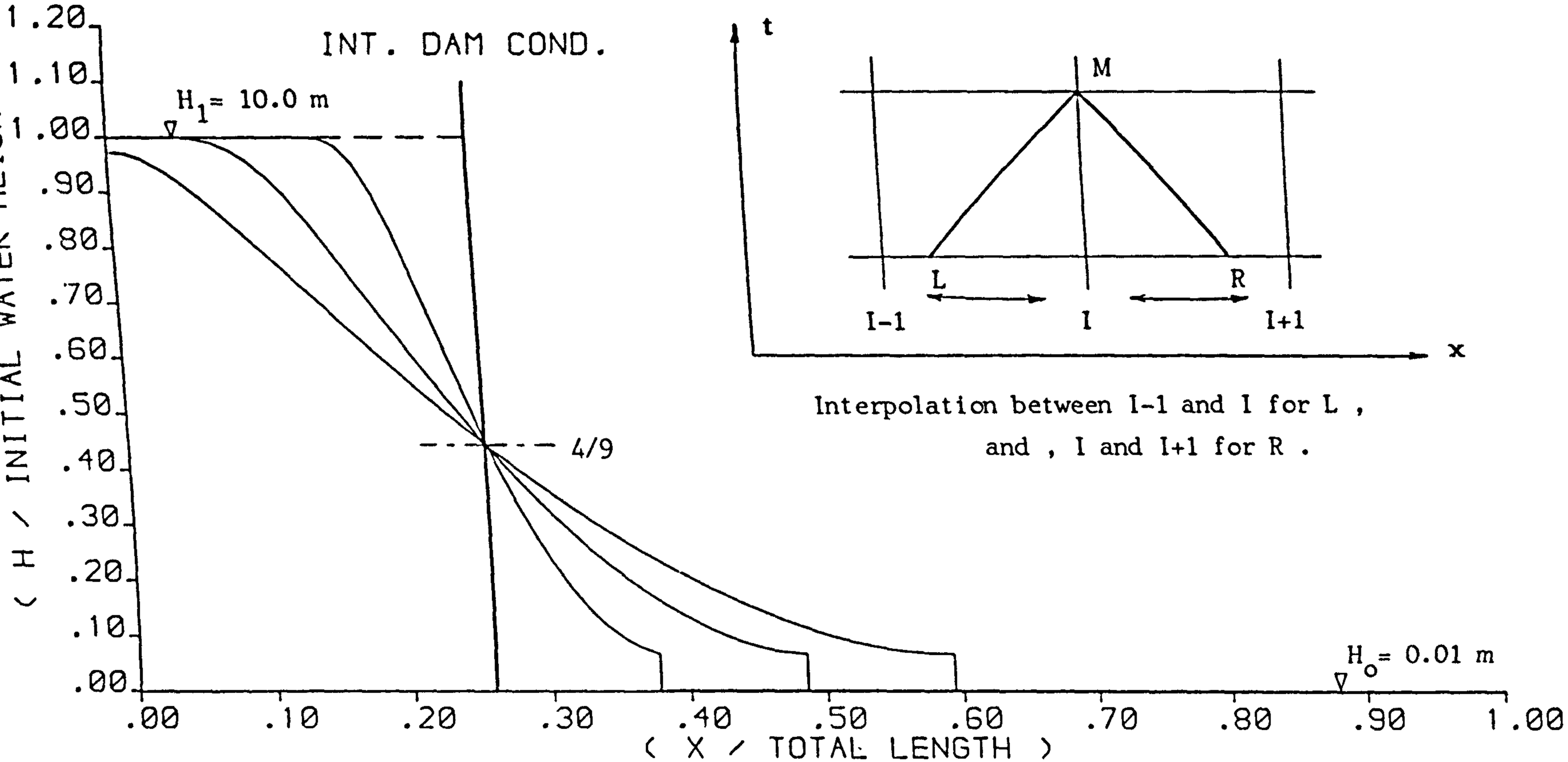

Interpolation between I-1 and I for L ,
and , I and I+1 for R .

FIGURE 3.18 : DAM – BREAK PROBLEM WITH SMOOTH WATER SURFACE , AT TIME t = 0.725 , 1.45 , and 2.175 sec. , H_1 / TOTAL LENGTH = 10 .

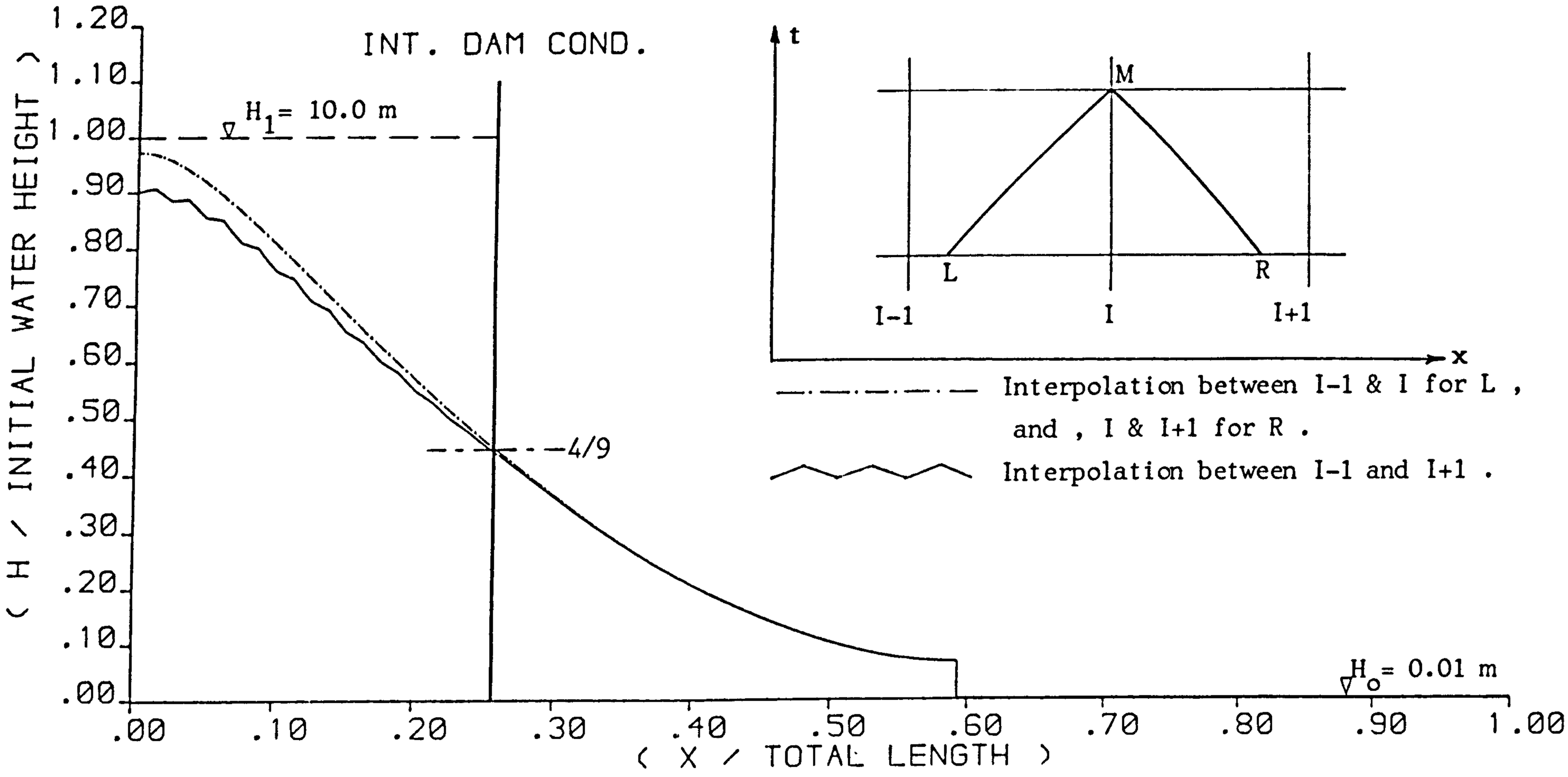

FIGURE 3.19 : COMPARISON BETWEEN THE SAW - TOOTHED SURFACE AND THE SMOOTH SURFACE , AT TIME t = 2.175 sec. , H_1 / TOTAL LENGTH = 10 .

CHAPTER FOUR

APPLICATIONS OF THE NUMERICAL TECHNIQUE

4.1 Introduction

Arising from the last chapter, two primary numerical models and three others for computing dam-break flood waves have been developed in this thesis. These models are based on the characteristics method together with the shock fitting method.

Before describing the models, common features are presented in section 4.3. These are:- the basic assumptions made in the development of the numerical models; the solution of the singularity at time (t=0) in order to start the computation; the calculation of specific points in the flow domain (like upstream and downstream boundary points, and supercritical points); the Colebrook-White (C-W) resistance formula; the negative wave characteristics.

Following the above are two sections, each describing primary situation. These are the plain channel (parallel sides) in X-T space and the expanded channel (divergent sides) or the contracted channel (convergent sides) in R-T space, together with the numerical results for each. Combinations of these primary cases lead to three further models which will be discussed, both physically and numerically, in Chapters five and six.

4.2 Definition of Dam-Break

Sudden destruction of a dam can result in a highly unsteady flow, with a forward wave advancing over a dry or a wet channel and

a back disturbance propagating into still water above the dam. Thus the dam-break problem in its simplest form is the determination of flow profiles resulting from sudden release of water initially held at rest behind the dam wall. The forward and backward waves are generally called positive and negative waves respectively. In the physical world the situations belonging to this category include the flash flood resulting from dam failures, collapse of the water column created in the atmosphere by an underwater explosion and the runoff in a step channel after rapid and intense rainfall on an impervious surface. In this work, a dam is supposed to be suddenly and completely destroyed at zero time. The problem is then to determine the subsequent motion of the water along the channel length x or (r) and for all time t.

4.3 Development of the Numerical Model

4.3.1 Basic Assumptions

The basic assumptions follow those usually made in numerical models of dam-break problems, namely:-

A. Flow Conditions:

1. One-dimensional flow (no transverse waves).
2. Shallow-water wave theory (neglecting vertical acceleration).
3. The flow velocity is uniform in a transverse section, i.e., the velocity-distribution coefficients are equal to unity.
4. No air entrainment.

B. Initial Conditions:

1. Instantaneous release of water initially at rest.

2. (i) Dry-bed downstream of release opening.

(ii) Wet-bed downstream of release opening.

3. No effect of release method on the outflow.

C. Channel Conditions:

1. (i) Prismatic, impermeable channel.

(ii) Non-prismatic, impermeable channel.

2. (i) Infinite reservoir extending upstream.

(ii) Bounded reservoir extending upstream.

3. No lateral inflow or outflow.

4. Boundary roughness is expressed by Barr's (1976) generalisation of the Colebrook-White (C-W) function.

4.3.2 Singularity at Time (t=0)

Referring to Figure 4.1(a), the discontinuity in the water depth H at the dam position when the time (t=0) prevents the starting of the numerical solution precisely at time (t=0). This singularity in the solution was solved by starting the computation at some later time (t > 0). In order to do this the analytical solution of Ritter (1892) may be used to give the starting flow profile at that time (t > 0). Although employed by many investigators, Ritter's solution has been shown to express the positions of the water surface only at high time values ($t\sqrt{g/H_1} > 2$) approximately [Martin (1983)]. This leaves some doubt as to the early time computation on that basis and a different approach is used in this work which depends on Stoker's theory (1957).

When the dam is destroyed a shock wave develops on the downstream

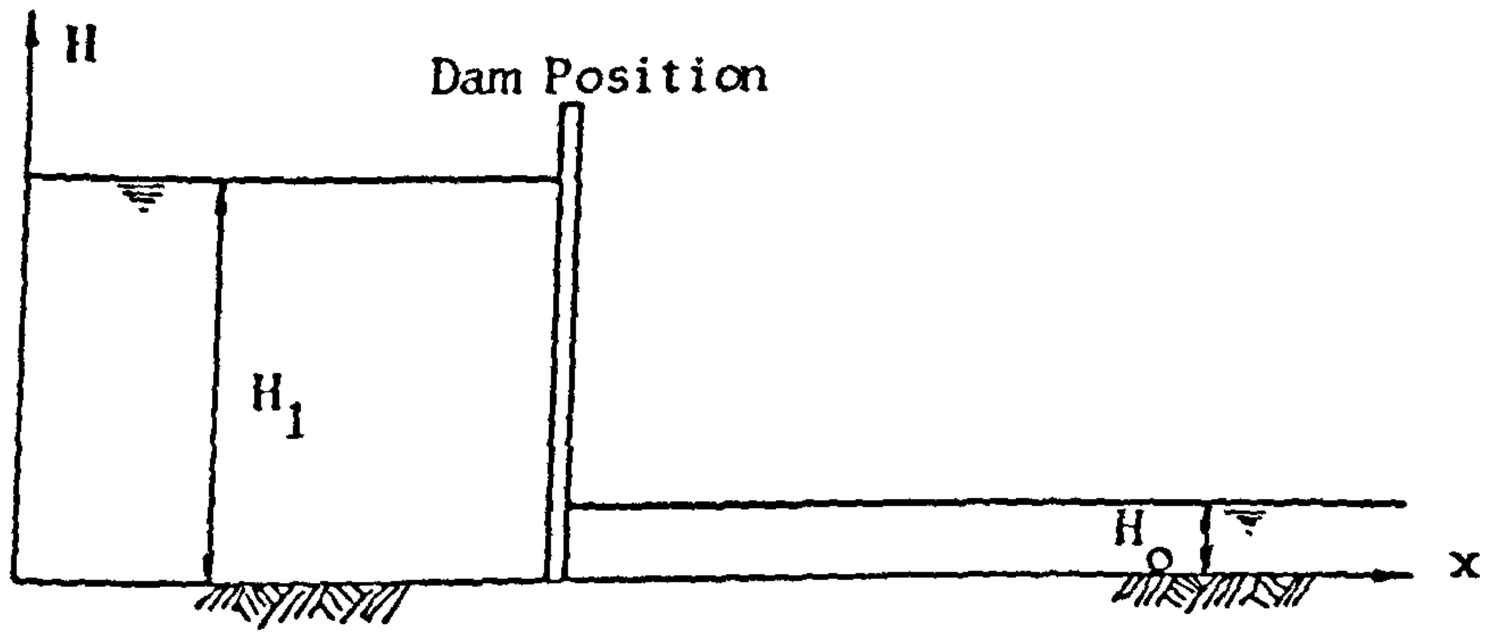

(a) Water Depth Discontinuity at Time t = 0

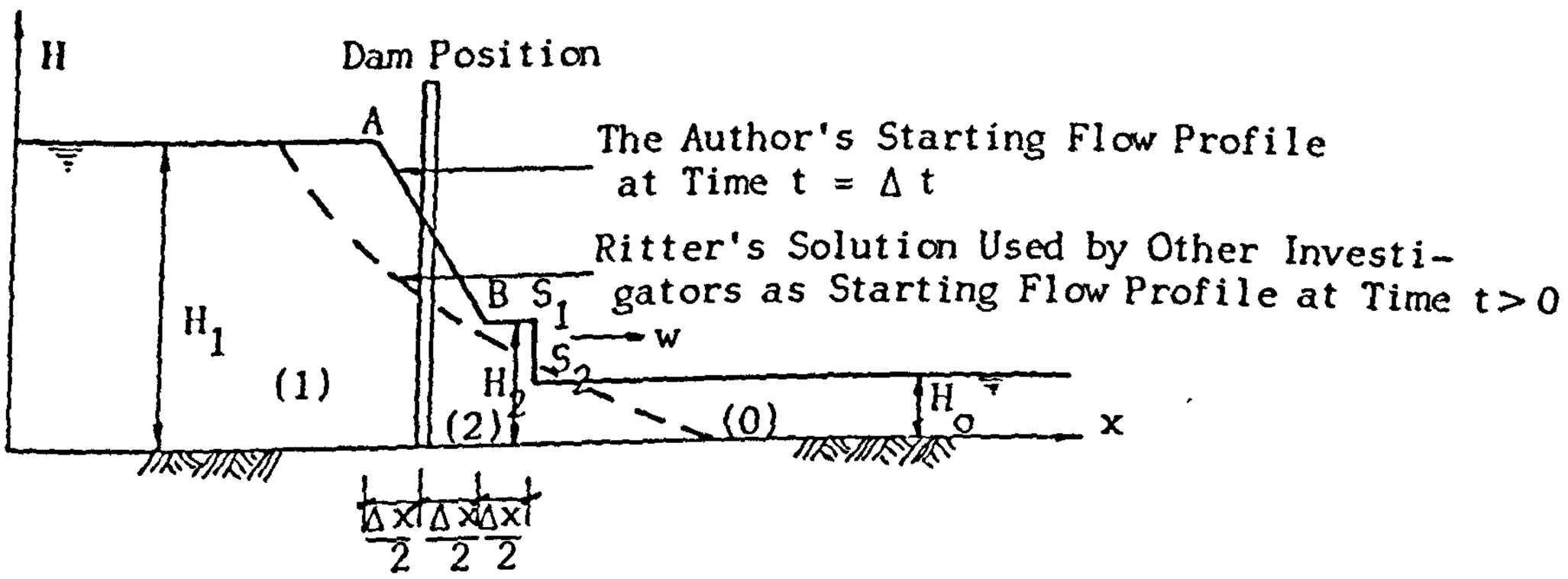

(b) Water Position at Initial Time t

The horizontal displacement is exaggerated.

Figure 4.1 : Singularity and Its Solution at the Initial Time

side arising from the downward vertical acceleration of water upstream. In fact, since all the water at the dam position instantaneously acquires a velocity different from zero, the shock will also be created instantly on the downstream side. On this basis, the initial conditions are posed as shown in Figure 4.1(b).

In order to start the numerical solution, at a very small time

(t=Δt) the water column is assumed to be tilted from the vertical with a shock moving downstream and a negative wave upstream. Depending partly on Ritter's solution, the author is assuming that the shock will travel a distance downstream which is twice that covered by the negative wave upstream in the same time. Therefore, at time (t=Δt), the negative wave moves ($\frac{1}{2}$ Δx) while the shock will move Δx as indicated in Figure 4.1(b). In this case, there are three unknowns; the shock velocity w, the shock depth H_2 and the water velocity u_2 just behind the shock. For given conditions upstream and downstream of the dam (u_1, H_1, u_o, and H_o) the values w, H_2 and u_2 may then be calculated according to Stoker's theory (1957) connecting state (2) with state (1). Since the quantity (u+2c) is a constant along the straight characteristic between the two states, it follows therefore that:

$$u_2 + 2c_2 = u_1 + 2c_1 \qquad (4.1)$$

or

$$u_2 + 2\sqrt{gH_2} = u_1 + 2\sqrt{gH_1} \quad \text{while } c = \sqrt{gH} \qquad (4.2)$$

Together with the shock equations from chapter three; (3.69) and (3.71),

$$w = \frac{u_2H_2 - u_oH_o}{H_2-H_o} \qquad (4.3)$$

and

$$(w-u_o)^2 = \frac{gH_2}{2H_o}\ (H_o+H_2) \qquad (4.4)$$

Thus Stoker's solution, i.e. equations (4.2) through to (4.4), allows the determination of the depth H_2, propagation speed w, and the velocity of water u_2 just behind the bore. In order to cover any given conditions for the states (1) and (0), u_1 and u_o are left in the equations (4.2) through to (4.4). With still water upstream and downstream (u_o=u_1=0) explicit solution of the three equations is possible for all values of the ratio (H_o/H_1) between zero and one. In this way w, u_2 and H_2 can be found a short time after the initial singular condition, in order to start the general computation.

Referring to Figure 4.1(b), the points A and B are two adjacent grid points, i.e. there is no grid point at the dam position. This is to prove that there is no special condition at the dam and that the numerical model gives results which agree with the condition at the dam position, as stated by the analytical solution. This will be shown in section 4.4.1. The water depth and the velocity at point A are H_1 and u_1 and at point B are H_2 and u_2 respectively. At the shock points S_1 and S_2 the water depth and the velocity are H_2, u_2 and H_o, u_o respectively.

The shock moves to a new position (say S') during the next time step Δt. To obtain an estimate of the new position S', the shock velocity w at point S is used. The calculation at point S' was described in section 3.4.4 whilst the rest of the grid points are treated normally by the characteristics equations as illustrated in section 3.3.1. Variations occur at certain points in the interpolation process as explained in the next section.

4.3.3 Interior Points

To avoid the time consuming iteration which arises in the case of non-linear interpolation, linear (or first-order) interpolation is employed as already formulated in Chapter Three. Thus care must be taken to choose the correct pair of adjacent grid points, when interpolating the values of x_R, u_R and c_R for subcritical and supercritical flow, as shown in Figure 4.2. However, interpolation

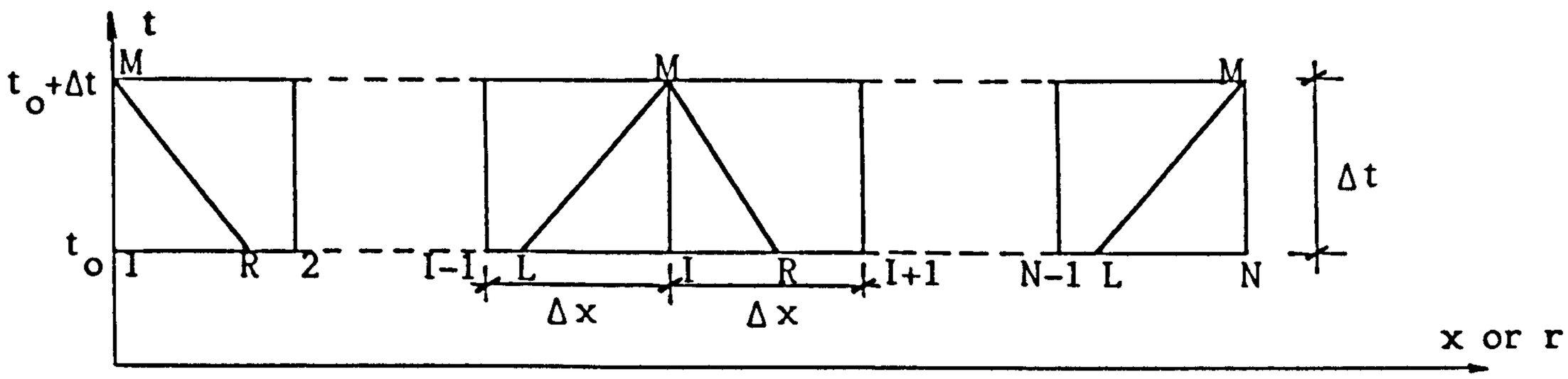

(a) Subcritical Flow

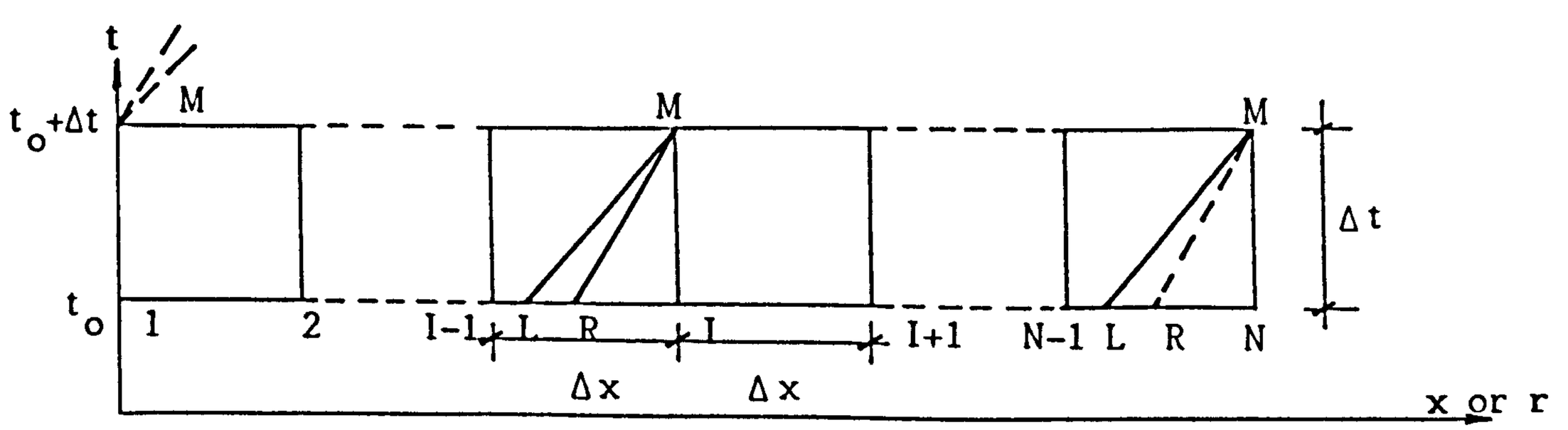

(b) Supercritical Flow

Figure 4.2 : Characteristics on a Specified-Time-Interval Grid Net in One-Dimensional Flow

of x_L, u_L and c_L is the same both for subcritical and supercritical flow. To test which pair of the two adjacent grid points should be used in the interpolation of x_R, u_R and c_R, the following procedure

is carried out:

1. Use the two grid points (I-1) and (I+1) to interpolate the two points L and R in order to find M, since the interpolation between these two grid points is the same for subcritical and supercritical flow points.

2. Compute the Froude number at point M.

3. Make a choice between the left and right pair of the grid points, depending upon whether the Froude number so computed is greater than or less than unity. Then the values at point M will be found according to the last interpolating pairs of the two adjacent grid points.

In case of bounded reservoir upstream and bounded channel downstream the boundary conditions upstream and downstream are functions of the dependent variable H (or c) only, since the velocity u is zero. Hence there is only one characteristic line from each boundary point M extended backward in time for both subcritical and supercritical flow as illustrated in Figure 4.2. From this characteristic line the only unknown H (or c) can be found.

For reservoir and channel both extending infinitely, upstream and downstream respectively, the boundary conditions are functions of the two dependent variables H (or c) and u. Also there is only one characteristic line from each boundary point M extended backward in time when the flow is subcritical. There are two unknowns and only one characteristic line at the boundary points M. The solution is possible if there is a special condition at the

boundary, such as a specified discharge. Also it is possible to apply the mirror image concept [Chowdhury (1982)] as described in

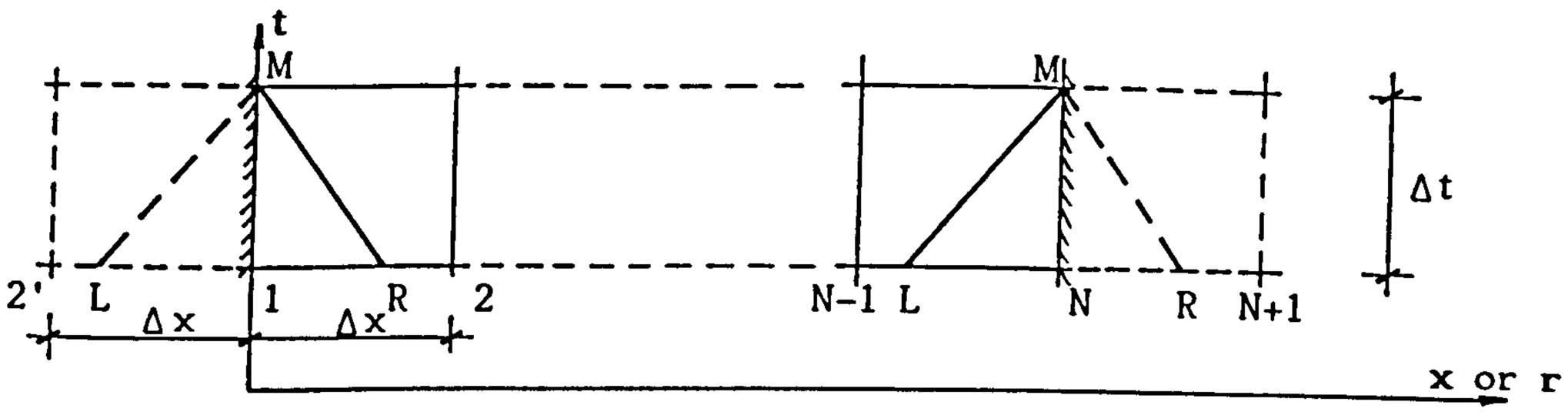

(a) Subcritical Flow

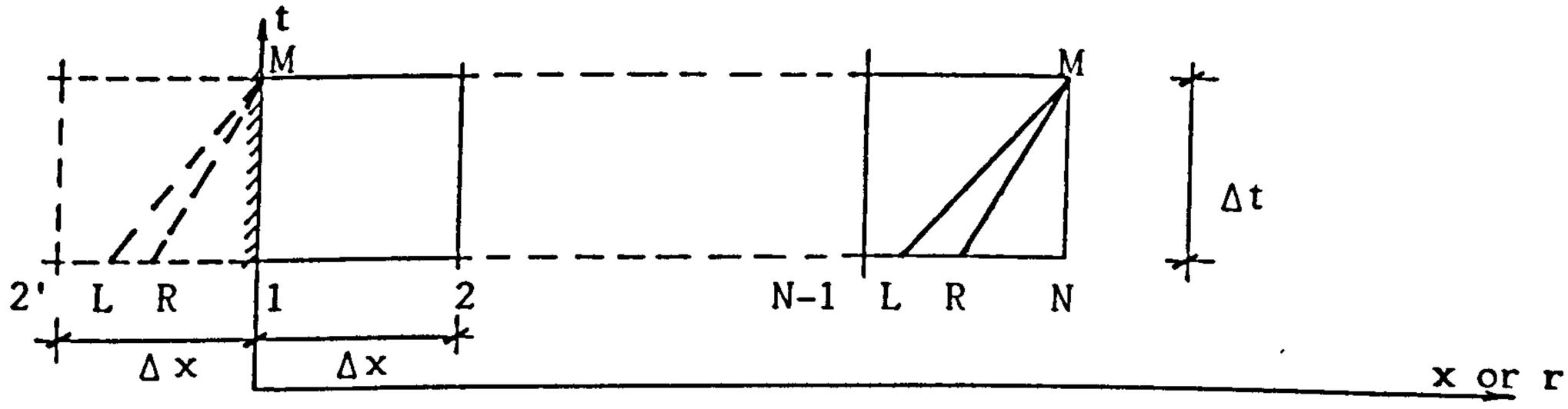

(b) Supercritical Flow

Figure 4.3 : The Mirror Image Concept at the Boundary Points

Figure 4.3(a). An imaginary domain at the outer side of the boundary is assumed and at the same time a flow field is introduced to the imaginary domain whose depth and velocity are reflections of those on the real domain. Thus, for the left boundary

$$u_{2'} = -u_2 \quad ; \quad H_{2'} = H_2 \tag{4.5}$$

and for the right boundary

$$u_{N+1} = -u_{N-1} \; ; \quad H_{N+1} = H_{N-1} \tag{4.6}$$

Then the solution at point M in each boundary is possible.

For supercritical flow there are two characteristic lines from point M at the right boundary, so there is no need to the mirror image concept since the two lines are on the real side as shown in Figure 4.3(b). While, at the left boundary there is no characteristic line at the real side and the mirror image is not appropriate. Both variables must then be specified independently since they are unaffected by changes within the problèm area.

In fact , the mirror image concept appears simply as an elaborate technique for setting u=0.

4.3.4 Boundary Resistance Formula

In the past, considerations of simplicity in mathematical manipulation have led either to the Chezy formula or to the Manning formula in terms which represent the unsteady frictional resistance. The only attempt (to the best knowledge of the author) to apply the generalised Colebrook-White (C-W) resistance formula in the dam-break problem was made by Das (1978) and Barr and Das (1980). After an extensive review of the existing resistance formulae by Das (1978), the Colebrook-White function, as generalised by Barr (1976), was chosen to assess the range of effect of resistance. In such a form this generalisation is explicit for friction factor and generates appropriate transition routes for different resistance types. The advantage of using the Colebrook-White function, as opposed to the use of the Manning or of the Chezy type, is that the latter cannot be held to deal with other than totally rough turbulent

flow on any consistent basis. This is particularly relevant where comparisons are to be made with unsteady flows at laboratory scale. Therefore the Colebrook-White function continues to be appropriate for the resistance term in the present work.

The direct application of the Colebrook-White formula is implicit for friction factor λ . An explicit approximation to this transition formula was given by Barr (1973).

The generalised Colebrook-White resistance formula adopted here is:

$$\frac{1}{\sqrt{\lambda}} = 2.\text{Log}\left(\frac{3.7d_e}{K}\right) - 2A\ \text{Log}\left\{\left[\text{Log}^{-1}\left(\frac{2H}{ER_{**}^{W}+1}\right)\right]^{1/A} + \left(\frac{3.283}{R_{**}}\right)^{1/A}\right\} \qquad (4.7)$$

where d_e is the equivalent diameter of the open channel, replacing pipe diameter, which is given by four times the area of flow divided by the wetted perimeter; K is the Nikuradse's equivalent sand roughness size, R_{**} is an approximation for the roughness Reynold's number R_*, and A,E,H,W are the indices and constants required for control of the transition route to match experimental evidence. By definition:

$$R_* = \frac{\sqrt{\lambda}}{8} \cdot \frac{1}{d_e/K} .R \qquad (4.8)$$

where R is Reynold's number ud_e/ν and for explicit calculation

$$R_* \simeq R_{**} = 0.2149\ \frac{Q^{0.89}K}{\nu^{0.89}d_e 1.89} \qquad (4.9)$$

where Q is discharge and ν is kinematic viscosity. The friction slope S_f appearing in the characteristic conditions is then given by

$$S_f = \frac{\lambda u^2}{2gd_e} \qquad (4.10)$$

4.3.5 Negative Wave Characteristics

Referring to Figure 4.4 (at the end of the chapter) it appears that numerically obtained depth profiles approach the horizontal tangentially. This is not theoretically true since the negative wave front represent a discontinuity in the slope of forward characteristics emanating from the undisturbed zone in the reservoir. The depression wave front is therefore, in theory , a discontinuity in the slope of the depth profile. Evidently an interpolation across it is incorrect as illustrated in Figure 4.5. In order to find the dependent variables at point M, the values of u and c must be known at points L and R by interpolating between the grid points as explained in Chapter Three. In the case of a negative surge, point L would be on the wave path and not on the grid line; therefore the interpolation should be along the wave path.

The view was taken that a more precise computation of the negative wave would lead to an excessively complicated and time-consuming model. It seemed likely that any error in the negative wave would be confined to the upstream grid point and small in the context of the entire flood wave computation.

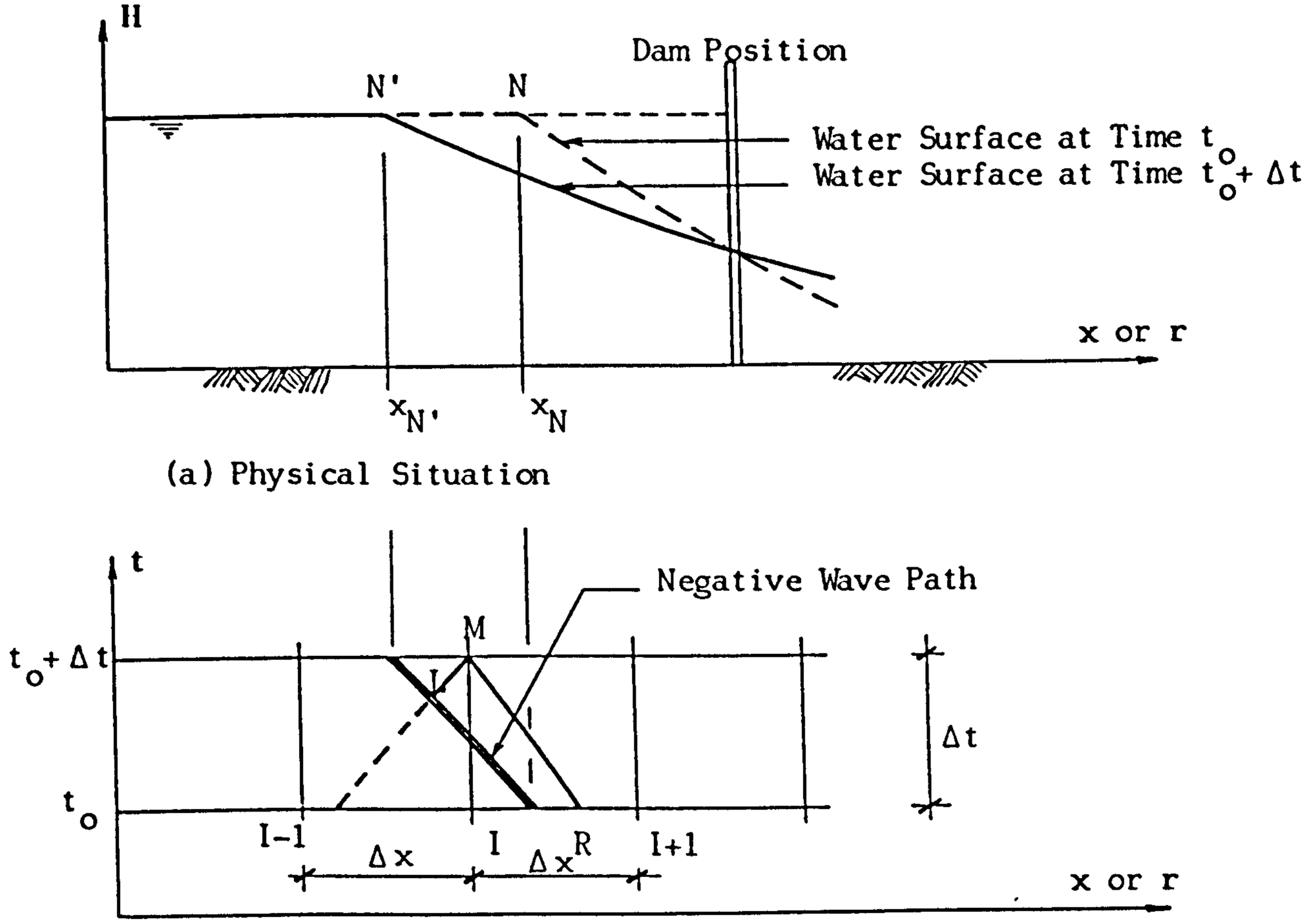

Figure 4.5 : Discontinuity Manifest in Negative Wave Propagation and Smoothed Numerically

According to Chen (1982), a comparative computation of the negative wave supported this view. Here, further evidence is given by the comparison made between the author's (X-T) numerical model and Ritter's solution, as shown in Figure 4.6. Linear interpolation is used between two adjacent grid points [i.e. between (I-1) and I one hand and I and (I+1) on the other]. The space increment, Δx, was chosen to give a reasonably large total number of grid points (N=81) along the entire computational line (being the total distance occupied by the reservoir and the downstream channel

of 100 m). The initial upstream water depth H_1 was 10.0 m and the fictitious downstream water depth H_o was 0.001 m so as to simulate the dry bed.

Figure 4.6 shows a good agreement between the numerical model and the analytical solution, but some smoothing of the numerical depth profile appears at the upstream end of the reservoir. In order to reduce this effect a fine mesh spacing seemed necessary on the reservoir side only rather than throughout the entire flow. A number of numerical experiments were conducted with (1/2 Δt) and (1/3 Δt) chosen as time increment in the reservoir while Δt was the time increment in the downstream channel side as usual.

Figure 4.7 demonstrates how an interface separates the two regions of different mesh sizes Δt and (1/3 Δt). The stability consideration would, in general, limit the overall time step to that for the region with the smaller Δx (say $\Delta x'$). We can, however, calculate points in the two regions at different time steps, each being governed by the stability condition in its own region. Points in the interior of the regions may be calculated in a straightforward manner whilst the only difficulties arise at the interface between them. We can see in Figure 4.7 that solution of point M_1 is normal, with L_1 being found by linear interpolation betweeen (I-1) and I, at time t_o, and R_1 similarly from I and (I+1), also at time t_o. However, we can proceed to point M_2 by obtaining L_2 by interpolation between (I-1) and I at time (t_o + 1/3 Δt) whilst still determining R_2 between I and (I+1) at time t_o. This process can continue during the total time of integration from t_o to (t_o + Δt). The rest of the

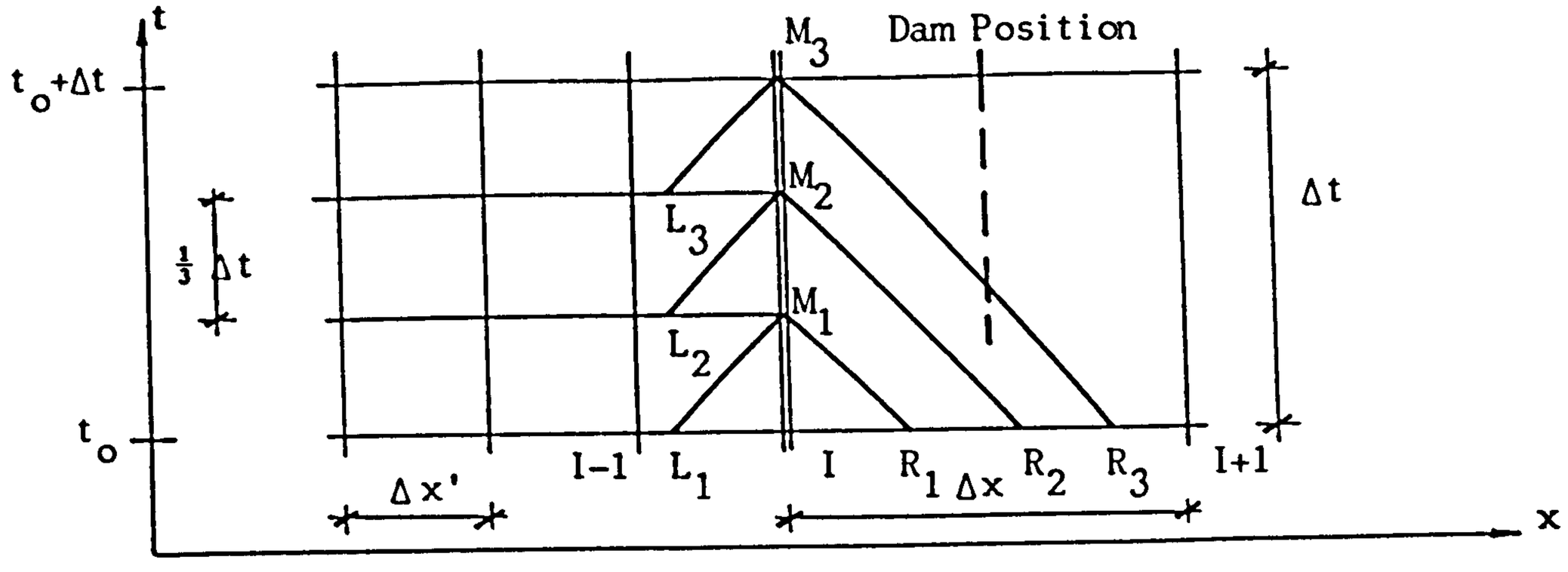

Figure 4.7 : Calculation at an Interface when the Time Step of the Integration is Not Equal in the Two Regions

points (I+1) and so on, at time ($t_o + \Delta t$), in the right-hand region may then be calculated so that the whole solution is determined at a common time and the process may be repeated.

This scheme is capable of extension to a multiplicity of regions in each of which the mesh size is the same but differs from that in neighboring regions by an appreciable factor. The time step of integration in each region is then calculated to give stability in that region and the region with smallest time step found. The calculations start in this region and the solution is built up to suit the smaller of the time steps required in the two adjacent regions. The solution in that region may then be calculated and this continues, at each stage building the solution up to the region with the larger time step until finally the whole solution is again obtained at a common time. This process results in a substantial economy of computer time when compared with the alternative of a large number of equally spaced points throughout.

Figure 4.8 is the numerical result from such an (X-T) model where the nested-grid is used. In the reservoir region the time step of (1/2 Δt) is used which makes the total number of the grid points (N) = 106. With a homogeneous increment a total of 81 were employed in the normal model whose results appear in Figure 4.6. Comparing the depth profile from the nested model with the one from Ritter's solution, in each case, indicates better agreement and less damping in the former than in the latter discretisation for the same problem. Trying another time increment for the reservoir region, which is (1/3 Δt), makes the total number of the grid points 128 as shown in Figure 4.9. A small improvement, only, in the profile took place which indicates that (1/2 Δt) is enough to improve the model.

Figure 4.10 is the result of a homogeneous step (X-T) model with large number of grid points. In order to improve the model rather more than with the nested-grid with (1/3 Δt) upstream, the number of the grid points must reach 401.

Comparing the depth profiles in the last four Figures; 4.6, 4.8, 4.9 and 4.10, is not easy since the differences are small. Therefore Figure 4.11 contains the four depth profiles which are, from top to bottom, the fine mesh for whole flow with total grid points 401, the nested-grid of (1/3 Δt) at the reservoir region with total number of grid points 128, the nested-grid of (1/2 Δt) with total grid points 106, and the moderate mesh with number of grid points 81. Clearly there is better improvement by using a universally fine mesh rather than a nested-grid but the difference is small while the time of computation is much greater. Also the difference between

the nested-grid of (1/3 Δt) and (1/2 Δt) is very small, confirming that the nested-grid of (1/2 Δt) is a reasonable compromise, keeping the computational time low.

The advantages of three point interpolation were indicated in section 3.5. To emphasise this, results from a model with two point interpolation are presented in Figure 4.12. This shows a large damping in the reservoir region together with the saw-toothed surface previously discussed in Chapter Three. The same conditions as in the original model (Figure 4.6) were applied except that the interpolation was between (I-1) and (I+1).

The use of a coarse grid in the reservoir is undesirable, despite some argument in its favour from the Courant condition, given a fixed overall time-step. The prior requirement of resolution is demonstrated in Figure 4.13. This indicates a large damping in the depth profile for the reservoir region where the distance increment is double the one in the downstream channel (i.e. $2\Delta x$). This makes the total number of the grid points 71.

As a general conclusion, to assume completely smooth negative waves is to over simplify. The nested-grid scheme with (1/2 Δt) upstream gives a good compromise with much lower computer times than the fine mesh scheme of (N=401) grid points. The ordinary model with a moderate number of grid points gives reasonably good results. Although a proper treatment of the negative wave requires further work, the present model provides excellent simulation of 90% of the flow profile and that in the main area of interest.

4.4 X-T Model

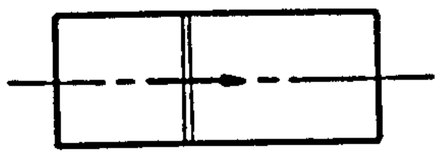

4.4.1 Typical Features of Numerical Results

Figure 4.14 represents a typical example of depth profile computations at different successive times (from 0.725 sec.to 4.350 sec.), with the initial water depth upstream of 10.0 m & downstream the negligibly small H_o = 0.01 m; in a rectangular, horizontal, and frictionless channel. A check calculation showed that mass was conserved with errors of less than 0.5 percent. The flow profiles all intersect the dam line very close to the height of $(4/9\ H_1)$ coinciding with that derived mathematically by Ritter. The computed velocity at this point also agrees with his value of $2c_1/3$.

The effect of bed slope is shown in Figure 4.15 where a succession of flow profiles are computed for times of (0.684-2.736 sec.). Conditions are the same as in Figure 4.14 but with a bed slope (S_o=0.02) and a smaller fictitious base flow depth = 0.001 m. An increase in frontal speed with a decrease in frontal height may be observed.

4.4.2 Comparison with Previous Works

Experimental data on the dam-break problem is required not only to allow full assessment of the numerical (X-T) model but also to justify extensions of the same principles in the development of the radial (R-T) model. According to the literature survey, there is hardly sufficient data to test the radial model thoroughly.

Experiments by Das (1978) had been previously conducted in the same Hydraulics Laboratory of this University and were obviously

appropriate. Two rectangular horizontal flumes had been used for the experiment. The larger flume was 110 ft (33.53 m) long, 5 ft (1.529 m) wide and 1.5 ft (0.457 m) deep. A plate, at 25 ft (7.62 m) from the upstream end, acted as a dam. The bed of the flume was made of steel plate plastered with white paint and had been taken to be hydraulically smooth.

The smaller flume was 14.5 ft (4.42 m) in length, 1.25 ft (0.381 m) in width and 0.65 ft (0.198 m) deep. As in the large flume, a gate was placed at 2.5 ft (0.762 m) from the upstream reservoir end to act as a dam. Thus the length of the reservoir of the small flume was 1/10ths of the length of the large flume reservoir. The flume was made of perspex. Experimental data on this flume was taken for both smooth and rough bed conditions. The roughnesses used were single and double layers of steel wire mesh. In both the flumes the gate was lifted manually at a sufficiently high speed to simulate sudden collapse.

Water depths with respect to time at different cross-sections of the flumes and the position of the front, with respect to time, for different configurations of upstream and downstream initial depths extracted from Das's experiments are compared with the (X-T) numerical model. The computed profiles for the large flume with smooth bed are compared with the experimental data and presented in Figures 4.16 to 4.31. The front trajectories are also compared and presented in Figures 4.24(B) and 4.29(B) to 4.31(B) for the same flume. Further profile comparisons are made for the small flume with two different rough beds; Figure 4.32 for single layer mesh (K=0.044 ft), and Figure 4.33 for double layers mesh (K=0.127 ft). Both profiles are

computed with computations incorporating the generalised Colebrook-White (C-W) function as resistance formula. In all the comparative plots of surface profiles and front trajectories, it is seen that there is good agreement between the (X-T) numerical results and the experimental data, with an average error of 4.51% for the surface profiles and 9.24% for the front trajectories. Another form of assessment of the (X-T) numerical model may be made by the comparison of stage hydrographs. The (X-T) numerical model is compared on this basis with the five mathematical models and experimental data from Katopodes and Schamber (1983). Two models are based on the Saint-Venant equations for open channel flow; the characteristic model and the integrated finite-difference model. Three others are the approximate flood routing models; the zero-inertia implicit model, the kinematic-wave characteristic model, and the kinematic-shock-profile model. The experimental data was obtained at the Waterways Experiment Station (WES) [U.S. Corps of Engineers (1960)]. In that study, a plastic-coated plywood flume of rectangular cross section was used to simulate the dam-break flood wave. The flume was 400 ft (121.92 m) long, 4 ft (1.22 m) wide, set on a ½% slope, and terminated in a free overfall (as mentioned in section 2.3.7). The model dam was 1 ft (0.305 m) high and was located in the middle of the flume, as shown in Figure 4.34. In the first series of experiments, identified as being in a hydraulically smooth channel, a Manning (n=0.009) was found to accurately represent the resistance characteristics. In the second series, identified as in a rough channel, the Manning n was found to vary significantly with depth and the value adopted for computational purposes was 0.05, which is very high. The bed resistance S_f was approximated by:

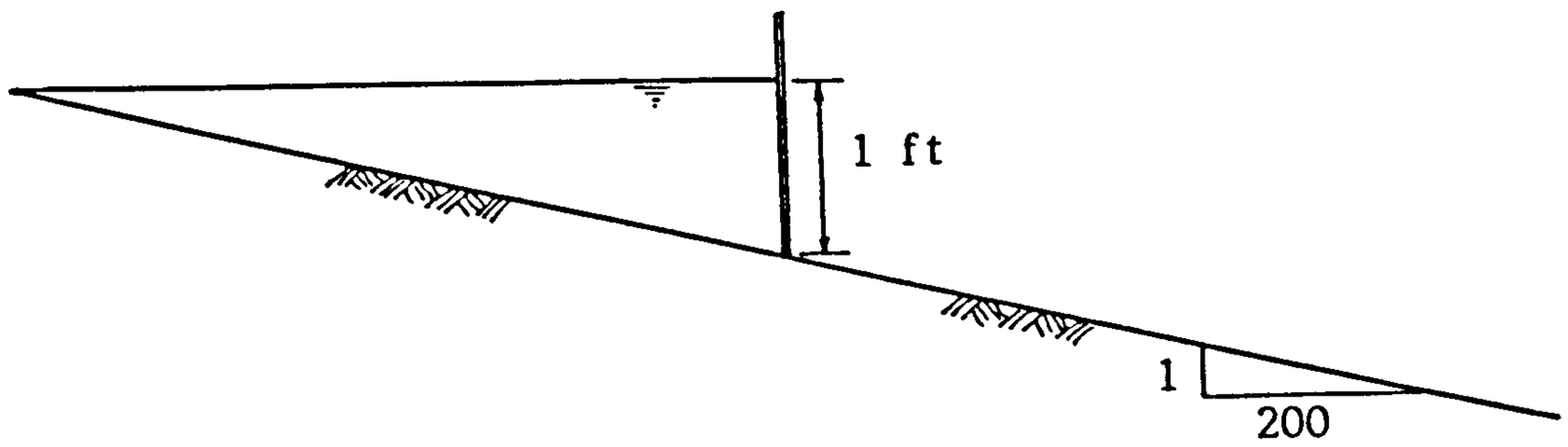

Figure 4.34 : Initial Depth Before Dam Burst

$$S_f = \frac{n^2 u^2}{C_u^2 R^{4/3}} \qquad (4.11)$$

where n = Manning coefficient of roughness, C_u = units coefficient (C_u=1 in the metric system, and C_u = 1.486 in the English system) and R = channel hydraulic radius.

Figures 4.35 and 4.36 show hydrographs computed by the (X-T) numerical model for the cases corresponding to both channels under full breach conditions, at two points 25.0 ft (7.62 m) and 150.0 ft (45.72 m) downstream of the dam site. Figures 4.37 and 4.38 show comparisons of the present (X-T) numerical model with the five models and the experimental data. It may be deduced that the present numerical model and the previous characteristic and integrated difference models yielded very close results, as may be expected since the three models were based on the same equations. Results from all dynamic models show a good agreement with the experimental (WES) data.

The present author has conducted some physical model tests of the (X-T) situation, whose comparison with the (X-T) numerical model will

be shown in Chapter Six. However sufficient confidence in the (X-T) numerical model had been gained from the above to encourage tests on the radial (R-T) numerical model which is developed next and on the same basis.

4.5 R-T Model

4.5.1 Convergent Sides

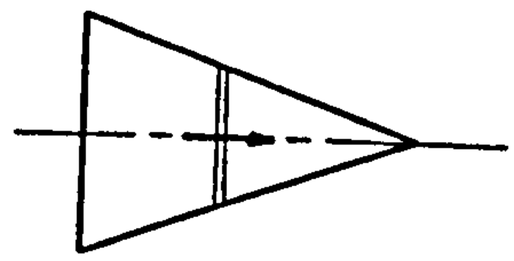

Referring to section 3.3.2, the main equations in characteristic form for radial flow through contracting channel, as shown in Figure 4.39, are:

$$\frac{dr}{dt} = u \pm c \tag{4.12}$$

and

$$[u \pm 2c]_1^2 = \int_{t_1}^{t_2} [\pm \frac{uc}{r} + g(S_o - S_f)]\, dt \tag{4.13}$$

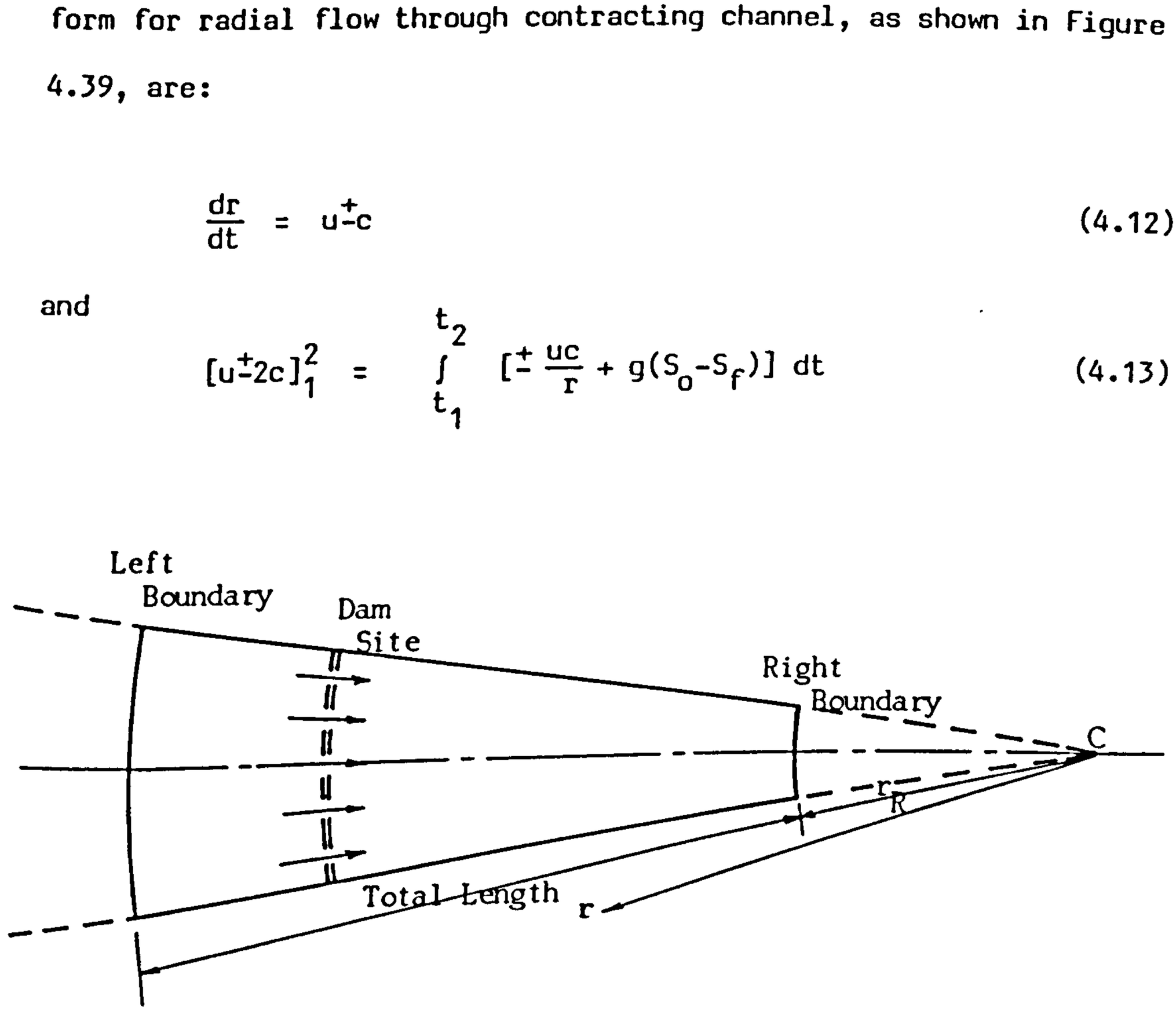

Figure 4.39 : Dam-Break in a Convergent Channel

Comparing the equations (3.58) and (4.13), the only difference is the

sign before the term $(\frac{uc}{r})$ which depends on whether the sides converge or diverge.

The flow converges towards the point C located at the extreme right of Figure 4.39. It may be anticipated that the radial movement causes both surface heights and mean velocities to <u>increase</u>; in Figures 4.40 to 4.46 are shown the effects of a contracting channel section having different values of r_R (the distance from the centre C). While the value of r_R increases from 0.0 to 400.0 m, the radial effect decreases until, when approaching $r_R = \infty$, the sides become parallel and the problem returns to that in (X-T) space. Figures 4.40 to 4.46 present the depth profiles for different times (from 0.684 sec. to 2.736 sec.) and for a depth upstream of the dam of 10.0 m and a 'fictitious' depth downstream of 0.001m. A clear comparison between the depth profiles for different values of r_R is presented in Figure 4.47 at 1.368 sec. and in Figure 4.48 at 2.736 sec. It may be seen that the depth profiles intersect the dam at heights <u>greater</u> than Ritter's ratio (4/9 H_1) but reducing to it for large values of r_R. The heights and velocities increase as the value of r_R decreases, which was expected.

In Figure 4.49 the present model for a contracting channel section has been applied to the conditions studied by Marshall and Menendez (1981) using the Random Choice Method (RCM). The initial conditions were; $H_o = 2$ m, $u_o = 0$ downstream of the dam and $H_1 = 10$ m, $u_1 = 0$ upstream of the dam. The flow converges towards the point located at the extreme left of the figure. The depth profiles are for time 150 sec., 300 sec., and 450 sec. Satisfactory agreement in the negative wave region (the reservoir region) can be observed. However,

the height and the velocity of the front, as predicted by this author are both less than those calculated by Marshall and Menendez. The error in mass conservation is less than 0.07%, in the (R-T) model, whilst larger errors appear to exist in a conservation check based on their results and presented in Figure 4.49(a).

4.5.2 Divergent Sides

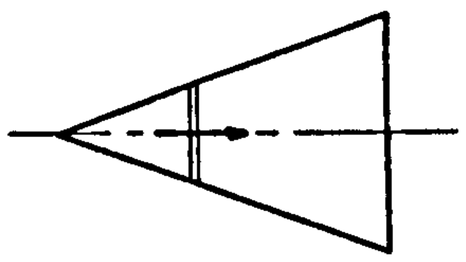

The main equations in characteristic form for radial flow through expanding channel, as shown in Figure 4.50, are:

$$\frac{dr}{dt} = u \pm c \tag{4.14}$$

and

$$[u \pm 2c]_1^2 = \int_{t_1}^{t_2} [\mp \frac{uc}{r} + g(S_o - S_f)\ ]\ dt \tag{4.15}$$

They are the same equations (3.57) and (3.58). Referring to Figure 4.50, the flow diverges from the point C located at the extreme left of the figure.

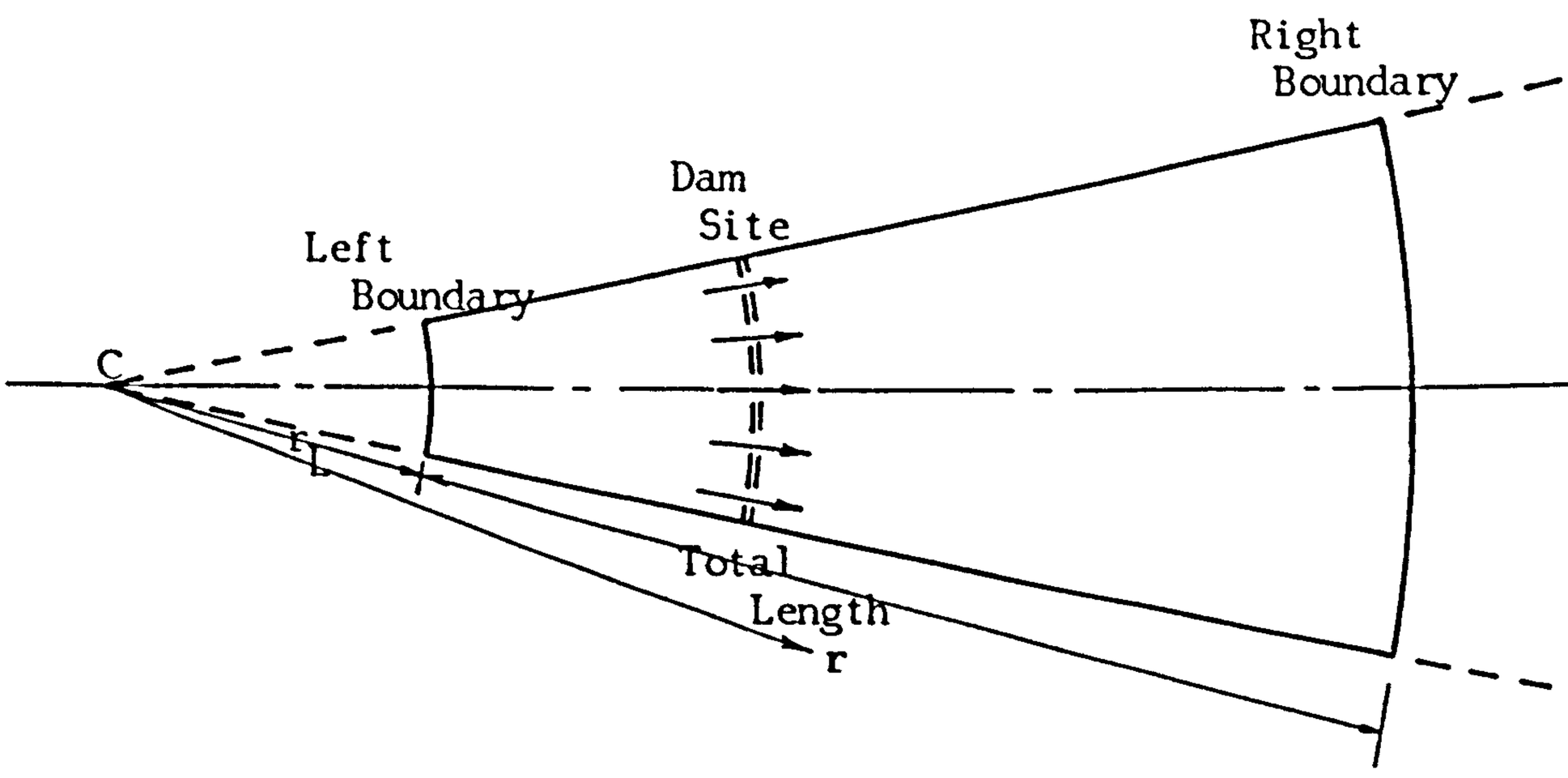

Figure 4.50 : Dam-Break in a Divergent Channel

Figures 4.51 to 4.57 show that the radial expansion causes the heights and the velocities to <u>decrease</u> when the value r_L decreases, where conditions are otherwise for Figures 4.40 to 4.46. As before, when r_L approaches infinity the sides become parallel and the problem returns to (X-T) space. The depth profiles presented in Figure 4.58 intersect the dam at heights <u>lower</u> than Ritter's ratio (4/9 H_1) and approach it for large values of r_L. Evidently the model of the expanding flow is consistent in predicting the converse of effects in the contracting case. The depth profile for a contracting section where r_R=0.0 is superimposed on Figure 4.58 and shows a clear transition from r_R=0, through r = ∞, to r_L=0 in both the contracting and the expanding cases. Smaller reservoir volume and a divergent channel in the expanding case cause a larger depression of the water depth profile by contrast with a smaller elevation of the profile for the contracting case at the same time. The contraction effects are emphasised at later times as shown in Figure 4.48 where the flow has increased upon reaching the narrower sections.

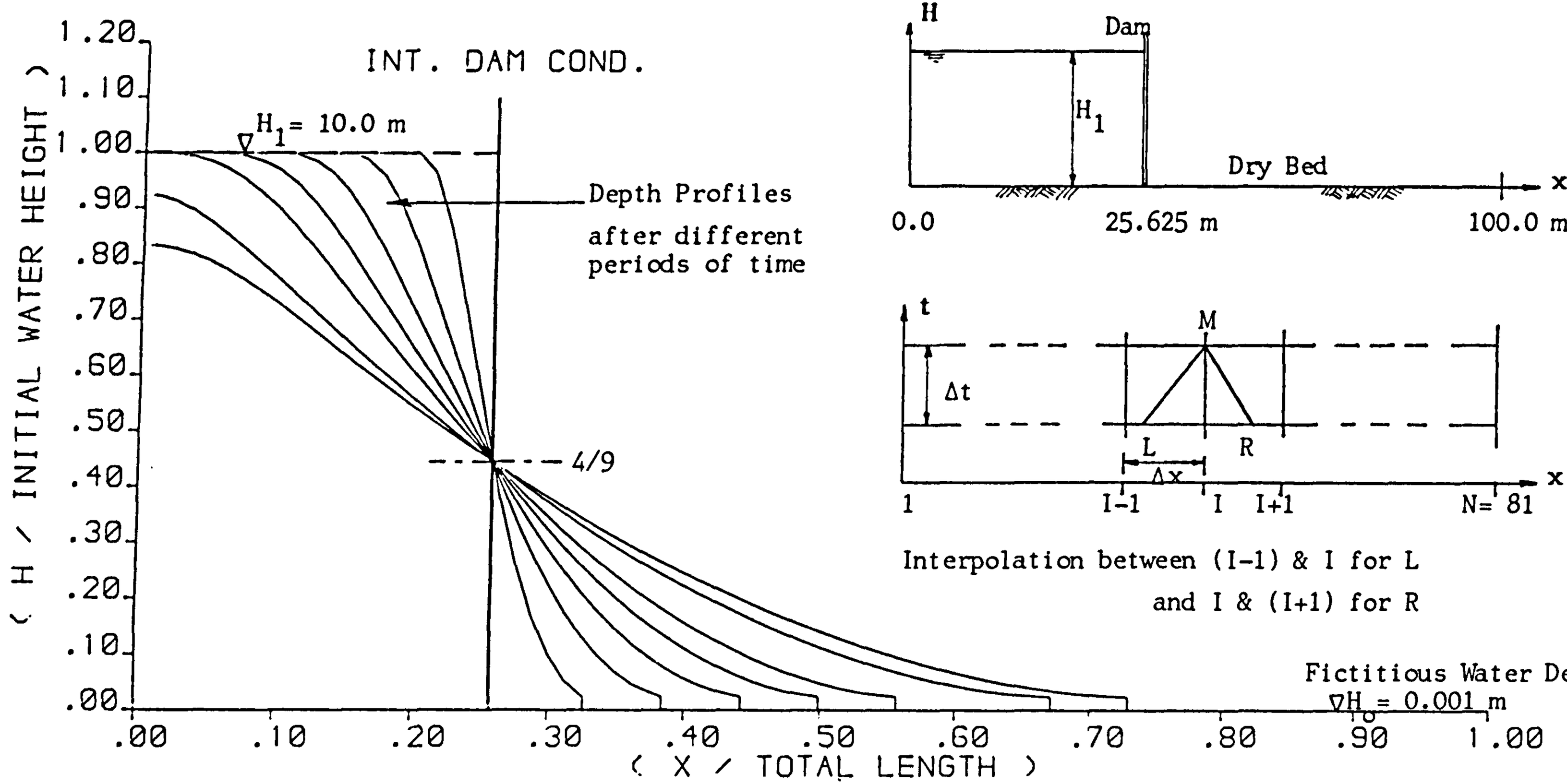

FIGURE 4.4 : DEPTH PROFILES APPROACH THE HORIZONTAL TANGENTIALLY , H_1 / TOTAL LENGTH = 10 .

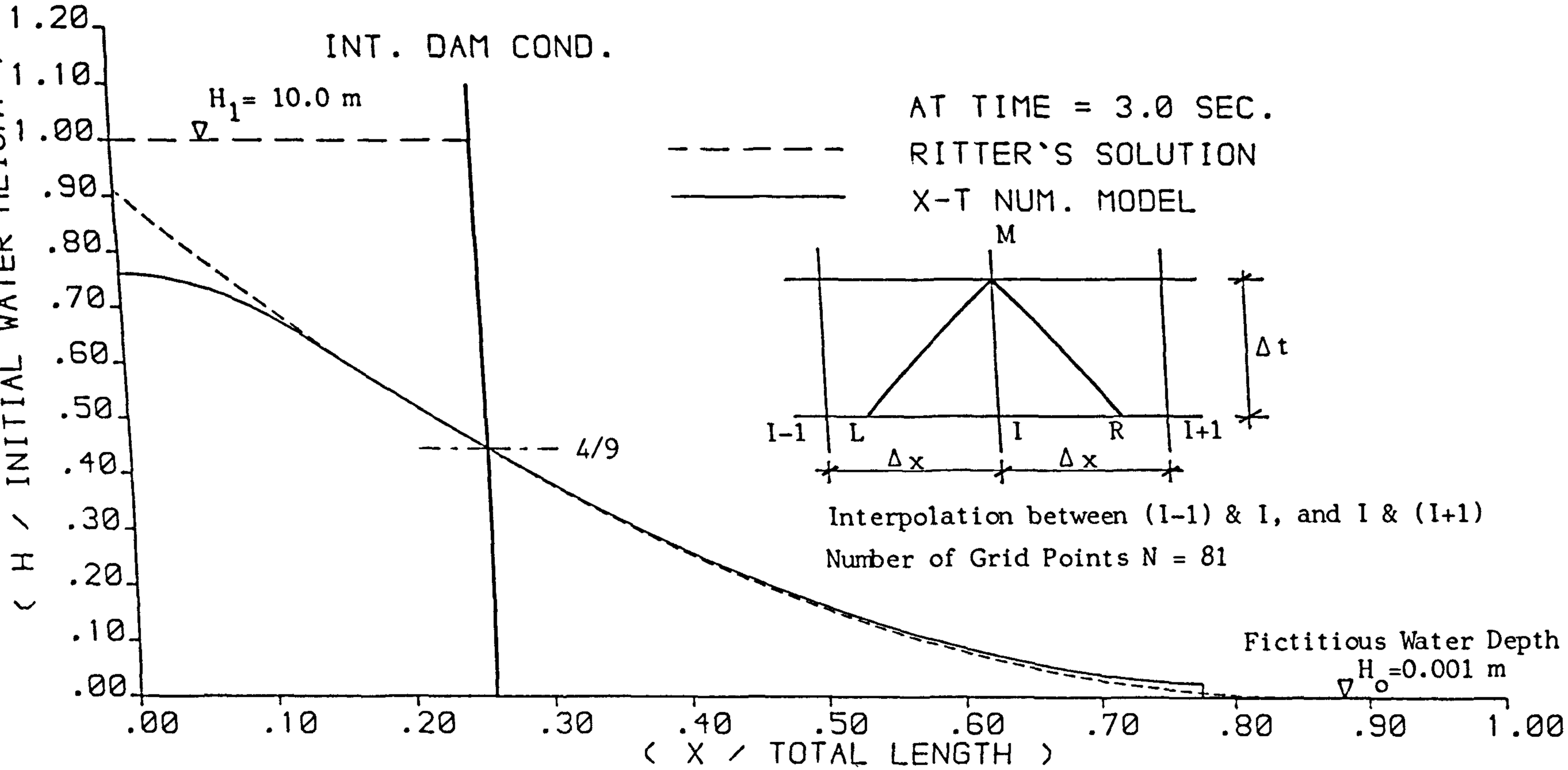

FIGURE 4.6 : COMPARISON BETWEEN THE NUMERICAL MODEL (X - T) AND RITTER'S SOLUTION , H_1 / TOTAL LENGTH = 10 .

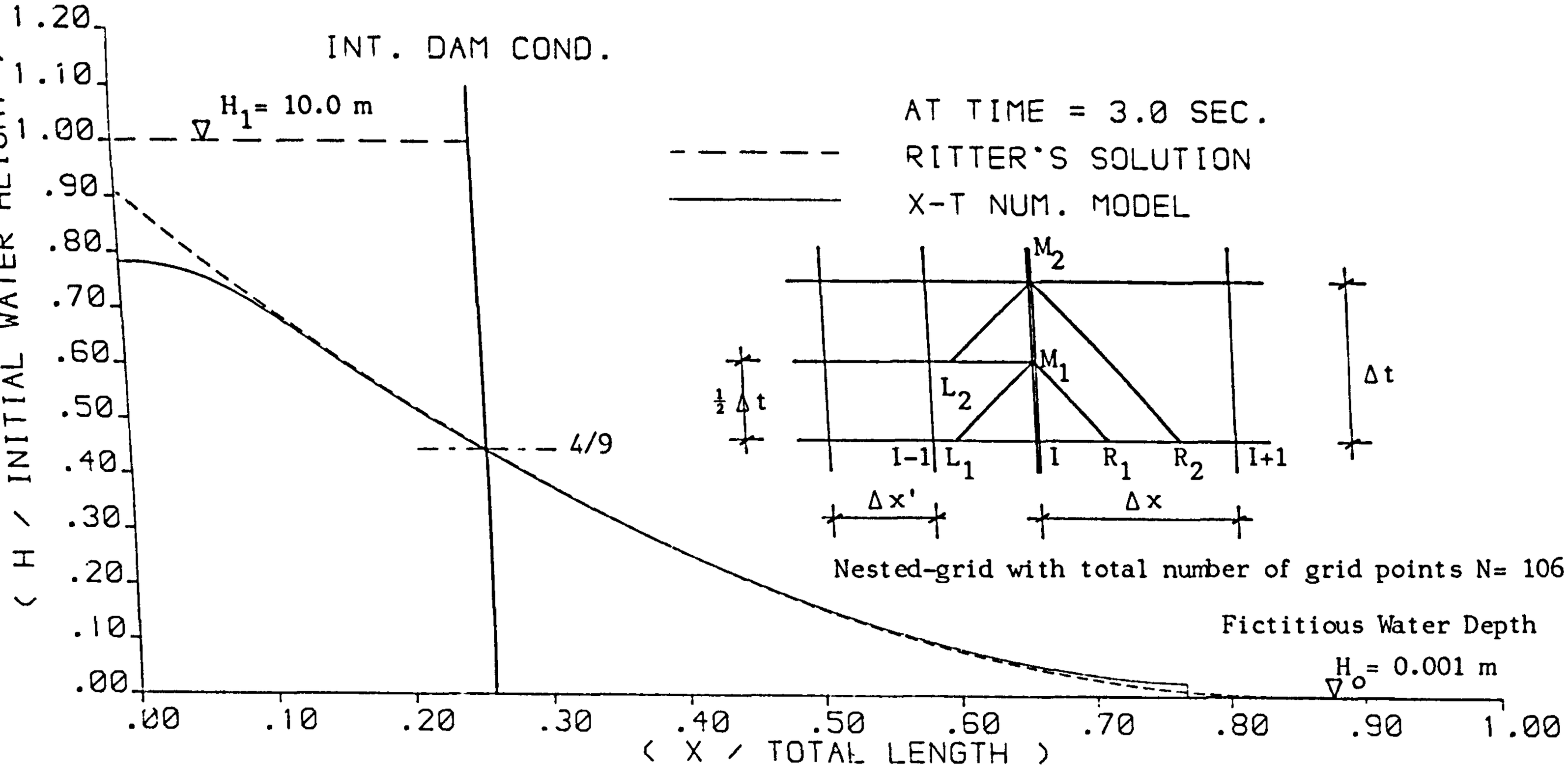

FIGURE 4.8 : NESTED – GRID MODEL WHERE THE TIME INCREMENT AT THE RESERVOIR IS $\frac{1}{2}$ THE TIME INCREMENT AT THE DOWNSTREAM CHANNEL , H_1 / TOTAL LENGTH = 10 .

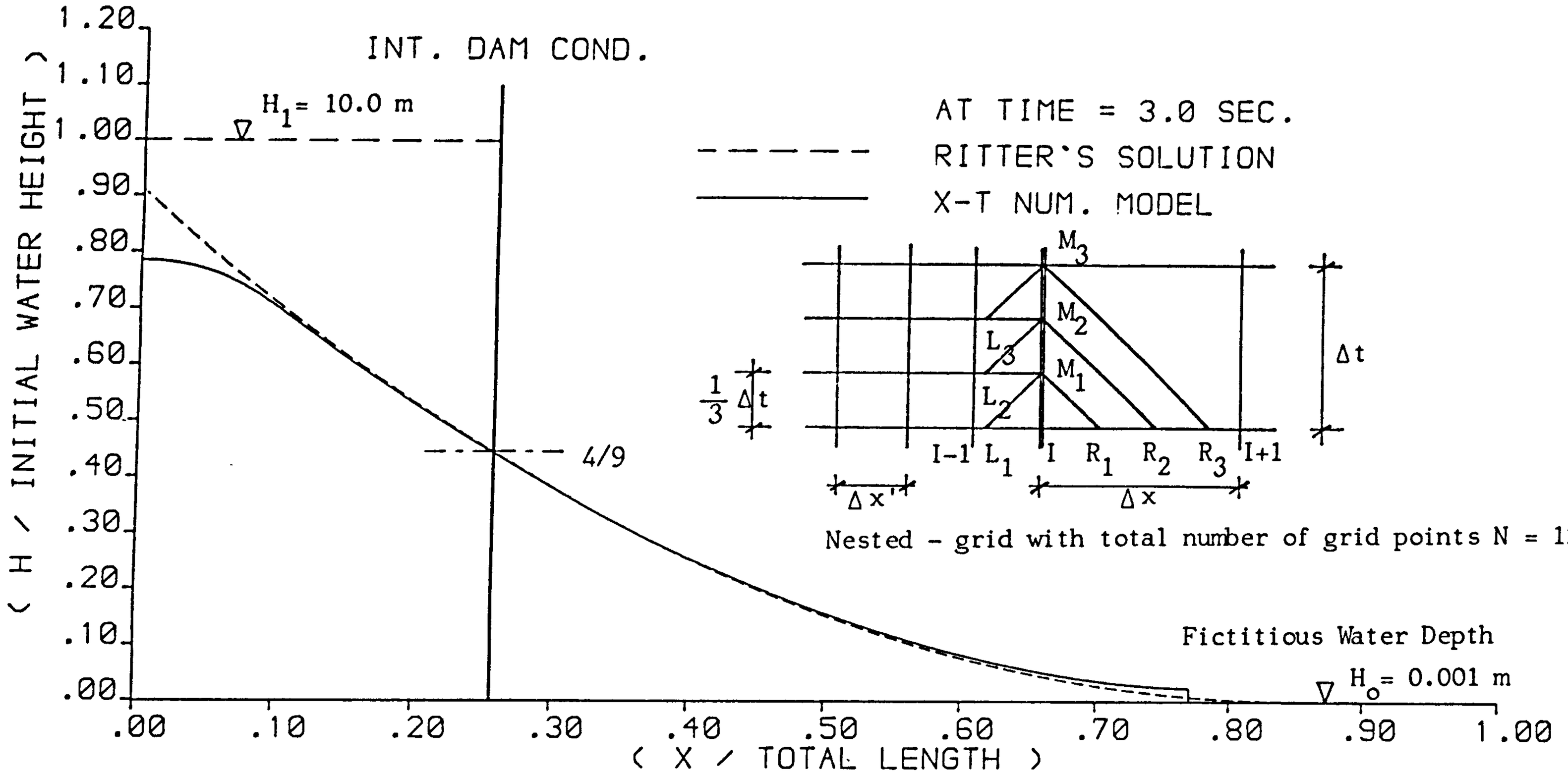

FIGURE 4.9 : NESTED - GRID MODEL WHERE THE TIME INCREMENT AT THE RESERVOIR REGION IS 1/3 THE TIME INCREMENT AT THE DOWNSTREAM CHANNEL , H_1 / TOTAL LENGTH = 10 .

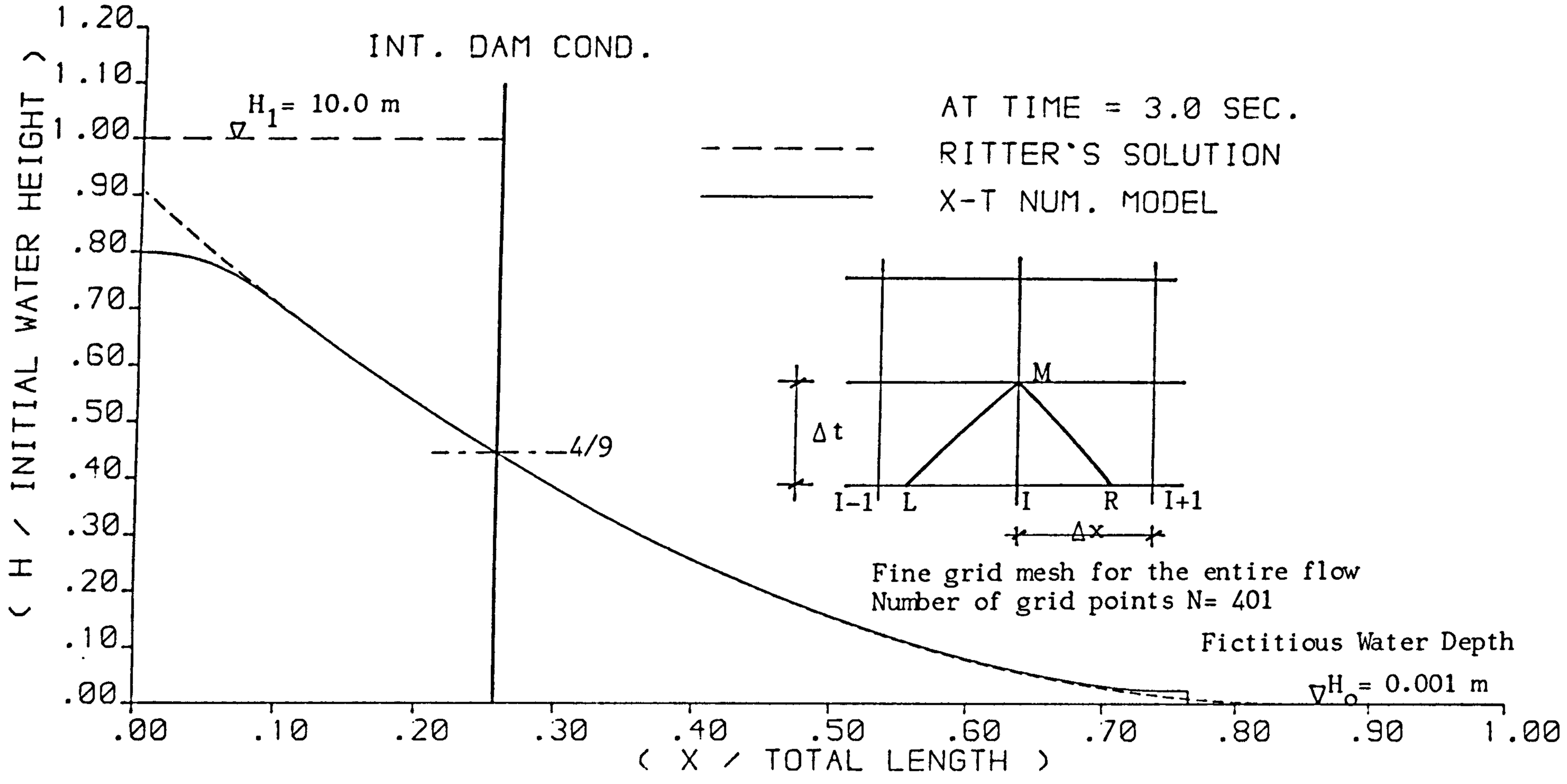

FIGURE 4.10 : X – T NUMERICAL MODEL WITH A LARGE NUMBER OF GRID POINTS (N = 401) ,H_1 / TOTAL LENGTH = 10 .

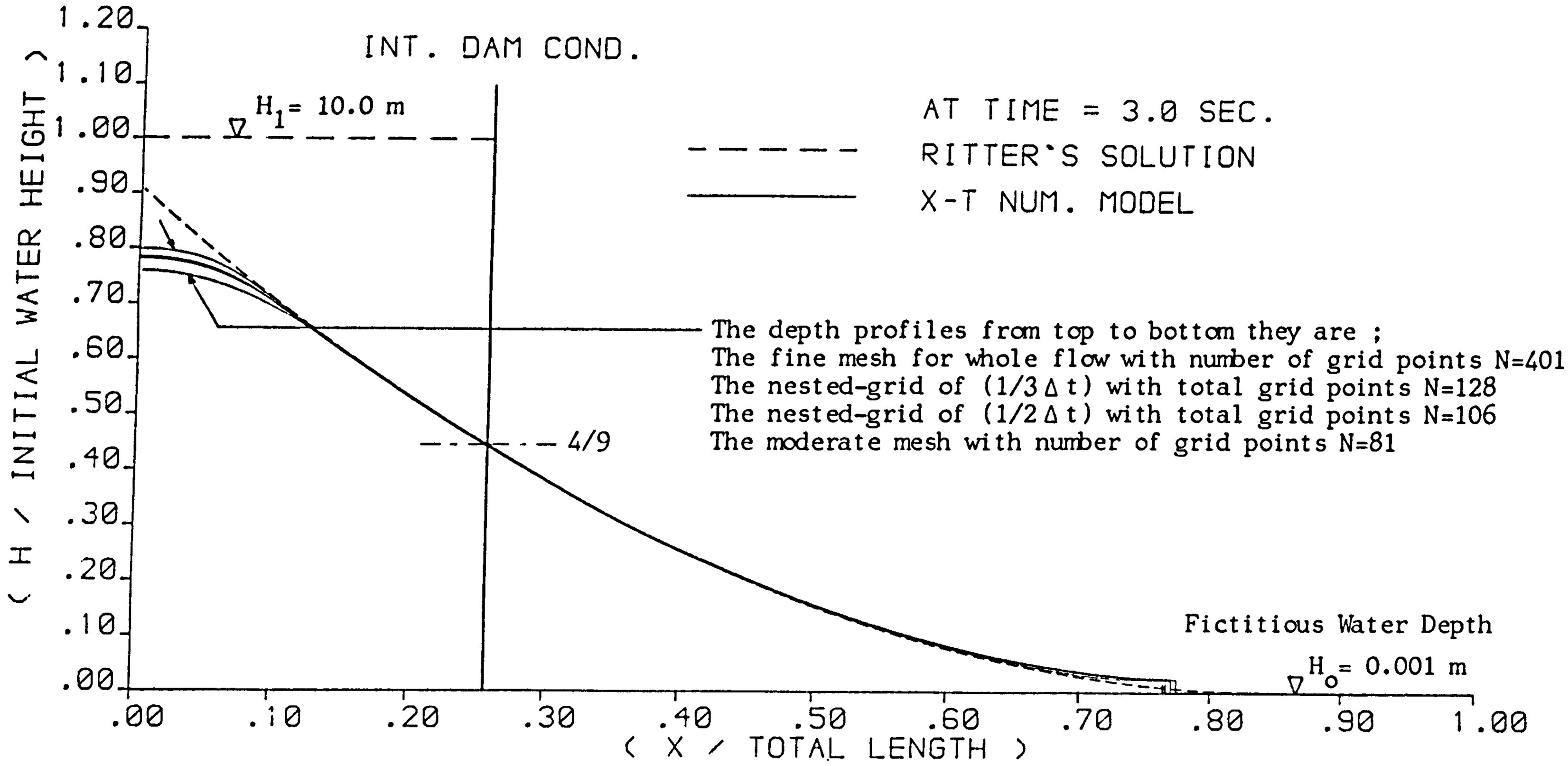

FIGURE 4.11 : COMPARING THE FOUR DEPTH PROFILES WITH RITTER'S SOLUTION , H_1 / TOTAL LENGTH = 10 .

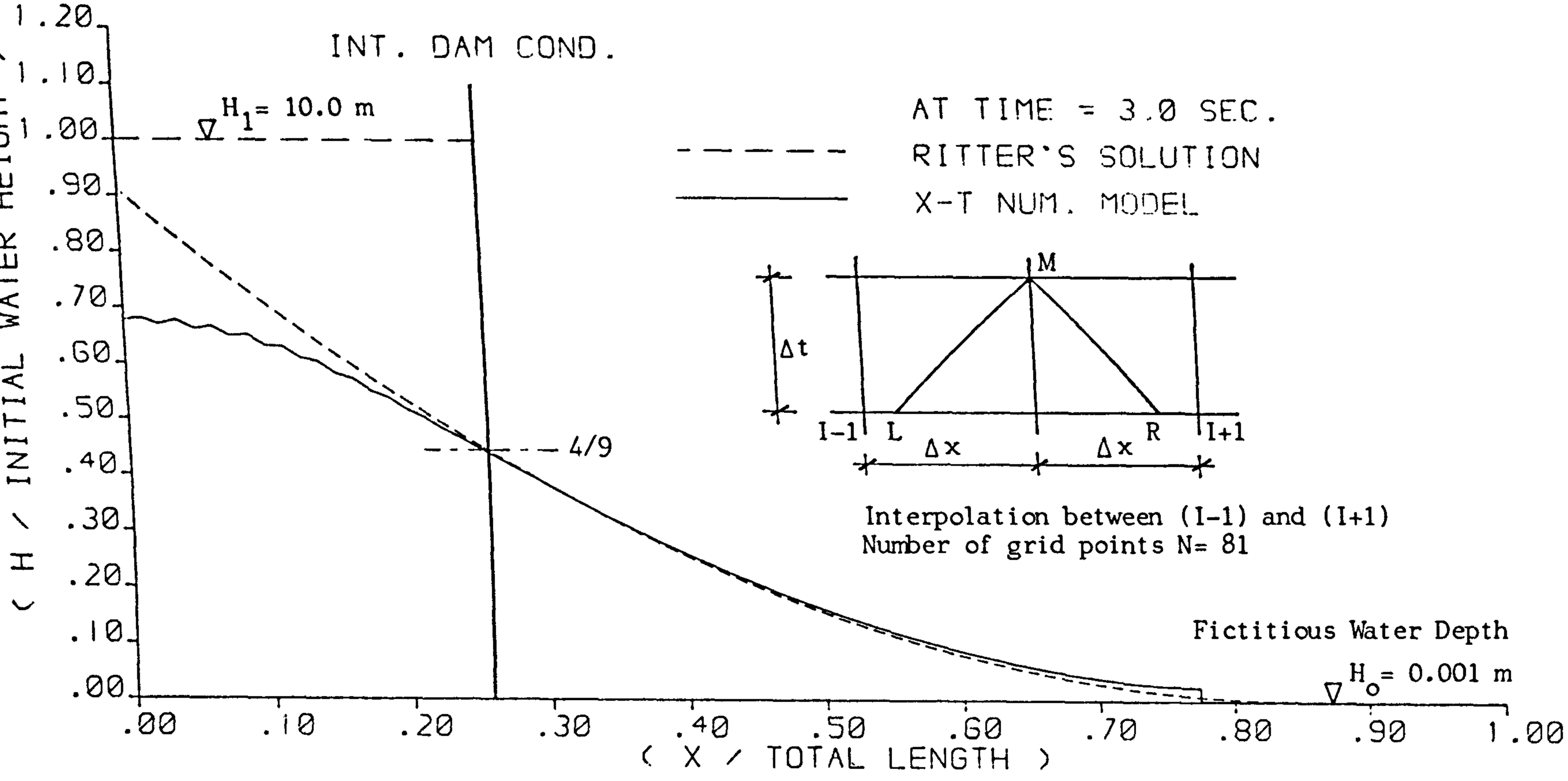

FIGURE 4.12 : COMPARING THE SAW – TOOTHED SURFACE WITH RITTER'S SOLUTION , H_1 / TOTAL LENGTH = 10 .

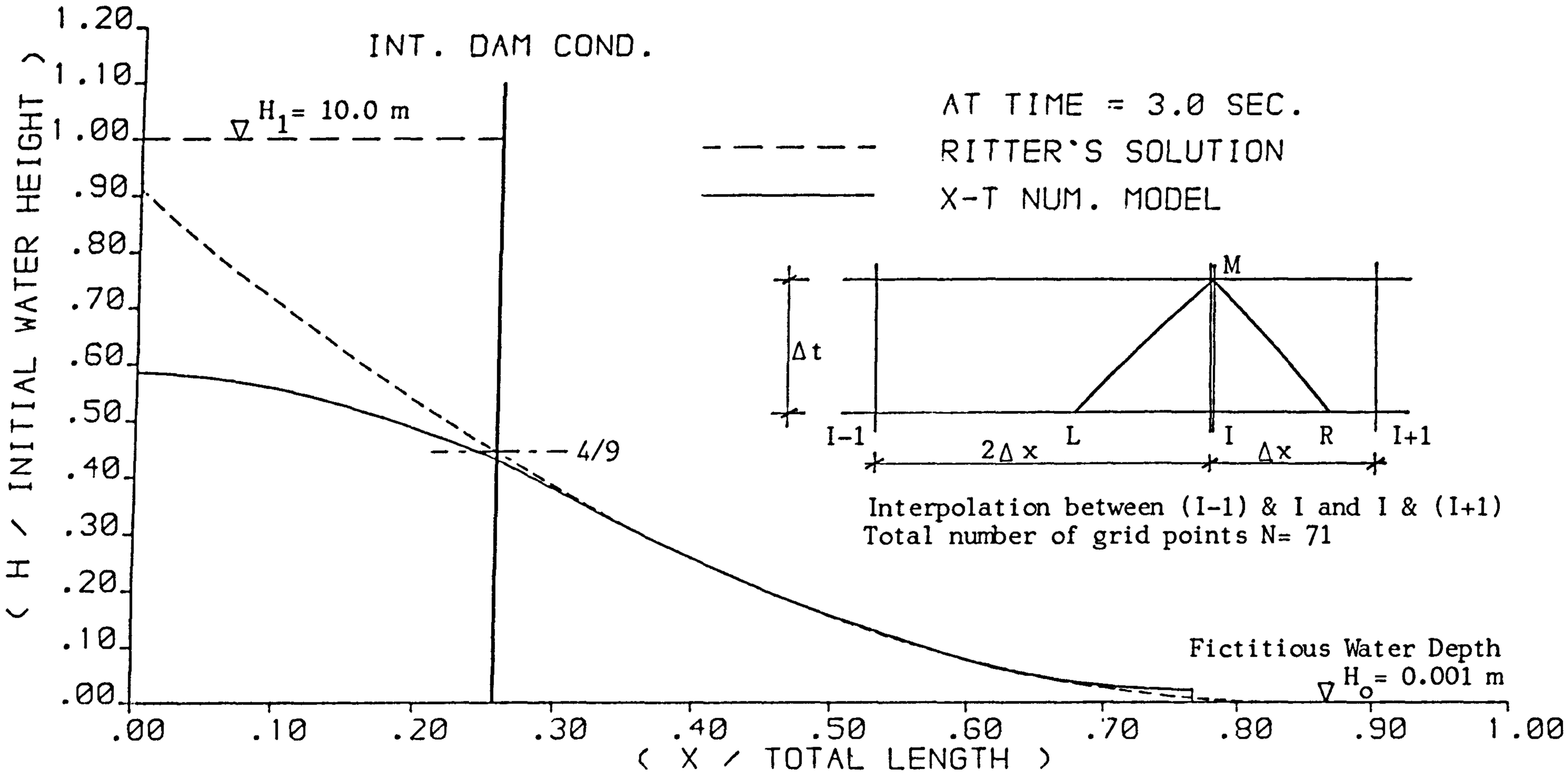

FIGURE 4.13 : COARSE MESH AT THE RESERVOIR REGION INTRODUCES LARGE DAMPING , H_1 / TOTAL LENGTH = 10 .

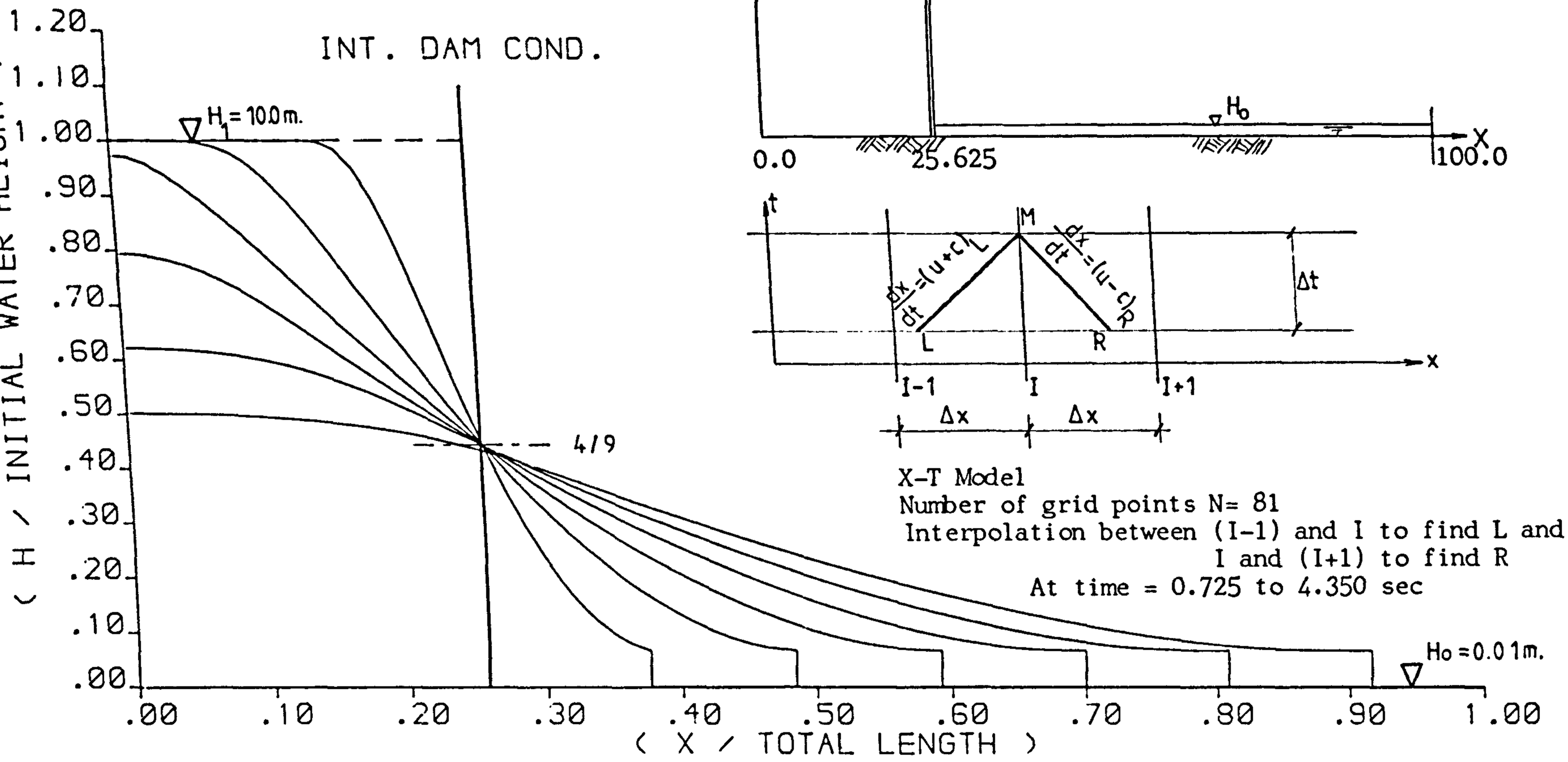

FIGURE 4.14 : COMPUTED TIME - VARYING FLOW PROFILES AFTER DAM BREAK .

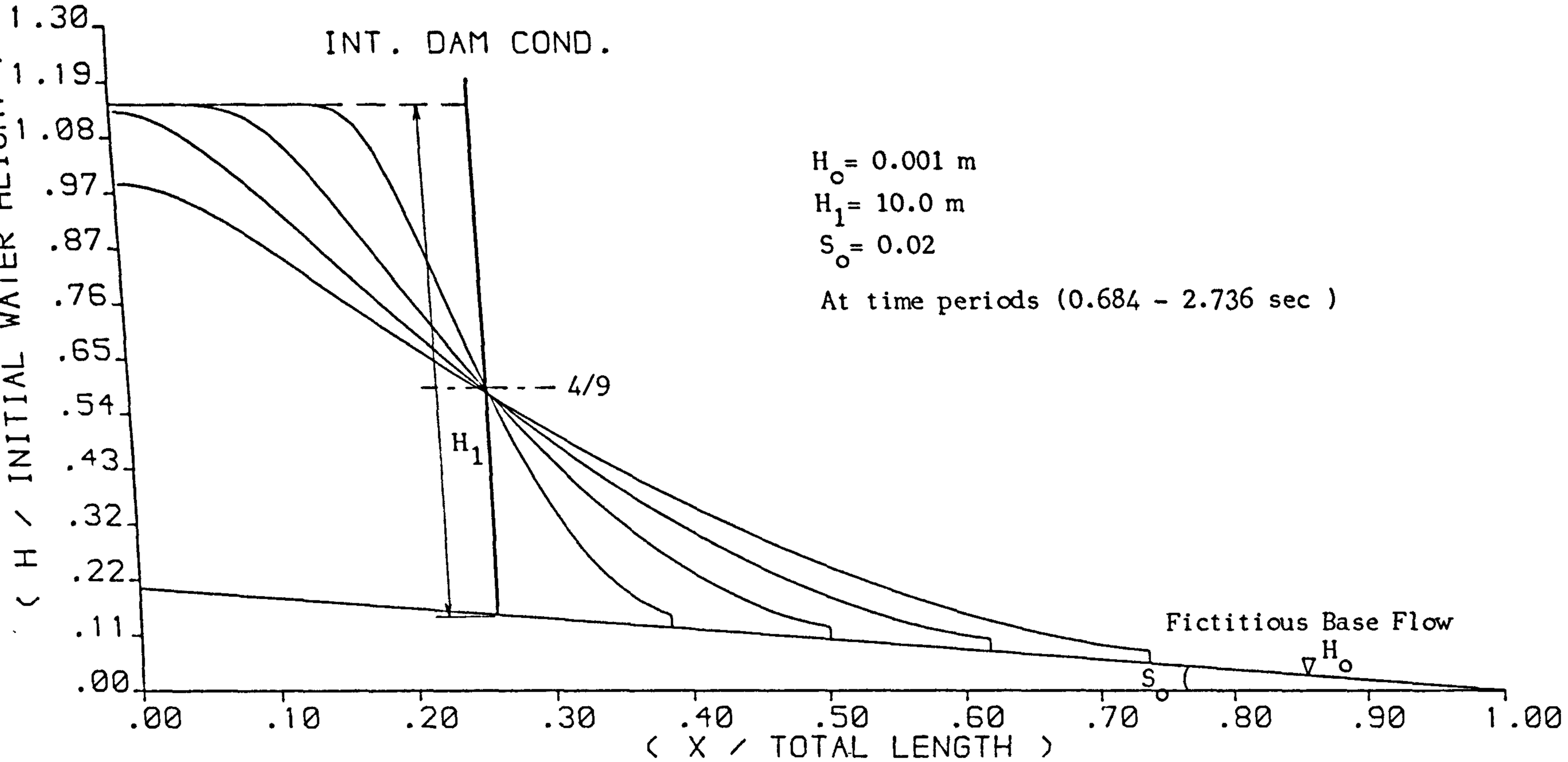

H_o = 0.001 m
H_1 = 10.0 m
S_o = 0.02

At time periods (0.684 - 2.736 sec)

FIGURE 4.15 : COMPUTED TIME – VARYING FLOW PROFILES AFTER DAM BREAK ON A CHANNEL WITH BED SLOPE S_o .

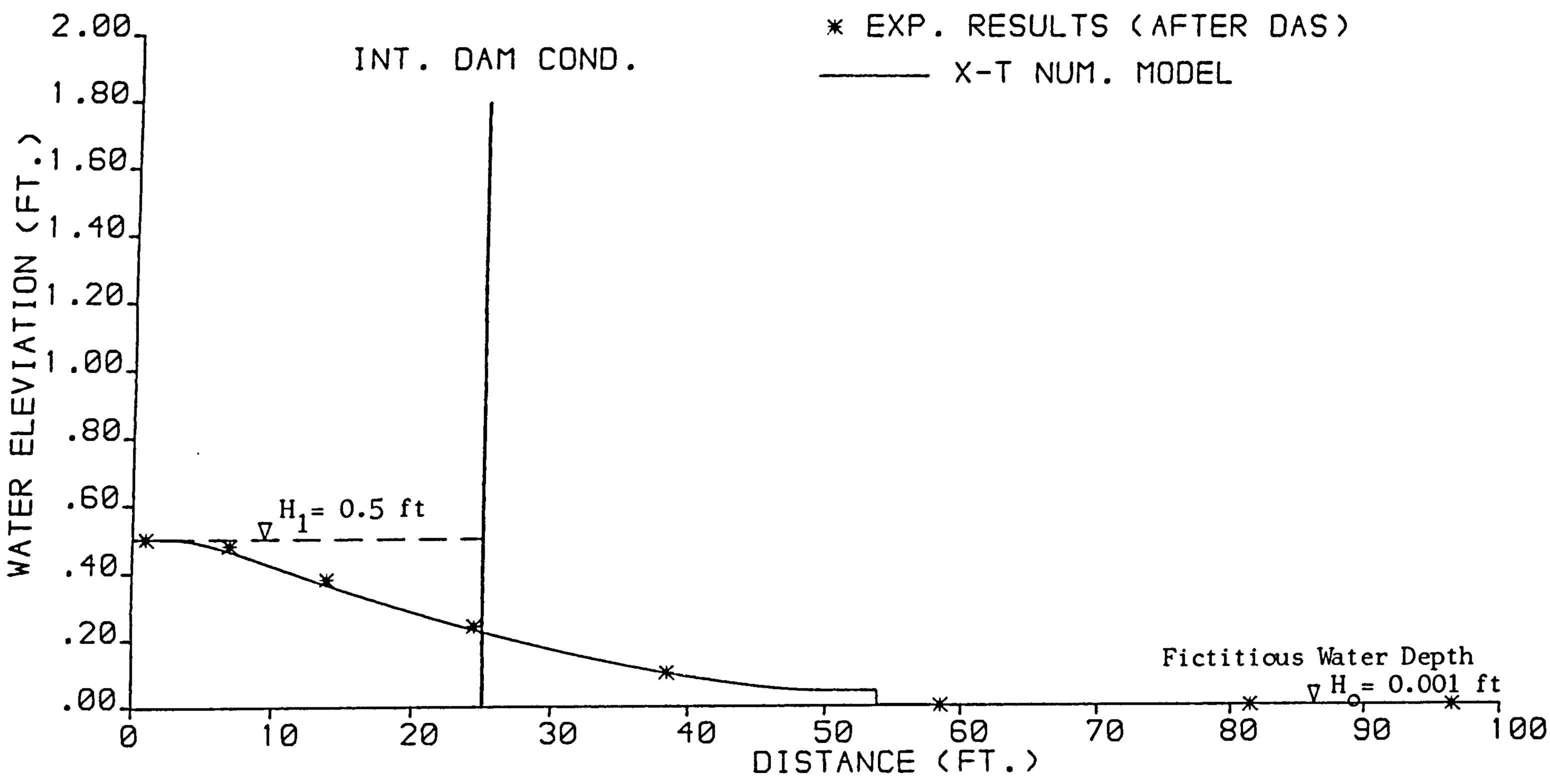

FIGURE 4.16 : COMPARISON OF EXPERIMENTAL DATA (AFTER DAS – LARGE FLUME WITH SMOOTH BED) AND X – T NUMERICAL PROFILE .

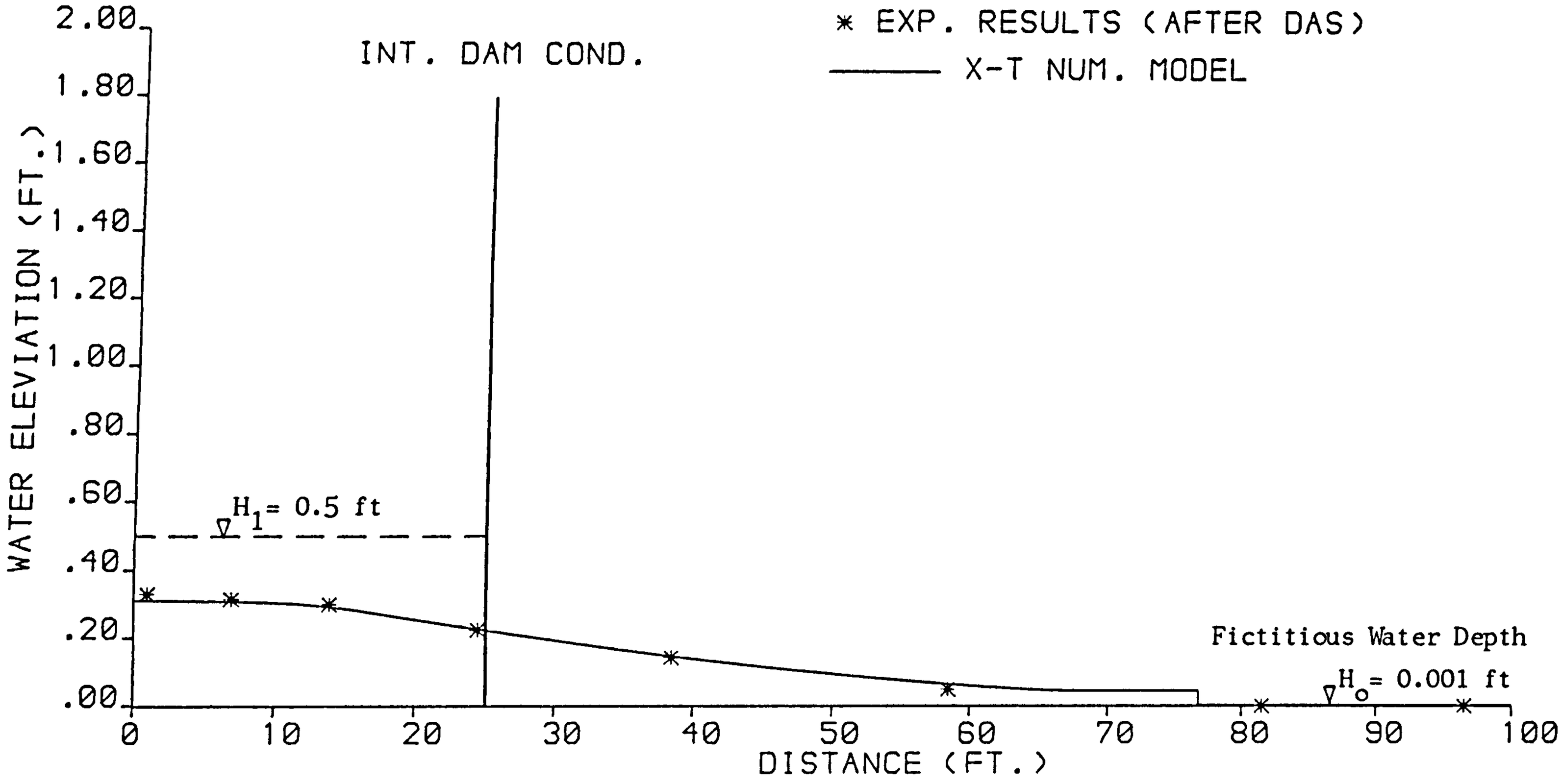

FIGURE 4.17 : COMPARISON OF EXPERIMENTAL DATA (AFTER DAS – LARGE FLUME WITH SMOOTH BED) AND X – T NUMERICAL PROFILE .

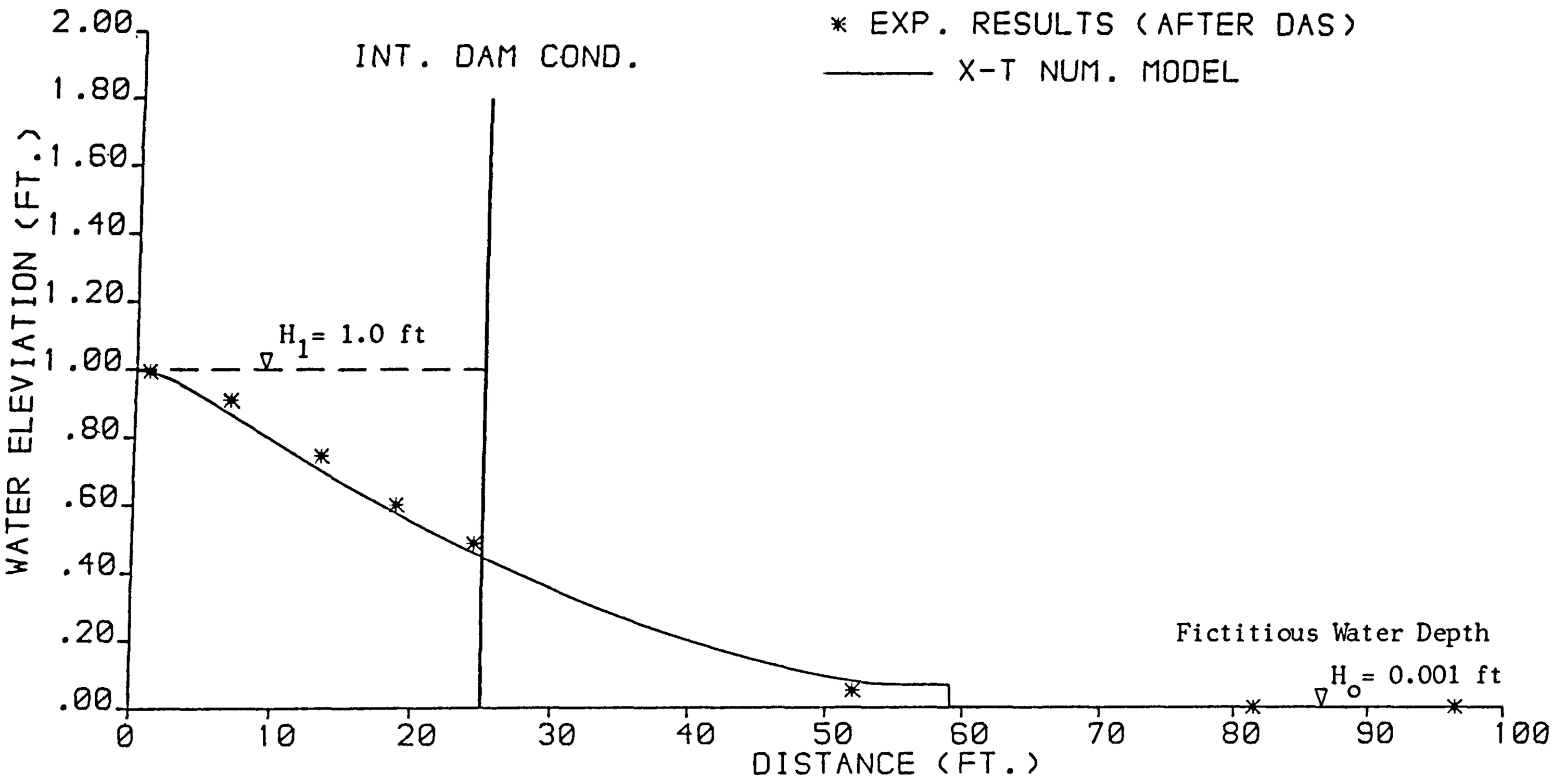

FIGURE 4.18 : COMPARISON OF EXPERIMENTAL DATA (AFTER DAS – LARGE FLUME WITH SMOOTH BED) AND X – T NUMERICAL PROFILE .

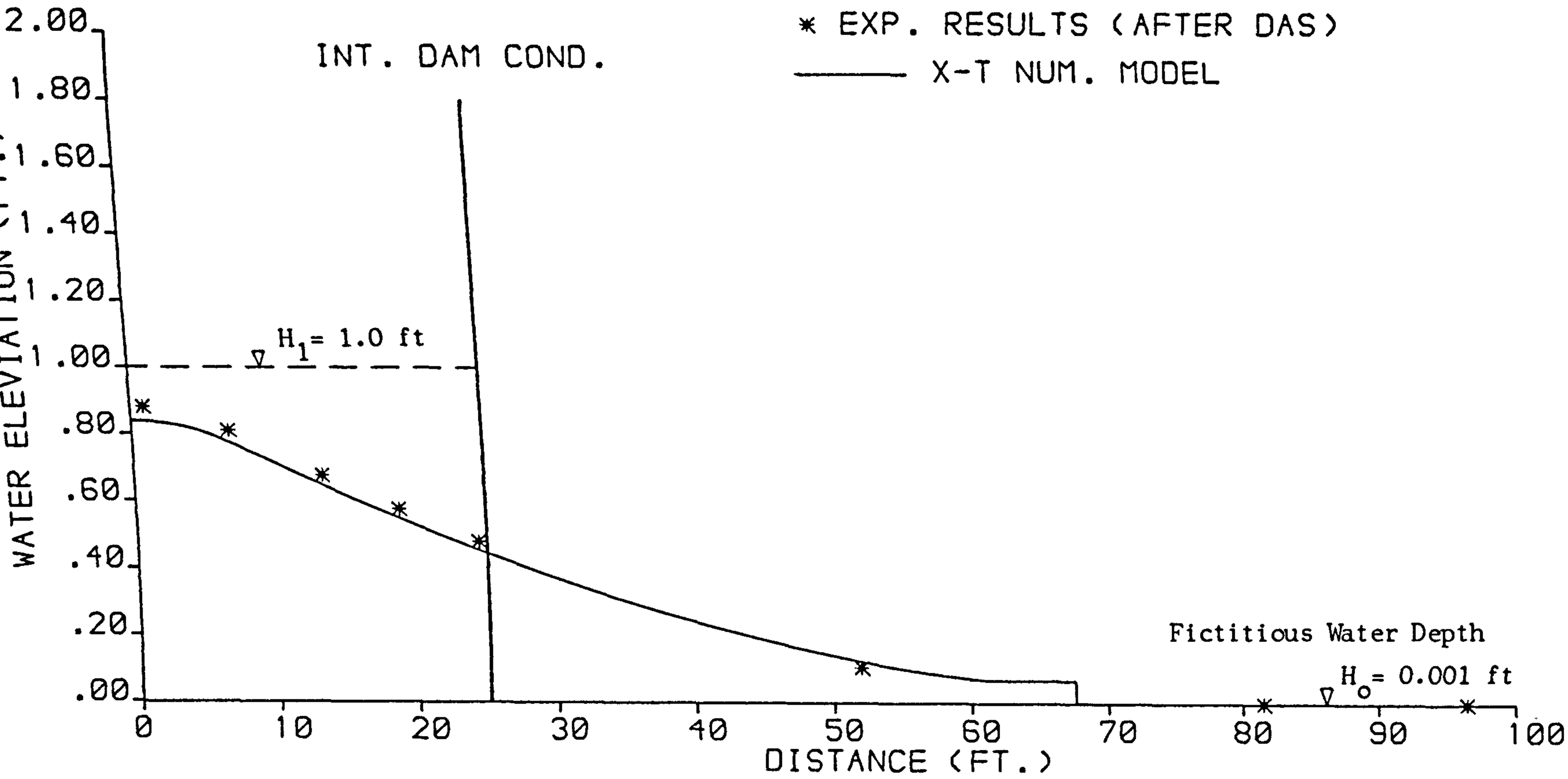

FIGURE 4.19 : COMPARISON OF EXPERIMENTAL DATA (AFTER DAS – LARGE FLUME WITH SMOOTH BED) AND X – T NUMERICAL PROFILE .

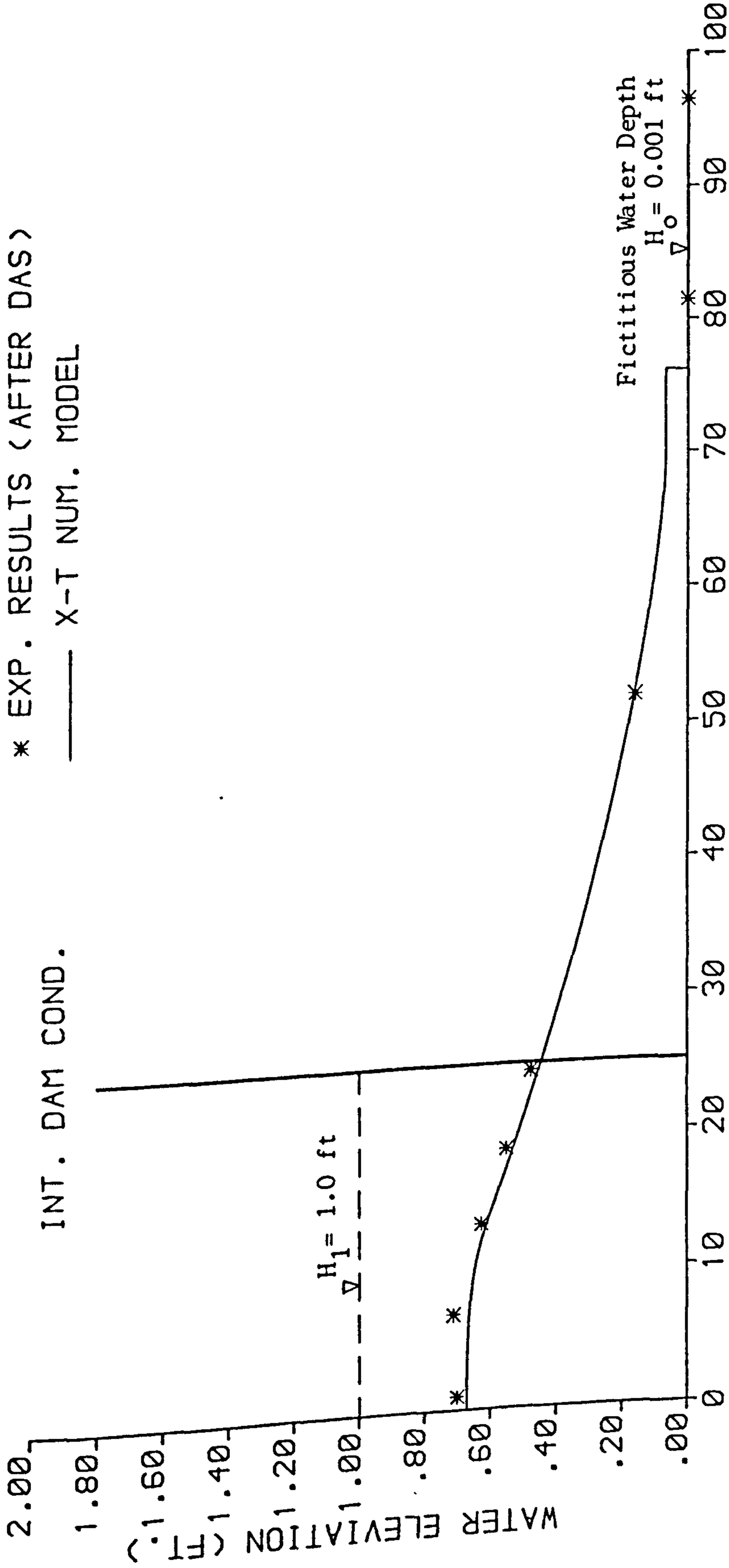

FIGURE 4.20 : COMPARISON OF EXPERIMENTAL DATA (AFTER DAS – LARGE FLUME WITH SMOOTH BED) AND X – T NUMERICAL PROFILE .

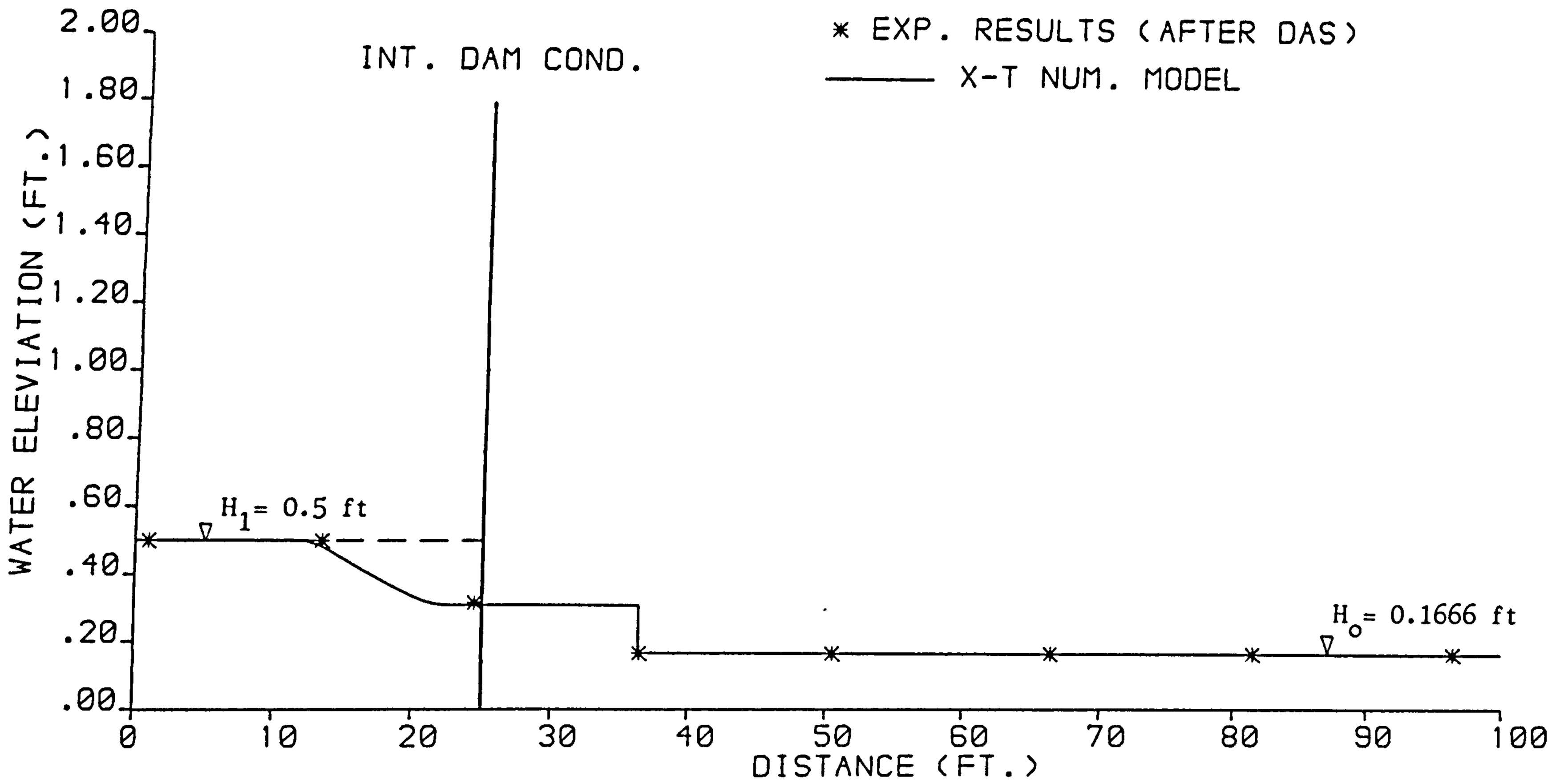

FIGURE 4.21 : COMPARISON OF EXPERIMENTAL DATA (AFTER DAS - LARGE FLUME WITH SMOOTH BED) AND X - T NUMERICAL PROFILE .

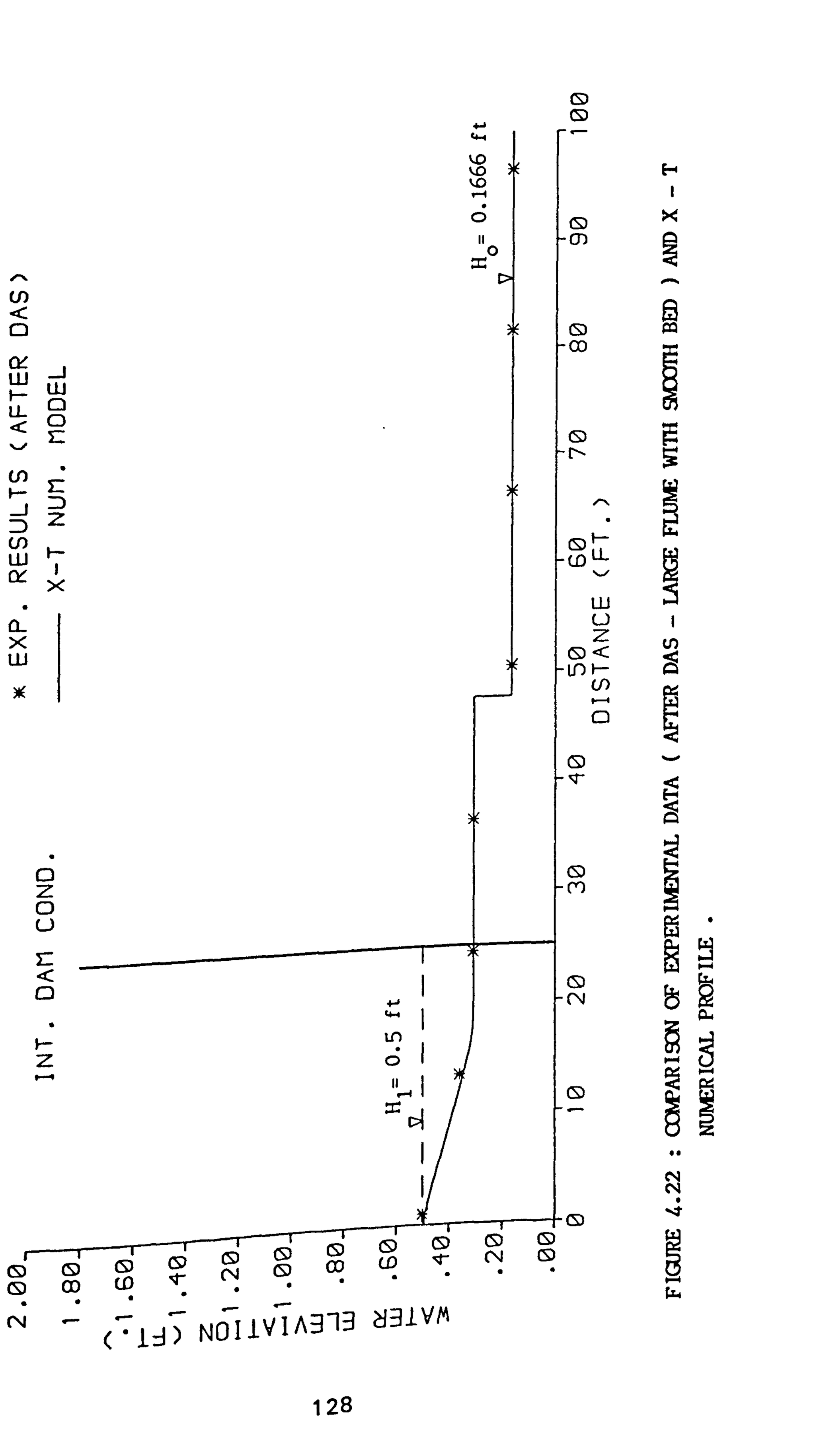

FIGURE 4.22 : COMPARISON OF EXPERIMENTAL DATA (AFTER DAS – LARGE FLUME WITH SMOOTH BED) AND X – T NUMERICAL PROFILE .

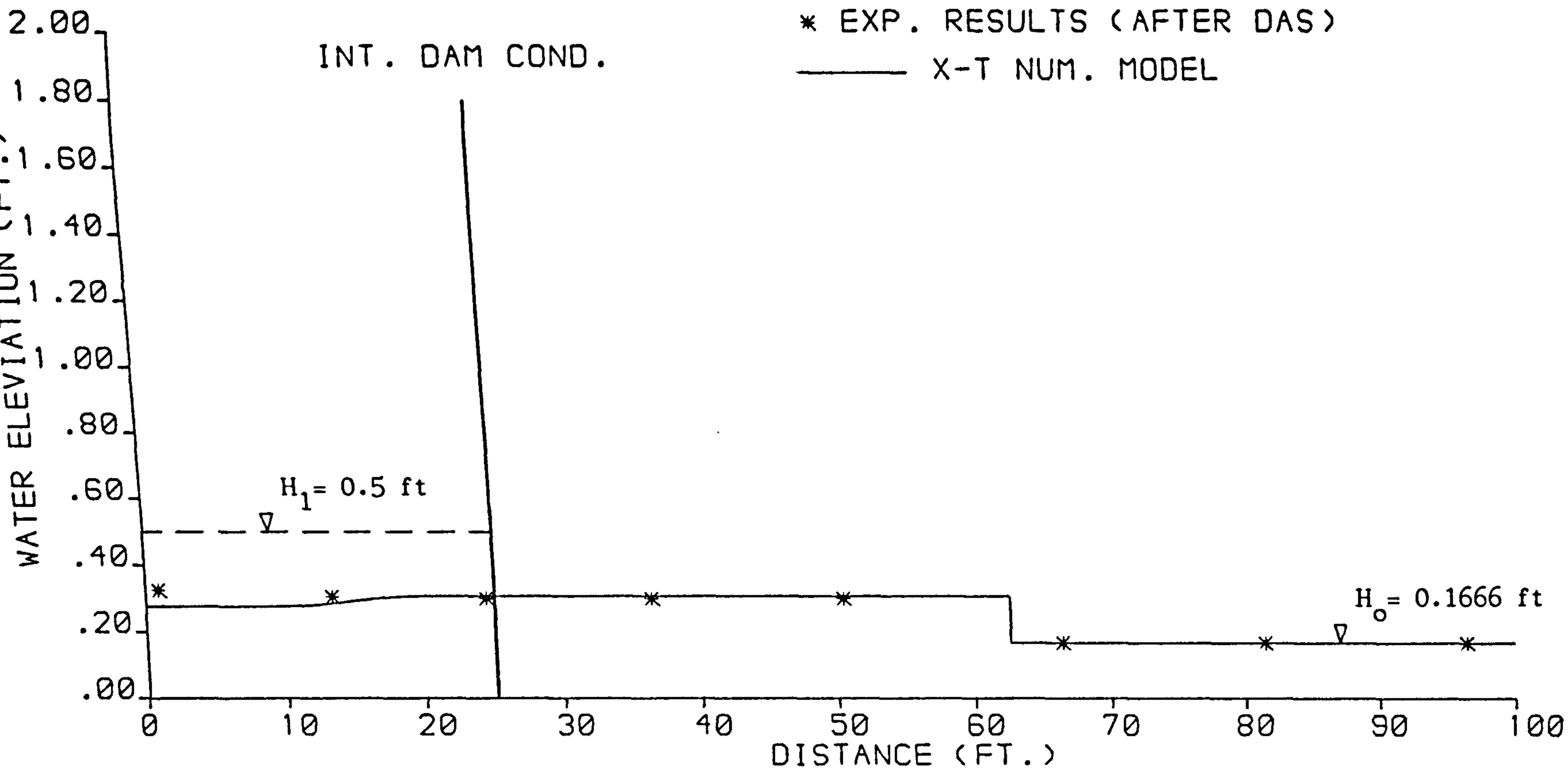

FIGURE 4.23 : COMPARISON OF EXPERIMENTAL DATA (AFTER DAS – LARGE FLUME WITH SMOOTH BED) AND X – T NUMERICAL PROFILE .

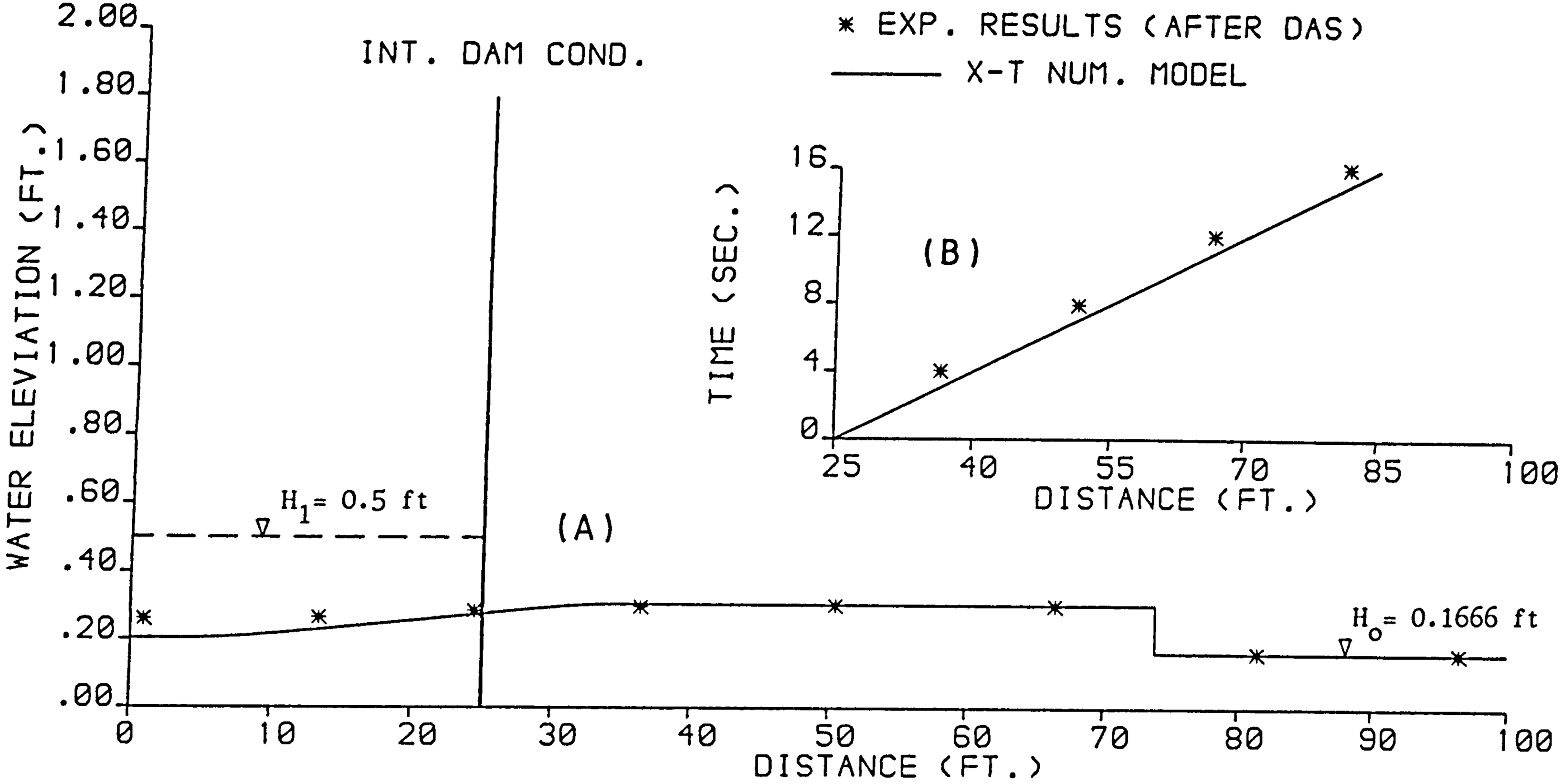

FIGURE 4.24 : COMPARISON OF EXPERIMENTAL DATA (AFTER DAS – LARGE FLUME WITH SMOOTH BED) AND X – T NUMERICAL (A) PROFILE AND (B) FRONT TRAJECTORY .

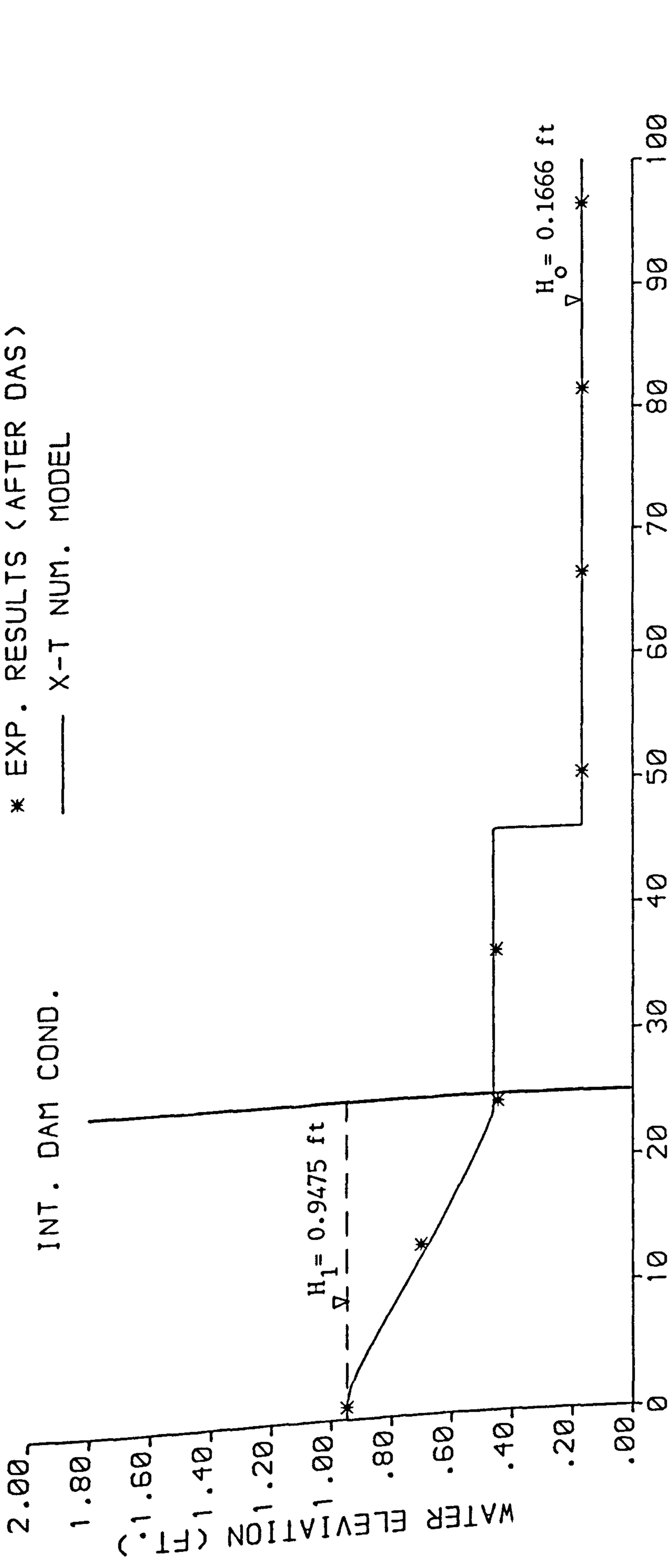

FIGURE 4.25 : COMPARISON OF EXPERIMENTAL DATA (AFTER DAS – LARGE FLUME WITH SMOOTH BED) AND X – T NUMERICAL PROFILE .

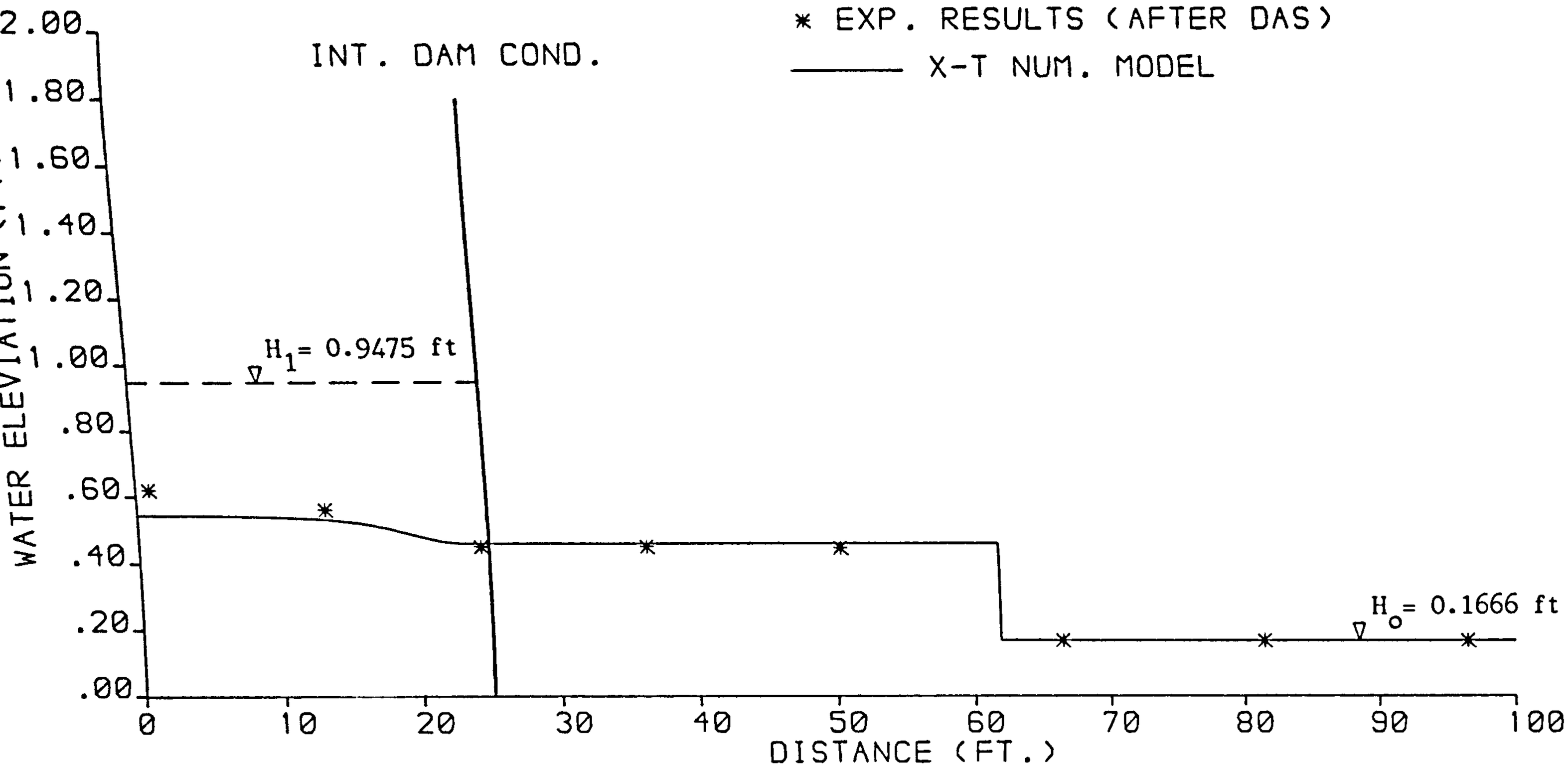

FIGURE 4.26 : COMPARISON OF EXPERIMENTAL DATA (AFTER DAS – LARGE FLUME WITH SMOOTH BED) AND X – T NUMERICAL PROFILE .

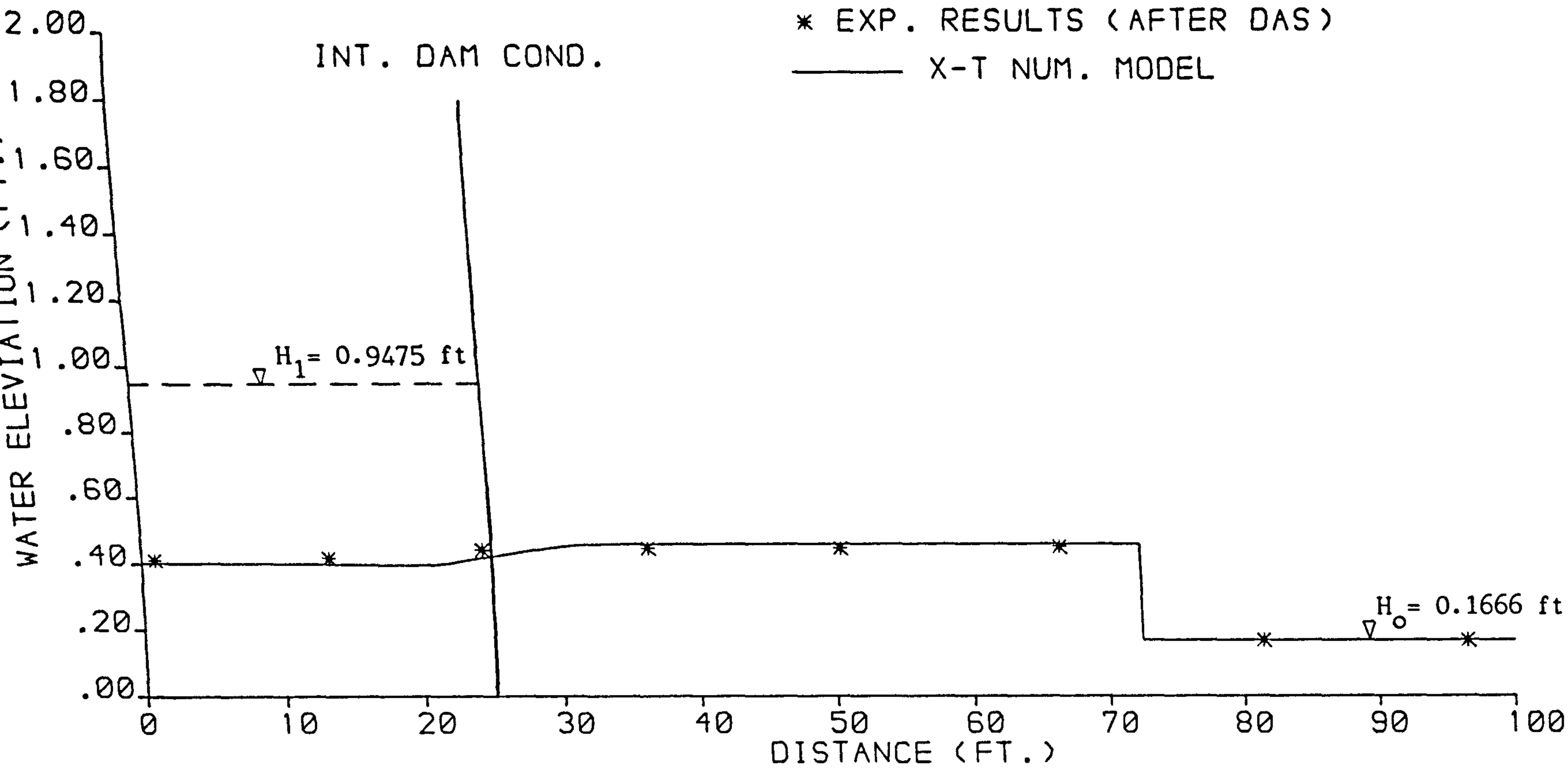

FIGURE 4.27 : COMPARISON OF EXPERIMENTAL DATA (AFTER DAS - LARGE FLUME WITH SMOOTH BED) AND X - T NUMERICAL PROFILE .

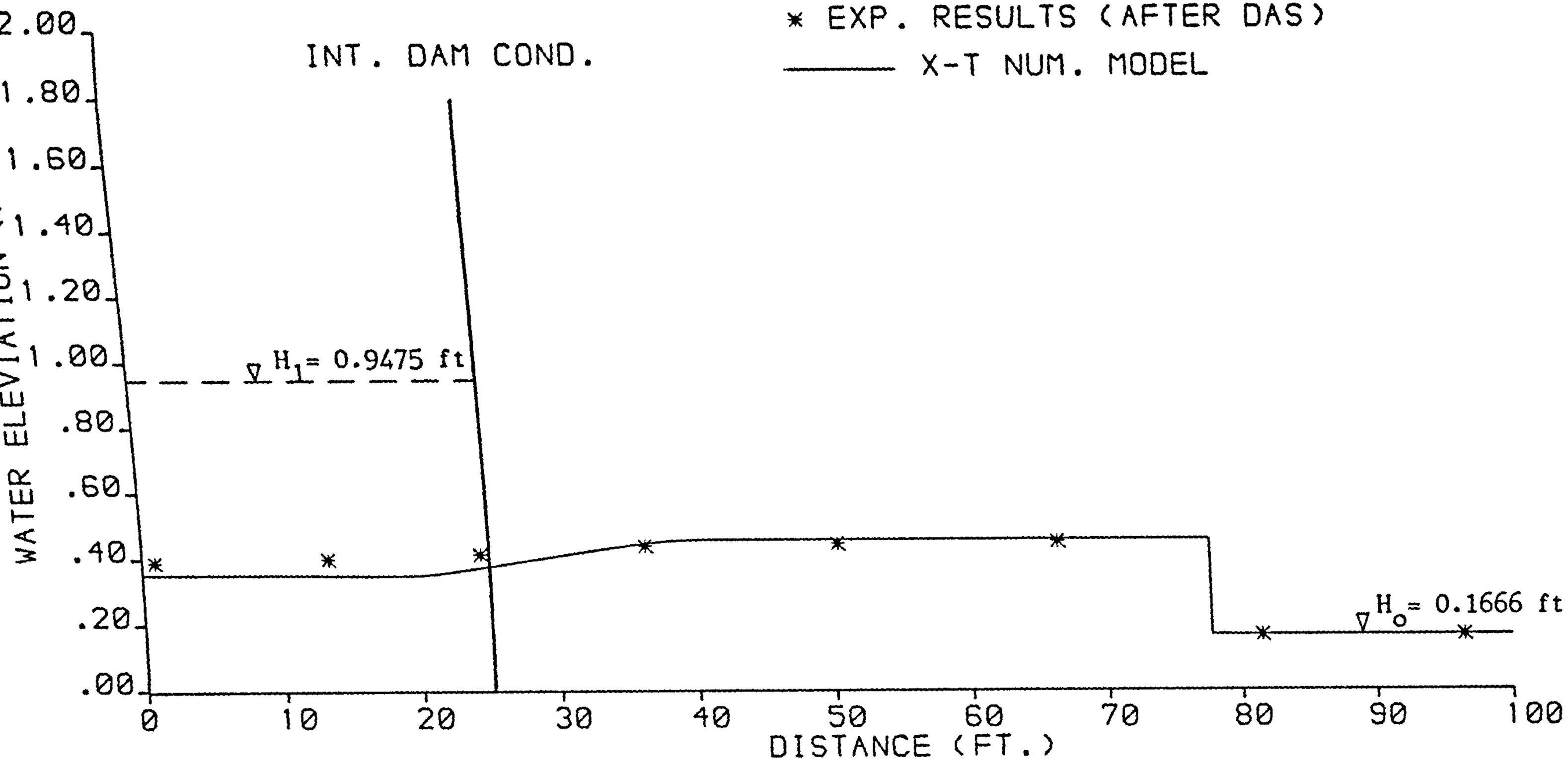

FIGURE 4.28 : COMPARISON OF EXPERIMENTAL DATA (AFTER DAS – LARGE FLUME WITH SMOOTH BED) AND X – T NUMERICAL PROFILE .

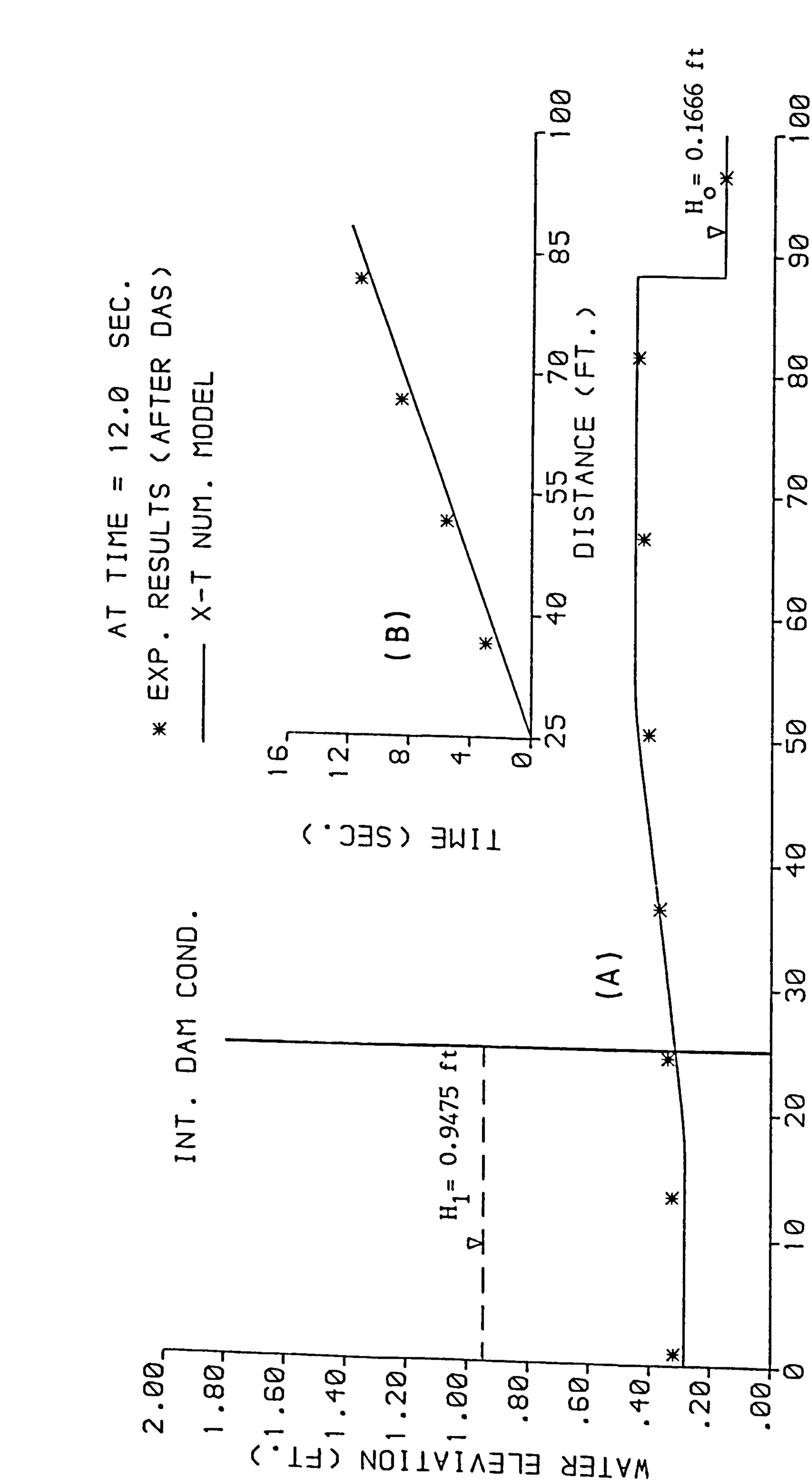

FIGURE 4.29 : COMPARISON OF EXPERIMENTAL DATA (AFTER DAS – LARGE FLUME WITH SMOOTH BED) AND X – T NUMERICAL (A) PROFILE AND (B) FRONT TRAJECTORY .

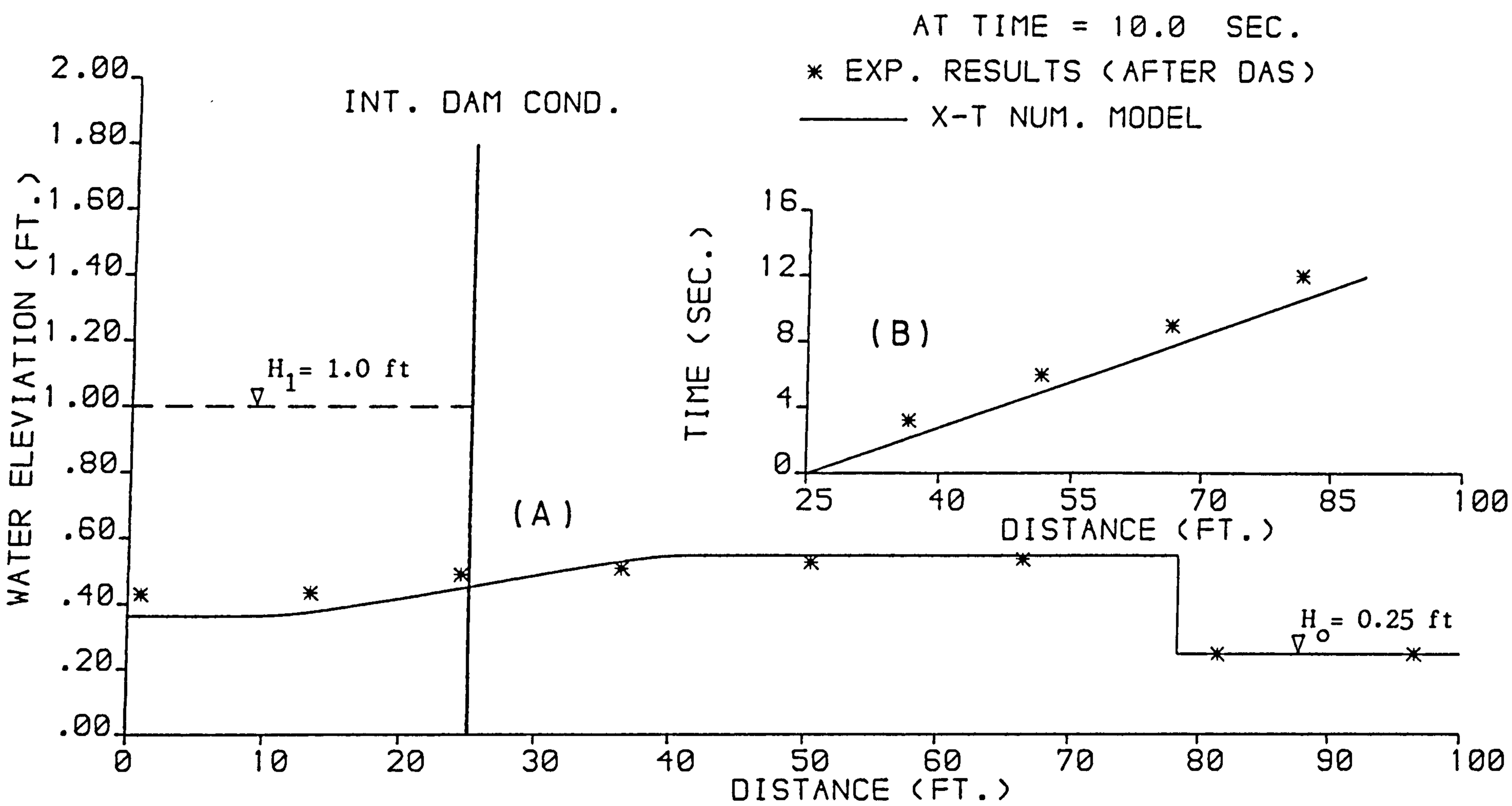

FIGURE 4.30 : COMPARISON OF EXPERIMENTAL DATA (AFTER DAS - LARGE FLUME WITH SMOOTH BED) AND X - T NUMERICAL (A) PROFILE AND (B) FRONT TRAJECTORY .

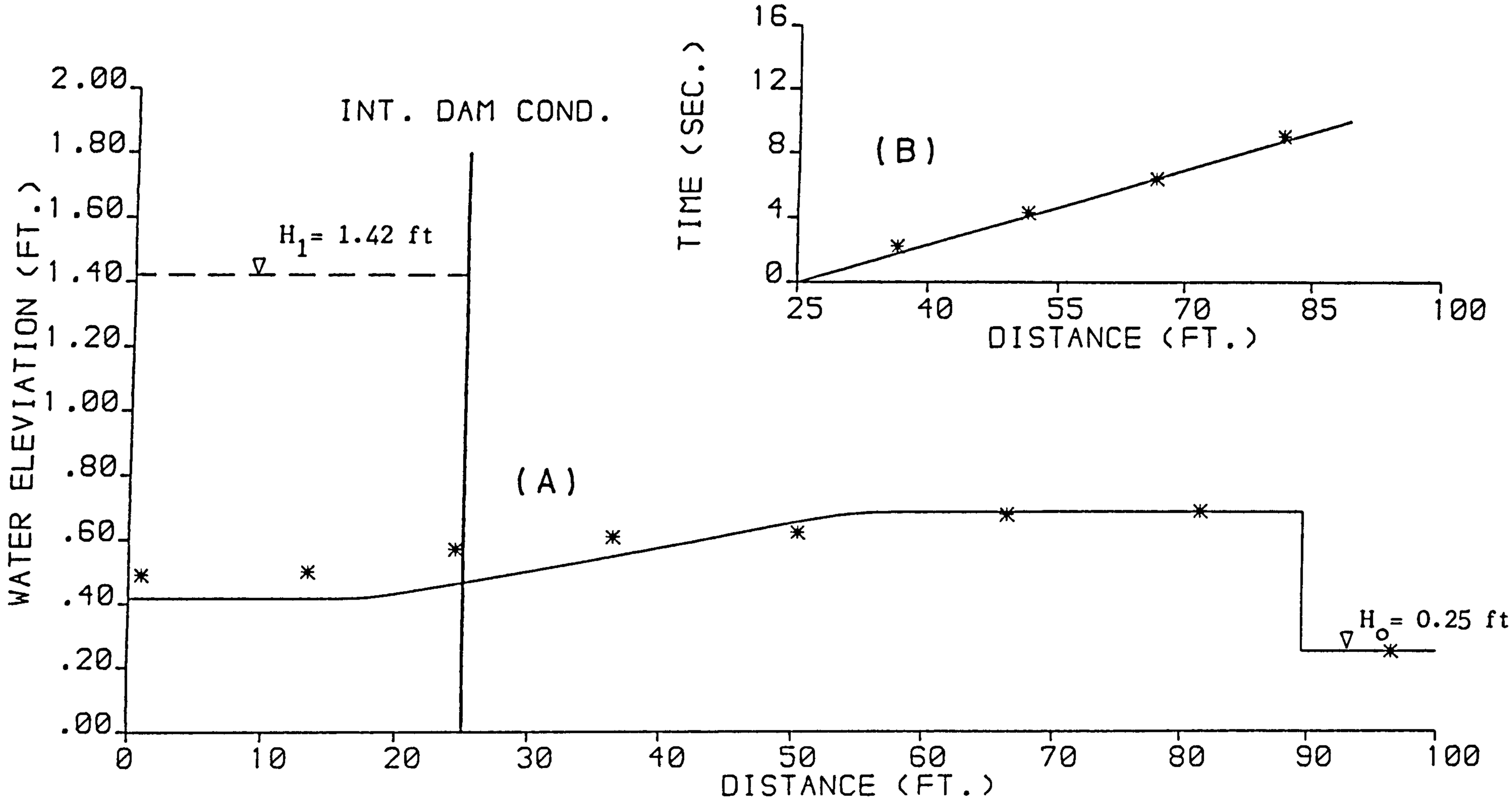

FIGURE 4.31 : COMPARISON OF EXPERIMENTAL DATA (AFTER DAS - LARGE FLUME WITH SMOOTH BED) AND X - T NUMERICAL (A) PROFILE AND (B) FRONT TRAJECTORY .

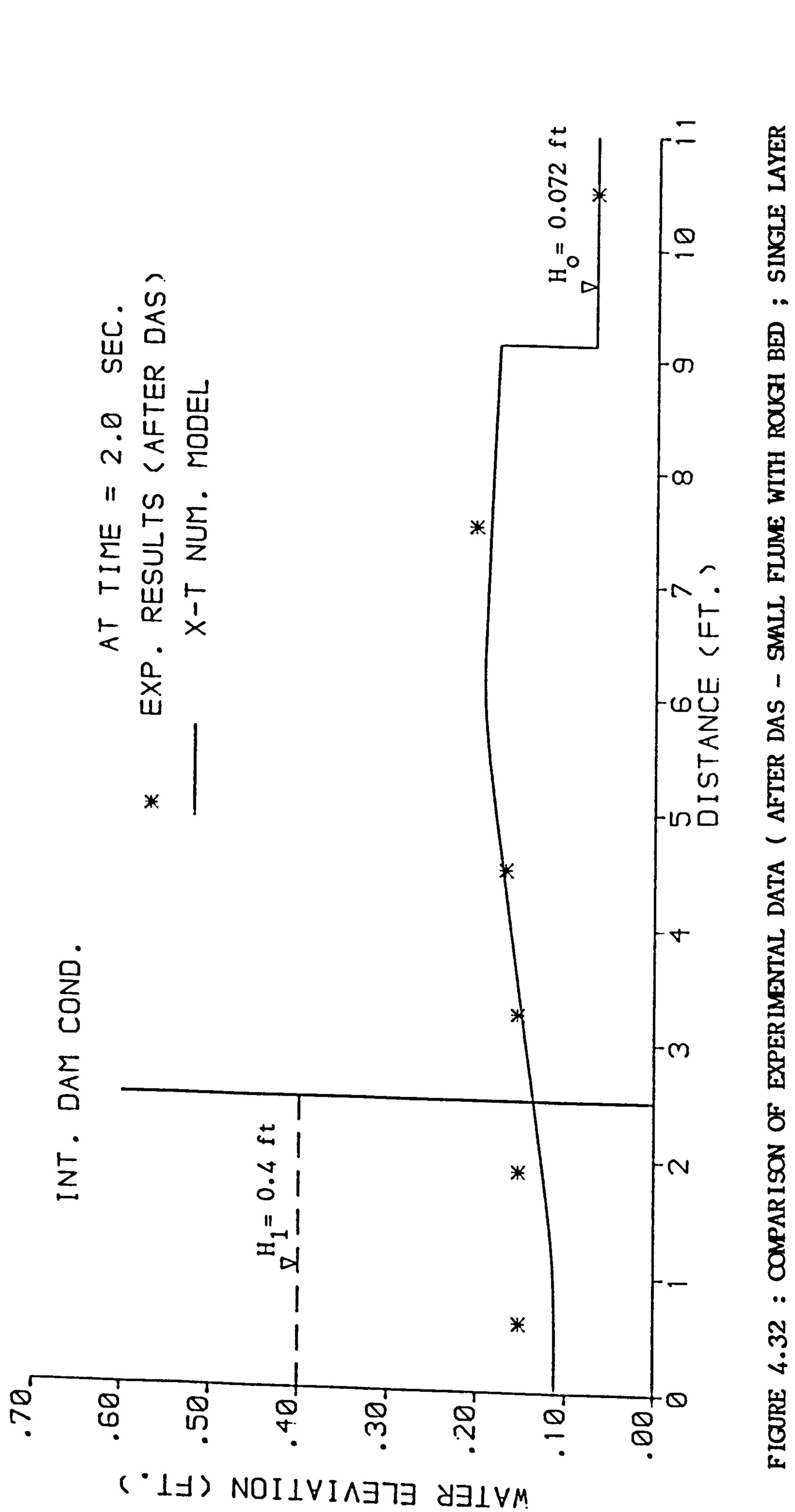

FIGURE 4.32 : COMPARISON OF EXPERIMENTAL DATA (AFTER DAS - SMALL FLUME WITH ROUGH BED ; SINGLE LAYER K = 0.044 ft) AND X – T NUMERICAL PROFILE .

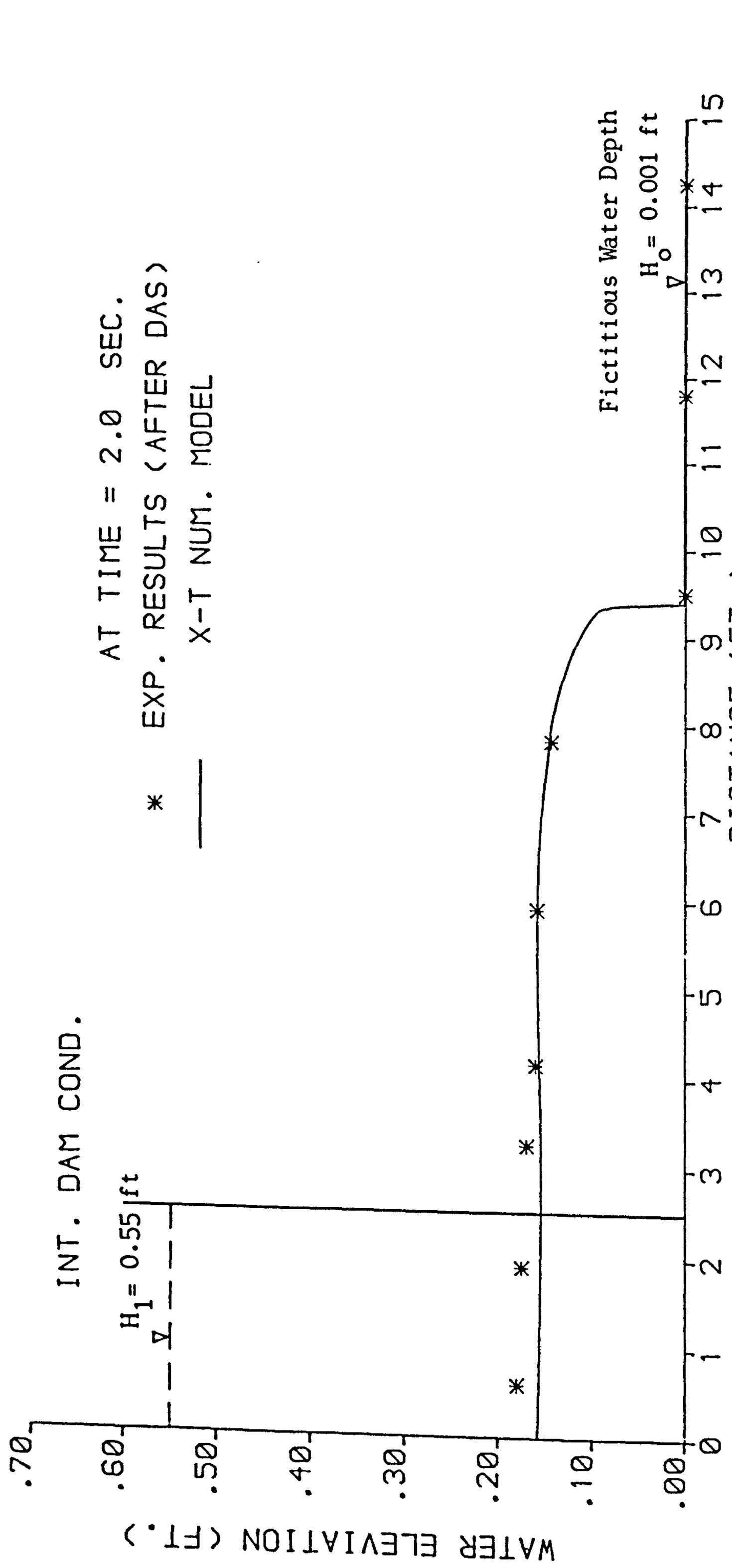

FIGURE 4.33 : COMPARISON OF EXPERIMENTAL DATA (AFTER DAS - SMALL FLUME WITH ROUGH BED ; DOUBLE LAYERS
K = 0.127 ft) AND X - T NUMERICAL PROFILE .

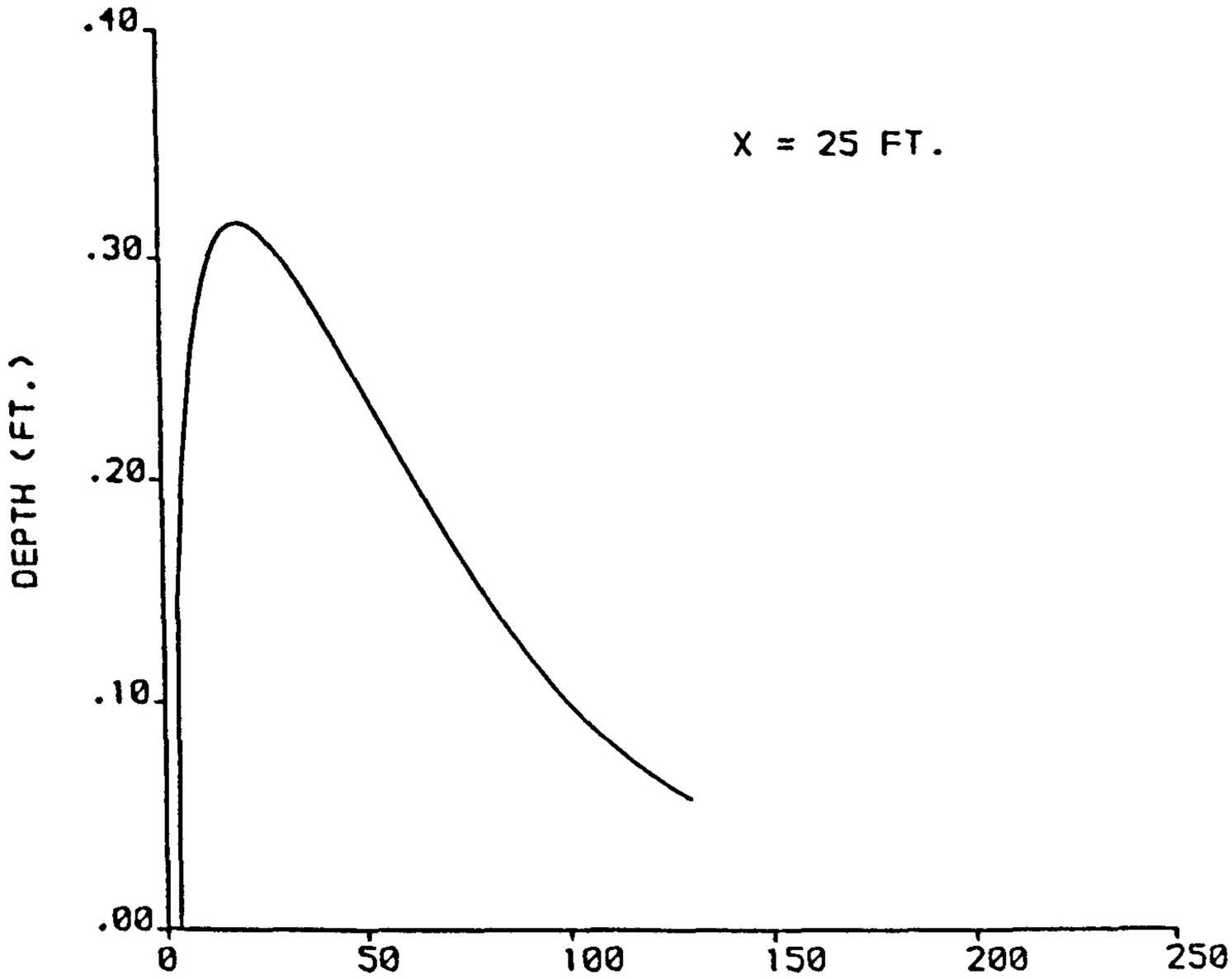

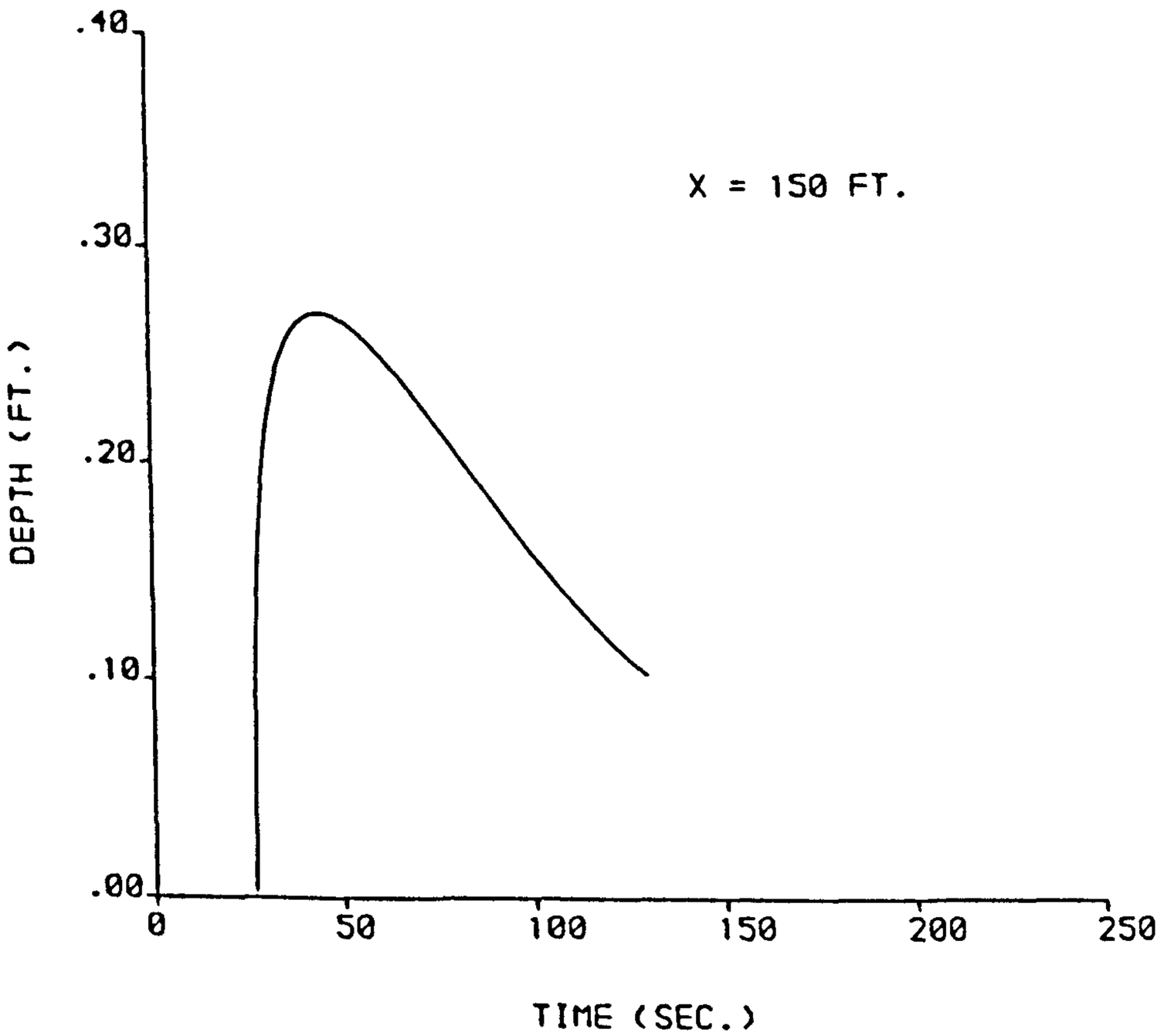

FIGURE 4.35 : STAGE HYDROGRAPH COMPUTED USING THE AUTHOR'S (X-T) NUMERICAL MODEL FOR A SMOOTH CHANNEL AS STUDIED BY KATOPODES AND SCHAMBER . (A COMPARISON WITH THEIR MODEL IS GIVEN IN FIGURE 4.37) .

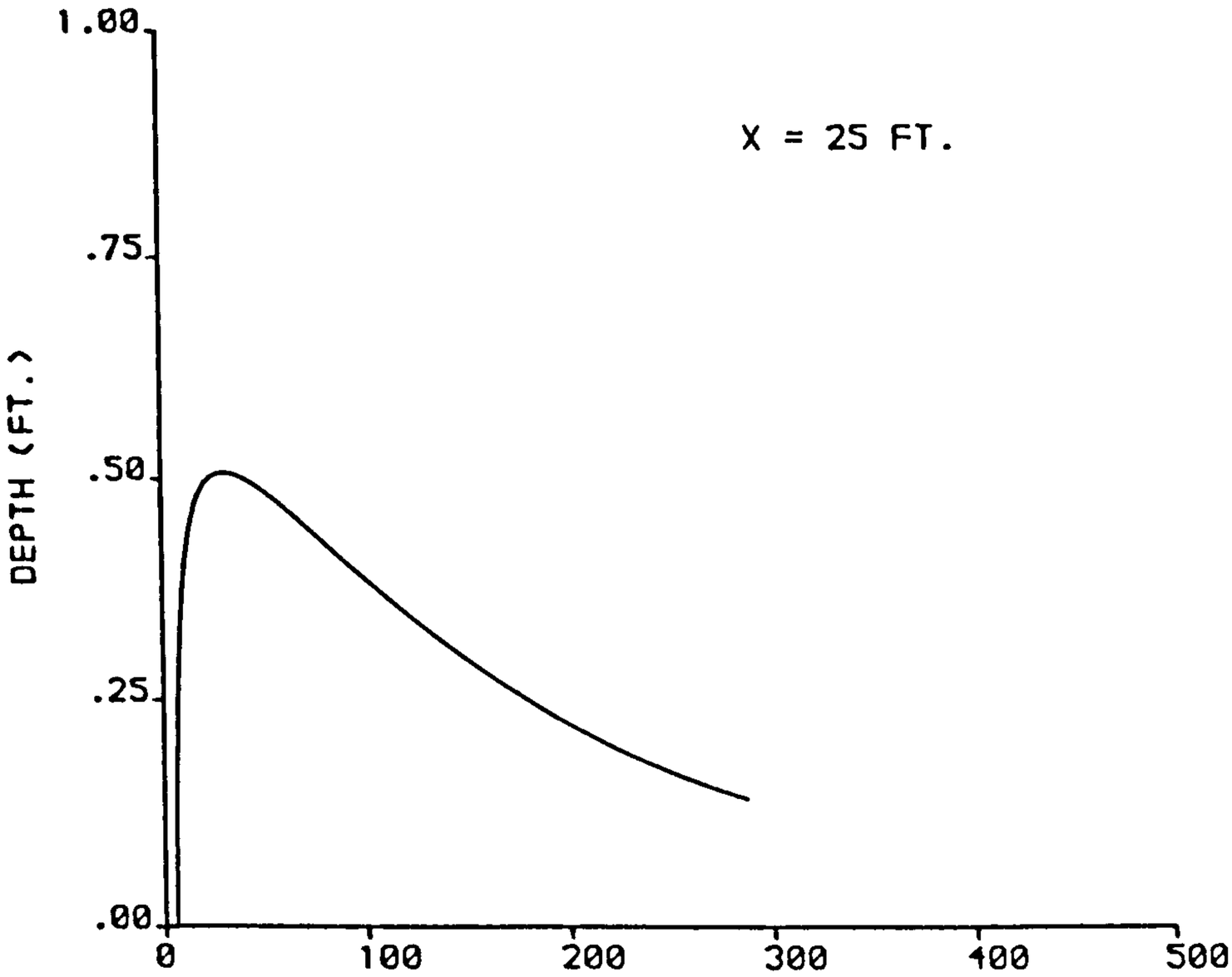

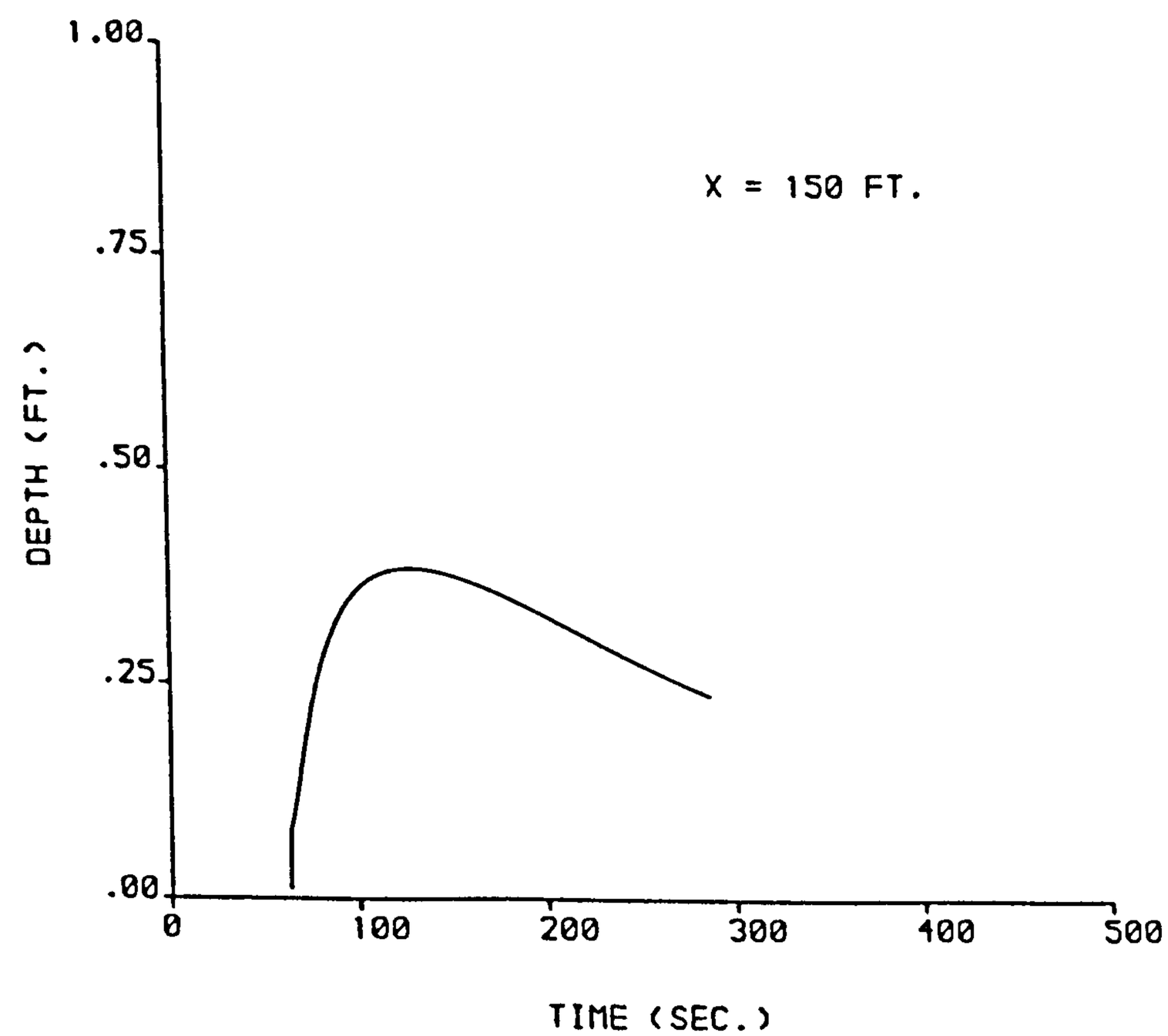

FIGURE 4.36 : STAGE HYDROGRAPH COMPUTED USING THE AUTHOR'S (X-T) NUMERICAL MODEL FOR THE ROUGH (n=0.05) CHANNEL AS STUDIED BY KATOPODES AND SCHAMBER . (SEE ALSO FIGURE 4.38)

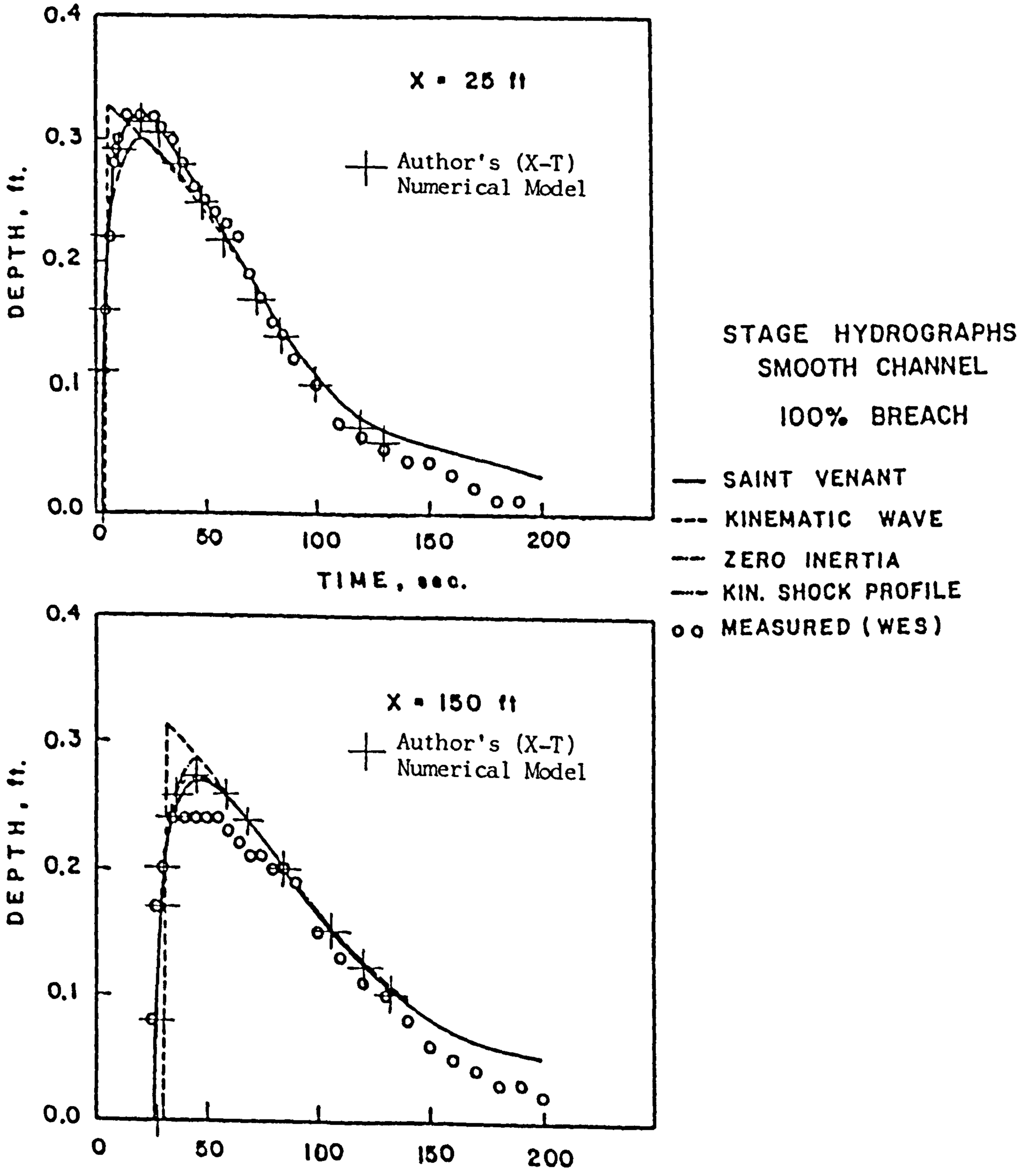

FIGURE 4.37 : COMPARISON OF AUTHOR'S STAGE HYDROGRAPHS IN FIGURE 4.35 WITH THOSE FROM KATOPODES AND SCHAMBER .

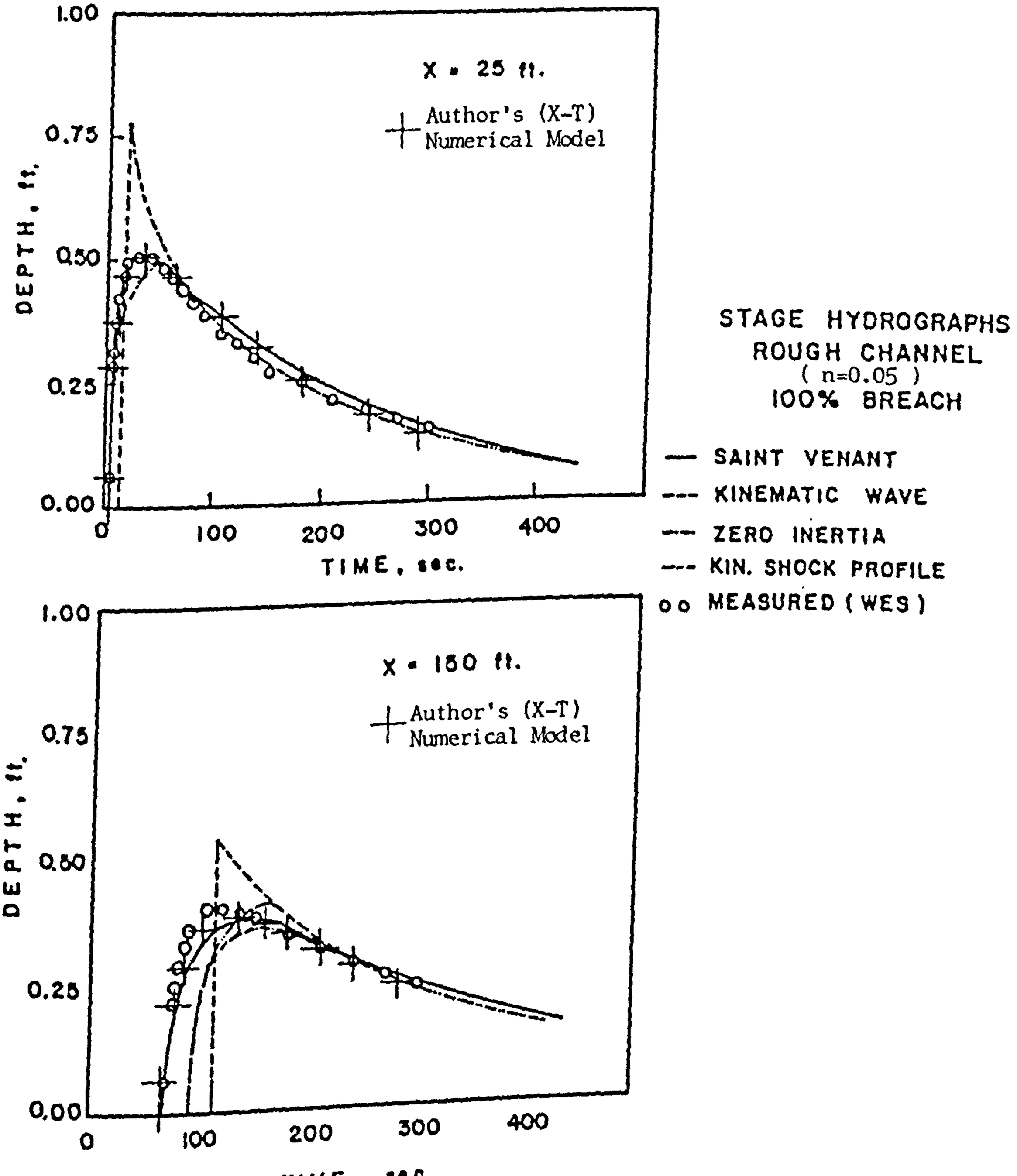

FIGURE 4.38 : COMPARISON OF AUTHOR'S STAGE HYDROGRAPHS IN FIGURE 4.36 WITH THOSE FROM KATOPODES AND SCHAMBER .

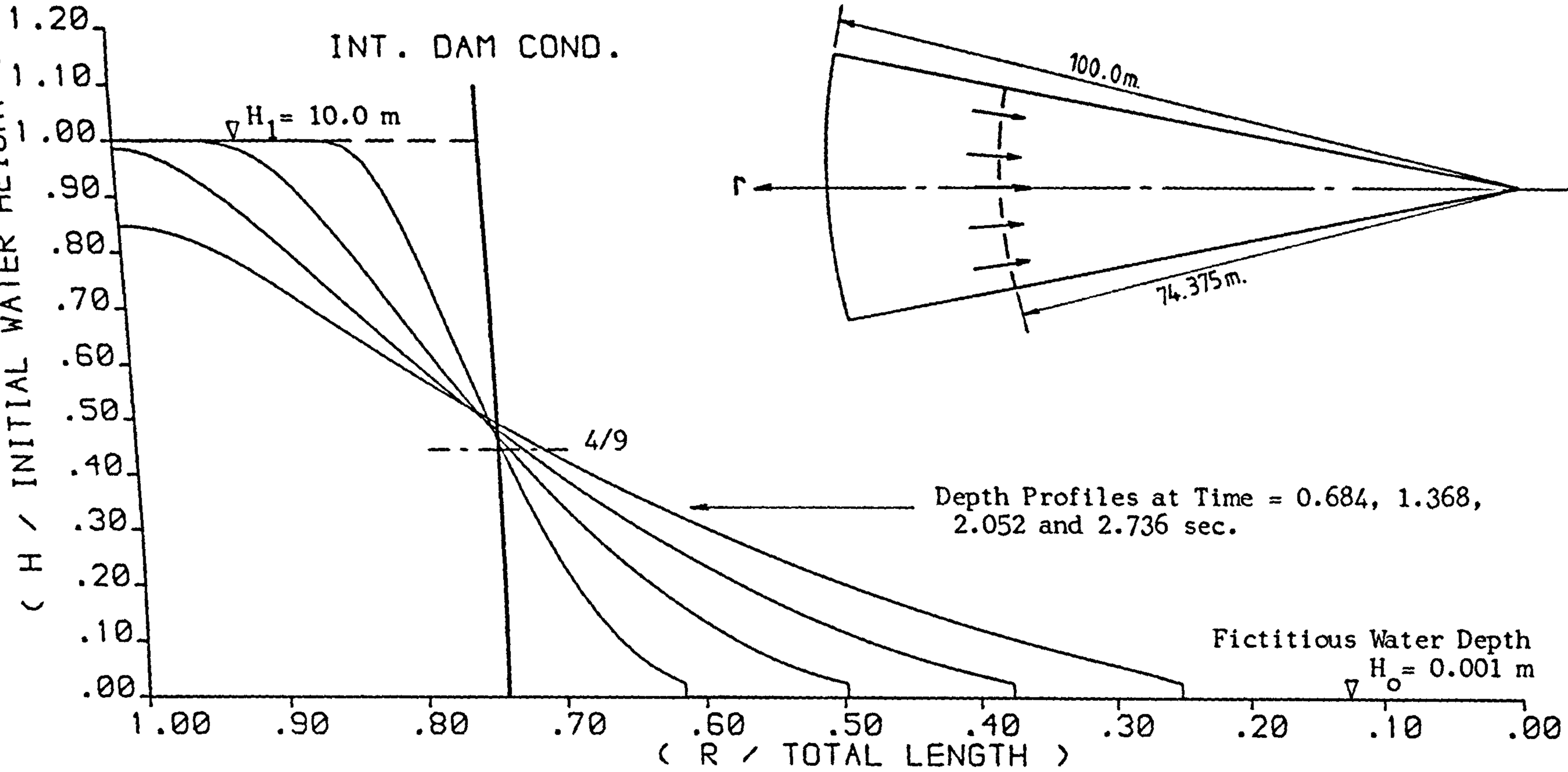

FIGURE 4.40 : DAM – BREAK WAVE THROUGH A CONTRACTING SECTION WHERE r_R= 0.0 .

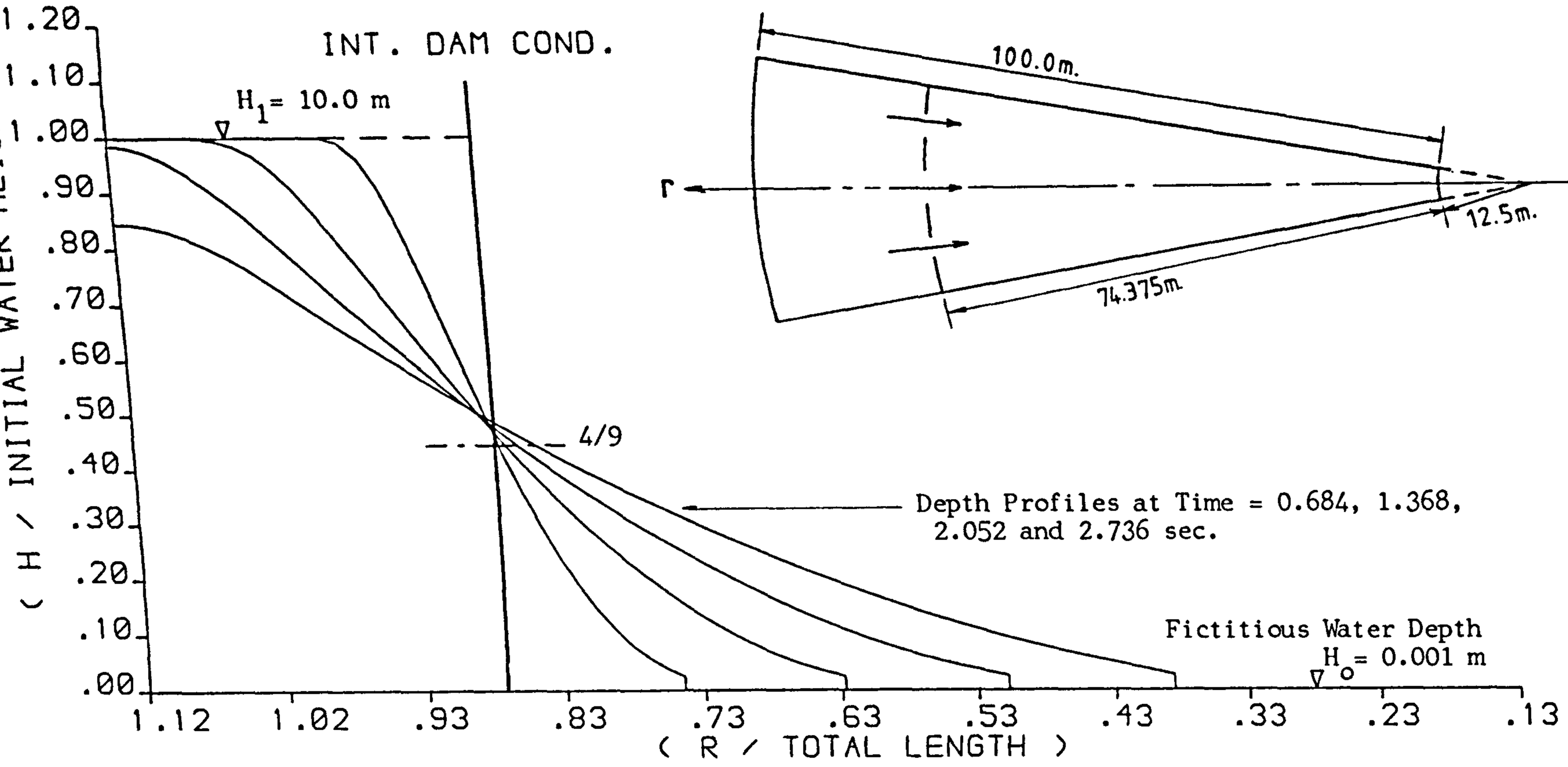

FIGURE 4.41 : DAM – BREAK WAVE THROUH A CONTRACTING SECTION WHERE r_R = 12.5 m .

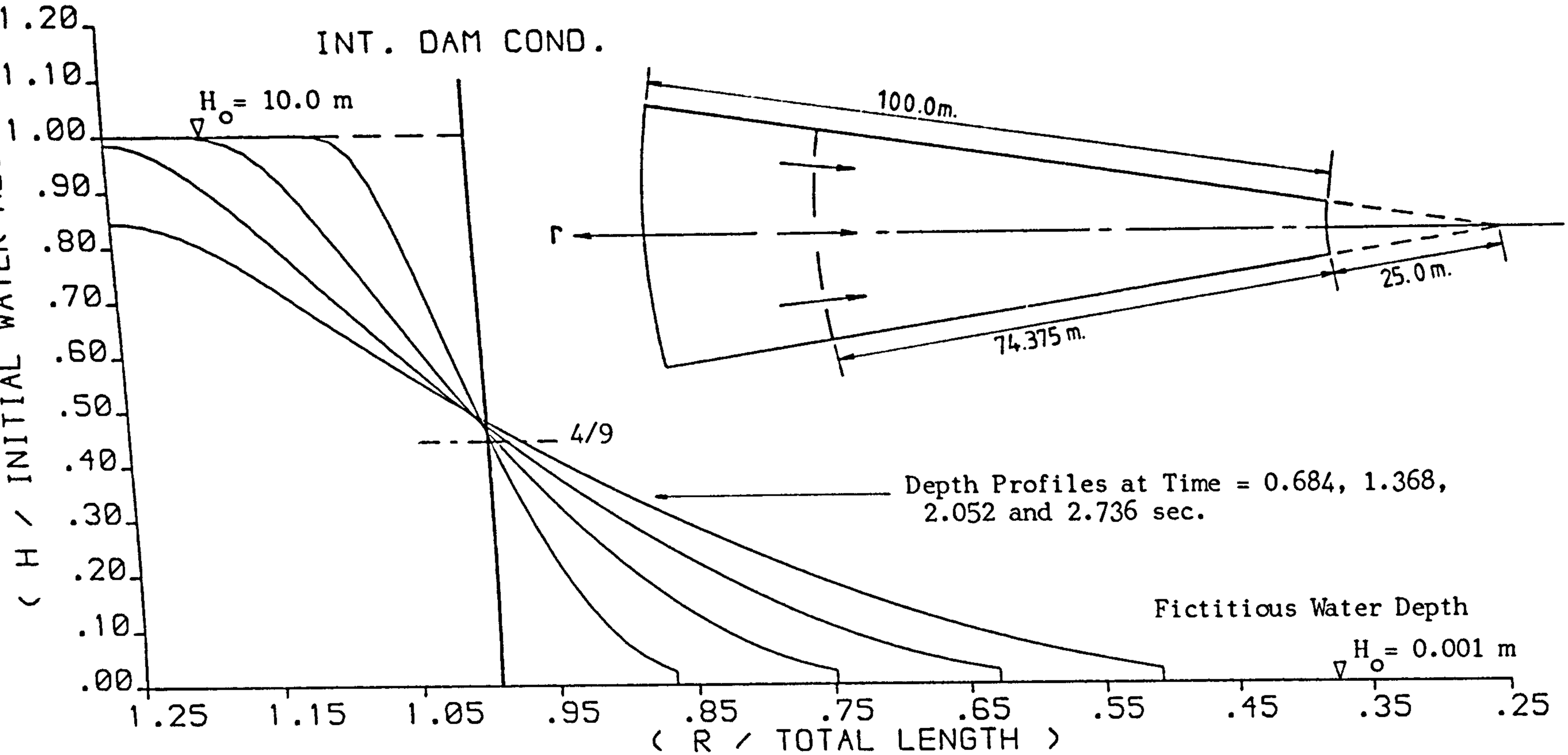

FIGURE 4.42 : DAM – BREAK WAVE THROUGH A CONTRACTING SECTION WHERE r_R = 25.0 m .

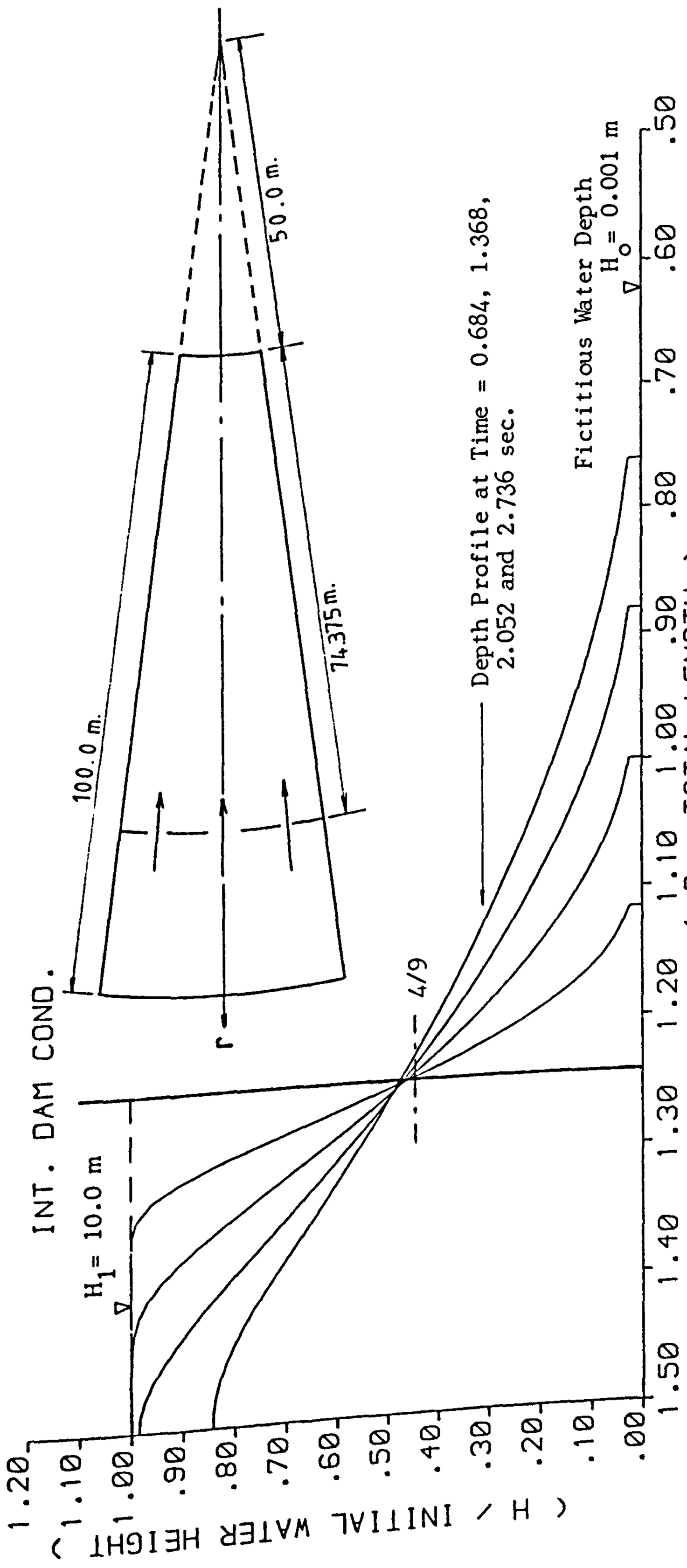

FIGURE 4.43 : DAM – BREAK WAVE THROUGH A CONTRACTING SECTION WHERE r_R = 50.0 m .

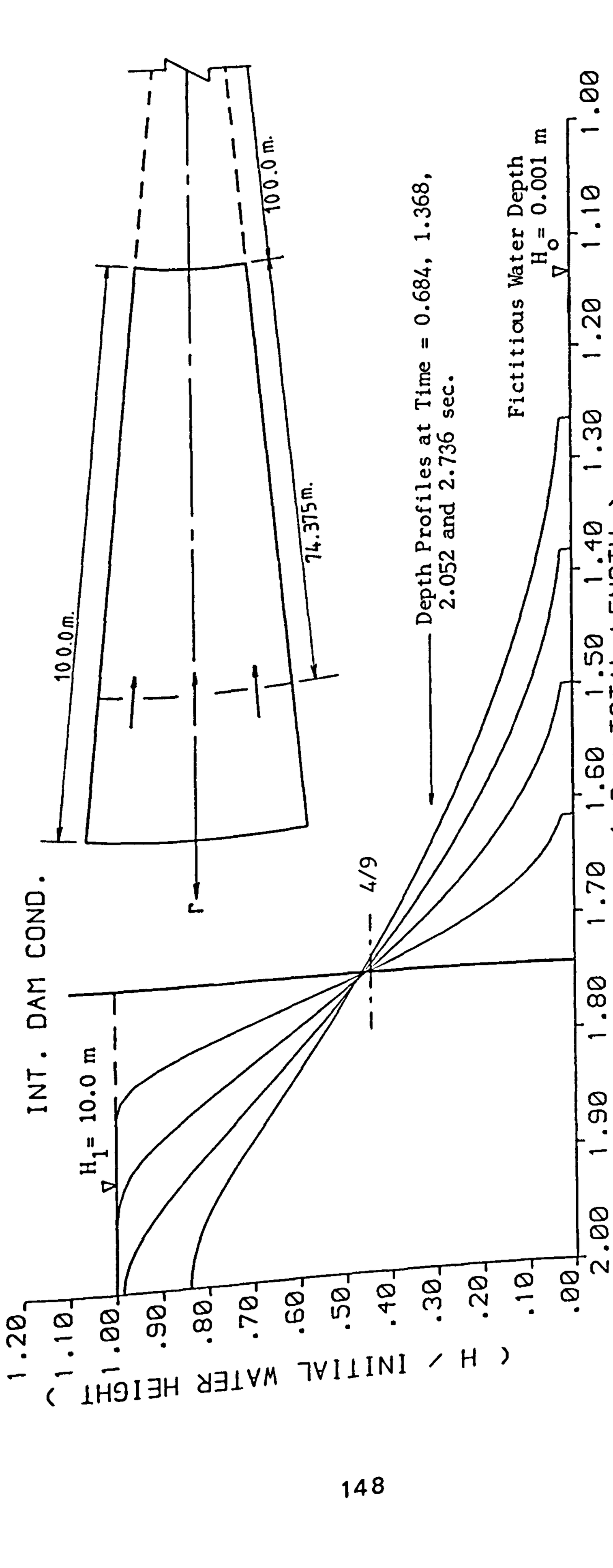

FIGURE 4.44 : DAM – BREAK WAVE THROUGH A CONTRACTING SECTION WHERE r_R = 100.0 m .

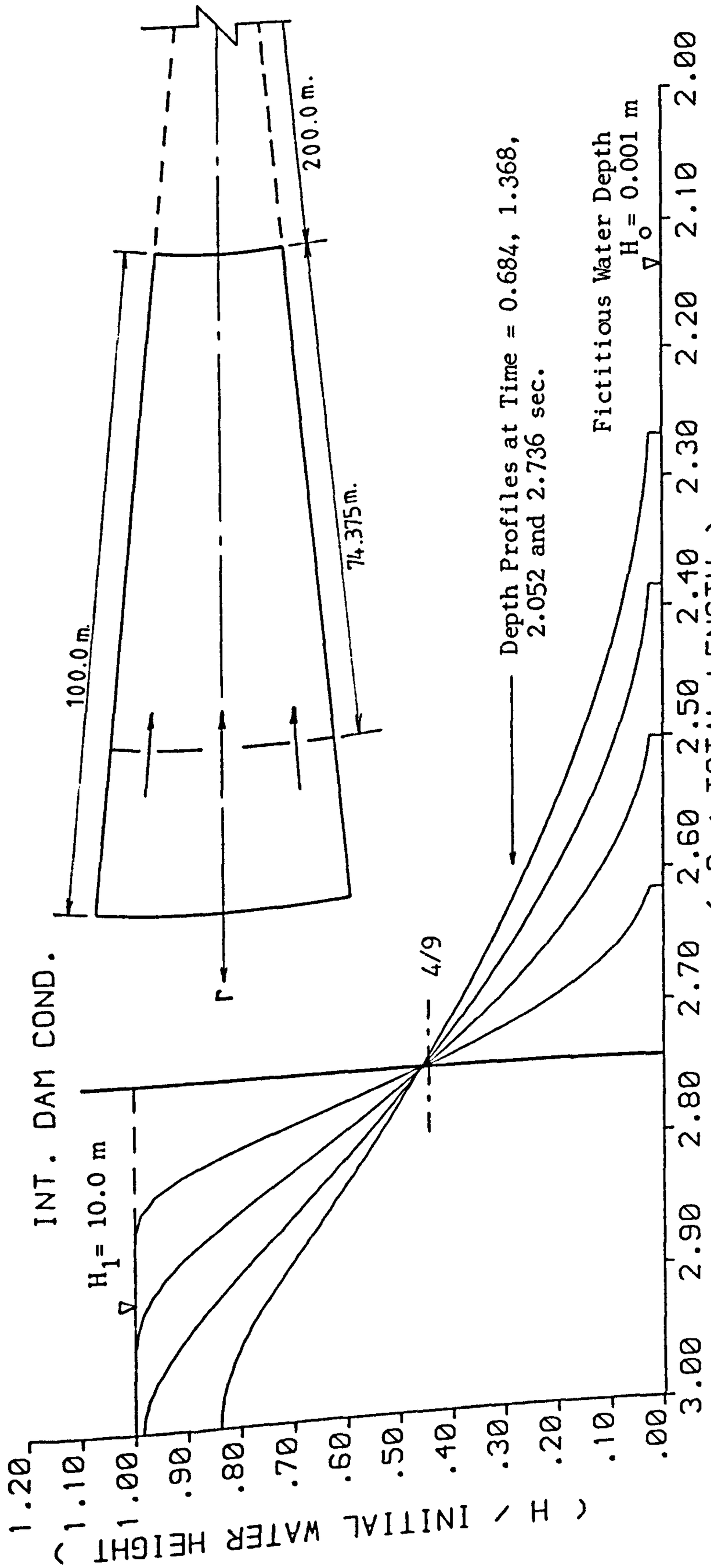

FIGURE 4.45 : DAM – BREAK WAVE THROUGH A CONTRACTING SECTION WHERE r_R = 200.0 m .

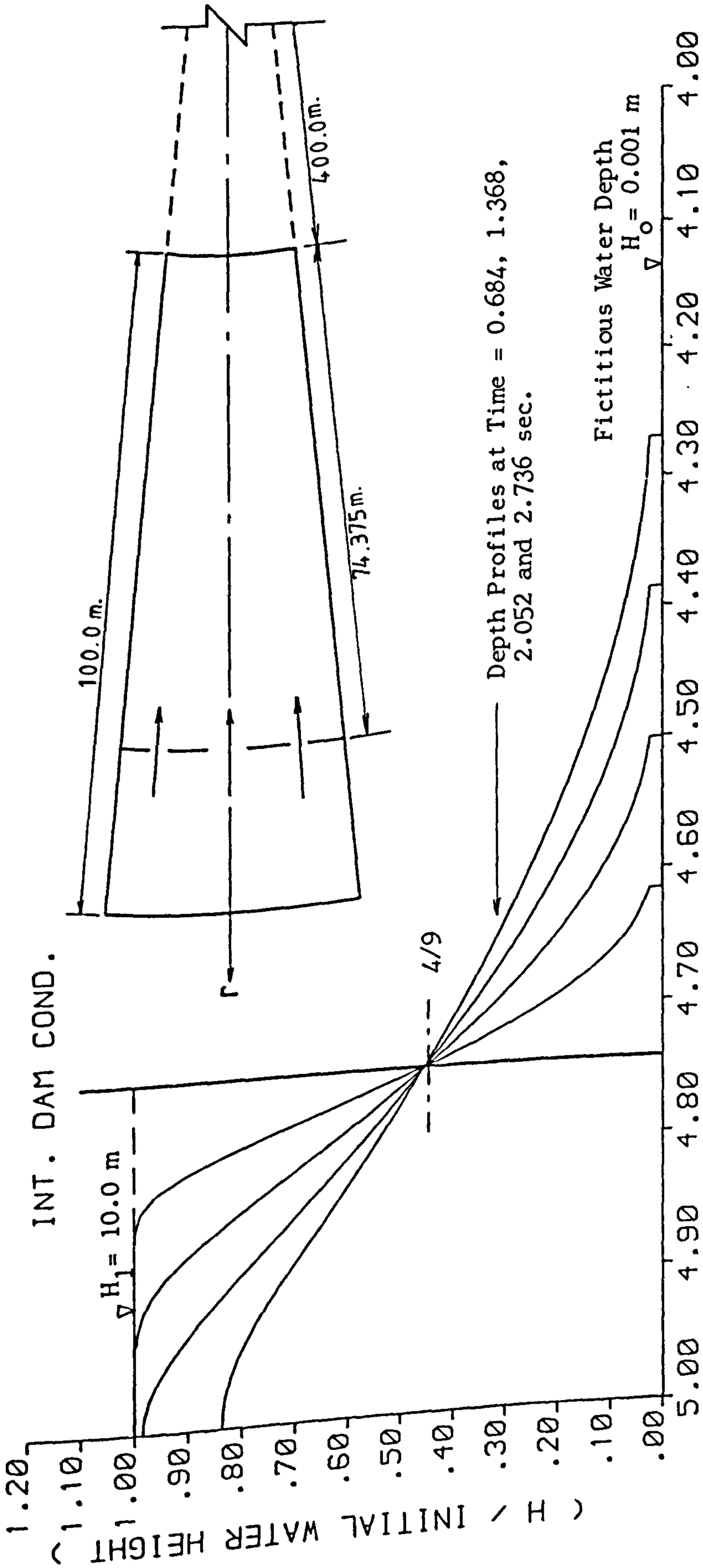

FIGURE 4.46 : DAM - BREAK WAVE THROUGH A CONTRACTING SECTION WHERE r_R = 400.0 m .

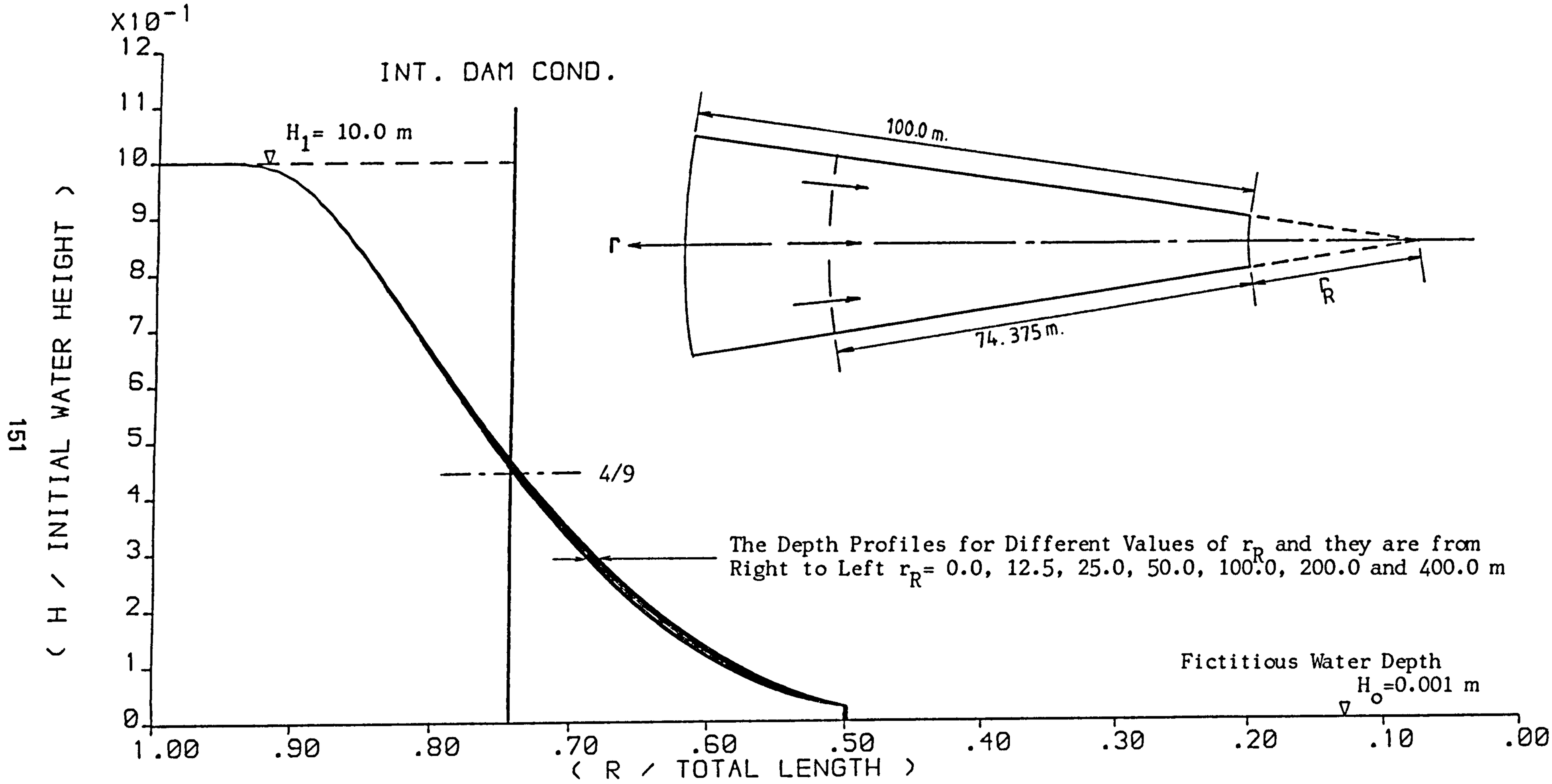

FIGURE 4.47 : DAM – BREAK WAVE THROUGH A CONTRACTING SECTION AT TIME = 1.368 sec WITH r_R= FROM 0.0 TO 400.0 m.

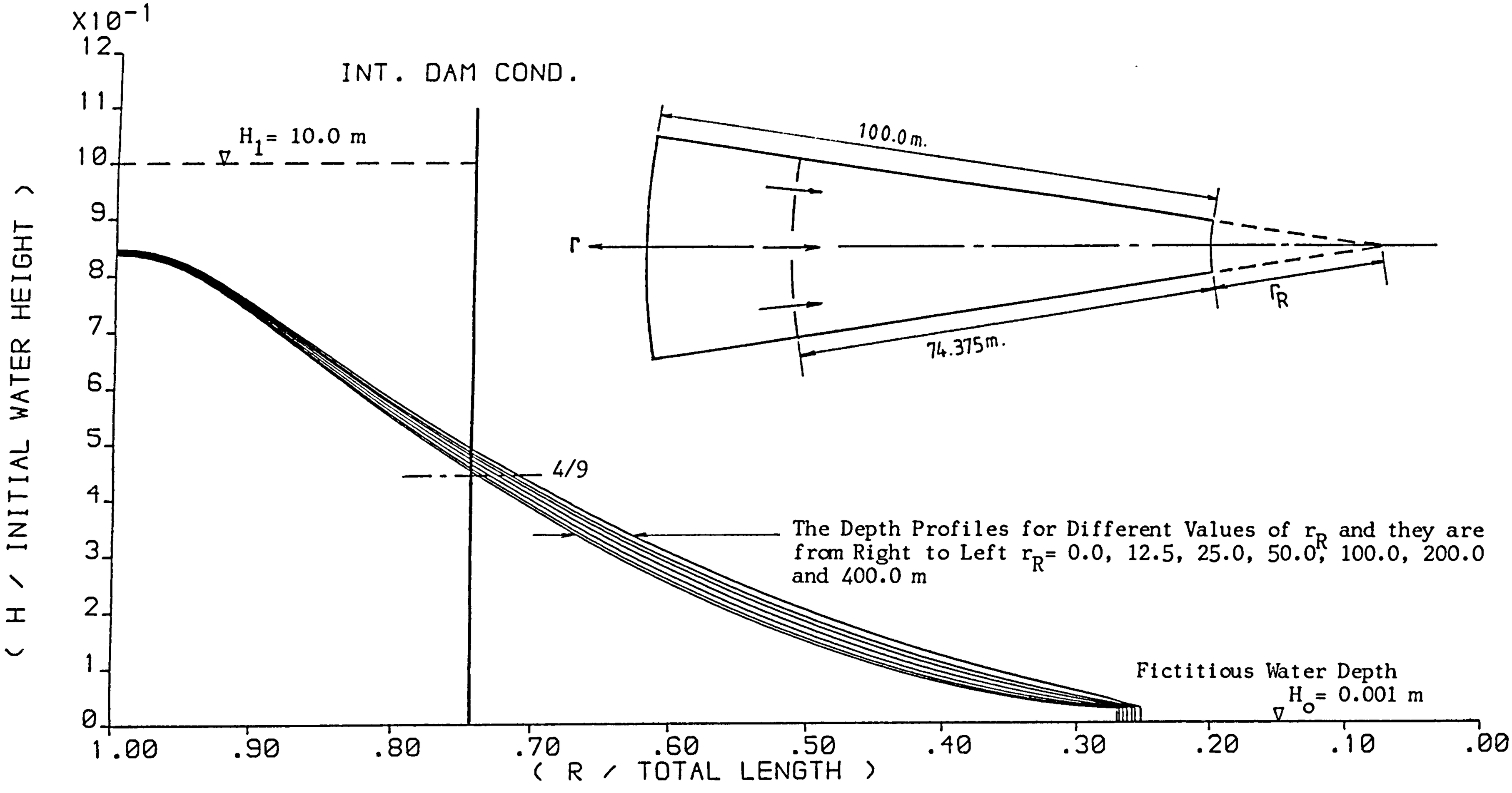

FIGURE 4.48 : DAM – BREAK WAVE THROUGH A CONTRACTING SECTION AT TIME = 2.736 sec WITH r_R = FROM 0.0 TO 400.0 m.

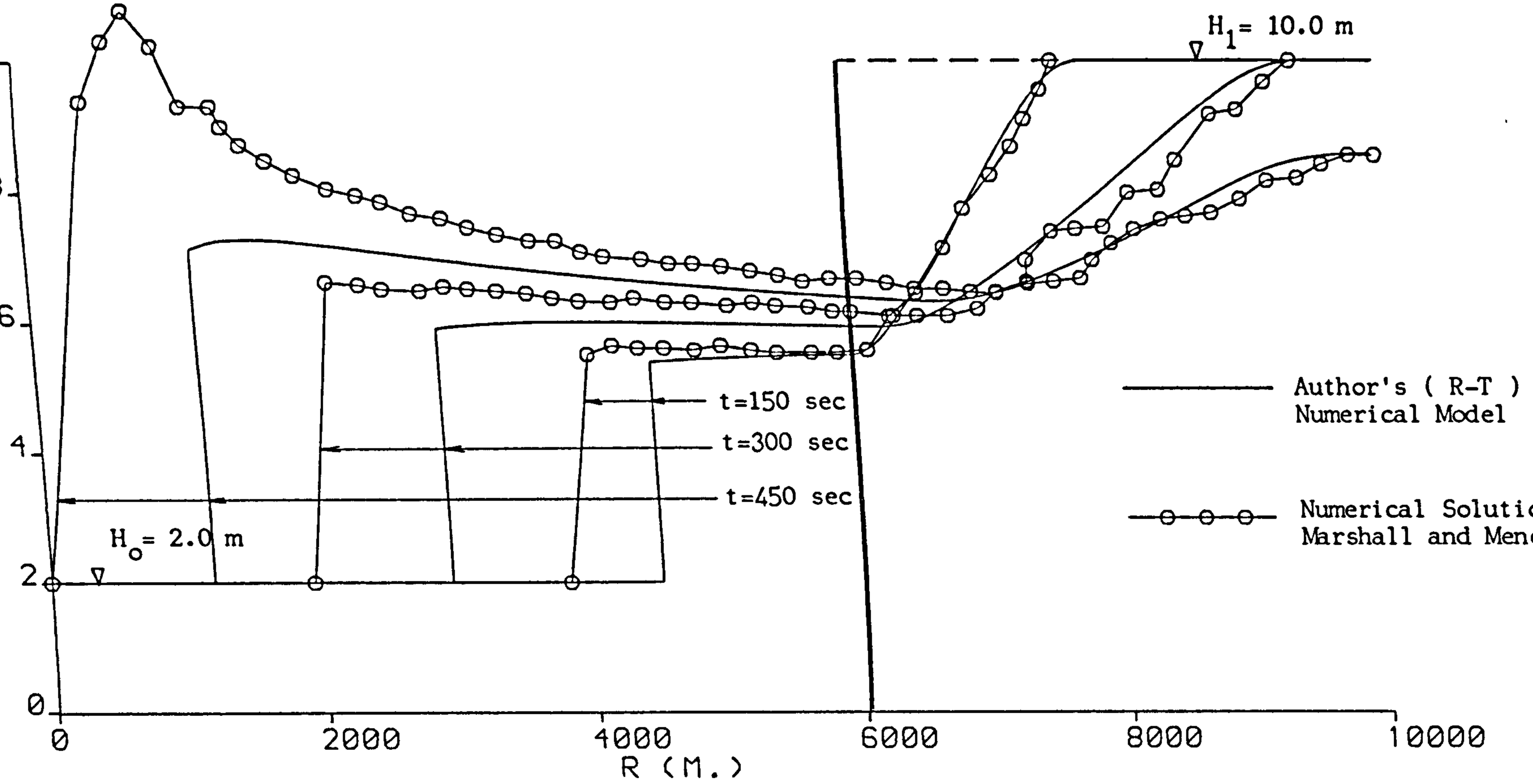

FIGURE 4.49 : THE COMPARISON OF THE DAM - BREAK WAVE THROUGH A CONTRACTING CHANNEL SECTION AS CALCULATED BY THE AUTHOR'S (R-T) NUMERICAL MODEL WITH THE NUMERICAL SOLUTION BY MARSHALL AND MENENDEZ .

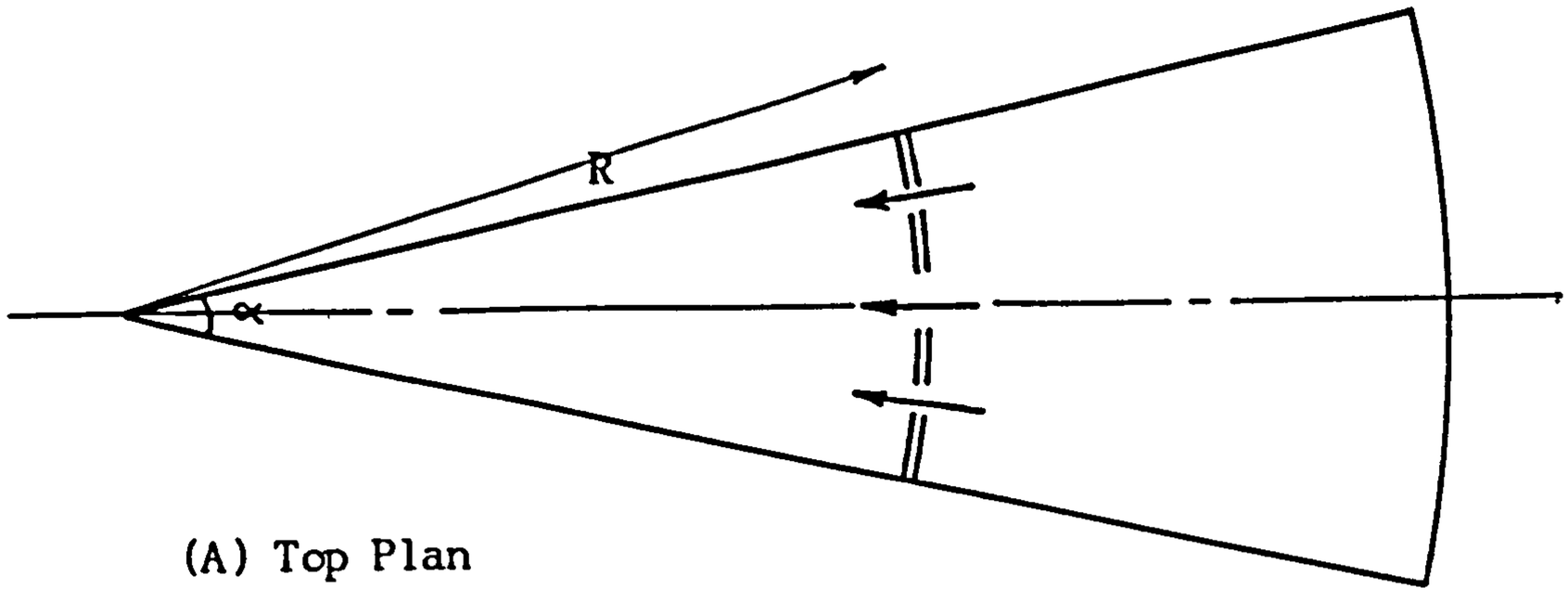

(A) Top Plan

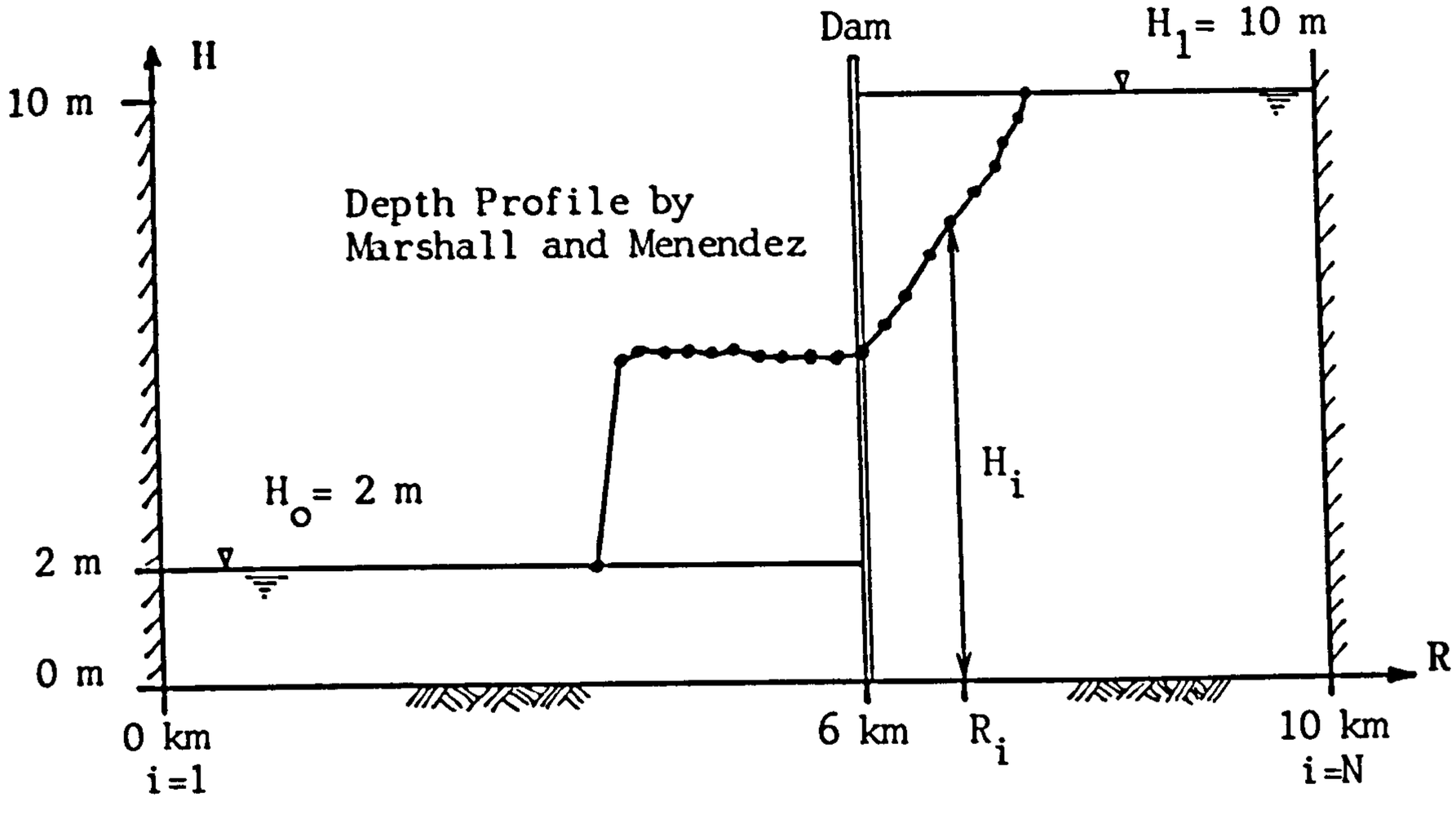

(B) Longitudinal Section

$$\text{Total Volume of Water Before Failure} = 10 \times 4000 \times \frac{10000 + 6000}{2} \times \propto + 2 \times 6000 \times \frac{0 + 6000}{2} \times \propto$$

$$\text{Total Volume of Water After Failure} = \sum_{i=1}^{i=N} \left(\frac{H_i + H_{i+1}}{2} \right) \times (R_i - R_{i+1}) \times \left(\frac{R_i + R_{i+1}}{2} \right) \times \propto$$

$$\%\ \text{Error} = \frac{\text{Volume Before Failure} - \text{Volume After Failure}}{\text{Volume Before Failure}} \times 100$$

Time sec	% Error in	
	The Author's Model	Marshall and Menendez Model
150	- 0.03	- 2.82
300	- 0.016	- 2.58
450	0.069	- 3.66

Note : The negative sign means the model is creating mass .

FIGURE 4.49 (a) : TYPICAL ESTIMATE OF ERRORS IN NUMERICAL MODEL MASS CONSERVATION .

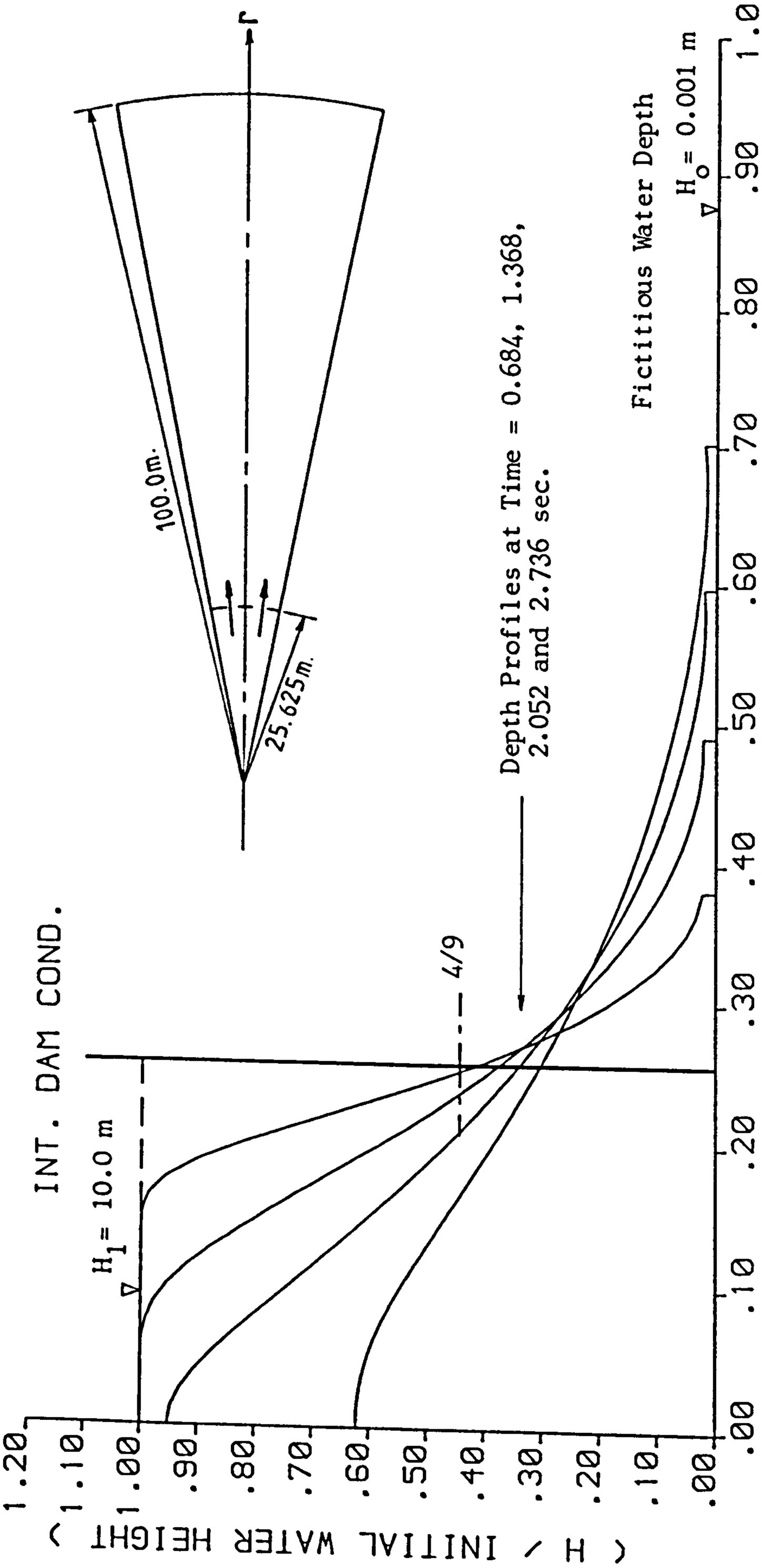

FIGURE 4.51 : DAM – BREAK WAVE THROUGH AN EXPANDING SECTION WHERE r_L = 0.0 .

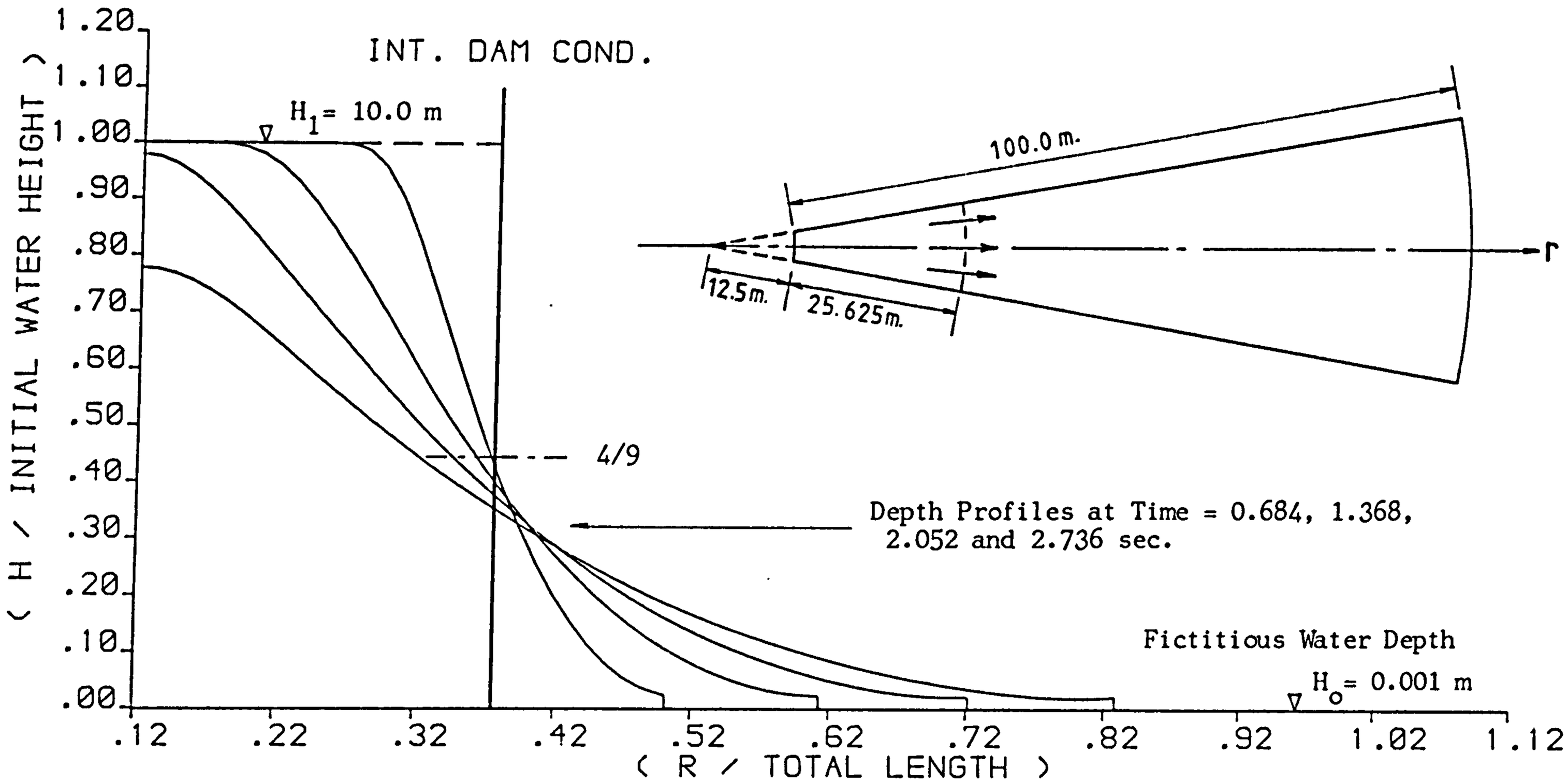

FIGURE 4.52 : DAM - BREAK WAVE THROUGH AN EXPANDING SECTION WHERE r_L = 12.5 m .

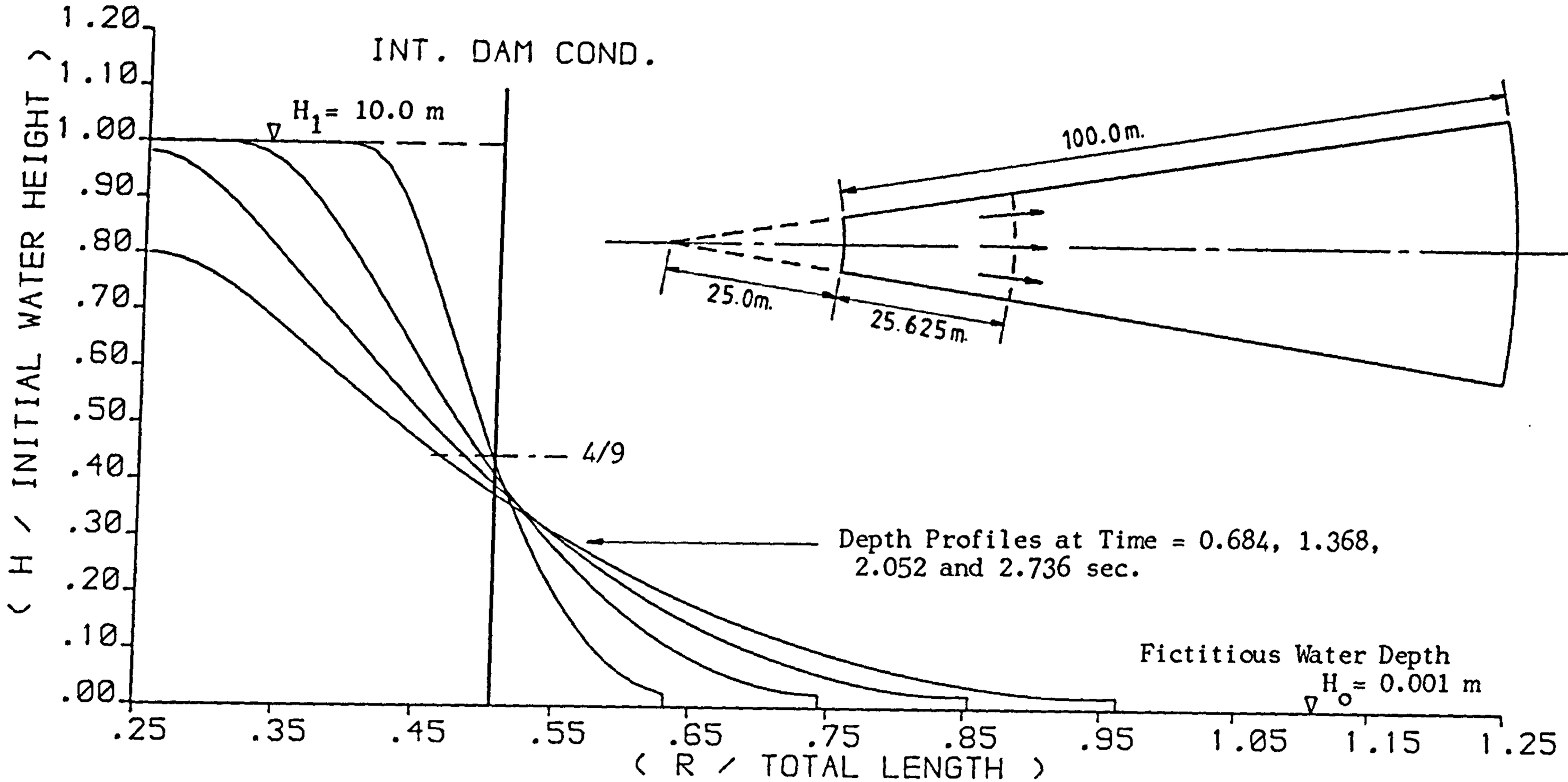

FIGURE 4.53 : DAM – BREAK WAVE THROUGH AN EXPANDING SECTION WHERE r_L = 25.0 m .

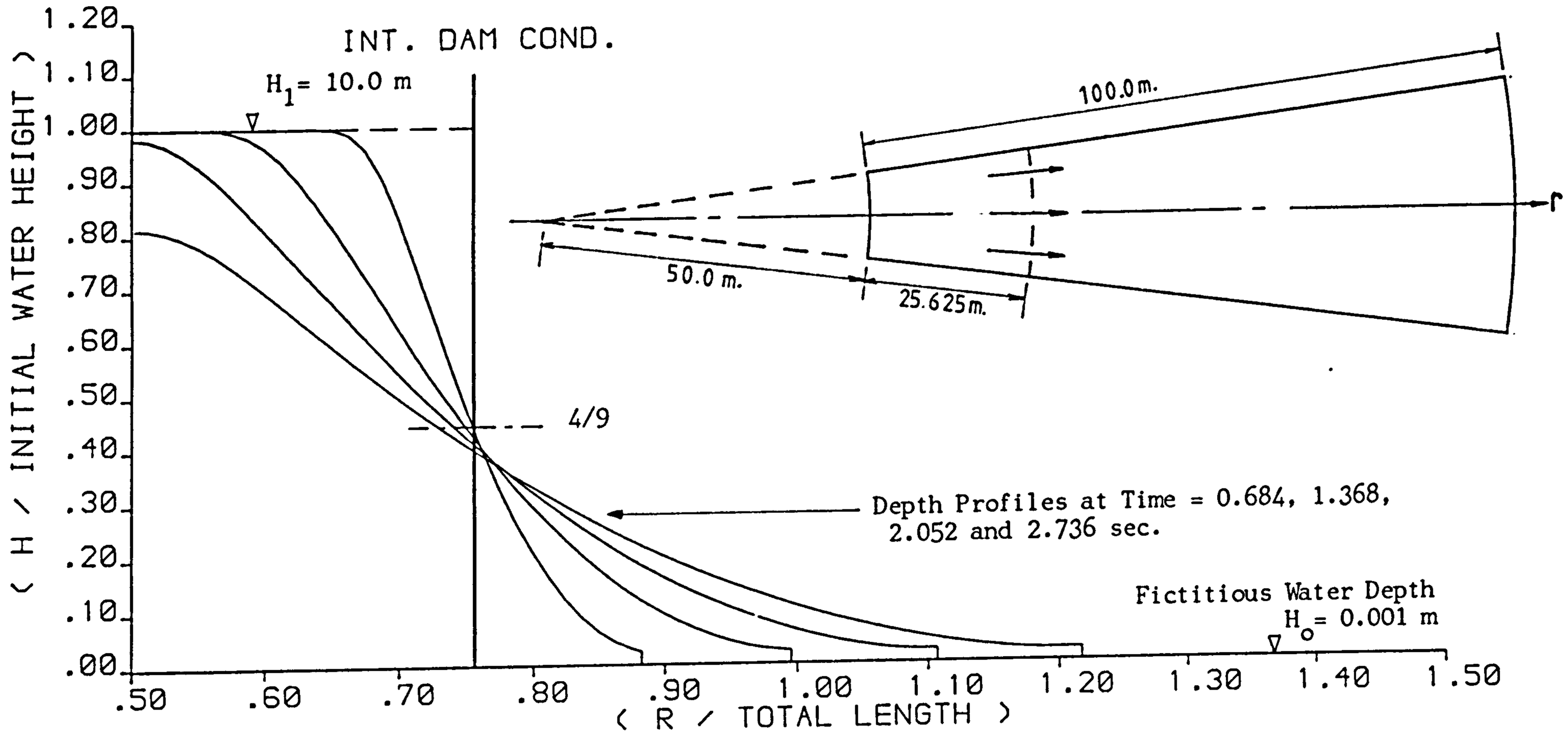

FIGURE 4.54 : DAM – BREAK WAVE THROUGH AN EXPANDING SECTION WHERE r_L= 50.0 m .

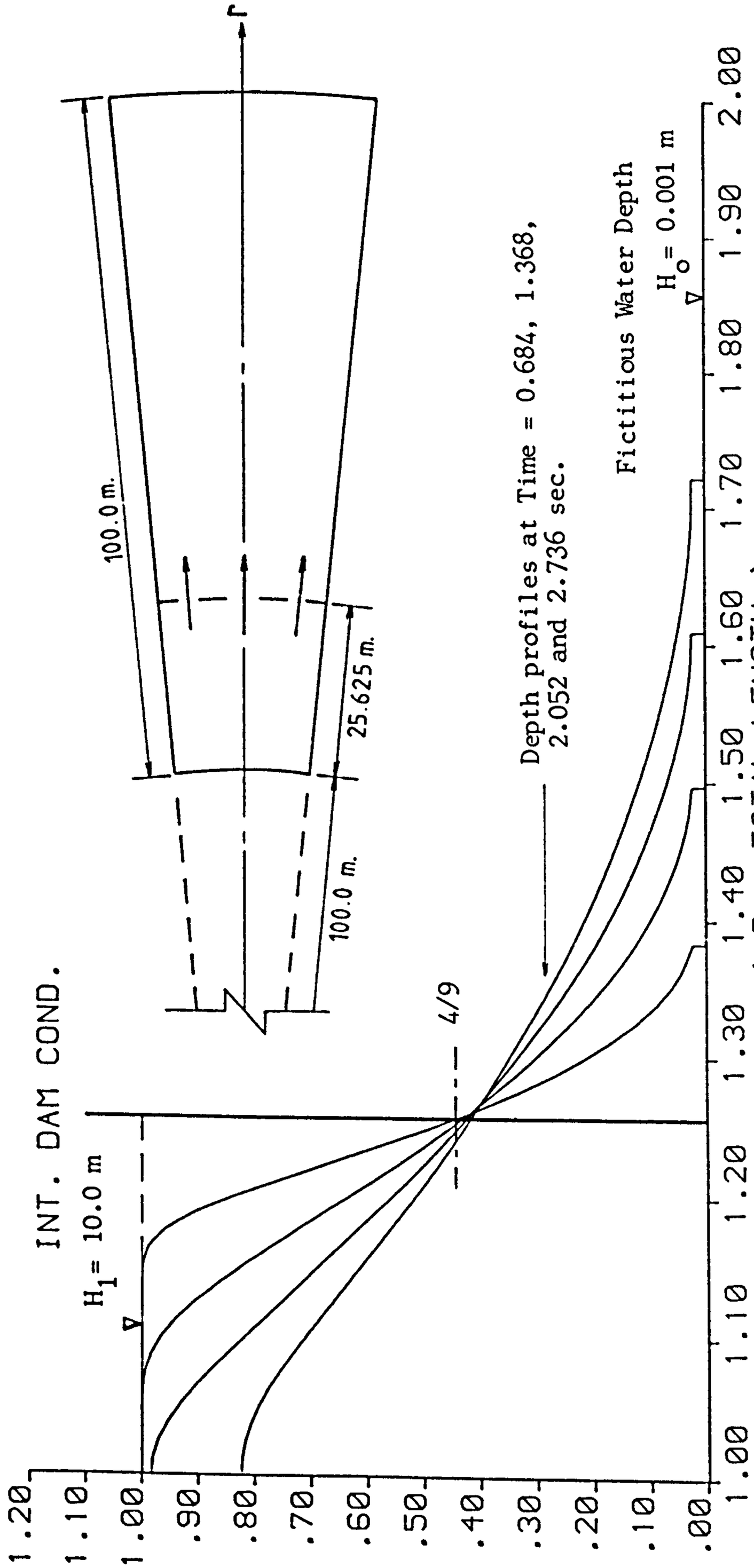

FIGURE 4.55 : DAM – BREAK WAVE THROUGH AN EXPANDING SECTION WHERE r_L = 100.0 m .

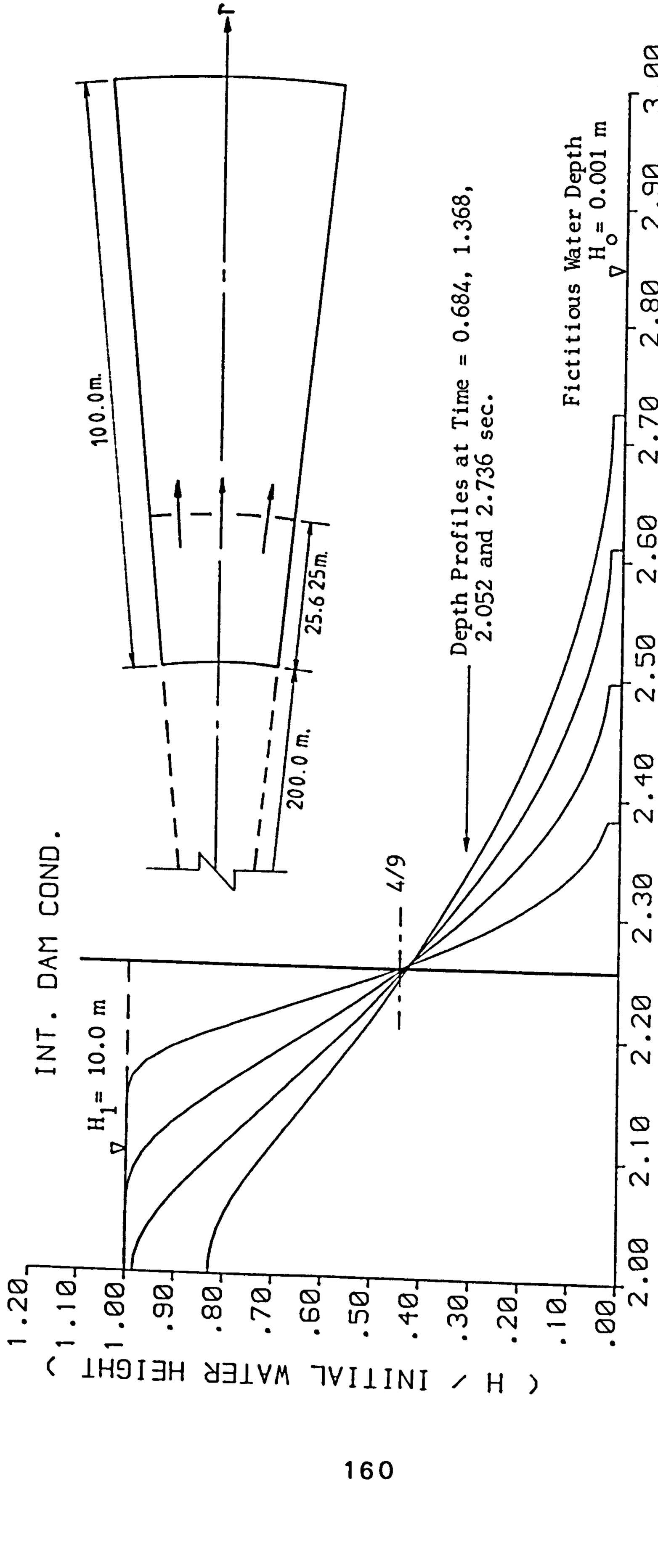

FIGURE 4.56 : DAM – BREAK WAVE THROUGH AN EXPANDING SECTION WHERE r_L = 200.0 m .

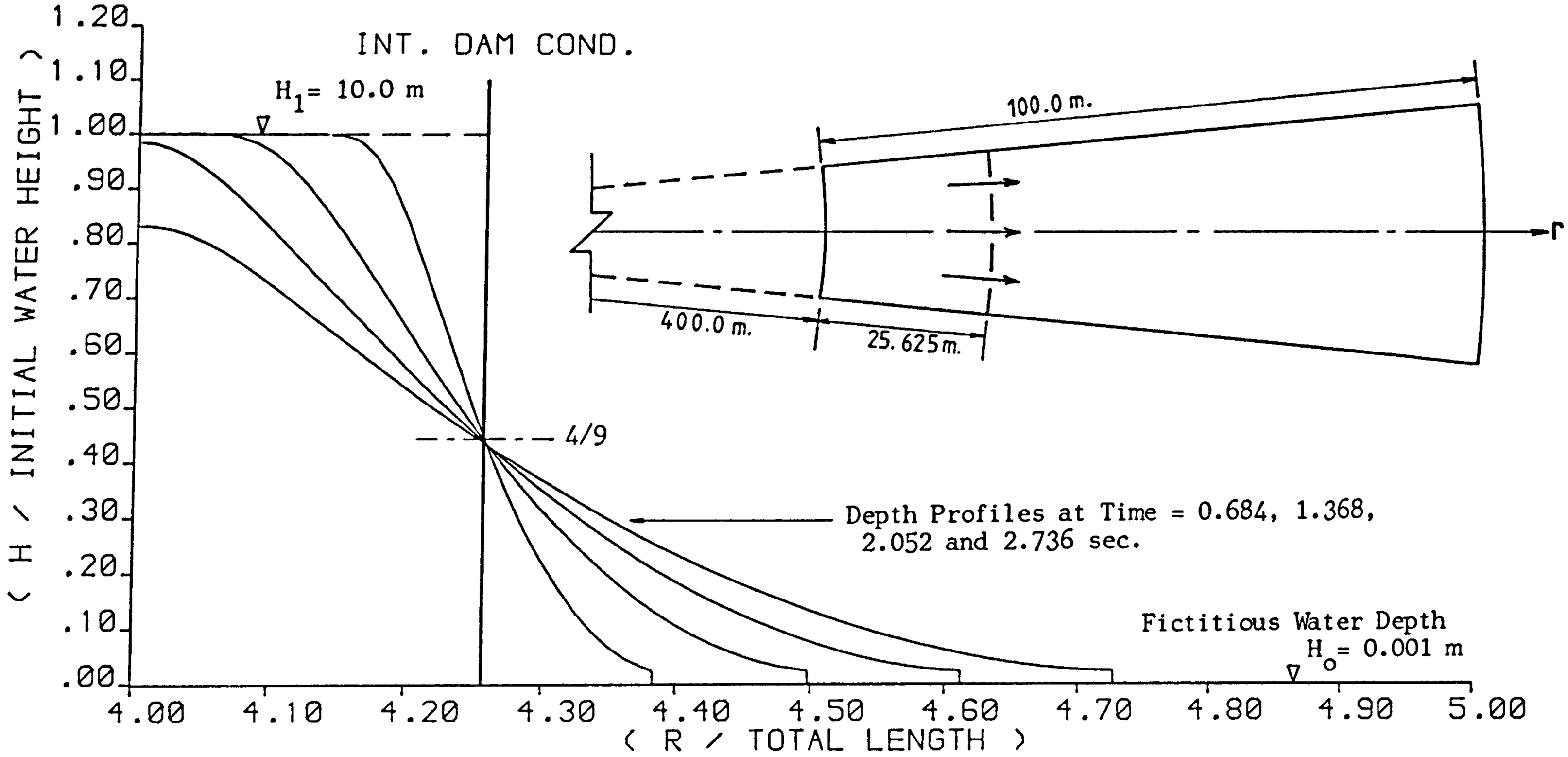

FIGURE 4.57 : DAM – BREAK WAVE THROUGH AN EXPANDING SECTION WHERE r_L = 400.0 m .

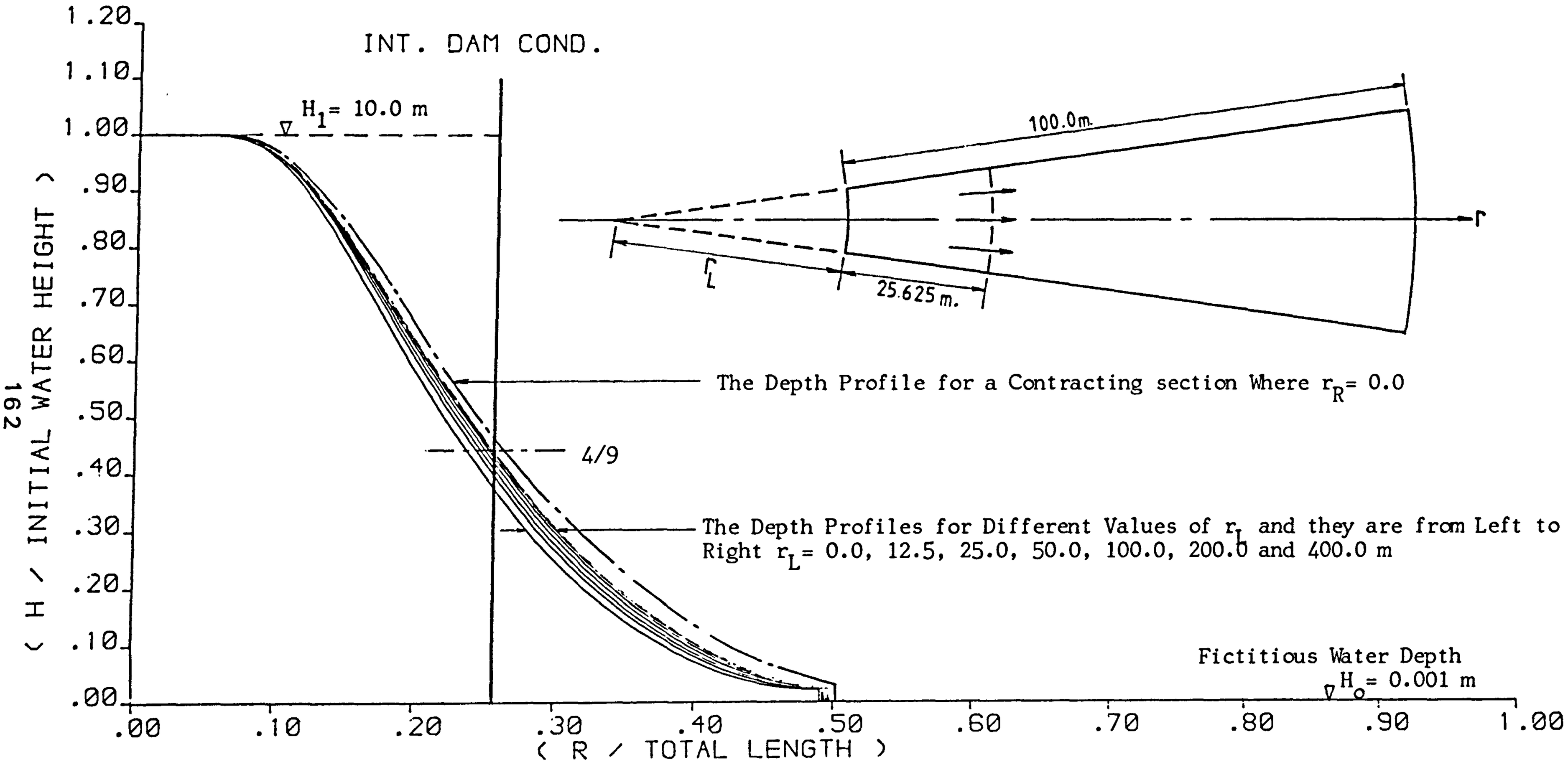

FIGURE 4.58 : DAM – BREAK WAVE THROUGH AN EXPANDING SECTION AT TIME = 1.368 sec WITH r_L FROM 0.0 TO 400.0 m.

CHAPTER FIVE
THE PHYSICAL MODELS

5.1 General Layout of Tests

The reservoir and the downstream channel can be simulated by connecting three main sections together, depending on the geometry. The three sections are (as mentioned in Chapter One):

1. Plain or parallel sides (X-T).
2. Contracted or convergent sides (R-T).
3. Expanded or divergent sides (R-T).

The numerical models for each of the above three sections, discussed singly in chapters three and four; may be connected together in pairs to produce three composite models, as follows:

1. Contracted - plain (RT-XT).
2. Contracted - expanded (RT-RT).
3. Plain - expanded (XT-RT).

For these three and the plain one, four physical models were built in the Hydraulics Laboratory of the University. The models were built from four plastic-coated plywood walls. Two walls for each side of the dam, the reservoir and the downstream channel, were placed and sealed on the base of large steel tank capable of containing each composite model. The wall joints were sealed by a metallic tape and the bed of each model was covered with clear smooth perspex. The gate which performed the role of a dam was fixed in the middle of the tank between two wing walls, as shown in Figure 5.1 (at the end of the chapter).

The first model was the plain (X-T) model with parallel sides giving a channel 0.1 m wide, 0.465 m deep and 4.085 m long of which 1.828 m acted as a reservoir, as illustrated in Figure 5.2. The main purpose of this model was as a further cross-check between the general performance of the experimental models and the numerical ones [since the (X-T) numerical model had already been tested against previous work in Chapter Four].

The second model was the contracted-plain (RT-XT) model with the same (X-T) downstream channel and a section upstream contracting from 0.259 m to 0.1 m having same length and depth as the (X-T) model, as illustrated in Figures 5.2 to 5.4.

The third model was the contracted-expanded (RT-RT) case in which the previous parallel section was replaced by a section downstream expanding from 0.1 m to 0.297 m also of the same length and depth as the former models, which is represented in Figures 5.2 and 5.5.

In the final model the above sequence was continued; the plain-expanded (XT-RT) model retained the same (RT-RT) downstream side and the previous (X-T) upstream side was reintroduced as illustrated in Figures 5.2 and 5.6.

5.2 Experimental Arrangements and Procedure

In all models the gate was lifted manually by a quick-lift mechanism. The gate moved freely in vertical, plastic grooves on each side of an aluminium frame. The gate was lifted by pulling a lever connected to the gate by a steel wire through a pulley, as

shown in Figures 5.1, 5.7 and 5.8. Thus the time required to lift the gate was less than 0.1 sec. which, being small compared with the wave propagation time, seemed likely to simulate full and instantaneous collapse of a dam.

Prior to the gate's removal, inflow created a reservoir upstream. As soon as the dam collapsed, the dam-burst wave moved downstream until it was reflected by the downstream dead end. Prior to reflection of the front, conditions could be described as representing the usual dam-break situation.

Water depths with respect to time were obtained at six different cross-sections along the channel, together with estimates of the position of the front. Different combinations of upstream and downstream initial depths were employed. Records were created largely by the joint use of a high speed tape recorder, a chart recorder, three Churchill-type wave probes upstream, and three pressure transducers downstream. Photographic evidence was also collected.

The six cross-sections were divided into three upstream and three downstream of the dam, being at 0.5, 1.0, 1.792, 2.5, 2.95, and 3.5 m. from the upstream end of the reservoir, as shown in Figure 5.9. At the reservoir side three wave probes were used in order to record the drop in the water elevation with time at three sections after lifting the gate. The first two probes P_1 and P_2 were connected to the chart recorder while the third probe P_3 was also connected to the tape recorder. Since the downstream channel was dry for a certain number of experiments the use of wave probes

was unsuitable and 'Gaeltec' pressure transducers were deployed. These were placed inside cups below holes in the bed of the downstream channel so as to transfer an initially small hydrostatic pressure from the channel to the transducers. The transducers were also connected to the tape recorder, as shown in Figures 5.10 to 5.13.

The upstream and downstream initial depths were measured by a point gauge against which the probes and the transducers were calibrated frequently.

5.3 Measurement of Depth with Respect to Time

The dam-break phenomena in the physical model takes a short time (1-2 sec.) so that extra care was taken to ensure accurate response of the measurement system. The tape recorder has four channels to which the three transducers and the probe P_3 were connected while the two probes P_1 and P_2 were connected to the chart recorder which had six channels. During the experiment the water depths at all six sections were registered by the chart recorder at its top speed (60 cm. min^{-1}). At the same time the depths at the four sections P_3, T_1, T_2 and T_3 were also recorded on tape at a speed of 3¾ inches$\cdot sec^{-1}$. After the experiment, the tape recorder was replayed at a slower speed (15/16 inches$\cdot sec^{-1}$) through the chart recorder at its top speed, thus spreading the wave over a larger time (exactly four times the original recording time). This made for the most accurate extraction of points for comparison with the numerical models.

Each experiment was repeated more than twice to allow for variations in the initial conditions. As the gate was operated manually

it was unlikely that the speed and the time of lifting the gate could be precisely repeated. However, for the majority of the experimental pairs, very little difference was observed between the wave features generated by nominally the same initial conditions. The results of two typical experiments are shown in Figure 5.14 as recorded by the chart recorder and a replay of the same two experiments is shown in Figures 5.15 and 5.16.

Prior to experiments, tests were carried out to find the effect of any flow disturbance by the probe P_3 on the waves, since the probe P_3 is very near to the gate. It was found that no measurable disturbance was created. In addition to this, because of the relative and variable narrowness at some sections, a friction effect was expected at the side walls. This was investigated by placing the three probes close to one of the walls in the (X-T) model and repeating one of the standard tests. The resulting wave fronts did not show any significant changes. It was difficult to make the same comparison for the downstream wave, because of the nature of the transducers.

5.4 Analysis of Physical Results

A summary of conditions for experimental runs in all the four models, giving the different initial upstream and downstream depths (H_1 and H_o respectively) is presented in Table 5.1.

Table 5.1 : Upstream and Downstream Depths (H_1 and H_o) Configurations

H_o/H_1	H_o (cm)		
	H_1=10 cm.	H_1=15cm.	H_1=20 cm.
0	Dry	Dry	Dry
0.025	0.25	0.375	0.5
0.05	0.5	0.75	1.0
0.1	1.0	1.5	2.0
0.176	1.76	2.64	3.52
0.2	2.0	3.0	4.0
0.4	4.0	6.0	8.0
0.8	8.0	12.0	-

In order to analyse the experimental charts, the opening time of the gate, not recorded thereon, must be known. A consistent estimate of this was obtained by using the numerical model. The time between opening the gate and the front reaching the section T_1 was assumed to be equal to the time calculated by the numerical model. It was subsequently observed that the first changes in the trace, from probe P_3, occurred very close to this estimate of failure time. Thus the starting time of the dam-break can be located and the analysis of each recording section can be made, giving attention to the various small distances separating the six pens the chart recorder.

The data obtained from the physical experiments, i.e. water depths at the six sections with respect to time, are compared with the numerical models in the next chapter. Four kinds of figures are presented; the water surface profiles at different times, the stage hydrographs at the six sections, the front trajectory and a comparison with Stoker's solution for the front height. According to Table 5.1, the total number of experimental runs for each model is 23, giving a total of 92 runs for the four models. Only a selection of these experiments is presented in Chapter Six, having a total number of 32, i.e. 8 experiments for each model as illustrated in Table 5.2.

Table 5.2 : A Selection of Experimental Runs from Each Model

H_o/H_1 ratio	H_o downstream	H_1 upstream
0	Dry	10
0.025	0.375	15
0.05	1.0	20
0.1	1.5	15
0.176	1.76	10
0.2	4.0	20
0.4	6.0	15
0.8	8.0	10

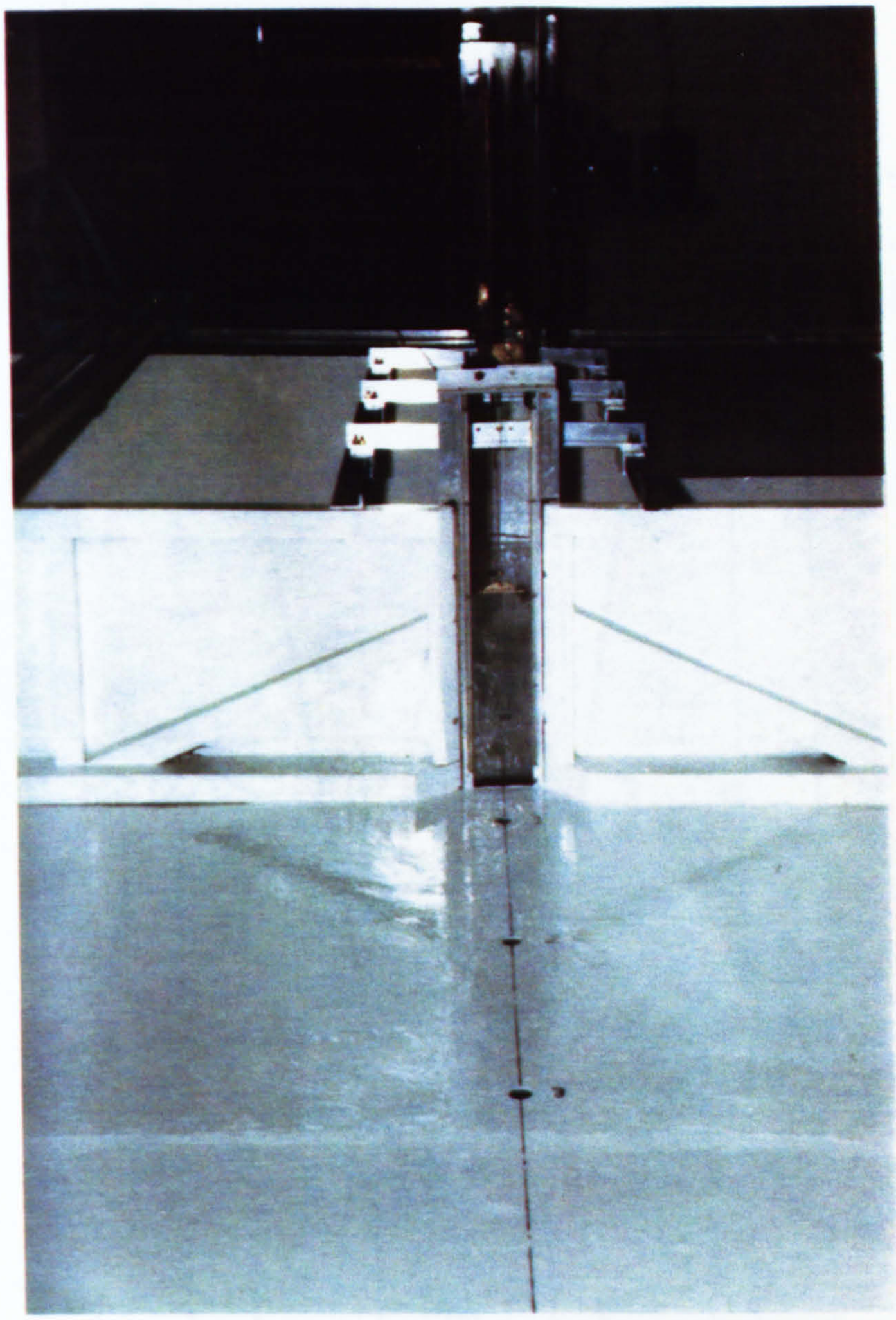

FIGURE 5.1 : THE GATE AND ITS CONTAINING WALLS IN THE STEEL TANK BEFORE BUILDING THE MODELS . THE POSITION OF THE DOWNSTREAM TRANSDUCERS CAN BE SEEN .

1-1 = X-T
2-2 = RT-XT
3-3 = RT-RT
4-4 = XT-RT

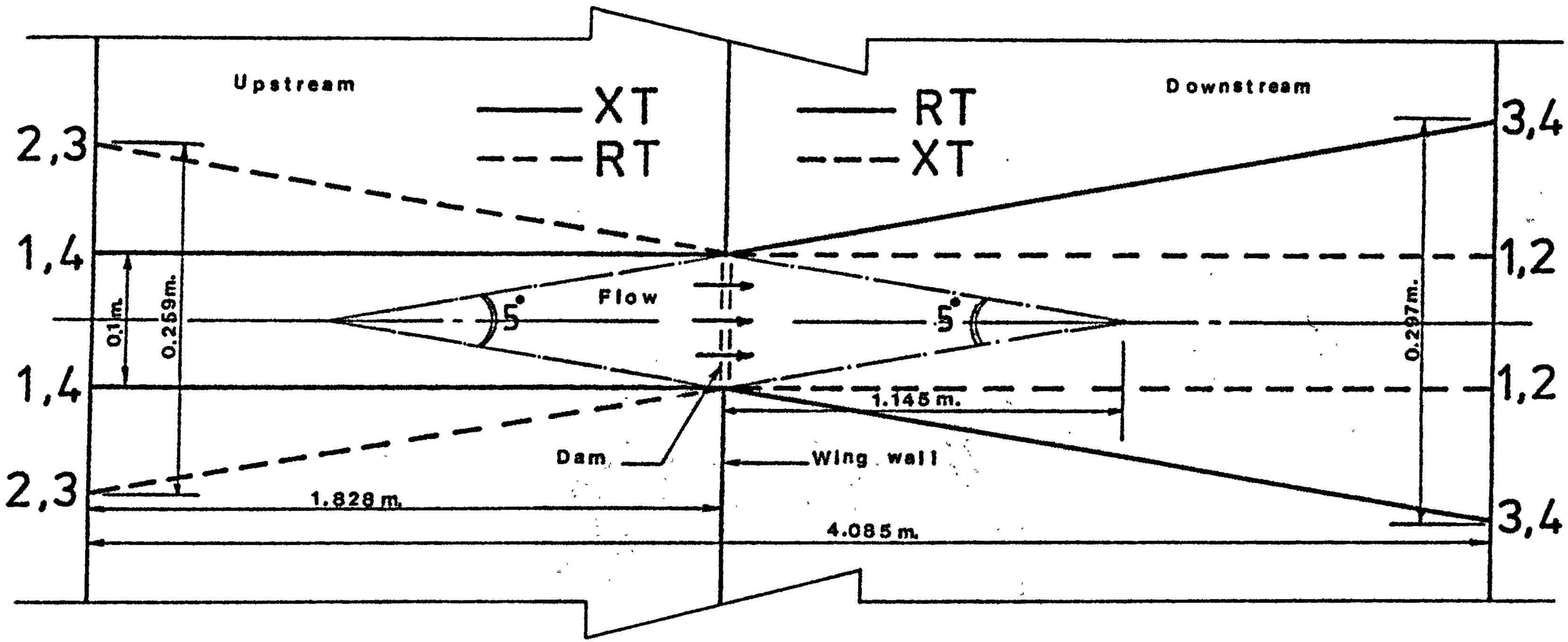

FIGURE 5.2 : PLAN OF LABORATORY TANK SHOWING SEQUENCE OF PHYSICAL MODEL TESTS 1 - 1 TO 4 - 4 .

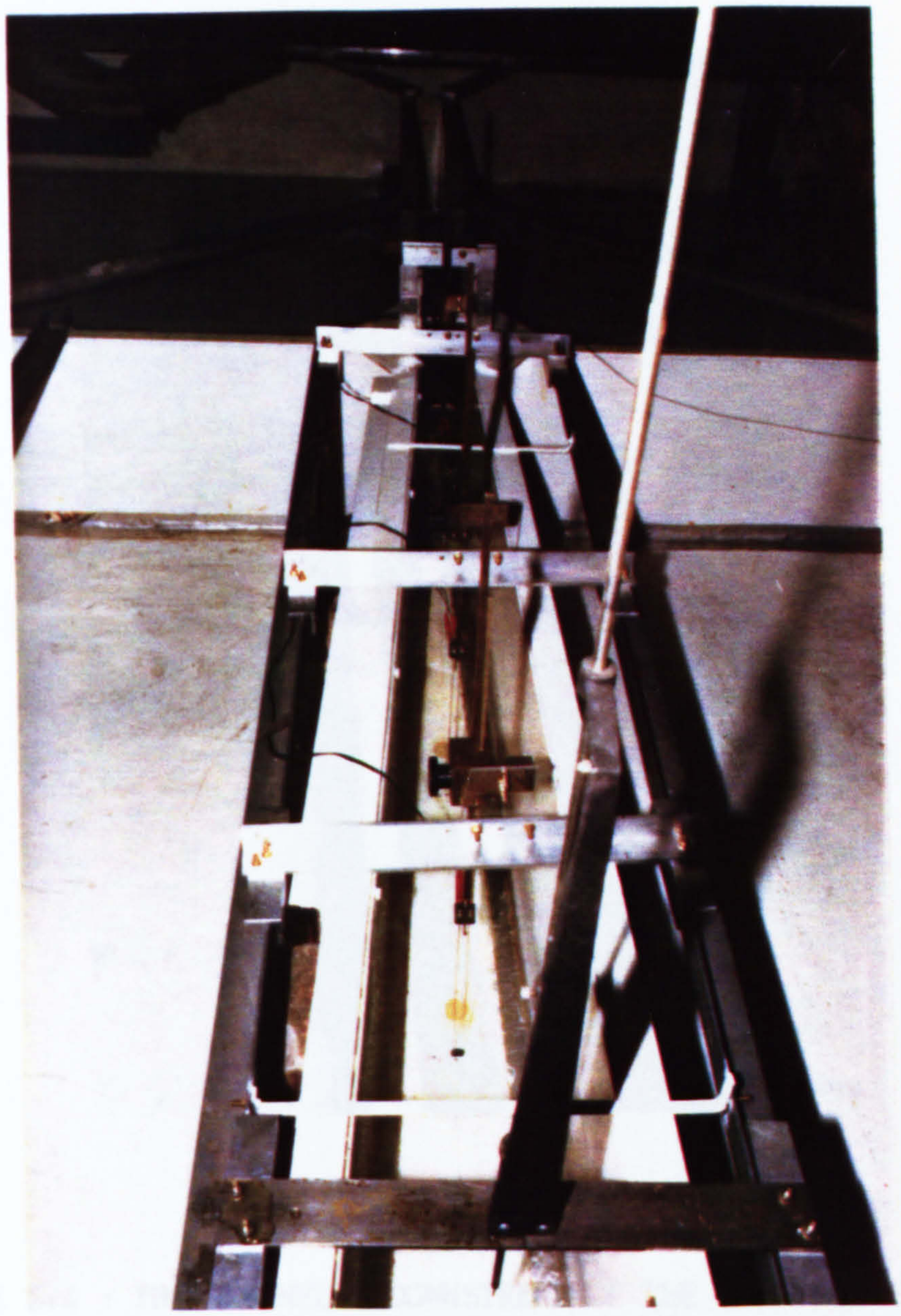

FIGURE 5.3 : THE RESERVOIR SIDE (UPSTREAM OF THE GATE) IN THE (RT-XT) MODEL , SHOWING PROBES AND DEPTH GAUGE .

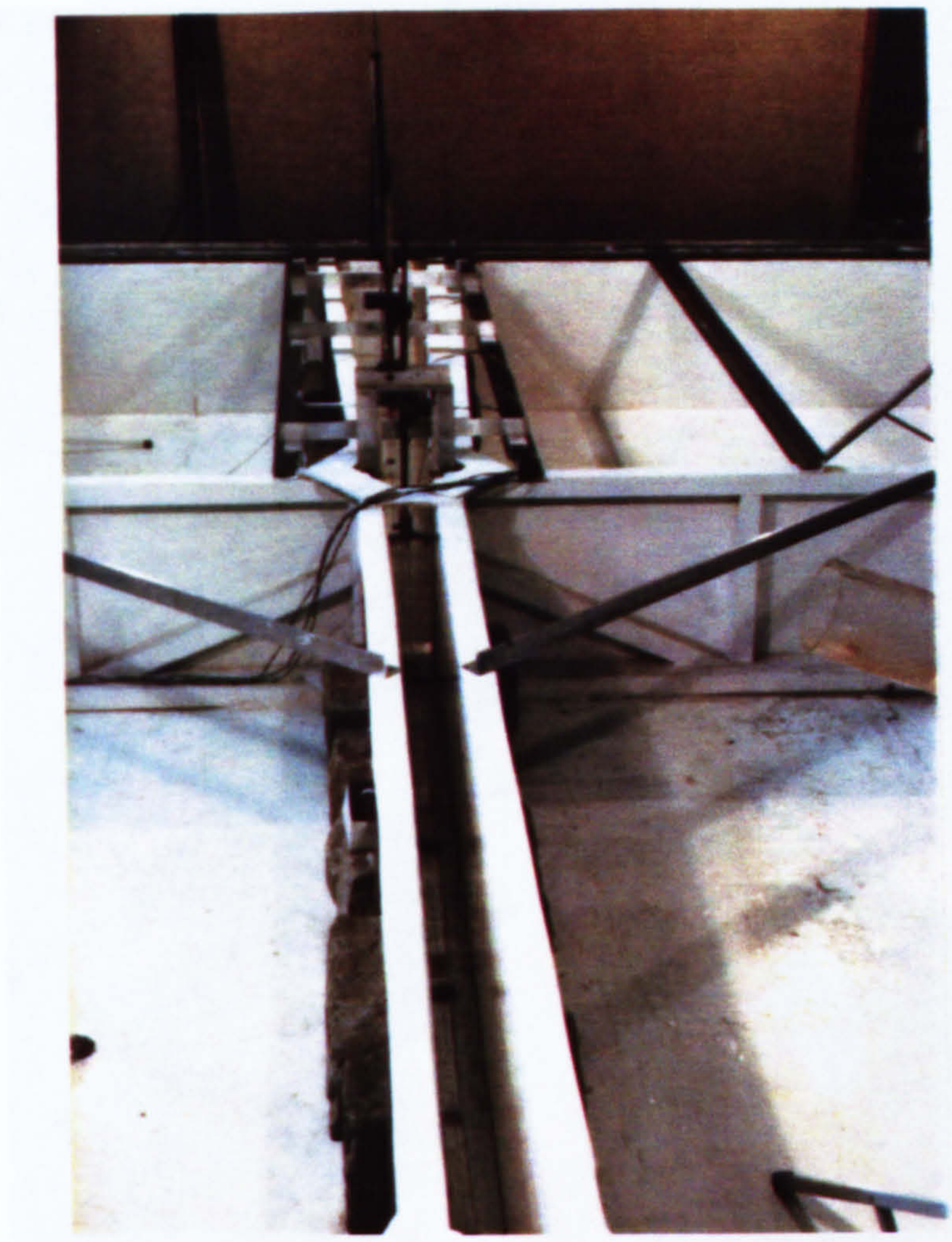

FIGURE 5.4 : THE CHANNEL (DOWNSTREAM OF THE GATE) IN THE (RT-XT) MODEL .

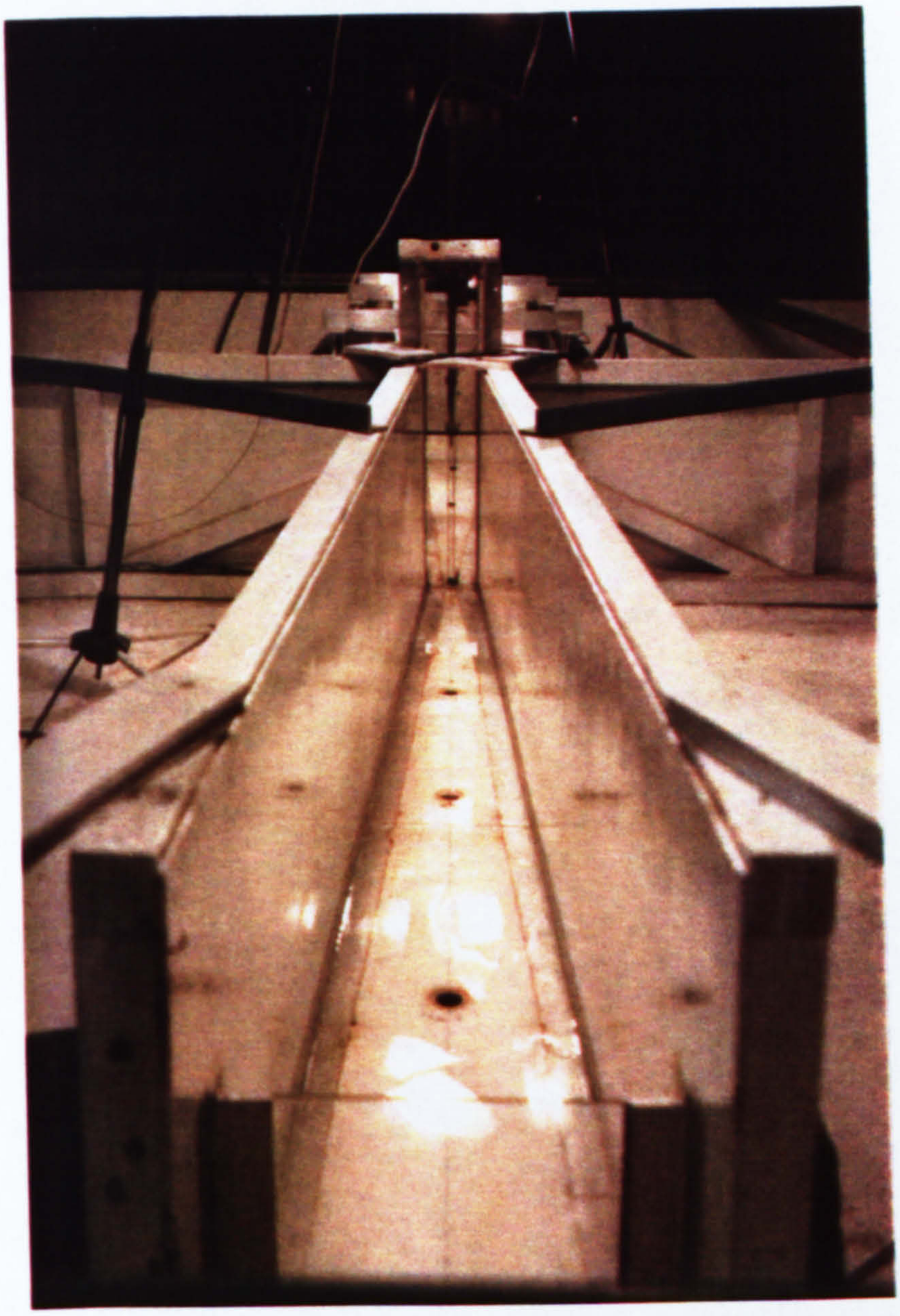

FIGURE 5.5 : THE EXPANDING CHANNEL (DOWNSTREAM OF THE GATE) IN THE (RT-RT) MODEL .

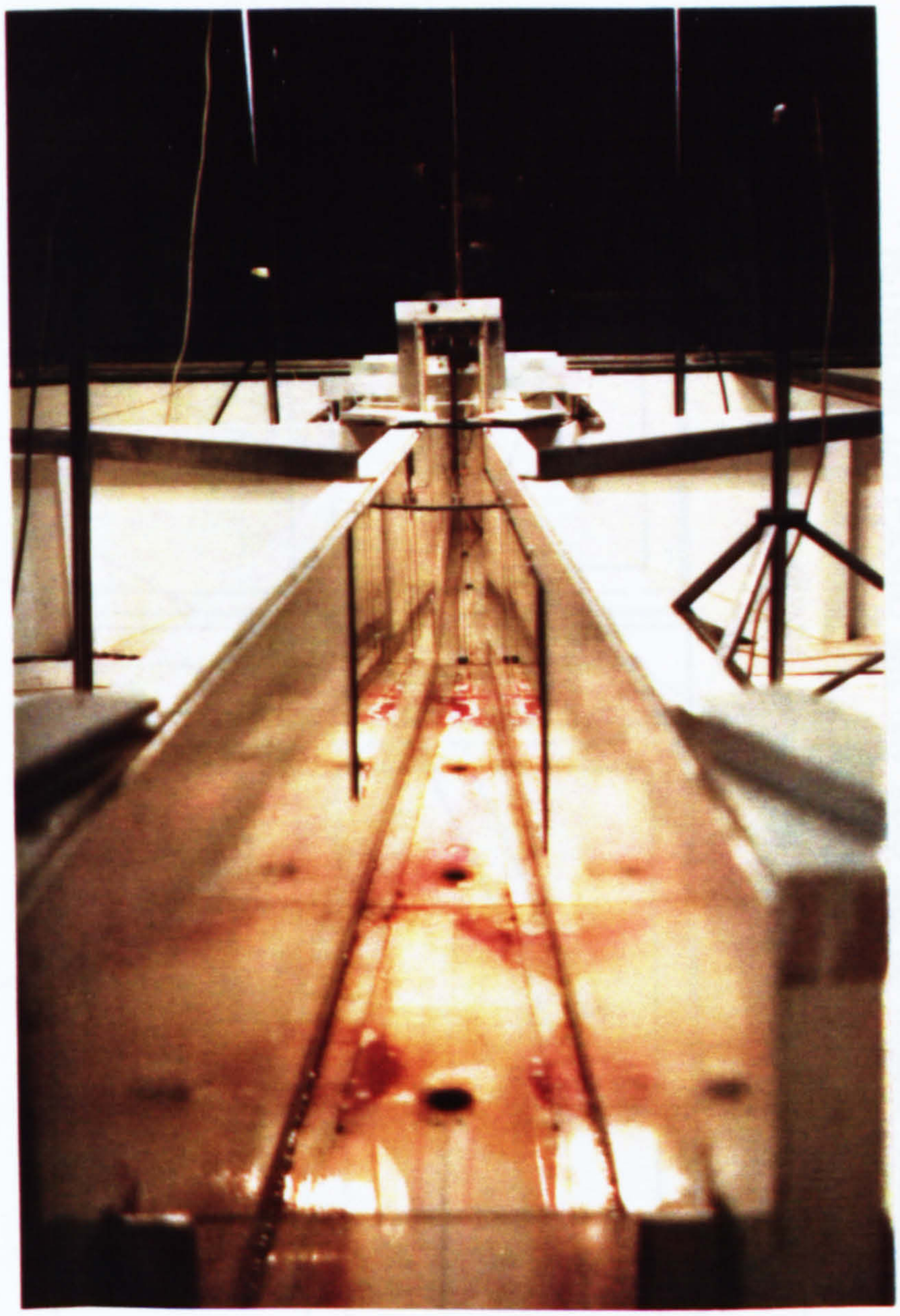

FIGURE 5.6 : THE DOWNSTREAM CHANNEL IN THE (XT-RT) MODEL , SHOWING MIRRORS ATTACHED TO THE SIDE WALLS FOR PHOTOGRAPHING THE FRONT .

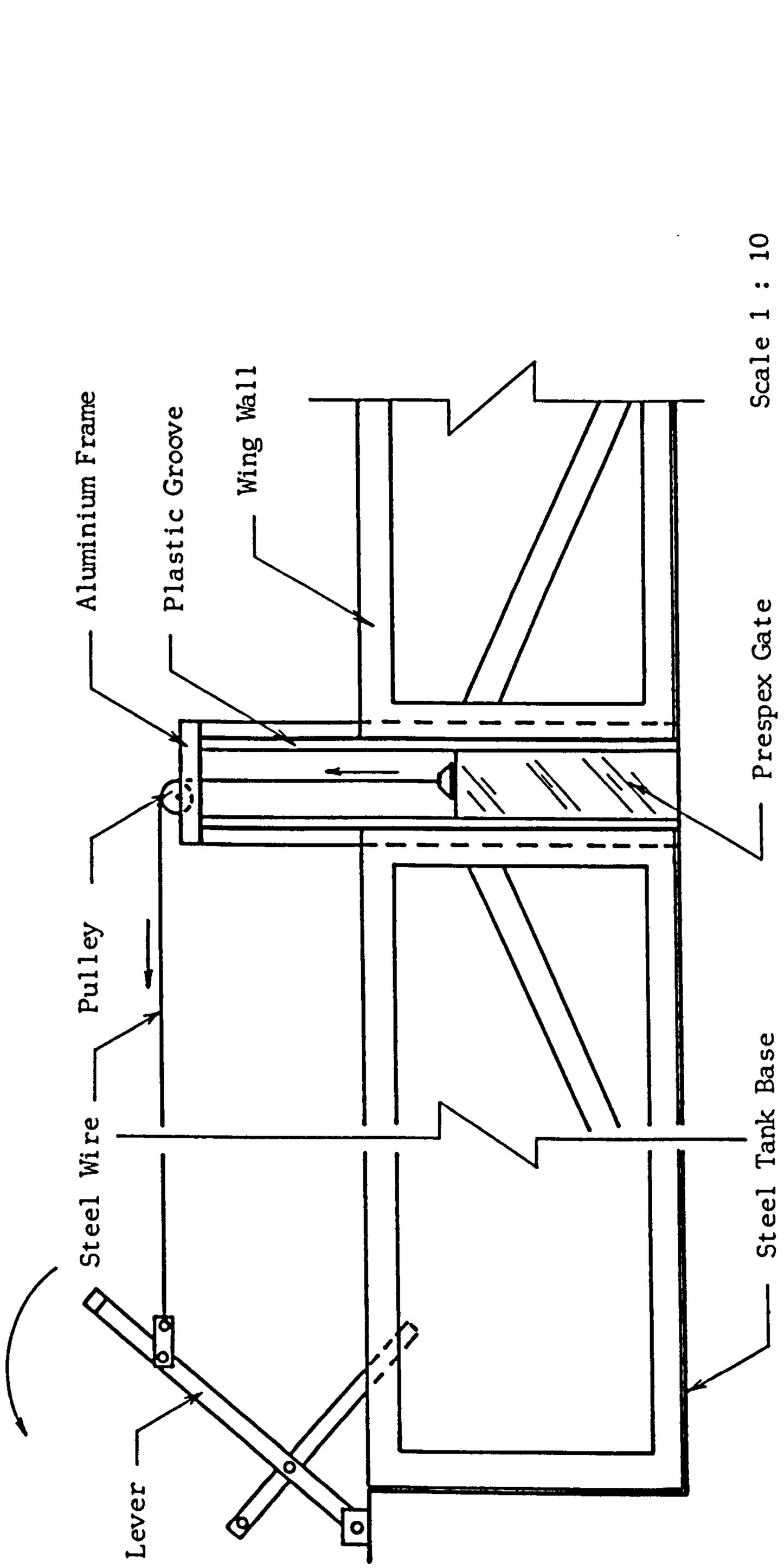

FIGURE 5.7 : GENERAL SKETCH OF THE GATE AND THE QUICK-LIFT MECHANISM .

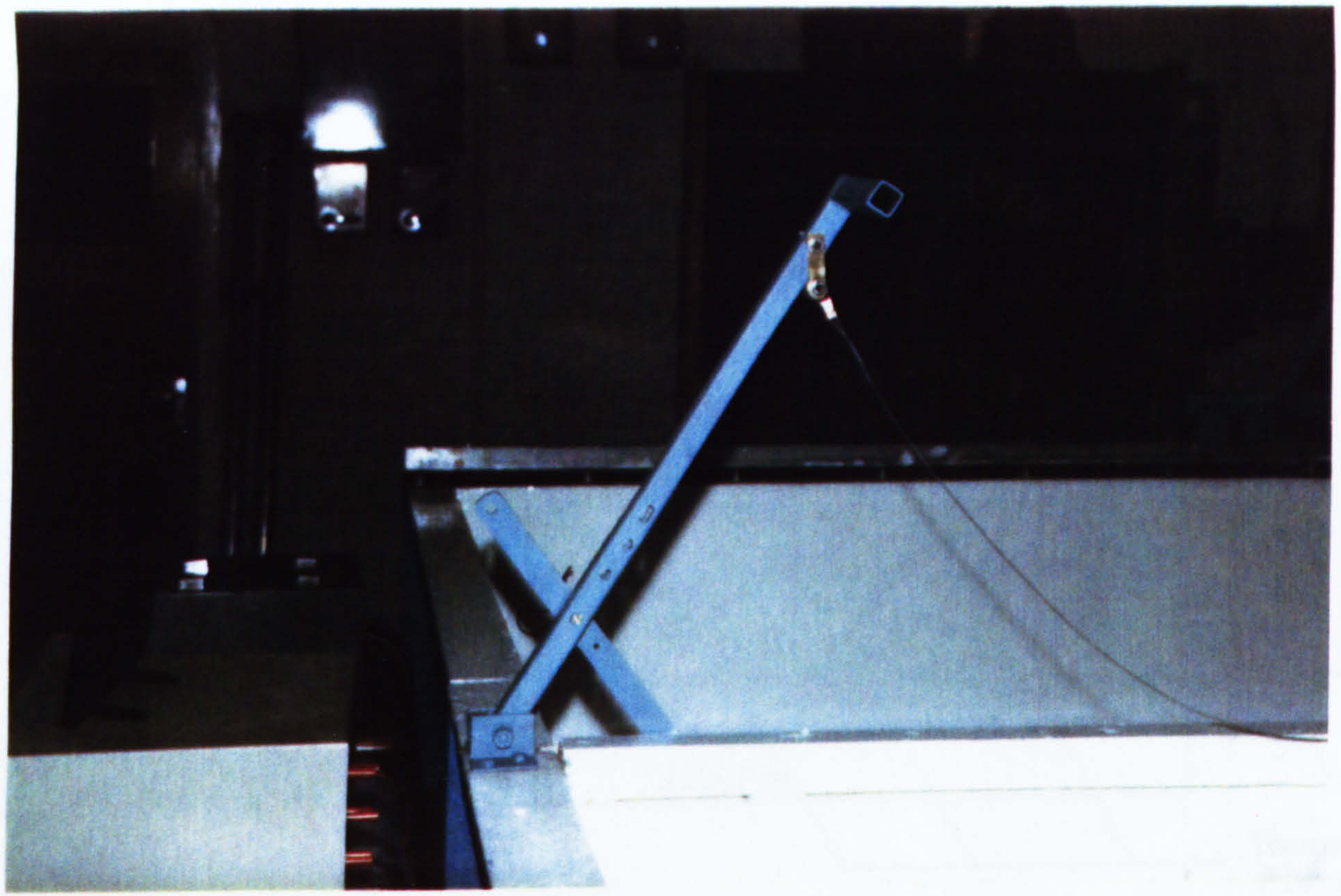

FIGURE 5.8 : THE LEVER AND THE STEEL WIRE BY WHICH THE GATE WAS LIFTED .

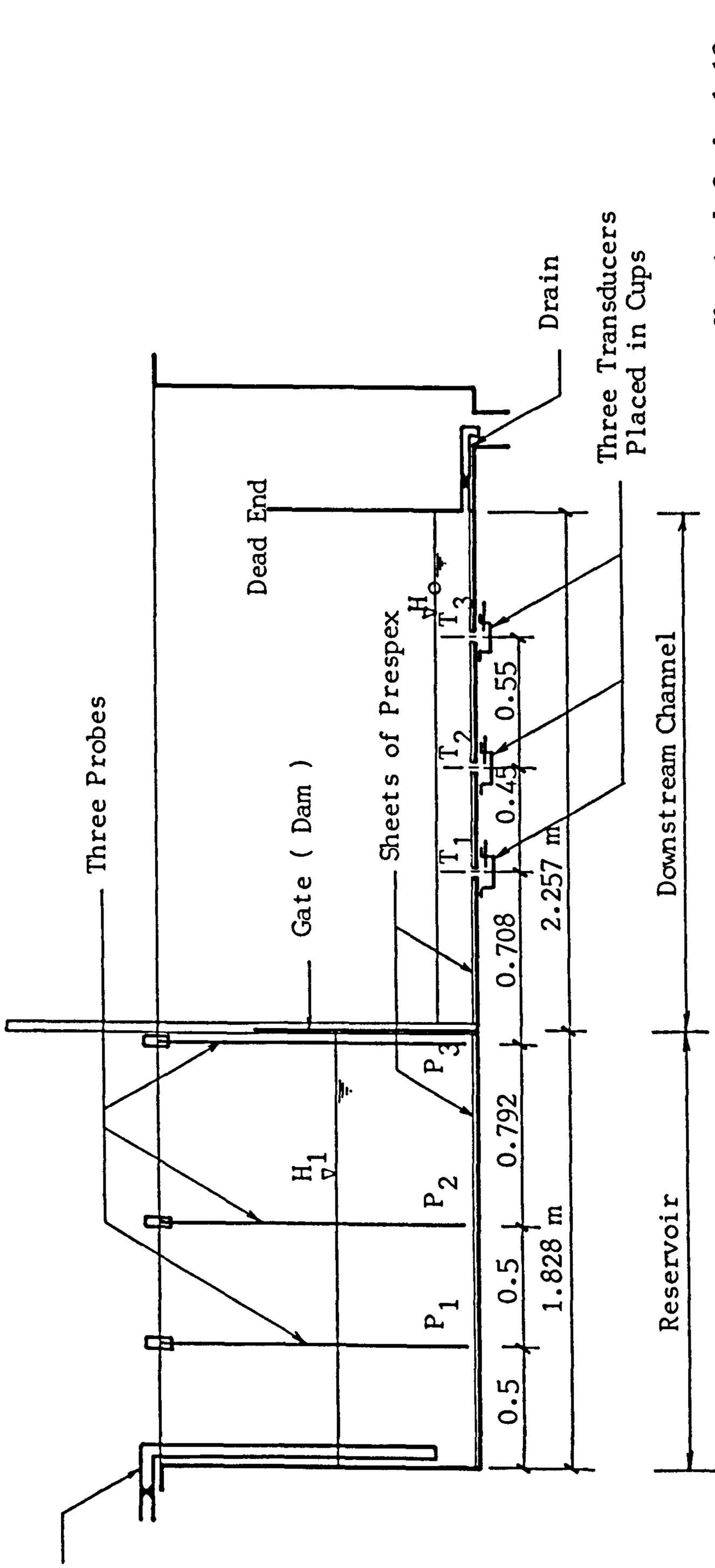

FIGURE 5.9 : LONGITUDINAL SECTION THROUH THE PHYSICAL MODELS .

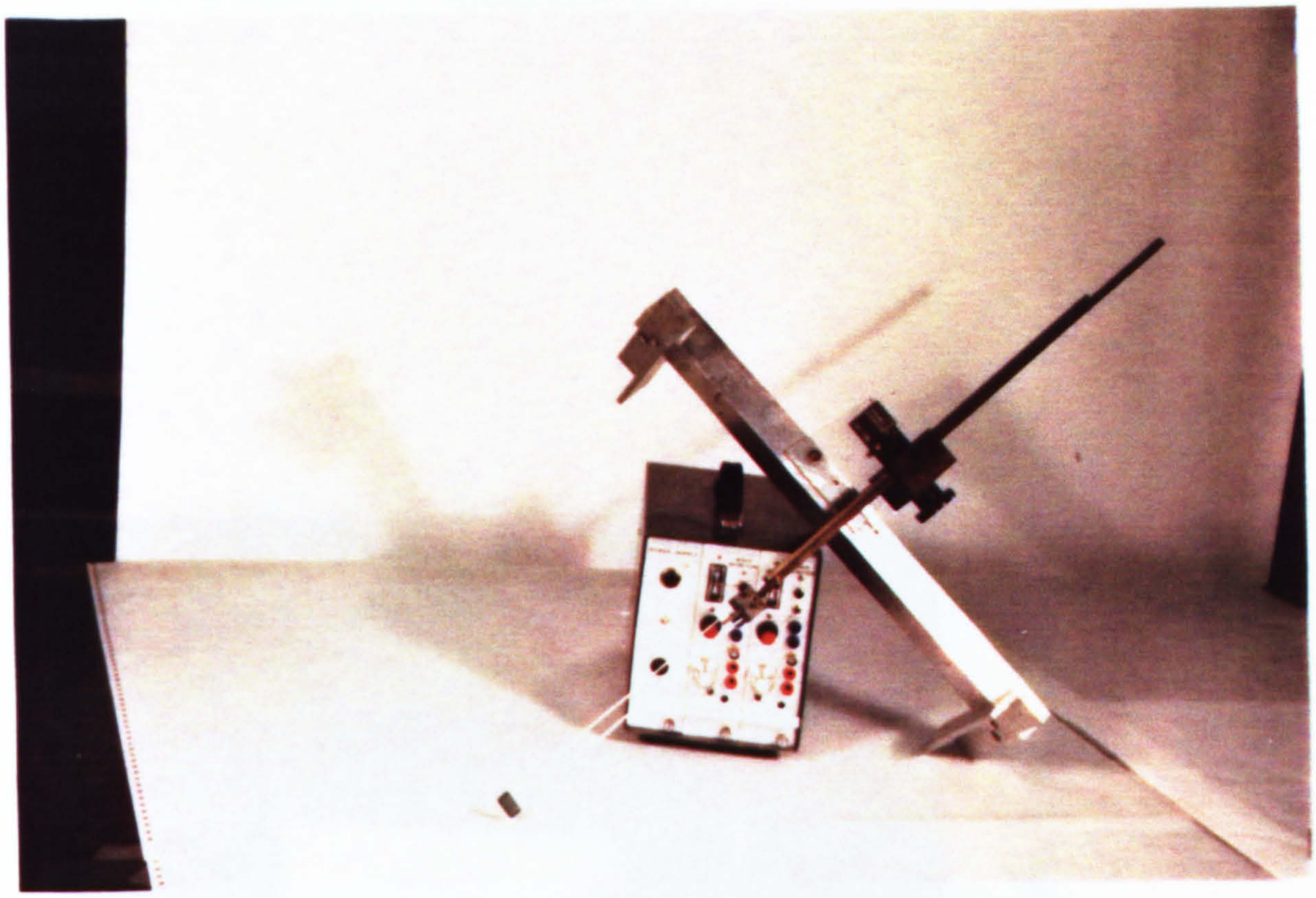

FIGURE 5.10 : PHOTOGRAPH OF THE PROBE AND THE WAVE MONITOR .

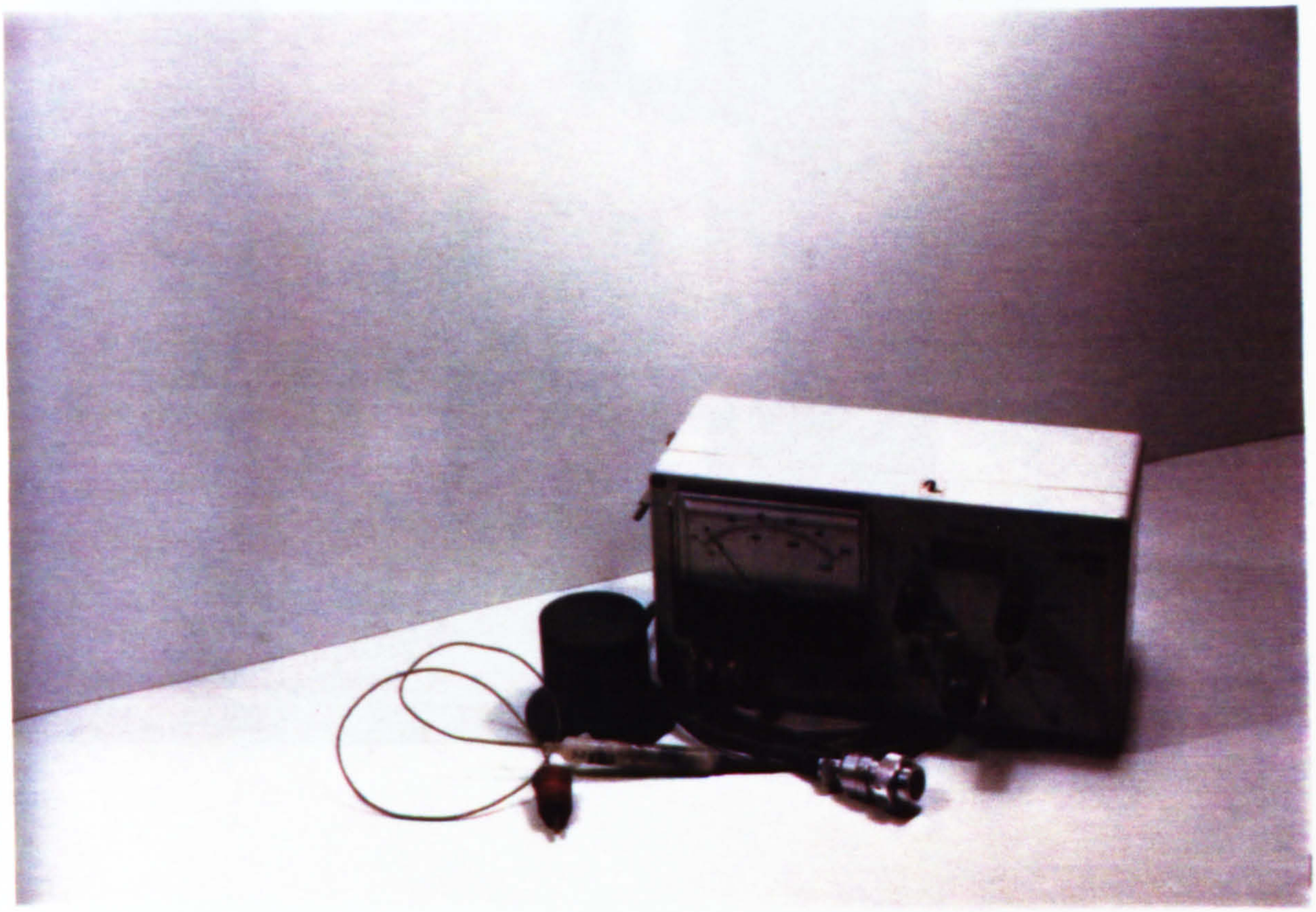

FIGURE 5.11 : PHOTOGRAPH OF THE TRANSDUCER, THE CUP, AND THE WAVE MONITOR .

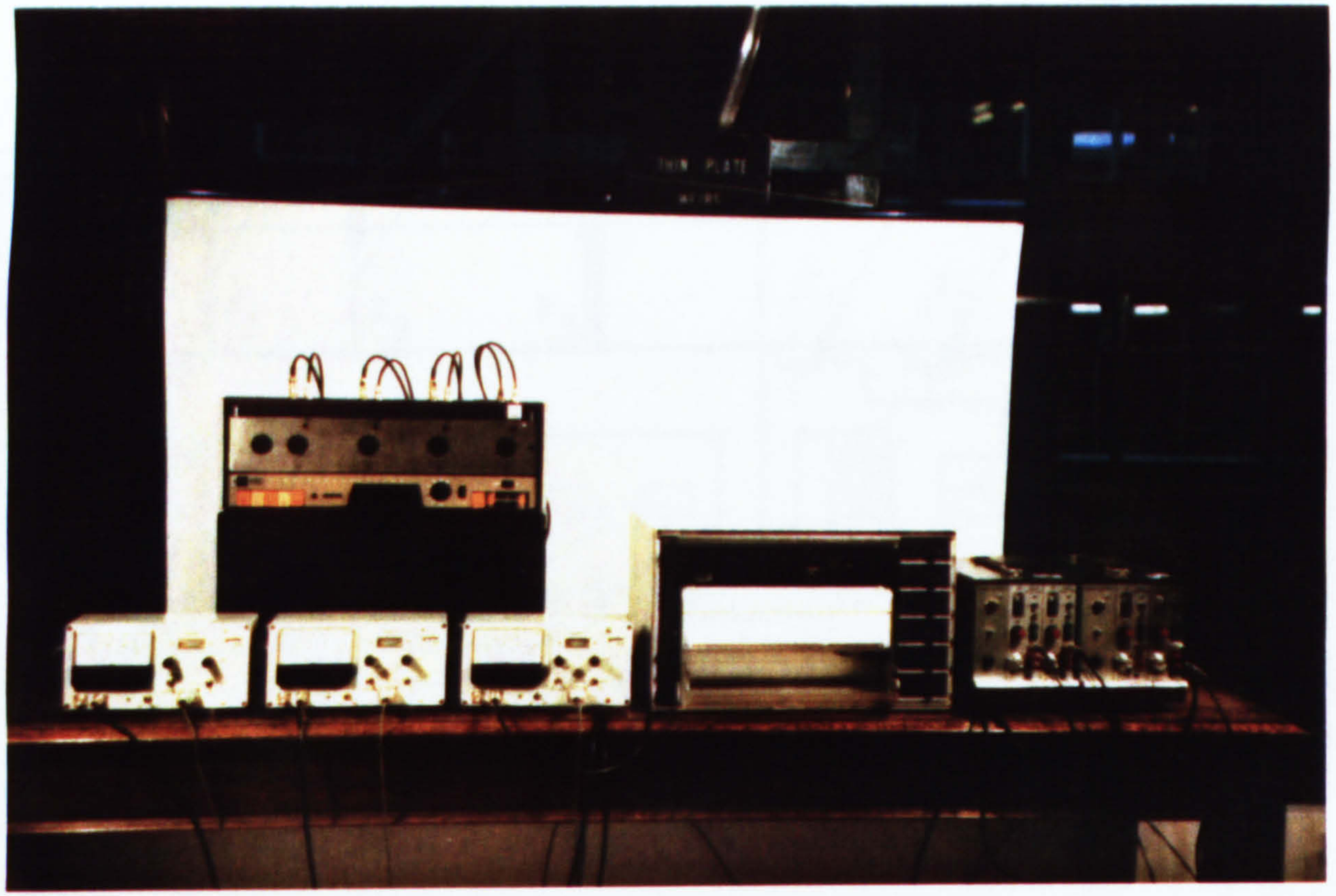

FIGURE 5.12 : PHOTOGRAPH OF THE INSTRUMENTATION SETUP .

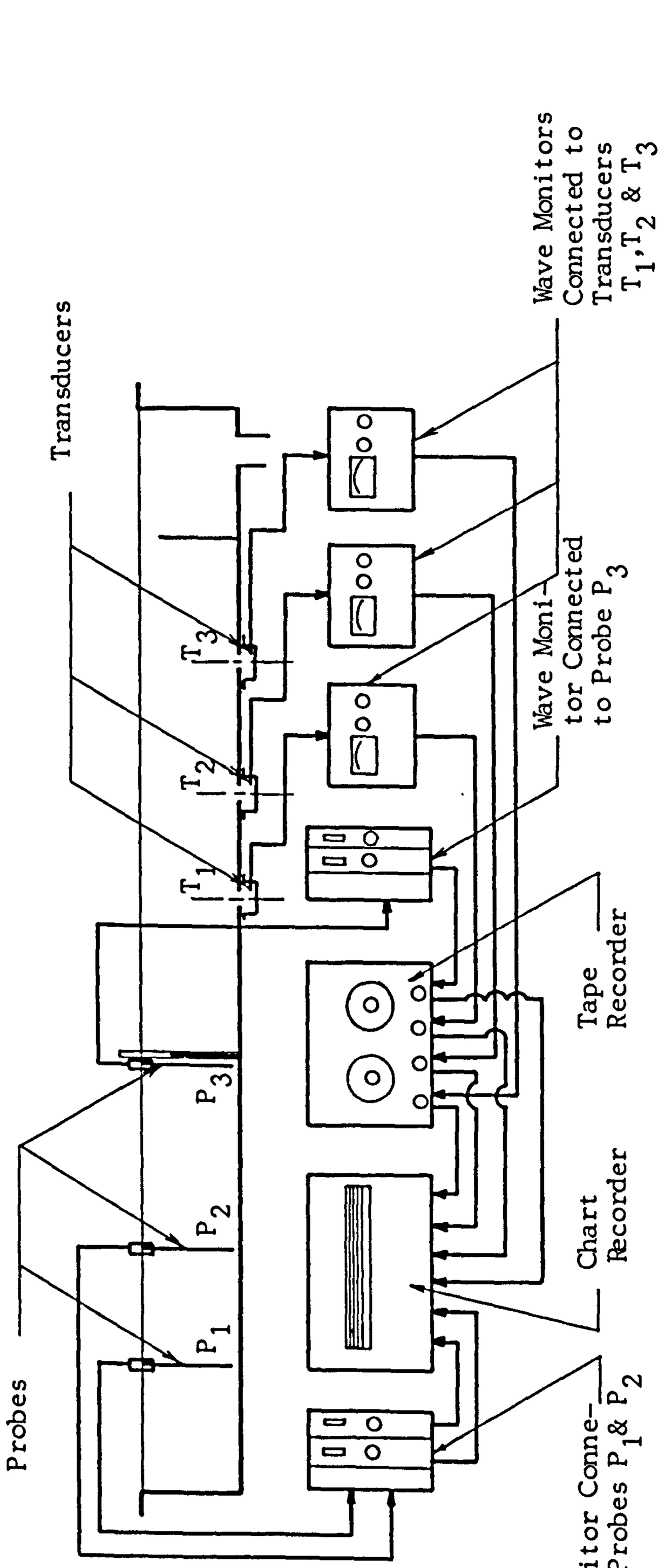

FIGURE 5.13 : SKETCH OF THE INSTRUMENTATION SETUP .

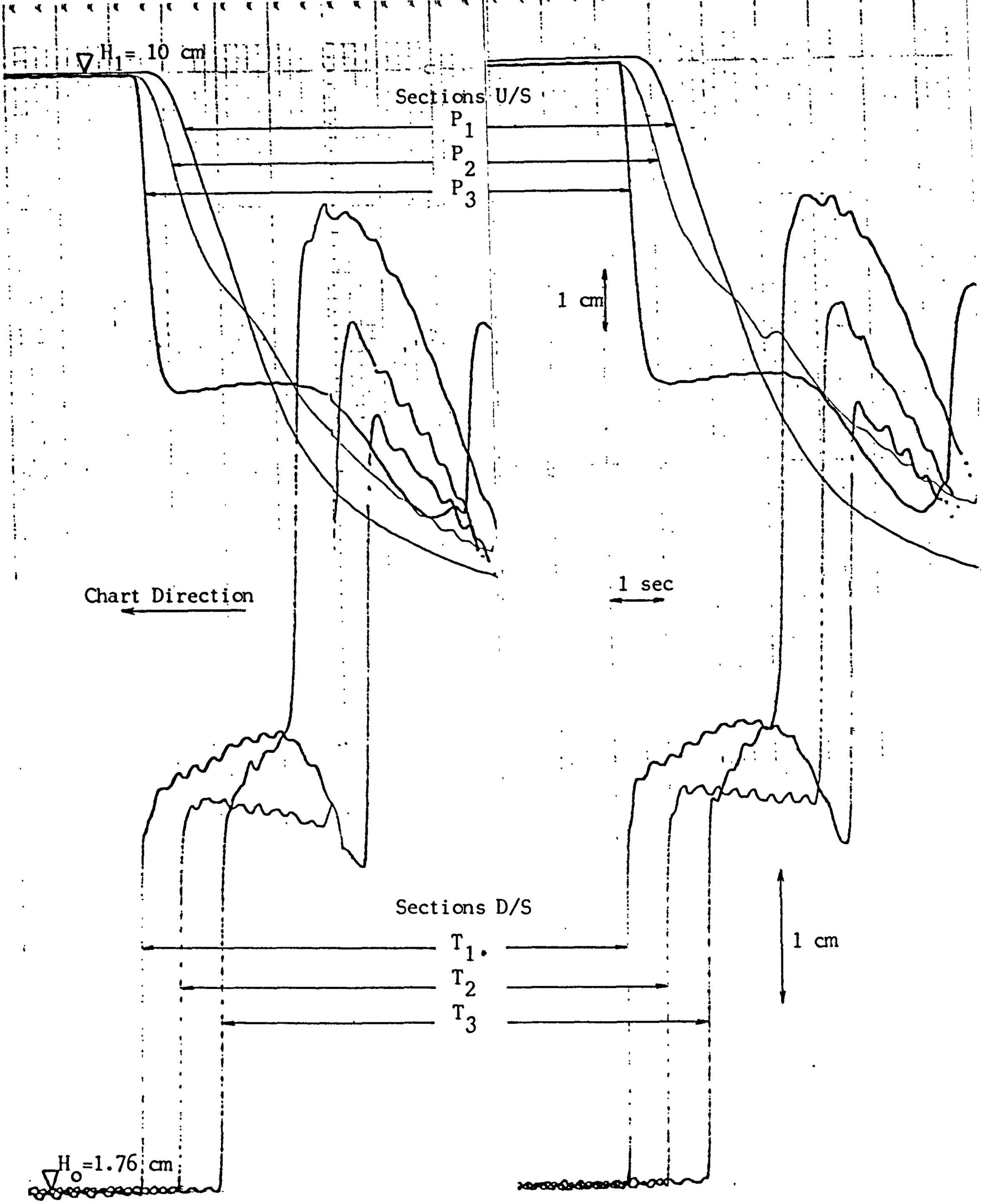

FIGURE 5.14 : RECORDED WATER LEVELS AT SIX RECORDING SECTIONS FOR TWO TYPICAL EXPERIMENTS .

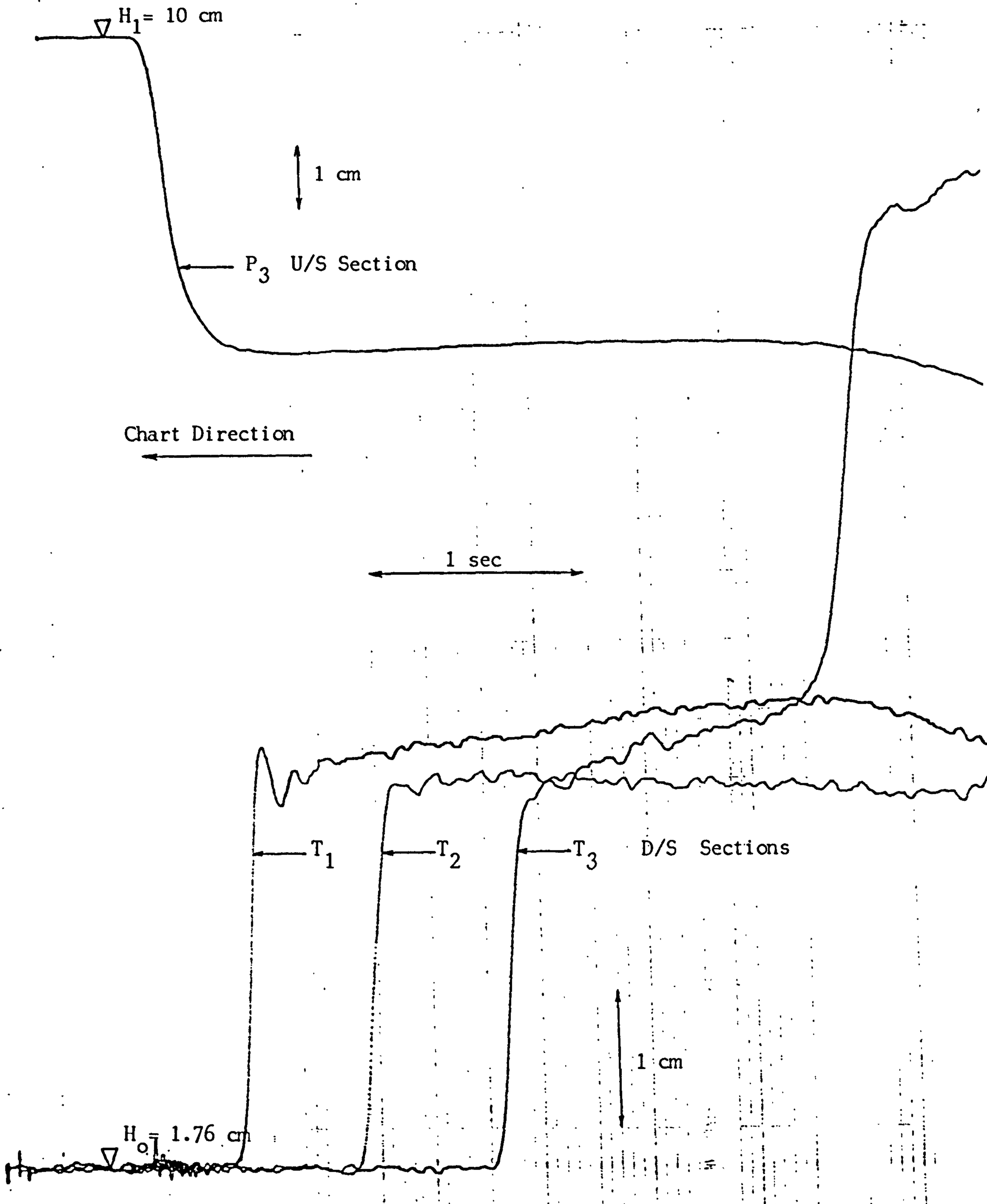

FIGURE 5.15 : REPLAY OF RECORDING EXPERIMENT (A) IN FIGURE 5.14 FOR FOUR RECORDING SECTIONS .

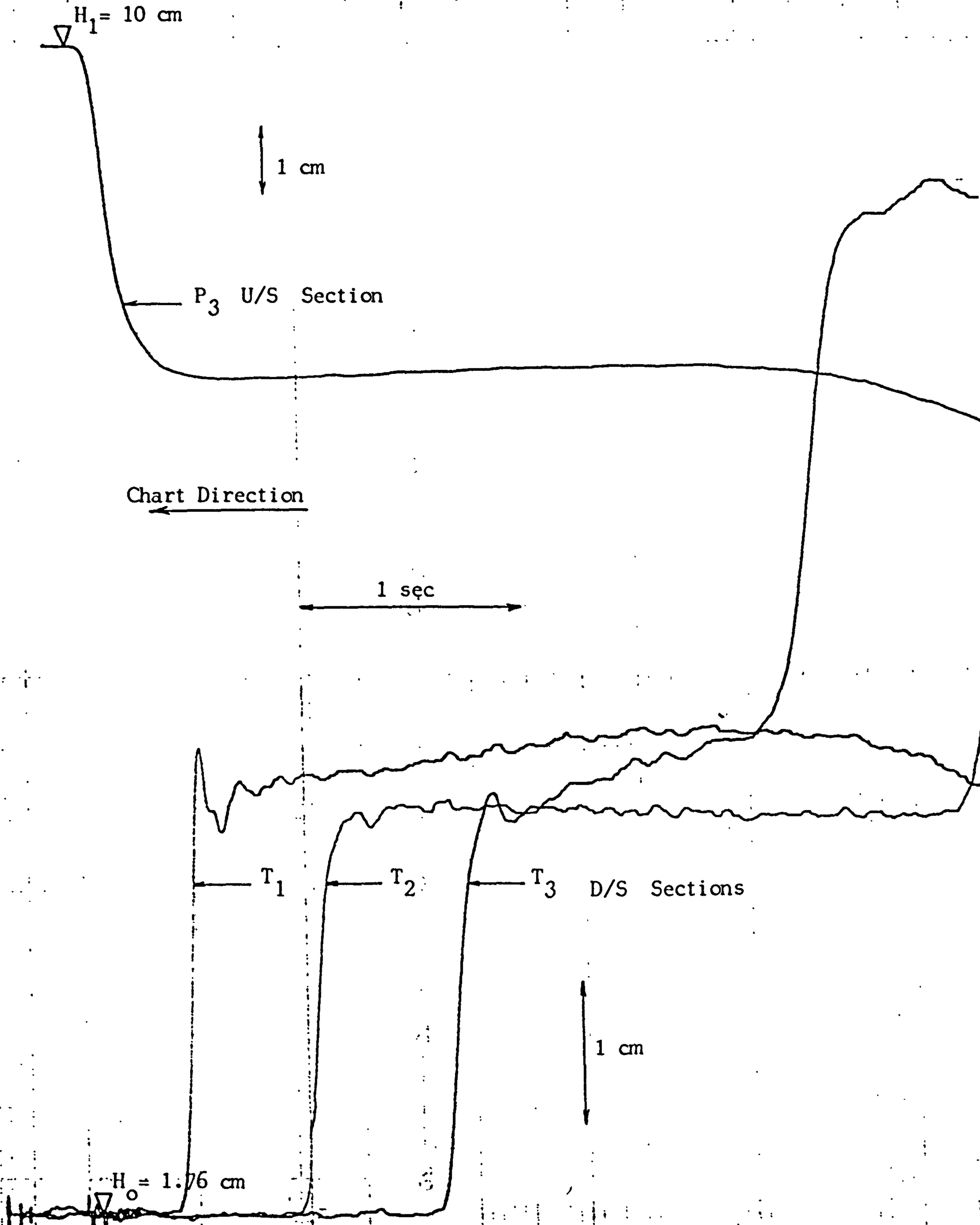

FIGURE 5.16 : REPLAY OF RECORDING EXPERIMENT (B) IN FIGURE 5.14 FOR FOUR RECORDING SECTIONS .

CHAPTER SIX

COMPARISON OF PHYSICAL AND NUMERICAL RESULTS

6.1 X-T Model

As indicated in Chapter 5, the physical X-T tests are regarded as an important verification of the numerical model, both as regards its performance against model data elsewhere and also for its confident extension to the R-T case. There was also concern that the two methods of depth measurement were each sufficiently accurate. The twin wire probes responded directly to depth variations (with a small surface tension error) whilst the sensors downstream responded rather to pressure. Provided the pressure remained close to hydrostatic, its transformation to an equivalent depth was justified. A water profile thus inferred from the physical model, which corresponded closely with numerical and analytical solutions in the X-T case, tends to confirm the position.

Both physical and numerical tests have therefore been compared firstly with Stoker's solution regarding the front height, as presented in Figure 6.1, for different ratios of (H_0/H_1) and different upstream water depth H_1 (see Table 5.1). Figures 6.2 to 6.31 contain both the numerical and experimental (X-T) data in three types of computer plots; the water depth profiles, the front trajectories, and the stage hydrographs. The water depth profiles are given at six different times for each run. The front trajectories consist of the time elapsed for the front to travel some distance downstream of the dam. The stage hydrographs are presented as variations with time of the dimensionless water depth (H/H_1) (the

water depth divided by the initial depth upstream the dam) at the six sections (three upstream the dam and three downstream the dam as shown in Figure 5.16). The experimental runs are for different ratios of the initial depths upstream and downstream the dam as illustrated in Table 5.2 where H_o/H_1 = 0, 0.025, 0.05, 0.1, 0.176, 0.2, 0.4 and 0.8 with initial water depths upstream of H_1 = 10, 15 and 20 cm. The reason for taking (H_o/H_1 = 0.176) was to confirm Stoker's theory that the maximum height of the front above the initial water level downstream the dam (H_2-H_0 = 0.32 H_1) occurs at this ratio, as shown in Figure 6.1. Since the front trajectories at the three sections (T_1, T_2 and T_3) can be read from the stage hydrographs plots, three plots only were presented for different initial depth ratios, as shown in Figures 6.4, 6.8 and 6.12.

A good agreement between the experimental and the numerical results (with a general difference less than 3%) in one hand and between the both and Stoker's solution (with a general difference less than 4%) in the other hand regarding to the front heights. Close agreement between computed and measured stage hydrographs (with a general difference less than 6%) further support the view that the experimental work is valid in testing the other three models. However, at high ratios (H_o/H_1 = 0.4 and 0.8), immediately after the dam break an oscillation with a small dip and recovery was noted in the experimental runs as shown in Figures 6.26, 6.27, 6.30 and 6.31. This oscillation seems to have been partly caused by the initial downsurge following the first movements of the gate, before the latter was clear of the downstream surface. Also some blurring of the initial portion of the downstream stage hydrograph inevitably

occurs as a result of the turbulent front-whereas the numerical model exhibits a rapid rise.

[6.2 RT-XT MODEL CONTINUED ON P.219
FIGURES 6.1 TO 6.31 FOLLOW DIRECTLY]

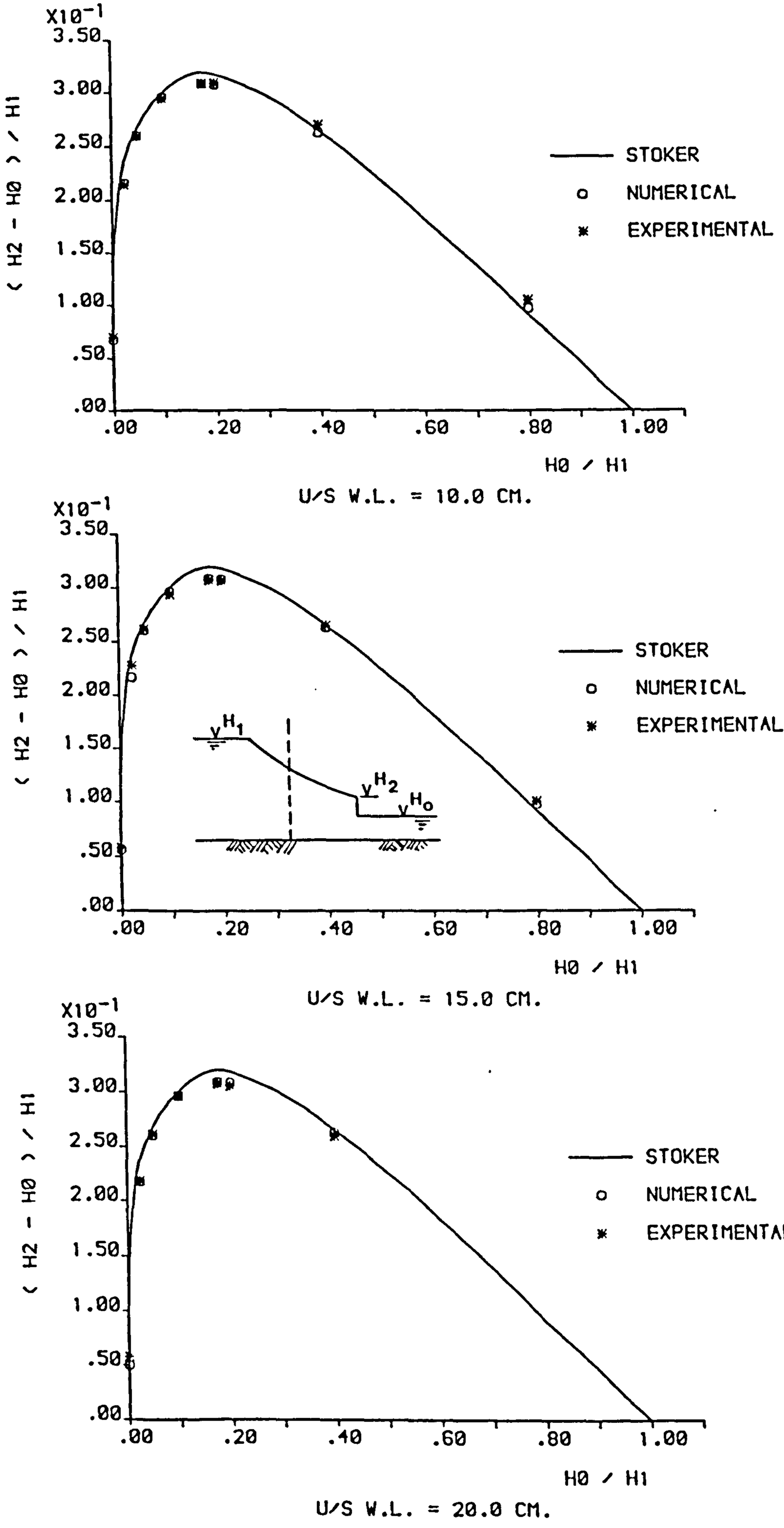

FIGURE 6.1 : COMPARISONS OF THE FRONT HEIGHTS RESULTING FROM THE (X-T) NUMERICAL AND PHYSICAL MODELS WITH STOKER'S SOLUTION .

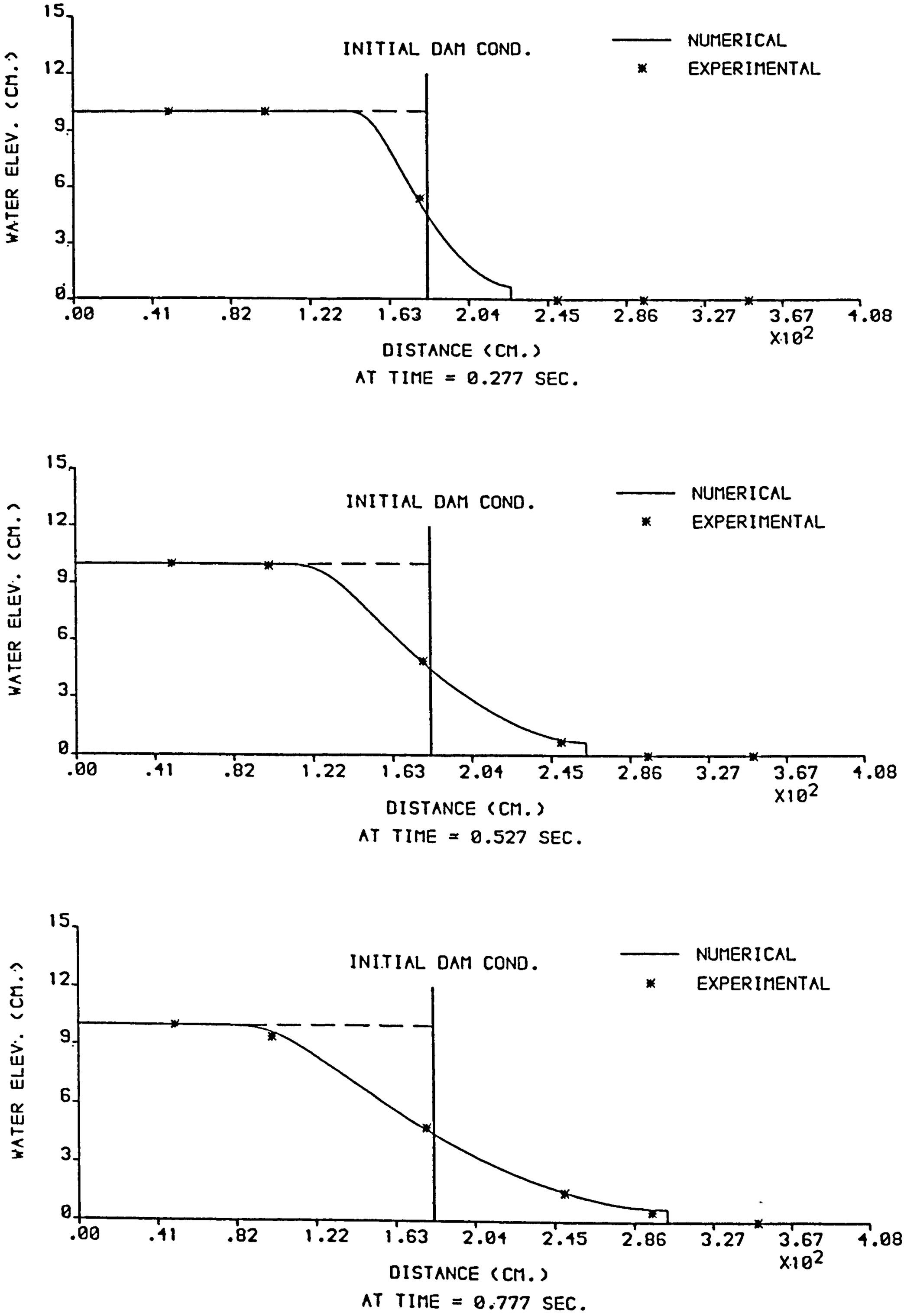

FIGURE 6.2 : NUMERICAL AND EXPERIMENTAL PROFILES FROM THE (X-T) MODEL , H_1 = 10 cm AND H_o = DRY .

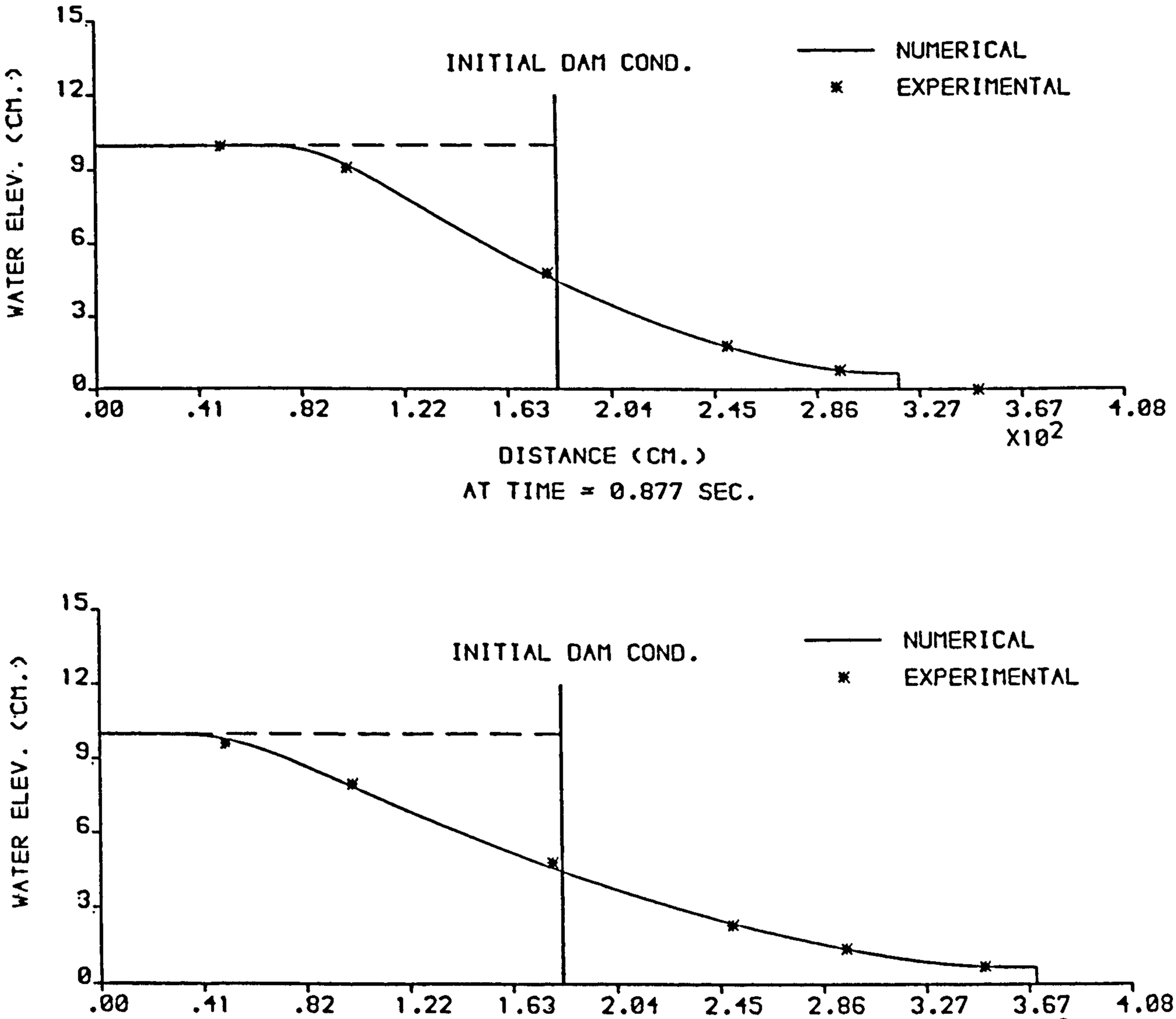

FIGURE 6.3 : NUMERICAL AND EXPERIMENTAL PROFILES FROM THE (X-T) MODEL , H_1 = 10 cm AND H_o = DRY .

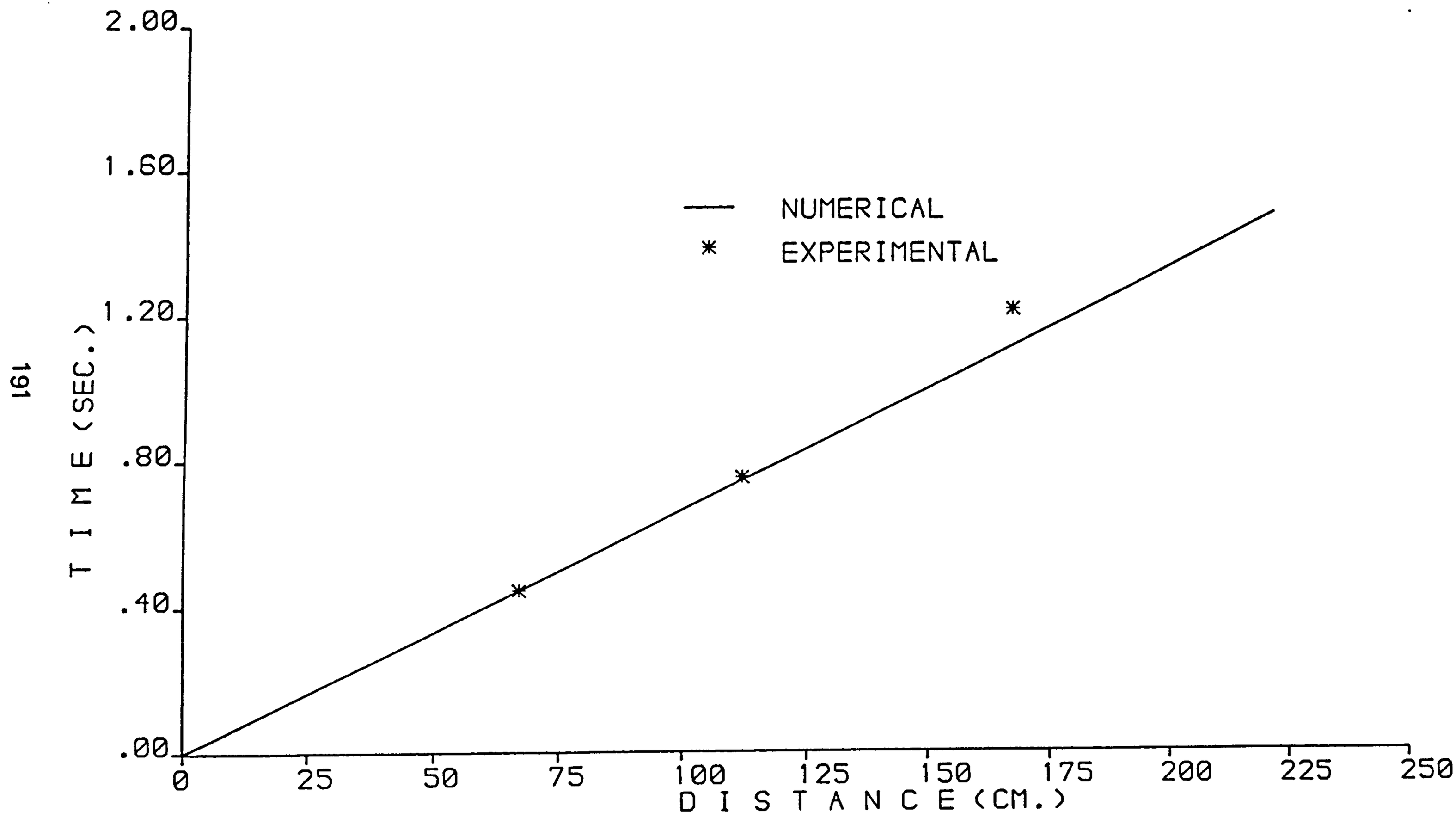

FIGURE 6.4 : NUMERICAL AND EXPERIMENTAL FRONT TRAJECTORIES FROM THE (X-T) MODEL , H_1 = 10 cm AND H_o = DRY.

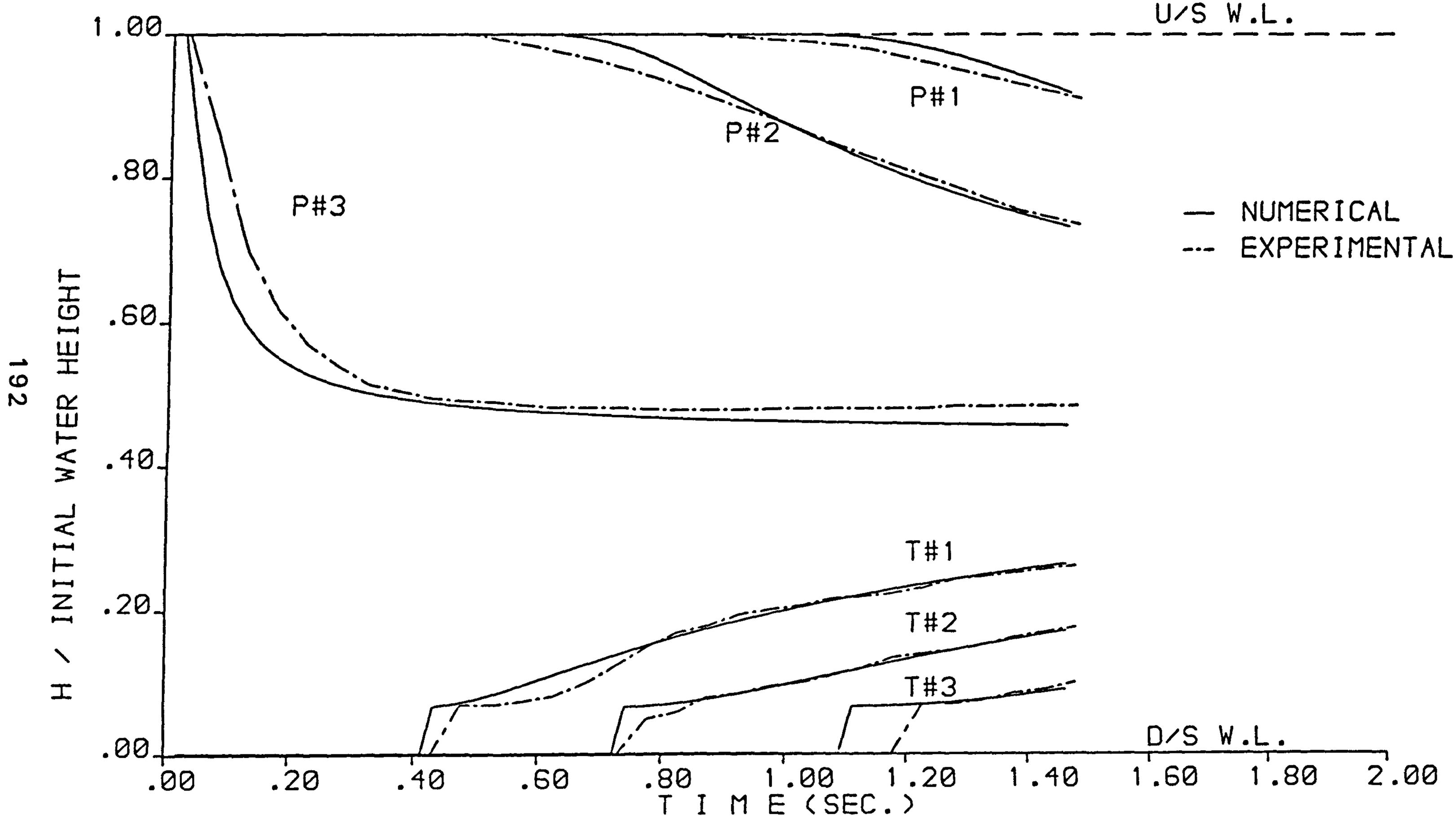

FIGURE 6.5 : NUMERICAL AND EXPERIMENTAL STAGE HYDROGRAPHS FROM THE (X-T) MODEL , H_1 = 10 cm AND H_o = DRY .

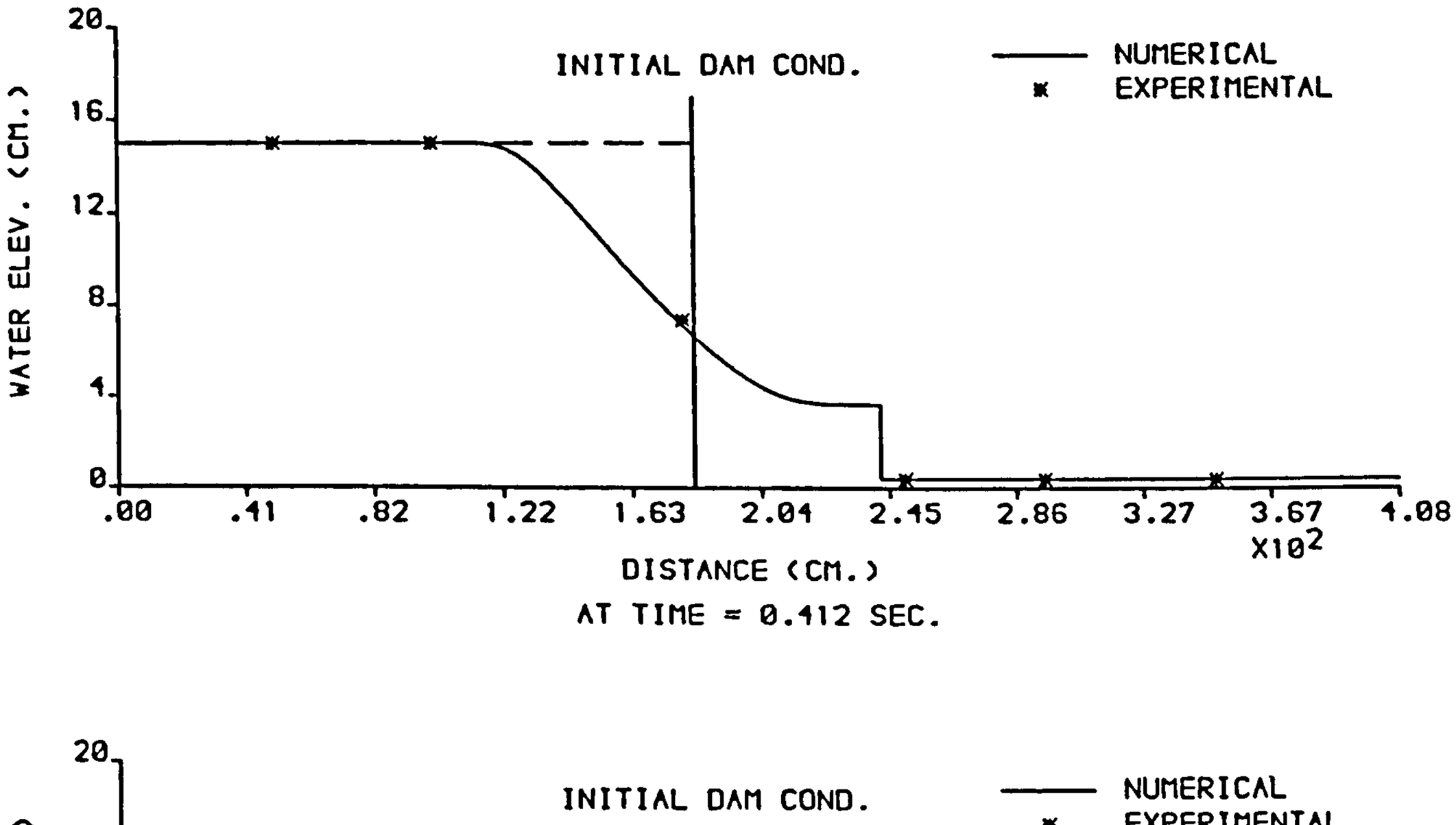

FIGURE 6.6 : NUMERICAL AND EXPERIMENTAL PROFILES FROM THE (X-T) MODEL , H_1 = 15 cm AND H_o = 0.375 cm .

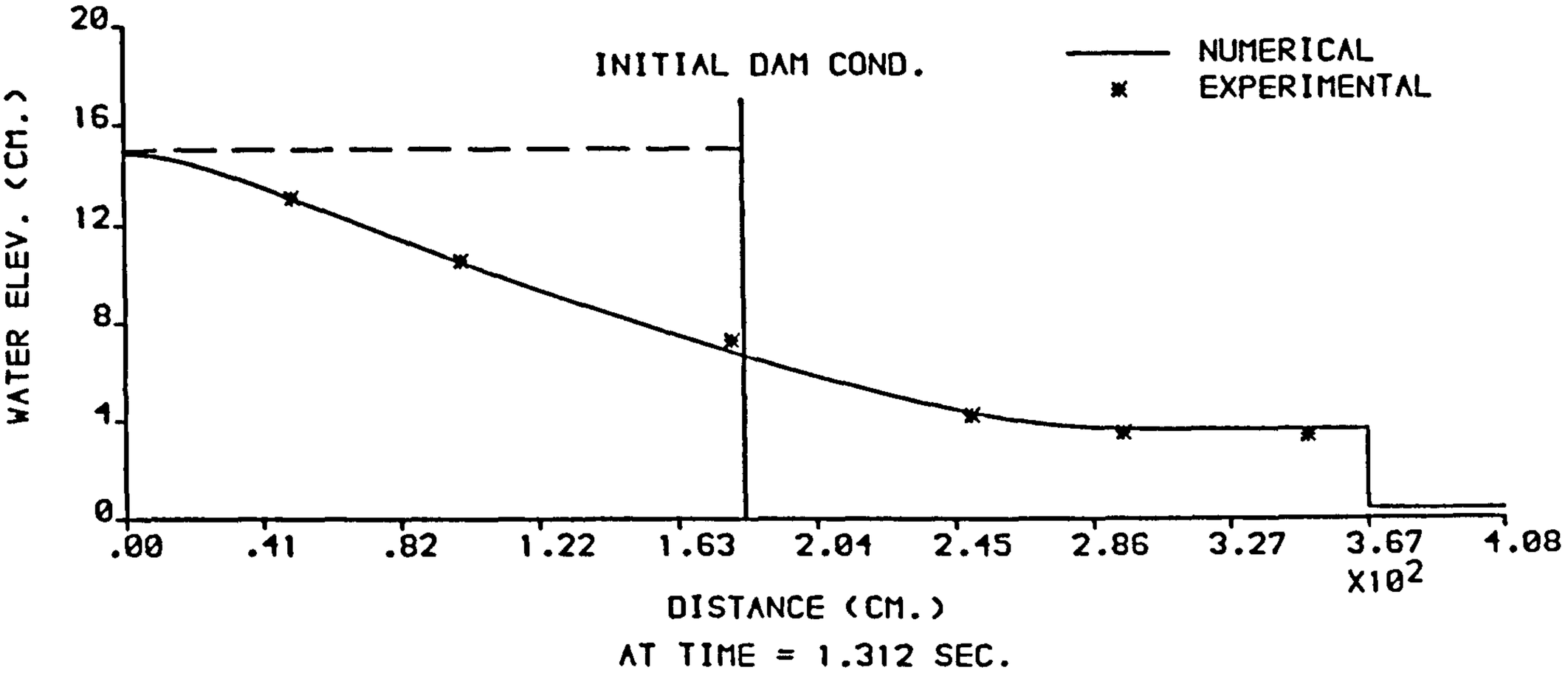

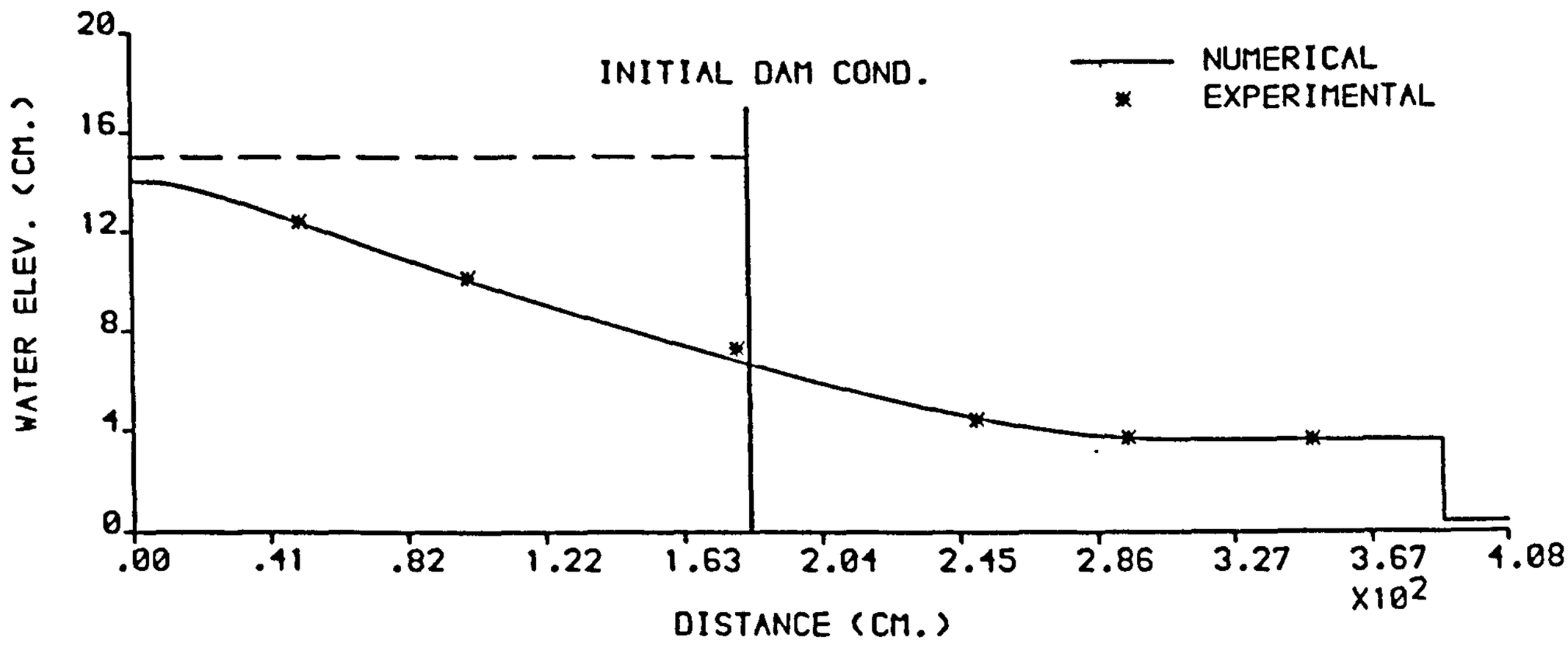

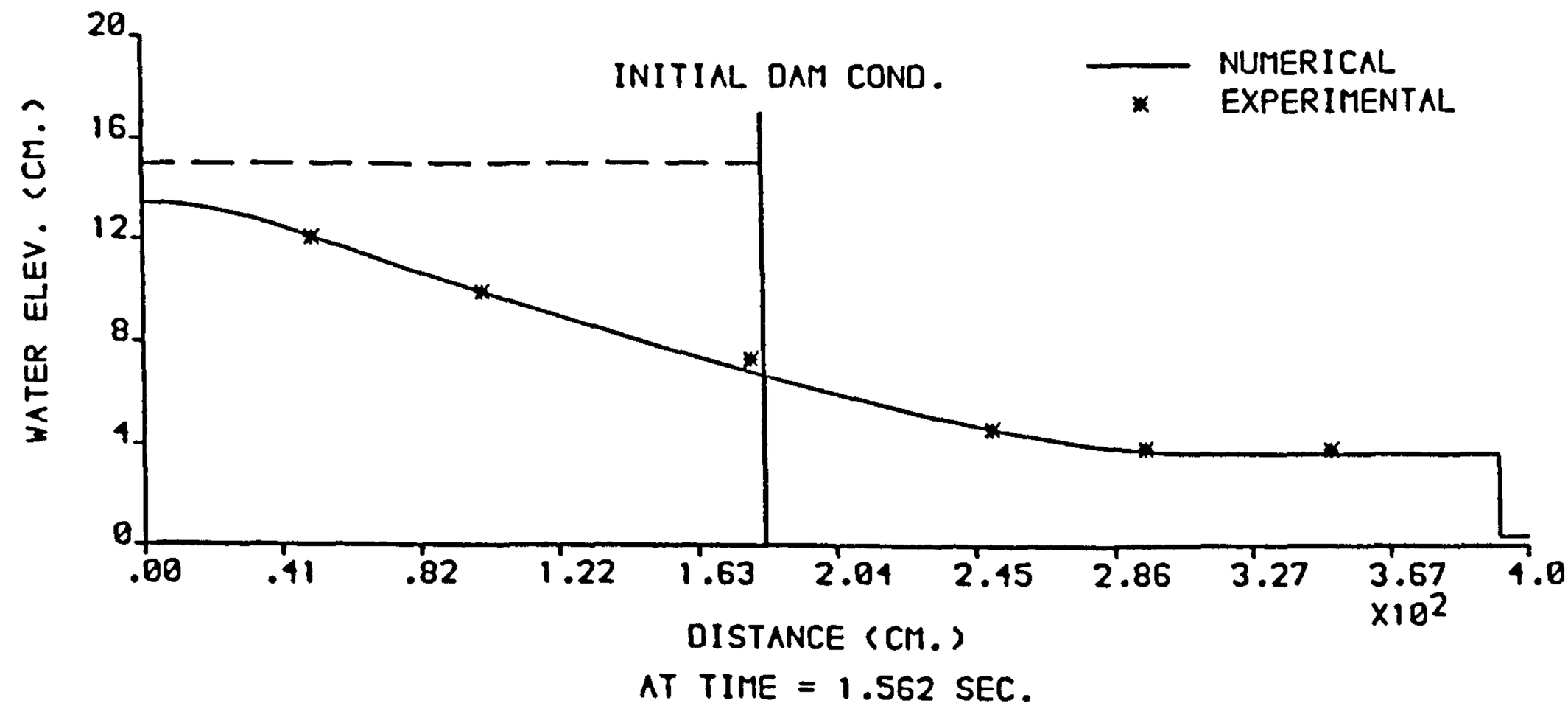

FIGURE 6.7 : NUMERICAL AND EXPERIMENTAL PROFILES FROM THE (X-T) MODEL , H_1 = 15 cm AND H_o = 0.375 cm .

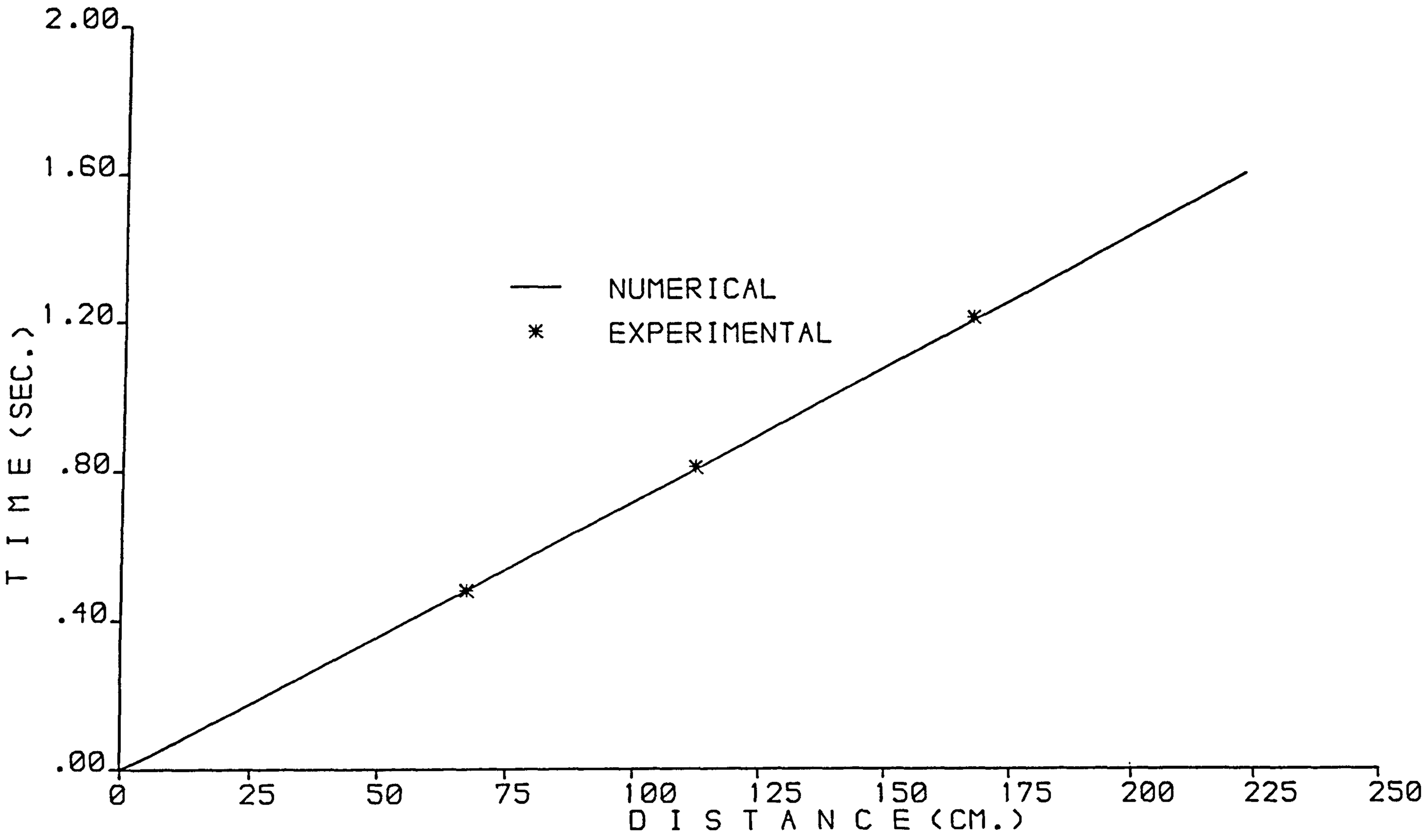

FIGURE 6.8 : NUMERICAL AND EXPERIMENTAL FRONT TRAJECTORIES FROM THE (X-T) MODEL , H_1 = 15 cm AND H_o = 0.375 cm.

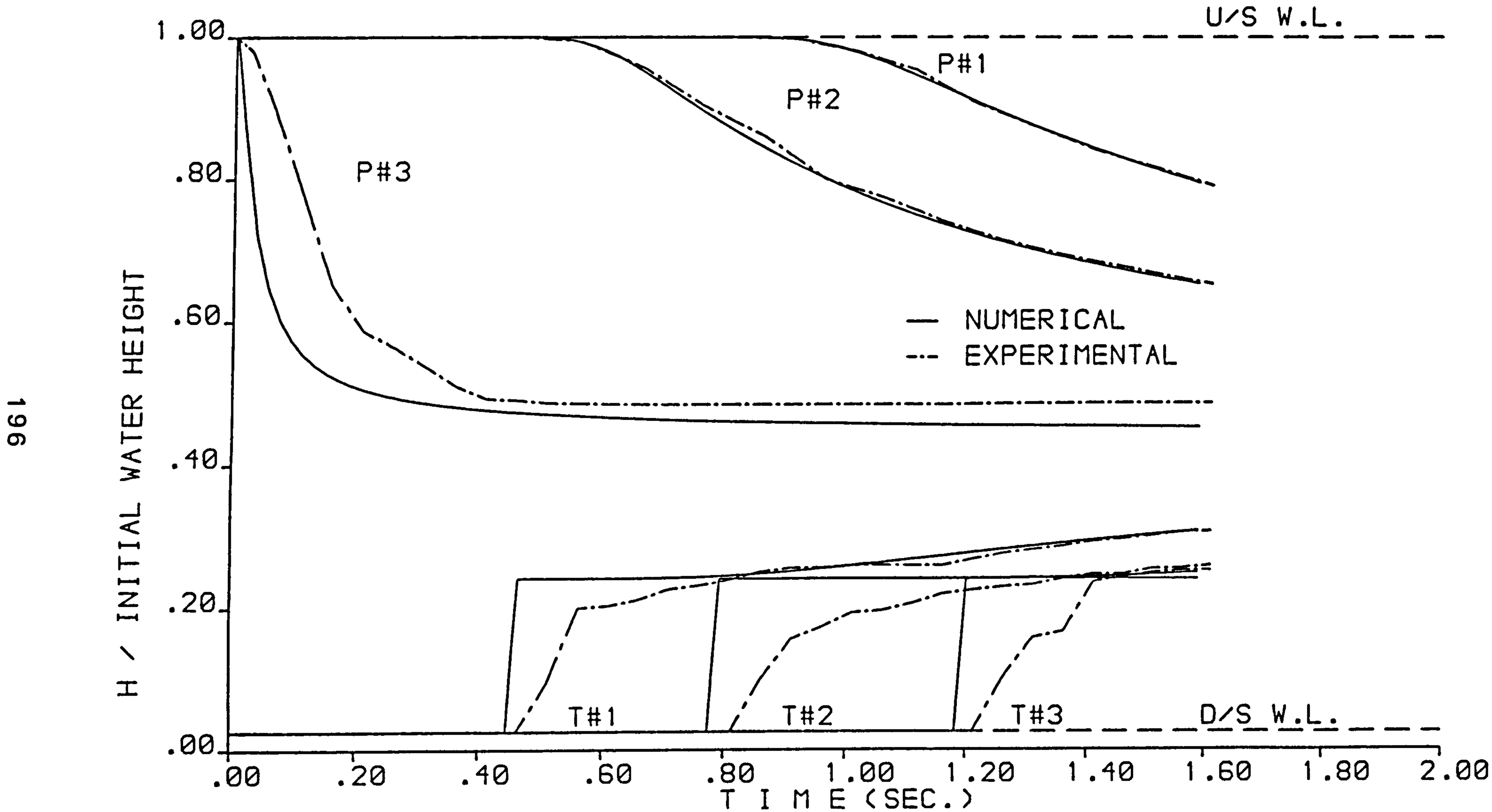

FIGURE 6.9 : NUMERICAL AND EXPERIMENTAL STAGE HYDROGRAPHS FROM THE (X-T) MODEL , H_1 = 15 cm AND H_o = 0.375 cm .

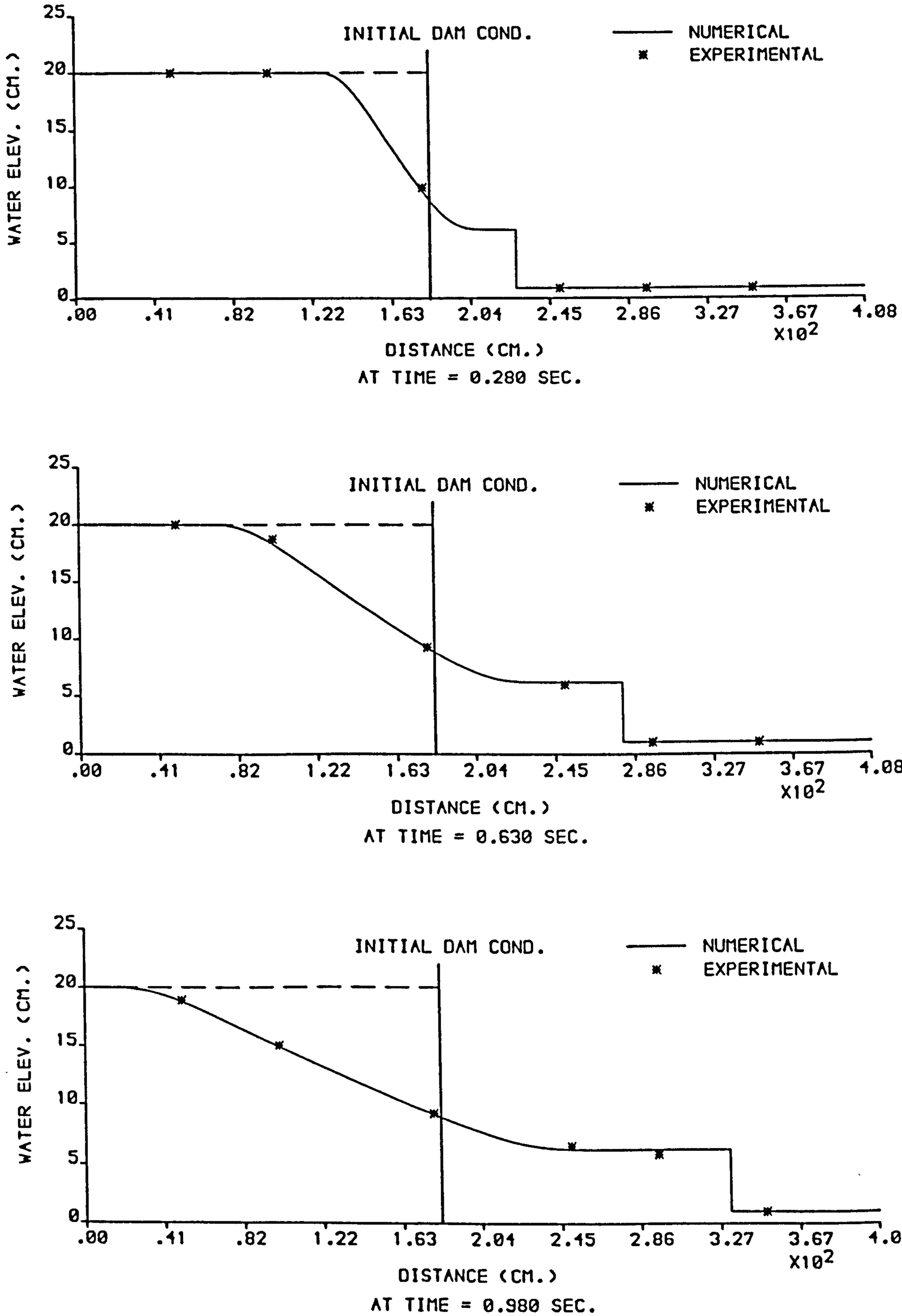

FIGURE 6.10 : NUMERICAL AND EXPERIMENTAL PROFILES FROM THE (X–T) MODEL , H_1 = 20 cm AND H_o = 1 cm .

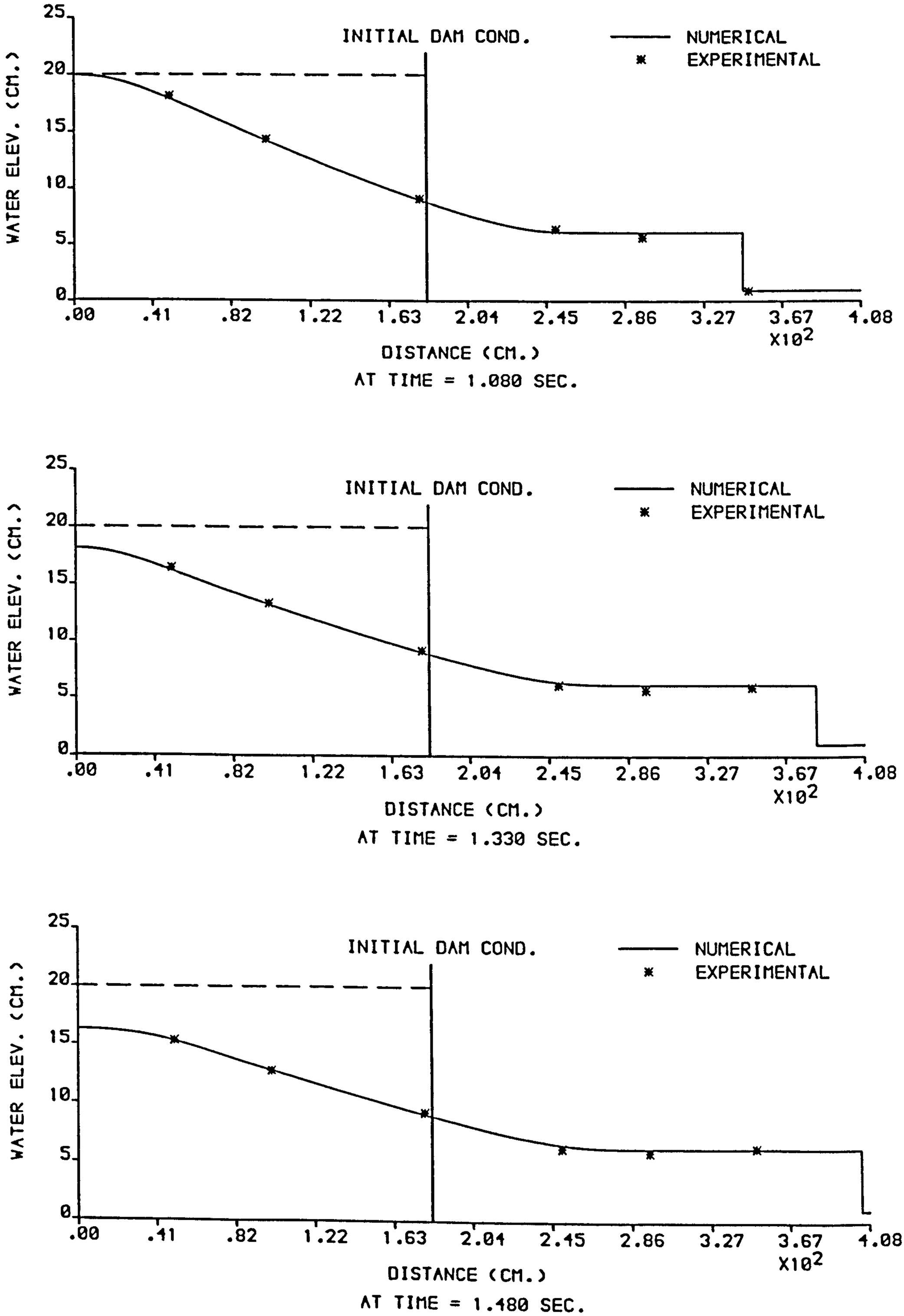

FIGURE 6.11 : NUMERICAL AND EXPERIMENTAL PROFILES FROM THE (X-T) MODEL , H_1 = 20 cm AND H_o = 1 cm .

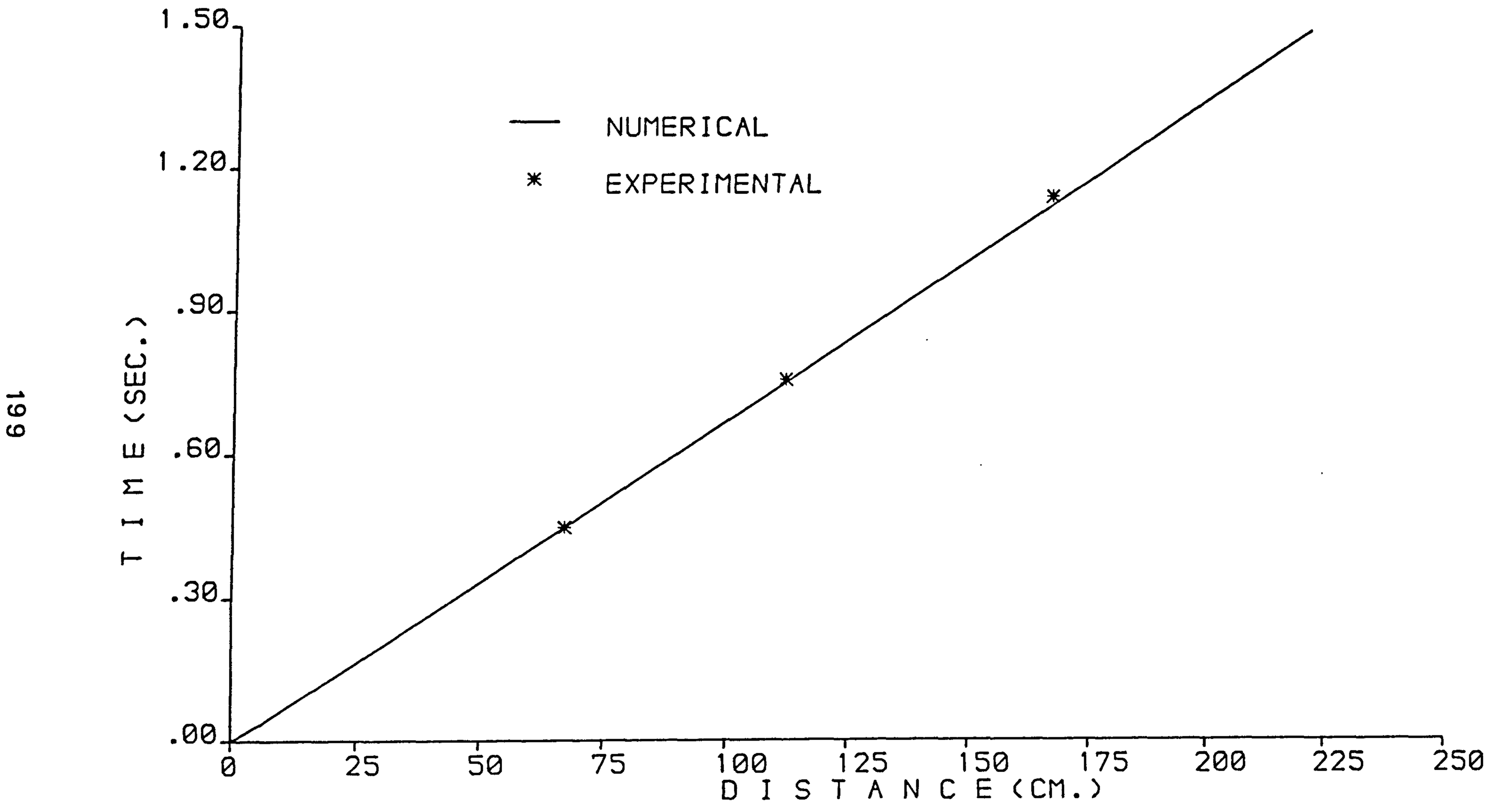

FIGURE 6.12 : NUMERICAL AND EXPERIMENTAL FRONT TRAJECTORIES FROM THE (X-T) MODEL , H_1 = 20 cm AND H_o = 1 cm.

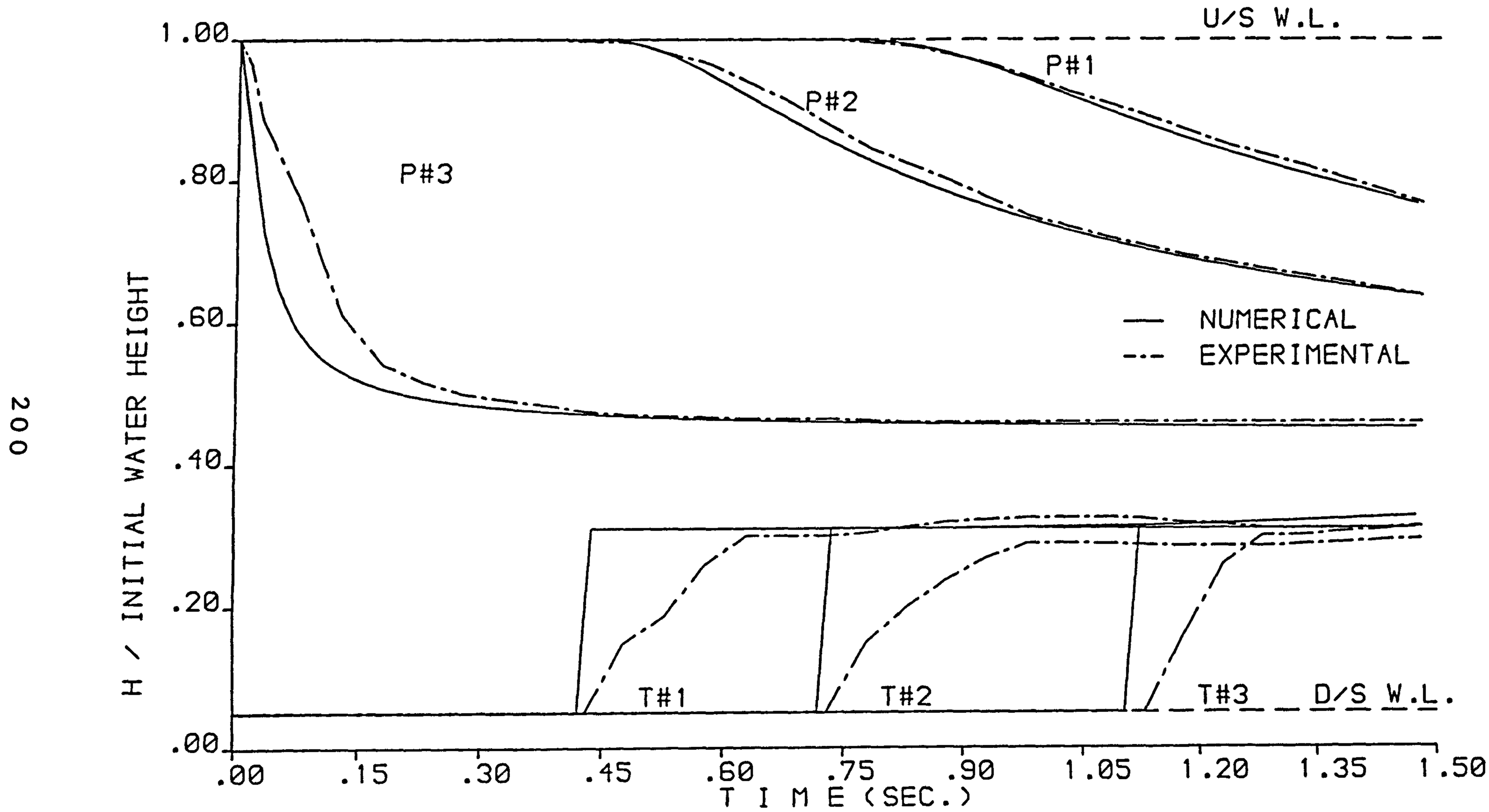

FIGURE 6.13 : NUMERICAL AND EXPERIMENTAL STAGE HYDROGRAPHS FROM THE (X-T) MODEL , H_1 = 20 cm AND H_o = 1 cm .

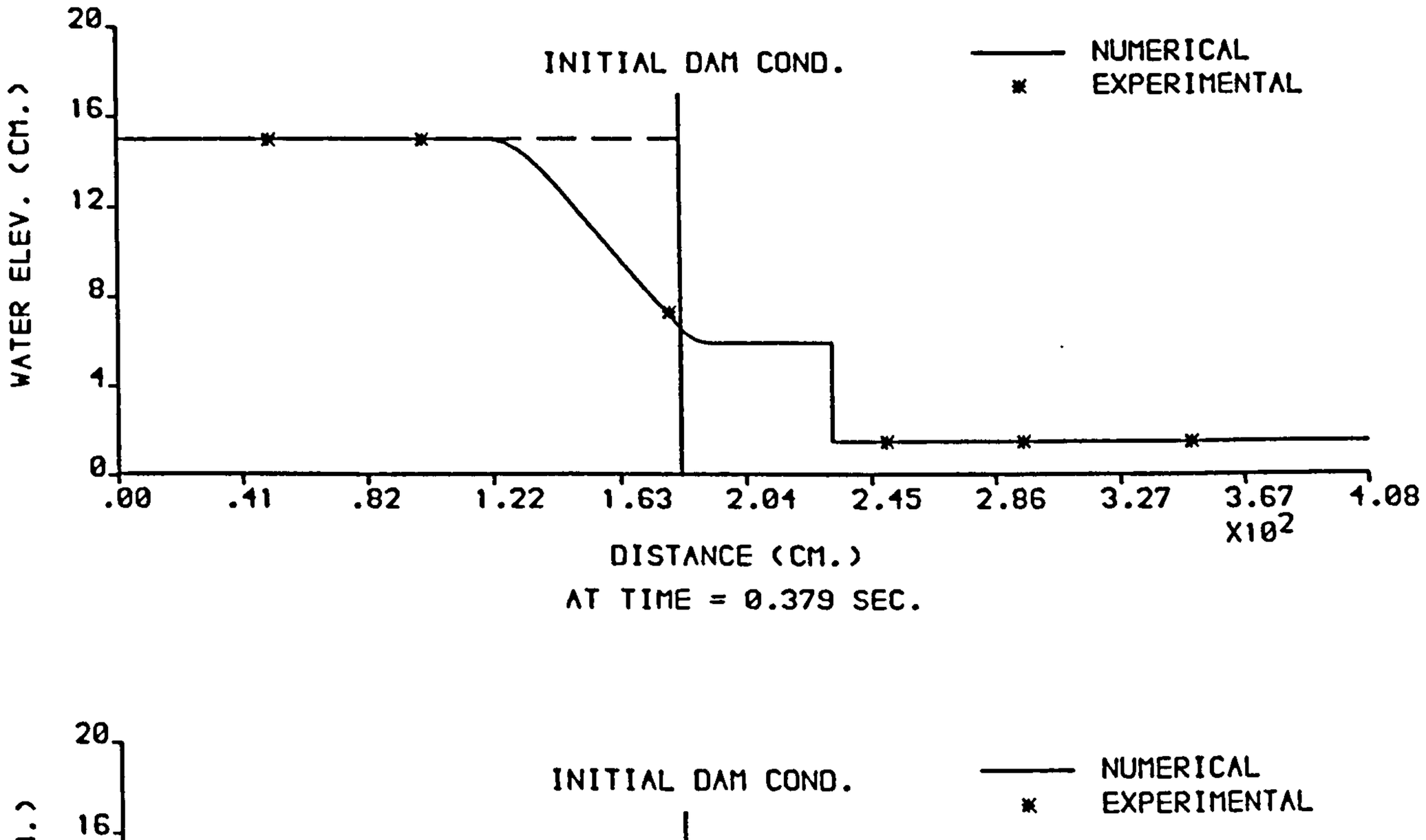

FIGURE 6.14 : NUMERICAL AND EXPERIMENTAL PROFILES FROM THE (X-T) MODEL , H_1 = 15 cm AND H_o = 1.5 cm .

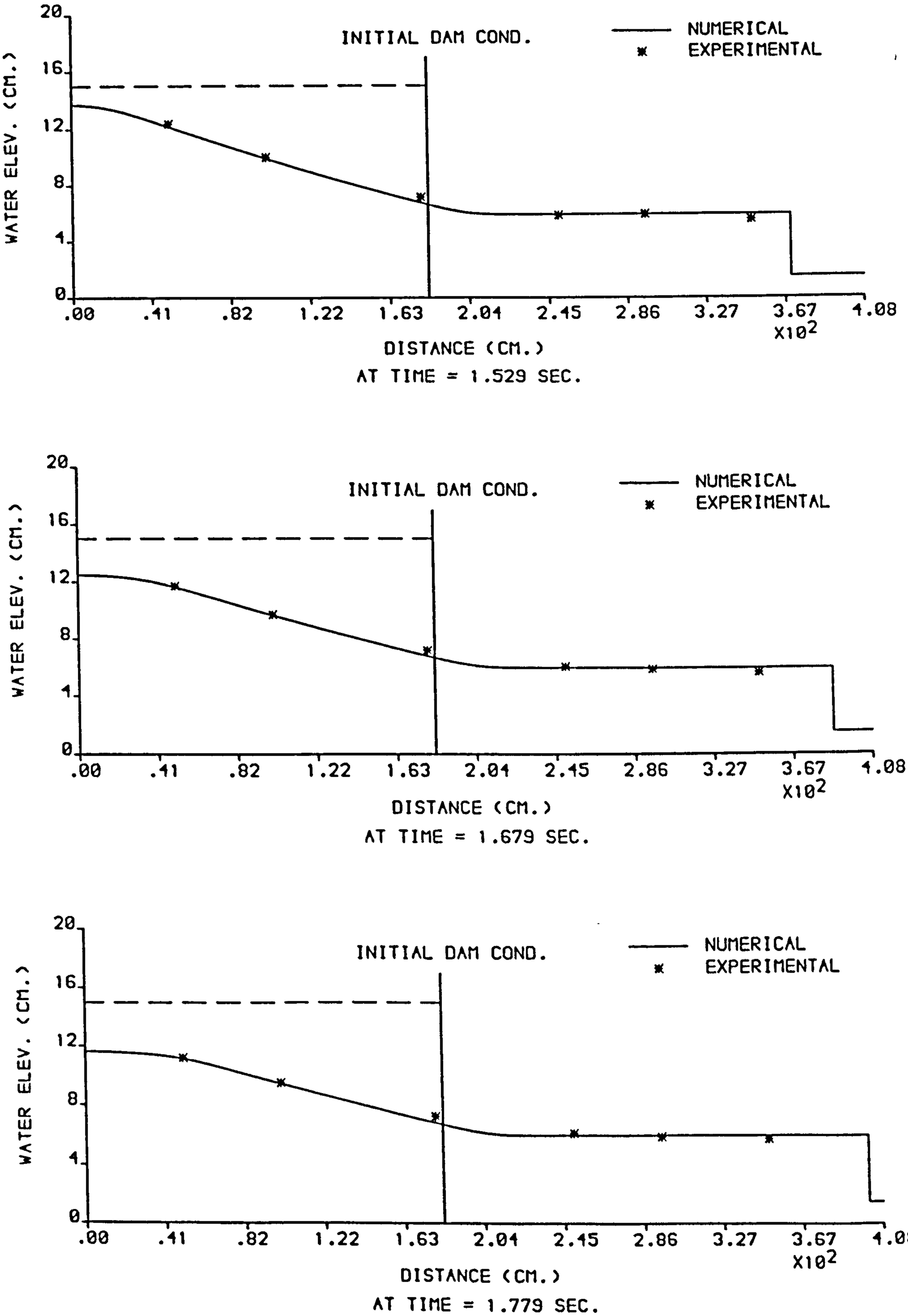

FIGURE 6.15 : NUMERICAL AND EXPERIMENTAL PROFILES FROM THE (X-T) MODEL , H_1 = 15 cm AND H_o = 1.5 cm .

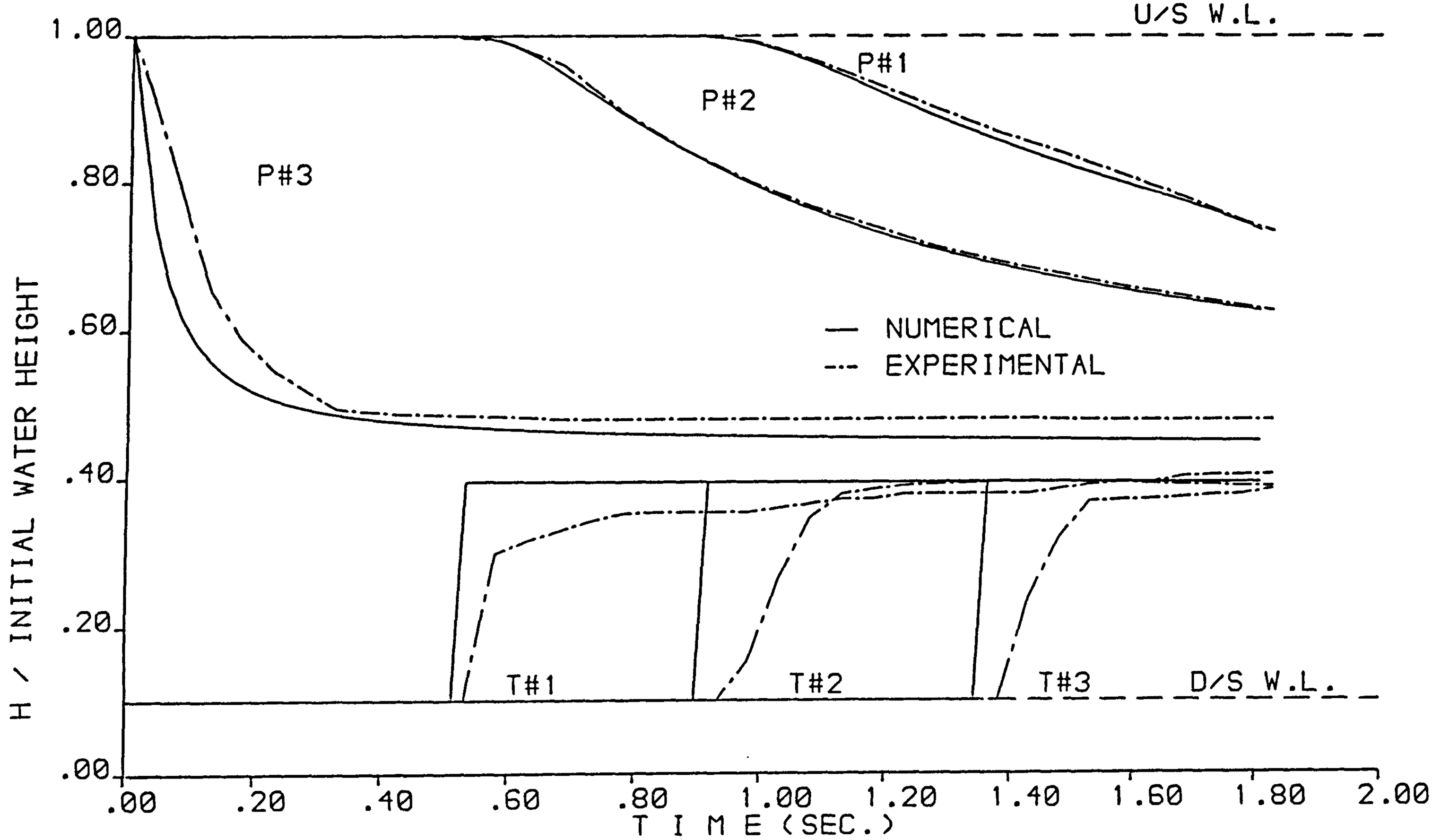

FIGURE 6.16 : NUMERICAL AND EXPERIMENTAL STAGE HYDROGRAPHS FROM THE (X-T) MODEL , H_1 = 15 cm AND H_o = 1.5 cm .

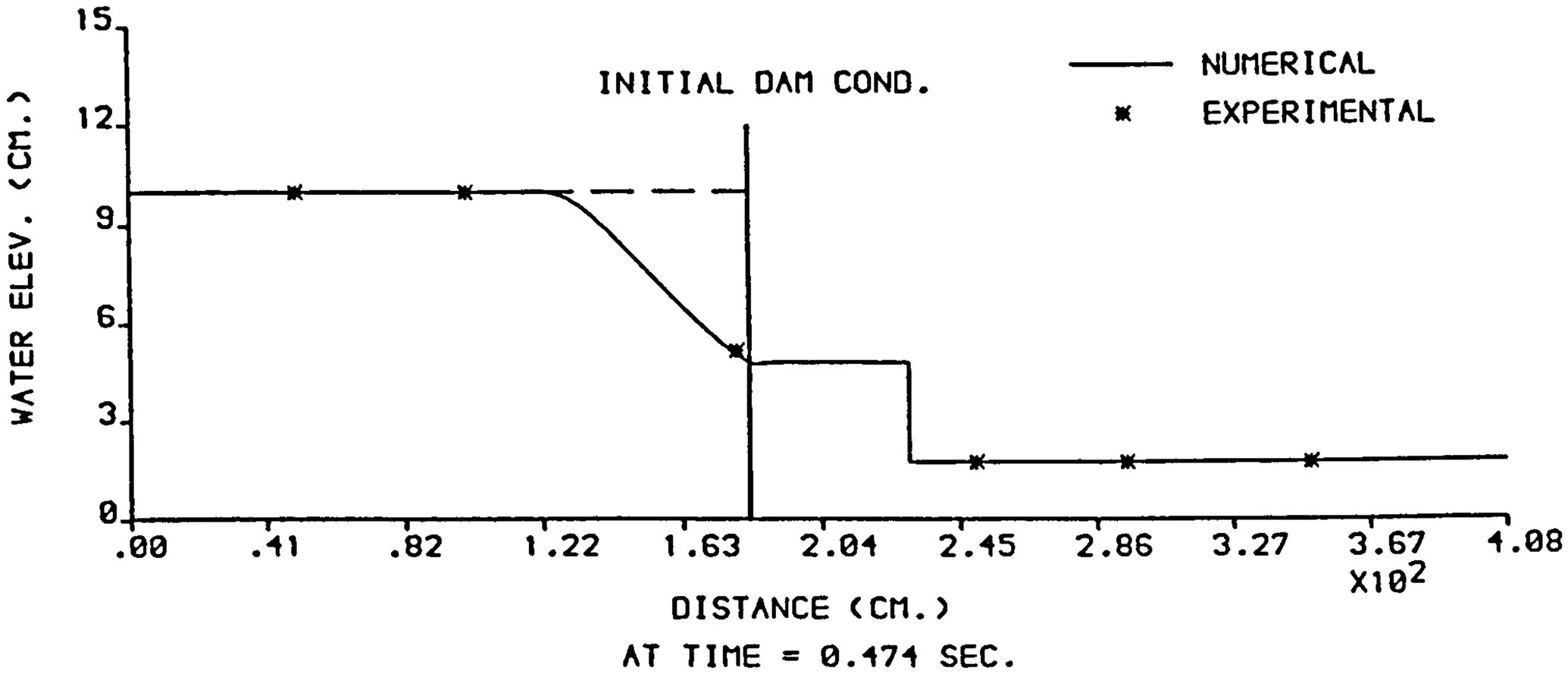

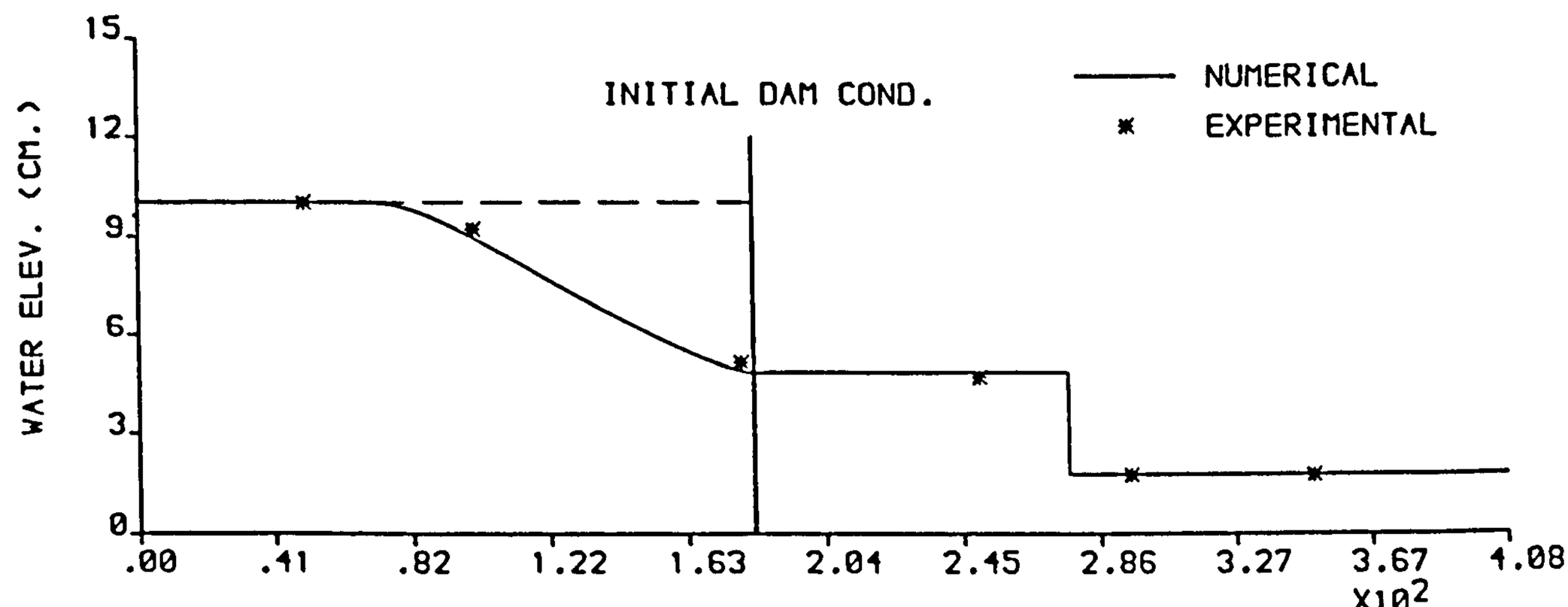

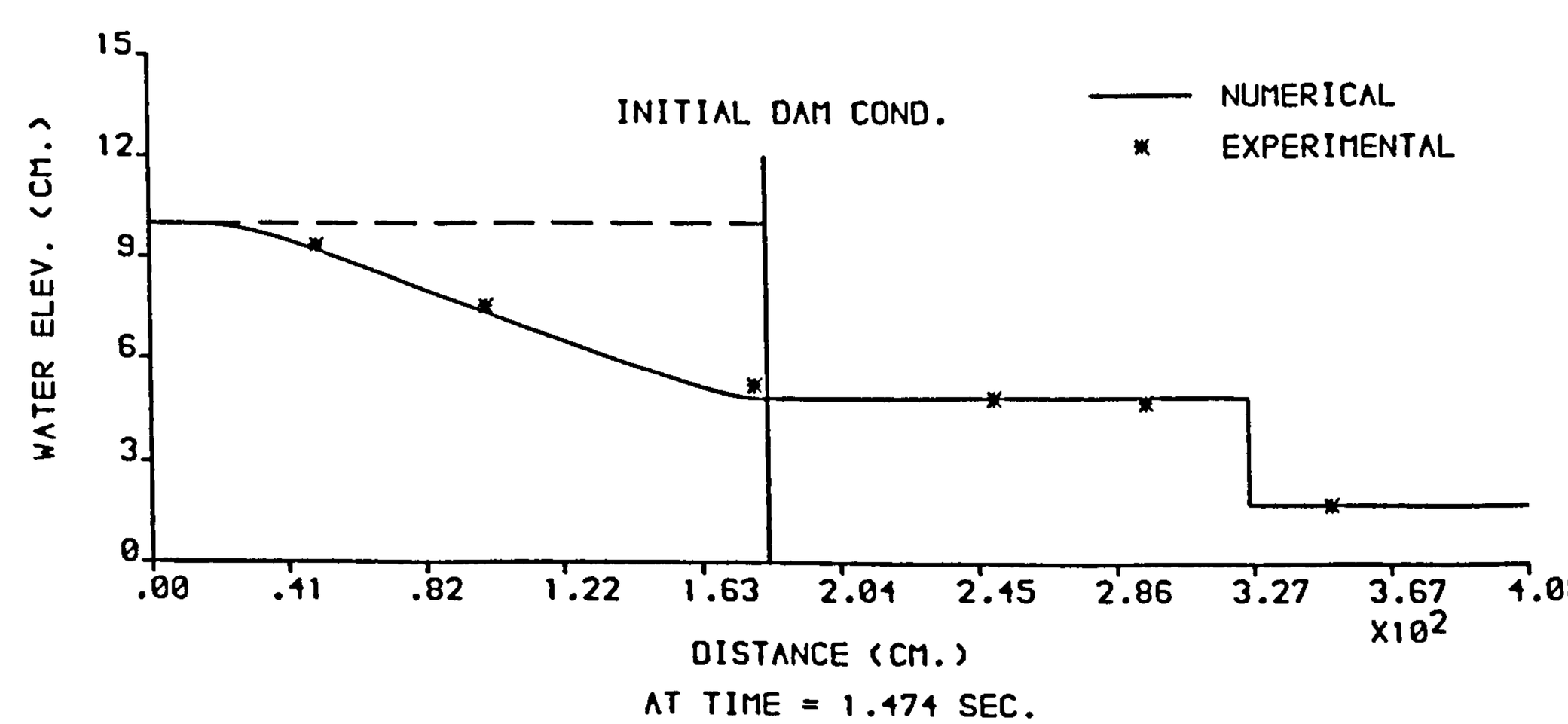

FIGURE 6.17 : NUMERICAL AND EXPERIMENTAL PROFILES FROM THE (X-T) MODEL , H_1 = 10 cm AND H_o = 1.76 cm .

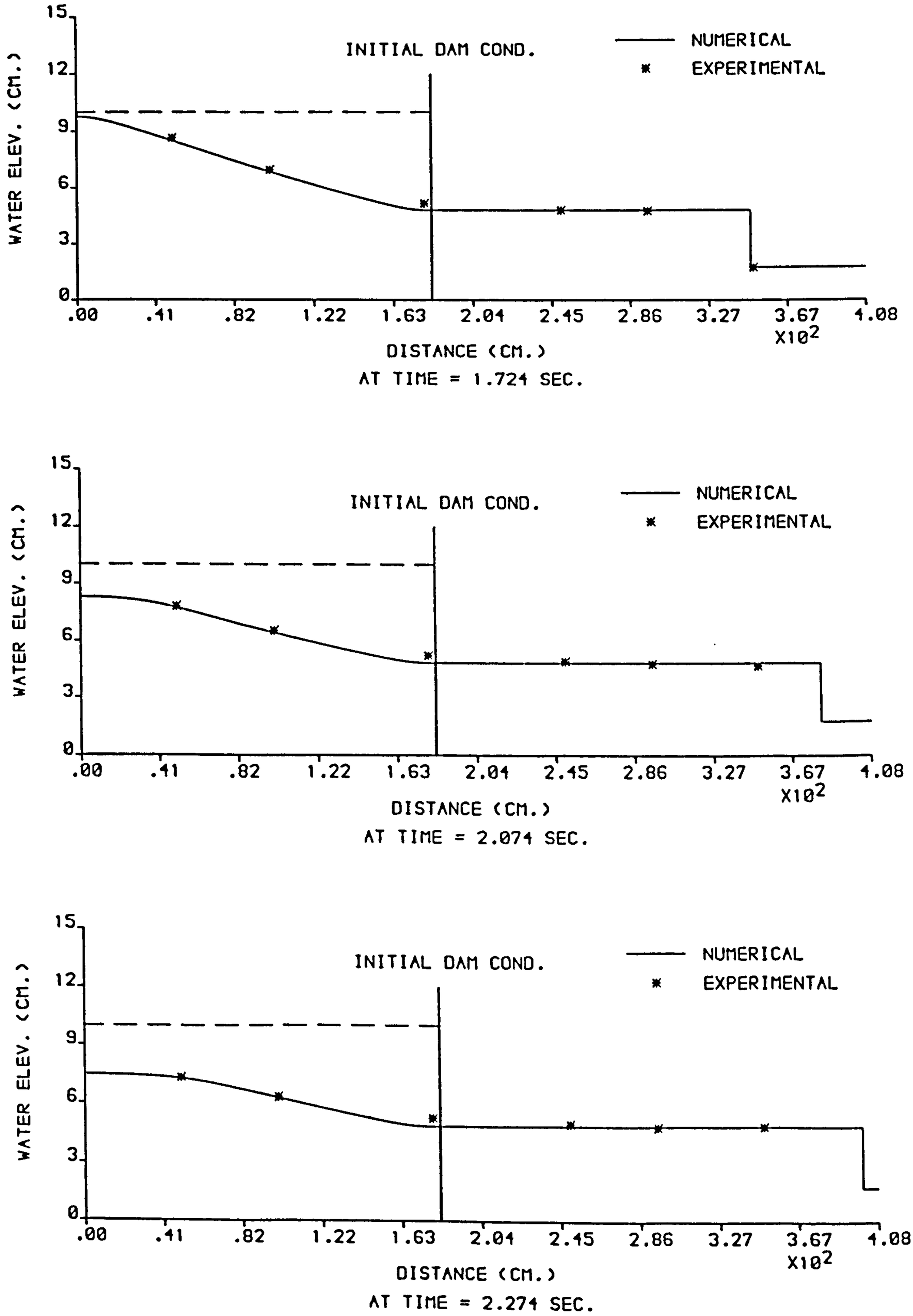

FIGURE 6.18 : NUMERICAL AND EXPERIMENTAL PROFILES FROM THE (X-T) MODEL , H_1 = 10 cm AND H_o = 1.76 cm .

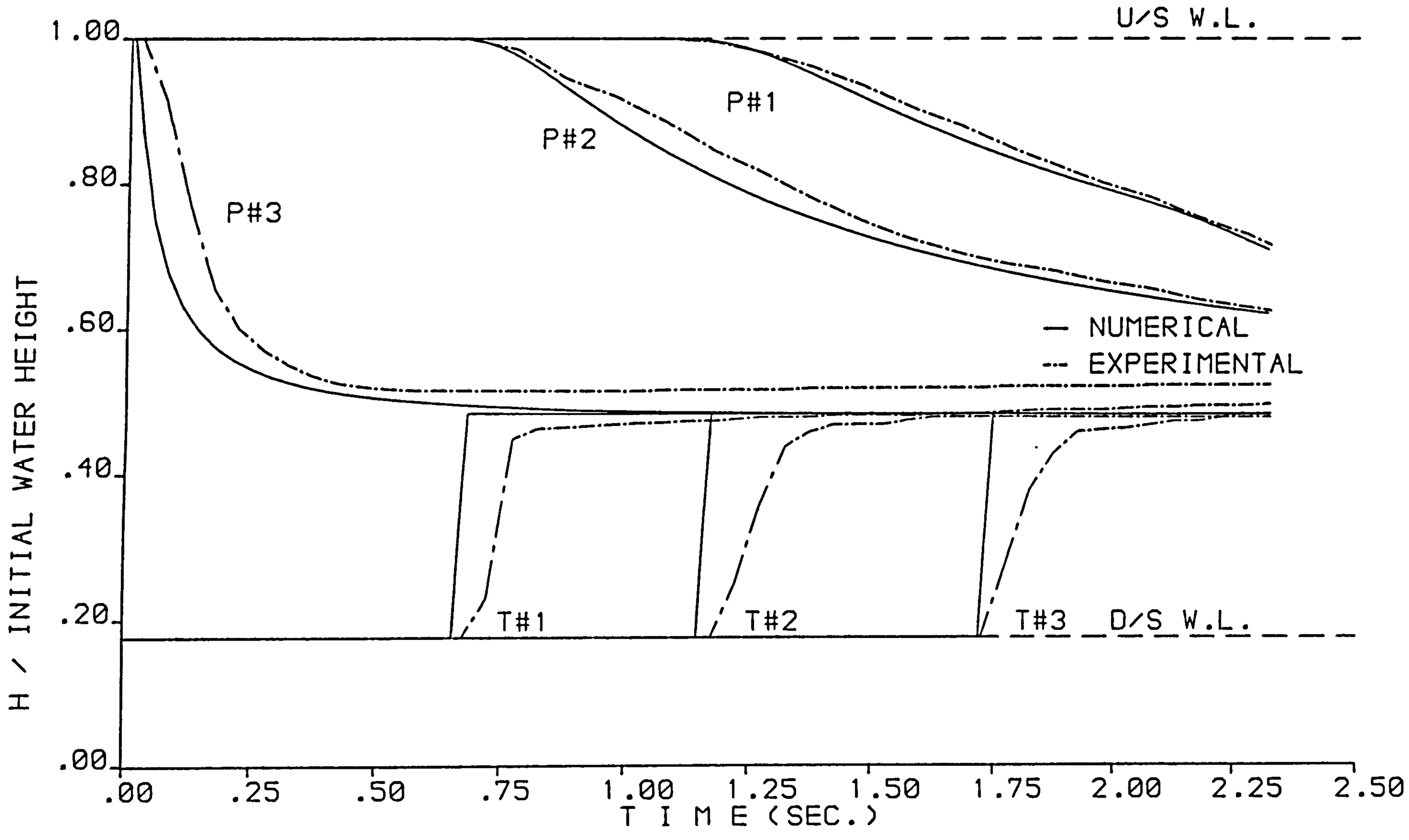

FIGURE 6.19 : NUMERICAL AND EXPERIMENTAL STAGE HYDROGRAPHS FROM THE (X-T) MODEL , H_1 = 10 cm AND H_o = 1.76 cm .

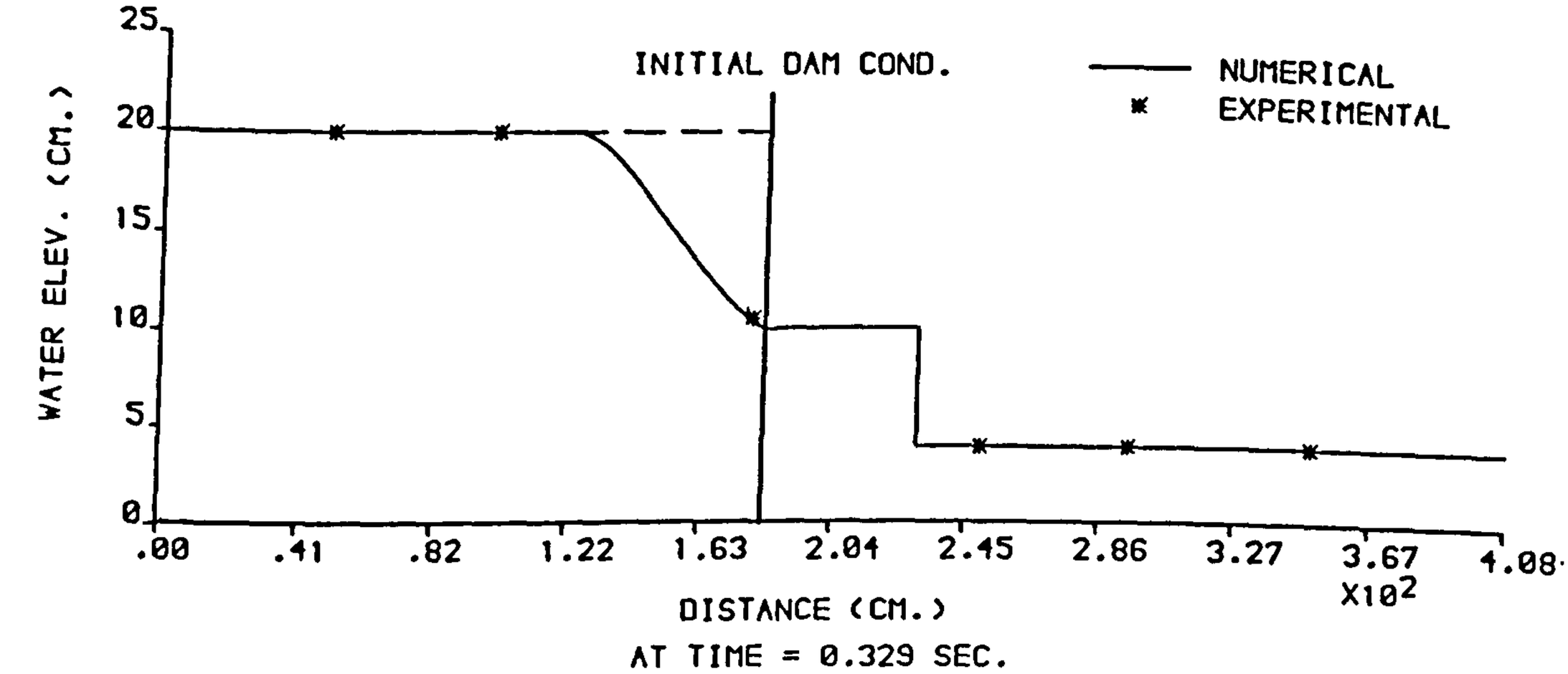

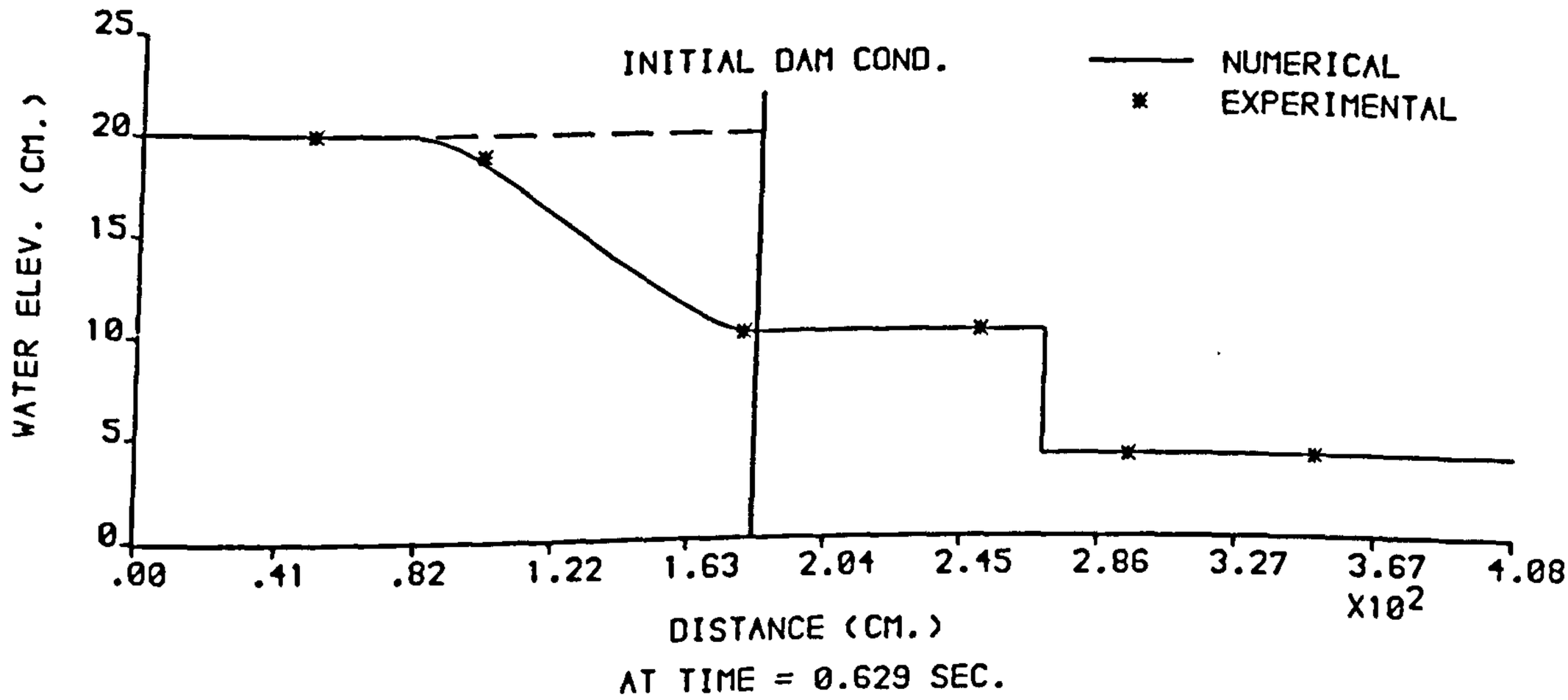

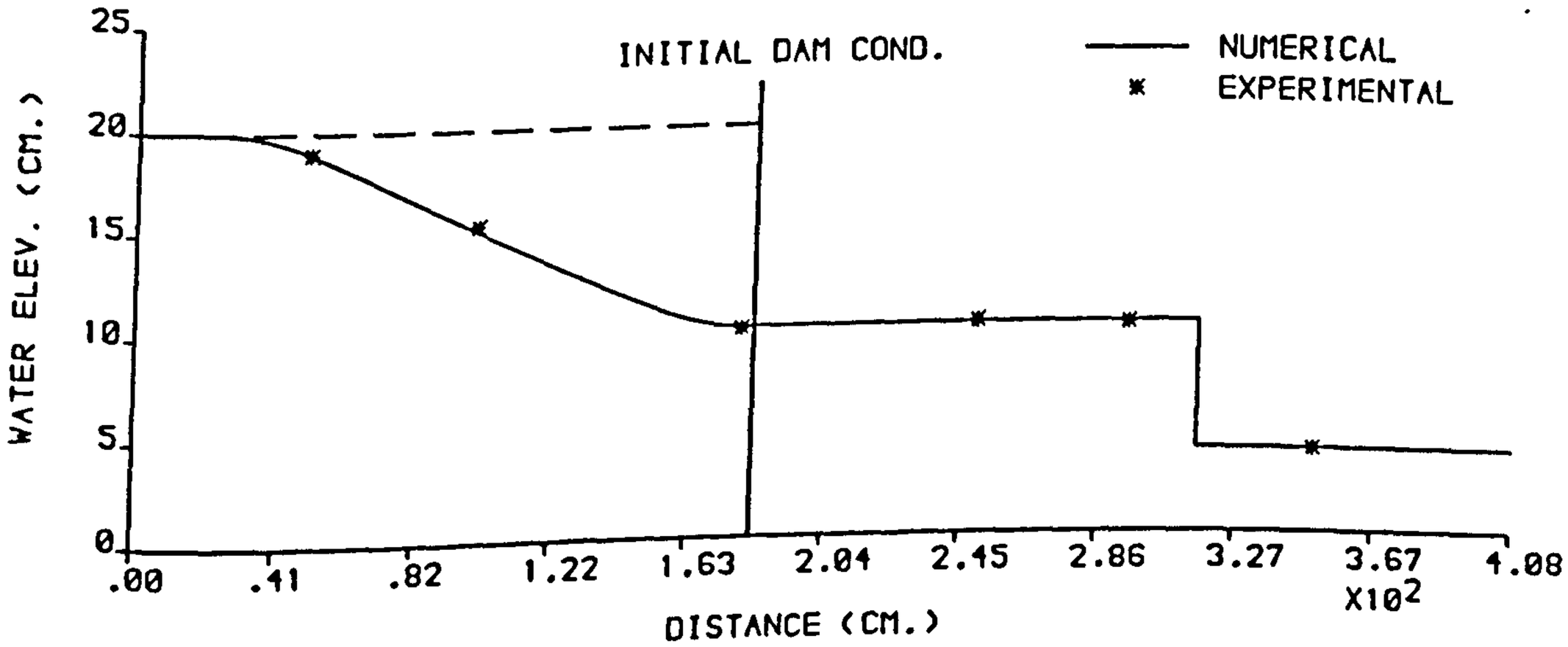

FIGURE 6.20 : NUMERICAL AND EXPERIMENTAL PROFILES FROM THE (X-T) MODEL , H_1 = 20 cm AND H_o = 4 cm .

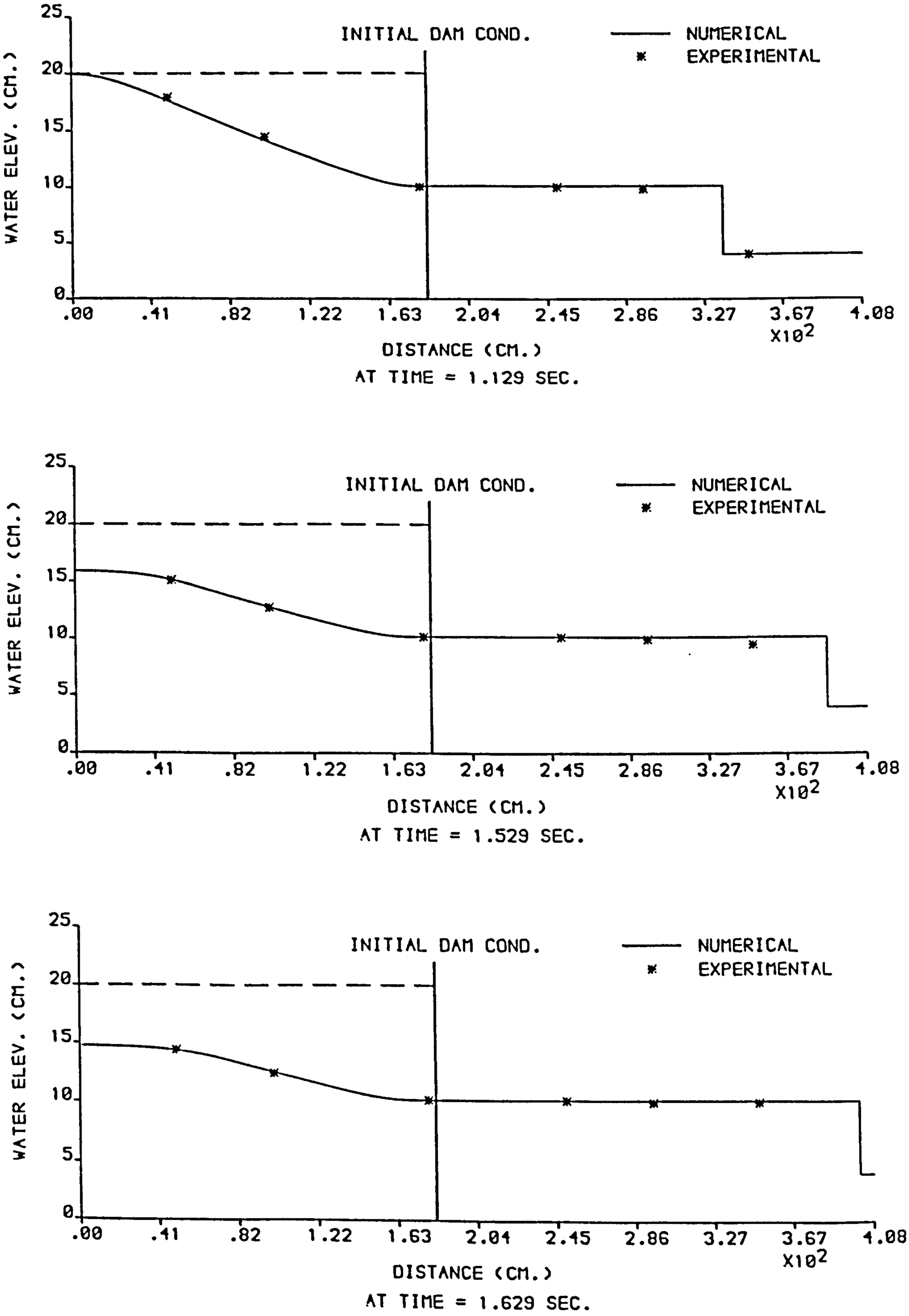

FIGURE 6.21 : NUMERICAL AND EXPERIMENTAL PROFILES FROM THE (X-T) MODEL , H_1 = 20 cm AND H_o = 4 cm .

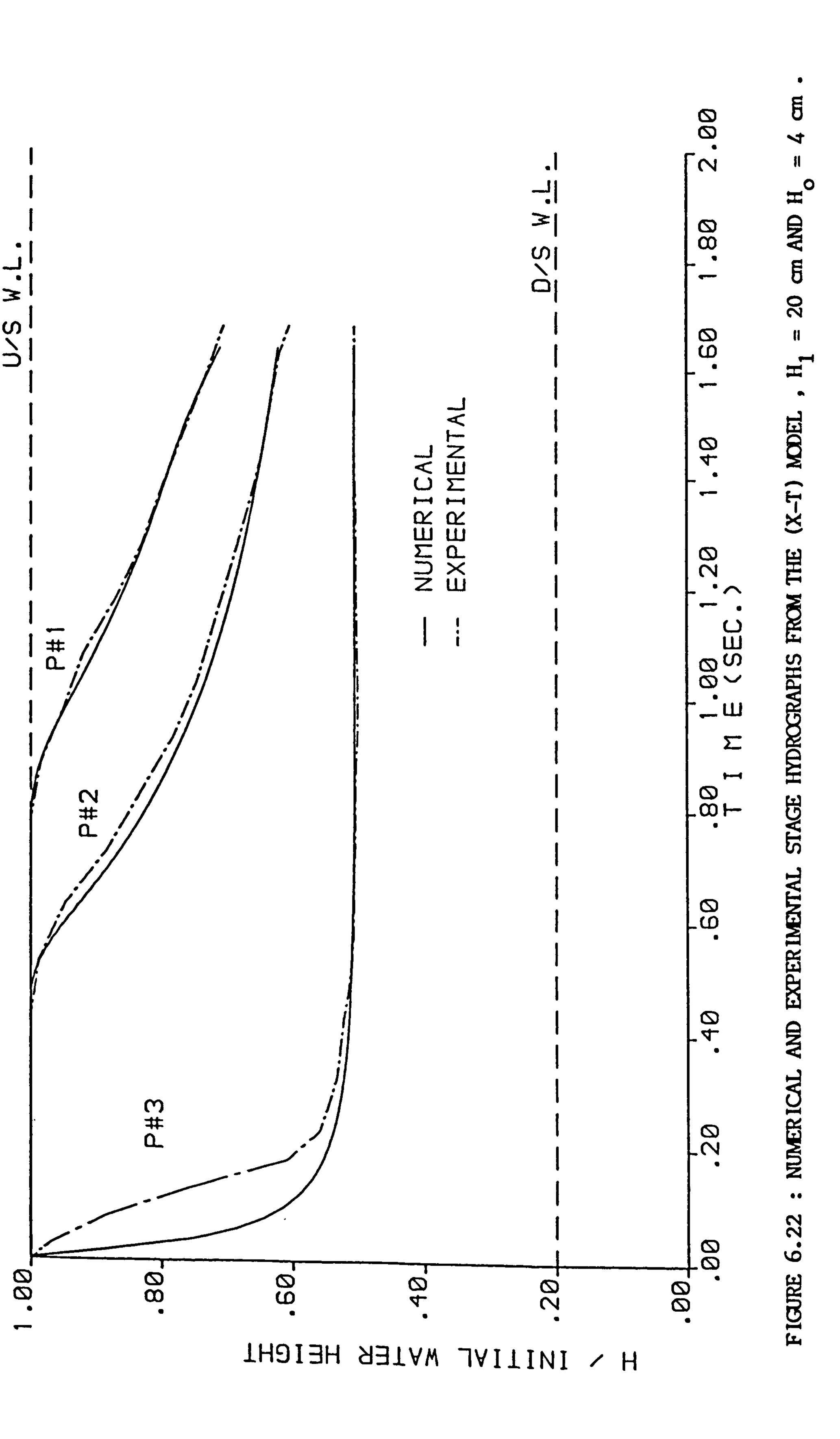

FIGURE 6.22 : NUMERICAL AND EXPERIMENTAL STAGE HYDROGRAPHS FROM THE (X-T) MODEL , H_1 = 20 cm AND H_o = 4 cm .

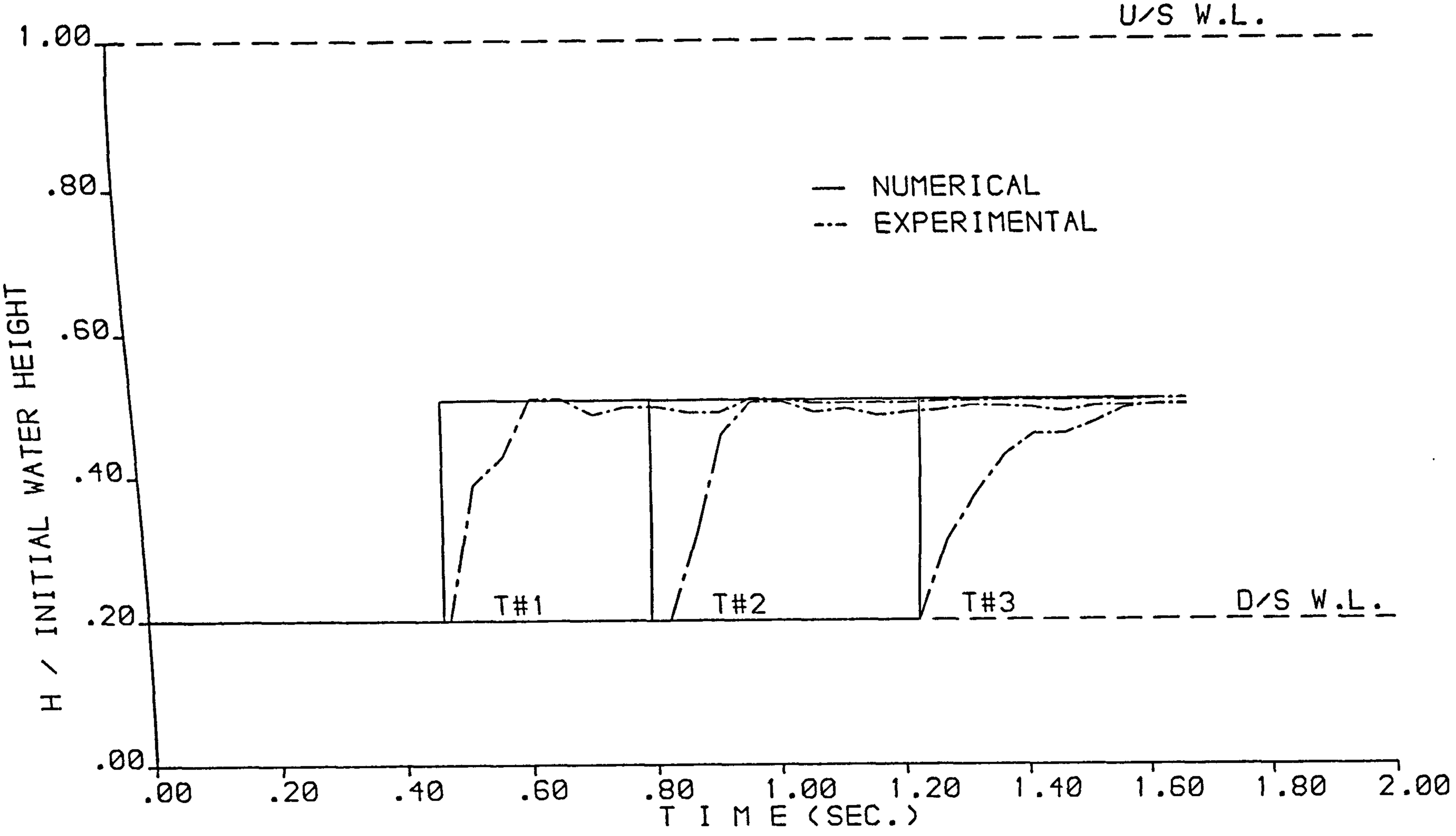

FIGURE 6.23 : NUMERICAL AND EXPERIMENTAL STAGE HYDROGRAPHS FROM THE (X-T) MODEL , H_1 = 20 cm AND H_o = 4 cm .

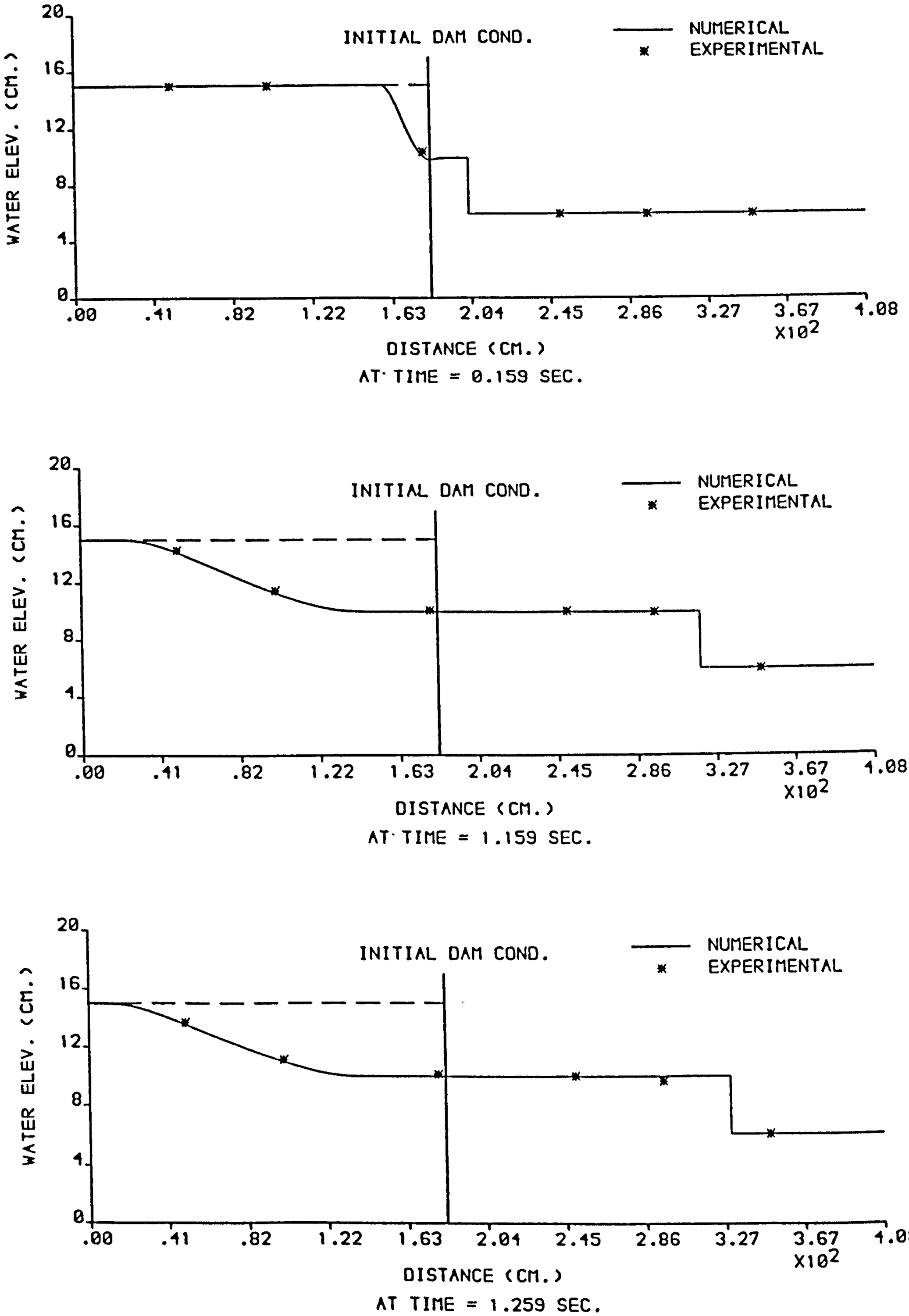

FIGURE 6.24 : NUMERICAL AND EXPERIMENTAL PROFILES FROM THE (X-T) MODEL , H_1 = 15 cm AND H_o = 6 cm .

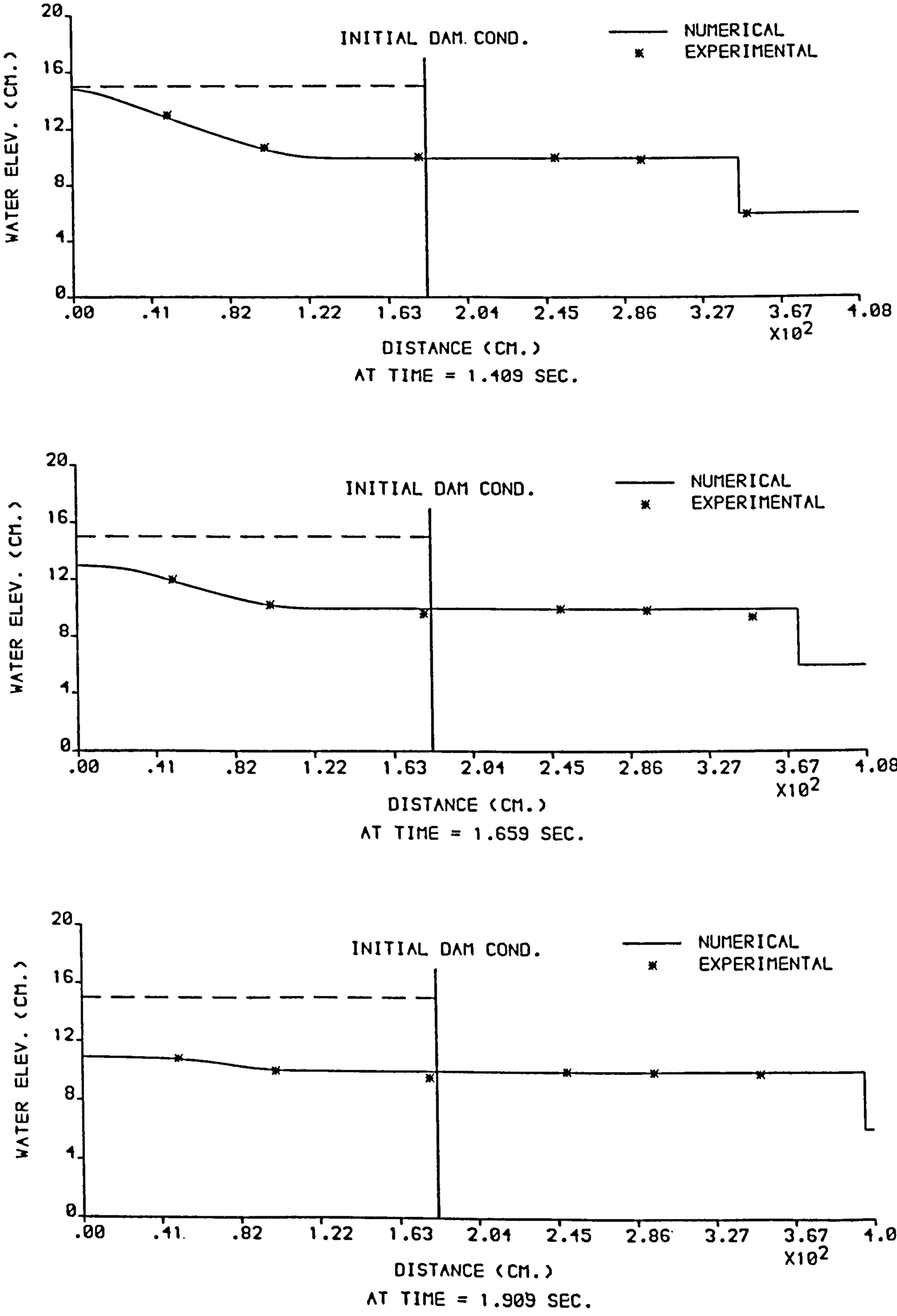

FIGURE 6.25 : NUMERICAL AND EXPERIMENTAL PROFILES FROM THE (X-T) MODEL , H_1 = 15 cm AND H_o = 6 cm .

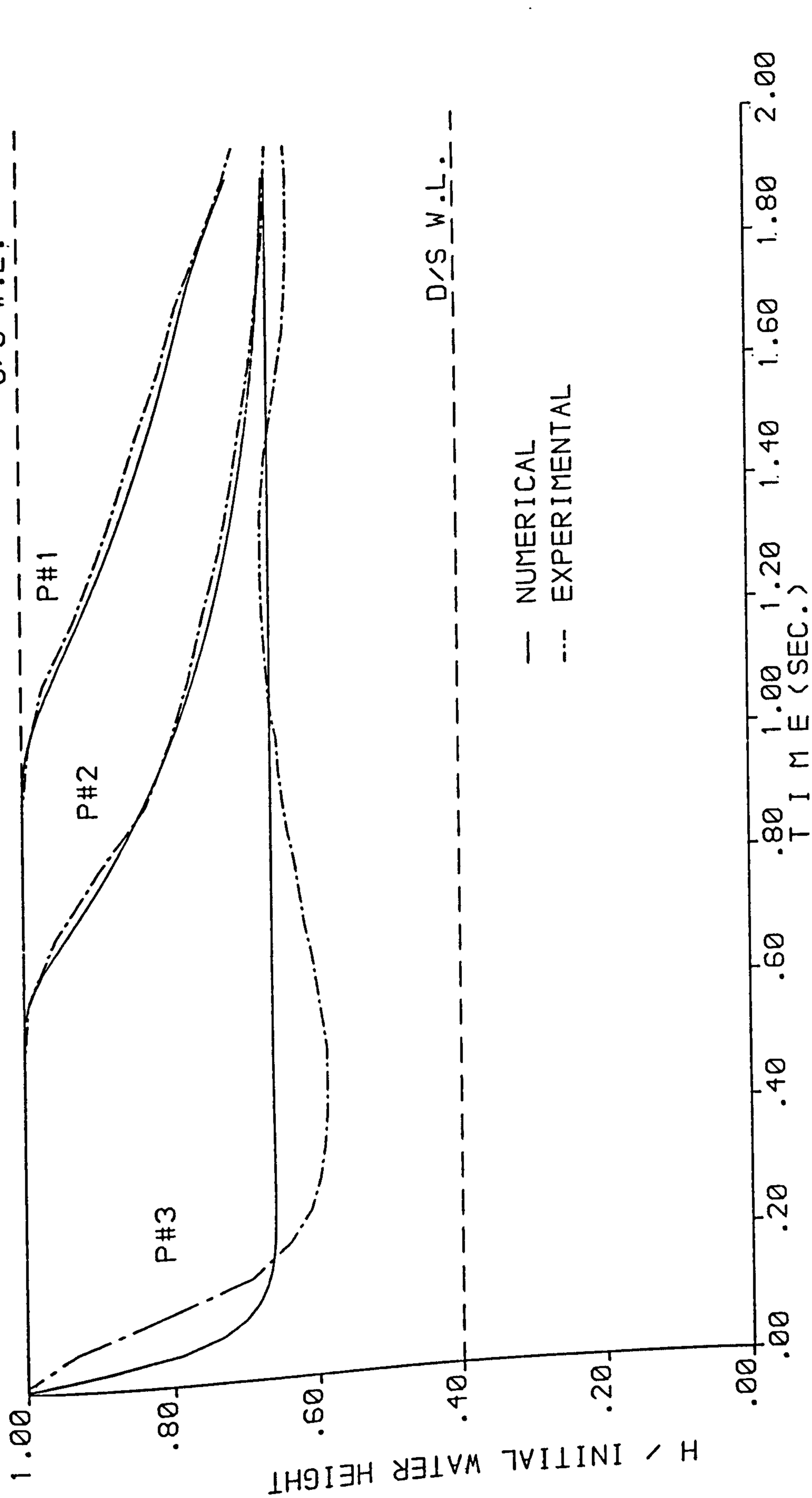

FIGURE 6.26 : NUMERICAL AND EXPERIMENTAL STAGE HYDROGRAPHS FROM THE (X-T) MODEL , H_1 = 15 cm AND H_o = 6 cm .

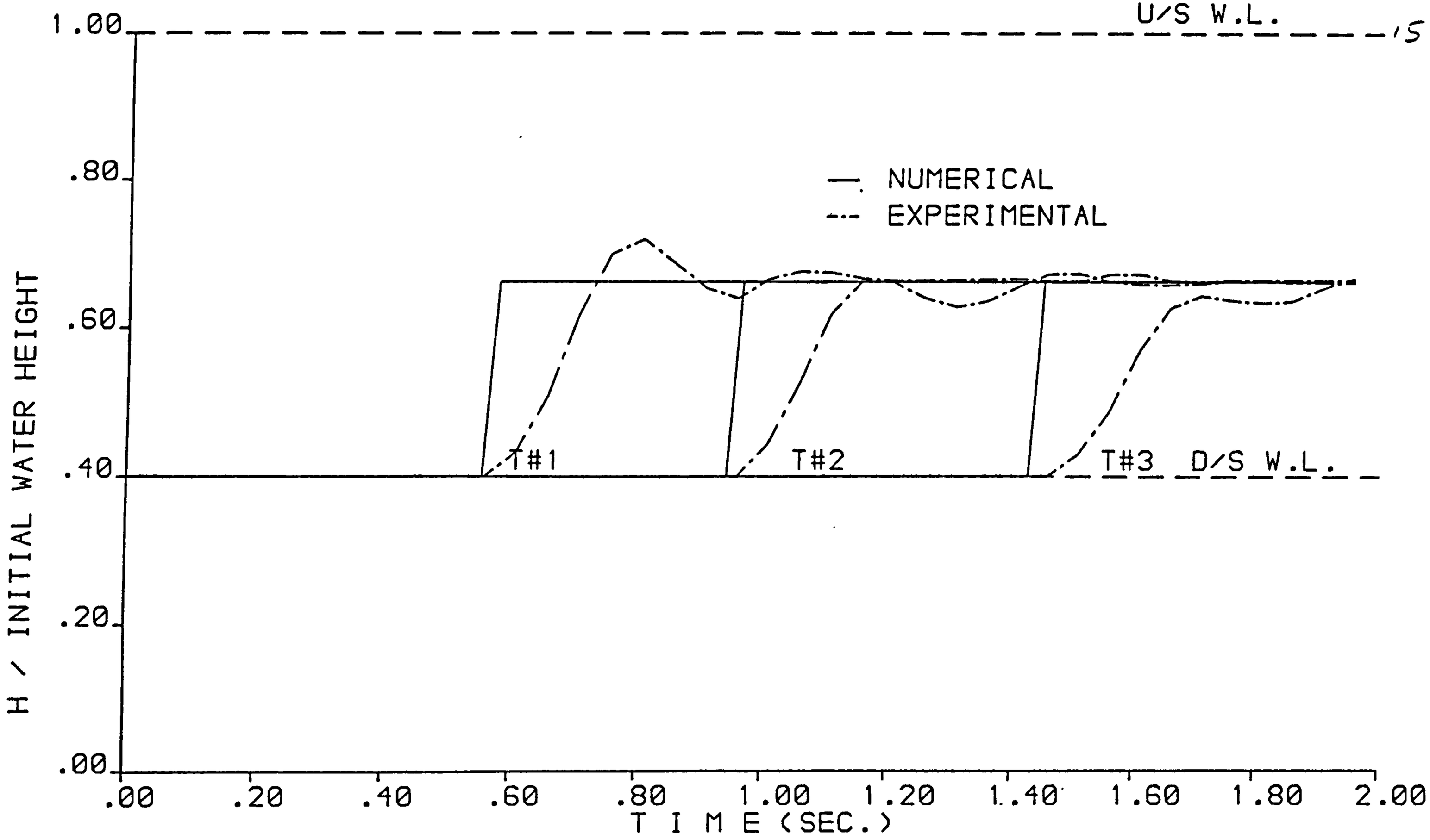

FIGURE 6.27 : NUMERICAL AND EXPERIMENTAL STAGE HYDROGRAPHS FROM THE (X-T) MODEL , H_1 = 15 cm AND H_o = 6 cm .

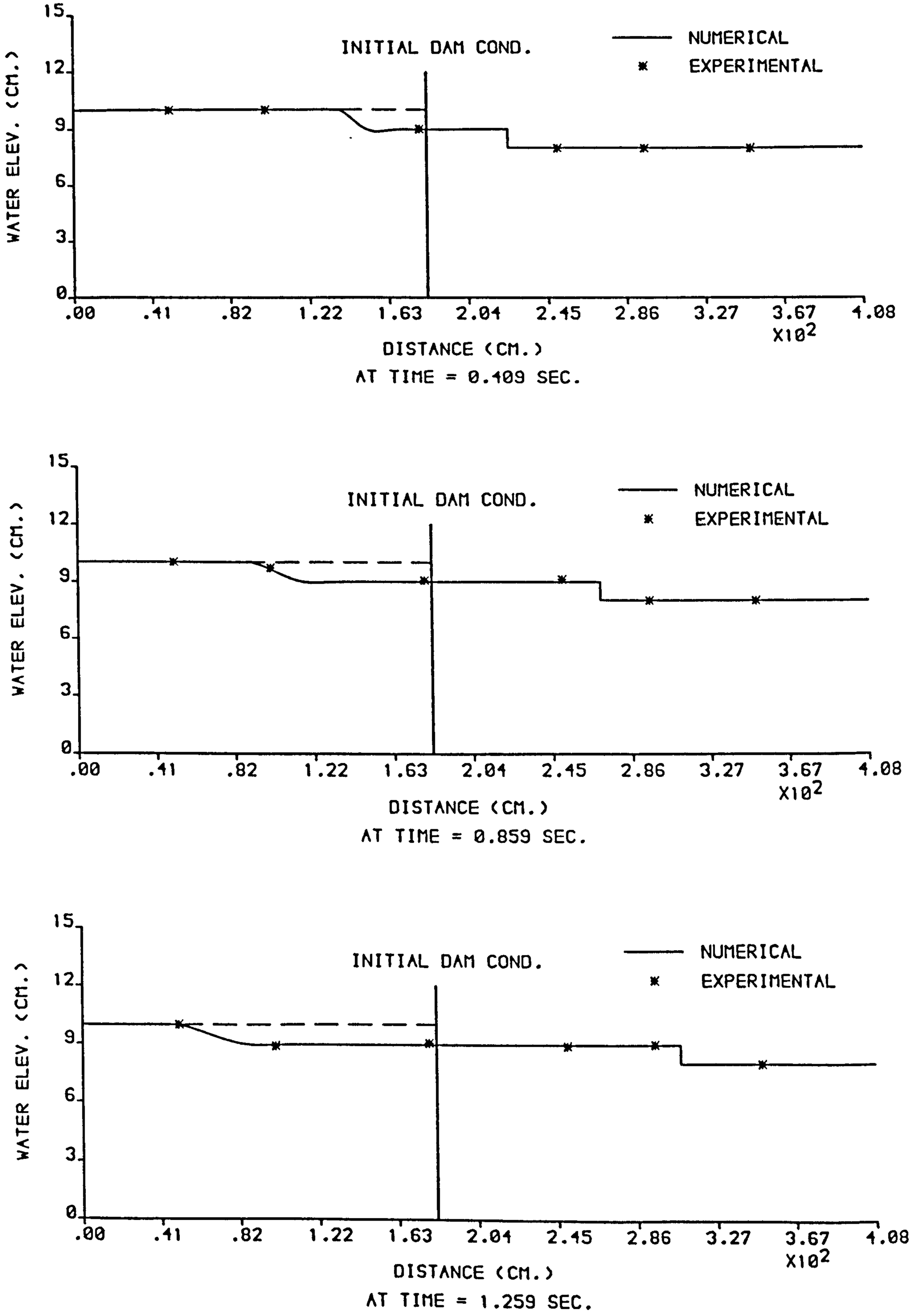

FIGURE 6.28 : NUMERICAL AND EXPERIMENTAL PROFILES FROM THE (X-T) MODEL , H_1 = 10 cm AND H_o = 8 cm .

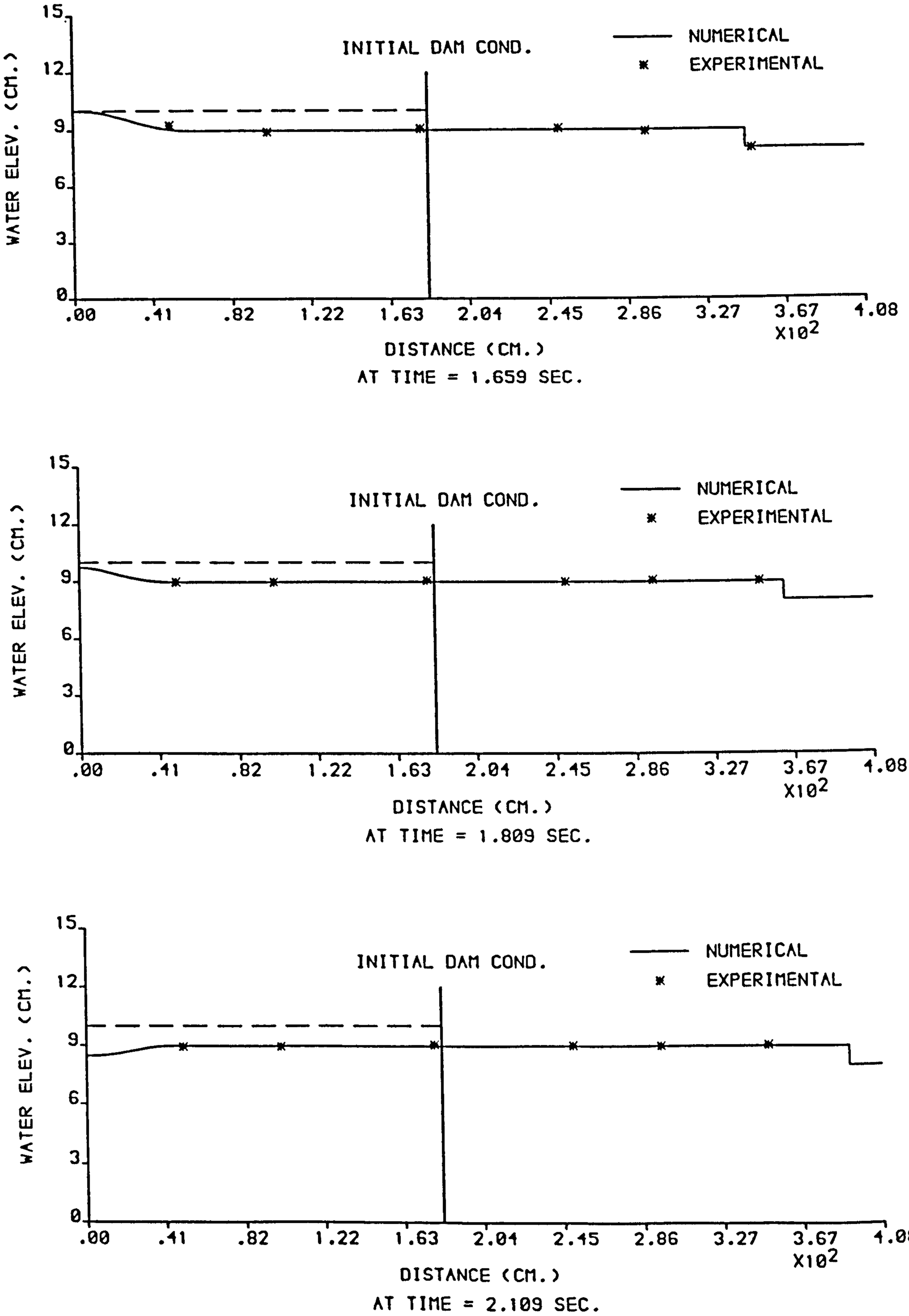

FIGURE 6.29 : NUMERICAL AND EXPERIMENTAL PROFILES FROM THE (X-T) MODEL , H_1 = 10 cm AND H_o = 8 cm .

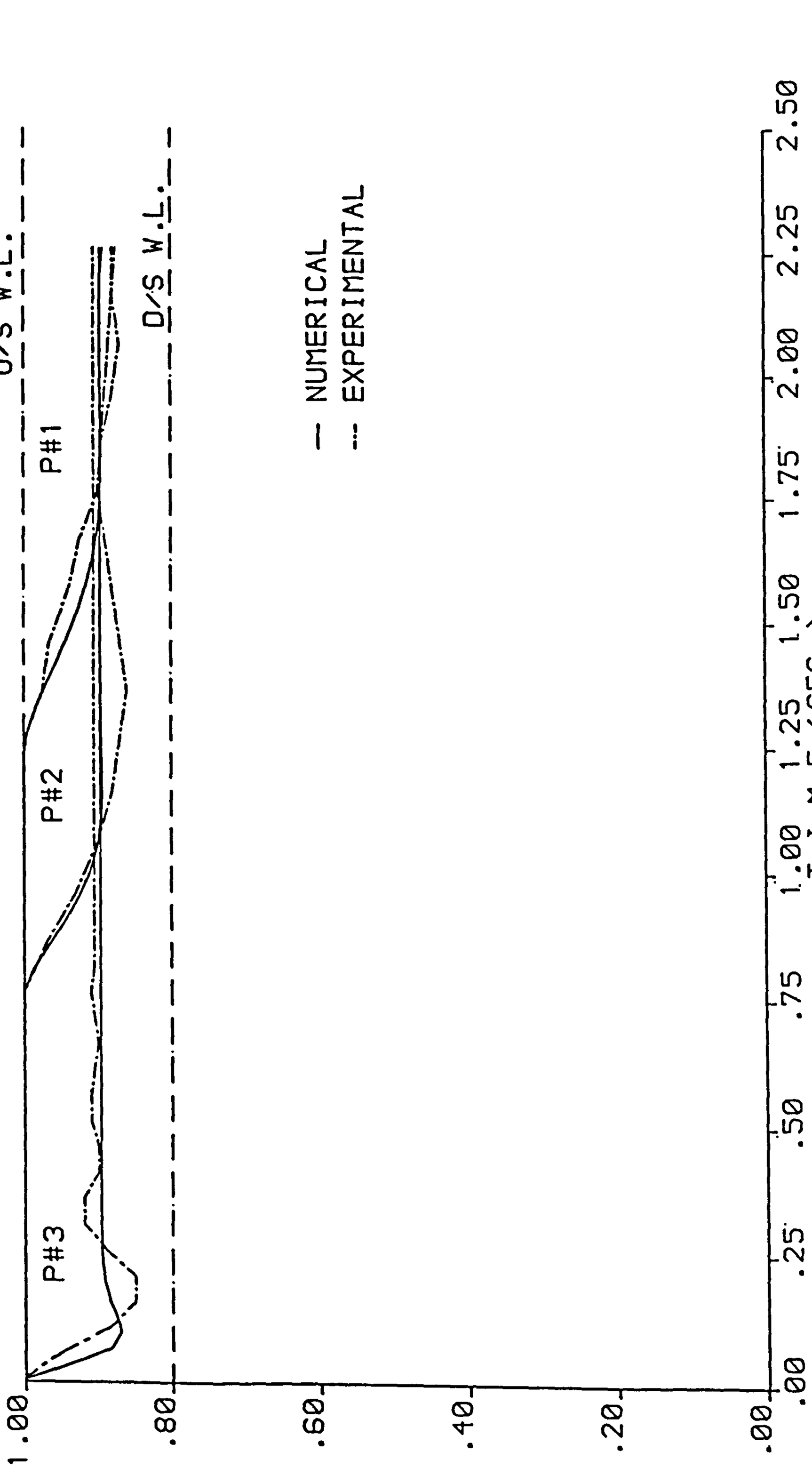

FIGURE 6.30 : NUMERICAL AND EXPERIMENTAL STAGE HYDROGRAPHS FROM THE (X- T) MODEL , H_1 = 10 cm AND H_o = 8 cm .

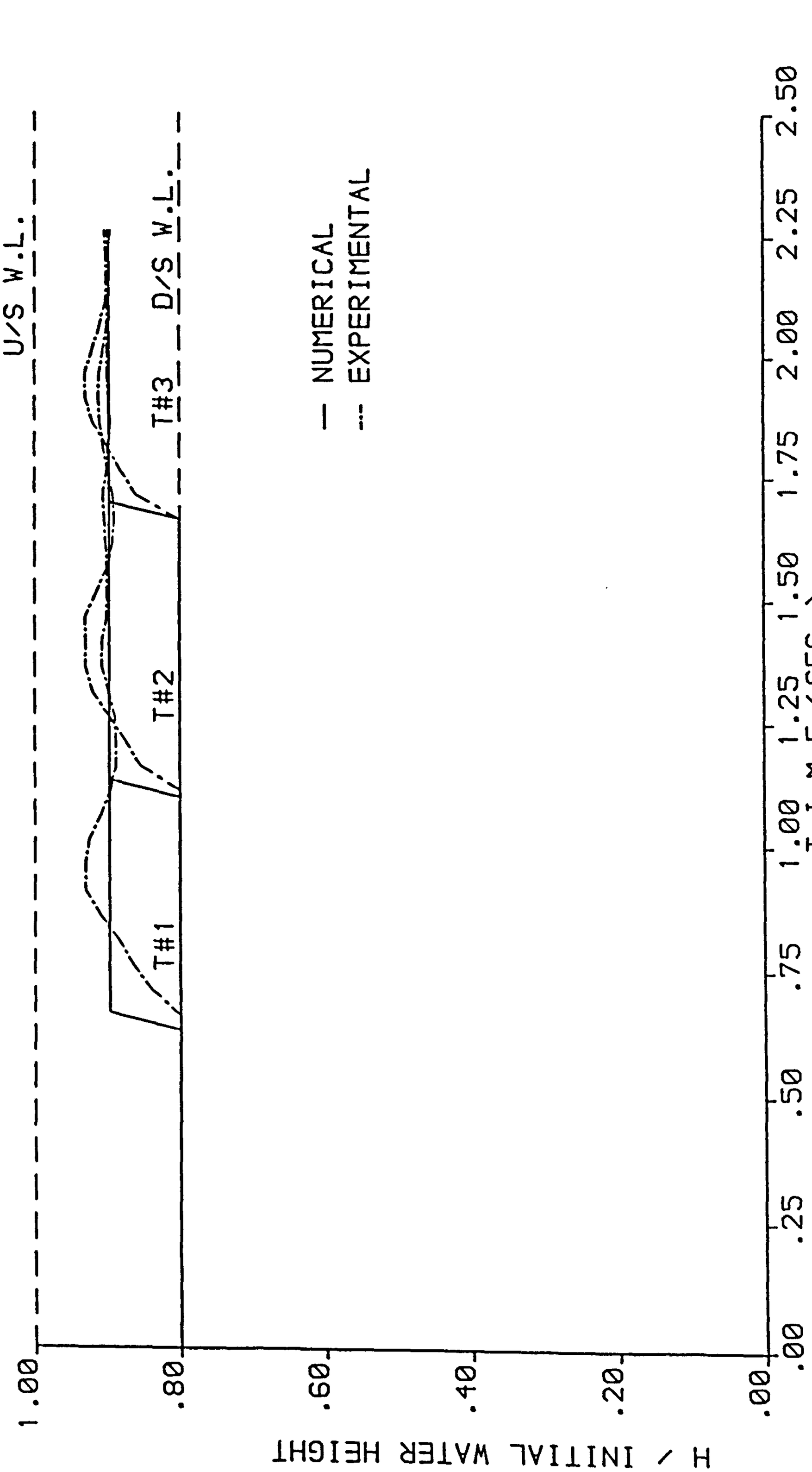

FIGURE 6.31 : NUMERICAL AND EXPERIMENTAL STAGE HYDROGRAPHS FROM THE (X-T) MODEL , H_1 = 10 cm AND H_o = 8 cm .

6.2 RT-XT Model

In this section the author attempts to assess the numerical (RT-XT) model which is a combination of the radial model (convergent sides) upstream of the dam and the plain (X-T) model (parallel sides) downstream. This assessment was aided by making a comparison between the results obtained from the physical model which is illustrated in Chapter Five and the numerical results.

Comparison of the front heights with Stoker's (X-T) solution was made for different ratios of initial water depths (H_o/H_1), as presented in Figure 6.32. The front height divided by the initial depth upstream $[(H_2-H_o)/H_1]$ versus the ratio of initial water depths (H_o/H_1) is plotted for Stoker's (X-T) solution, the numerical results and the experimental data for different water depths upstream. Close agreement between computed or measured front heights (with a general difference less than 4%) on one hand and Stoker's (X-T) solution (with a general difference less than 3.5%) suggests that the upstream reservoir shape has no effect on the front heights to some extent since the front height was slightly higher than in the X-T case with a general difference of 2%. However, both numerical and physically observed water depths upstream of the dam are generally higher than in the (X-T) model and exhibit a sharp drop in the water profile as it passes through the gate. Figure 6.33, photograph of the water profile at the gate and just behind it shows this phenomenon, also shown in Figure 6.34 an enlargement of the photograph in Figure 6.33.

Referring to Figures 6.35 to 6.60, numerical and experimental

dam-break results are now compared in two types of plots; the water depth profiles and the stage hydrographs, for the same ratios of initial water depths as in the (X-T) model. The agreement is good and the effect of changing the cross-section upstream is clearly exhibited by the depth profile plots, i.e. the depth of water becomes higher just behind the dam and then drops sharply when it reaches the dam. The difference between the numerical and experimental results generally was the same as in the X-T model.

[6.3 RT-RT MODEL CONTINUED ON P. 250
FIGURES 6.32 TO 6.60 FOLLOW DIRECTLY]

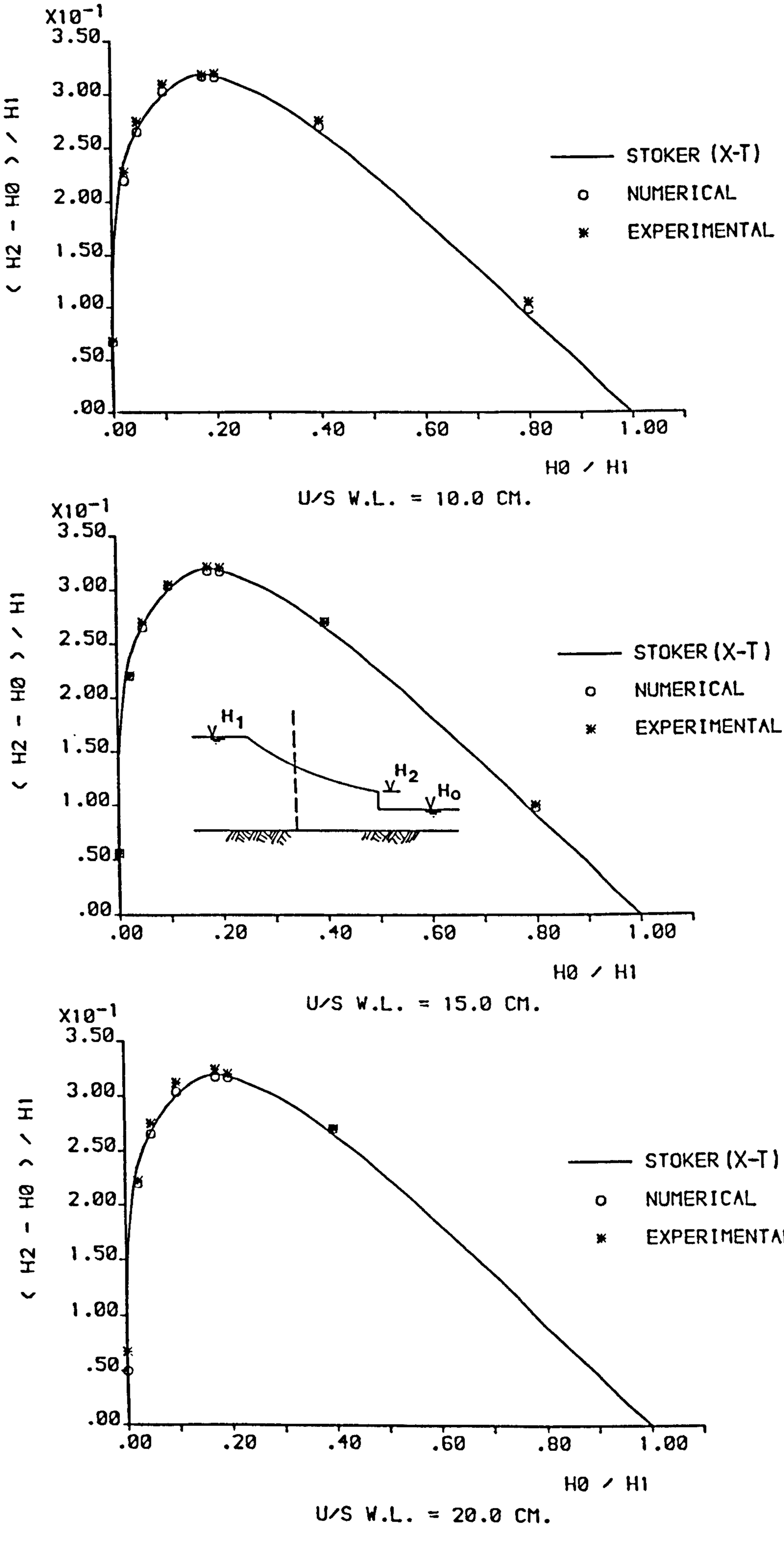

FIGURE 6.32 : COMPARISONS OF THE FRONT HEIGHTS RESULTING FROM THE (RT-XT) NUMERICAL AND PHYSICAL MODELS WITH STOKER'S (X-T) SOLUTION .

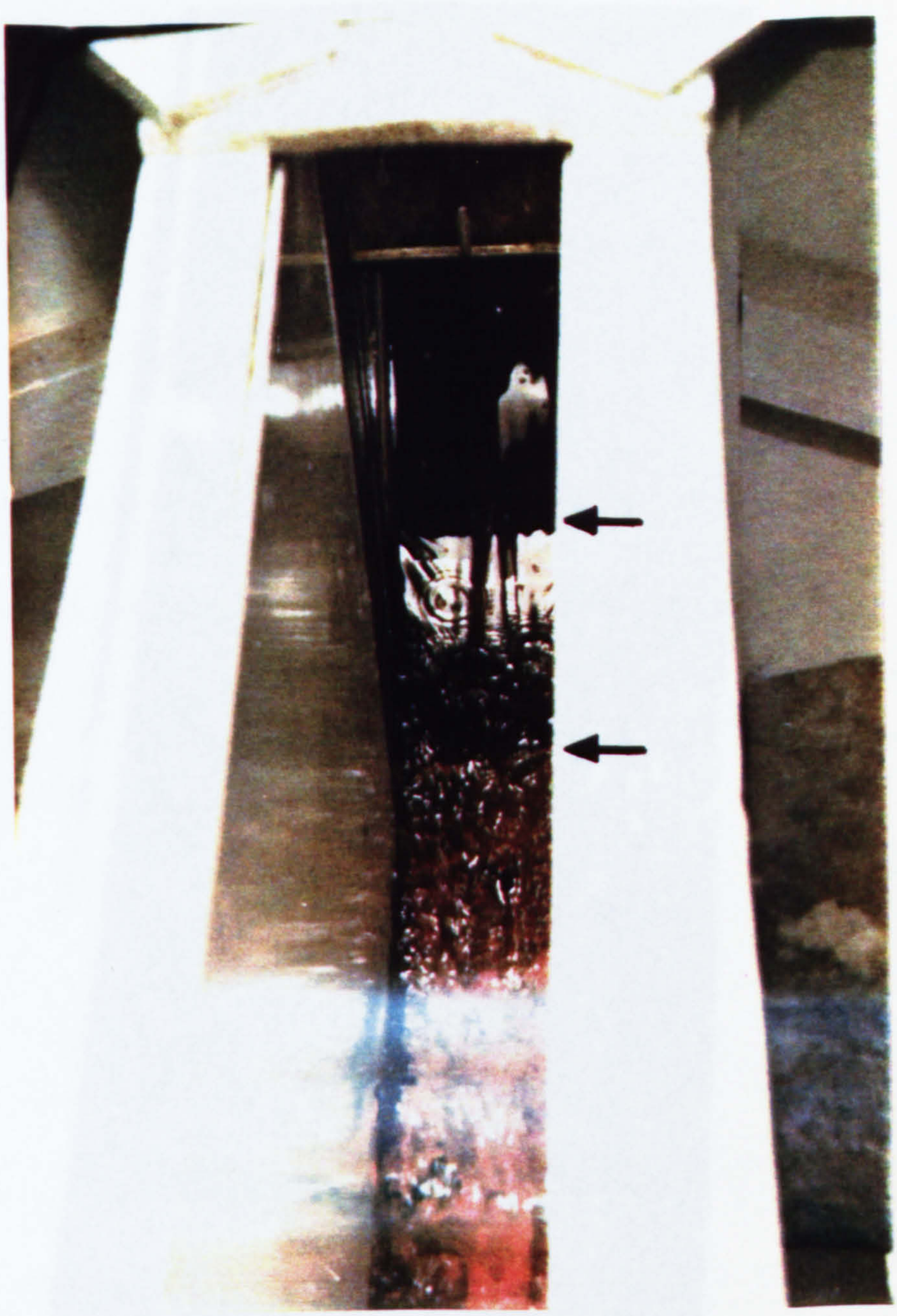

FIGURE 6.33 : PHOTOGRAPH OF THE WATER PROFILE AT THE GATE IN THE (RT - XT) MODEL . THE SHARP FALL IN THE PROFILE IS INDICATED BY THE ARROWS .

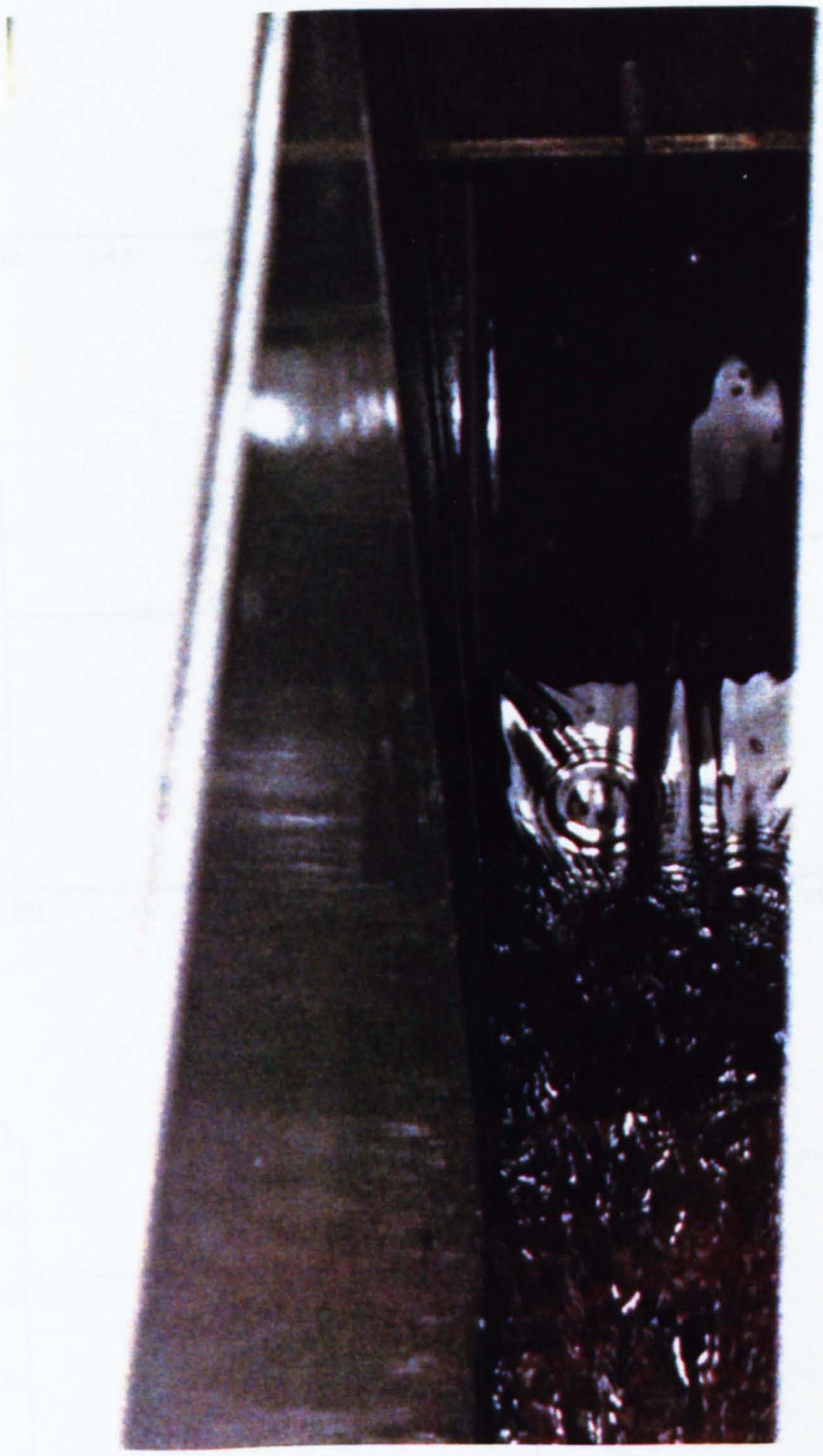

FIGURE 6.34 : ENLARGEMENT OF THE PHOTOGRAPH IN FIGURE 6.33 ; THE WATER PROFILE AT THE GATE IN THE (RT – XT) MODEL . SMALL CIRCULAR WAVEFRONTS ARE CAUSED BY DROPS FALLING FROM THE GATE .

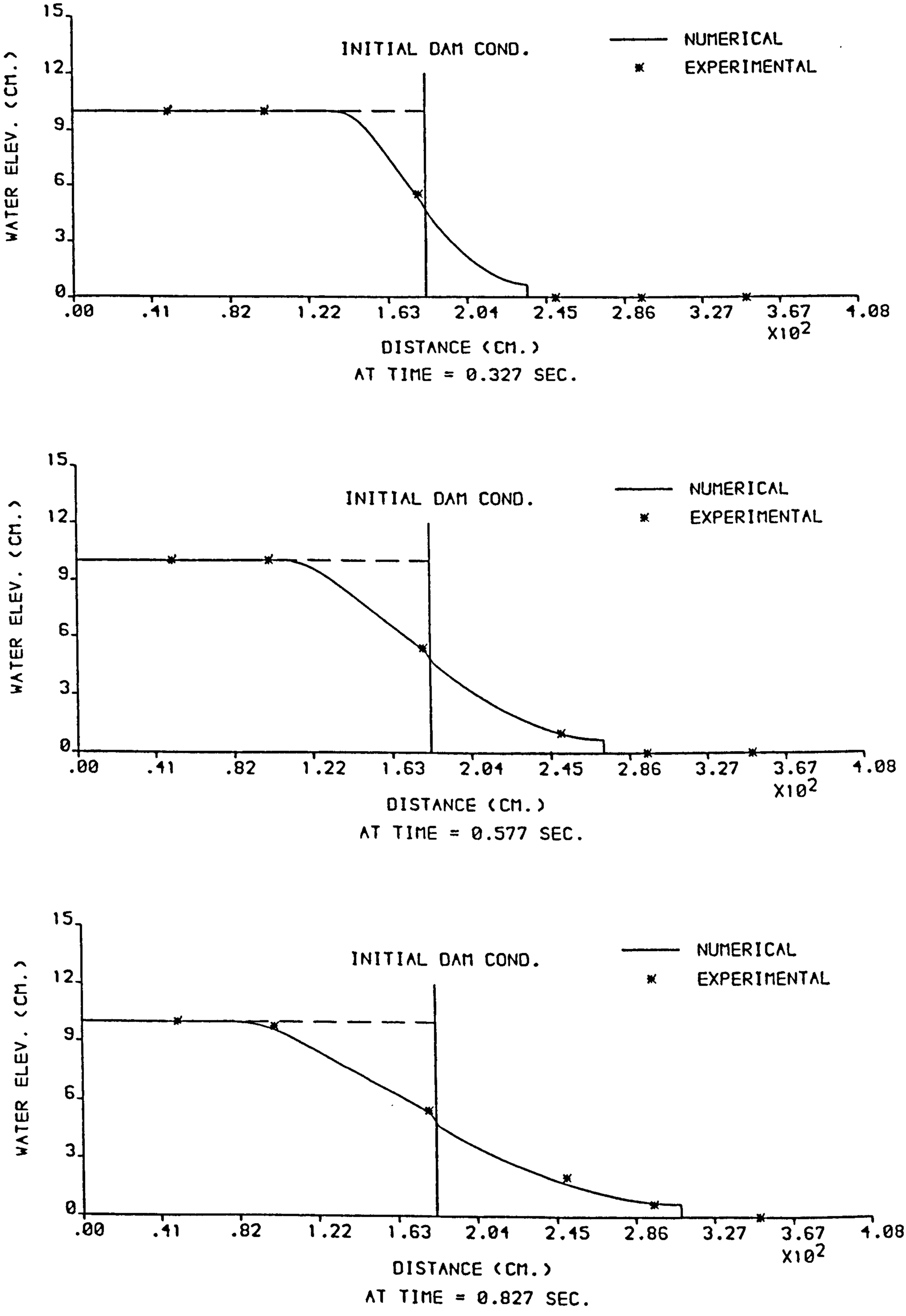

FIGURE 6.35 : NUMERICAL AND EXPERIMENTAL PROFILES FROM THE (RT-XT) MODEL , H_1 = 10 cm AND H_o = DRY .

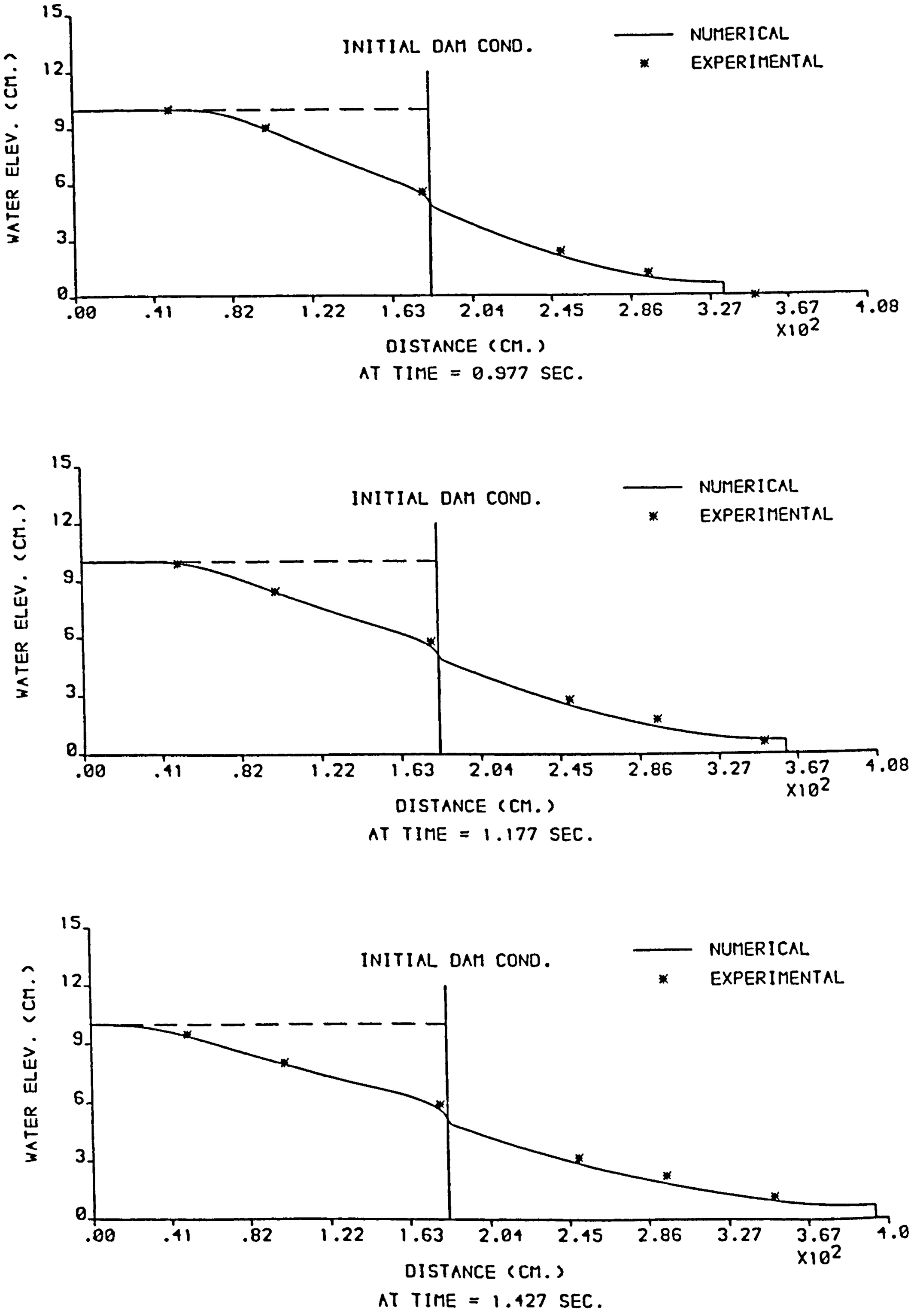

FIGURE 6.36 : NUMERICAL AND EXPERIMENTAL PROFILES FROM THE (RT-XT) MODEL , H_1 = 10 cm AND H_o = DRY .

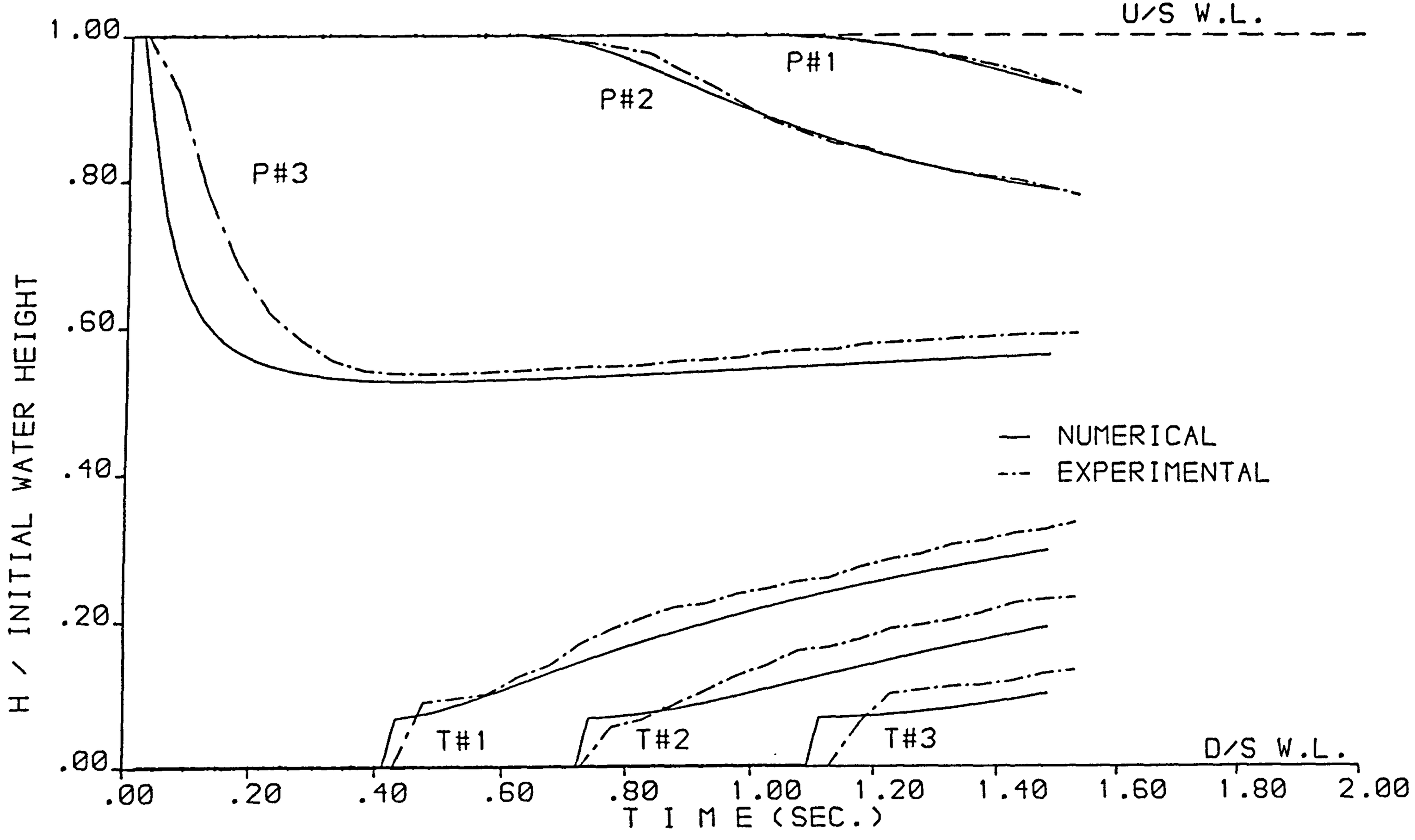

FIGURE 6.37 : NUMERICAL AND EXPERIMENTAL STAGE HYDROGRAPHS FROM THE (RT-XT) MODEL , H_1 = 10 cm AND H_o = DRY .

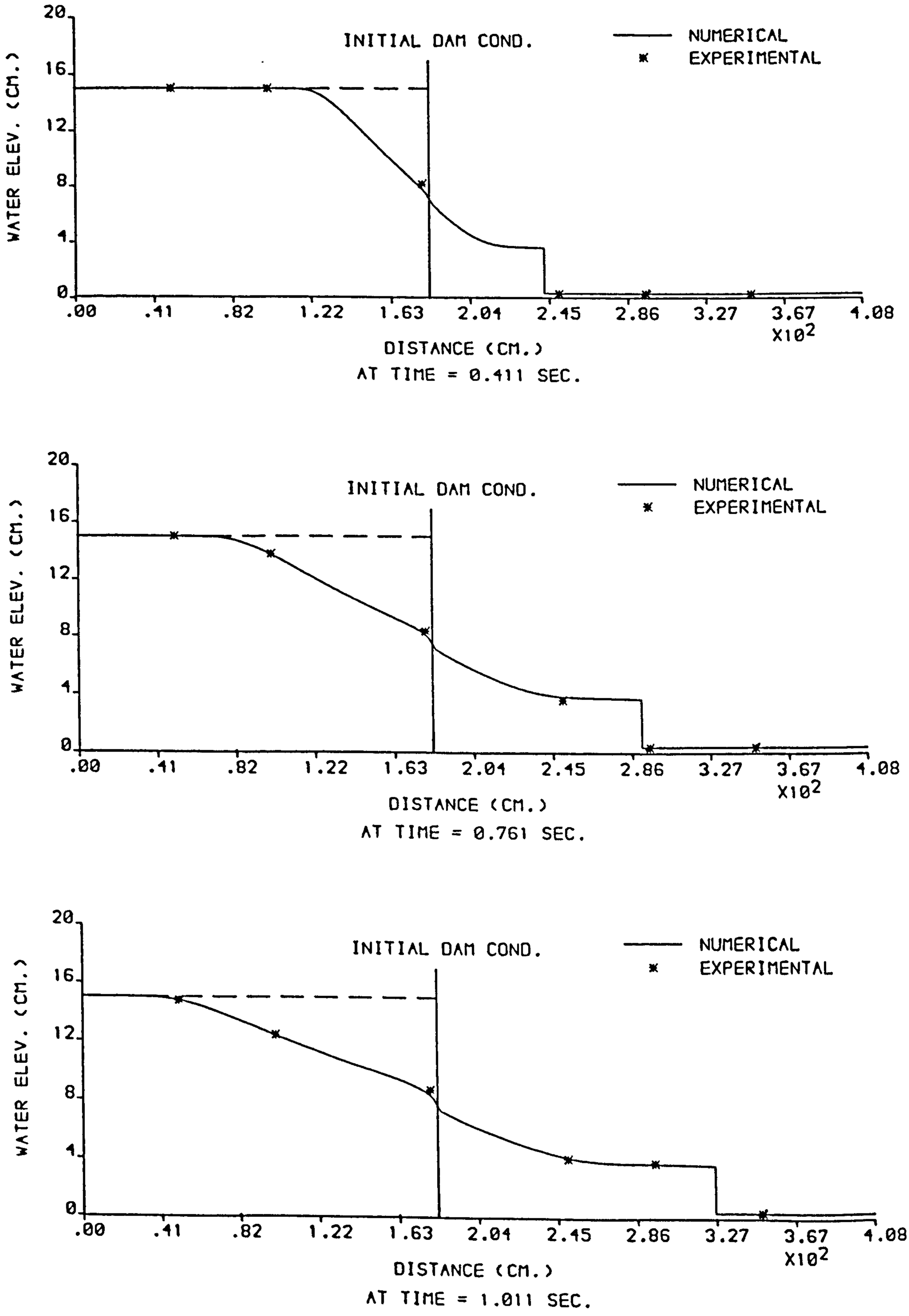

FIGURE 6.38 : NUMERICAL AND EXPERIMENTAL PROFILES FROM THE (RT-XT) MODEL , H_1 = 15 cm AND H_o = 0.375 cm .

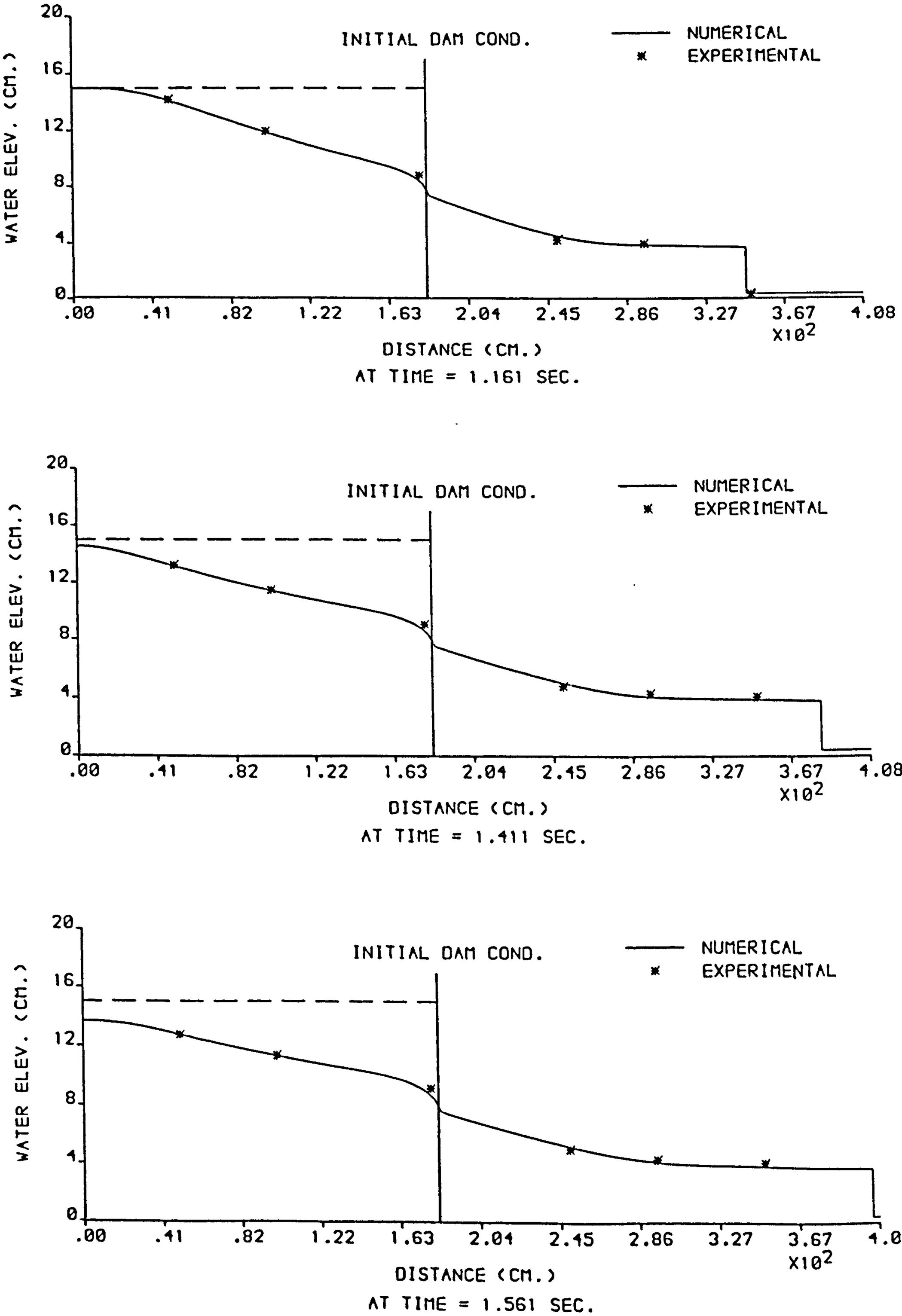

FIGURE 6.39 : NUMERICAL AND EXPERIMENTAL PROFILES FROM THE (RT-XT) MODEL , H_1 = 15 cm AND H_o = 0.375 cm .

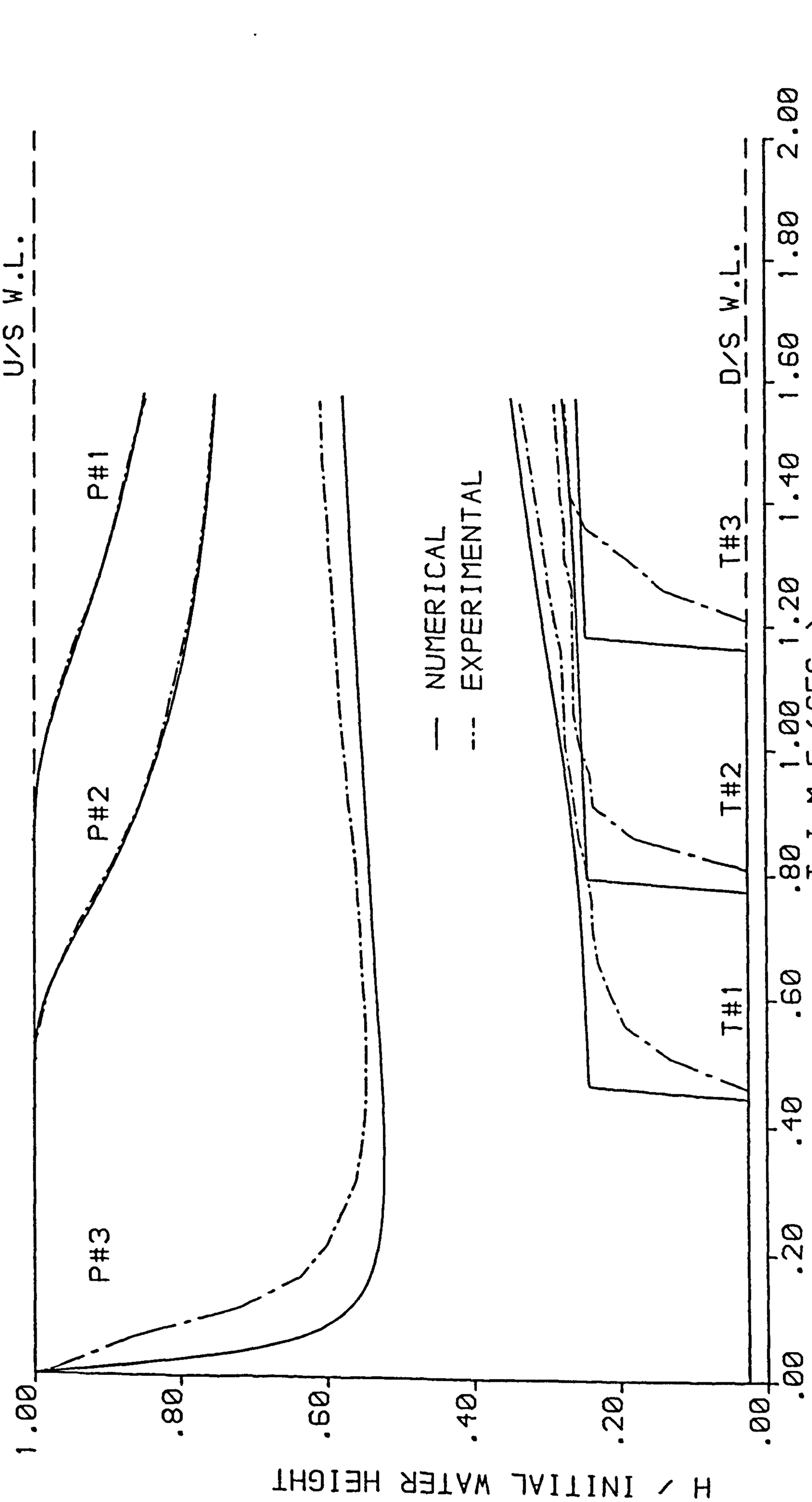

FIGURE 6.40 : NUMERICAL AND EXPERIMENTAL STAGE HYDROGRAPHS FROM THE (RT-XT) MODEL , H_1 = 15 cm AND H_o = 0.375 cm .

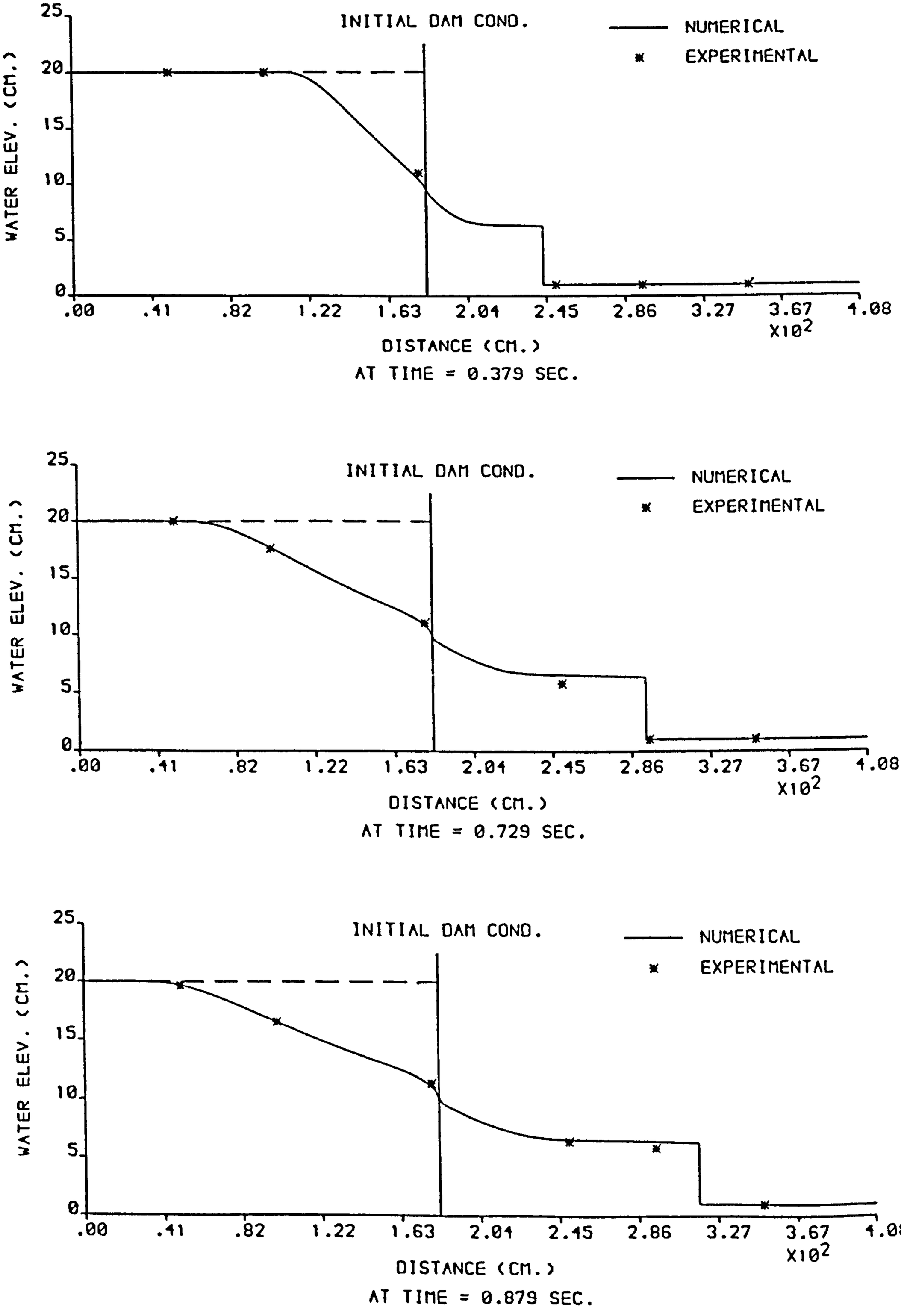

FIGURE 6.41 : NUMERICAL AND EXPERIMENTAL PROFILES FROM THE (RT-XT) MODEL , H_1 = 20 cm AND H_o = 1 cm .

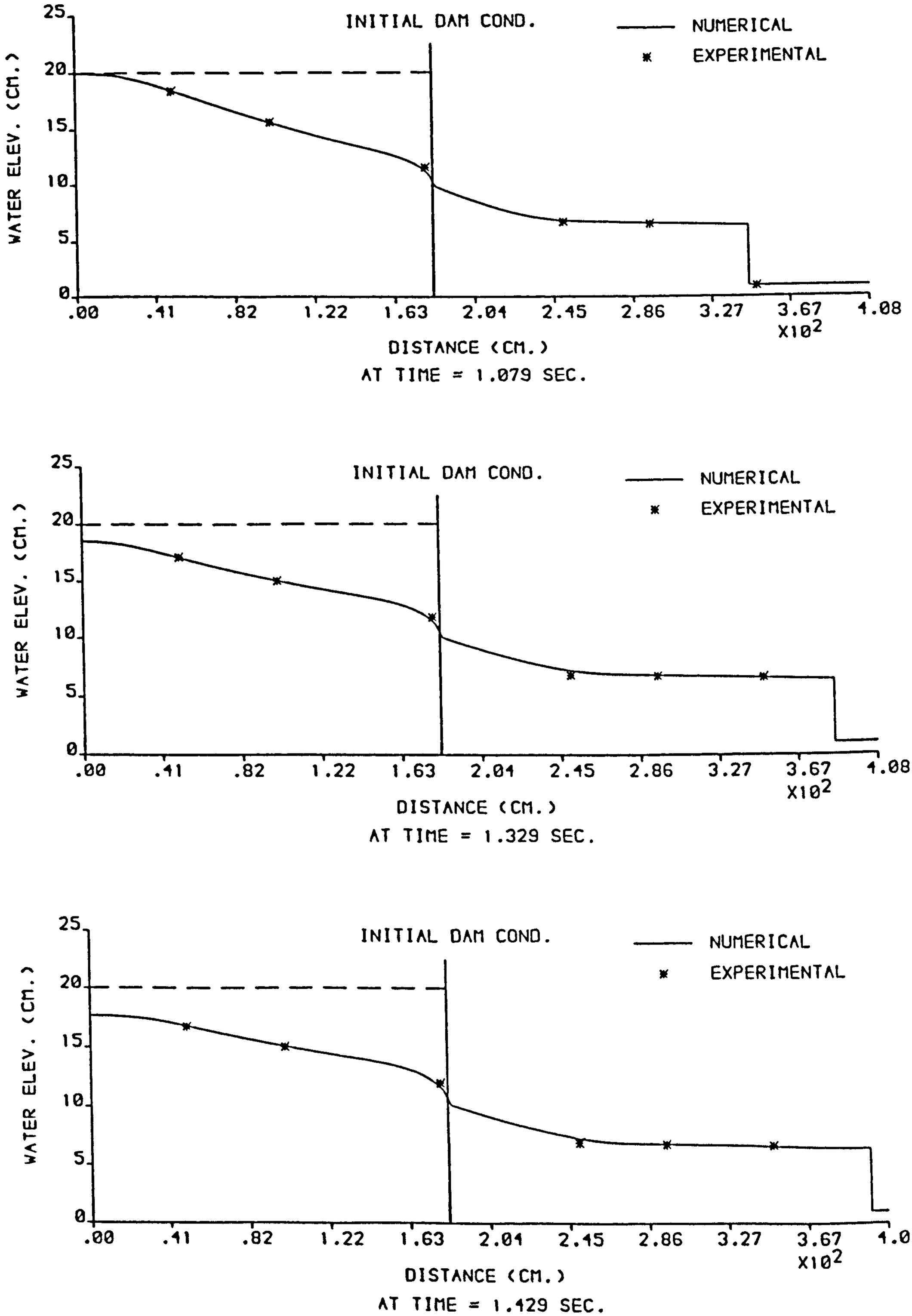

FIGURE 6.42 : NUMERICAL AND EXPERIMENTAL PROFILES FROM THE (RT-XT) MODEL , H_1 = 20 cm AND H_o = 1 cm .

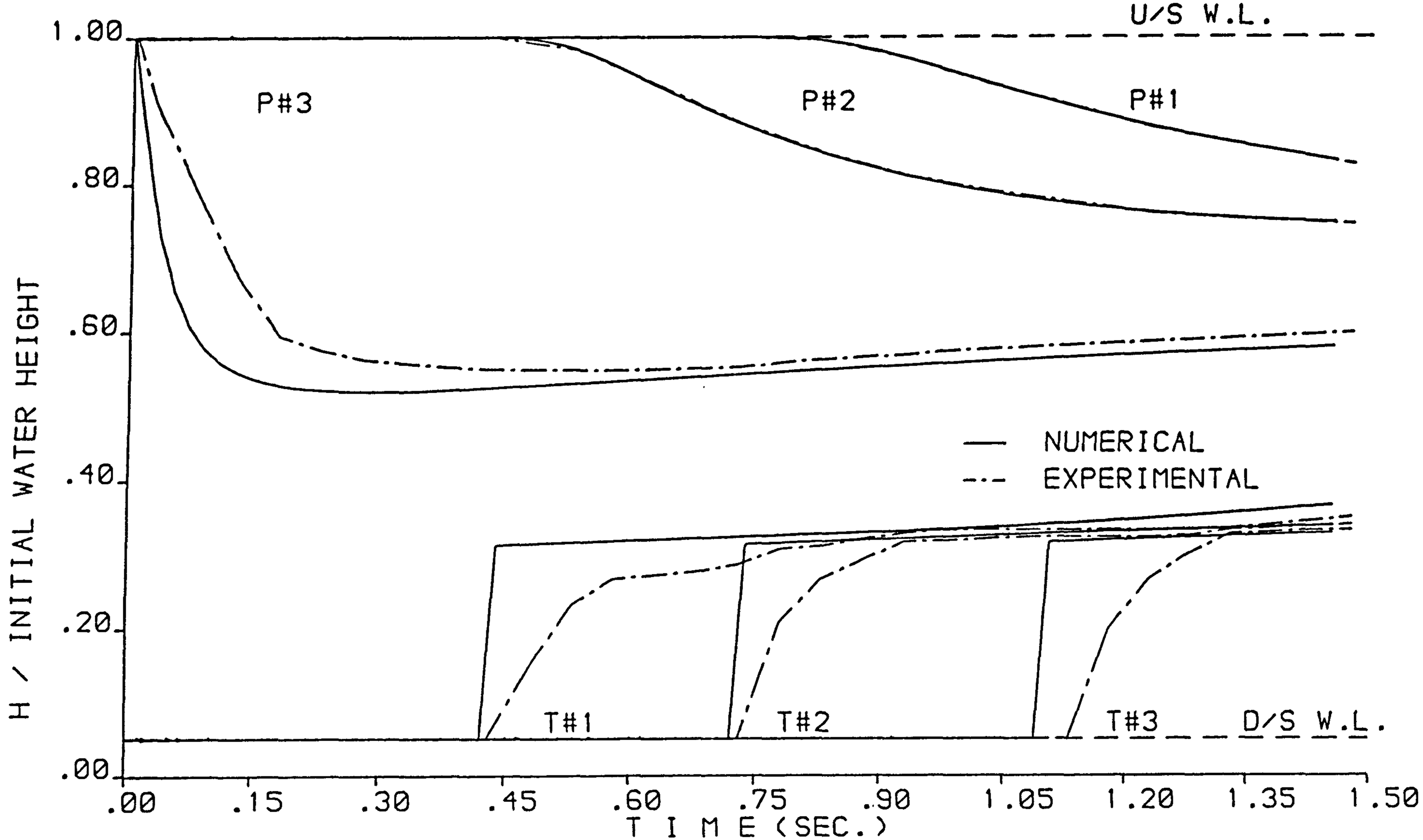

FIGURE 6.43 : NUMERICAL AND EXPERIMENTAL STAGE HYDROGRAPHS FROM THE (RT-XT) MODEL , H_1 = 20 cm AND H_o = 1 cm .

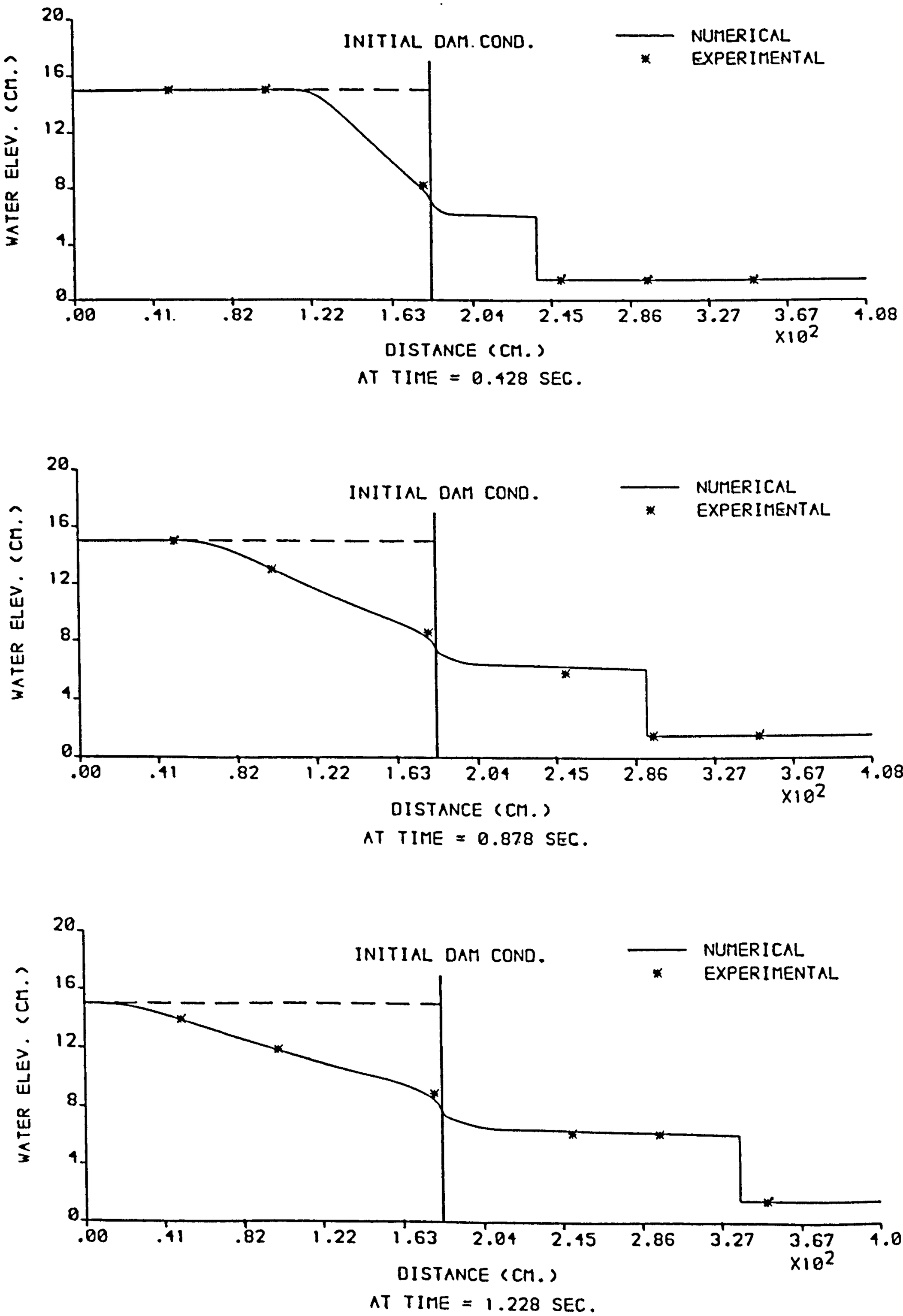

FIGURE 6.44 : NUMERICAL AND EXPERIMENTAL PROFILES FROM THE (RT-XT) MODEL , H_1 = 15 cm AND H_o = 1.5 cm .

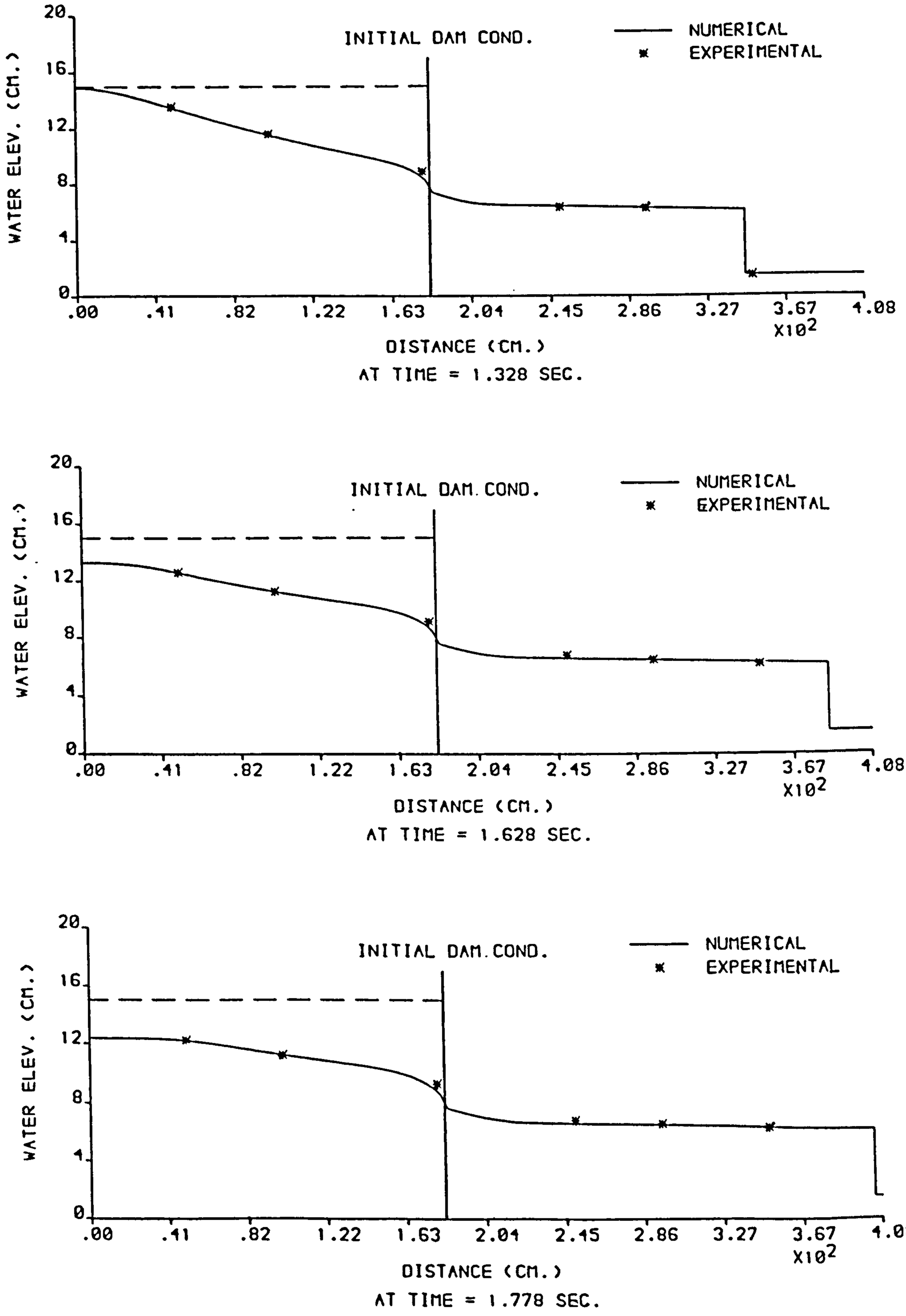

FIGURE 6.45 : NUMERICAL AND EXPERIMENTAL PROFILES FROM THE (RT-XT) MODEL , H_1 = 15 cm AND H_o = 1.5 cm .

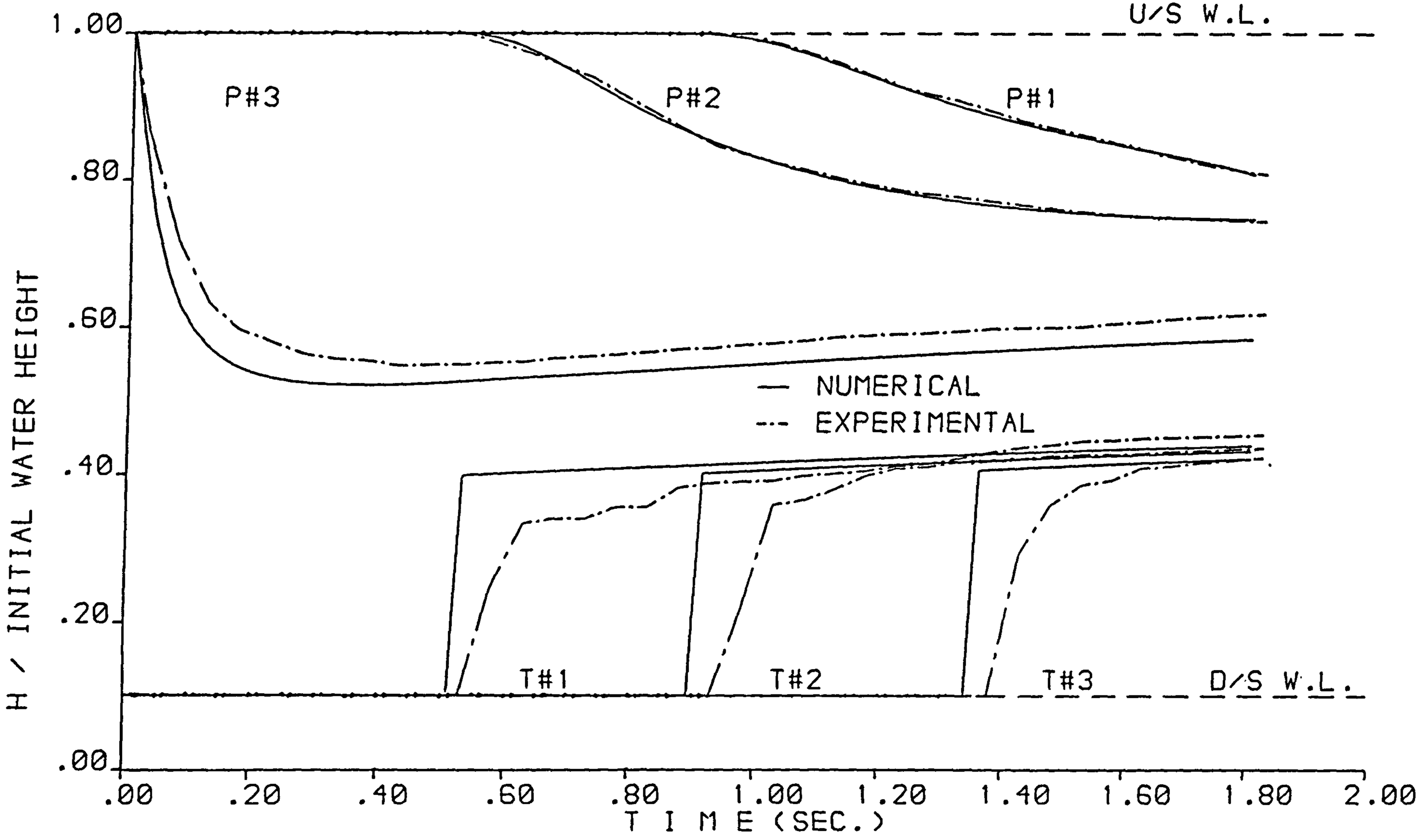

FIGURE 6.46 : NUMERICAL AND EXPERIMENTAL STAGE HYDROGRAPHS FROM THE (RT-XT) MODEL , H_1 = 15 cm AND H_o = 1.5 cm

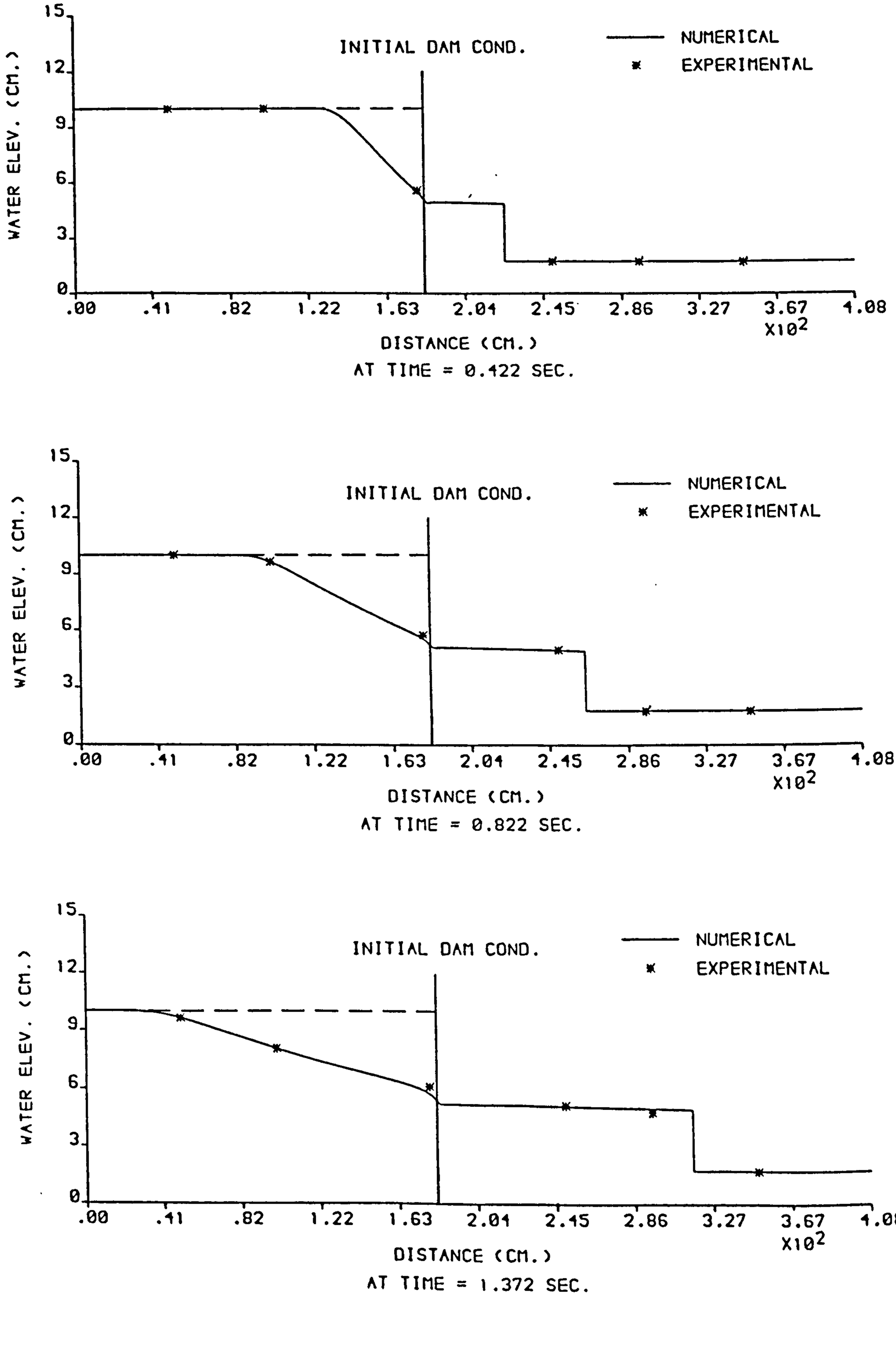

FIGURE 6.47 : NUMERICAL AND EXPERIMENTAL PROFILES FROM THE (RT-XT) MODEL , H_1 = 10 cm AND H_o = 1.76 cm .

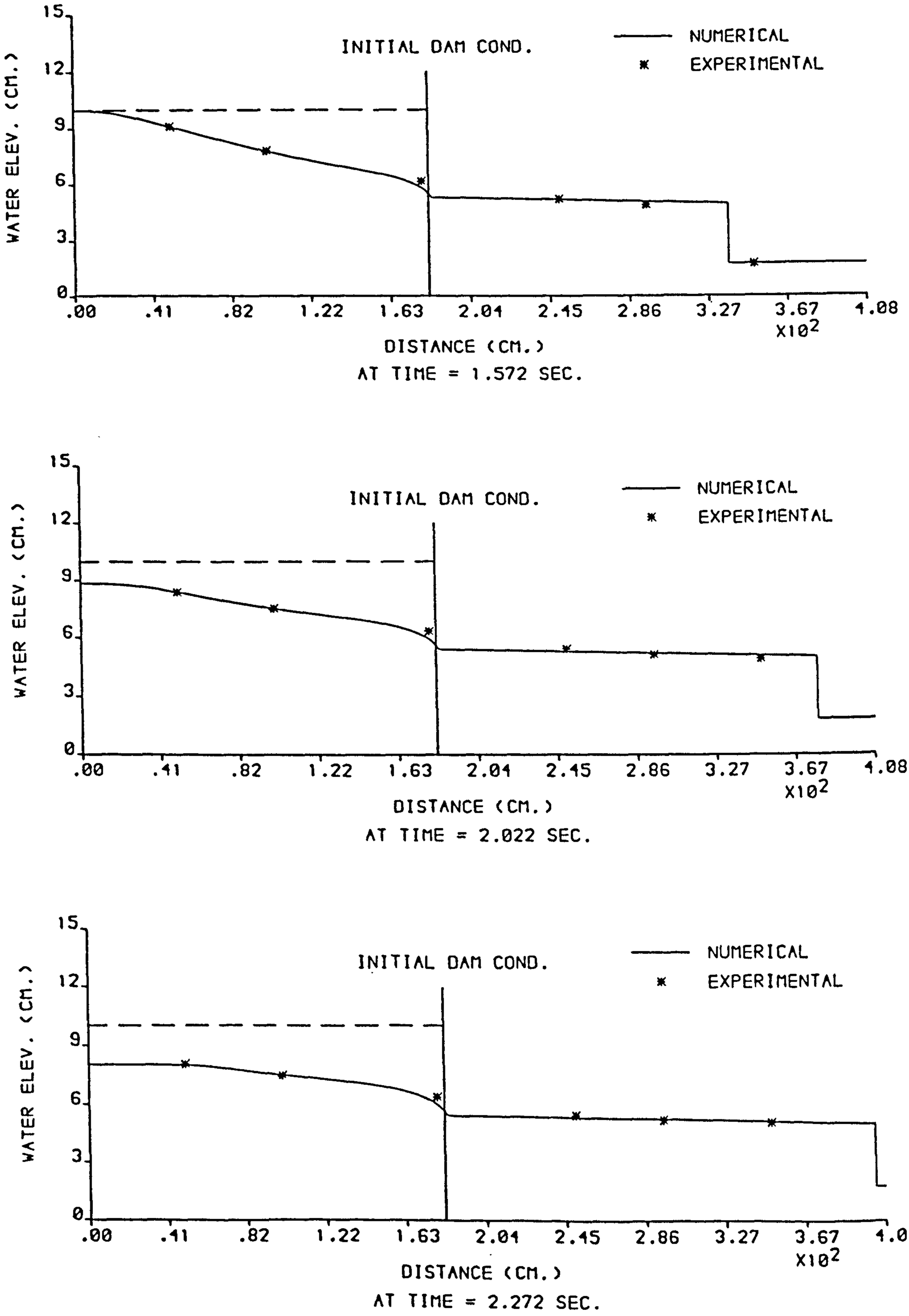

FIGURE 6.48 : NUMERICAL AND EXPERIMENTAL PROFILES FROM THE (RT-XT) MODEL , H_1 = 10 cm AND H_o = 1.76 cm .

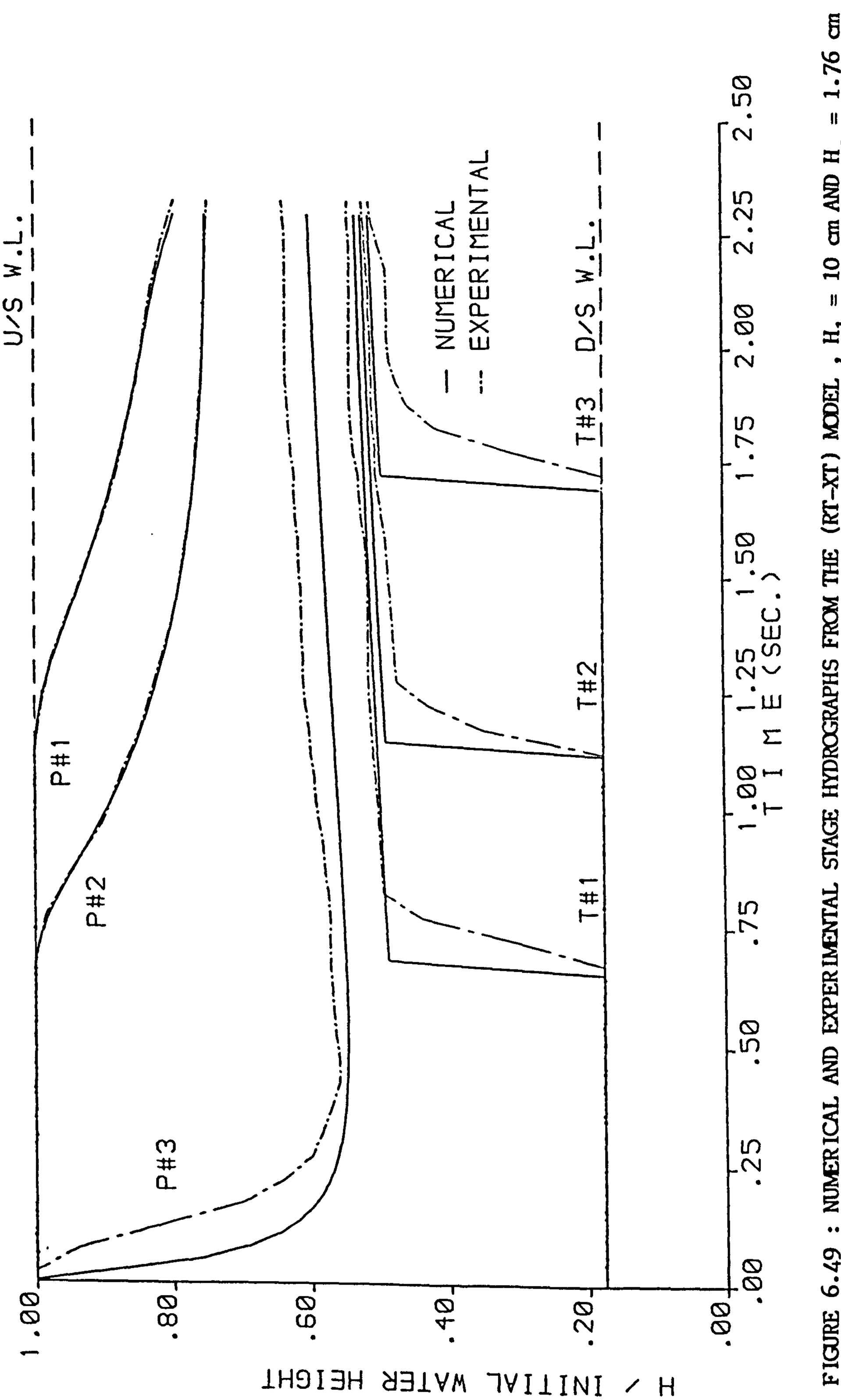

FIGURE 6.49 : NUMERICAL AND EXPERIMENTAL STAGE HYDROGRAPHS FROM THE (RT-XT) MODEL , H_1 = 10 cm AND H_o = 1.76 cm

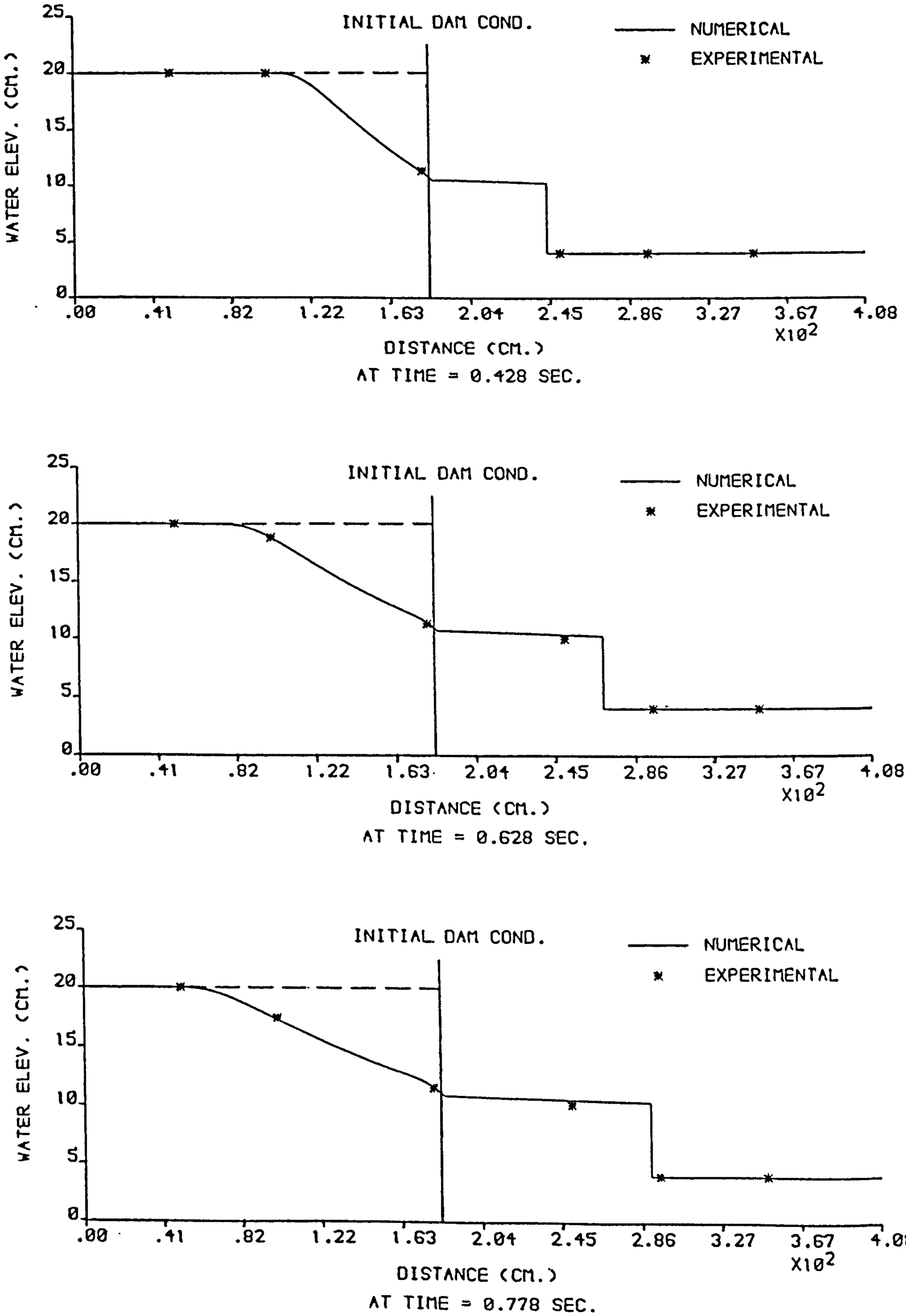

FIGURE 6.50 : NUMERICAL AND EXPERIMENTAL PROFILES FROM THE (RT-XT) MODEL , H_1 = 20 cm AND H_o = 4 cm .

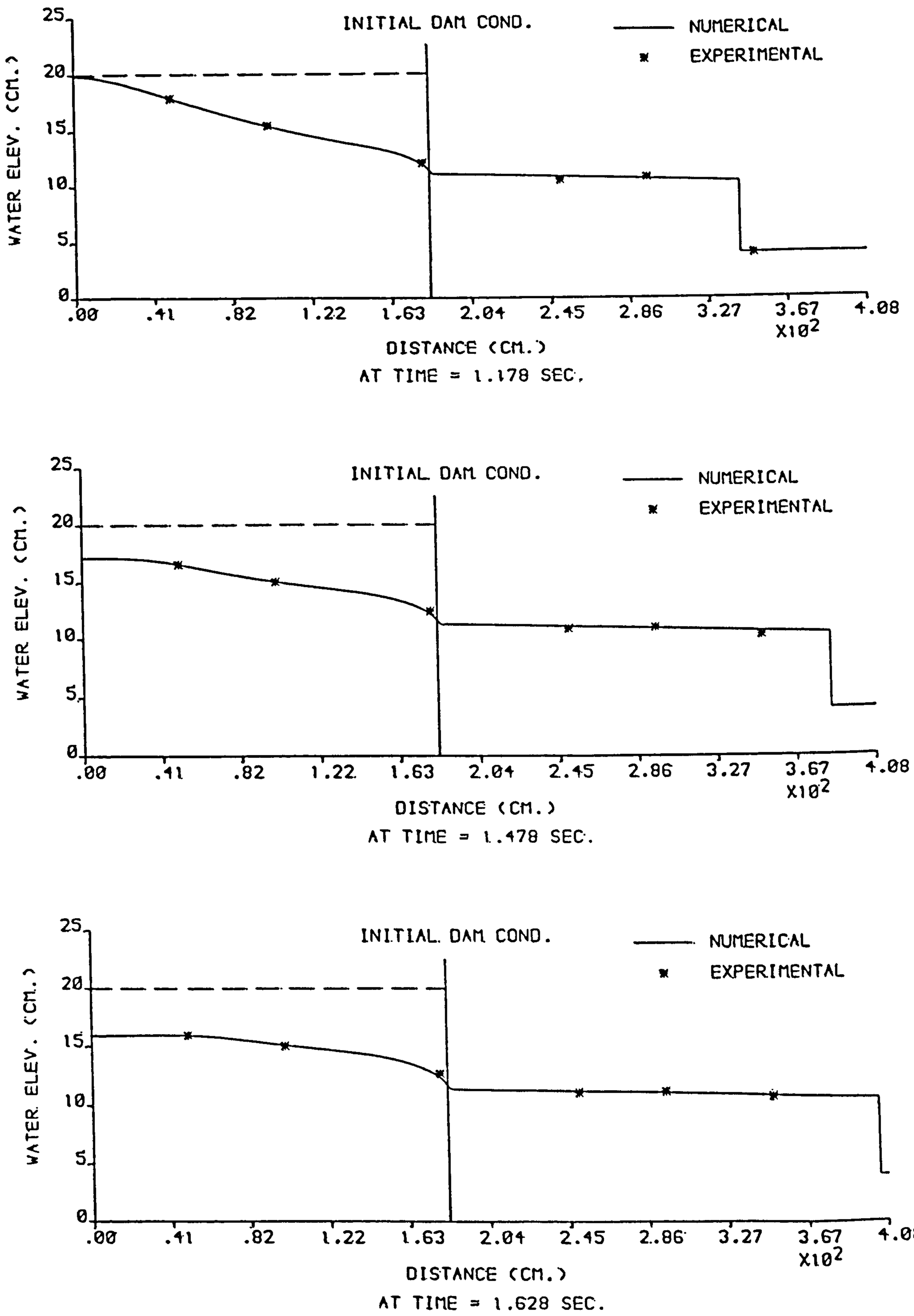

FIGURE 6.51 : NUMERICAL AND EXPERIMENTAL PROFILES FROM THE (RT-XT) MODEL , H_1 = 20 cm AND H_o = 4 cm .

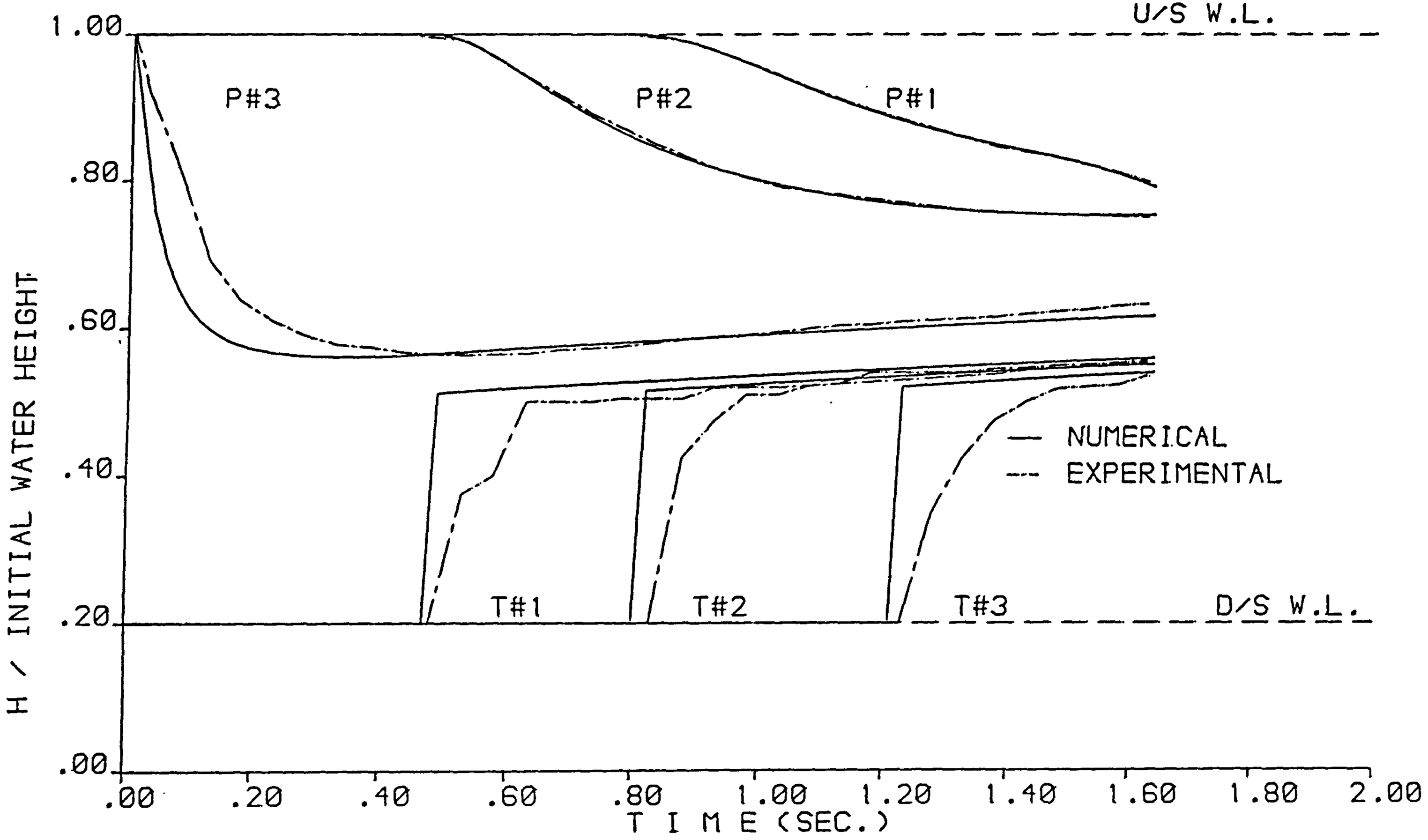

FIGURE 6.52 : NUMERICAL AND EXPERIMENTAL STAGE HYDROGRAPHS FROM THE (RT-XT) MODEL , H_1 = 20 cm AND H_o = 4 cm .

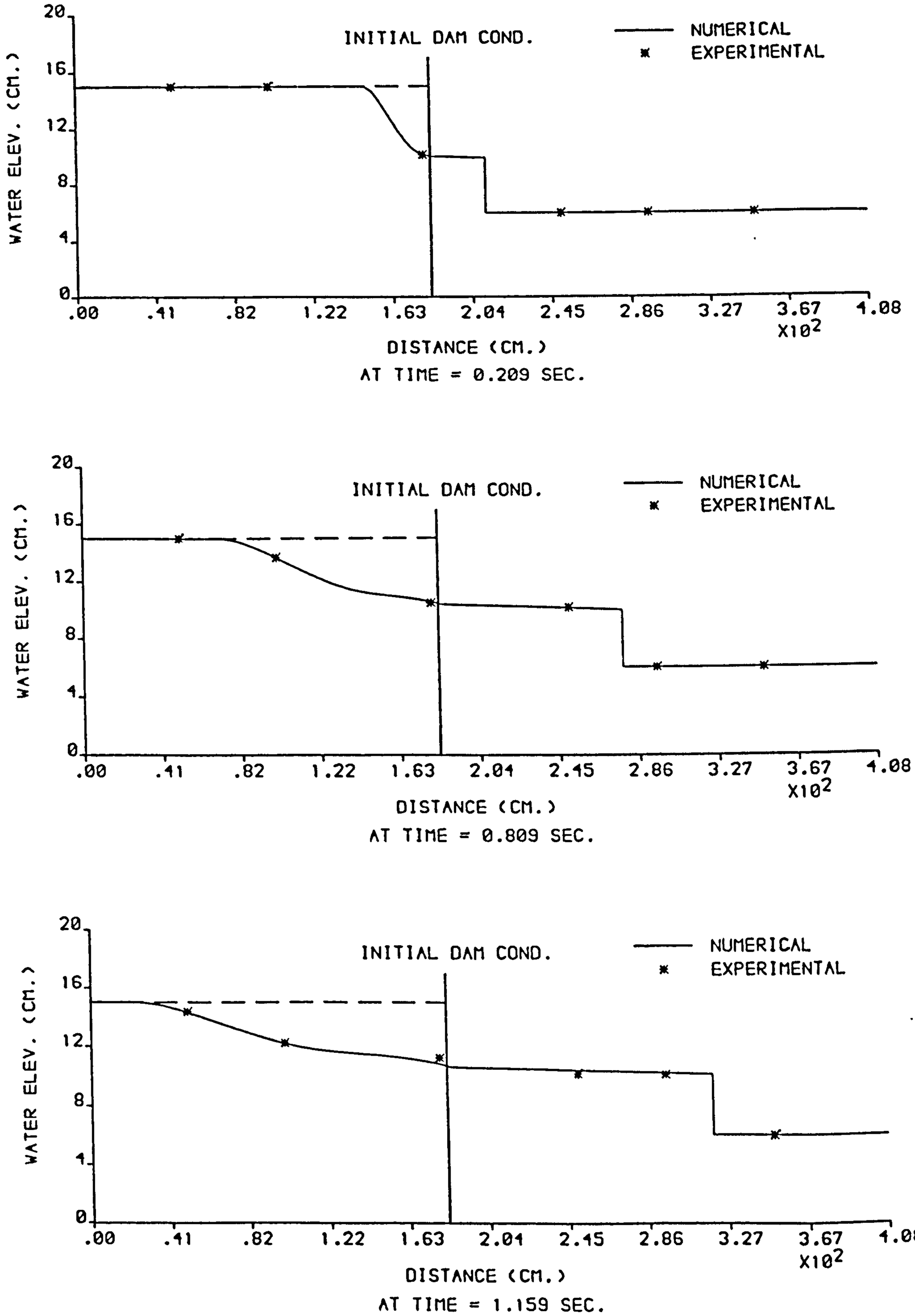

FIGURE 6.53 : NUMERICAL AND EXPERIMENTAL PROFILES FROM THE (RT-XT) MODEL , H_1 = 15 cm AND H_o = 6 cm .

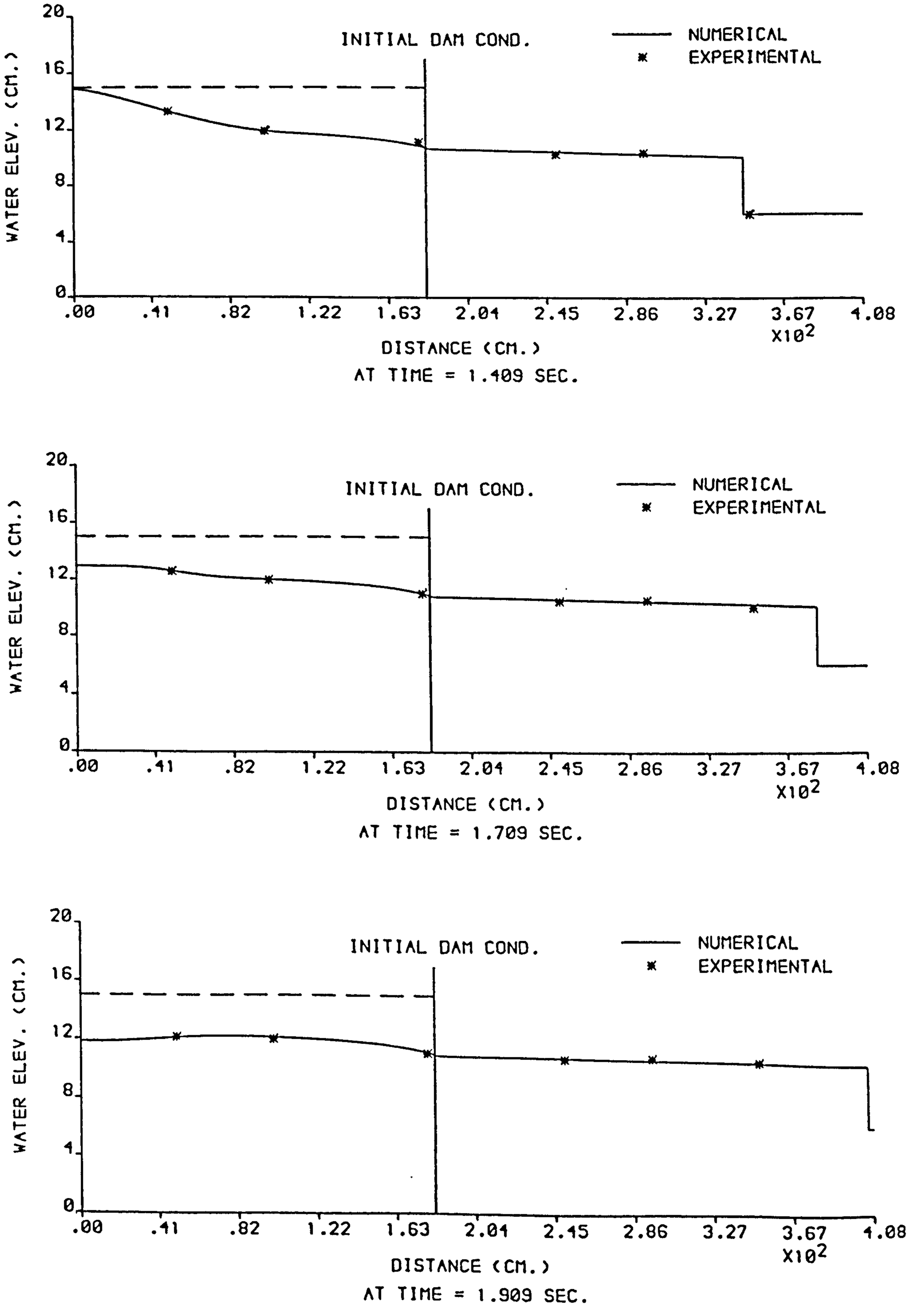

FIGURE 6.54 : NUMERICAL AND EXPERIMENTAL PROFILES FROM THE (RT-XT) MODEL , H_1 = 15 cm AND H_o = 6 cm .

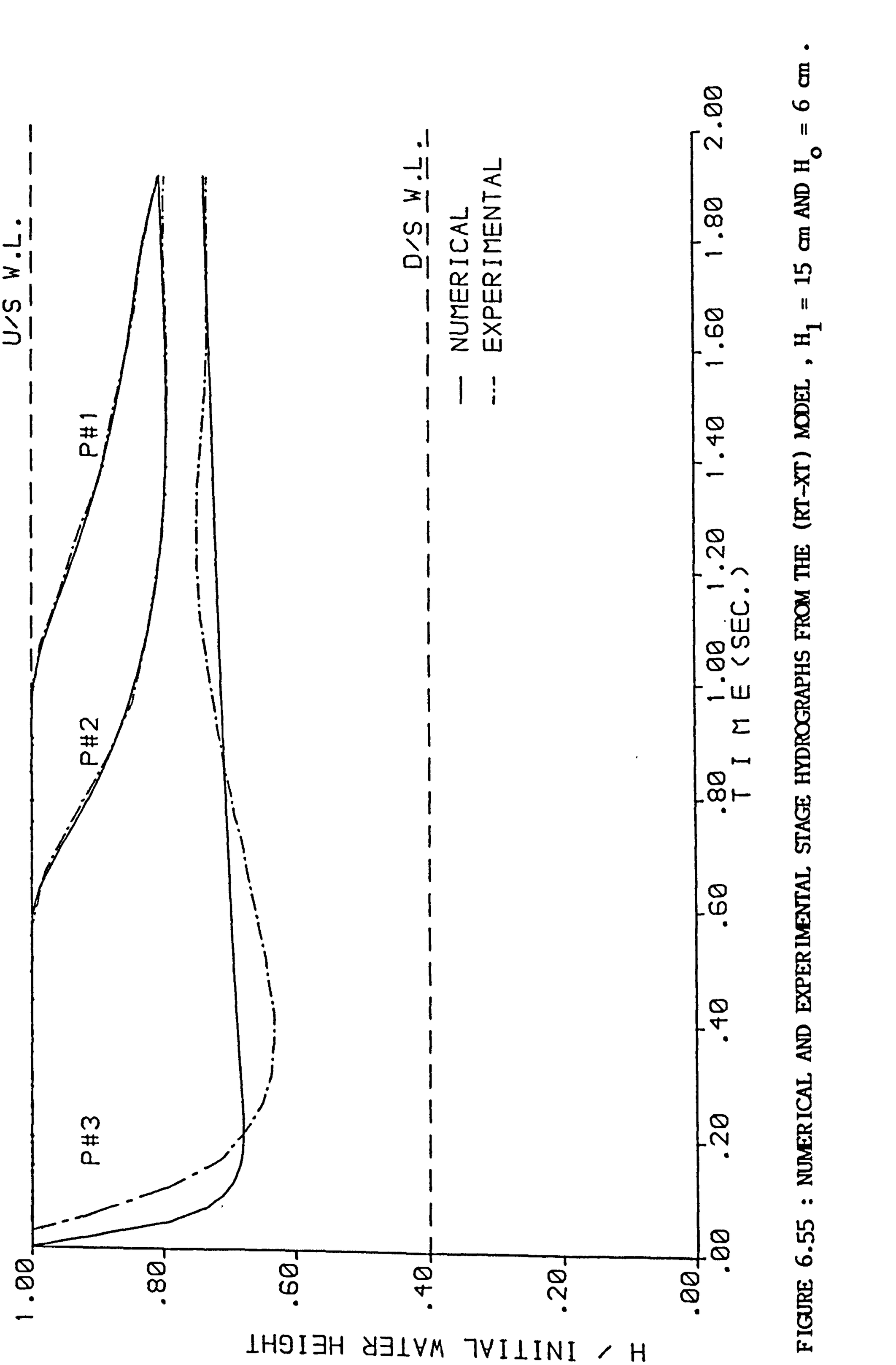

FIGURE 6.55 : NUMERICAL AND EXPERIMENTAL STAGE HYDROGRAPHS FROM THE (RT-XT) MODEL , H_1 = 15 cm AND H_o = 6 cm .

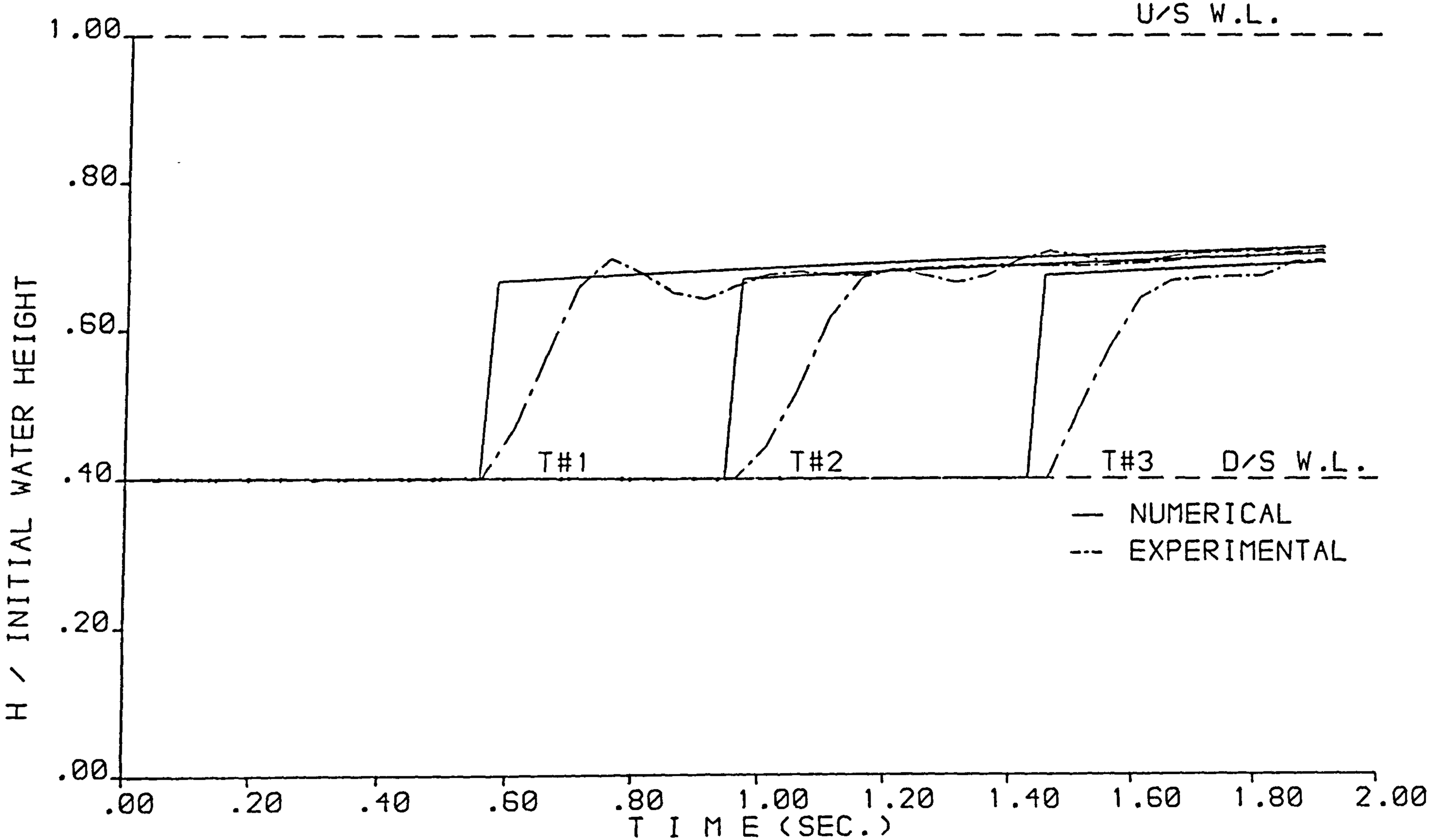

FIGURE 6.56 : NUMERICAL AND EXPERIMENTAL STAGE HYDROGRAPHS FROM THE (RT-XT) MODEL , H_1 = 15 cm AND H_o = 6 cm .

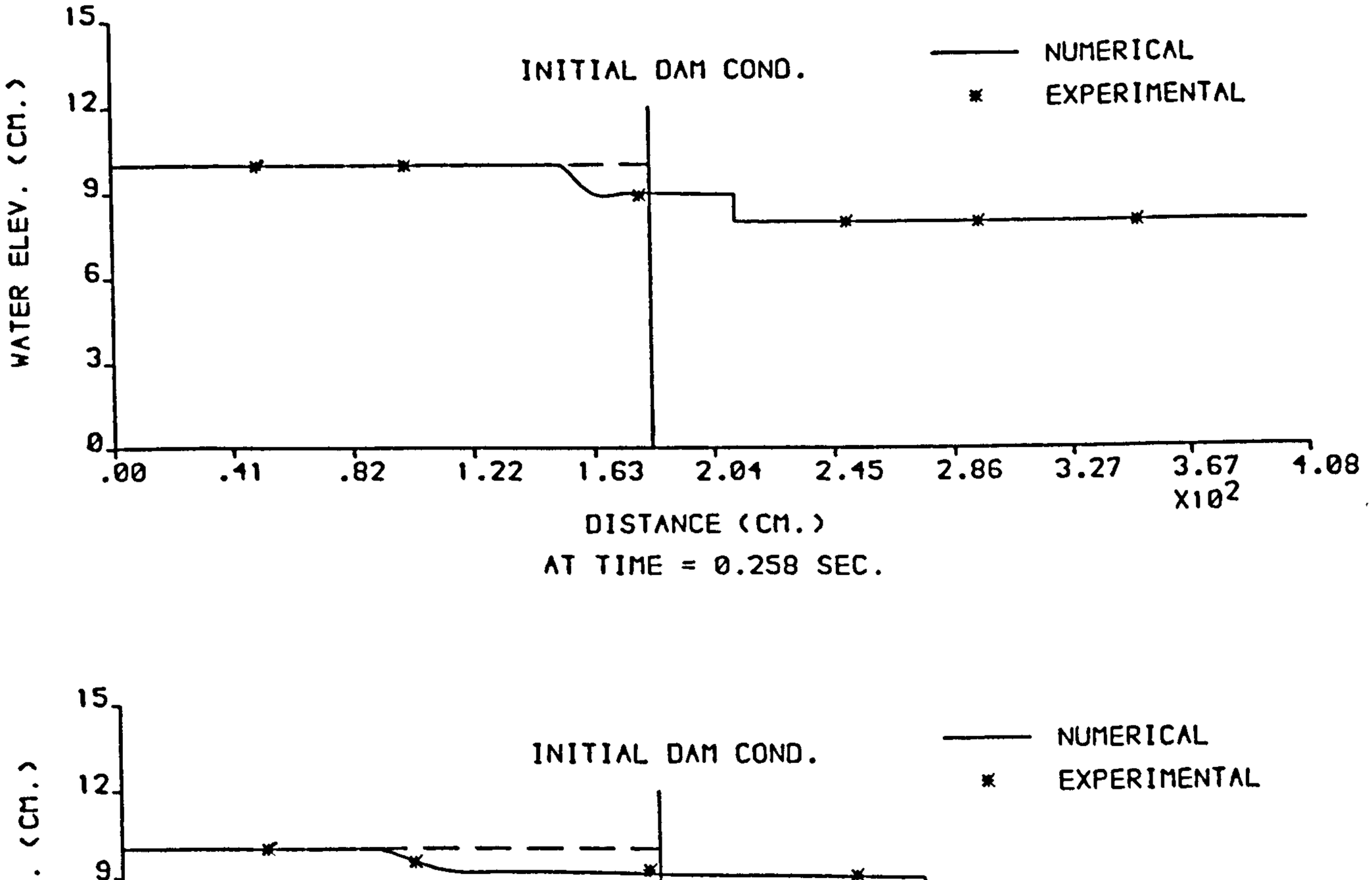

FIGURE 6.57 : NUMERICAL AND EXPERIMENTAL PROFILES FROM THE (RT-XT) MODEL , H_1 = 10 cm AND H_o = 8 cm .

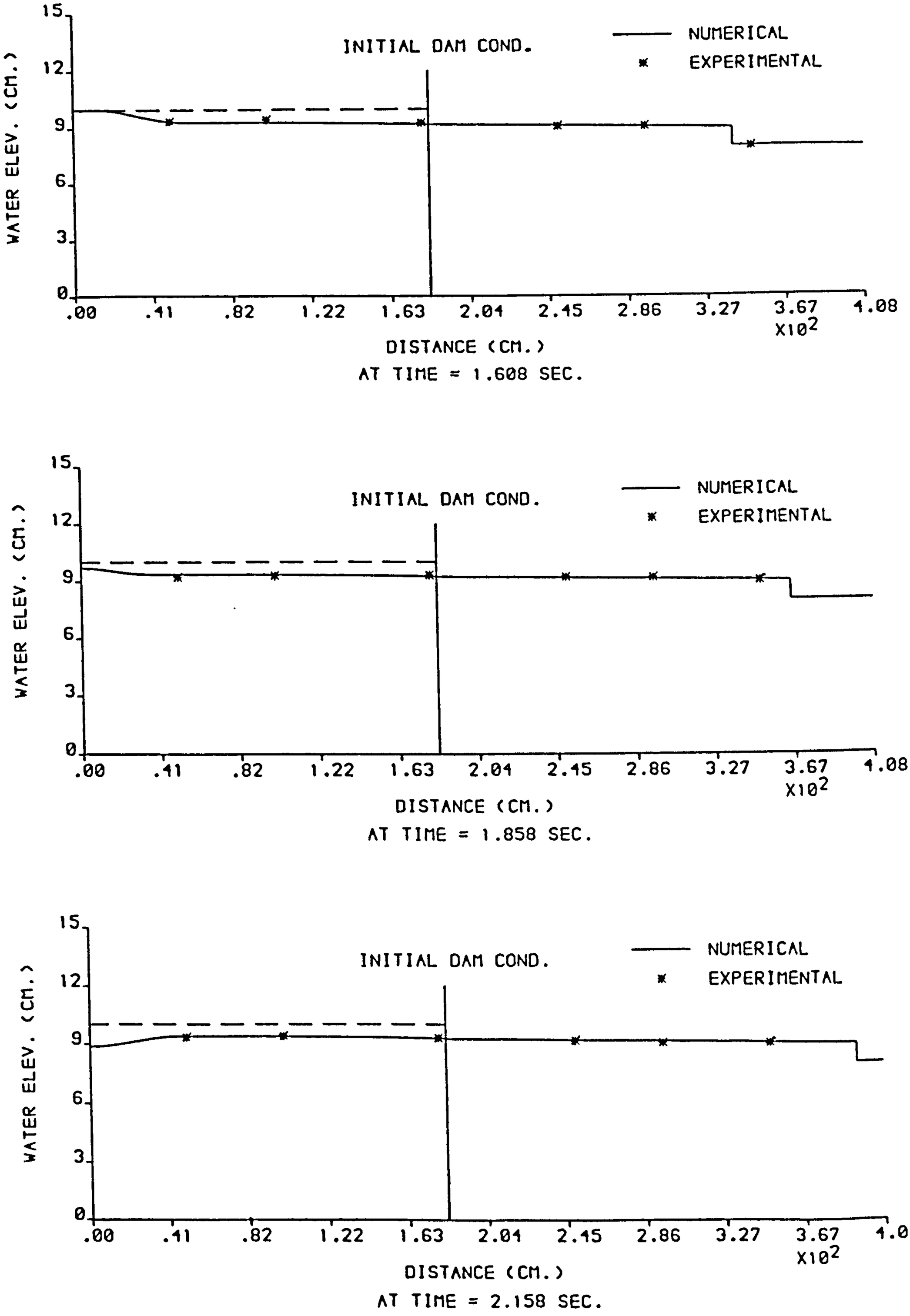

FIGURE 6.58 : NUMERICAL AND EXPERIMENTAL PROFILES FROM THE (RT-XT) MODEL , H_1 = 10 cm AND H_o = 8 cm .

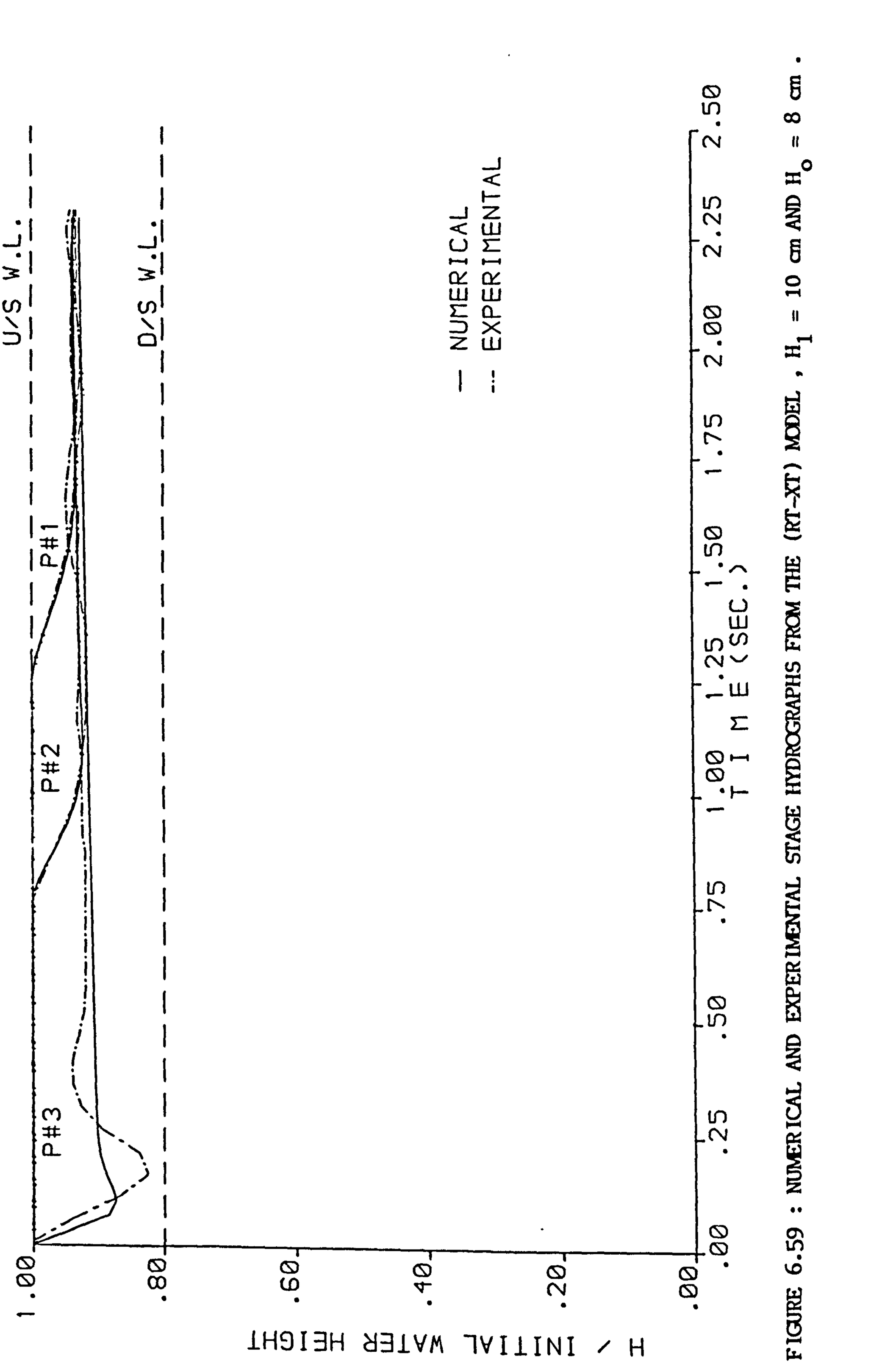

FIGURE 6.59 : NUMERICAL AND EXPERIMENTAL STAGE HYDROGRAPHS FROM THE (RT-XT) MODEL , H_1 = 10 cm AND H_o = 8 cm .

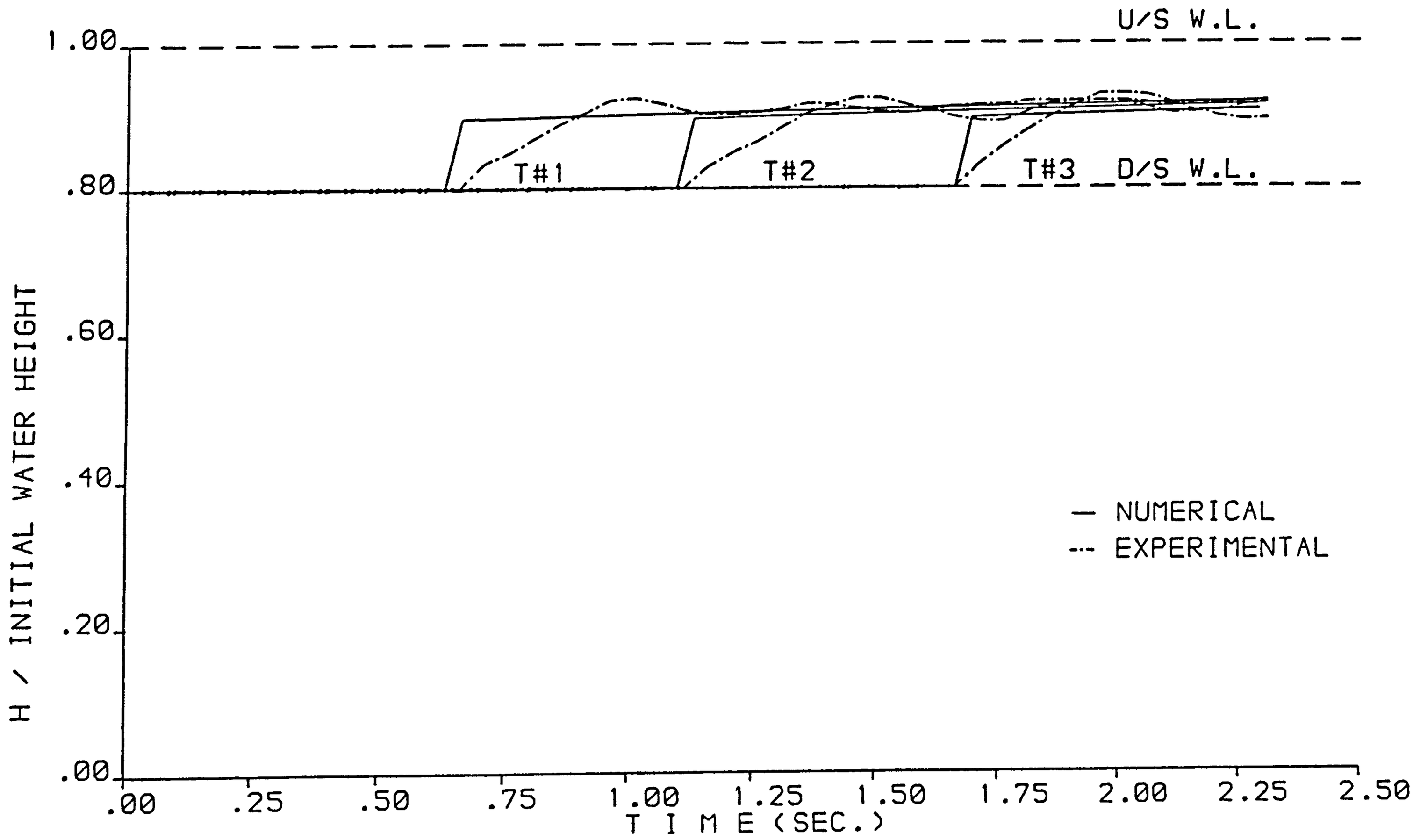

FIGURE 6.60 : NUMERICAL AND EXPERIMENTAL STAGE HYDROGRAPHS FROM THE (RT-XT) MODEL , H_1 = 10 cm AND H_o = 8 cm .

6.3 RT-RT Model

The numerical (RT-RT) model is a combination of two radial models, with convergent sides upstream and divergent sides downstream of the dam. In order to assess the numerical model a comparison between the numerical results and the experimental results is also carried out in this section.

In Figure 6.61, comparisons of the front heights resulting from the (RT-RT) numerical and physical models with Stoker's (X-T) solution, after dam-break, for different ratios of (H_o/H_1) and different initial depth upstream the dam as illustrated in the previous sections. The agreement between the numerical and the experimental results is good with a general difference less than 5%. The numerical results are slightly higher than the experimental results where the ratio (H_o/H_1) is less than (0.176) while the opposite is true for values more than (0.176). The front heights are substantially lower than the front heights (20% lower) which are computed either by Stoker's (X-T) solution or by the XT-RT model, presumably because of the more radical cross-section change now effected by the wall alignments upstream and downstream.

As for the X-T channel, if the dam-break wave propagates over dry bed downstream, there is no substantial shock at the front. A tip region of small heights is formed, which is pushed by the upstream mass of water, as shown in Figure 6.62. While the water surface is high just behind the dam a noticeable drop occurs in the water height after the dam. Since the walls were made of wood, mirrors were fitted inside to help in taking the photographs. Two

large mirrors were fixed on the both walls and the reflection of the water profile from one mirror to the other was taken its photograph.

As the flow passes through the expansion downstream the dam, the height of the wave front and the depths behind it are reduced, as shown both in Figure 6.63 and in Figure 6.64. Downstream of the dam a short reach exists with supercritical flow and a depression in the water profile. The reach ends with an oblique hydraulic jump. These phenomena are clearly defined in the comparative plots of Figures 6.65 to 6.90. The plots again consist of two types; the water depth profiles and the stage hydrographs, for the same ratios of initial water depths as previously in sections 6.1 and 6.2.

In all of Figures 6.65 to 6.90, the agreement is good between the physical and numerical results with a general difference less than 5%. The depth profile shows enhancement of the feature observed in the RT-XT model whilst now the sharp fall is connected to the wave front through an hydraulic jump, except where the bed is virtually dry downstream.

[6.4 XT-RT MODEL CONTINUED ON P. 281
FIGURES 6.61 TO 6.90 FOLLOW DIRECTLY]

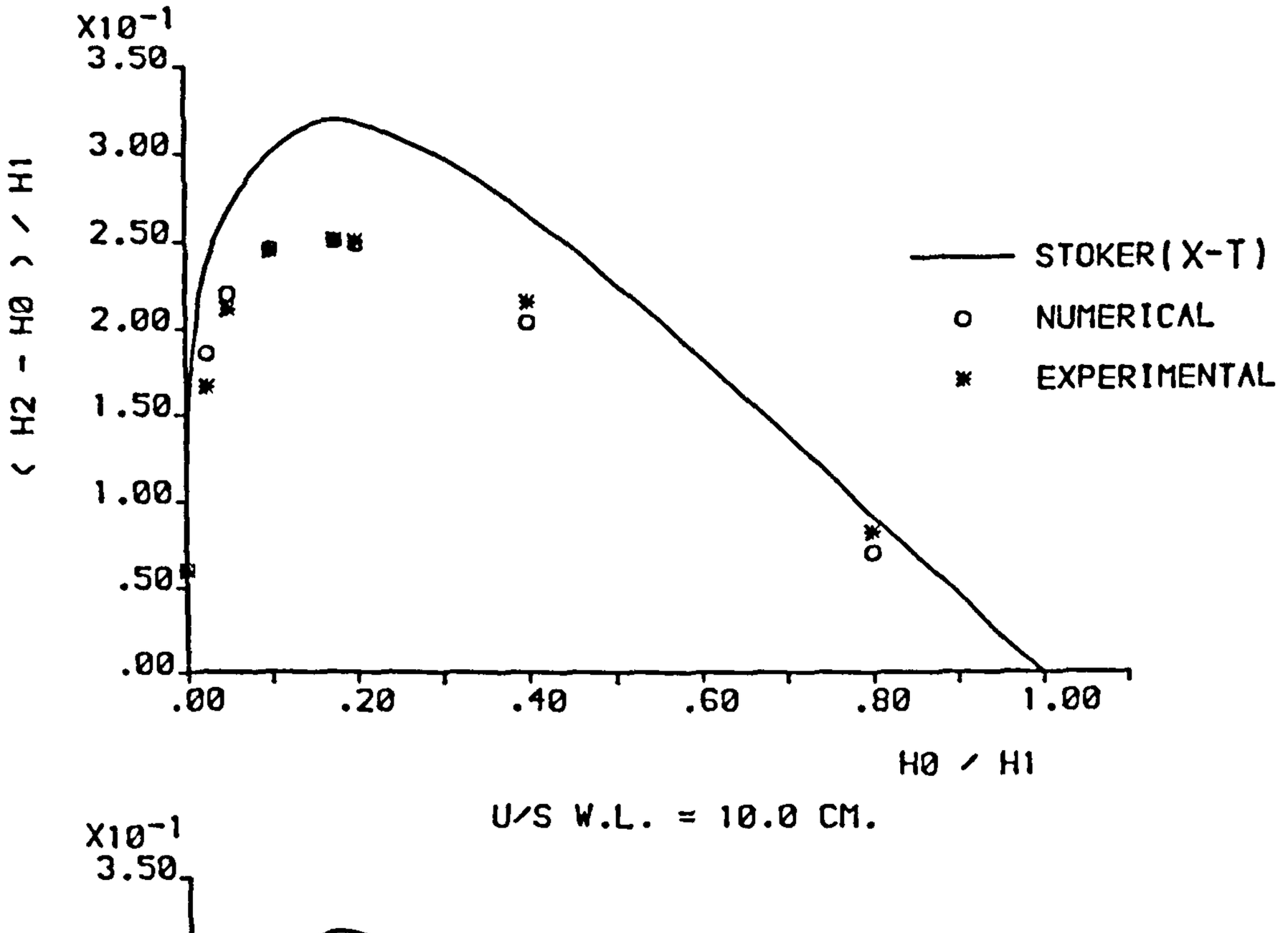

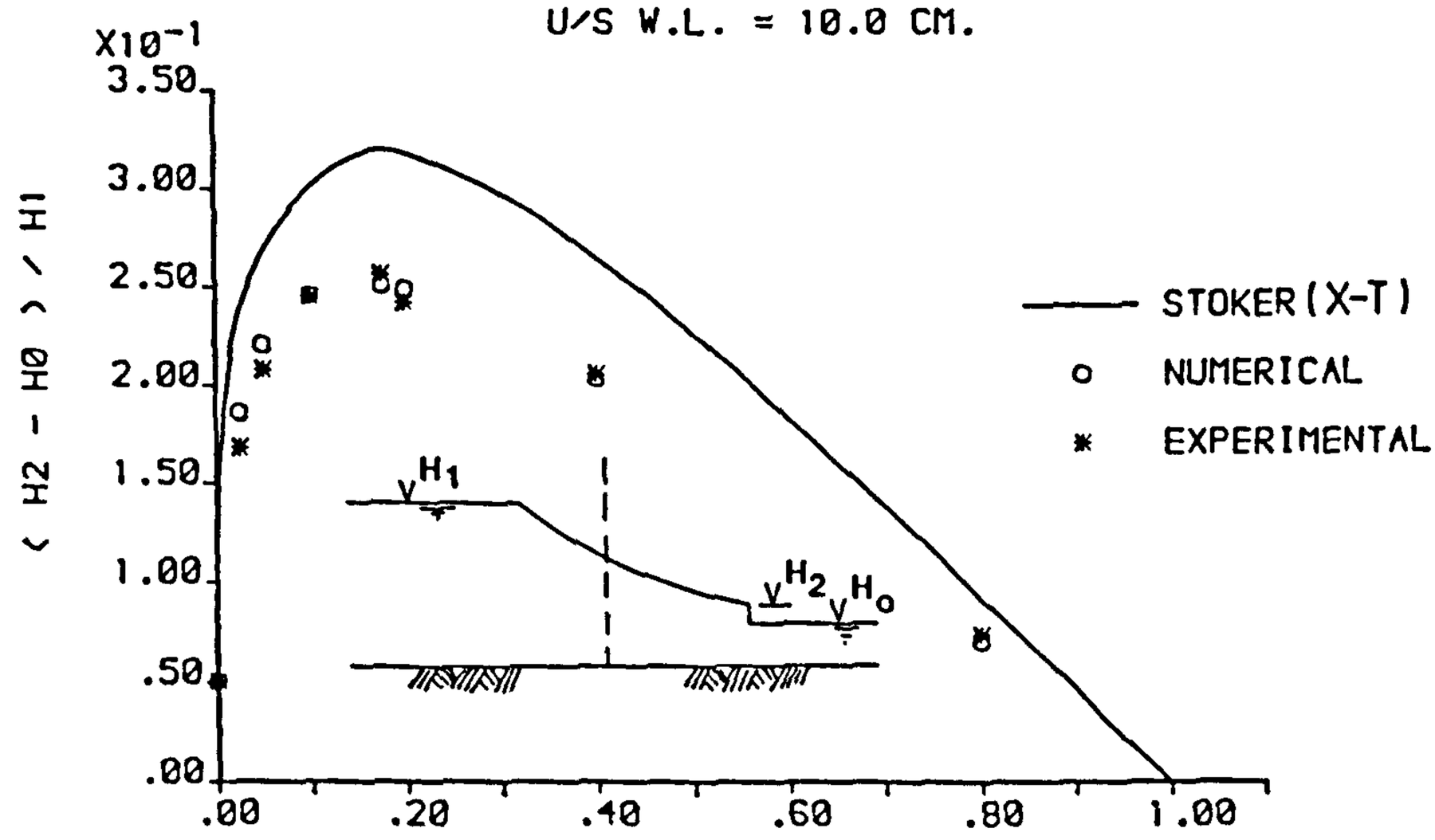

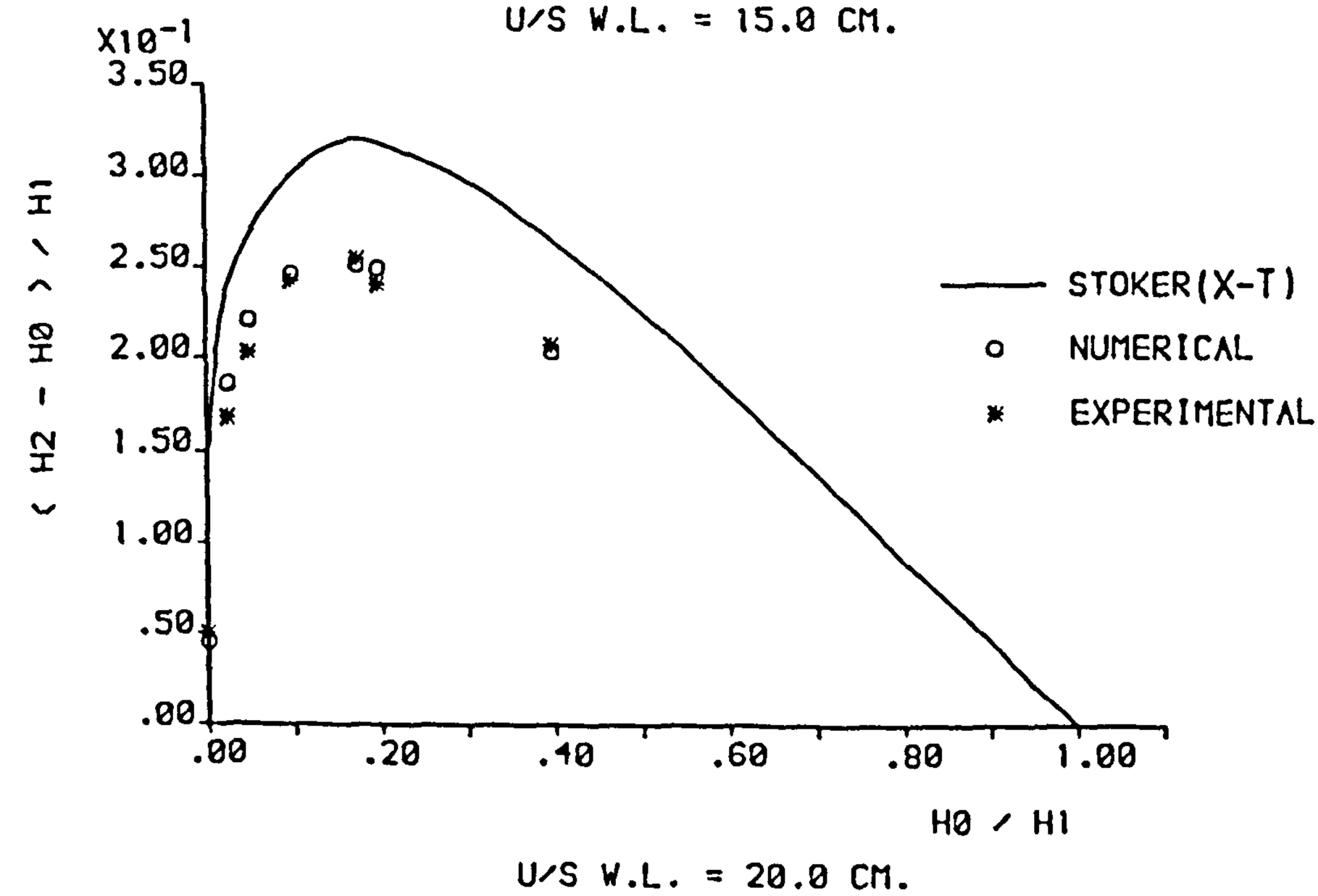

U/S W.L. = 20.0 CM.

FIGURE 6.61 : COMPARISONS OF THE FRONT HEIGHTS RESULTING FROM THE (RT-RT) NUMERICAL AND PHYSICAL MODELS WITH STOKER'S (X-T) SOLUTION .

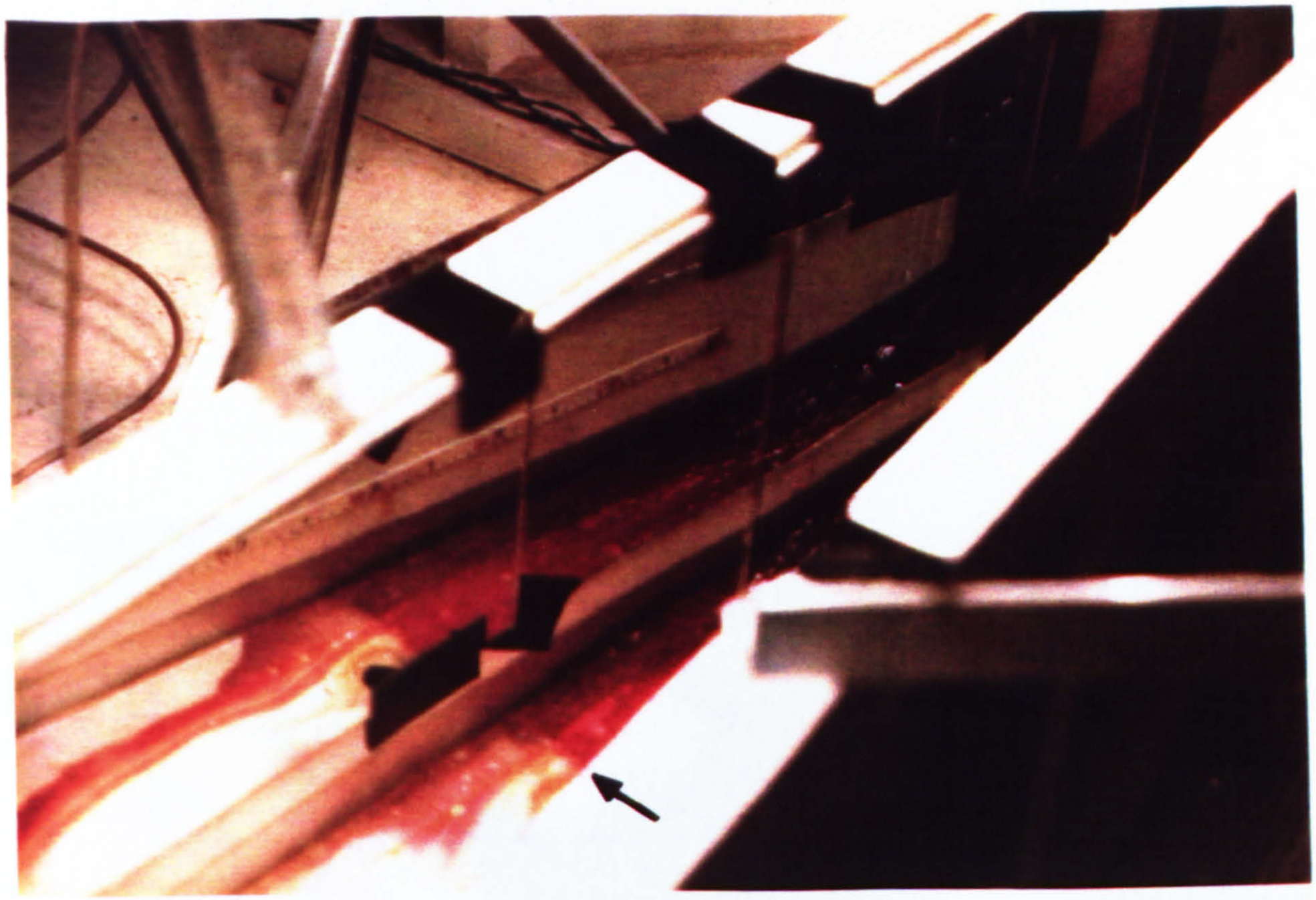

FIGURE 6.62 : PHOTOGRAPH OF THE WATER PROFILE DOWNSTREAM THE GATE IN THE (RT - RT) MODEL , H_1 = 15 cm AND H_o = DRY . THE FRONT IS MARKED BY THE ARROW .

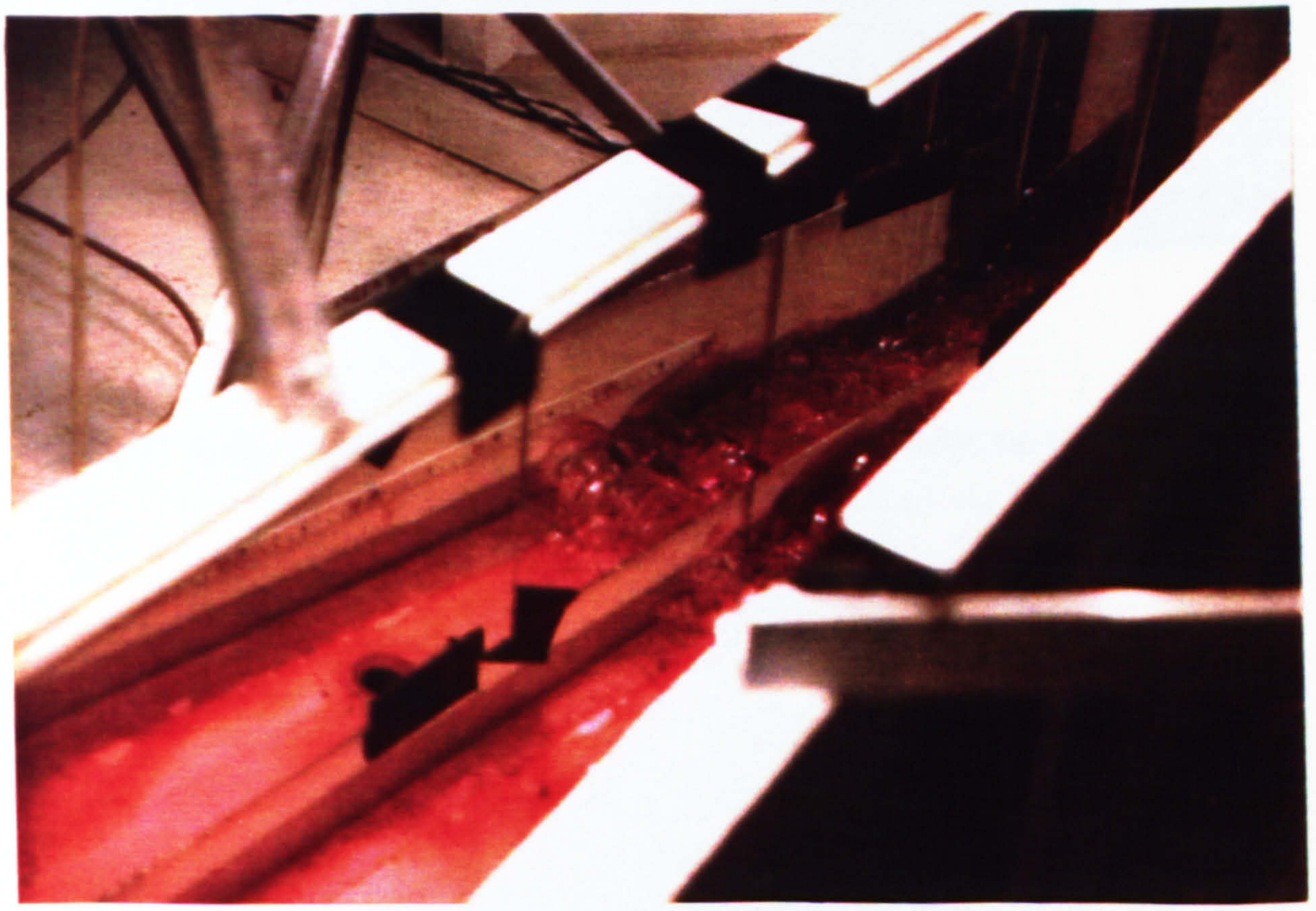

FIGURE 6.63 : PHOTOGRAPH OF THE WATER PROFILE DOWNSTREAM THE GATE IN THE (RT - RT) MODEL , H_1 = 15 cm AND H_o=1.5 cm . NOTE THE HEIGHT AND SHAPE OF THE FRONT .

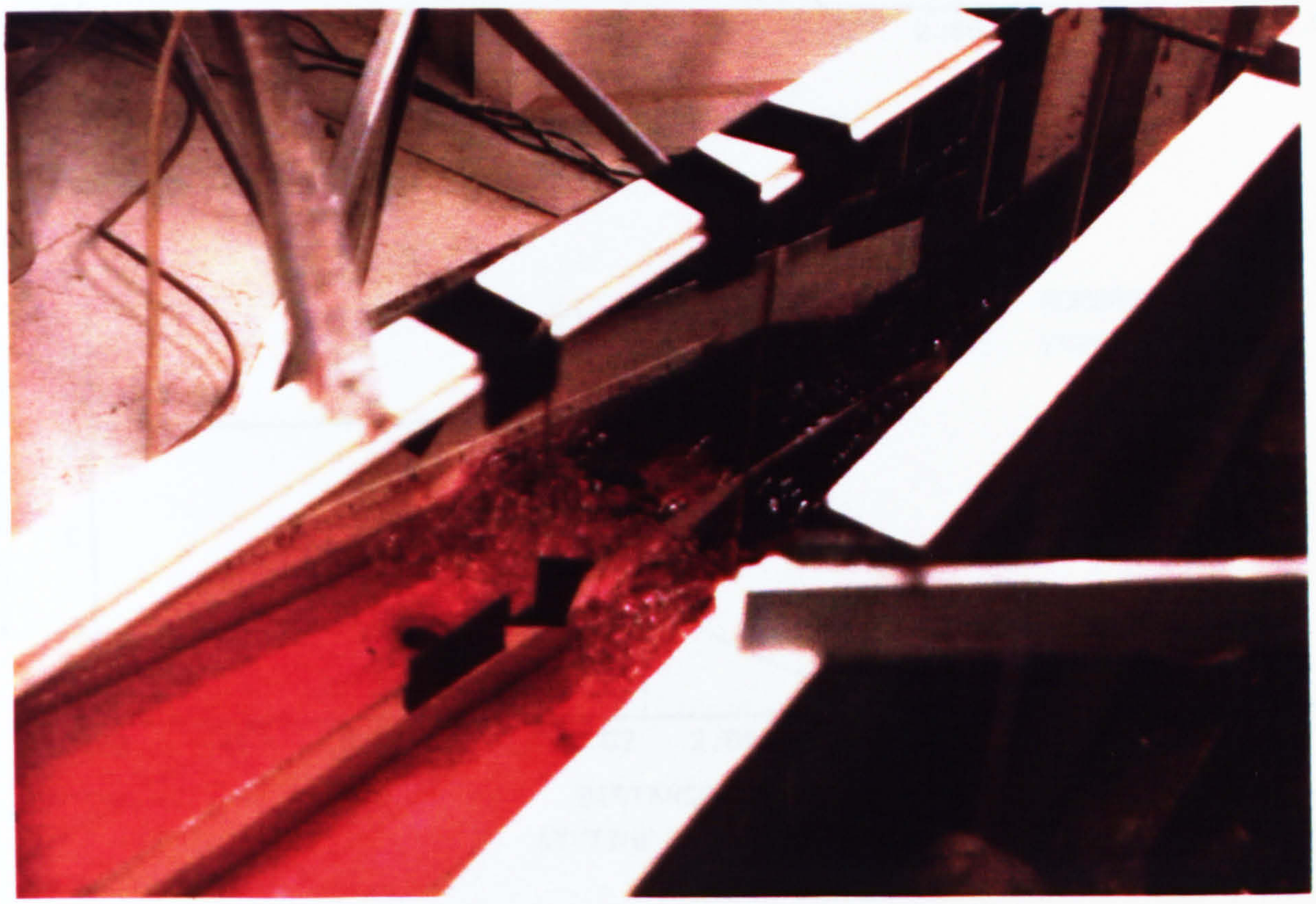

FIGURE 6.64 : PHOTOGRAPH OF THE WATER PROFILE DOWNSTREAM THE GATE IN THE (RT - RT) MODEL , H_1 = 15 cm AND H_o = 3 cm.

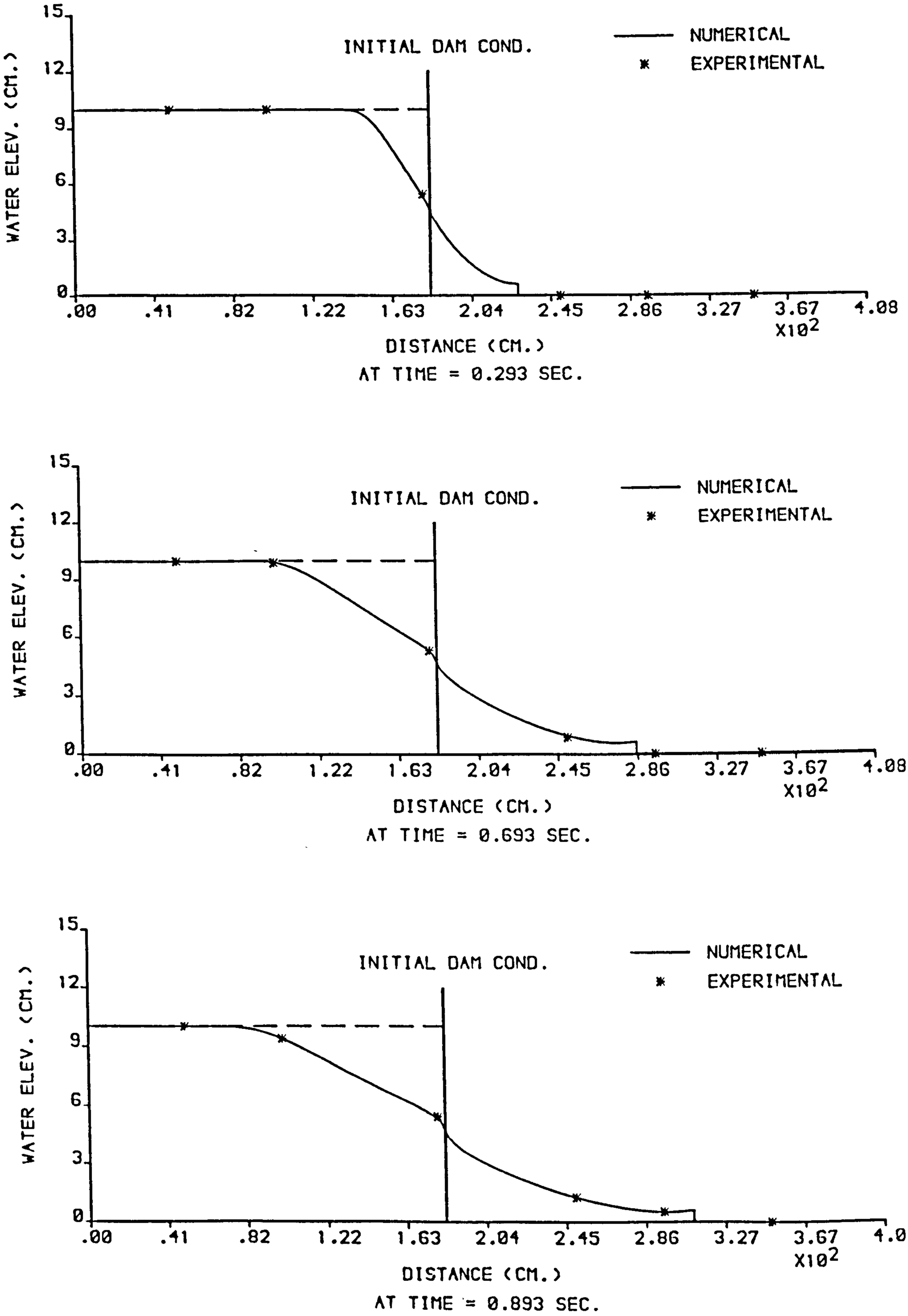

FIGURE 6.65 : NUMERICAL AND EXPERIMENTAL PROFILES FROM THE (RT-RT) MODEL , H_1 = 10 cm AND H_o = DRY .

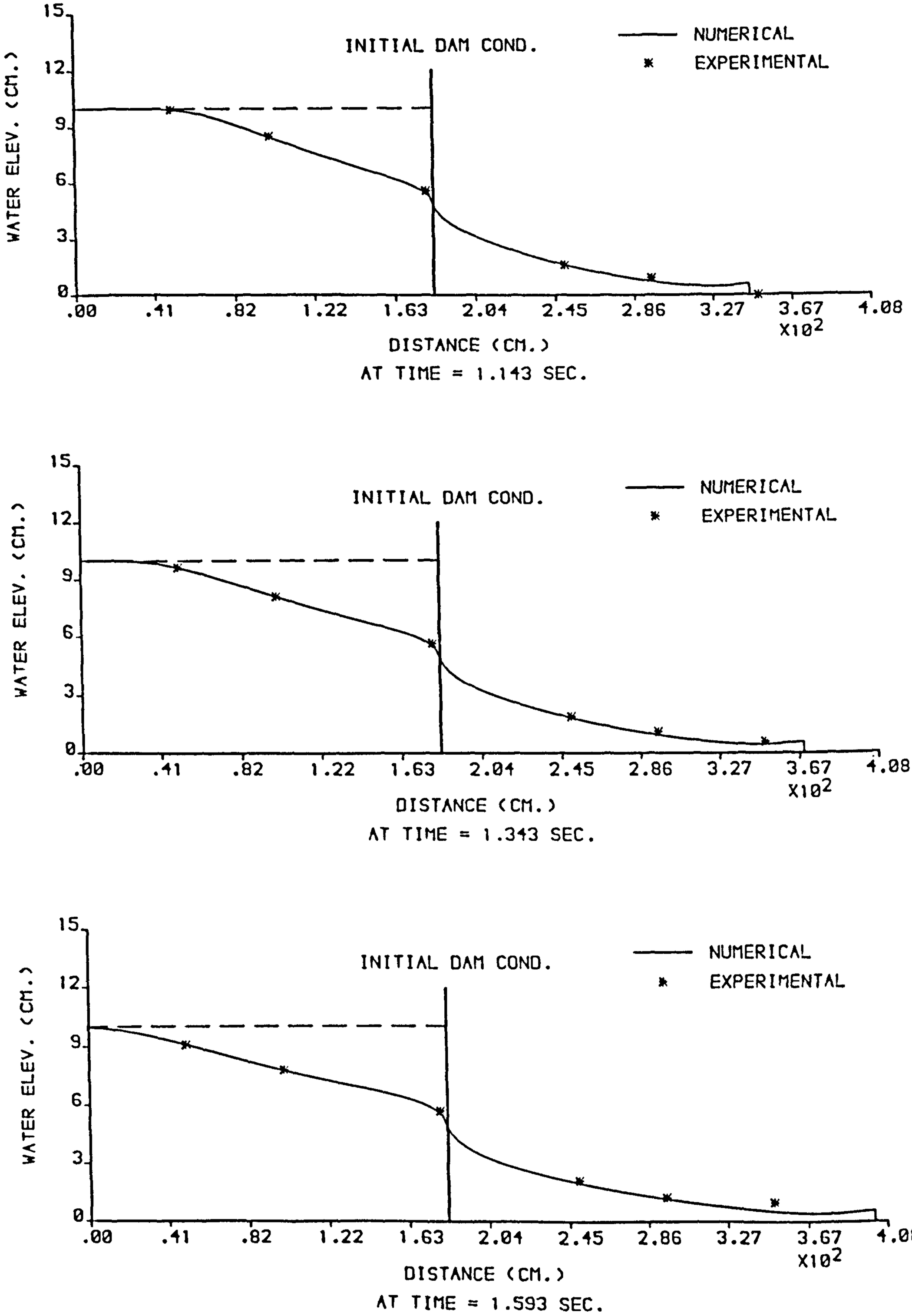

FIGURE 6.66 : NUMERICAL AND EXPERIMENTAL PROFILES FROM THE (RT-RT) MODEL , H_1 = 10 cm AND H_o = DRY .

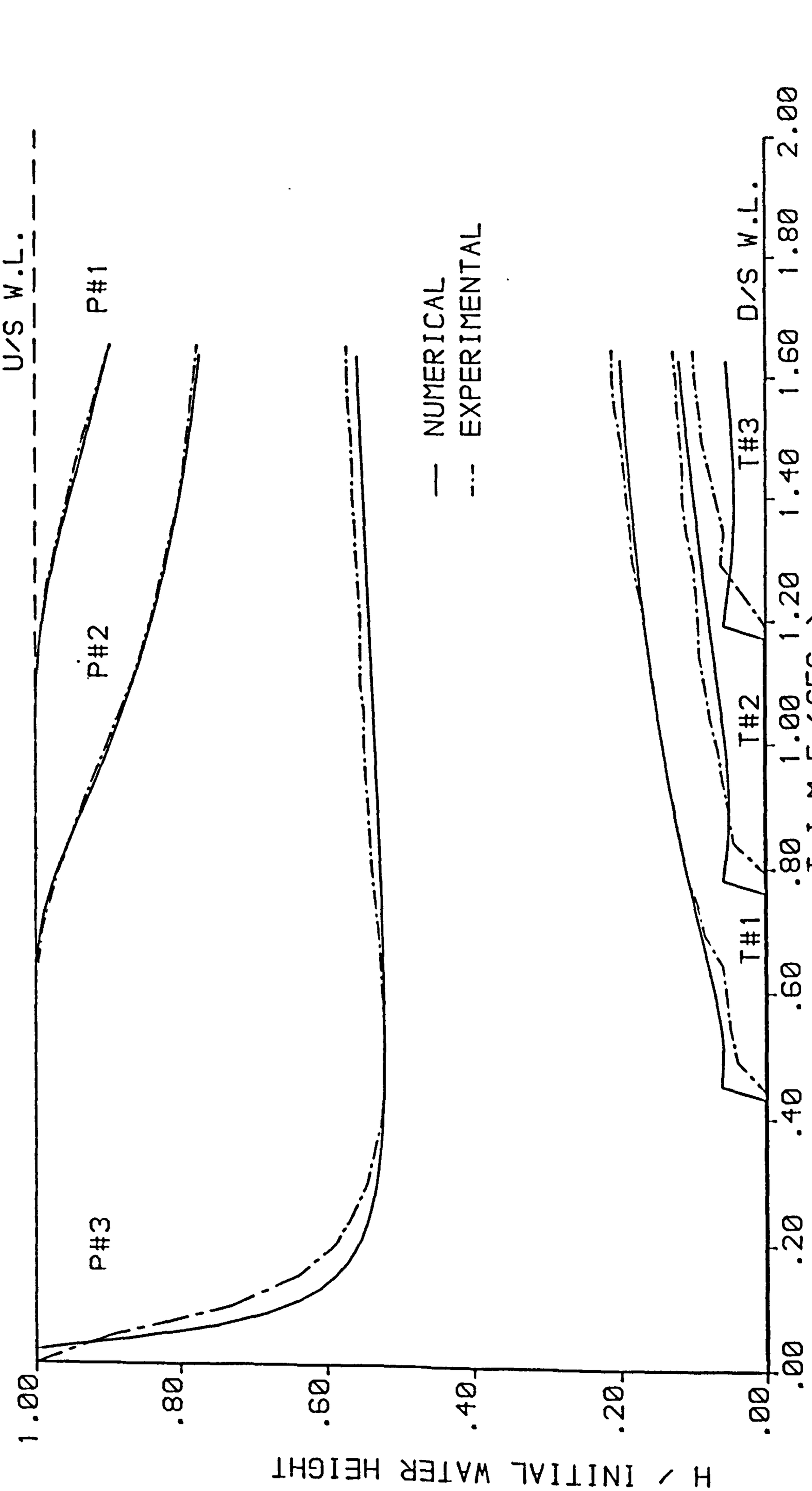

FIGURE 6.67 : NUMERICAL AND EXPERIMENTAL STAGE HYDROGRAPHS FROM THE (RT-RT) MODEL , H_1 = 10 cm AND H_o = DRY .

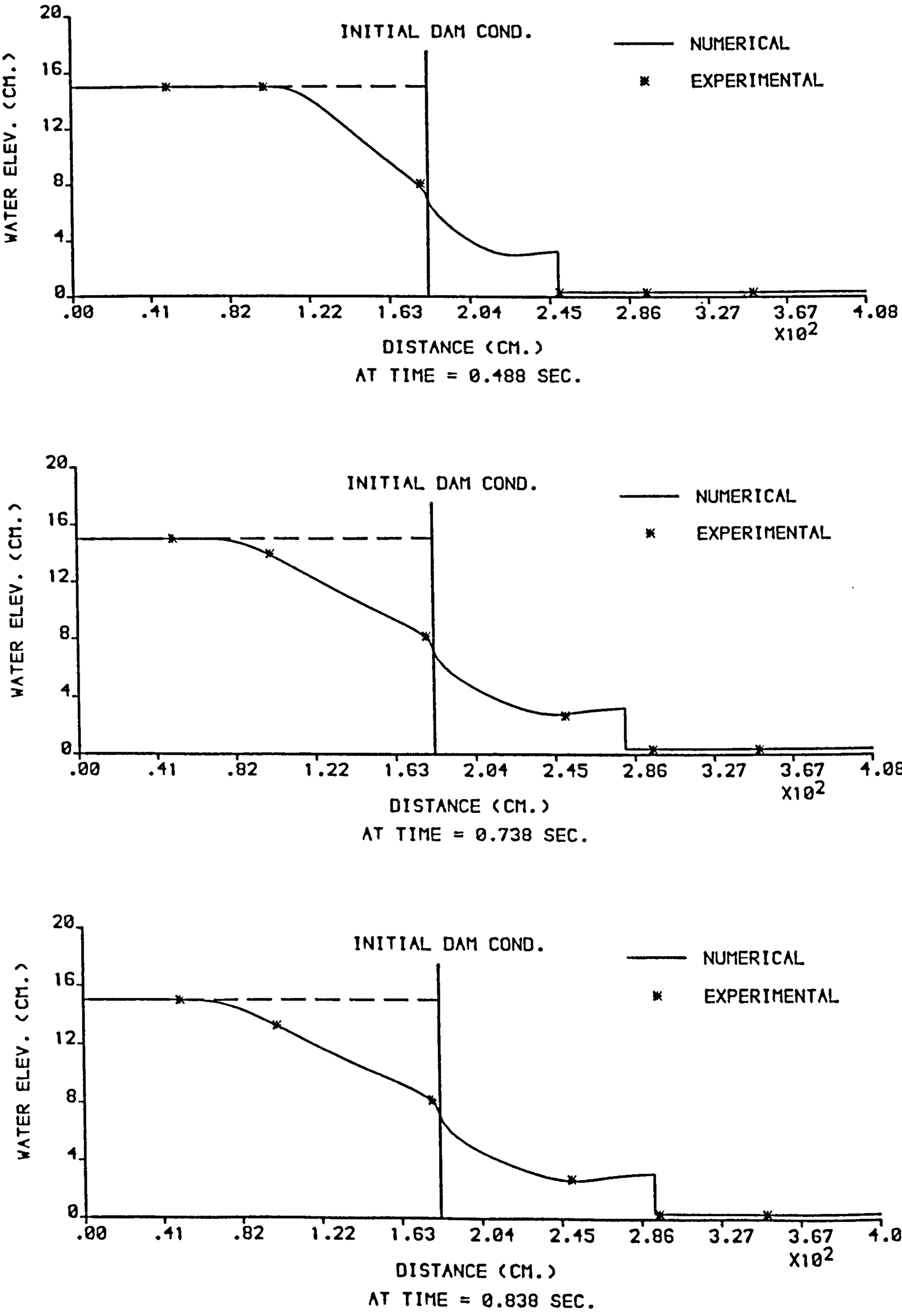

FIGURE 6.68 : NUMERICAL AND EXPERIMENTAL PROFILES FROM THE (RT-RT) MODEL , H_1 = 15 cm AND H_o = 0.375 cm .

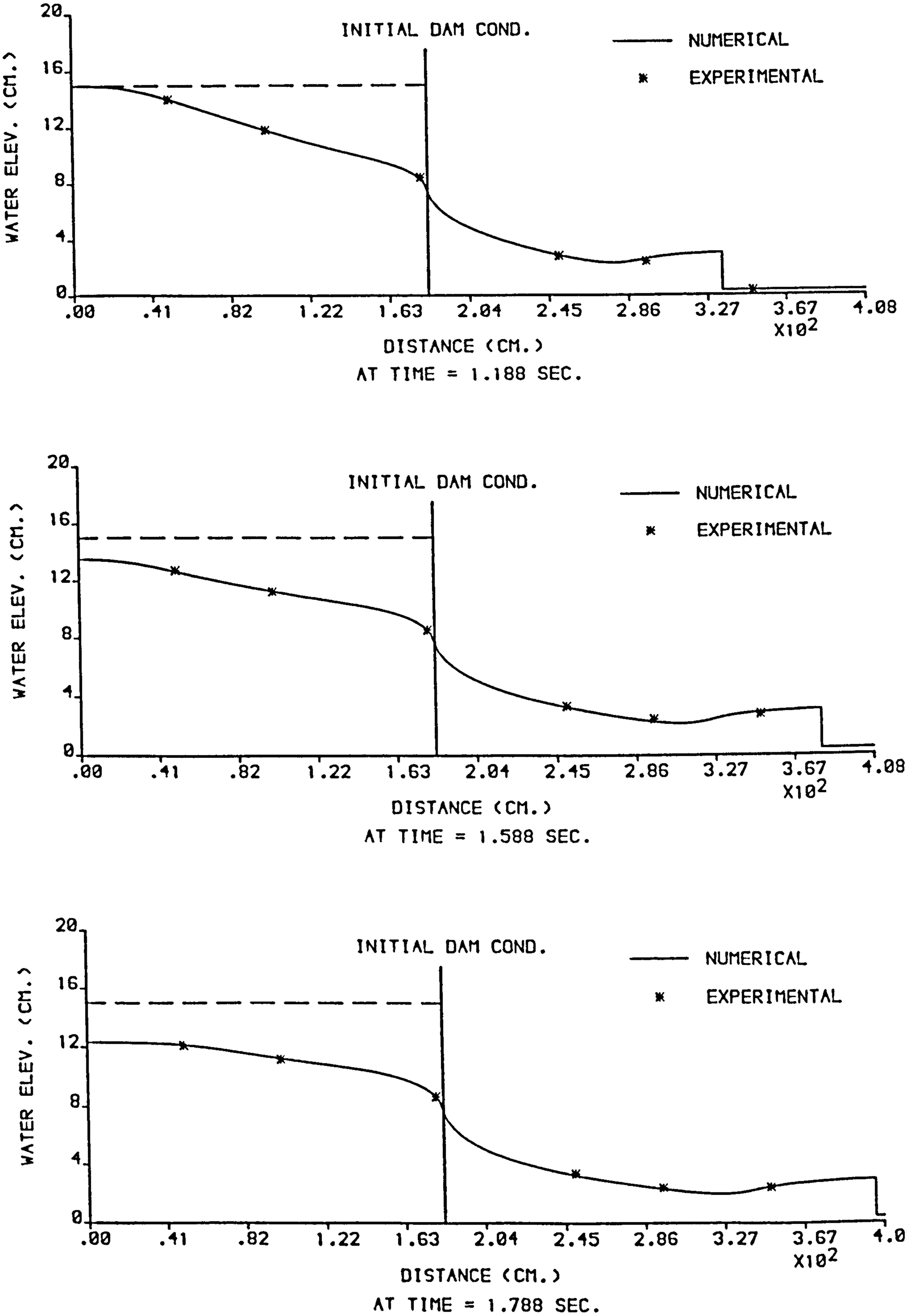

FIGURE 6.69 :NUMERICAL AND EXPERIMENTAL PROFILES FROM THE (RT-RT) MODEL , H_1 = 15 cm AND H_o = 0.375 cm .

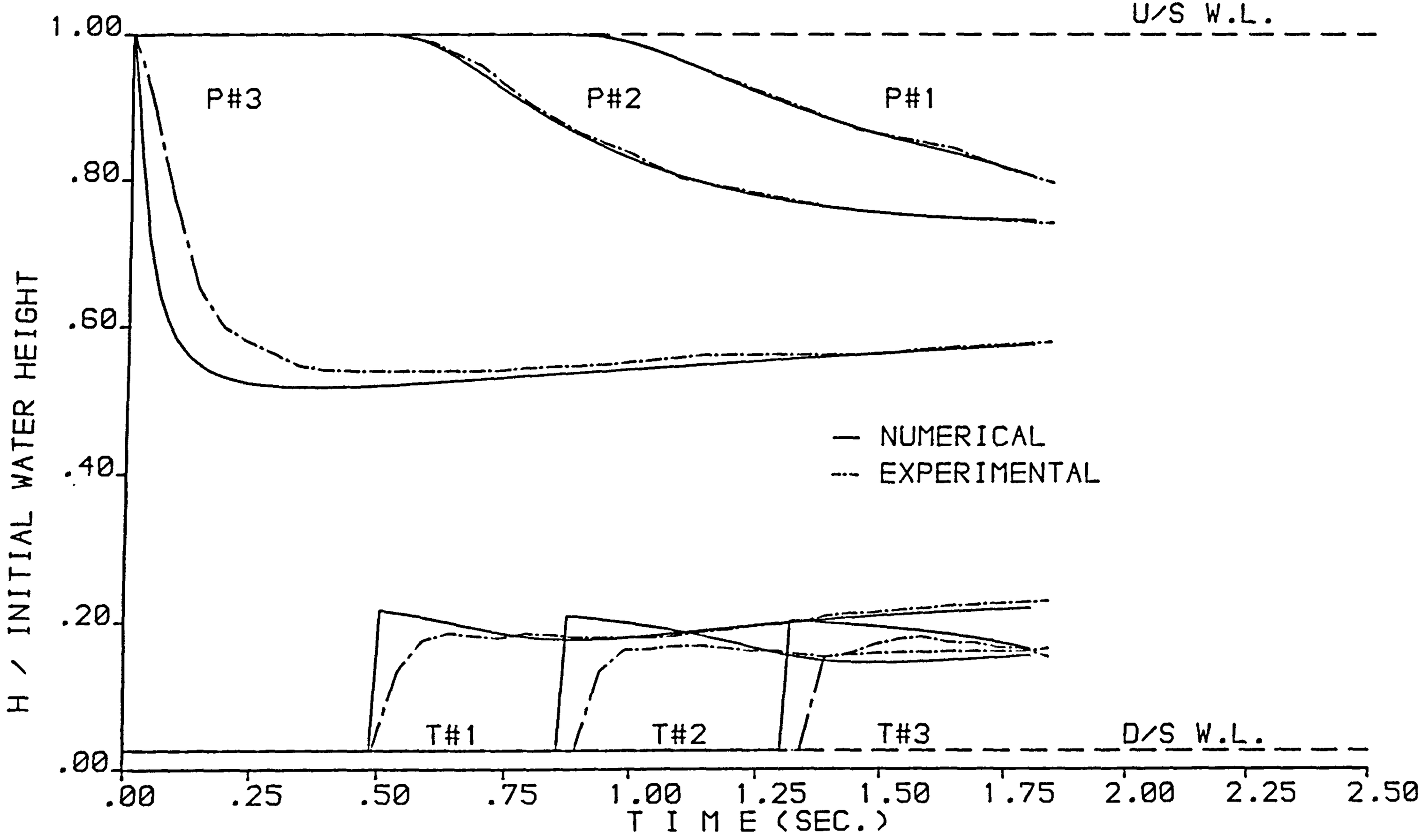

FIGURE 6.70 : NUMERICAL AND EXPERIMENTAL STAGE HYDROGRAPHS FROM THE (RT-RT) MODEL , H_1 = 15 cm AND H_o = 0.375 cm .

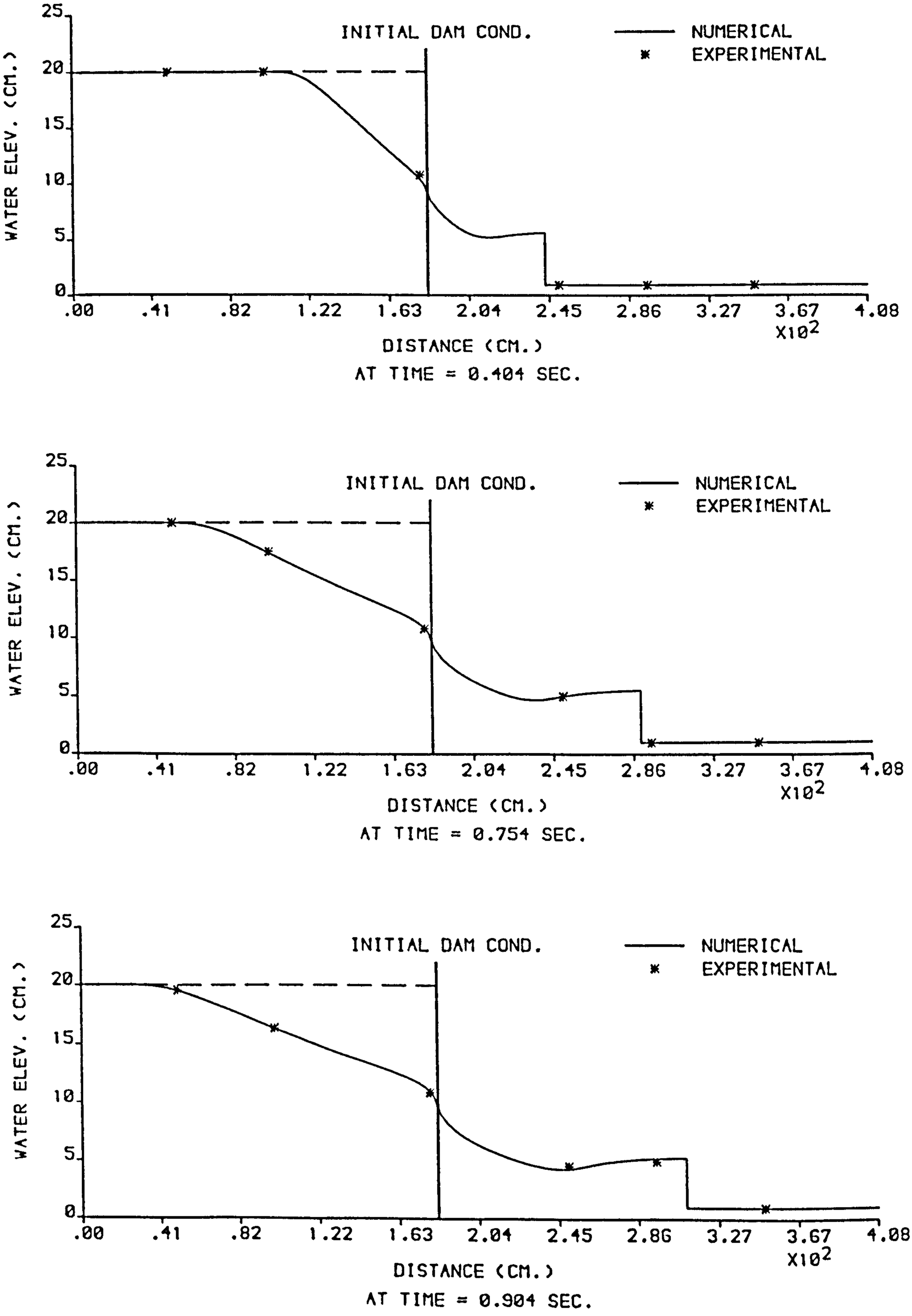

FIGURE 6.71 : NUMERICAL AND EXPERIMENTAL PROFILES FROM THE (RT-RT) MODEL , H_1 = 20 cm AND H_o = 1 cm .

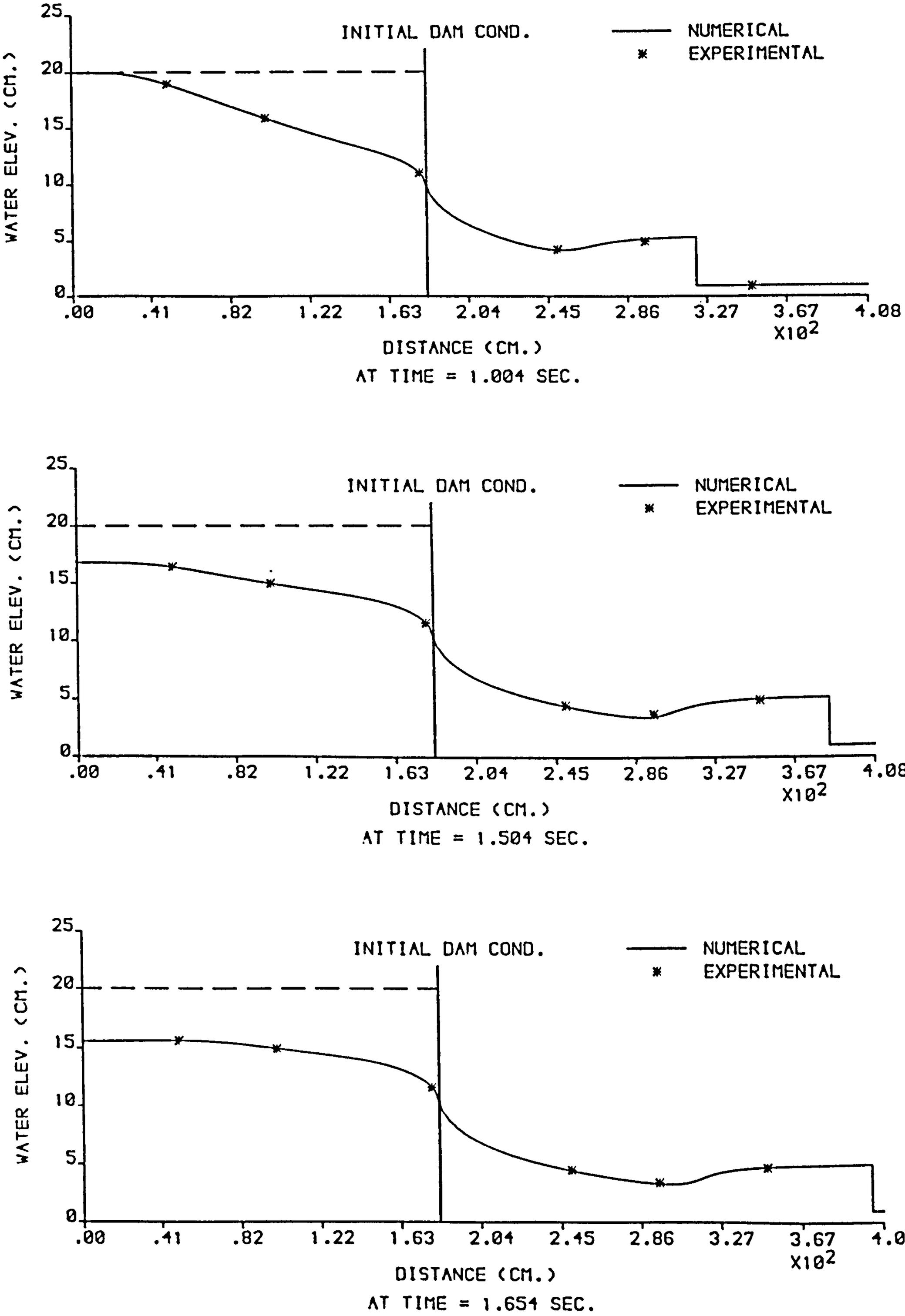

FIGURE 6.72 : NUMERICAL AND EXPERIMENTAL PROFILES FROM THE (RT-RT) MODEL , H_1 = 20 cm AND H_o = 1 cm .

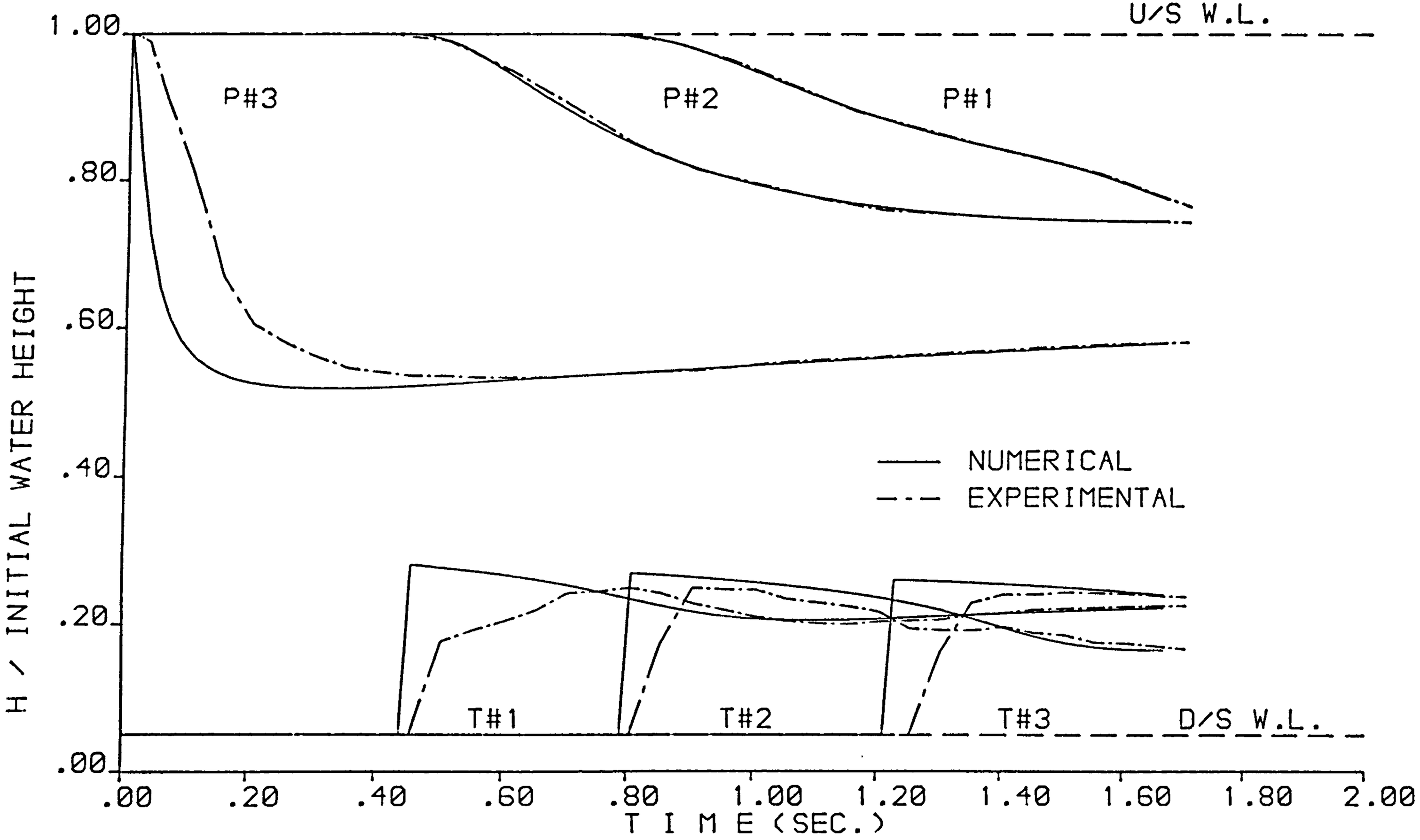

FIGURE 6.73 : NUMERICAL AND EXPERIMENTAL STAGE HYDROGRAPHS FROM THE (RT-RT) MODEL , H_1 = 20 cm AND H_o = 1 cm

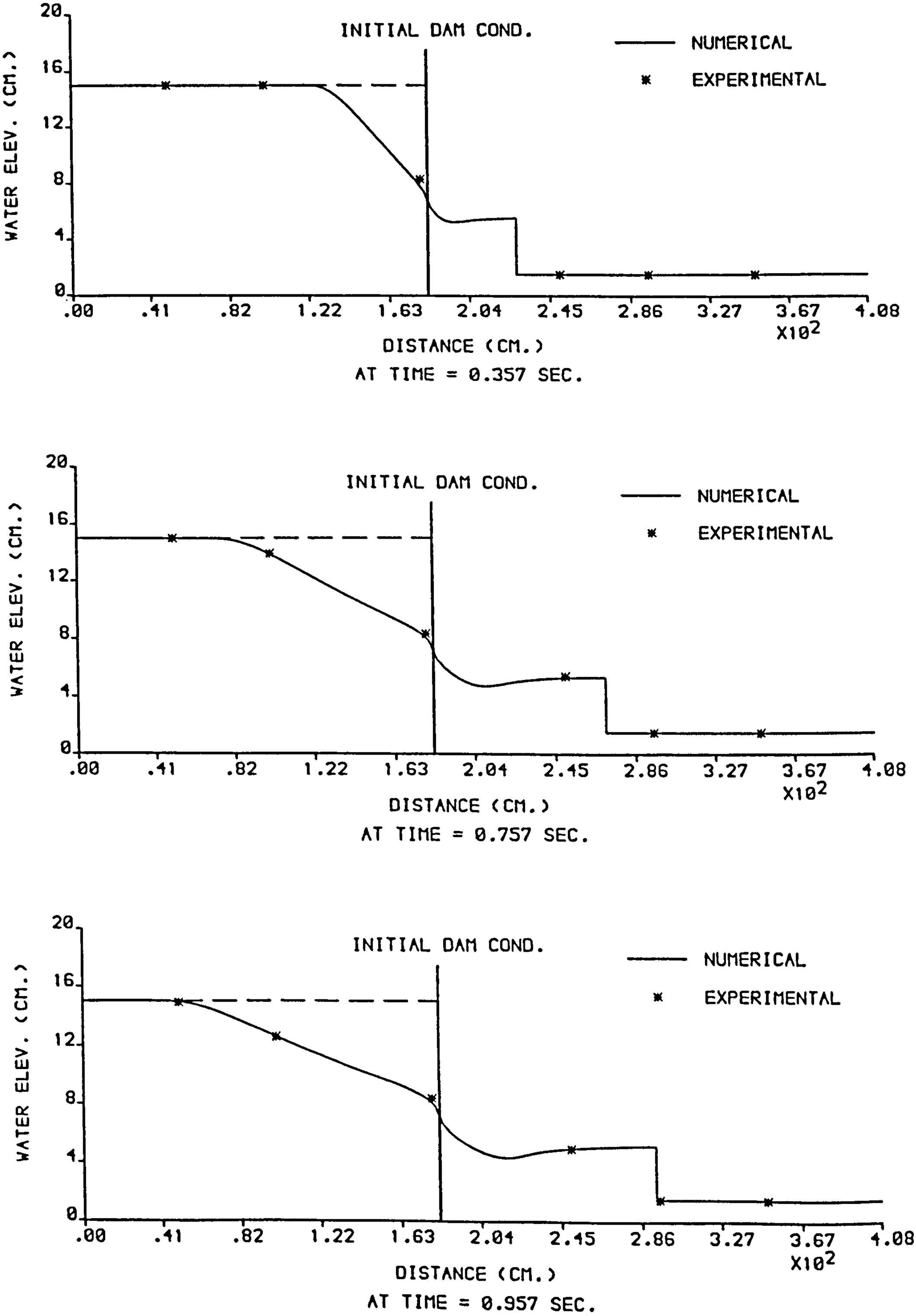

FIGURE 6.74 : NUMERICAL AND EXPERIMENTAL PROFILES FROM THE (RT-RT) MODEL , H_1 = 15 cm AND H_o = 1.5 cm .

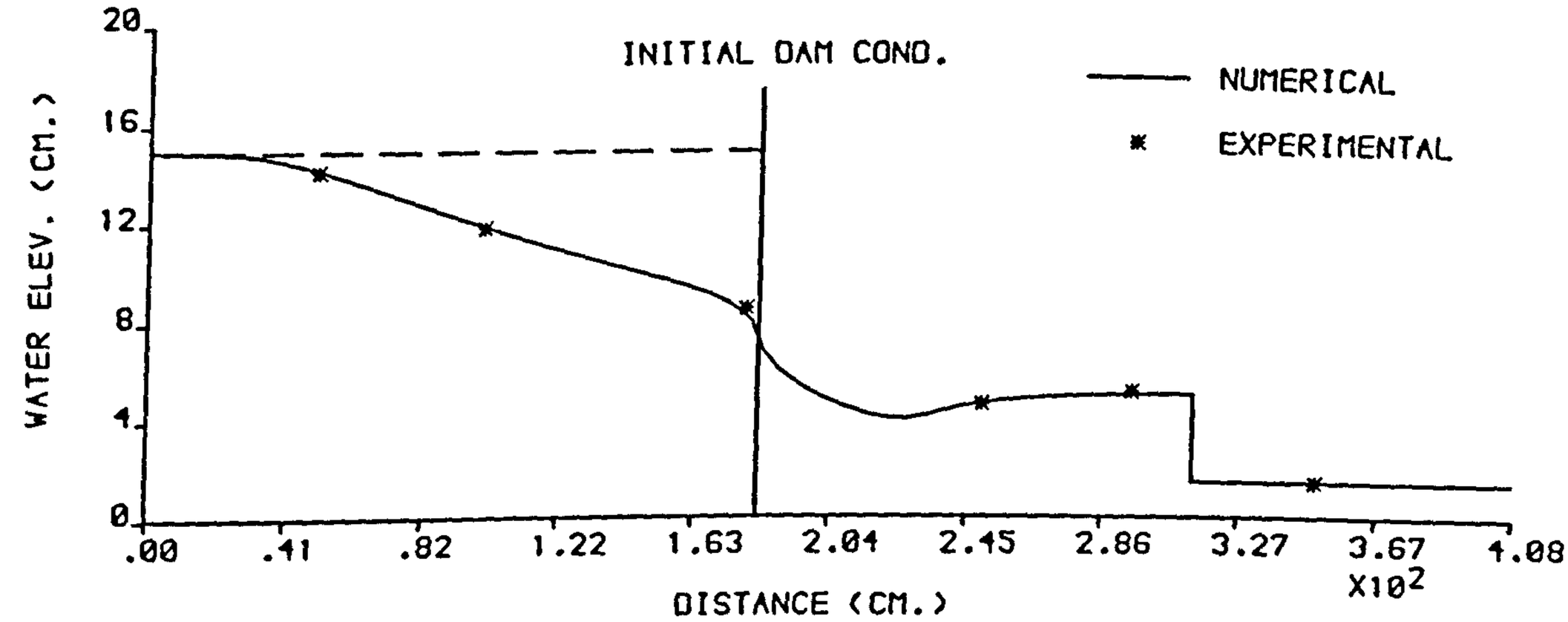

AT TIME = 1.157 SEC.

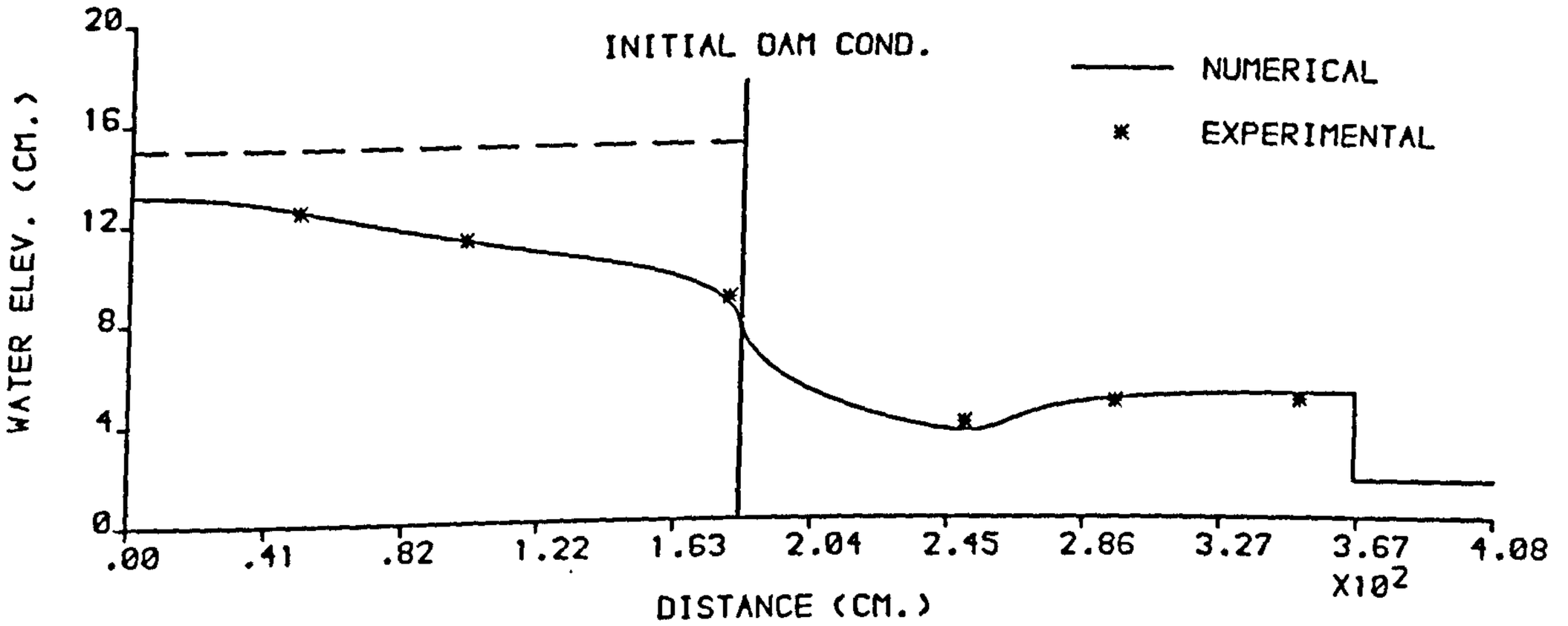

AT TIME = 1.657 SEC.

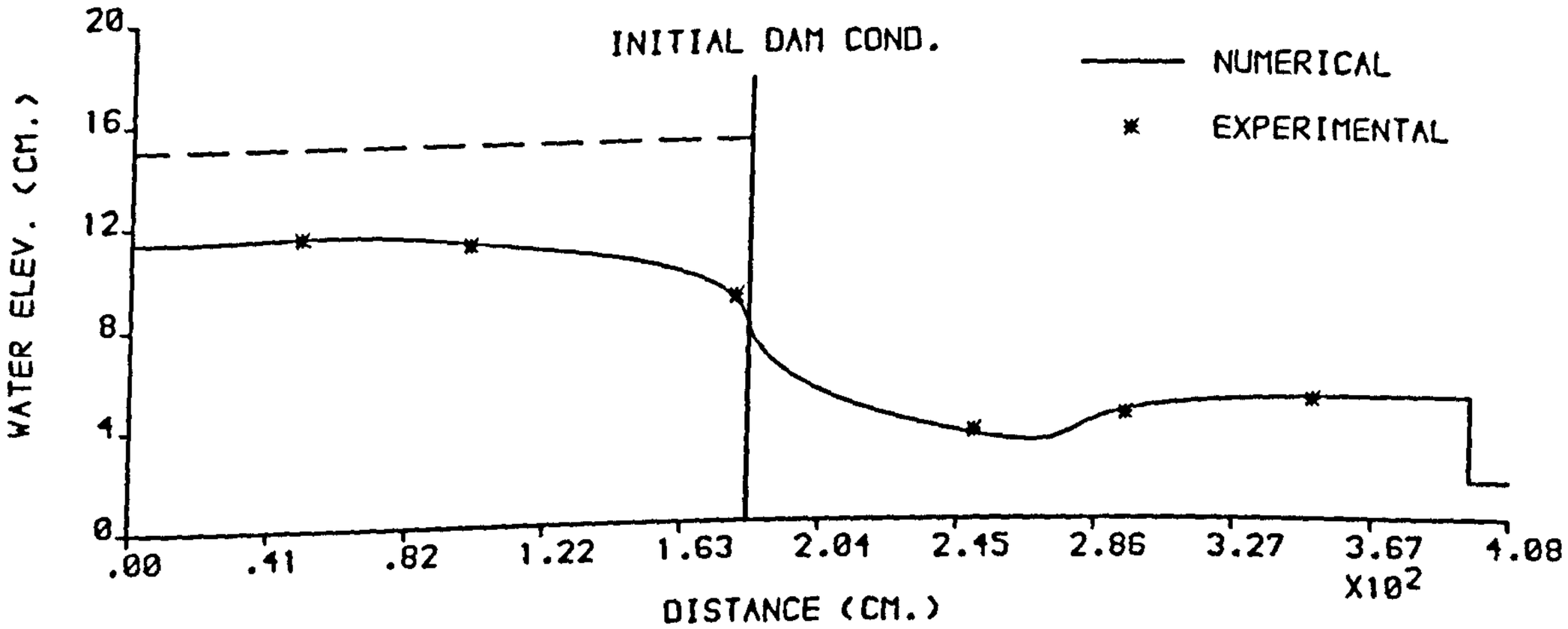

AT TIME = 1.957 SEC.

FIGURE 6.75 : NUMERICAL AND EXPERIMENTAL PROFILES FROM THE (RT-RT) MODEL , H_1 = 15 cm AND H_o = 1.5 cm .

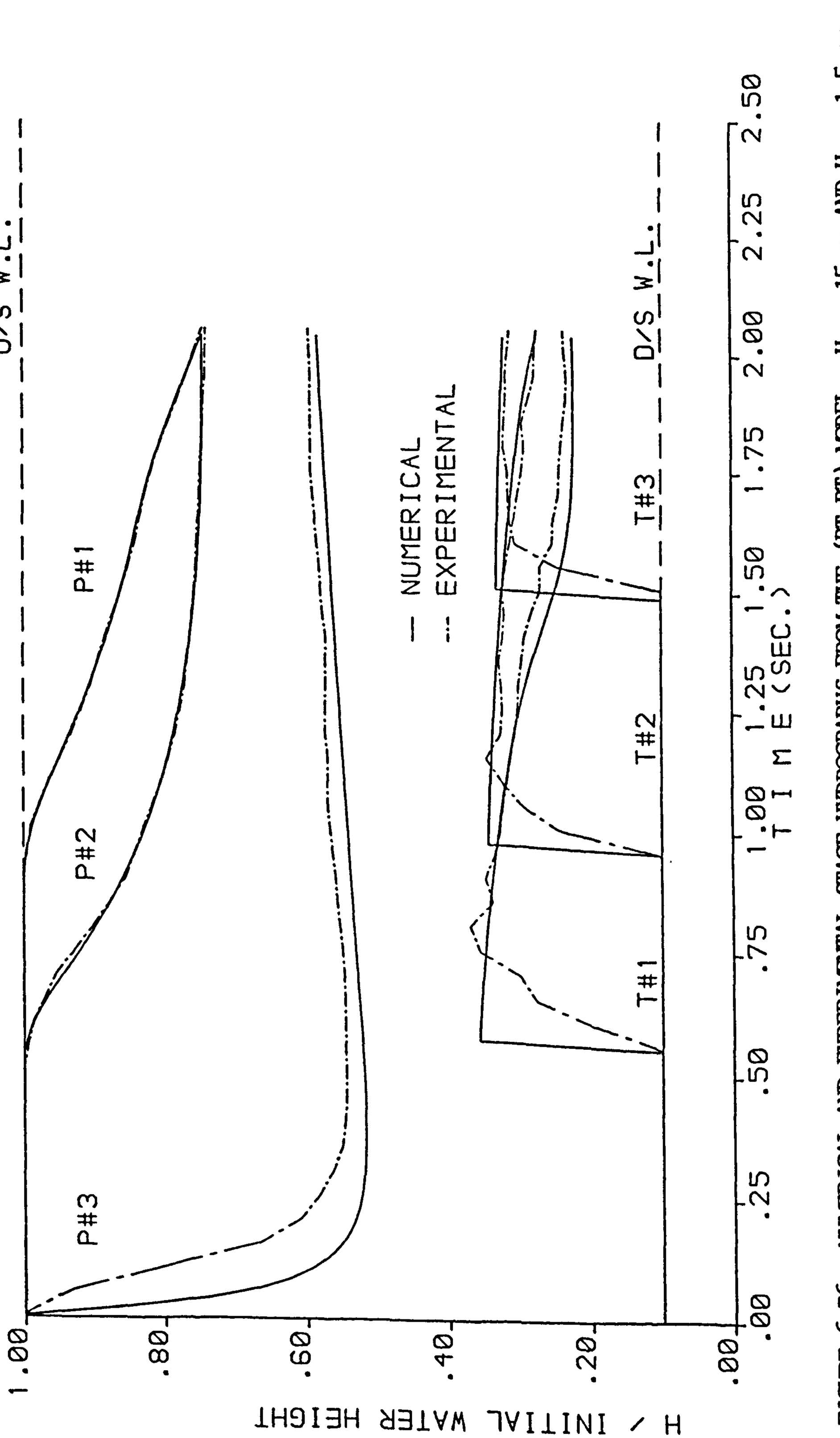

FIGURE 6.76 : NUMERICAL AND EXPERIMENTAL STAGE HYDROGRAPHS FROM THE (RT-RT) MODEL , H_1 = 15 cm AND H_o = 1.5 cm .

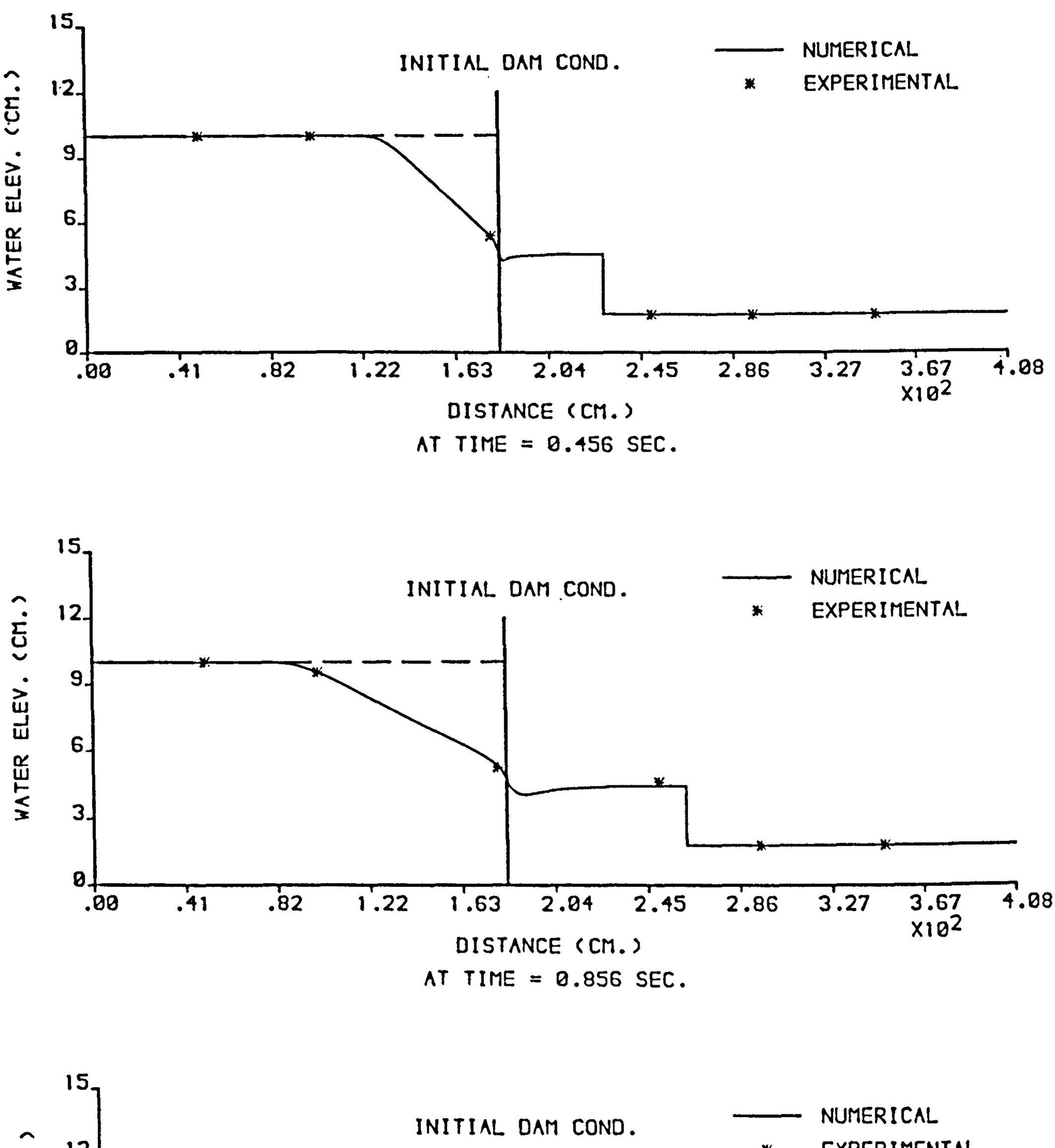

FIGURE 6.77 : NUMERICAL AND EXPERIMENTAL PROFILES FROM THE (RT-RT) MODEL , H_1 = 10 cm AND H_o = 1.76 cm .

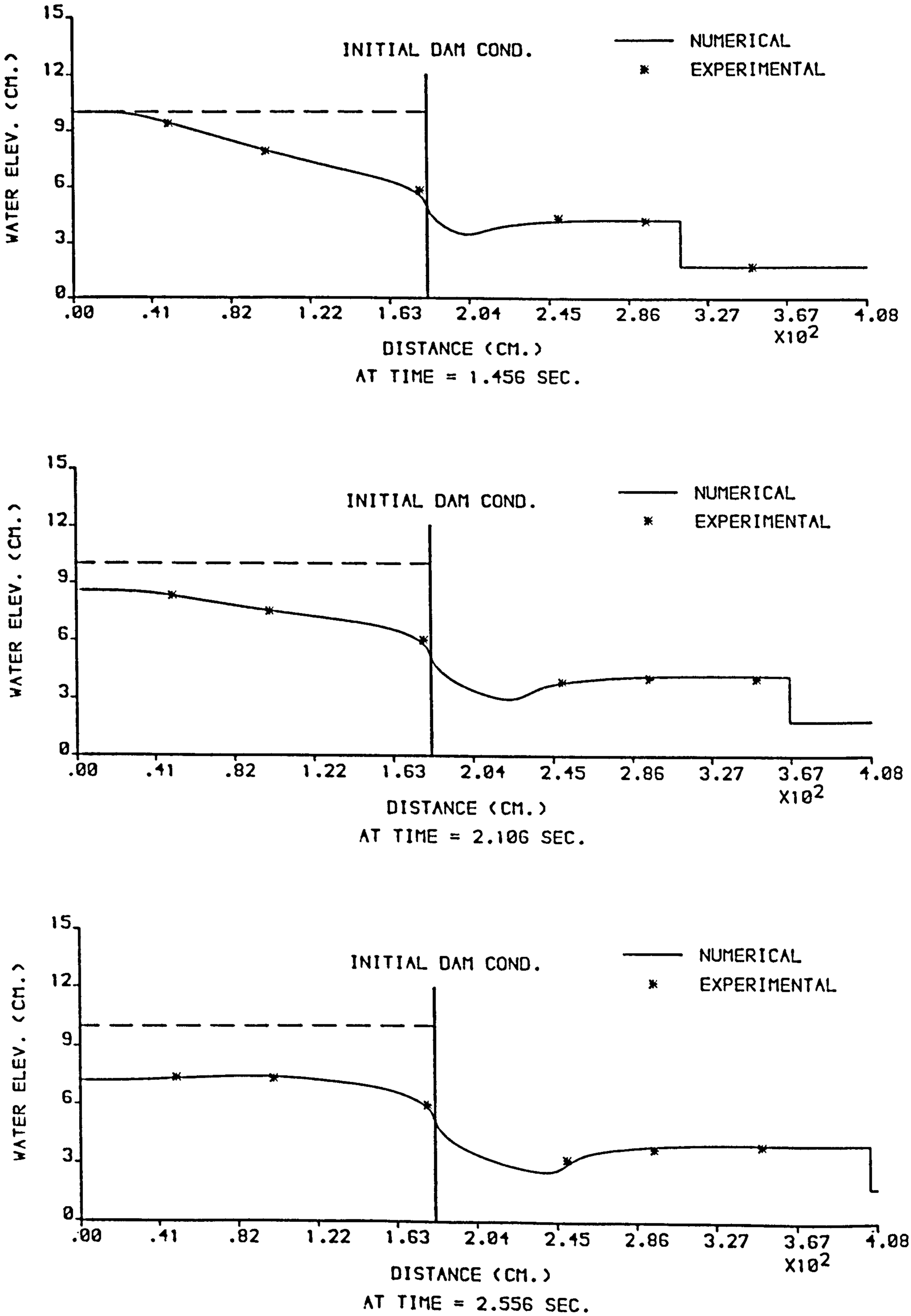

FIGURE 6.78 : NUMERICAL AND EXPERIMENTAL PROFILES FROM THE (RT-RT) MODEL , H_1 = 10 cm AND H_o = 1.76 cm .

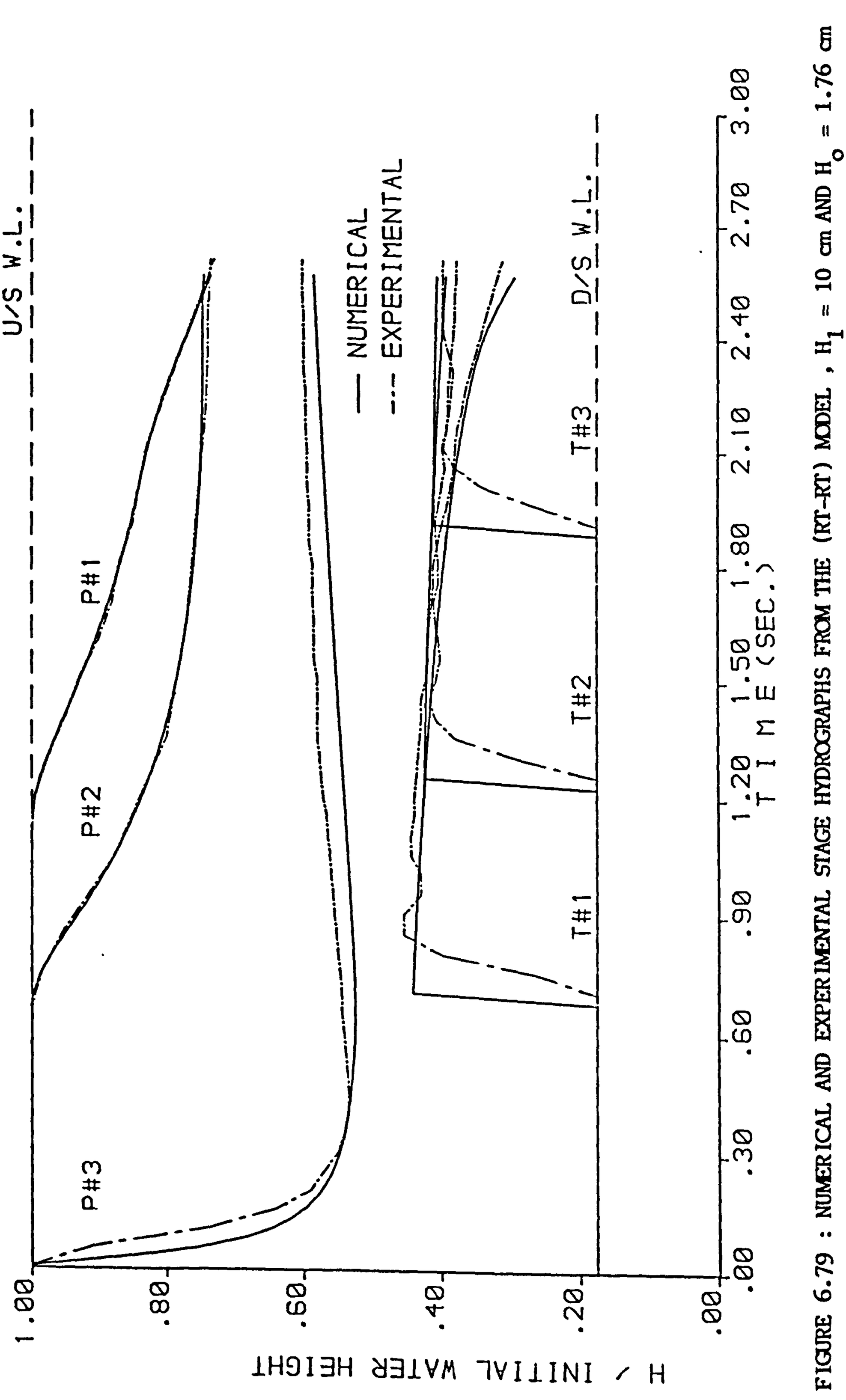

FIGURE 6.79 : NUMERICAL AND EXPERIMENTAL STAGE HYDROGRAPHS FROM THE (RT-RT) MODEL , H_1 = 10 cm AND H_o = 1.76 cm

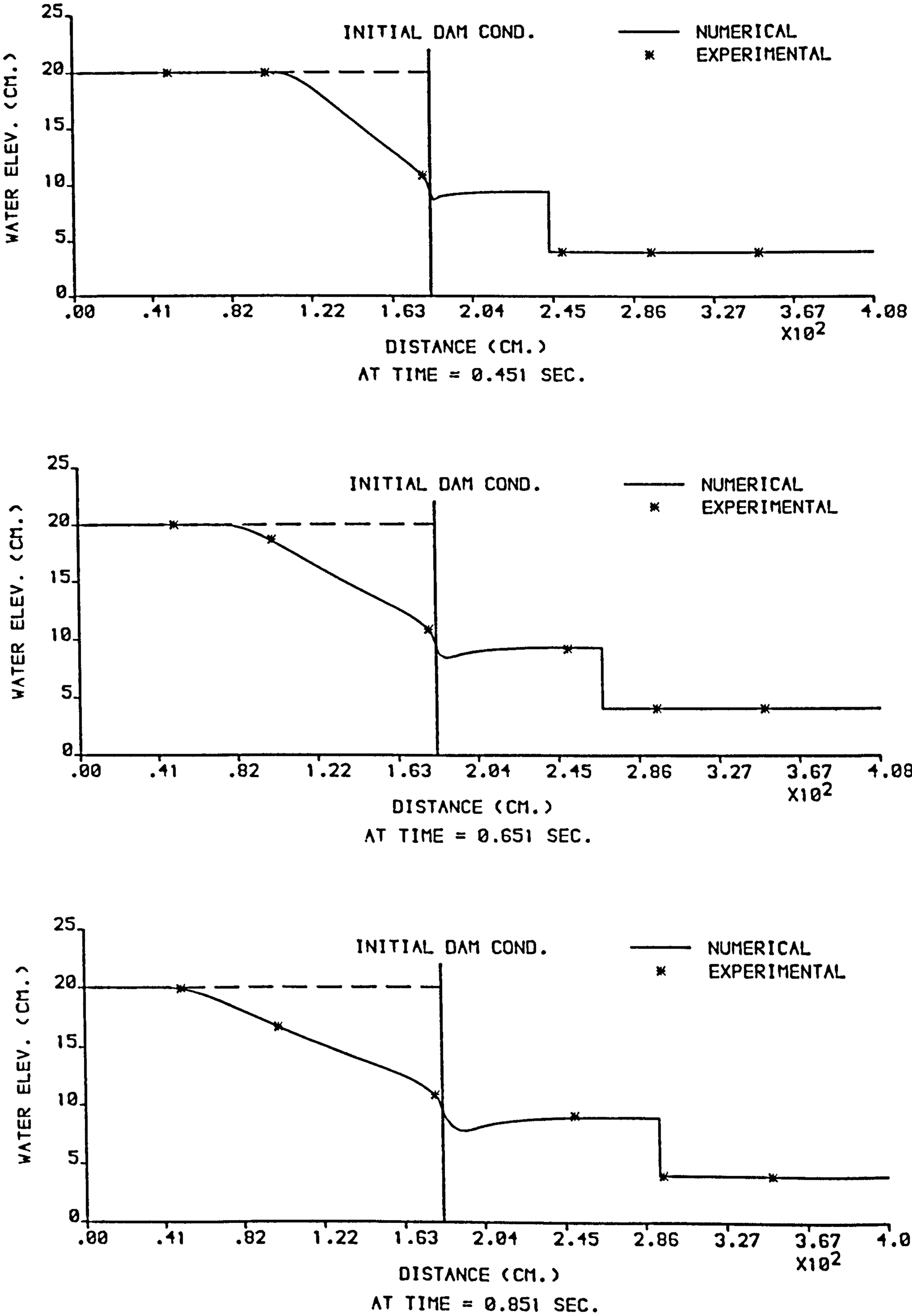

FIGURE 6.80 : NUMERICAL AND EXPERIMENTAL PROFILES FROM THE (RT-RT) MODEL , H_1 = 20 cm AND H_o = 4 cm .

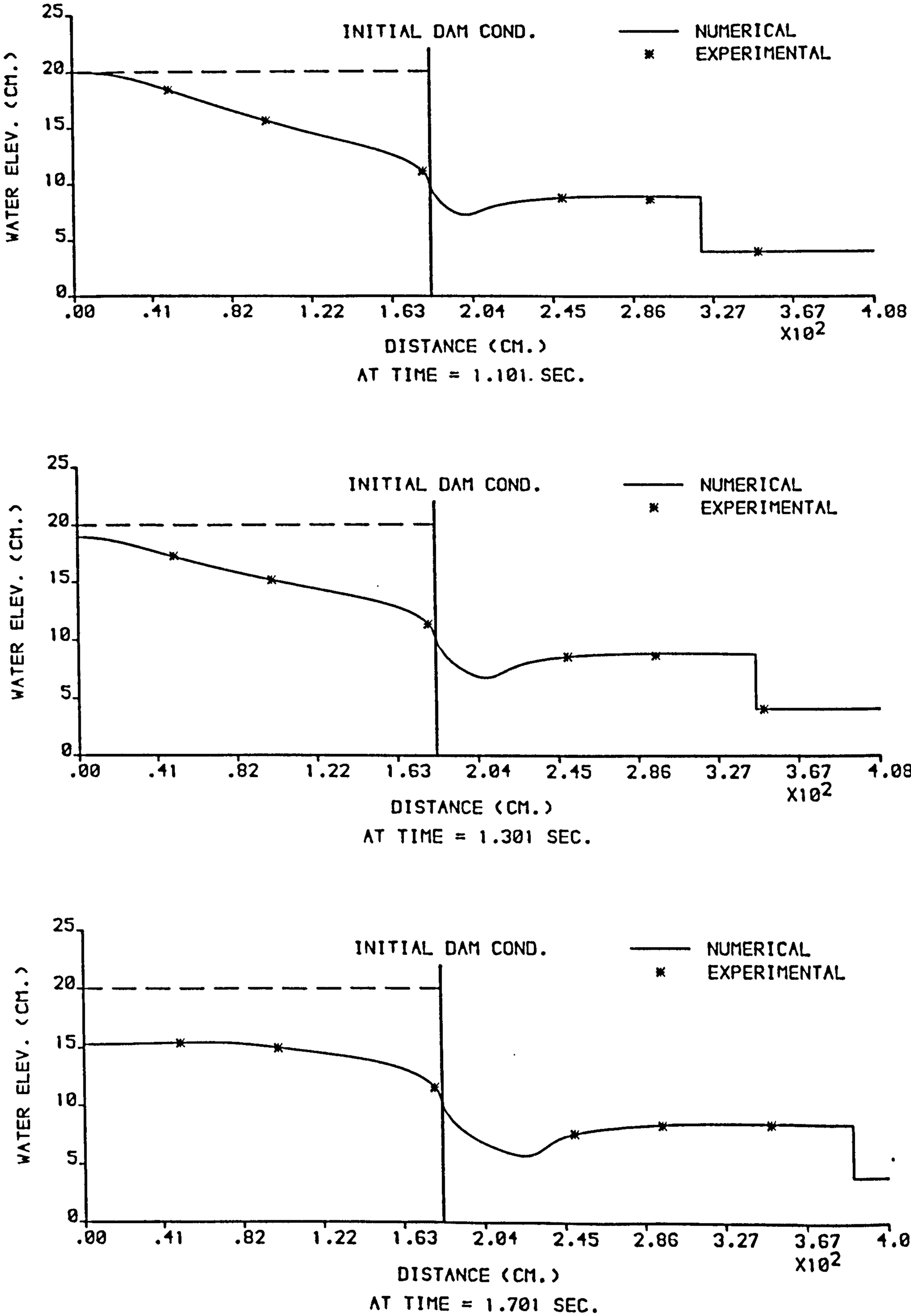

FIGURE 6.81 : NUMERICAL AND EXPERIMENTAL PROFILES FROM THE (RT-RT) MODEL , H_1 = 20 cm AND H_o = 4 cm .

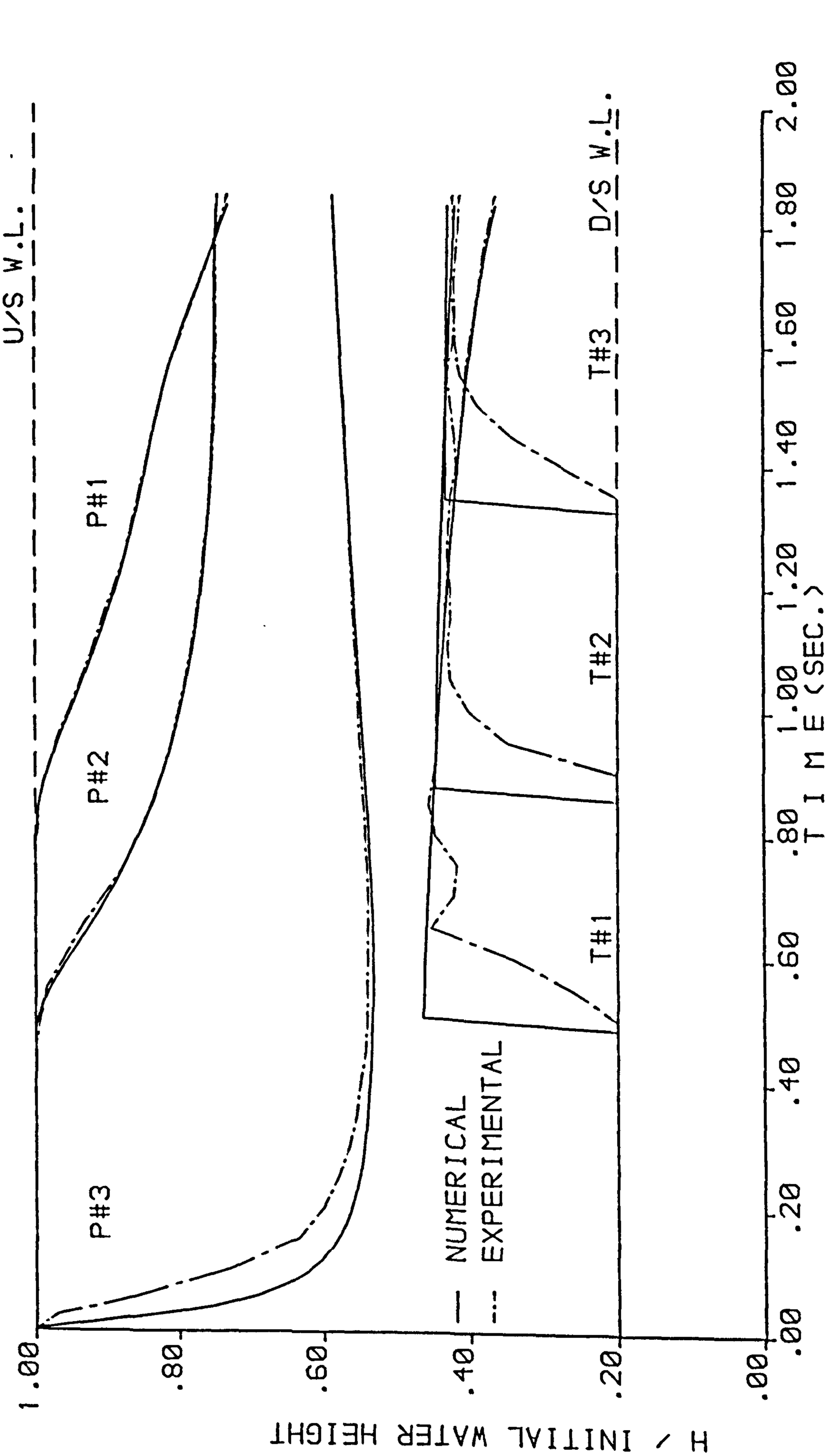

FIGURE 6.82 : NUMERICAL AND EXPERIMENTAL STAGE HYDROGRAPHS FROM THE (RT-RT) MODEL , H_1 = 20 cm AND H_o = 4 cm .

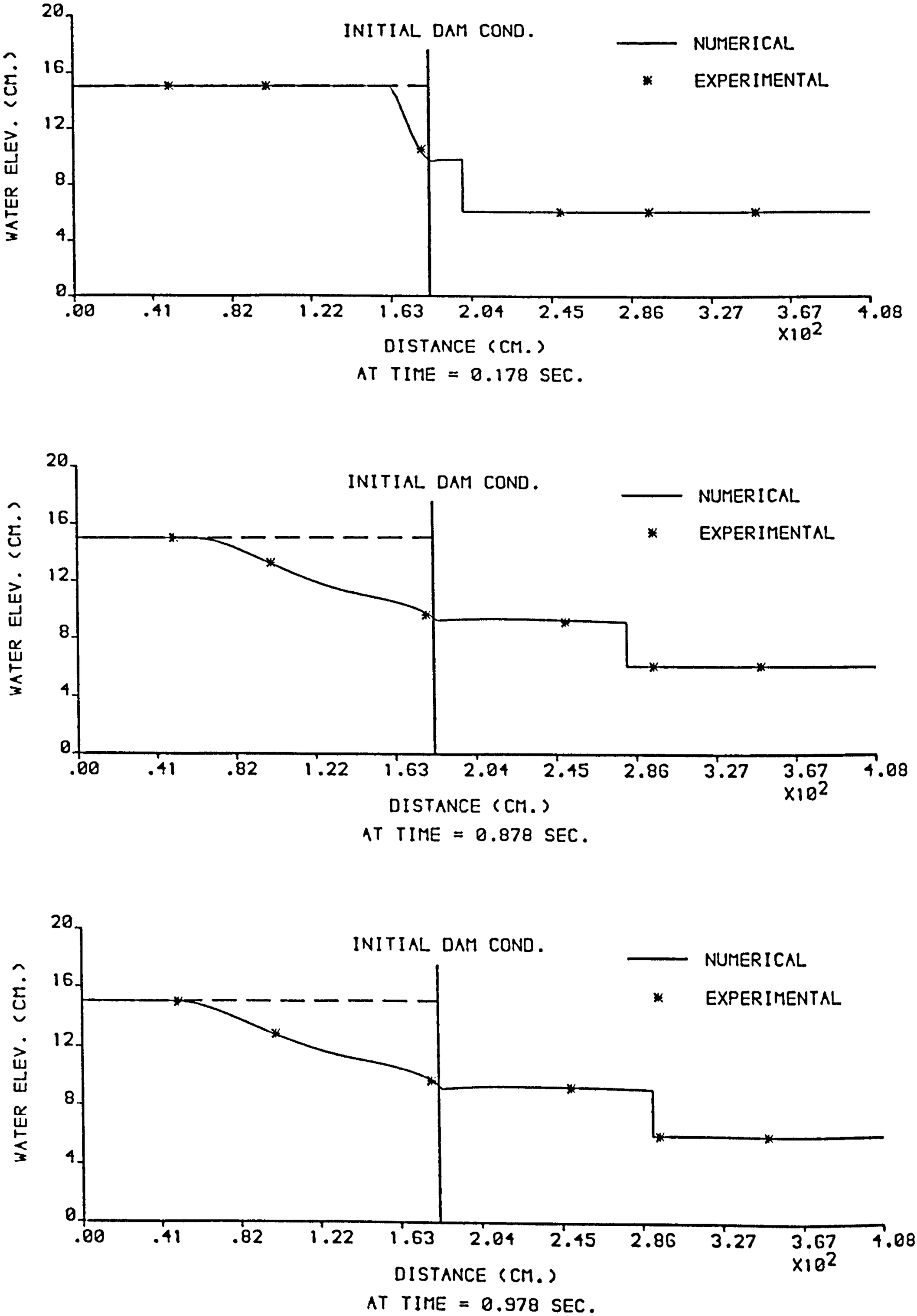

FIGURE 6.83 : NUMERICAL AND EXPERIMENTAL PROFILES FROM THE (RT-RT) MODEL , H_1 = 15 cm AND H_o = 6 cm .

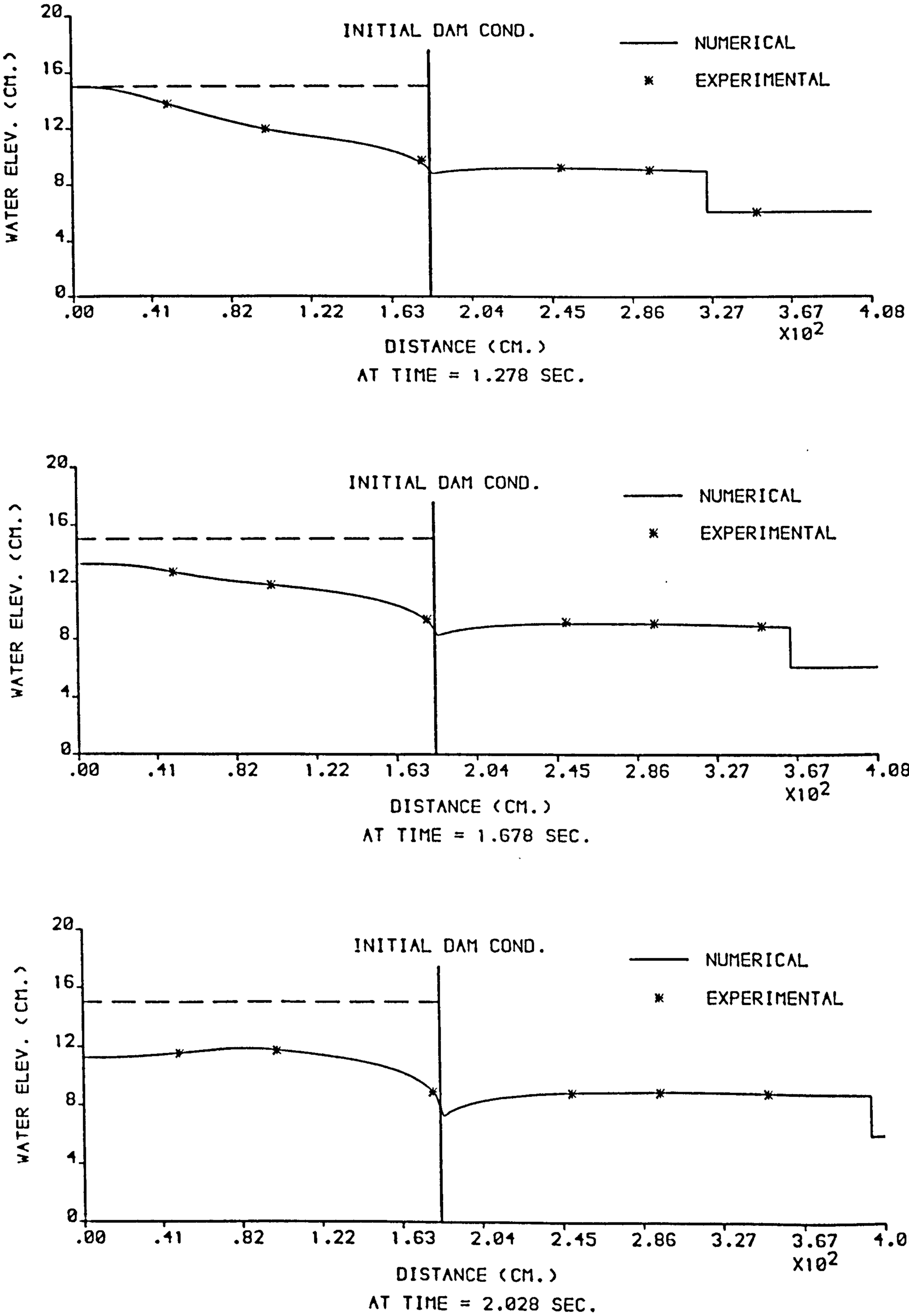

FIGURE 6.84 : NUMERICAL AND EXPERIMENTAL PROFILES FROM THE (RT-RT) MODEL , H_1 = 15 cm AND H_o = 6 cm .

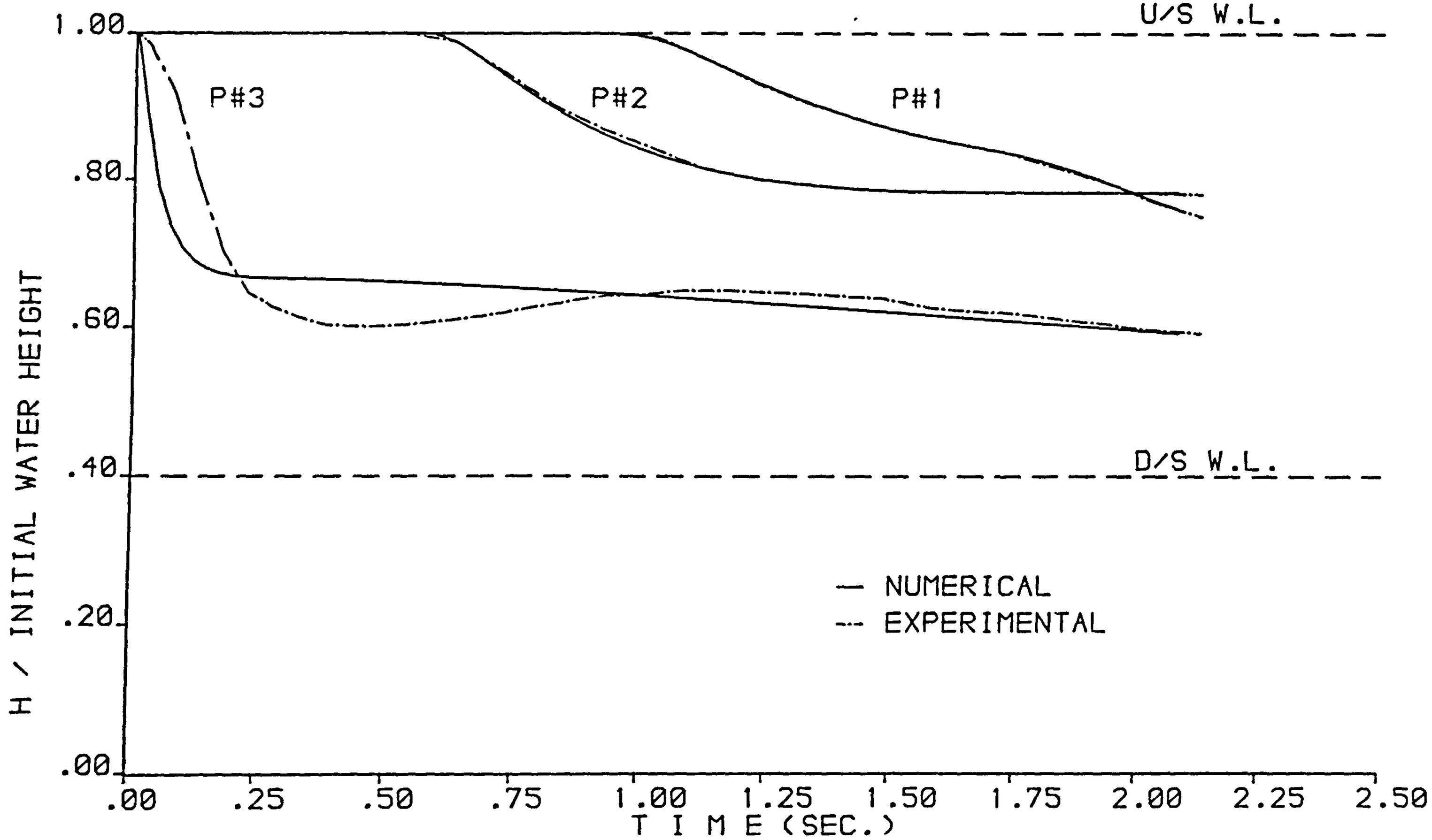

FIGURE 6.85 : NUMERICAL AND EXPERIMENTAL STAGE HYDROGRAPHS FROM THE (RT-RT) MODEL , H_1 = 15 cm AND H_o = 6 cm .

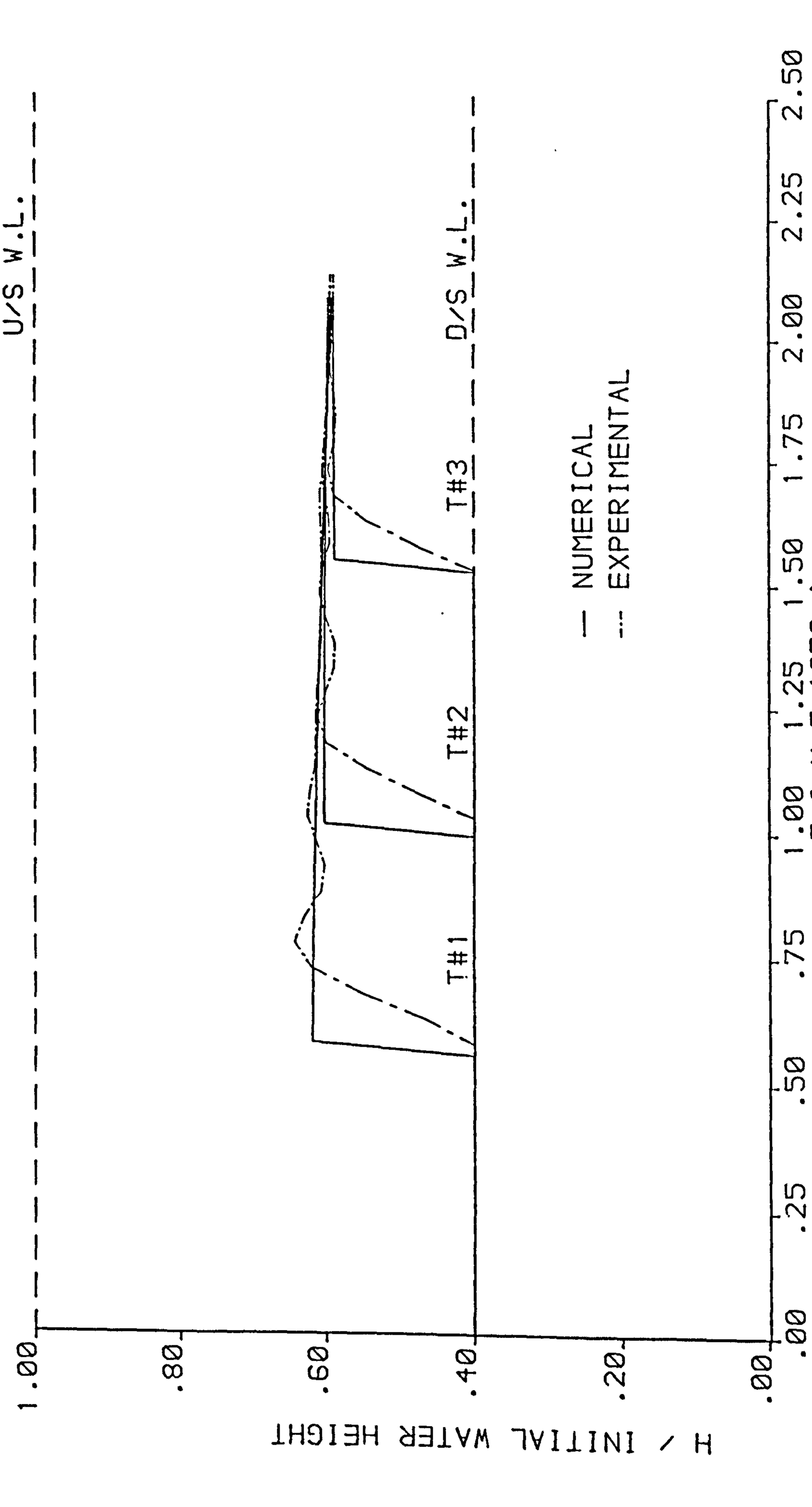

FIGURE 6.86 : NUMERICAL AND EXPERIMENTAL STAGE HYDROGRAPHS FROM THE (RT-RT) MODEL , H_1 = 15 cm AND H_o = 6 cm

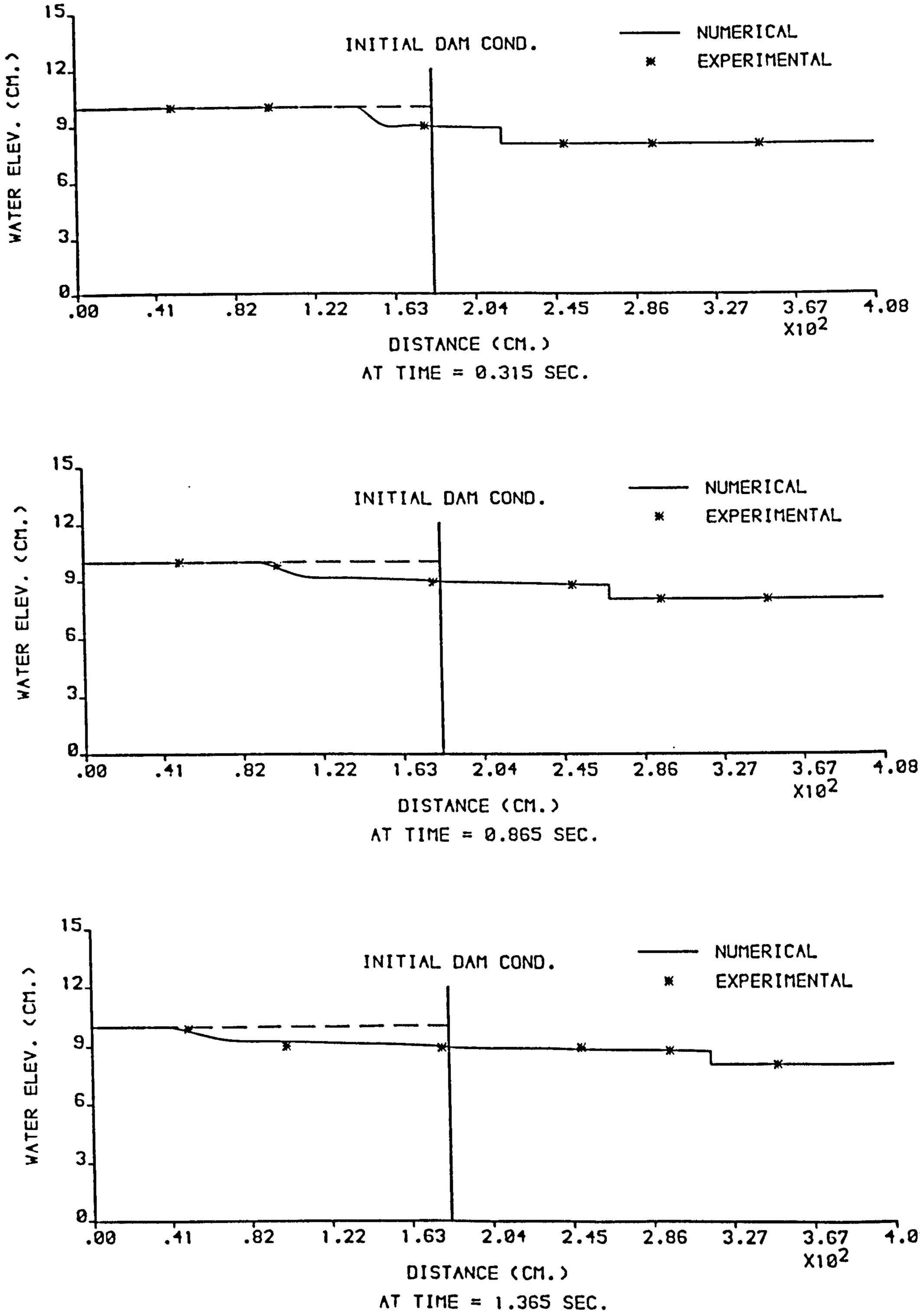

FIGURE 6.87 : NUMERICAL AND EXPERIMENTAL PROFILES FROM THE (RT-RT) MODEL , H_1 = 10 cm AND H_o = 8 cm .

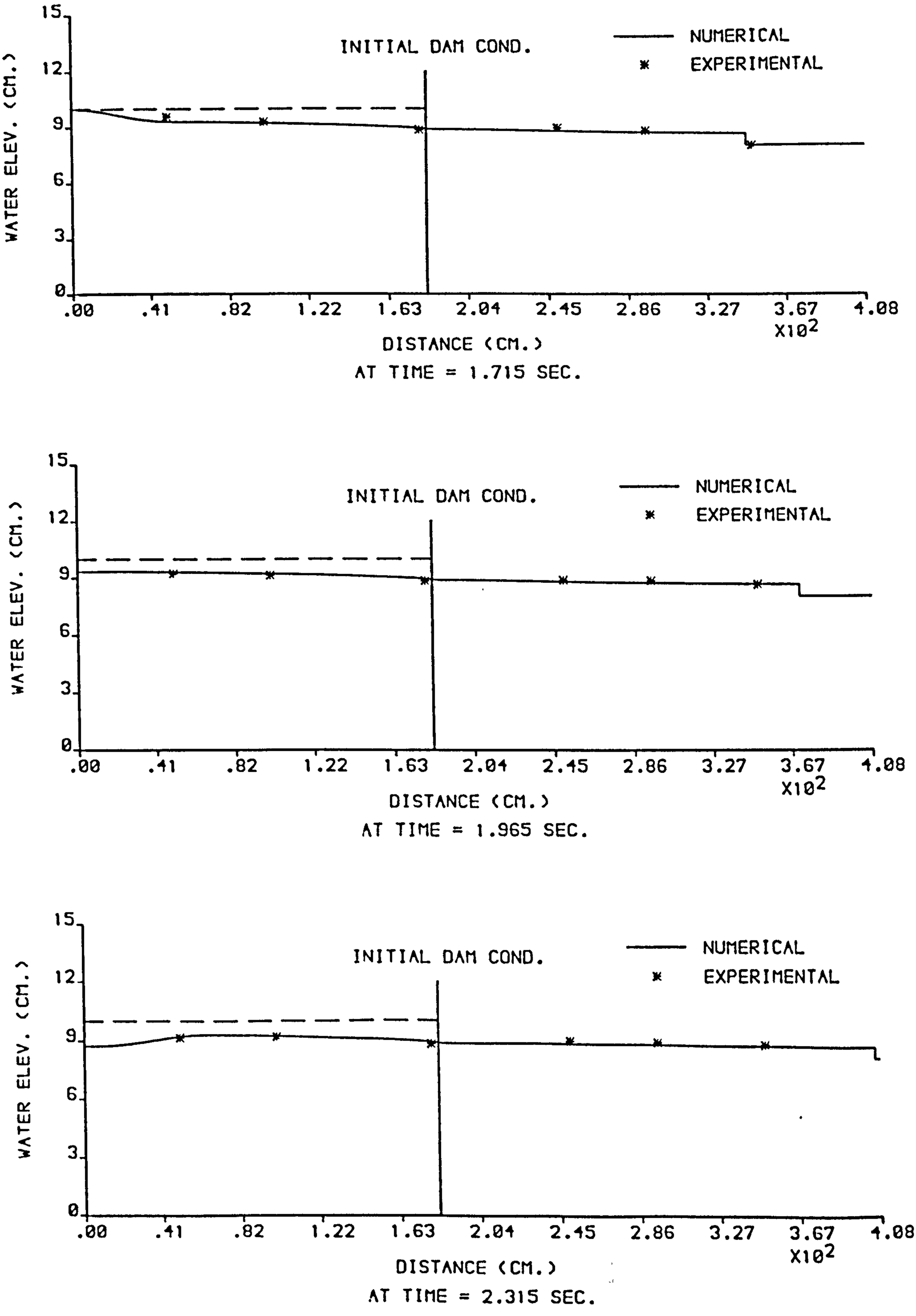

FIGURE 6.88 : NUMERICAL AND EXPERIMENTAL PROFILES FROM THE (RT-RT) MODEL , H_1 = 10 cm AND H_o = 8 cm .

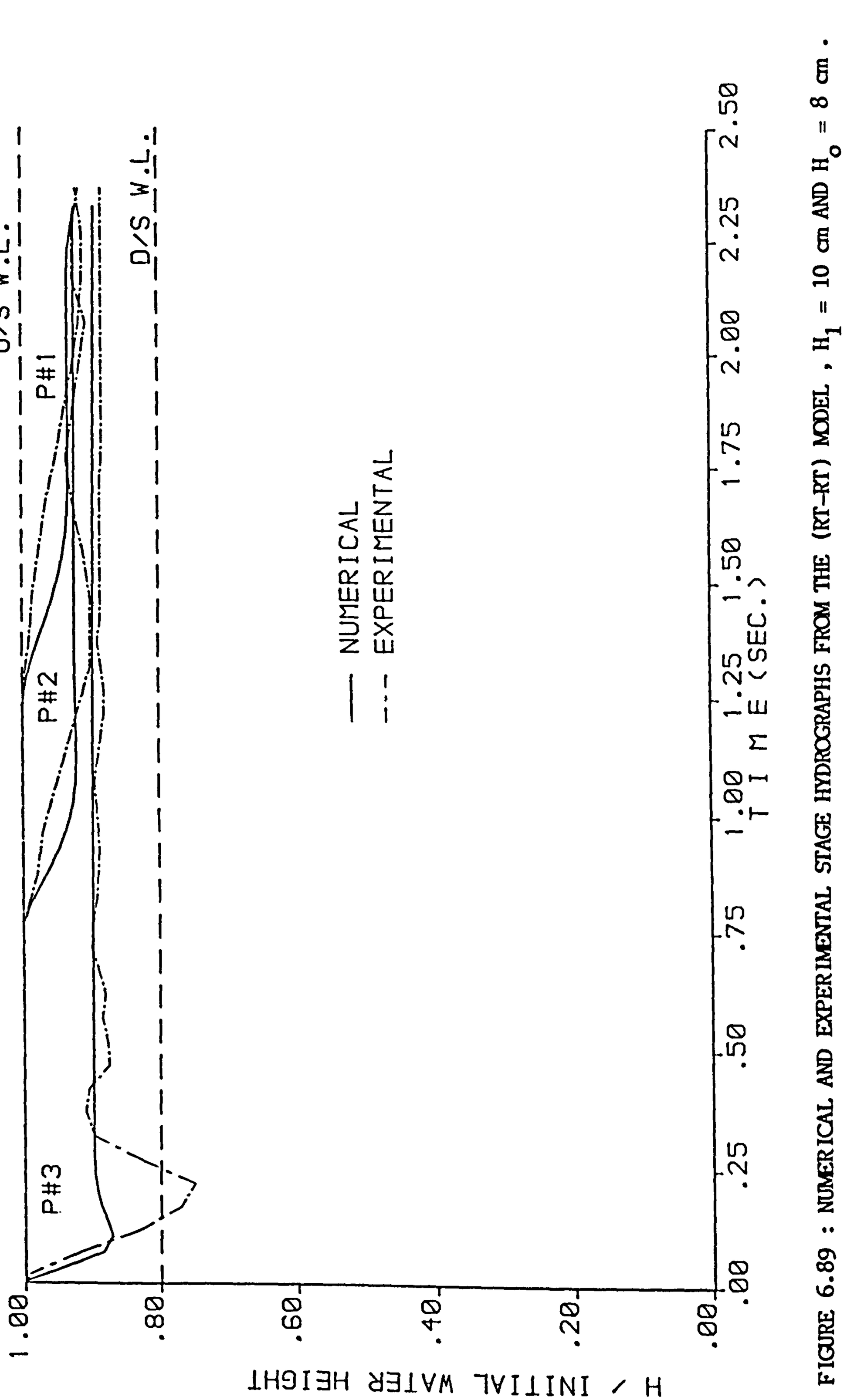

FIGURE 6.89 : NUMERICAL AND EXPERIMENTAL STAGE HYDROGRAPHS FROM THE (RT-RT) MODEL , H_1 = 10 cm AND H_o = 8 cm .

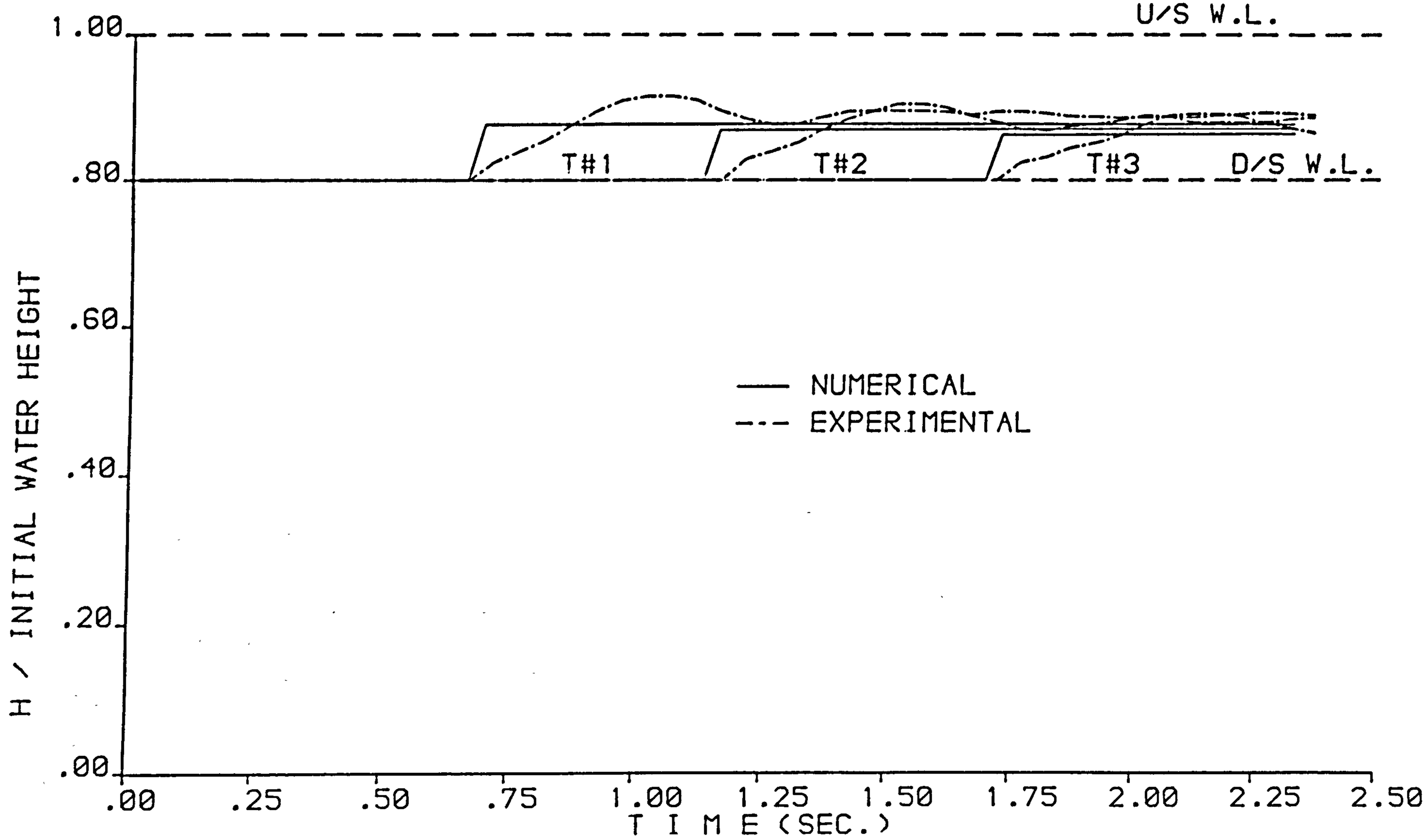

FIGURE 6.90 : NUMERICAL AND EXPERIMENTAL STAGE HYDROGRAPHS FROM THE (RT-RT) MODEL , H_1 = 10 cm AND H_o = 8 cm .

6.4 XT-RT Model

The numerical (XT-RT) model is a combination of the plain (X-T) model, with parallel sides upstream of the dam, and the radial (R-T) model, with divergent sides downstream. The assessment again begins by making a comparison of the front heights of the numerical model both with those of the physical model and with Stoker's (X-T) solution, as shown in Figure 6.91. The same ratios of (H_o/H_1) and the same initial depths upstream the dam were employed as in the previous sections. The same difference was also found as in the RT-RT model, while the front height was slightly lower (in general 2%) than the front height in the RT-RT case.

Referring to Figures 6.92 to 6.94, the same phenomena occurred as in the RT-RT model, but slightly less obviously. These phenomena are also defined in the comparisons given in each of Figures 6.95 to 6.120, having the same general differences as in the RT-RT model.

[6.5 OVERVIEW OF THE FOUR MODELS CONTINUED ON P.311
FIGURES 6.91 TO 6.120 FOLLOW DIRECTLY]

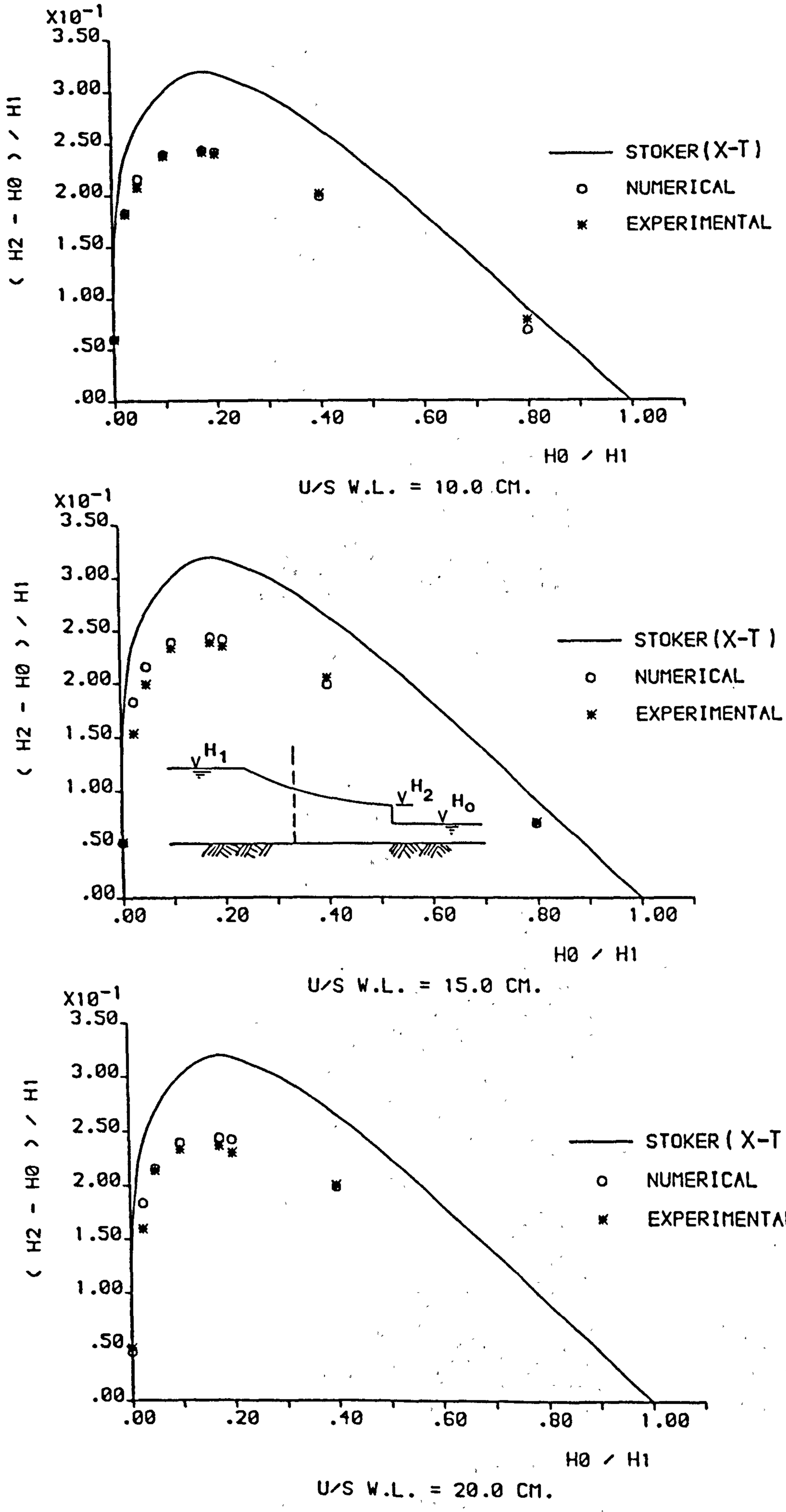

FIGURE 6.91 : COMPARISONS OF THE FRONT HEIGHTS RESULTING FROM THE (XT-RT) NUMERICAL AND PHYSICAL MODELS WITH STOKER'S (X-T) SOLUTION .

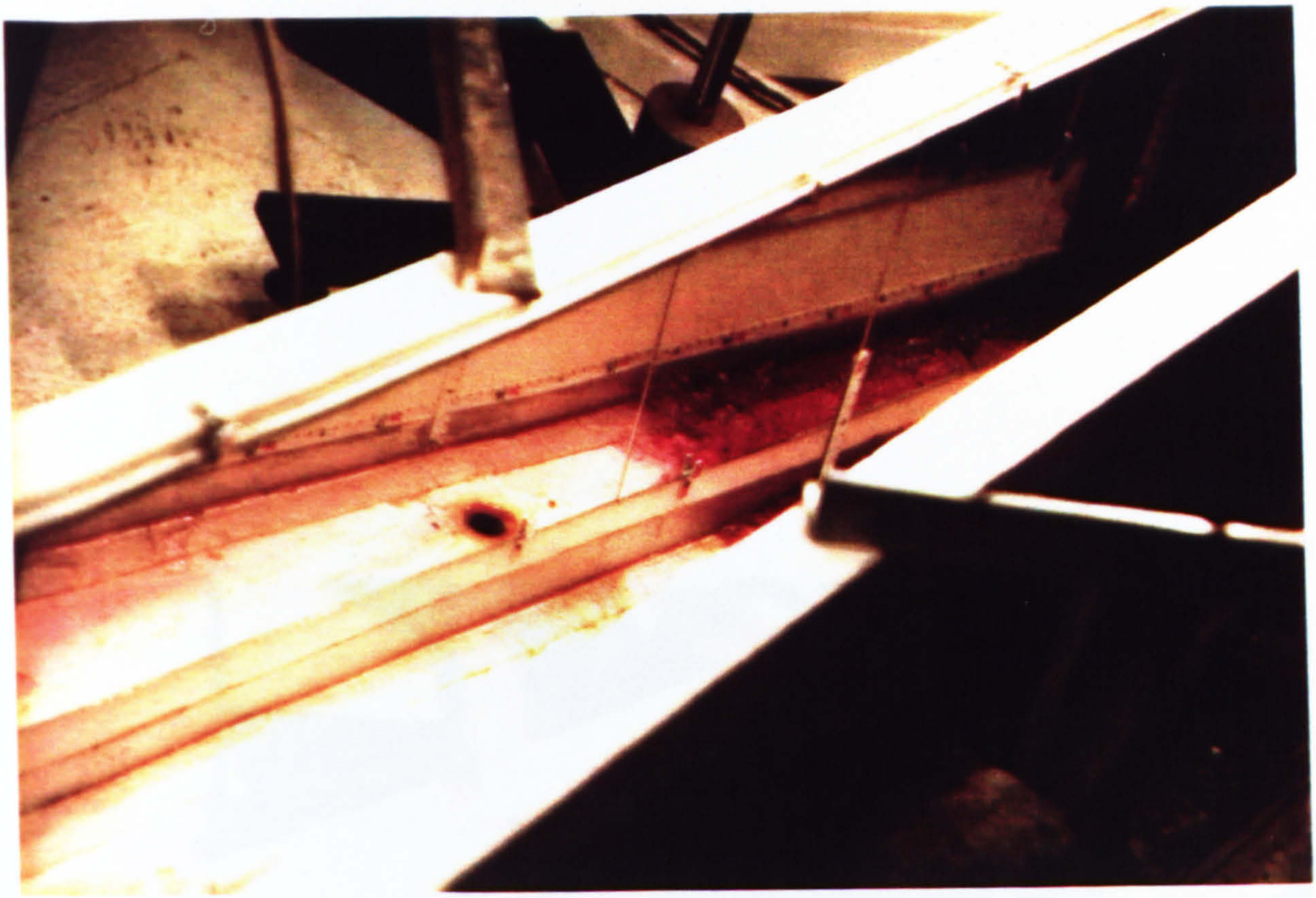

FIGURE 6.92 : PHOTOGRAPH OF THE WATER PROFILE DOWNSTREAM THE GATE IN THE (XT - RT) MODEL , H_1 = 15 cm AND H_o = DRY .

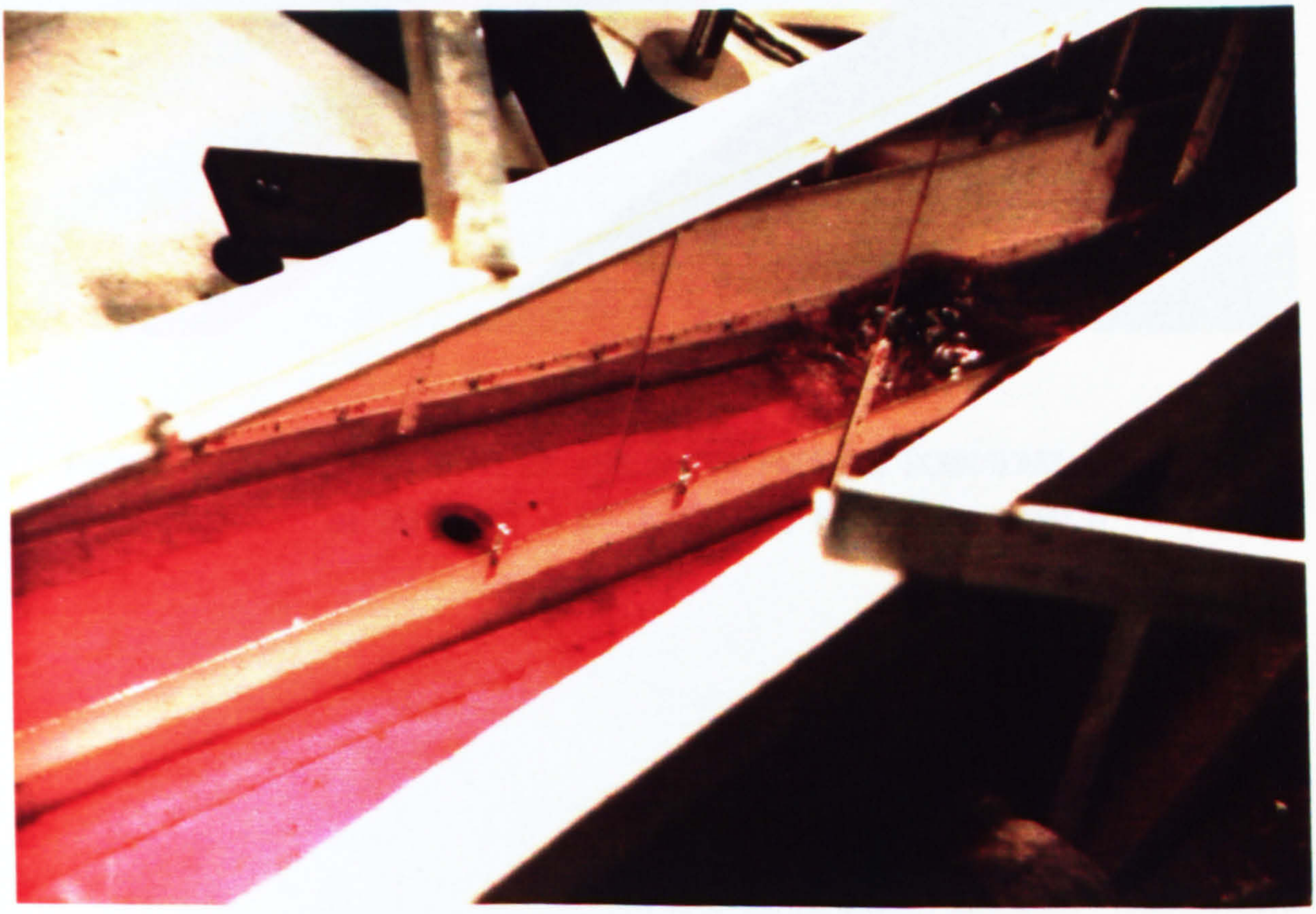

FIGURE 6.93 : PHOTOGRAPH OF THE WATER PROFILE DOWNSTREAM THE GATE IN THE (XT - RT) MODEL , H_1 = 15 cm AND H_o = 1.5 cm.

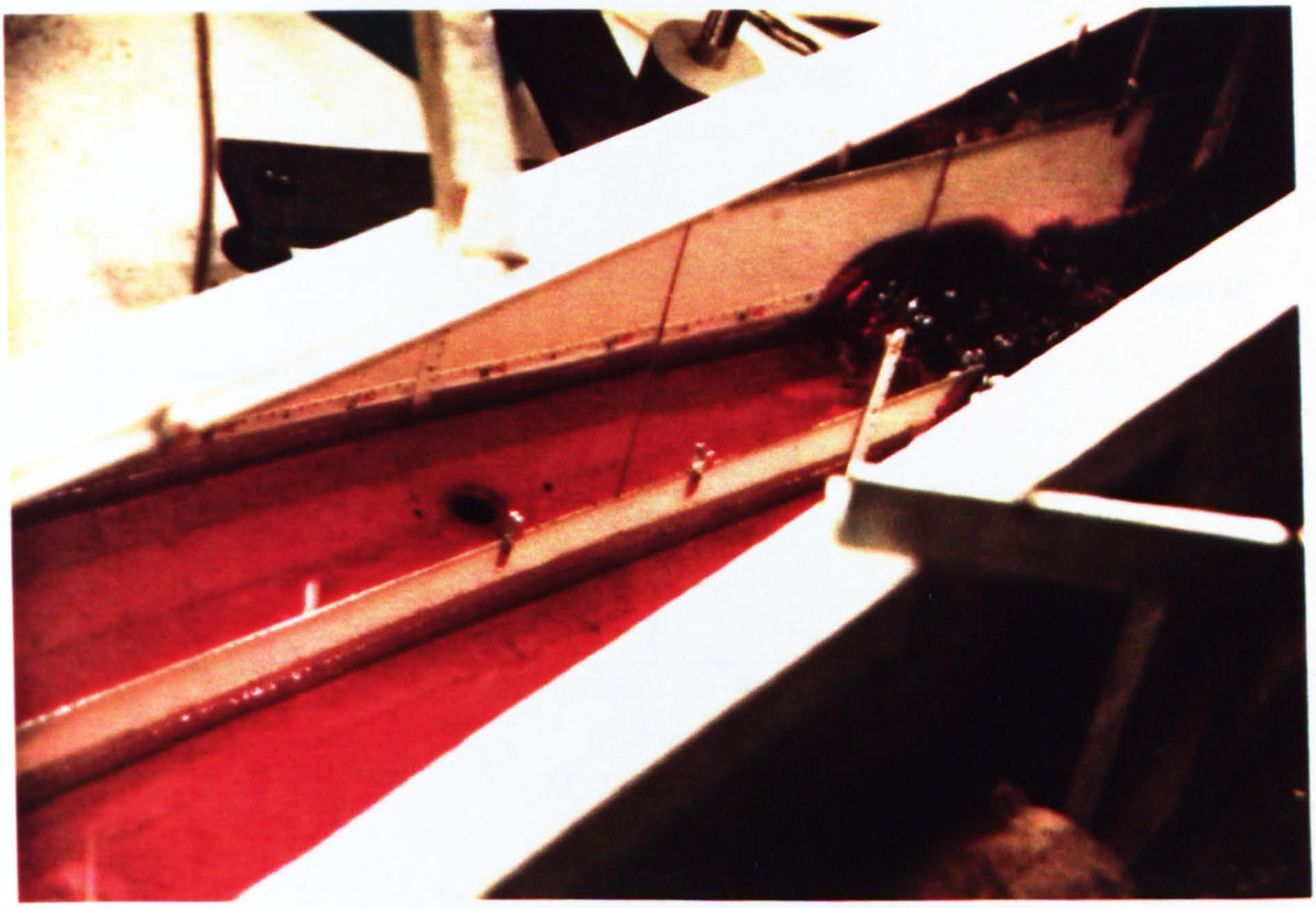

FIGURE 6.94 : PHOTOGRAPH OF THE WATER PROFILE DOWNSTREAM THE GATE IN THE (XT - RT) MODEL , H_1 = 15 cm AND H_o = 3 cm.

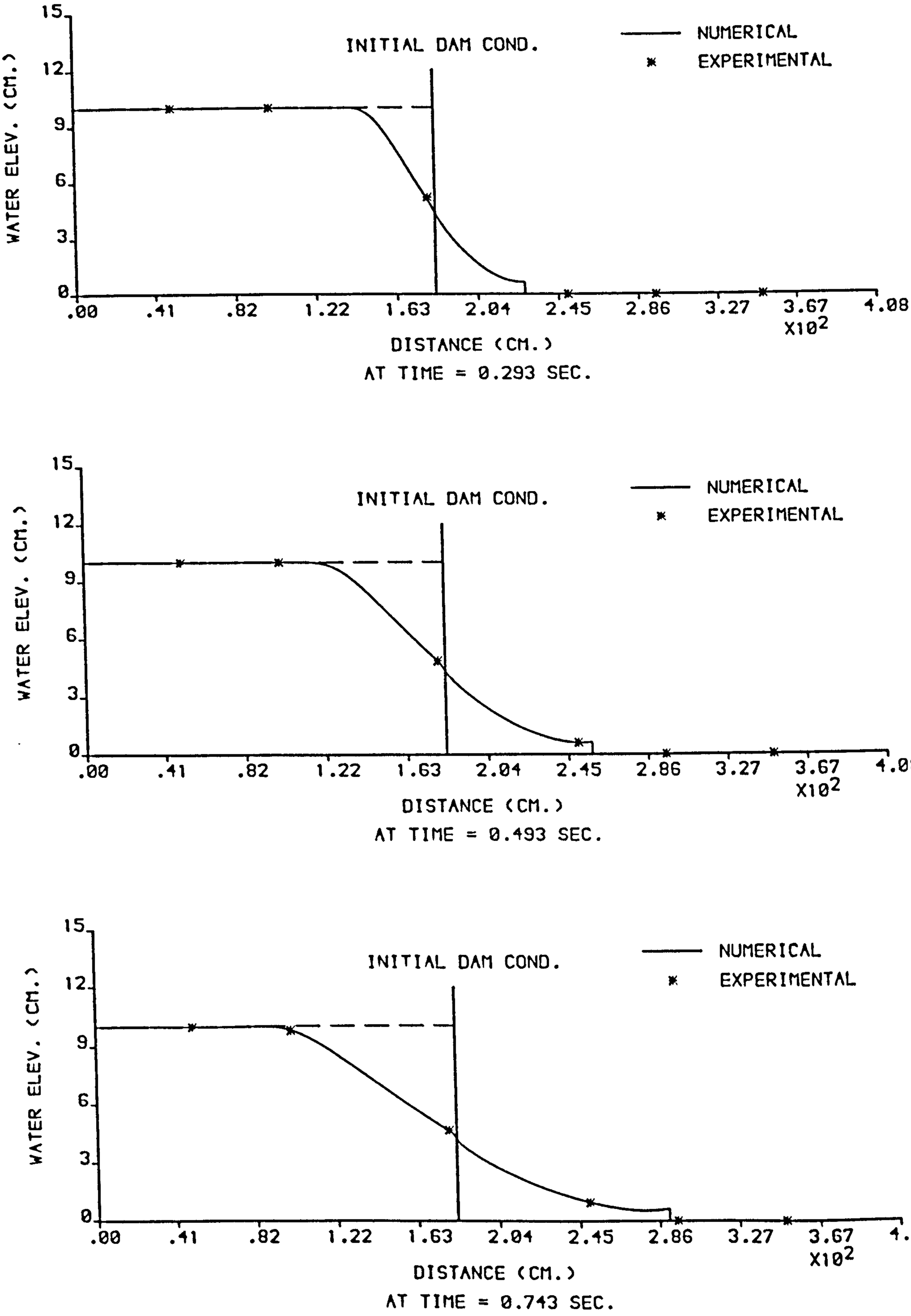

FIGURE 6.95 : NUMERICAL AND EXPERIMENTAL PROFILES FROM THE (XT-RT) MODEL , H_1 = 10 cm AND H_o = DRY .

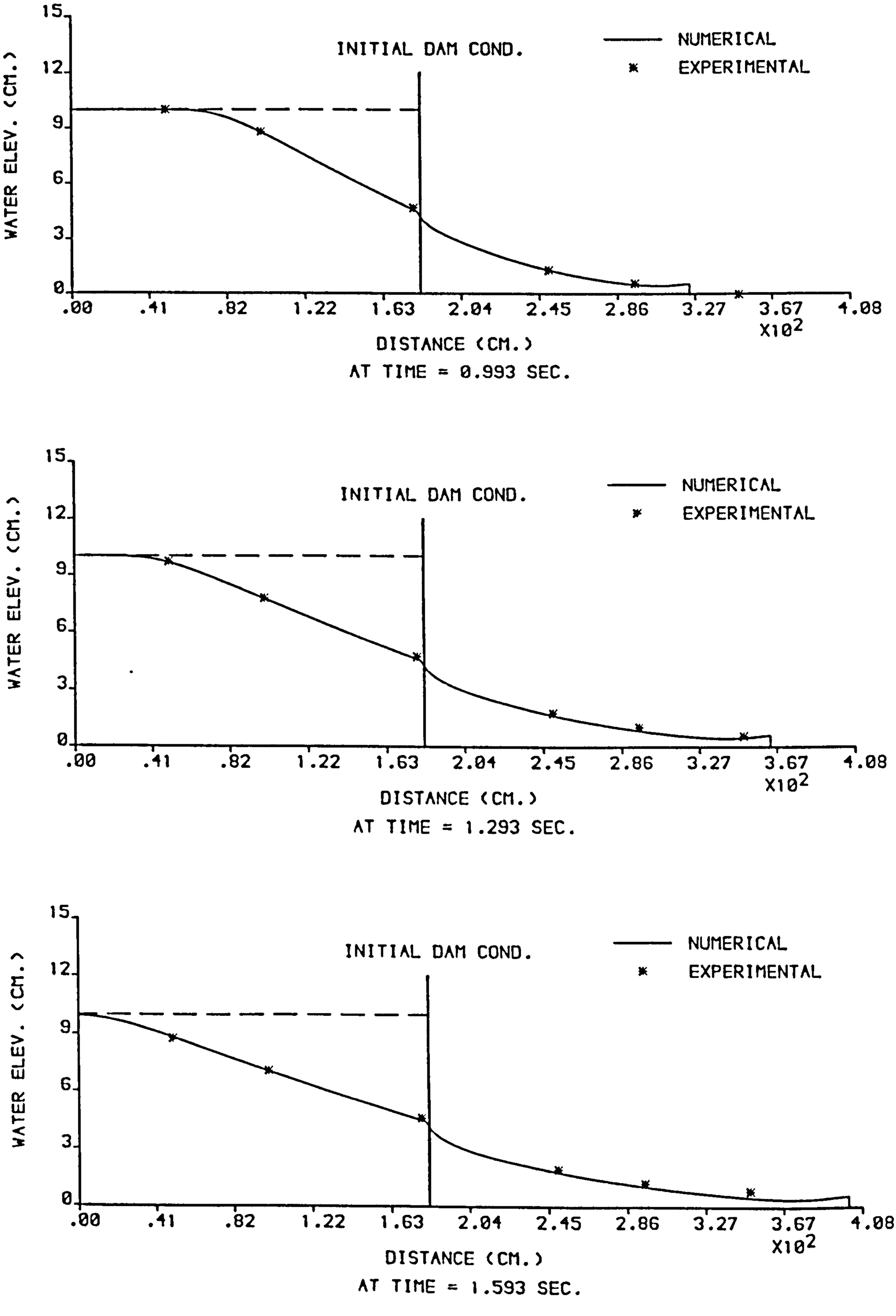

FIGURE 6.96 : NUMERICAL AND EXPERIMENTAL PROFILES FROM THE (XT-RT) MODEL , H_1 = 10 cm AND H_o = DRY .

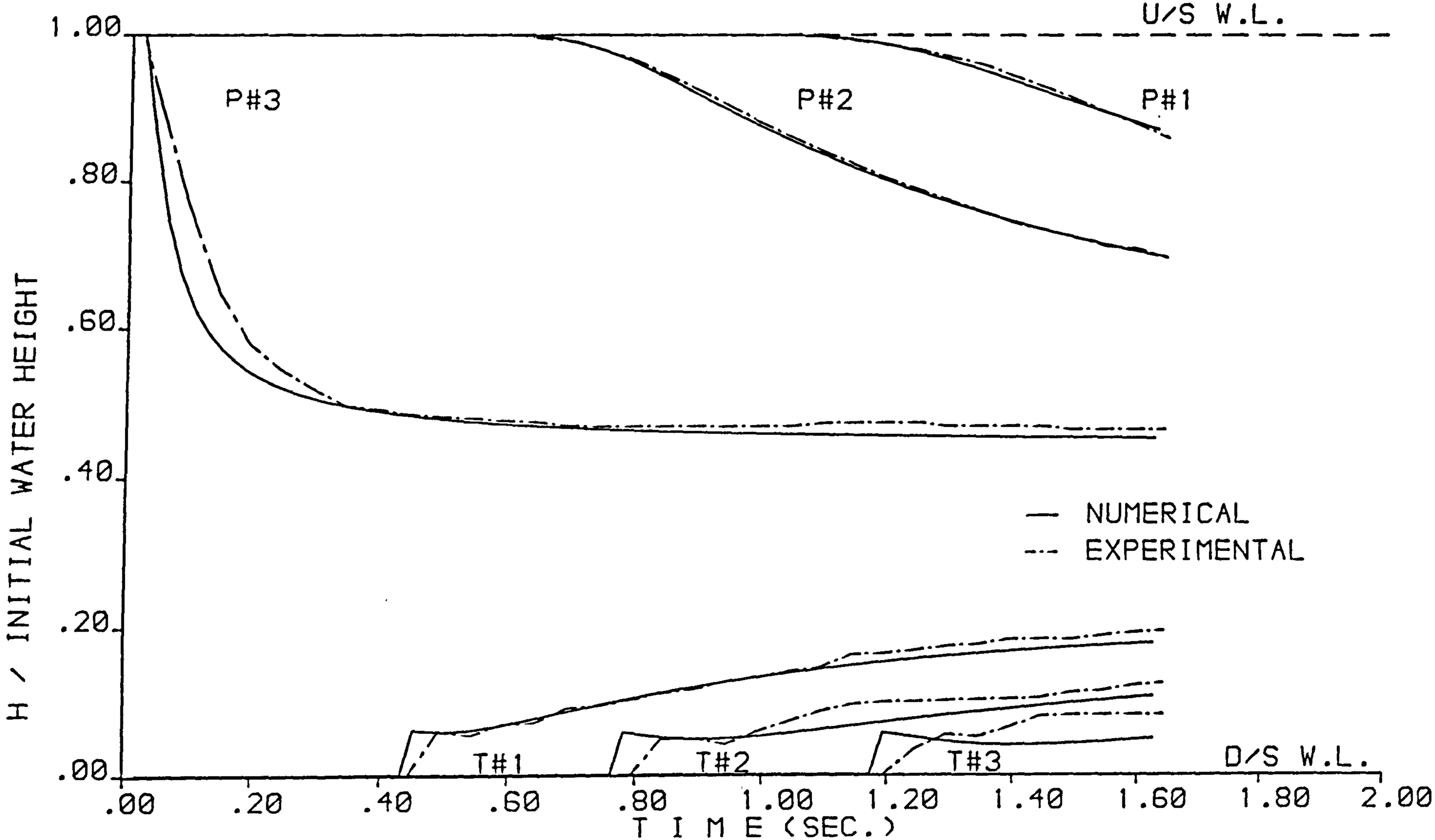

FIGURE 6.97 : NUMERICAL AND EXPERIMENTAL STAGE HYDROGRAPHS FROM THE (XT-RT) MODEL , H_1 = 10 cm AND H_o = DRY .

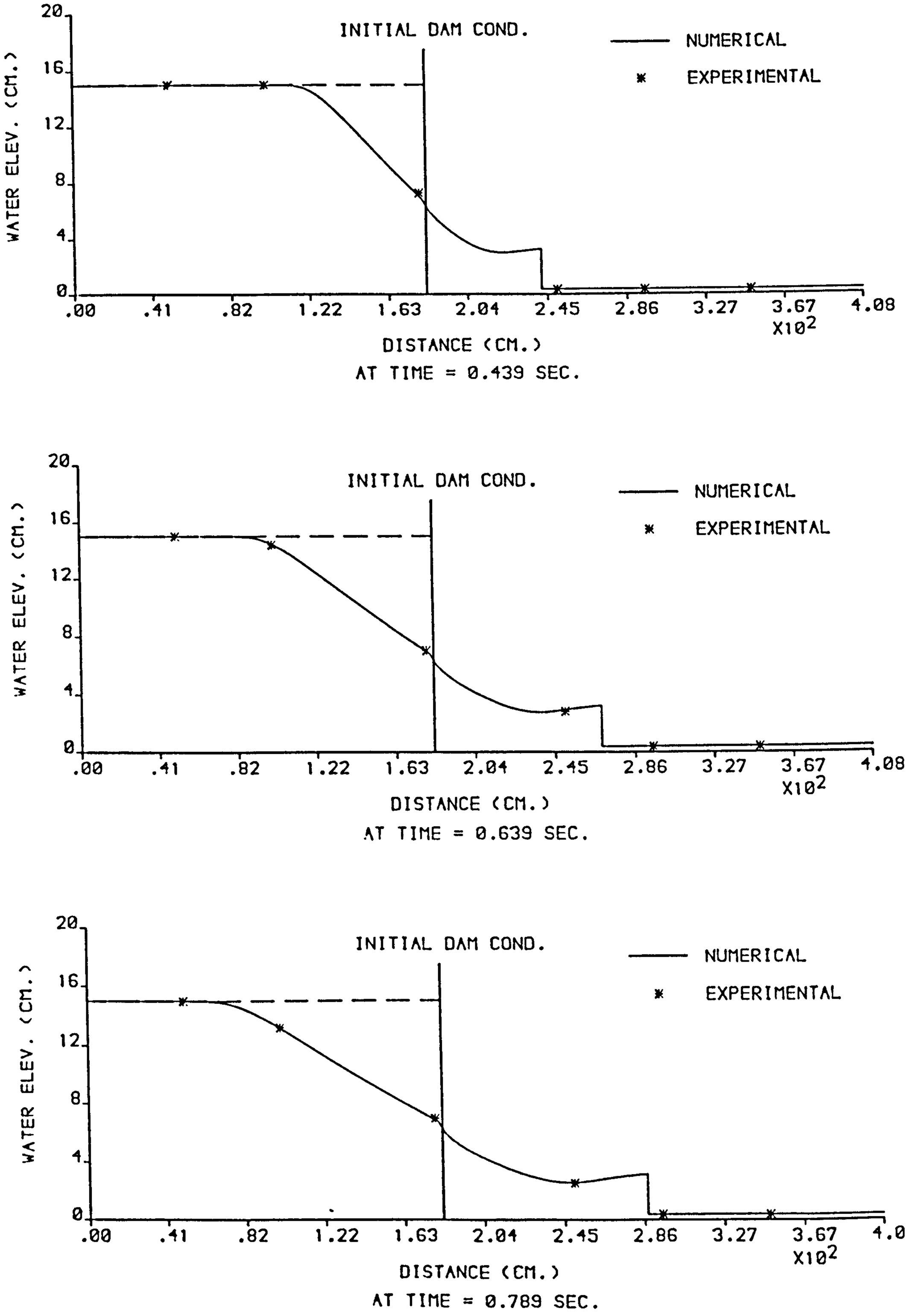

FIGURE 6.98 : NUMERICAL AND EXPERIMENTAL PROFILES FROM THE (XT–RT) MODEL , H_1 = 15 cm AND H_o = 0.375 cm .

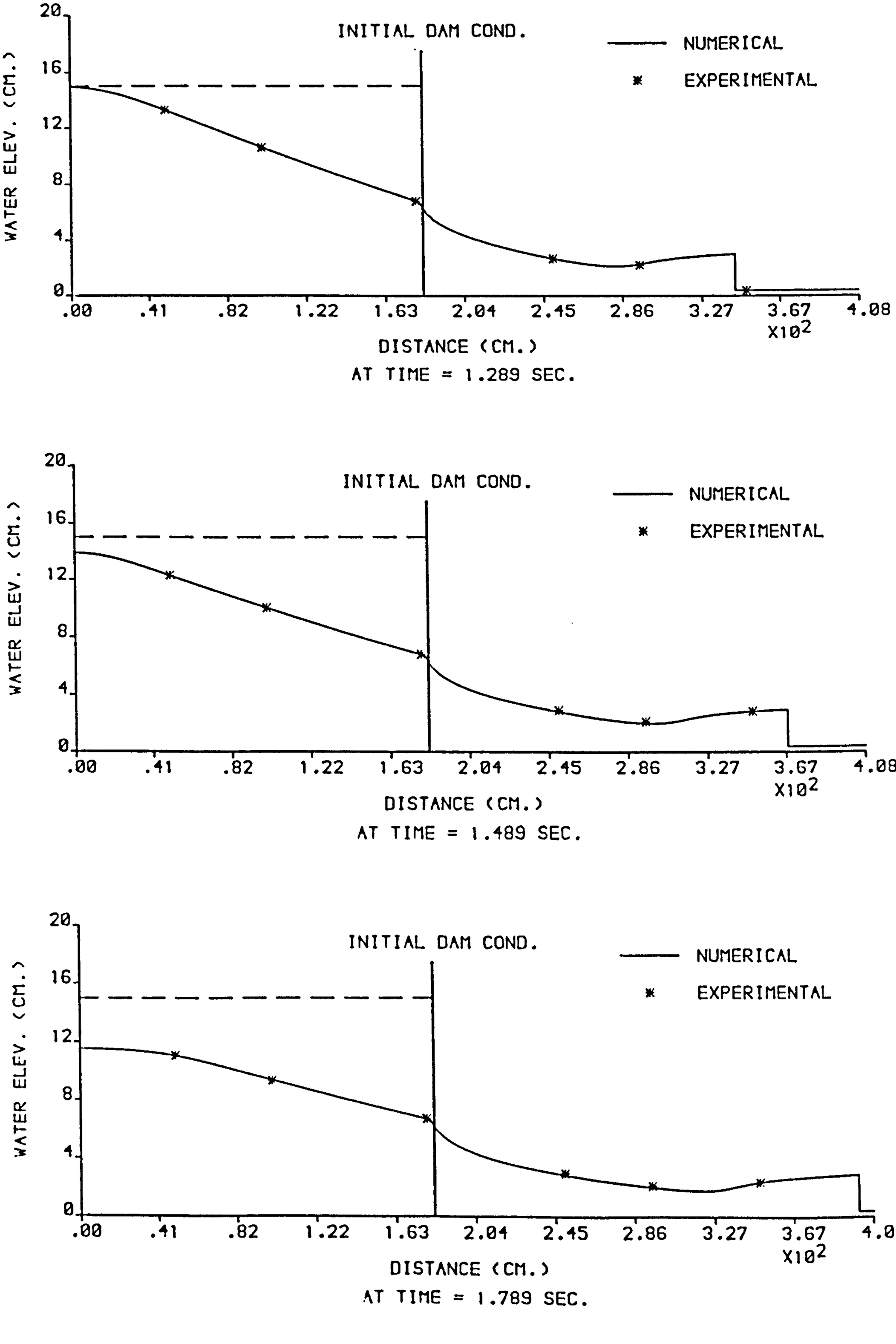

FIGURE 6.99 : NUMERICAL AND EXPERIMENTAL PROFILES FROM THE (XT-RT) MODEL , H_1 = 15 cm AND H_o = 0.375 cm .

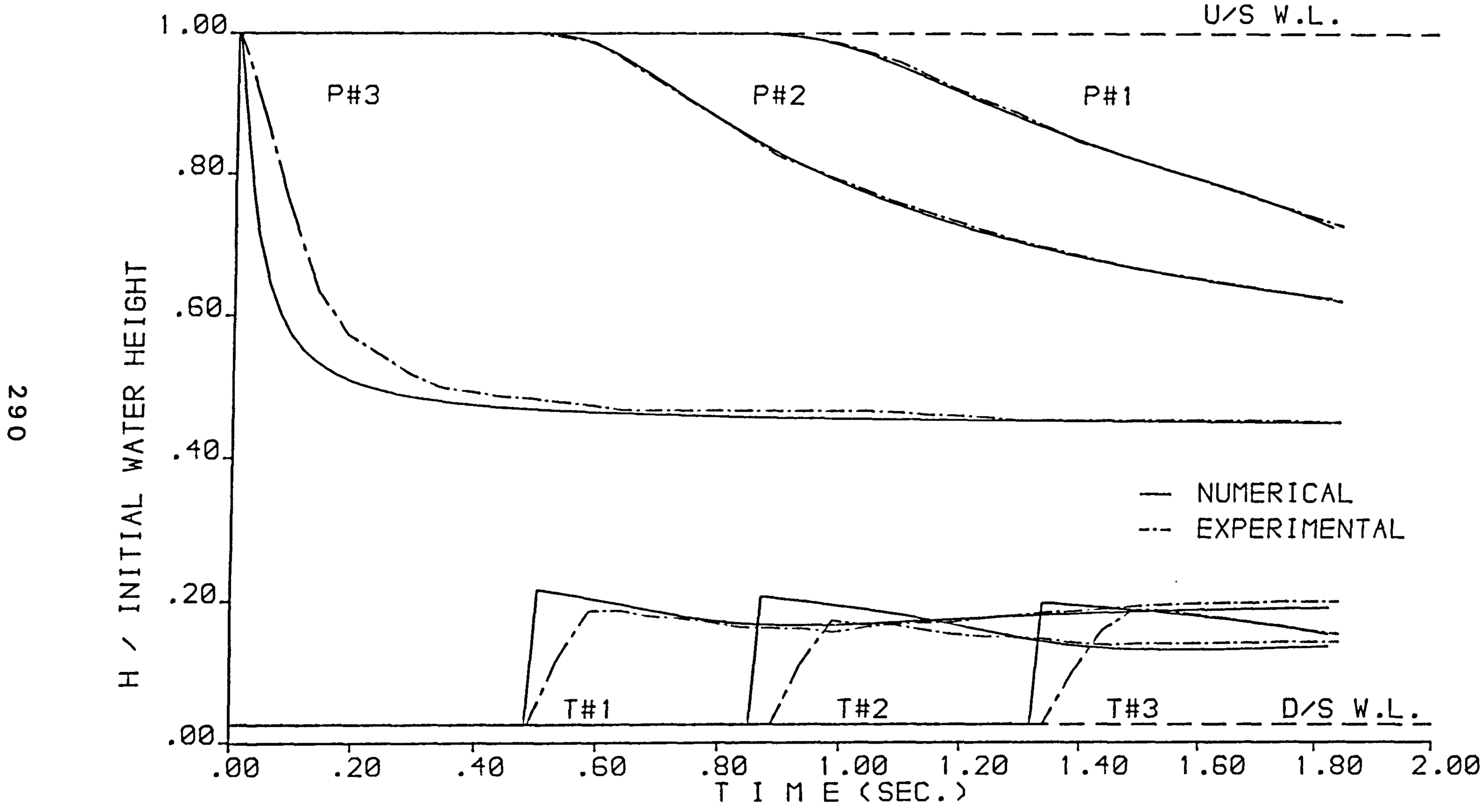

FIGURE 6.100 : NUMERICAL AND EXPERIMENTAL STAGE HYDROGRAPHS FROM THE (XT-RT) MODEL , H_1 = 15 cm AND H_o = 0.375 cm

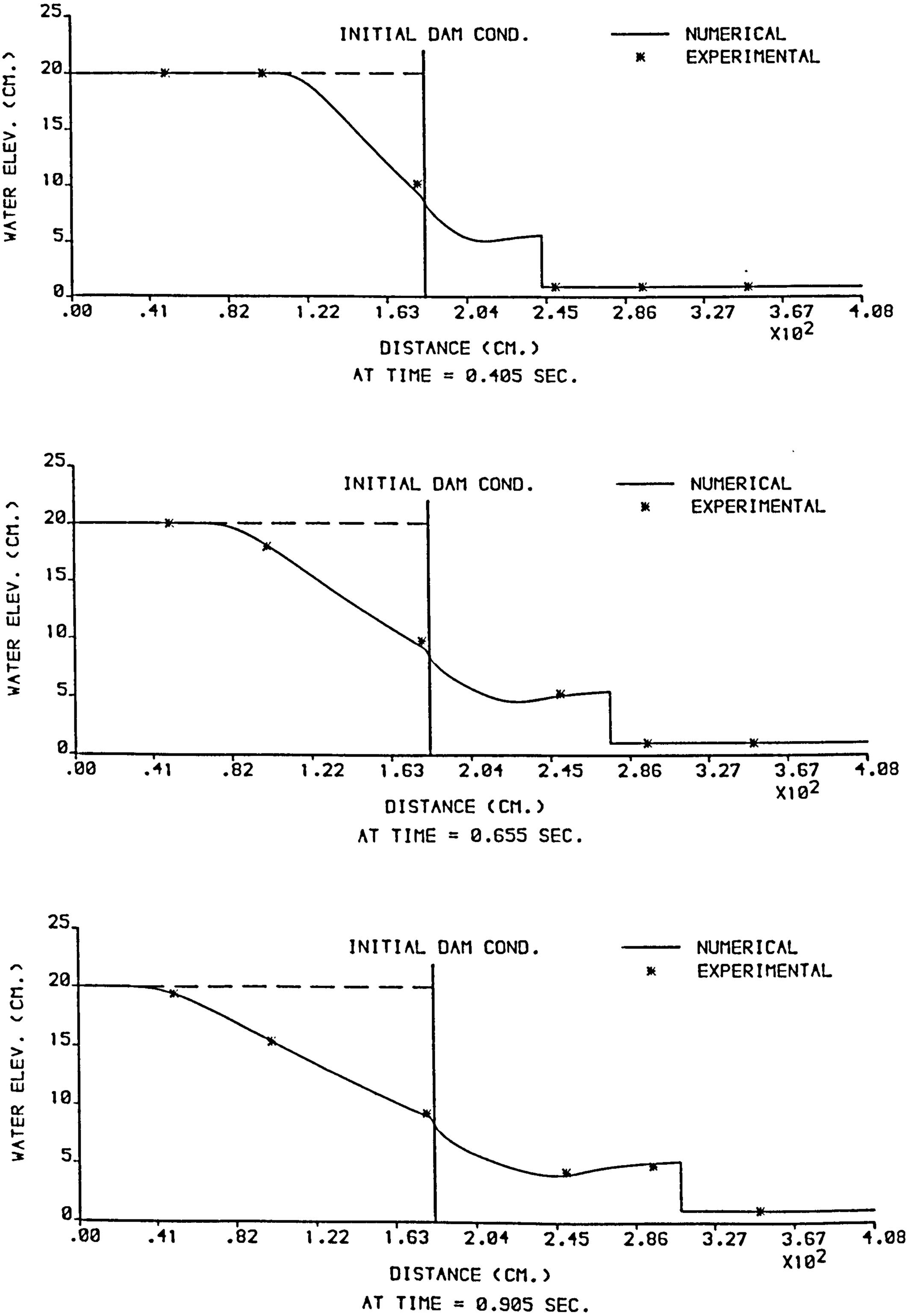

FIGURE 6.101 : NUMERICAL AND EXPERIMENTAL PROFILES FROM THE (XT-RT) MODEL , H_1 = 20 cm AND H_o = 1 cm .

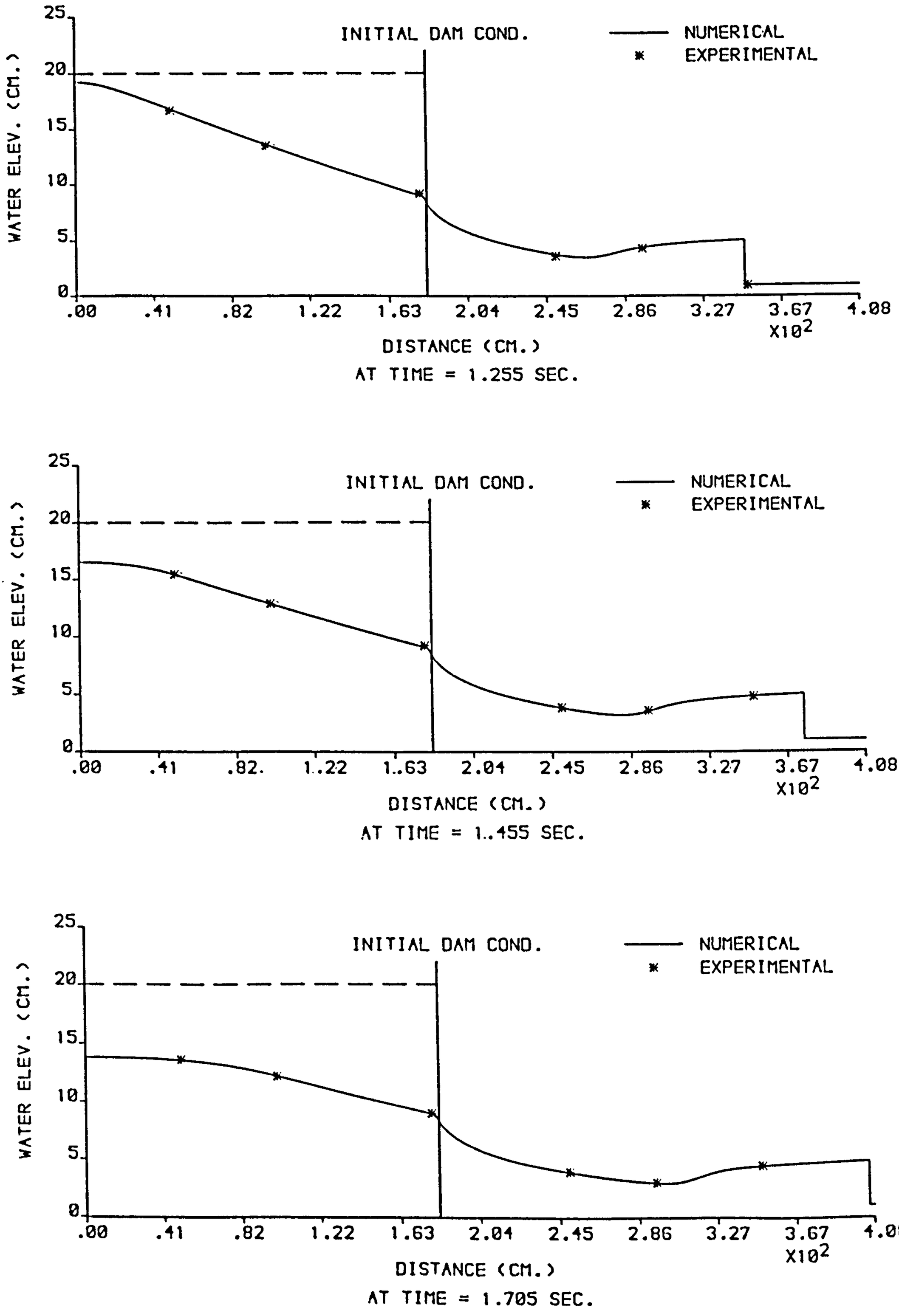

FIGURE 6.102 : NUMERICAL AND EXPERIMENTAL PROFILES FROM THE (XT-RT) MODEL , H_1 = 20 cm AND H_o = 1 cm .

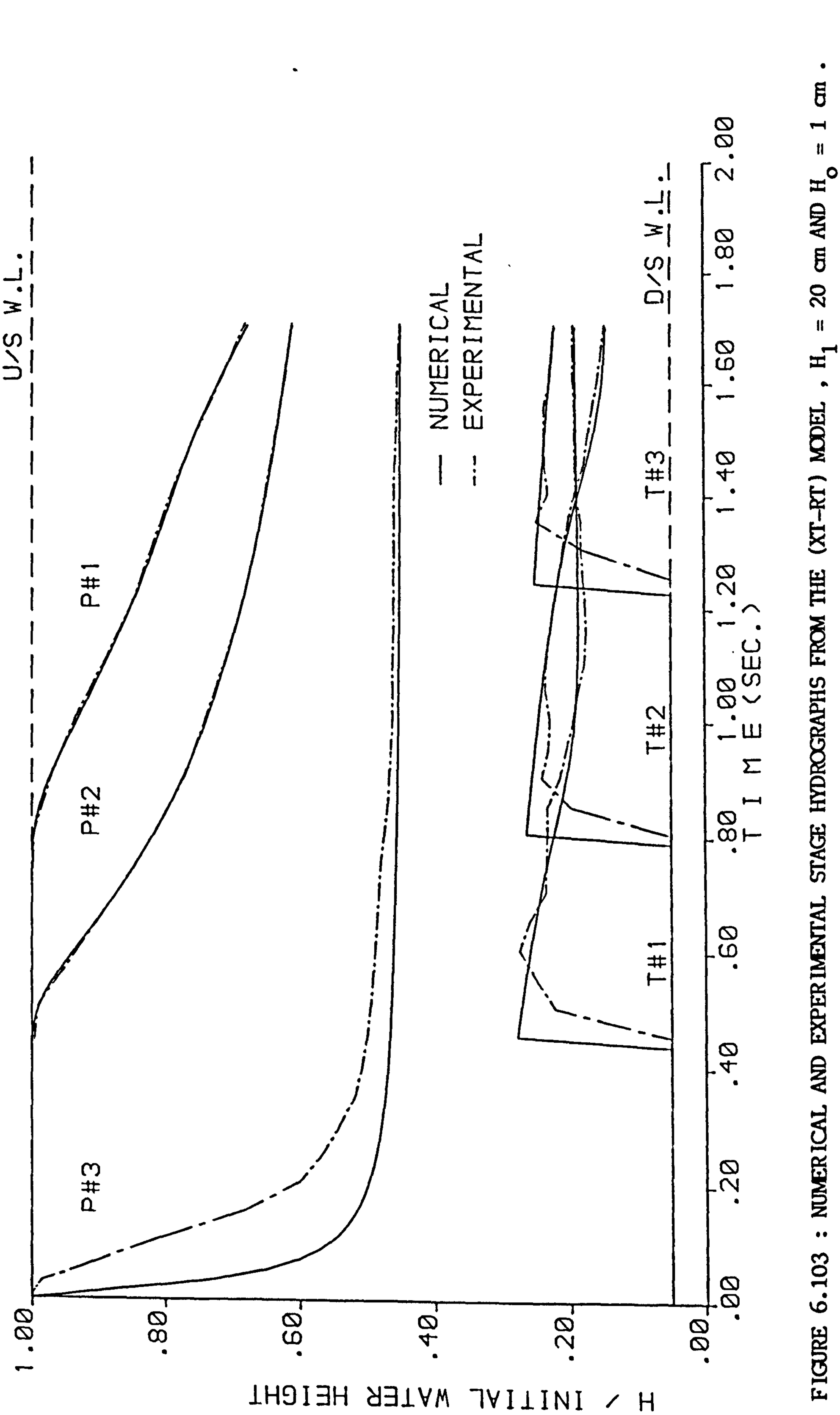

FIGURE 6.103 : NUMERICAL AND EXPERIMENTAL STAGE HYDROGRAPHS FROM THE (XT-RT) MODEL , H_1 = 20 cm AND H_o = 1 cm .

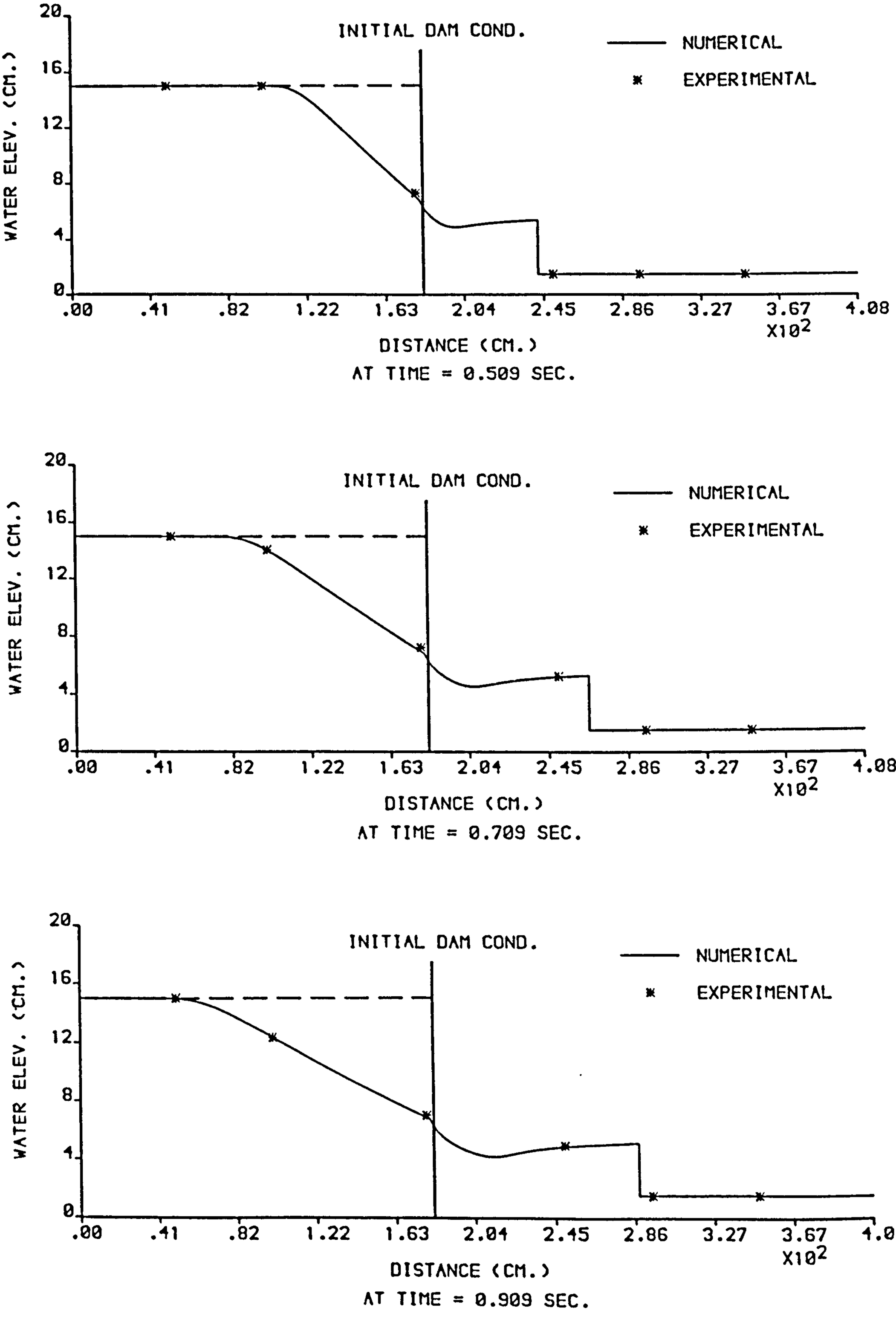

FIGURE 6.104 : NUMERICAL AND EXPERIMENTAL PROFILES FROM THE (XT-RT) MODEL , H_1 = 15 cm AND H_o = 1.5 cm .

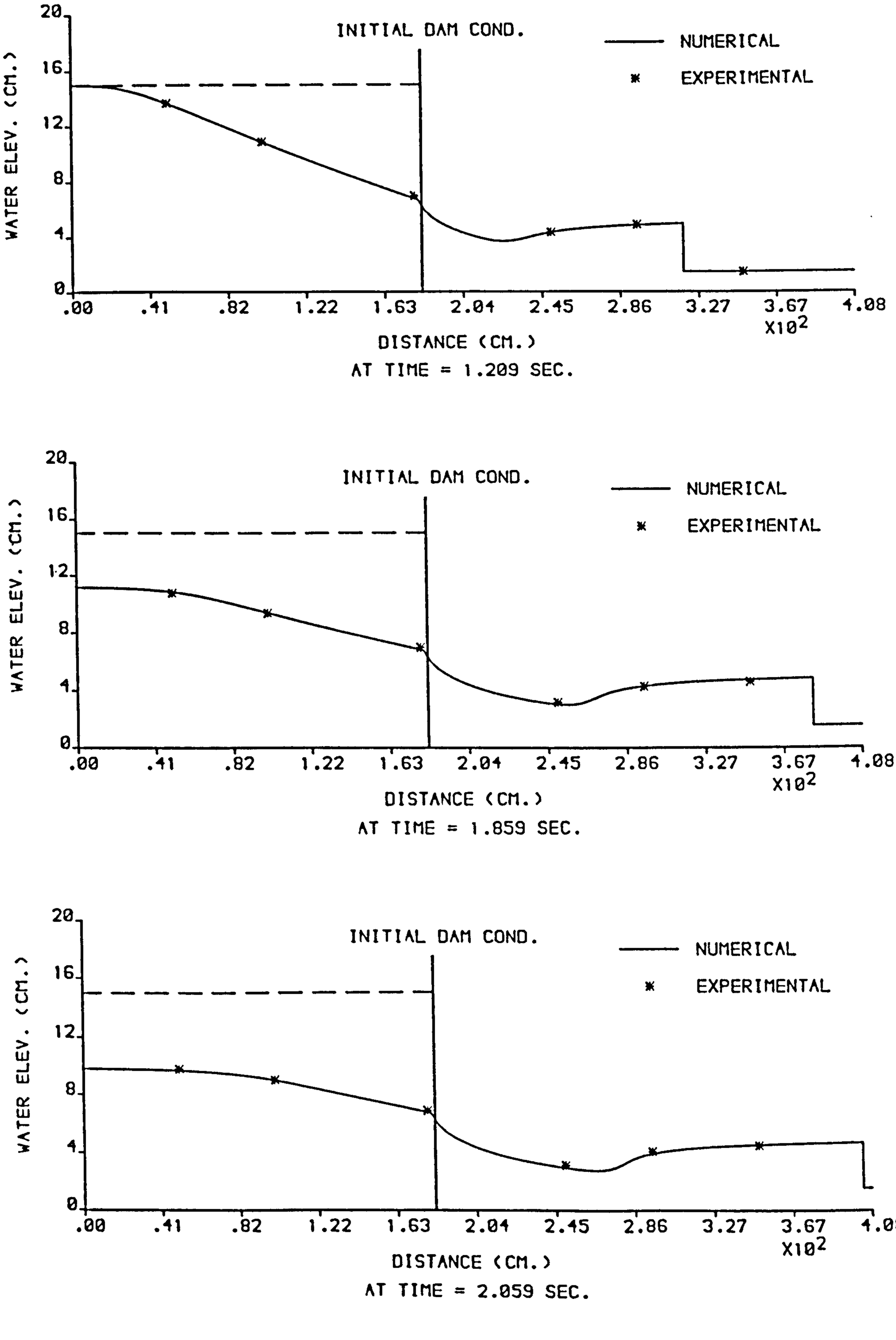

FIGURE 6.105 : NUMERICAL AND EXPERIMENTAL PROFILES FROM THE (XT-RT) MODEL , H_1 = 15 cm AND H_o = 1.5 cm .

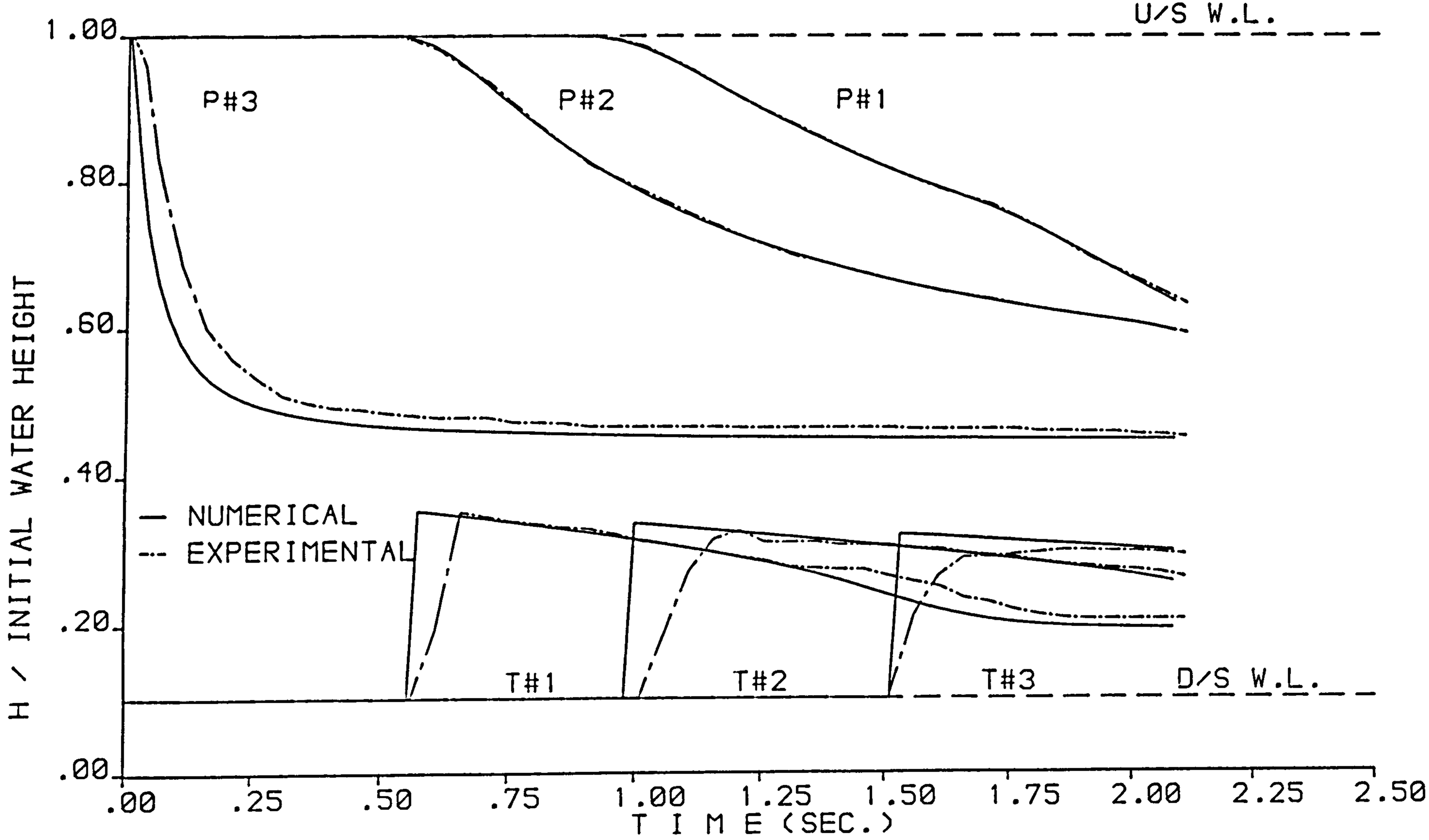

FIGURE 6.106 : NUMERICAL AND EXPERIMENTAL STAGE HYDROGRAPHS FROM THE (XT-RT) MODEL , H_1 = 15 cm AND H_o = 1.5 cm .

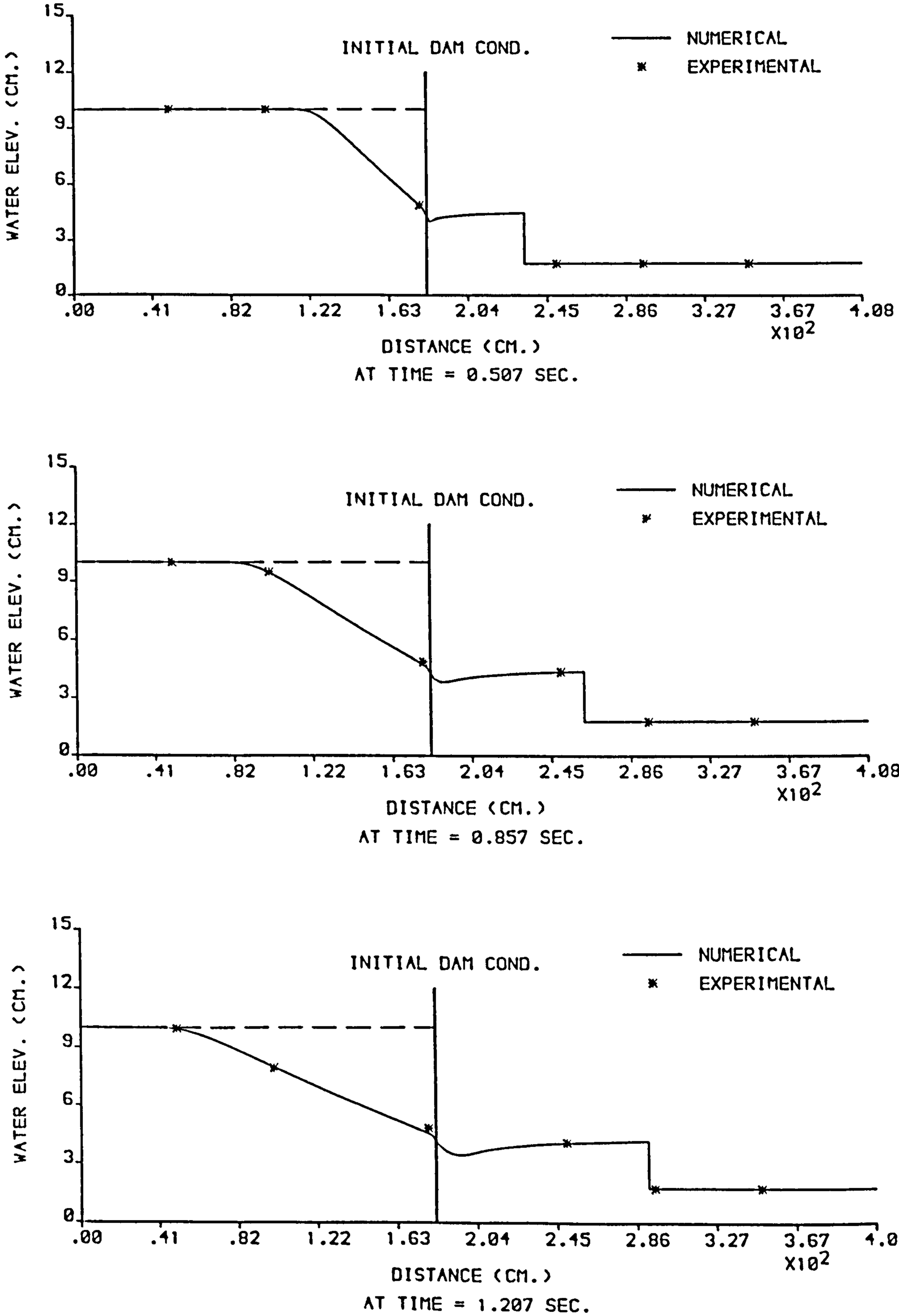

FIGURE 6.107 : NUMERICAL AND EXPERIMENTAL PROFILES FROM THE (XT-RT) MODEL , H_1 = 10 cm AND H_o = 1.76 cm .

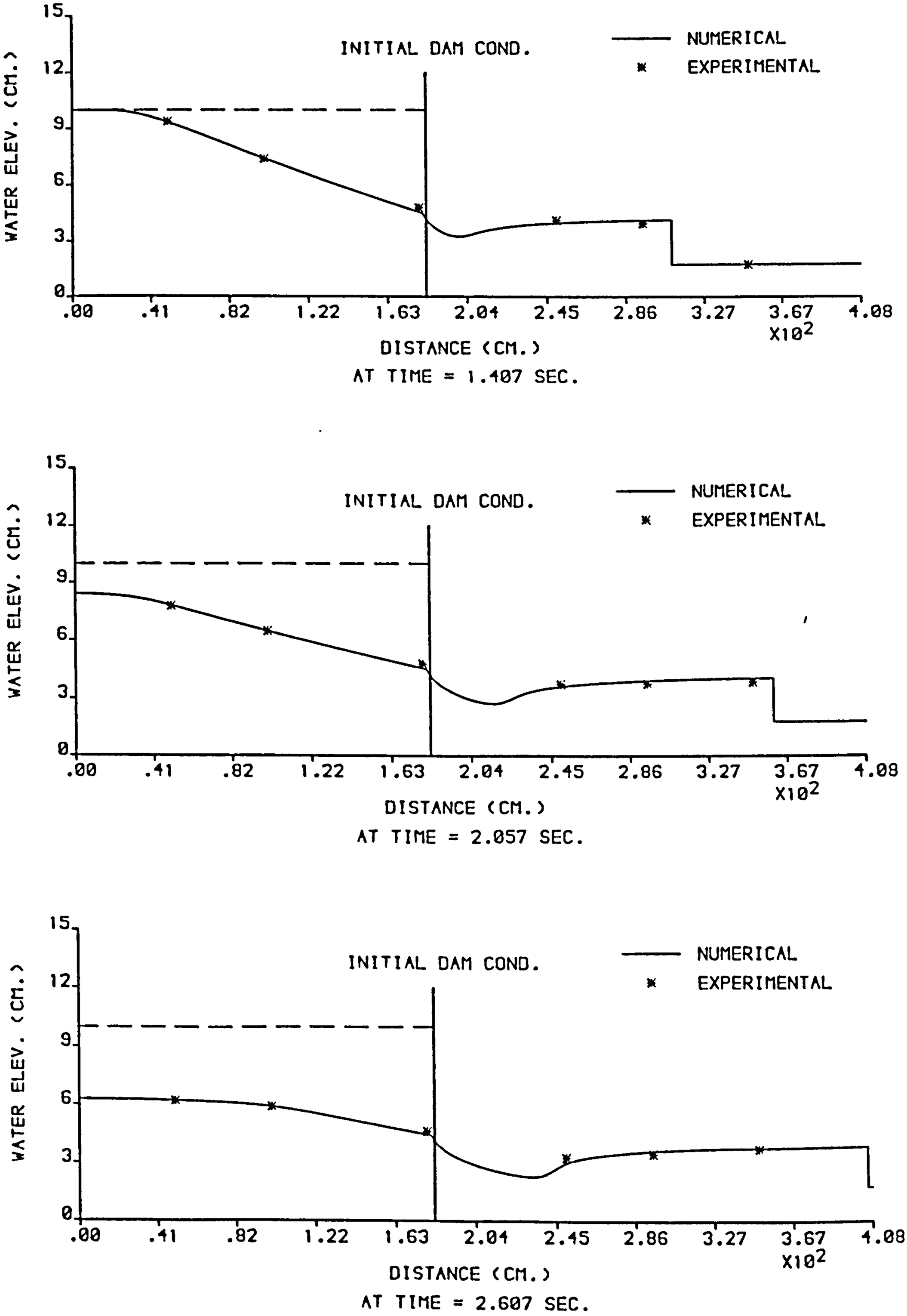

FIGURE 6.108 : NUMERICAL AND EXPERIMENTAL PROFILES FROM THE (XT-RT) MODEL , H_1 = 10 cm AND H_o = 1.76 cm .

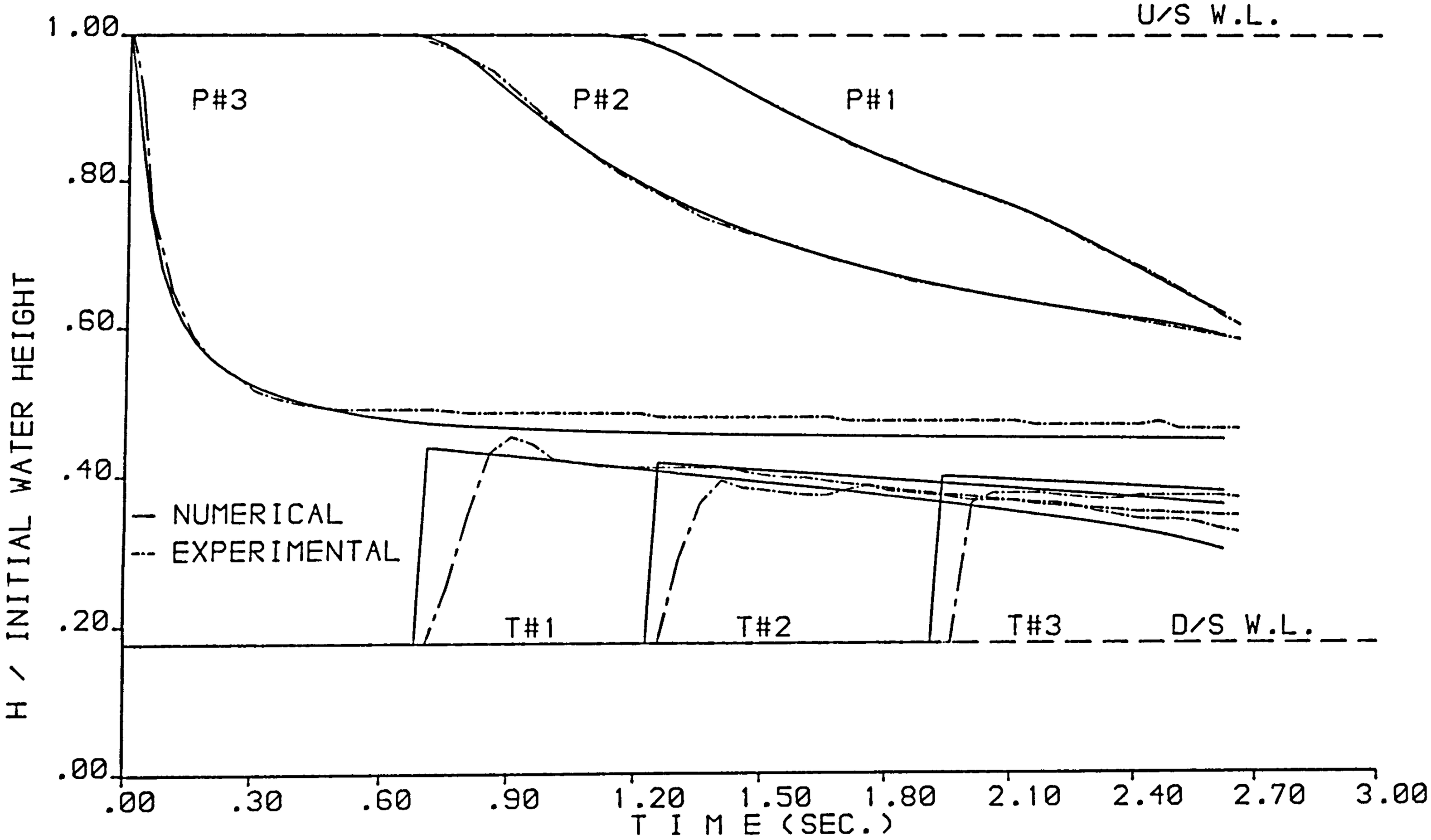

FIGURE 6.109 : NUMERICAL AND EXPERIMENTAL STAGE HYDROGRAPHS FROM THE (XT-RT) MODEL , H_1 = 10 cm AND H_o = 1.76 cm .

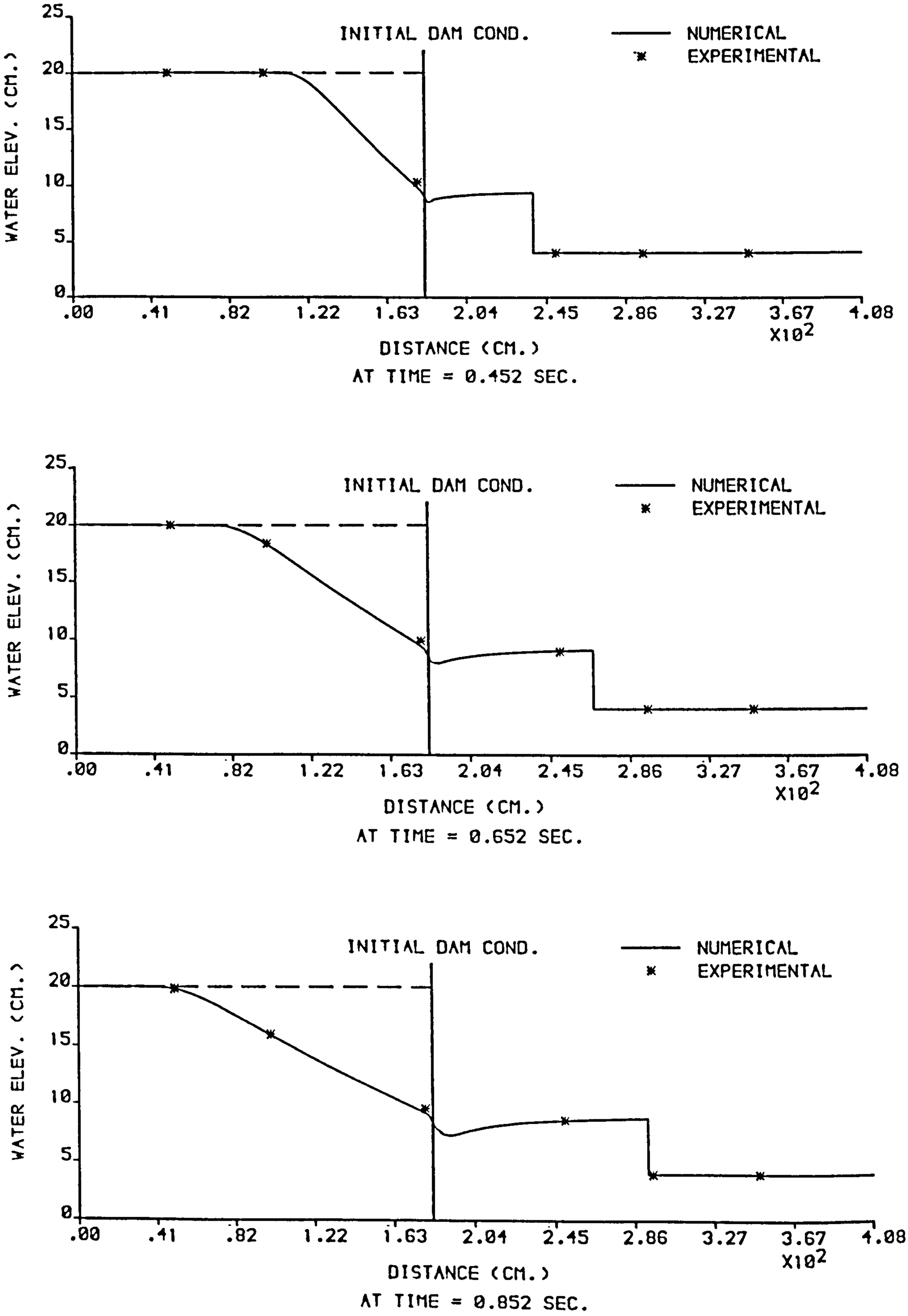

FIGURE 6.110 : NUMERICAL AND EXPERIMENTAL PROFILES FROM THE (XT-RT) MODEL , H_1 = 20 cm AND H_o = 4 cm .

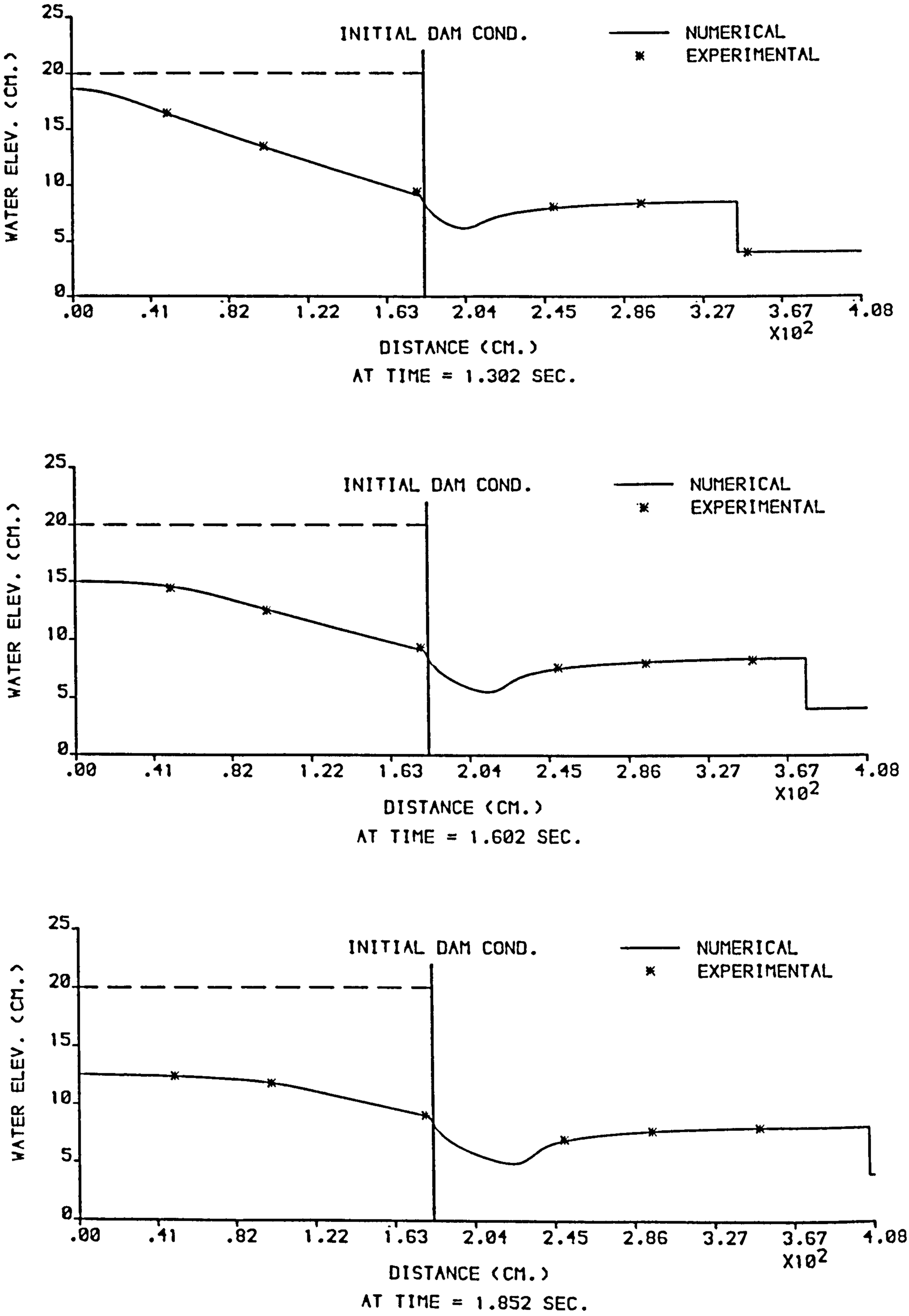

FIGURE 6.111 : NUMERICAL AND EXPERIMENTAL PROFILES FROM THE (XT-RT) MODEL , H_1 = 20 cm AND H_o = 4 cm .

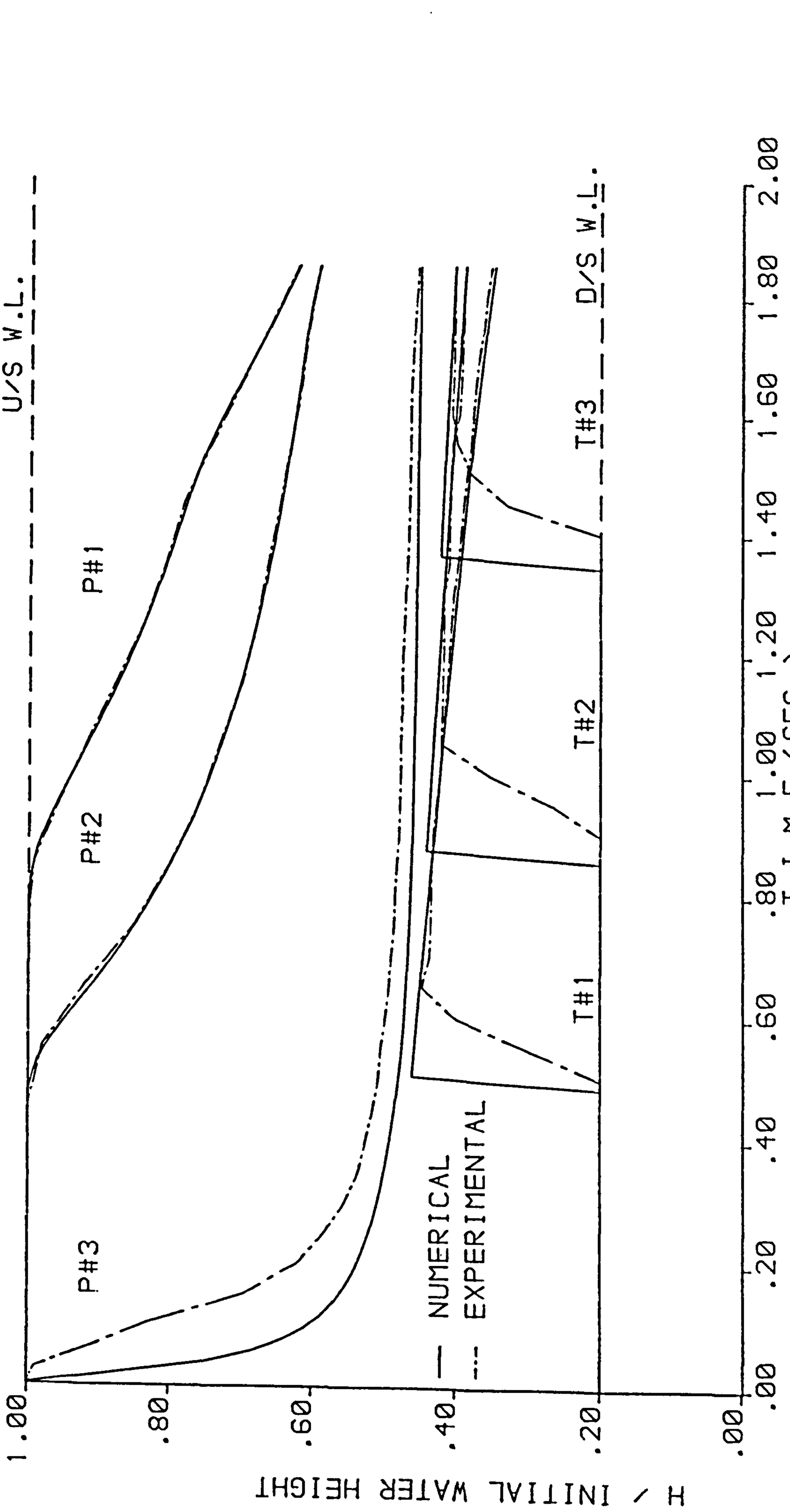

FIGURE 6.112 : NUMERICAL AND EXPERIMENTAL STAGE HYDROGRAPHS FROM THE (XT-RT) MODEL , H_1 = 20 cm AND H_o = 4 cm .

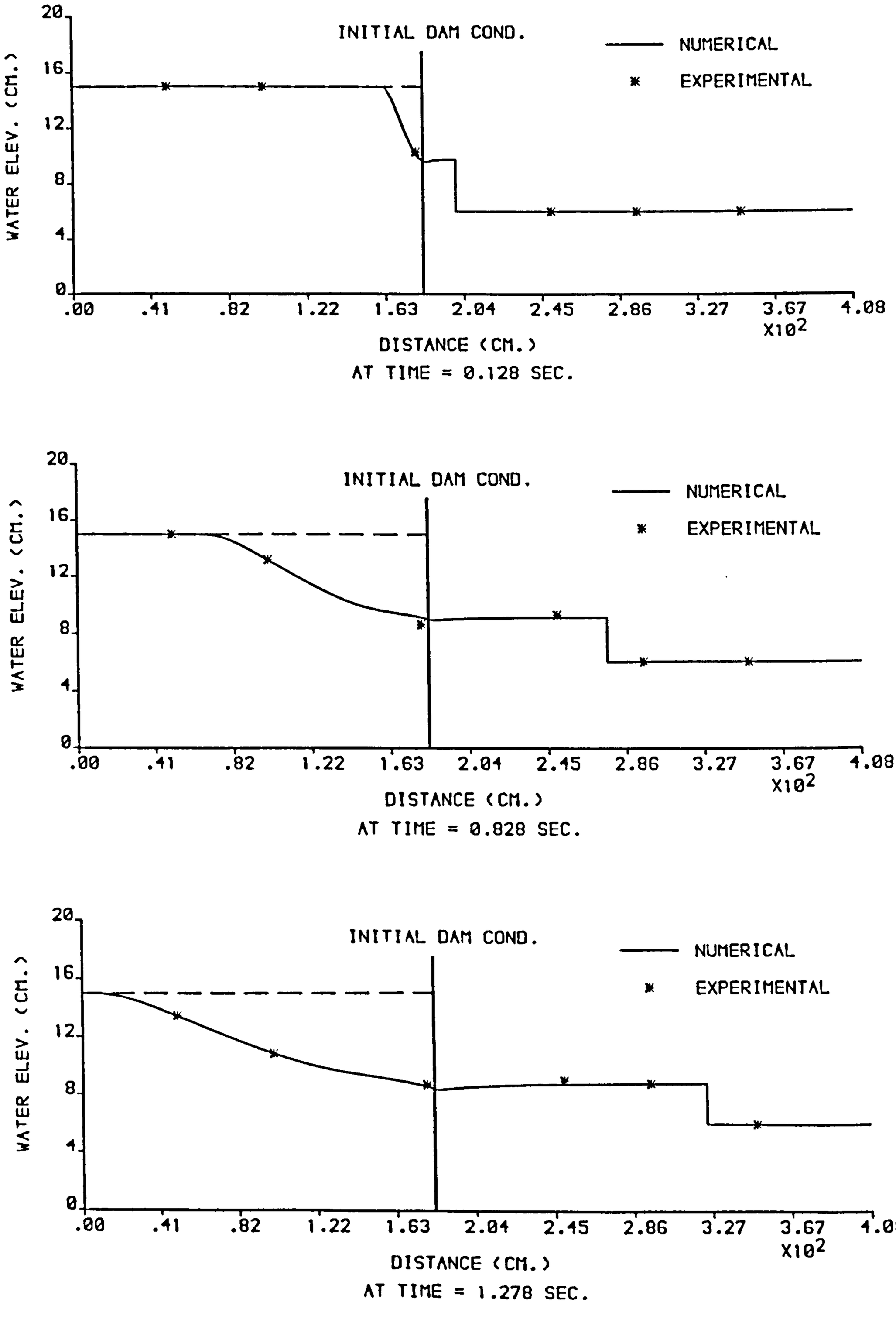

FIGURE 6.113 : NUMERICAL AND EXPERIMENTAL PROFILES FROM THE (XT–RT) MODEL , H_1 = 15 cm AND H_o = 6 cm .

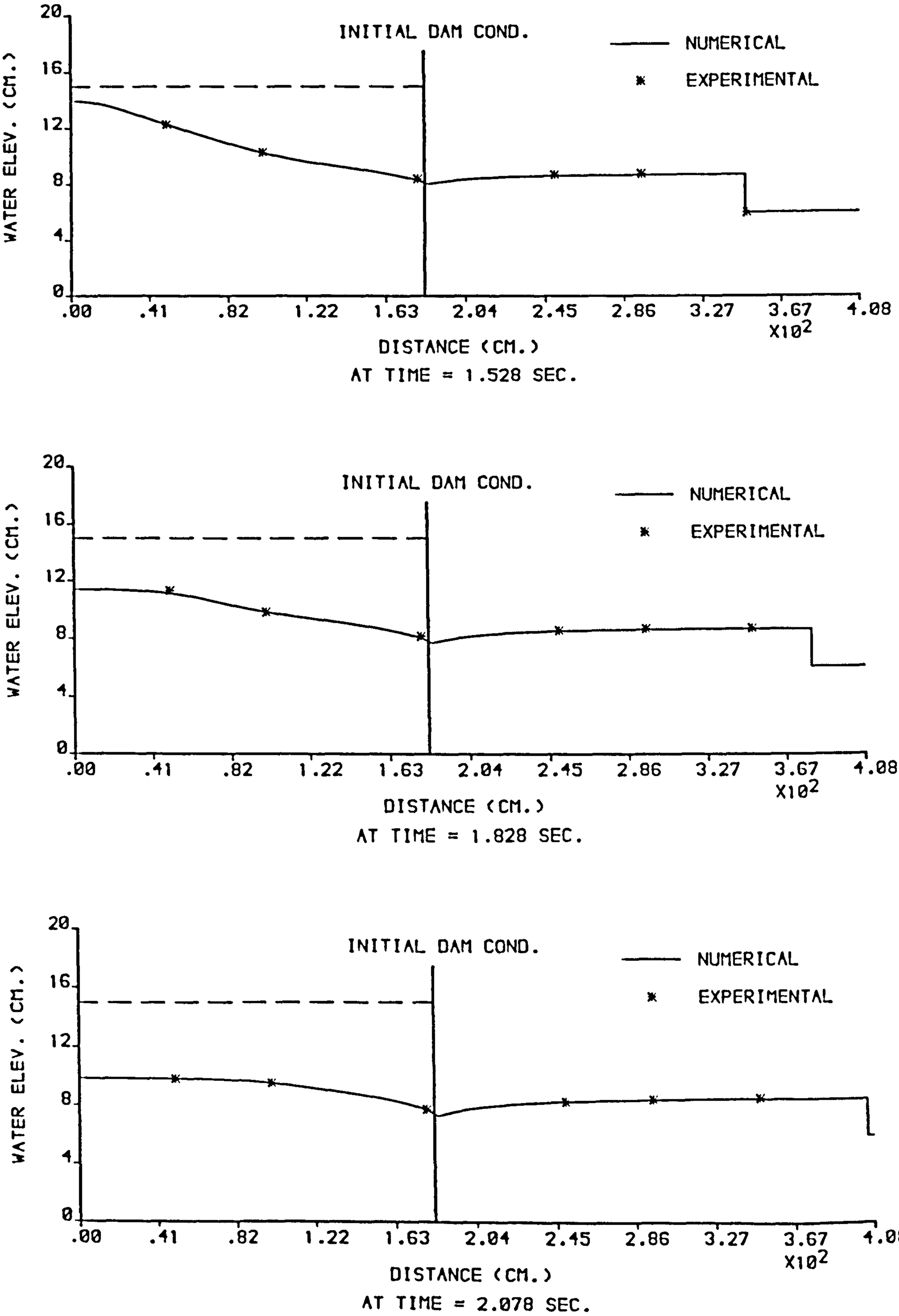

FIGURE 6.114 : NUMERICAL AND EXPERIMENTAL PROFILES FROM THE (XT-RT) MODEL , H_1 = 15 cm AND H_o = 6 cm .

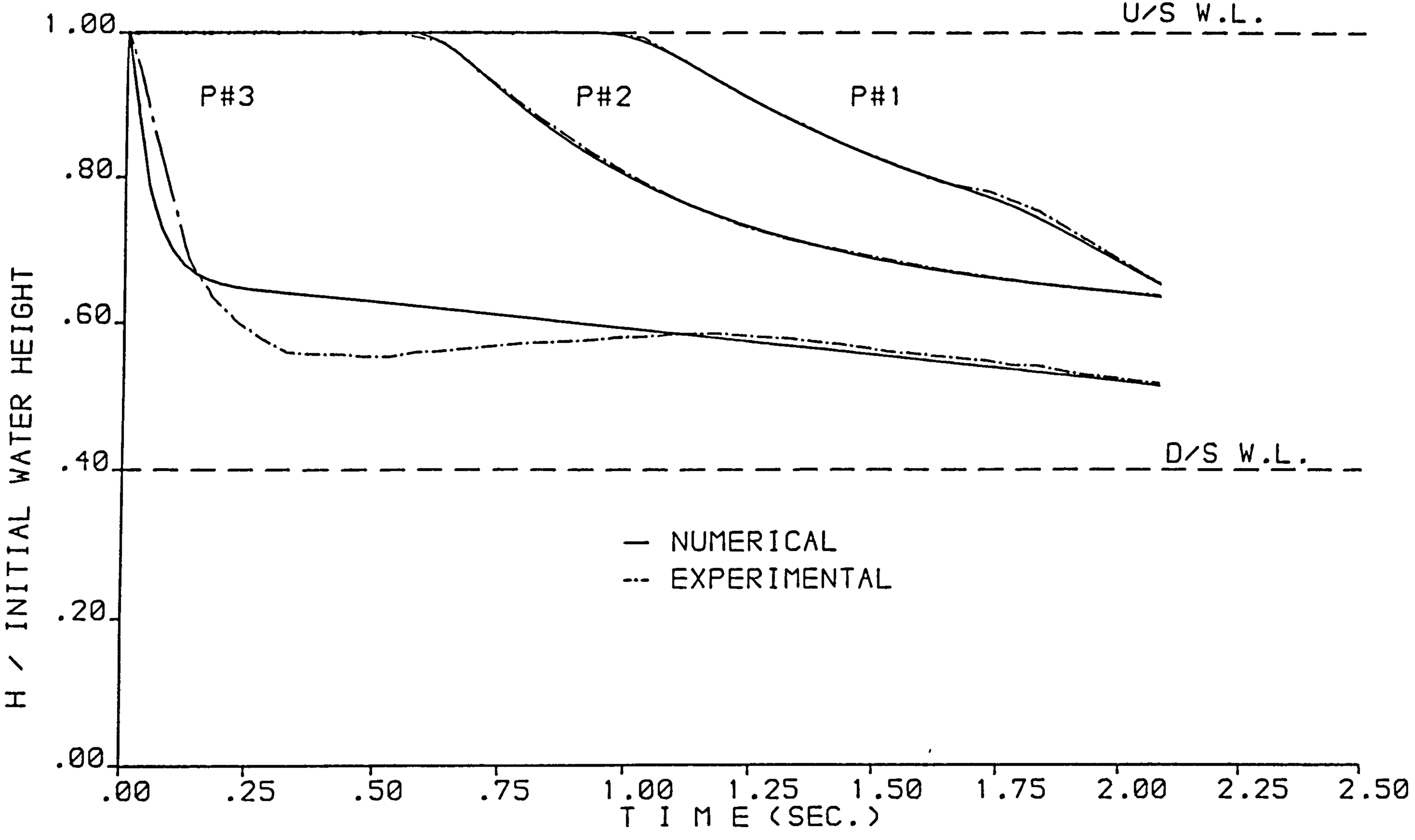

FIGURE 6.115 : NUMERICAL AND EXPERIMENTAL STAGE HYDROGRAPHS FROM THE (XT-RT) MODEL , H_1 = 15 cm AND H_o = 6 cm .

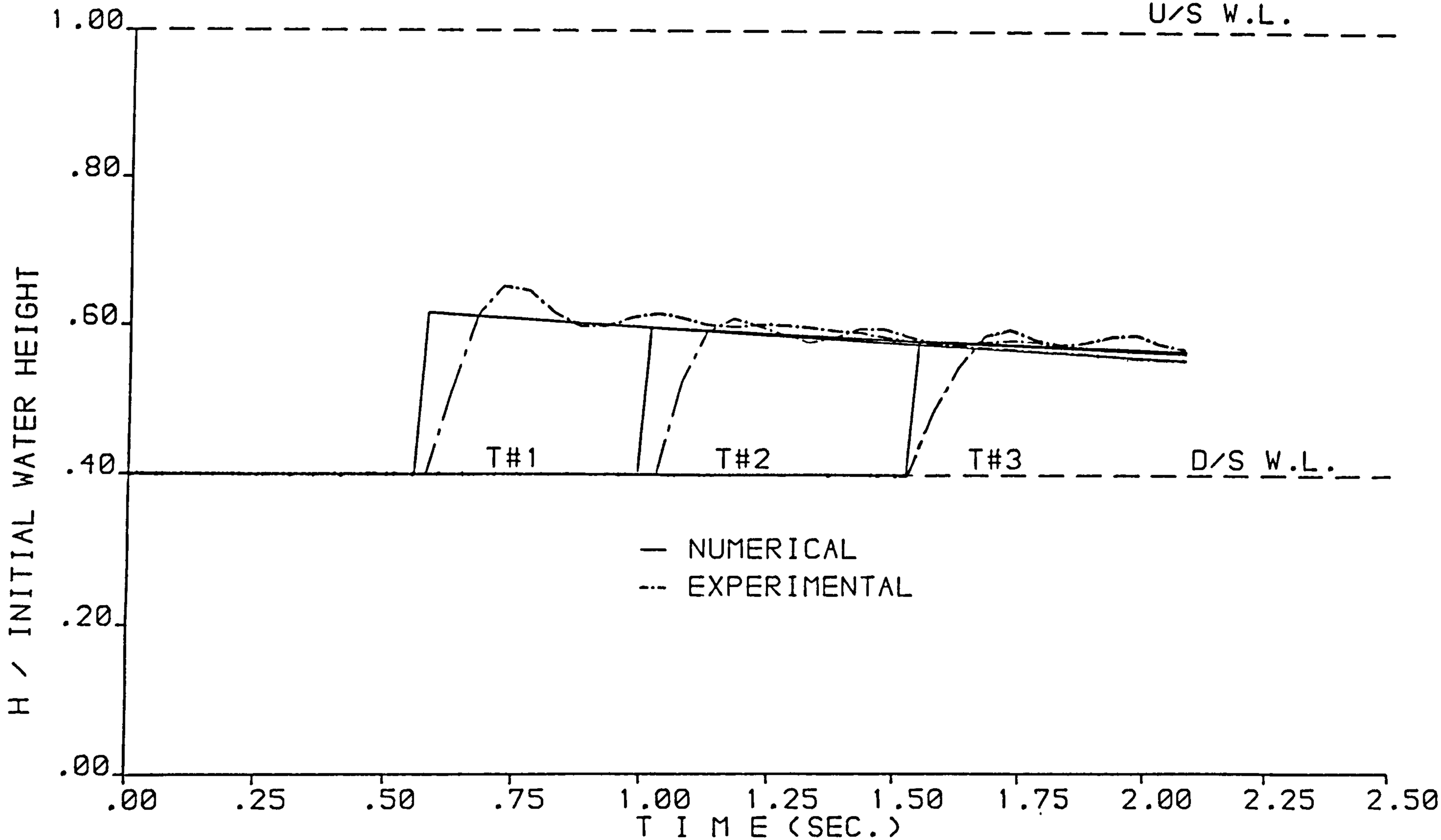

FIGURE 6.116 : NUMERICAL AND EXPERIMENTAL STAGE HYDROGRAPHS FROM THE (XT-RT) MODEL , H_1 = 15 cm AND H_o = 6 cm .

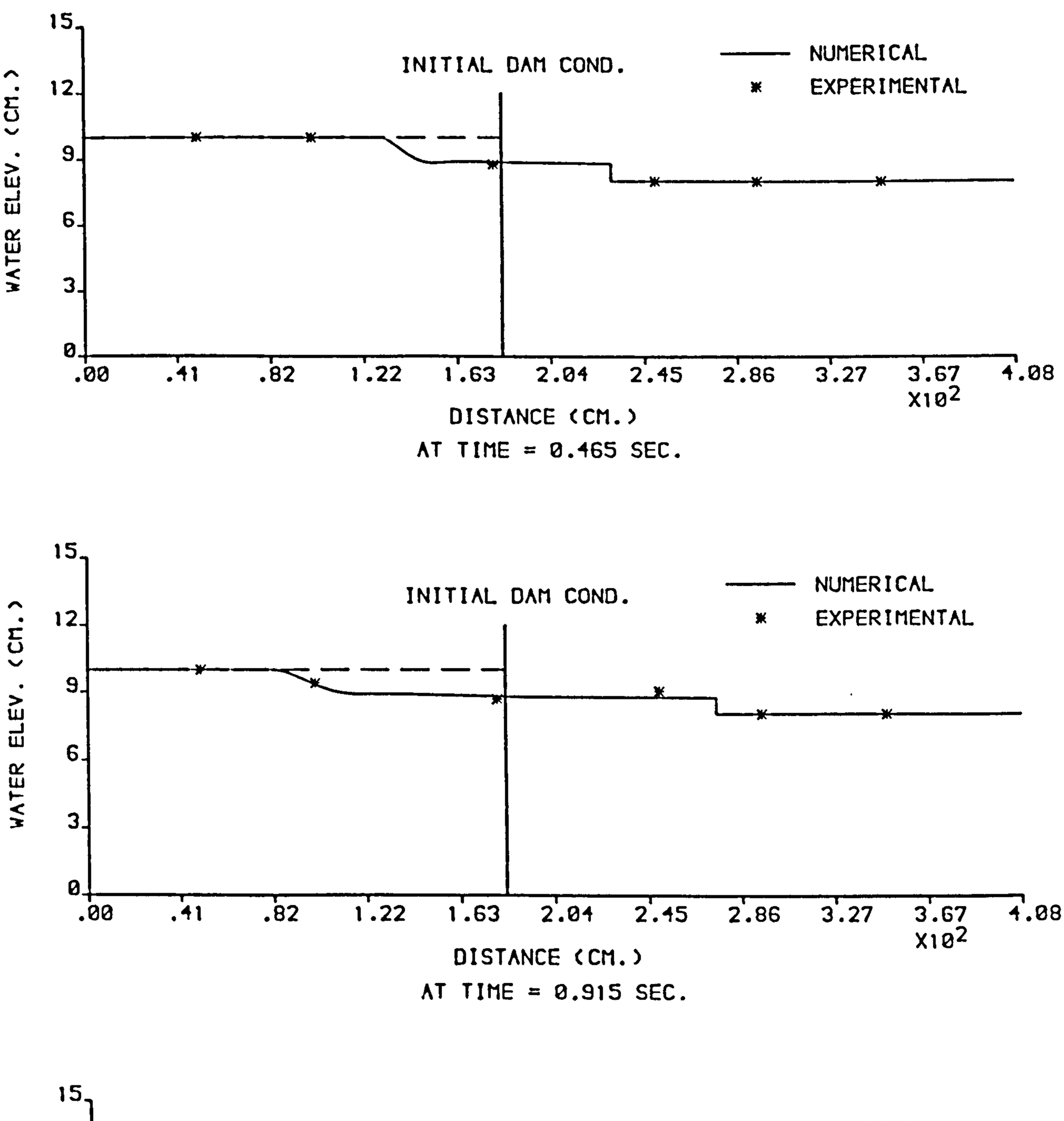

FIGURE 6.117 : NUMERICAL AND EXPERIMENTAL PROFILES FROM THE (XT-RT) MODEL , H_1 = 10 cm AND H_o = 8 cm .

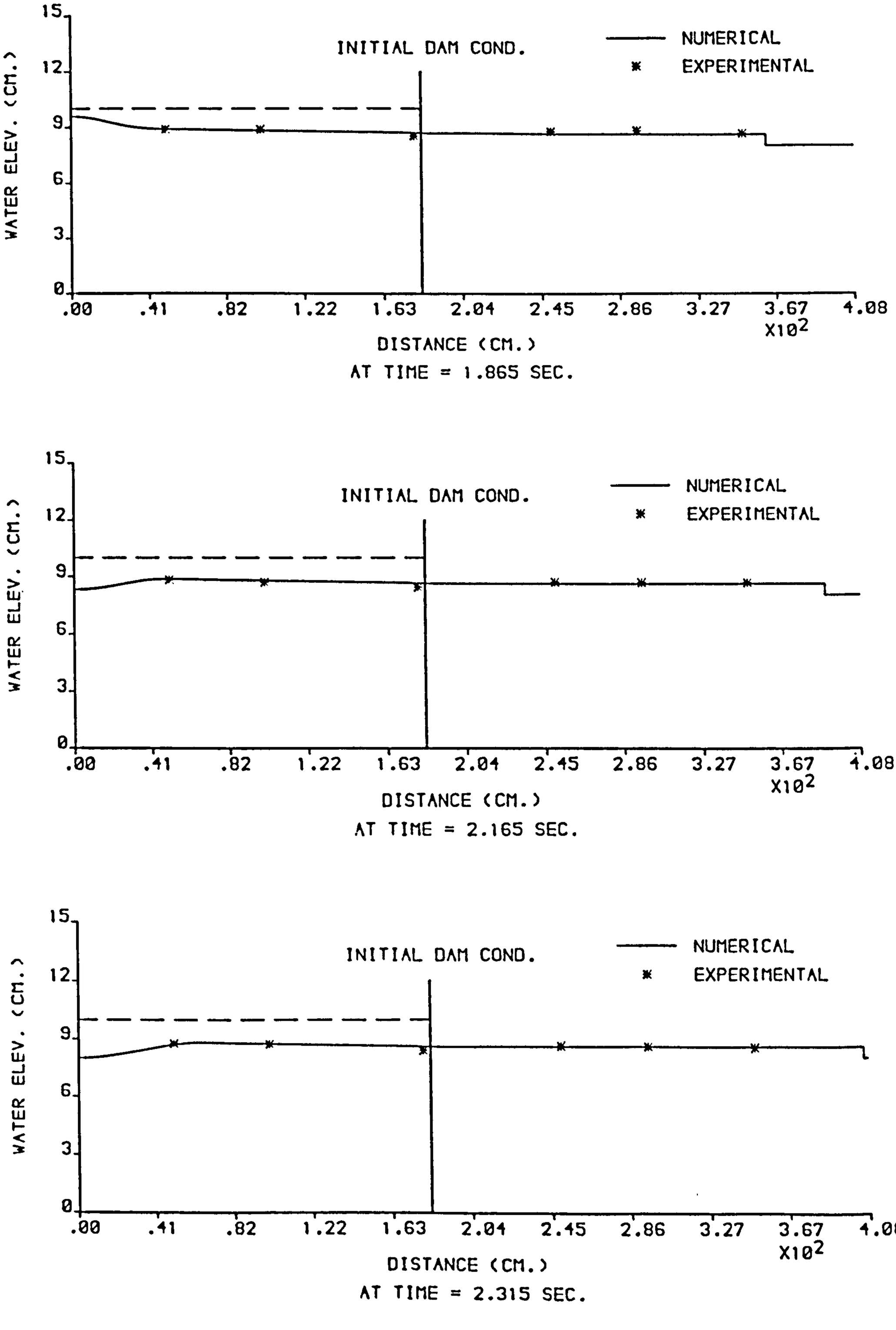

FIGURE 6.118 : NUMERICAL AND EXPERIMENTAL PROFILES FROM THE (XT–RT) MODEL , H_1 = 10 cm AND H_o = 8 cm .

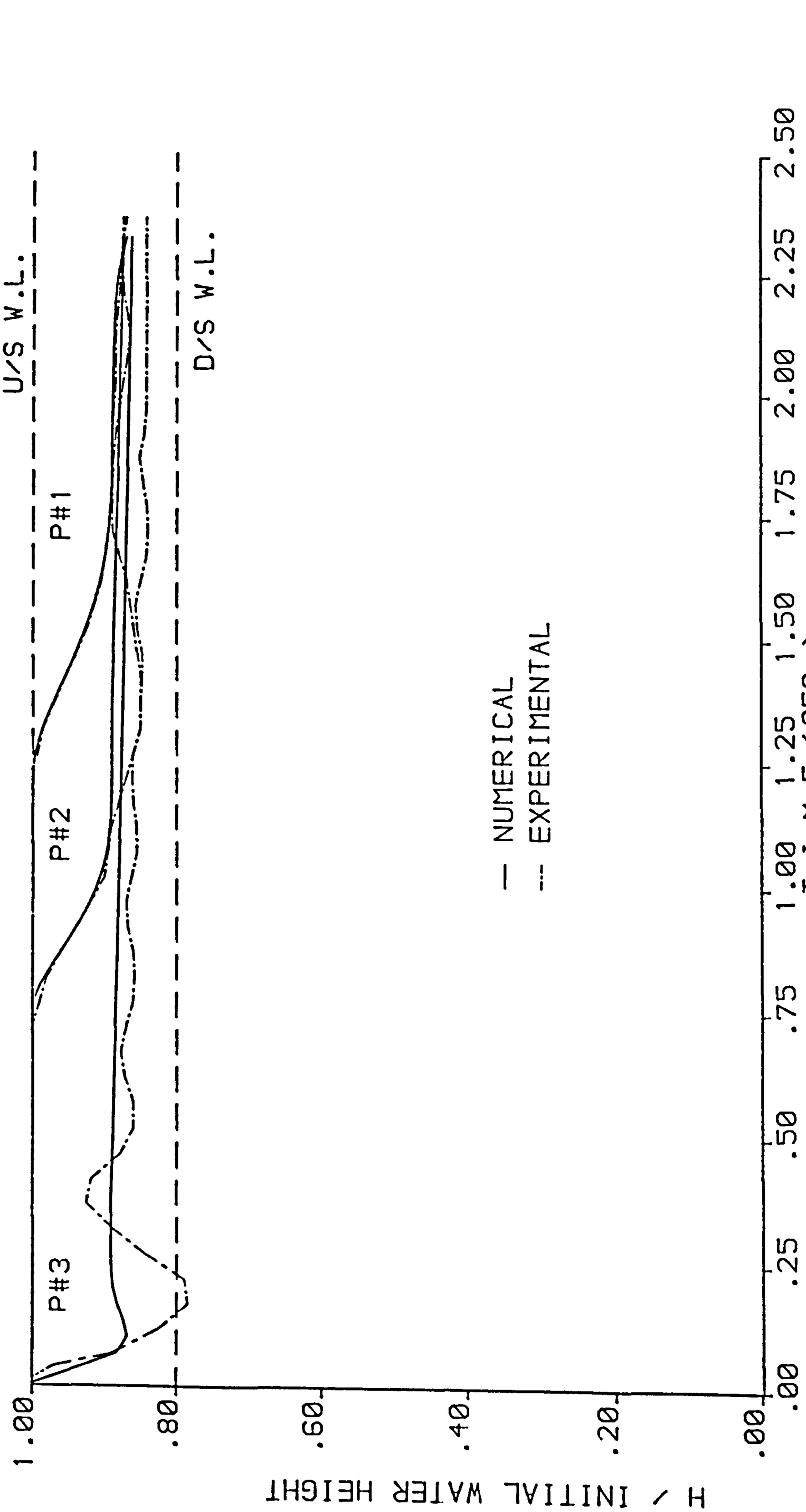

FIGURE 6.119 : NUMERICAL AND EXPERIMENTAL STAGE HYDROGRAPHS FROM THE (XT-RT) MODEL , H_1 = 10 cm AND H_o = 8 cm .

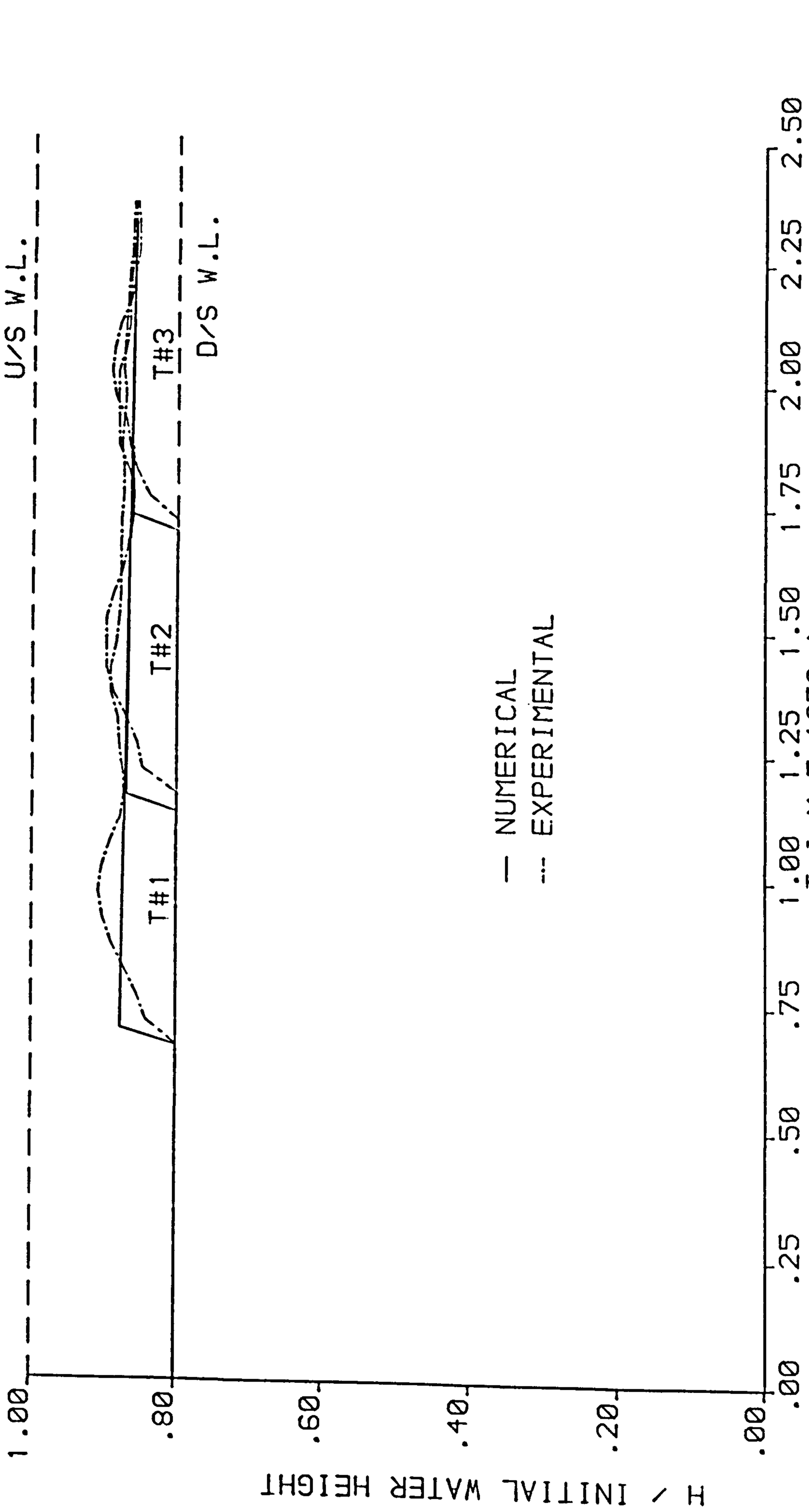

FIGURE 6.120 : NUMERICAL AND EXPERIMENTAL STAGE HYDROGRAPHS FROM THE (XT-RT) MODEL , H_1 = 10 cm AND H_o = 8 cm .

6.5 Overview of the Four Models

In this section, a comparison of the four physical and numerical models is presented. In order to make the comparison clear, Figures 6.121 to 6.128 are presented on two facing pages.

Figure 6.121 illustrates the comparisons of model front heights with Stoker's (X-T) solution. In all cases, the difference between the numerical and experimental results generally less than 5%. Stoker's (X-T) solution lies close to those from (X-T) and (RT-XT) models, but it is substantially (20%) higher than in the (RT-RT) and (XT-RT) models.

Comparing the front heights of the (X-T) and (RT-XT) models, shows the front heights in the (RT-XT) to be slightly (say 2%) higher in general than in the (X-T) model. A somewhat higher figure applies for downstream depths close to those consistent with maximum front height. The same occurs in the (RT-RT) model whose front heights are higher than those in the (XT-RT) model. Evidently the converging R-T reservoir, of greater area than in X-T space, enhances the momentum supply per unit width and encourages a higher downstream surge. Conversely, the R-T expansion downstream both encourages greater energy dissipation and also decreases the momentum supply (per unit width) - leading to lower surges.

The value of the shock fitting method in the simulation is clear. Figure 6.122 presents instantaneous profiles from the four models, where the initial depth upstream is (H_1 = 10 cm) and dry bed downstream. The profiles were selected so that, in each case, the front had reached the same point downstream of the dam, although the time

required to do so was different. The same time was required in the (X-T) and (RT-XT) models and which was lower (by 11.6%) than for the (RT-RT) and (XT-RT) models. This is consistent with the wave fronts of the (X-T) and (RT-XT) model being higher in depth and faster than those of the (RT-RT) and (XT-RT) models for the reasons above. The water depth profiles of the (X-T) and (XT-RT) models are cutting the dam site at height (0.444 and 0.424) of H_1 respectively. The first of these figures supports Stoker's theory since the walls are parallel upstream of the dam (plain reservoir) whilst the second is slightly lower than the (4/9) ratio in the case of (XT-RT) model because of the divergent sides in the downstream channel. Conversely, the water depth profiles of the (RT-XT) and (RT-RT) models are higher than the ratio (4/9) being 0.516 and 0.498 respectively. This is because of the convergent walls upstream of the dam in both models whilst the divergent walls downstream in the RT-RT model supress the increase. The water depth in the (RT-RT) and (XT-RT) models falls suddenly at the transition section (at the dam site).

As downstream depth ratios increase up to and beyond the critical value of 0.138, we may eventually expect a 'drowning' of the accelerating flow through the dam site. Prior to this, a transition from the supercritical flow immediately below the dam to subcritical flow behind the front appears - in the form of a weak hydraulic jump. This feature is well demonstrated by physical and numerical models of R-T downstream cases especially in Figures 6.123 to 6.128.

The general comparisons between experimental and numerical results and also of both these with Stoker for the front heights indicate small differences. For a summary of these differences see Table 6.1.

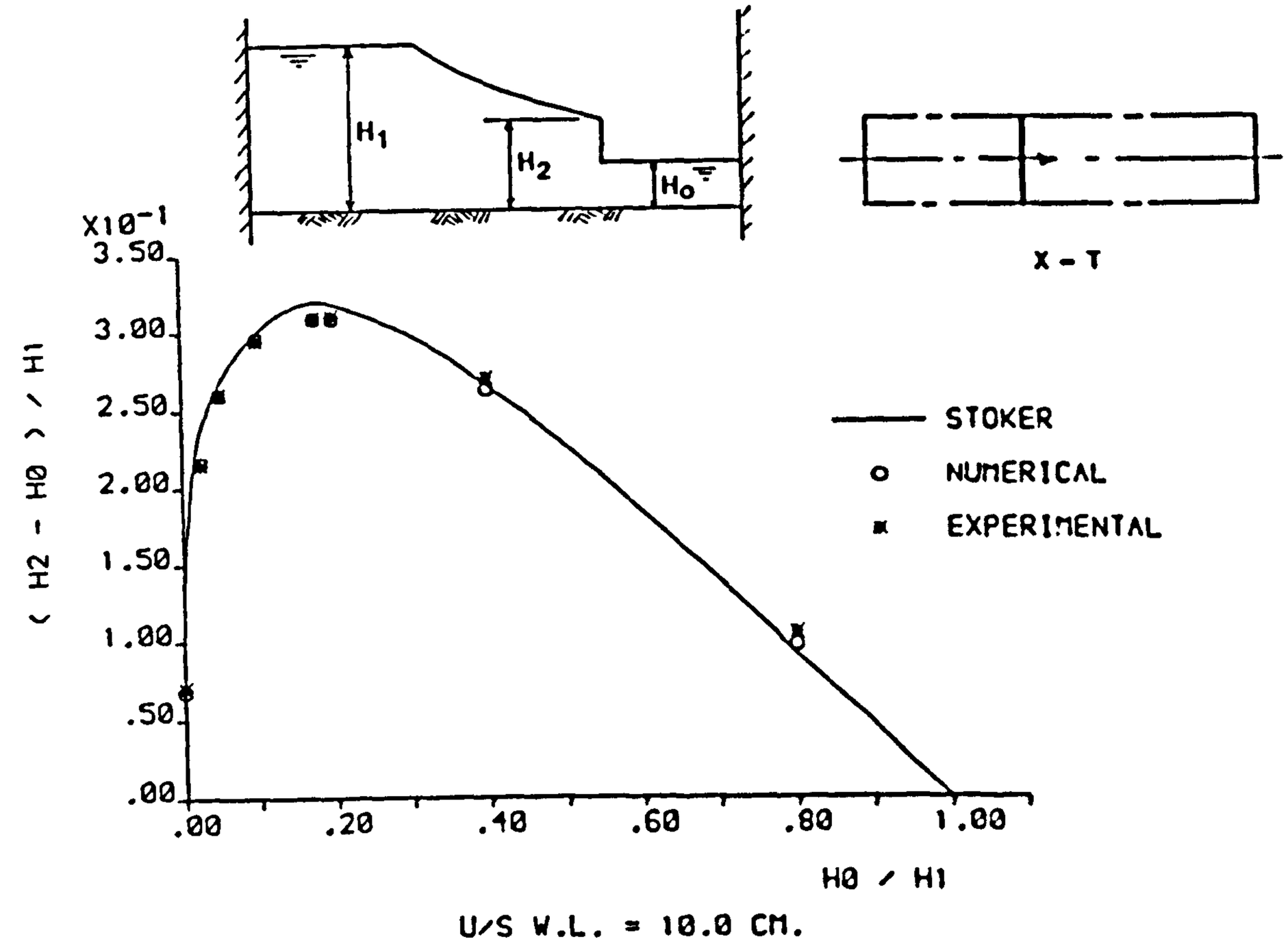

(A) The (X-T) Model

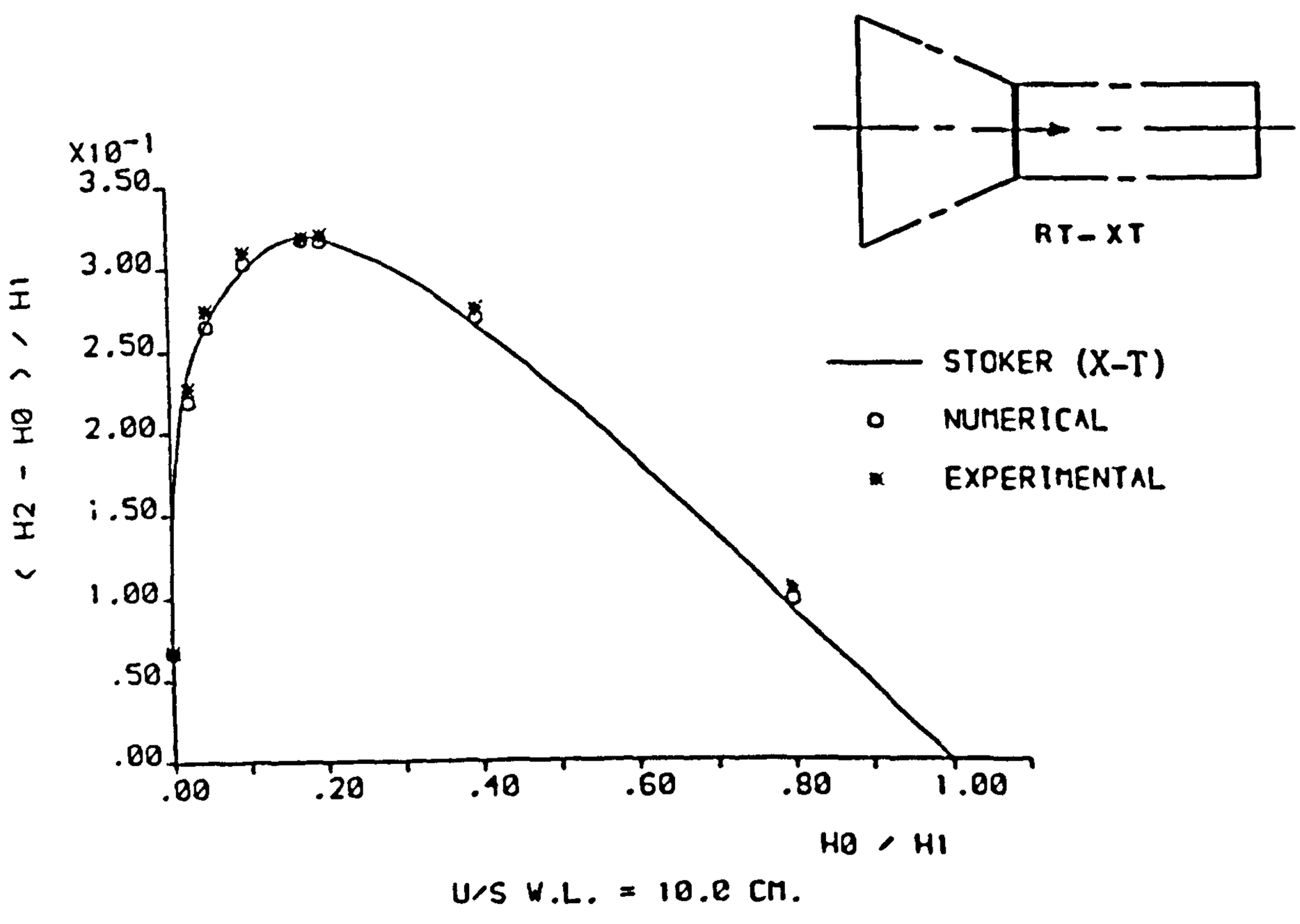

(B) The (RT-XT) Model

FIGURE 6.121 : COMPARISONS OF THE FRONT HEIGHTS RESULTING FROM THE FOUR NUMERICAL AND PHYSICAL MODELS WITH STOKER'S (X-T) SOLUTION .

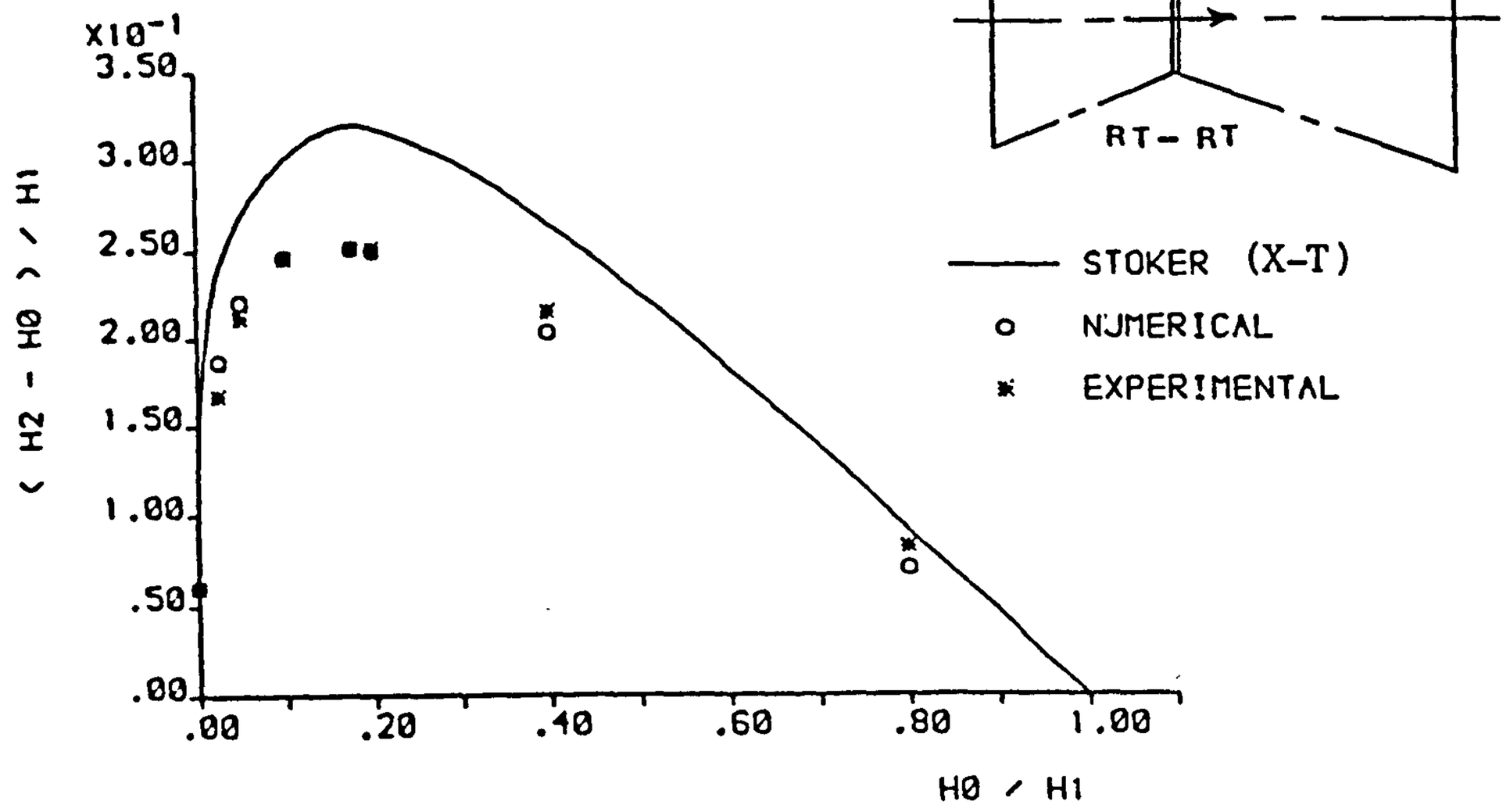

(C) The (RT-RT) Model

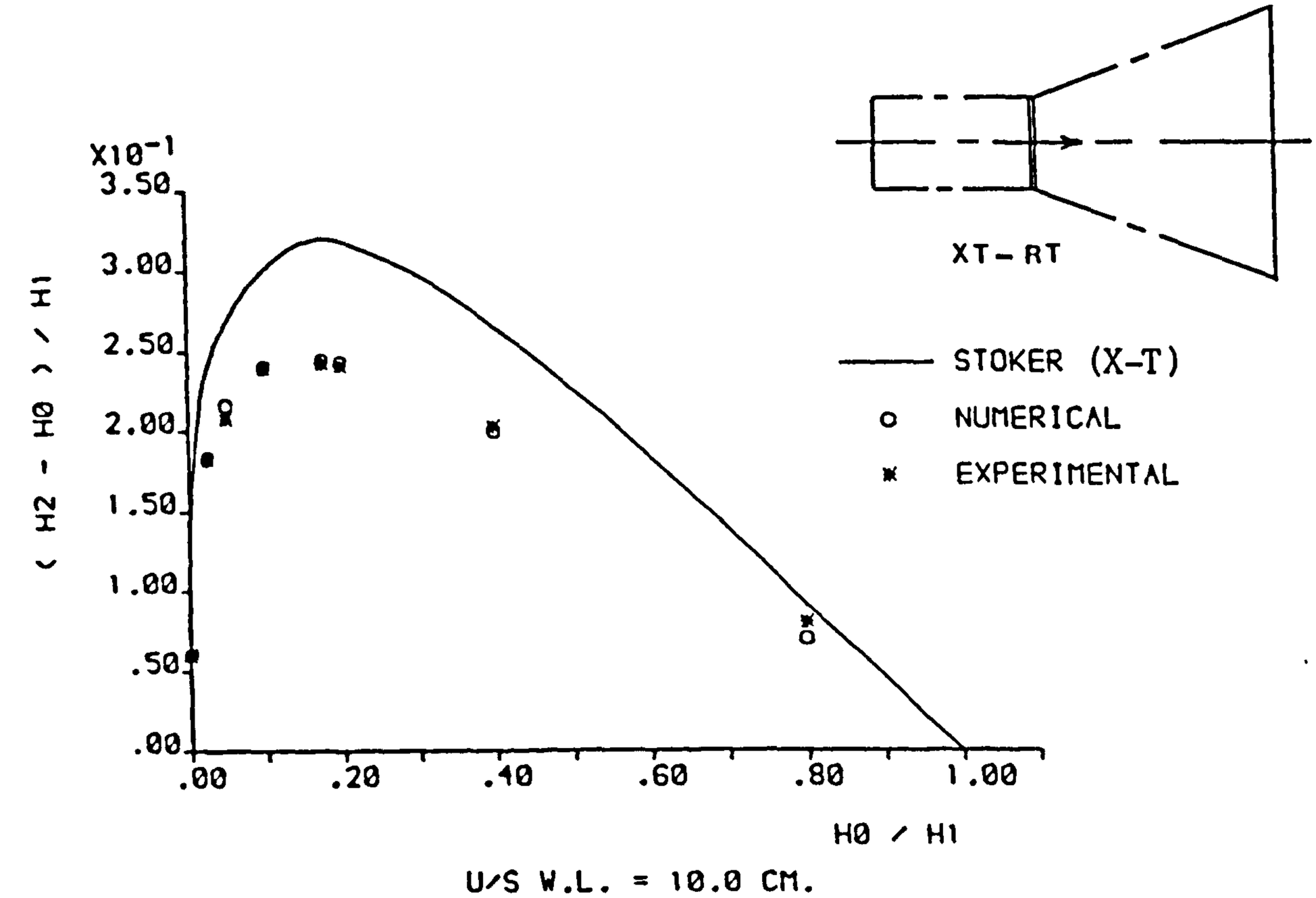

(D) The (XT-RT) Model

FIGURE 6.121 : CONT.

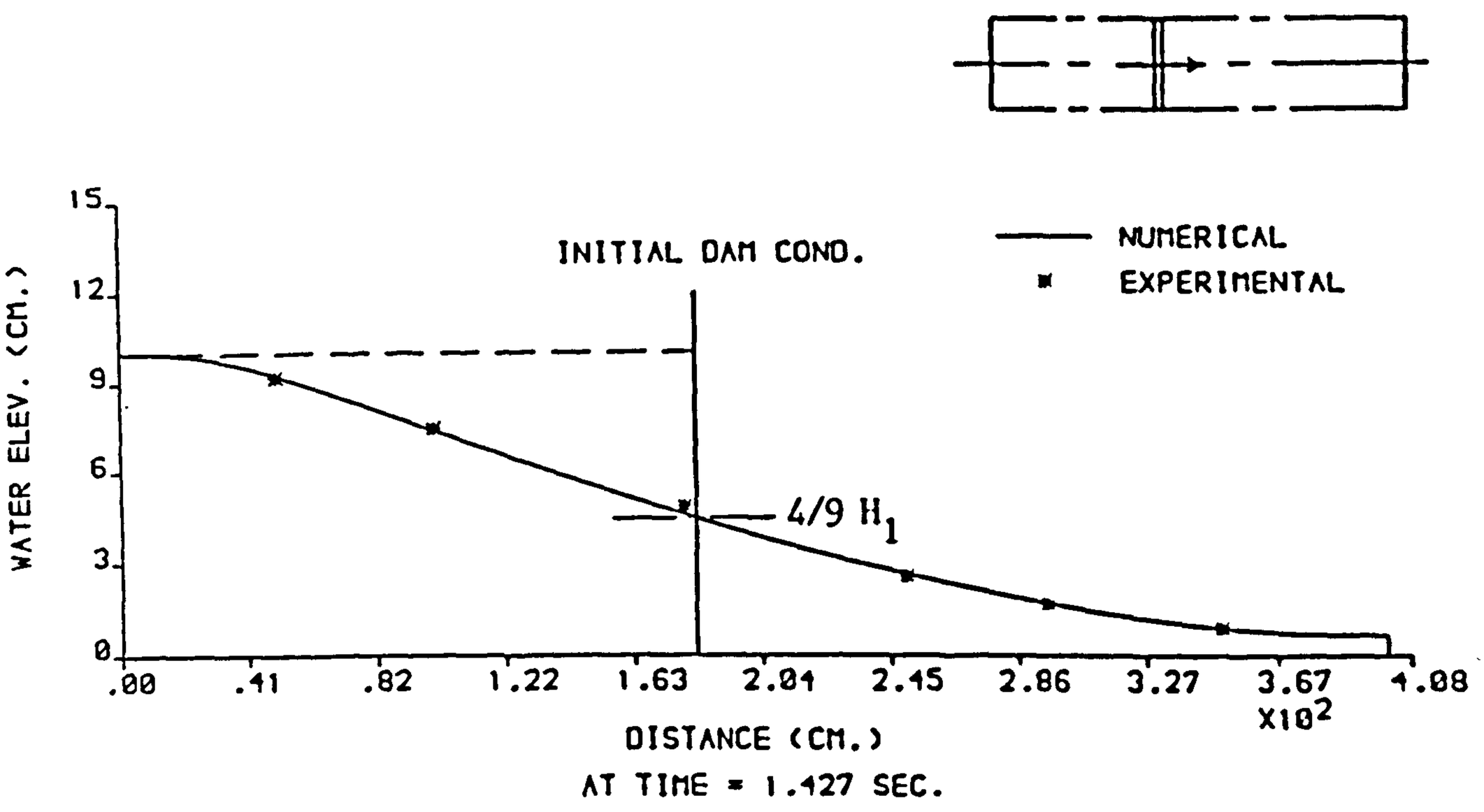

(A) The (X-T) Model

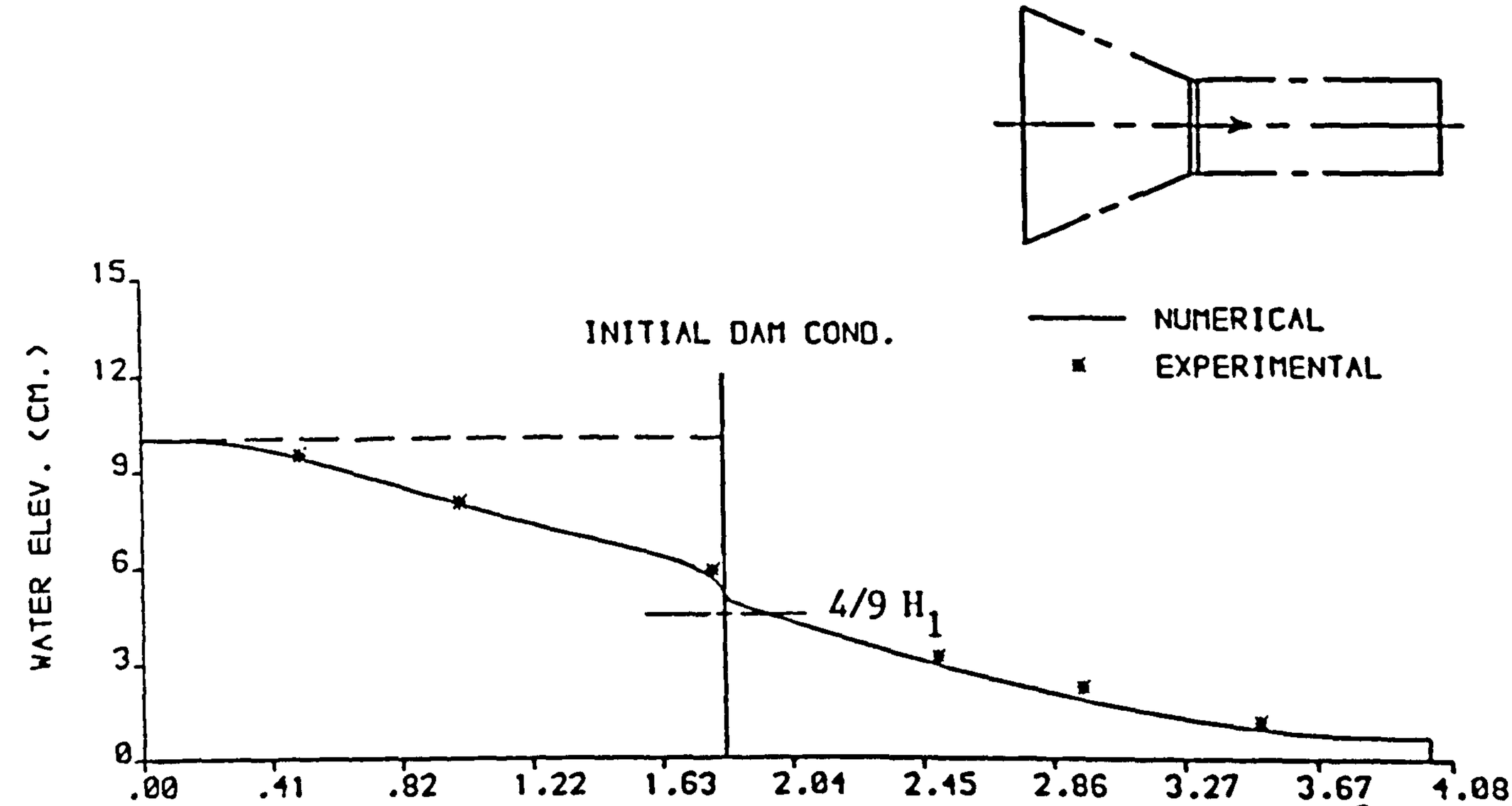

(B) The (RT-XT) Model

FIGURE 6.122 : COMPARISONS OF NUMERICAL AND EXPERIMENTAL PROFILES FROM THE FOUR MODELS , H_1 = 10 cm AND H_o = DRY , $H_o / H_1 = 0$.

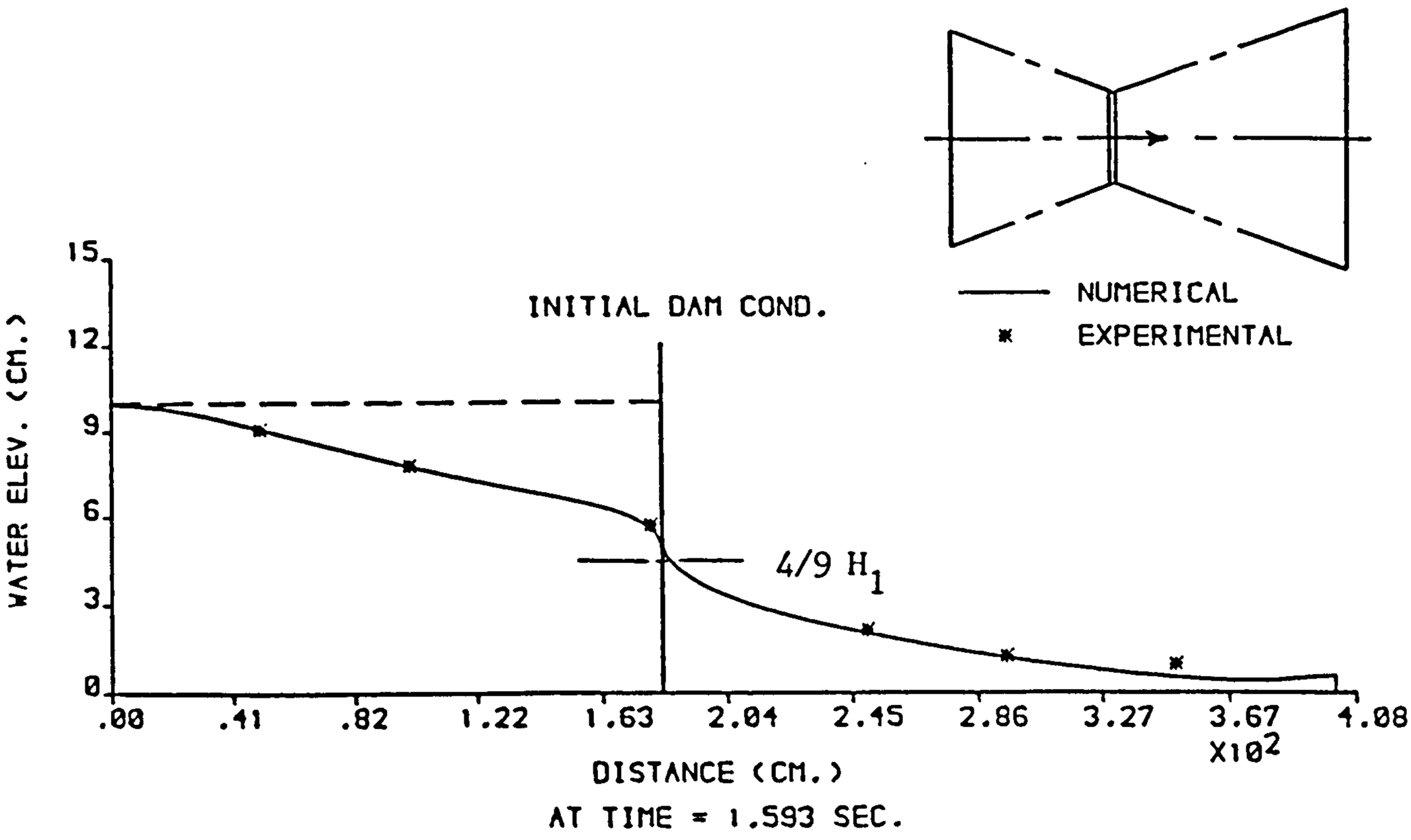

(C) The (RT-RT) Model

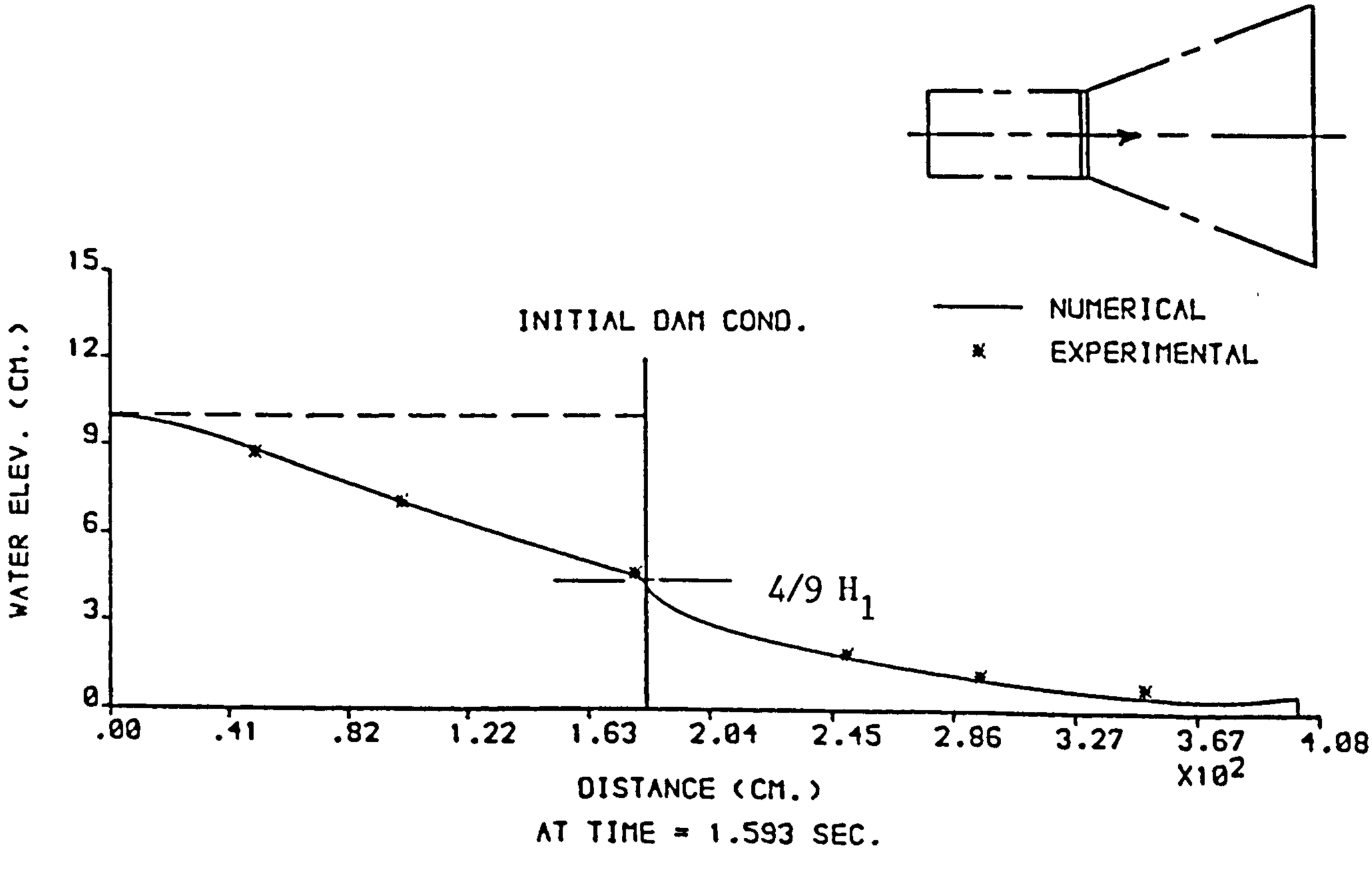

(D) The (XT-RT) Model

FIGURE 6.122 : CONT.

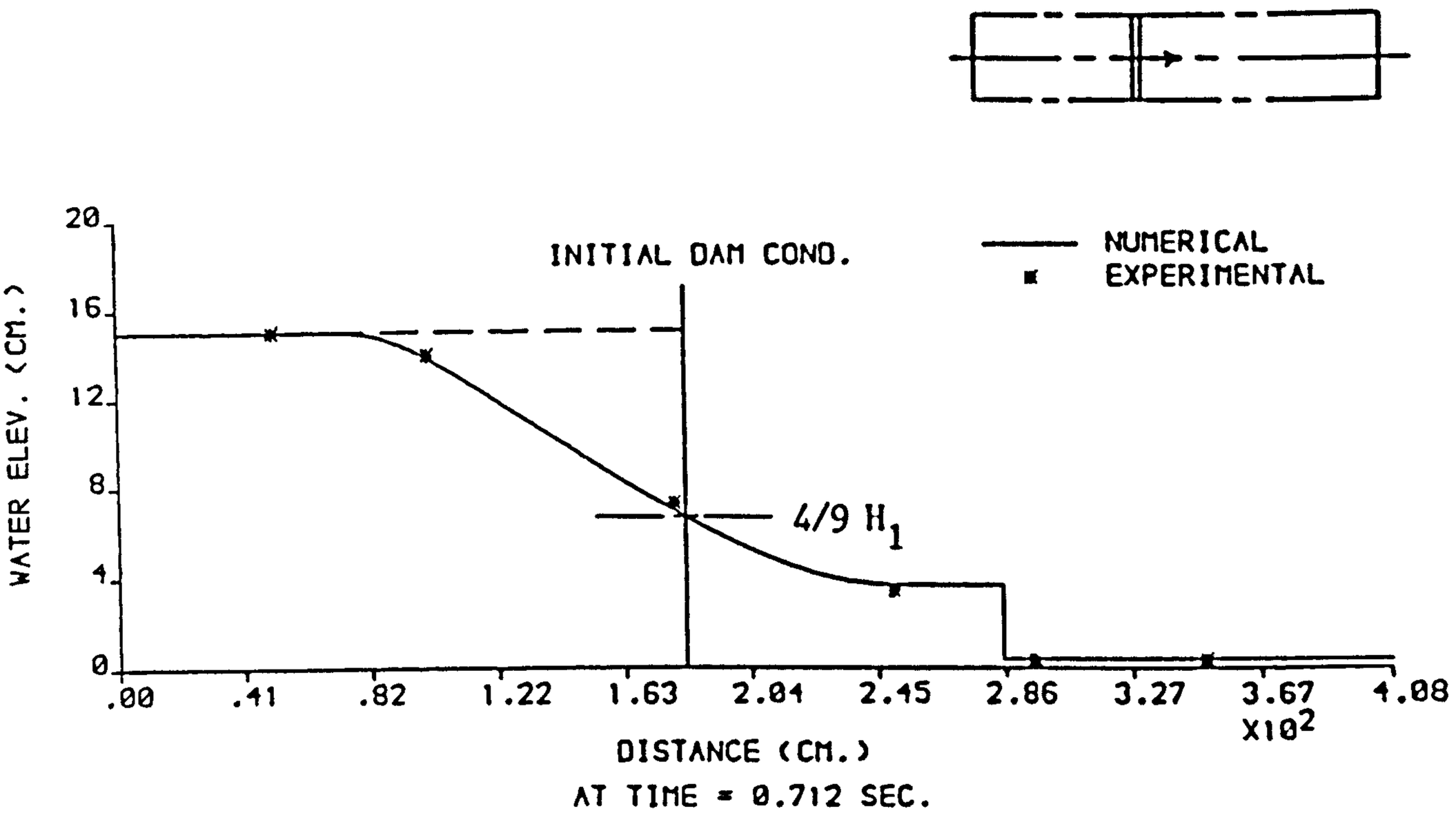

(A) The (X-T) Model

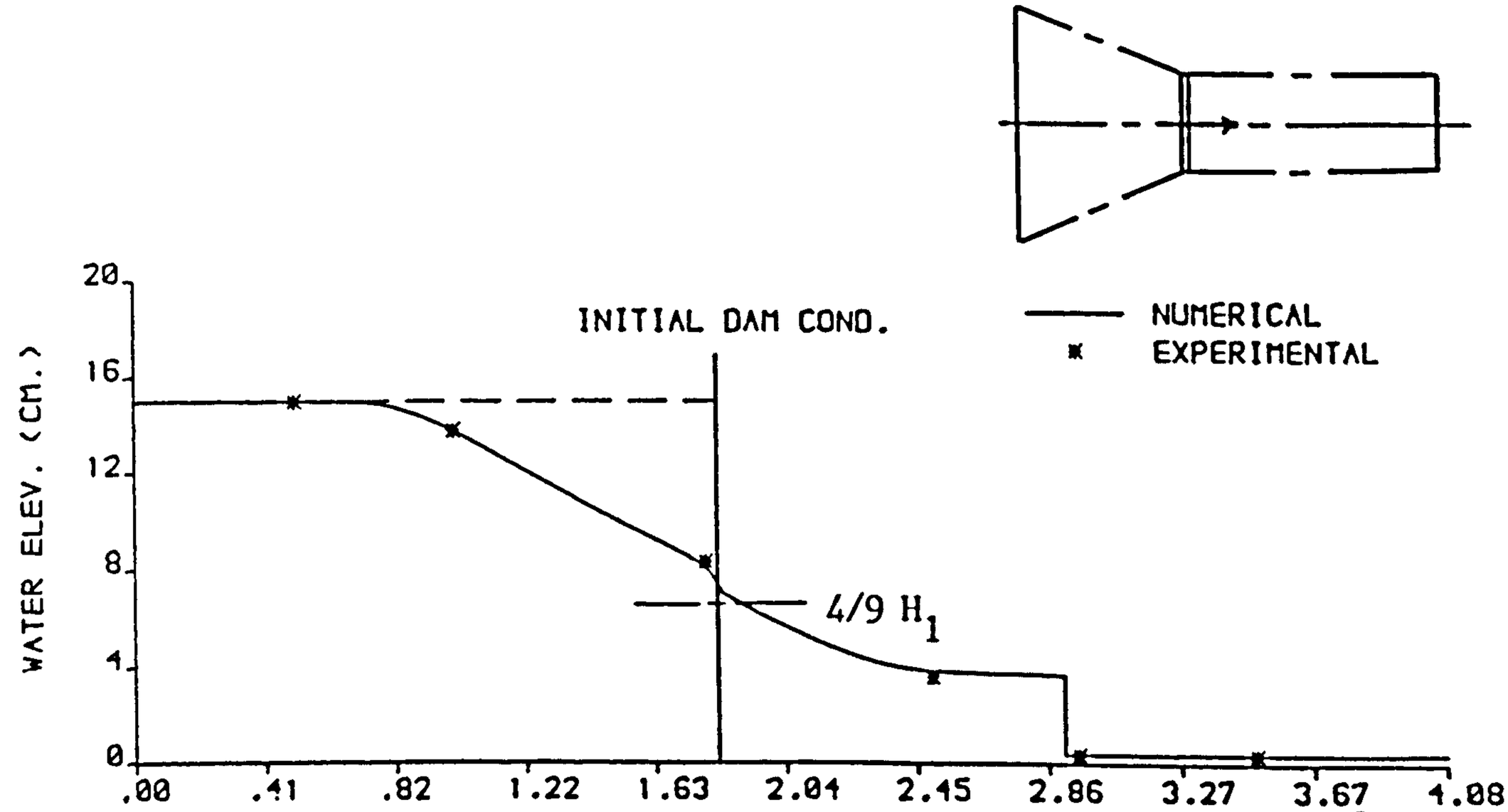

(B) The (RT-XT) Model

FIGURE 6.123 : COMPARISONS OF NUMERICAL AND EXPERIMENTAL PROFILES FROM THE FOUR MODELS , H_1 = 15 cm AND H_o = 0.375 cm, H_o / H_1 = 0.025 .

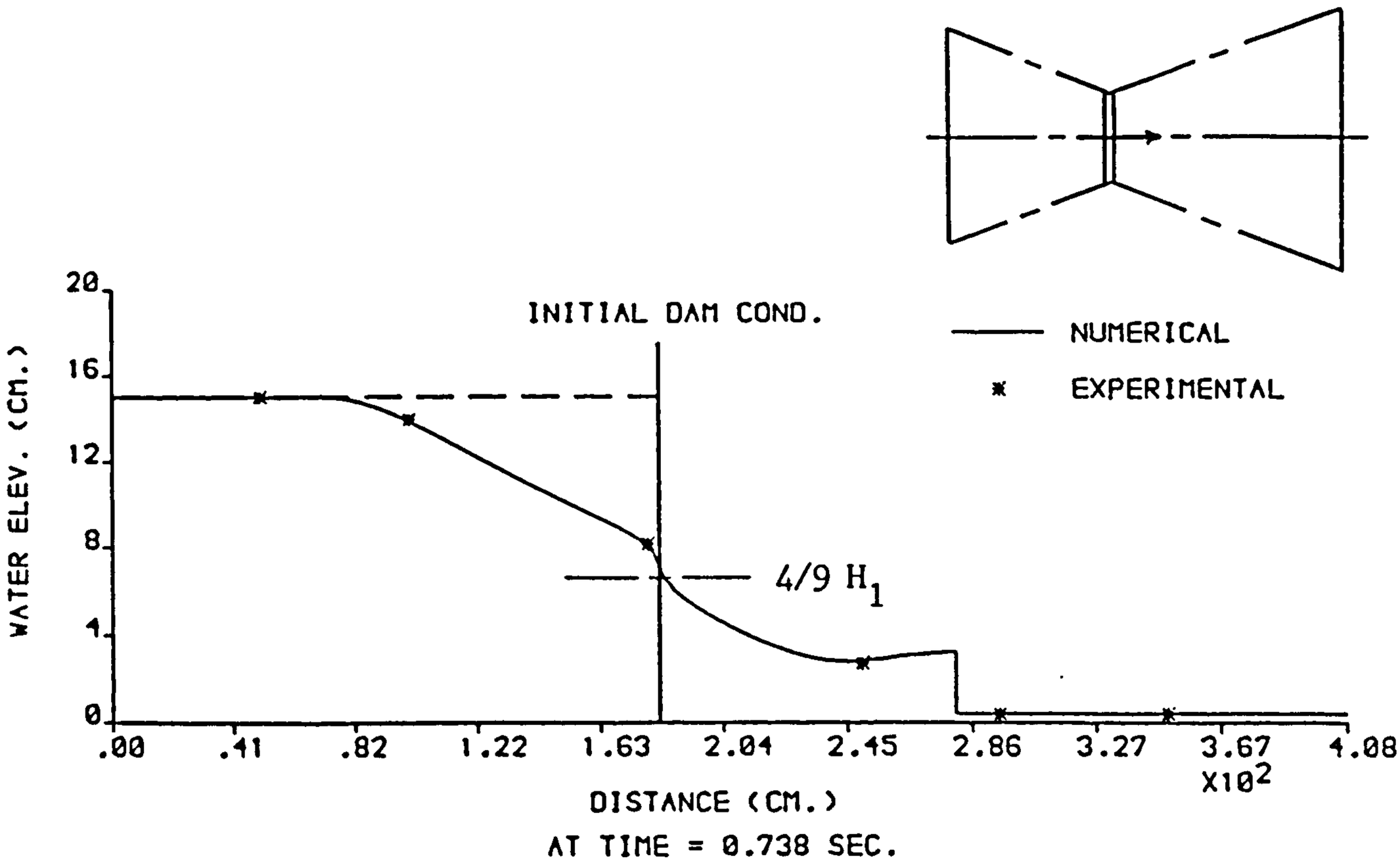

(C) The (RT-RT) Model

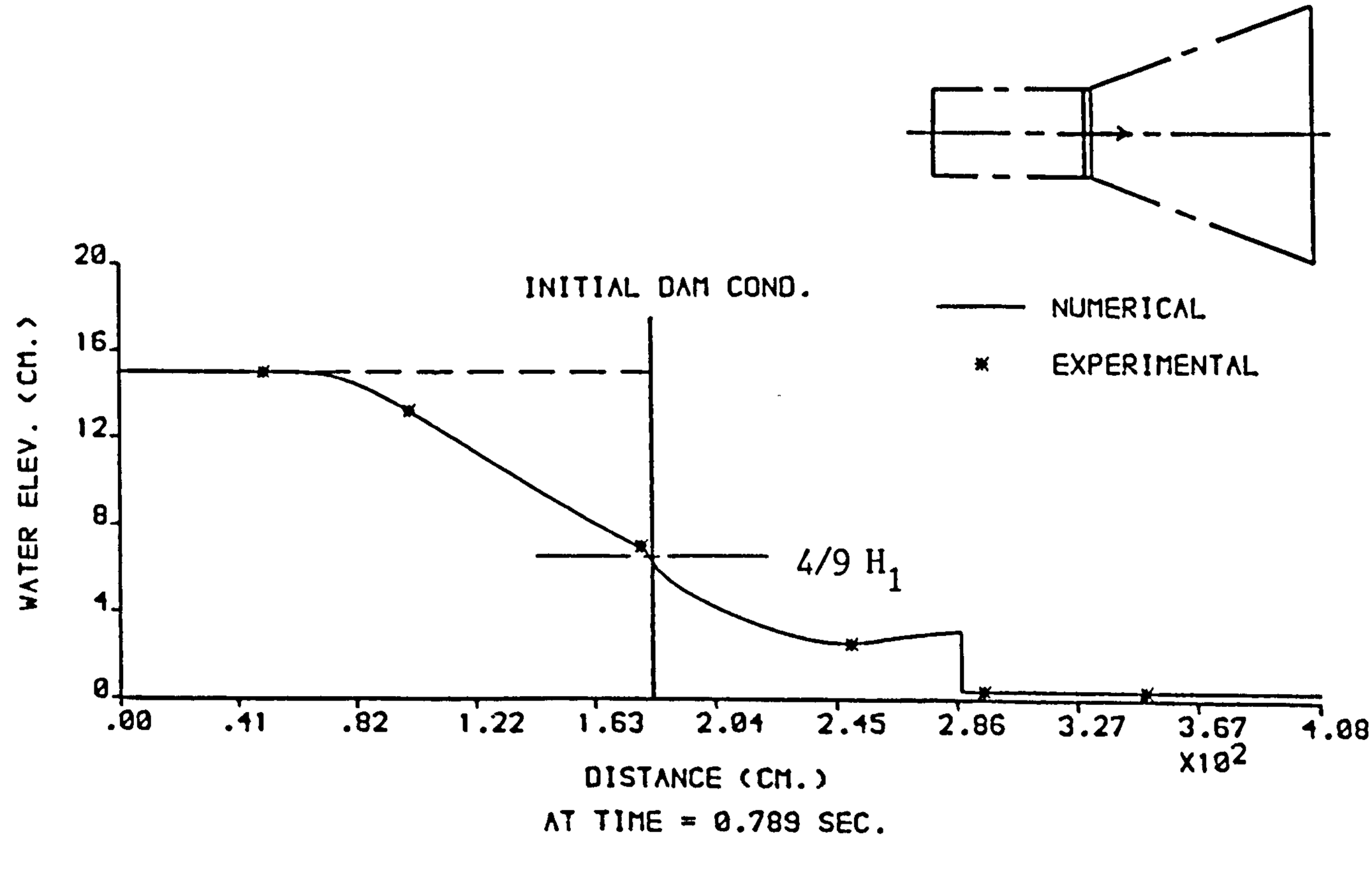

(D) The (XT-RT) Model

FIGURE 6.123 : CONT.

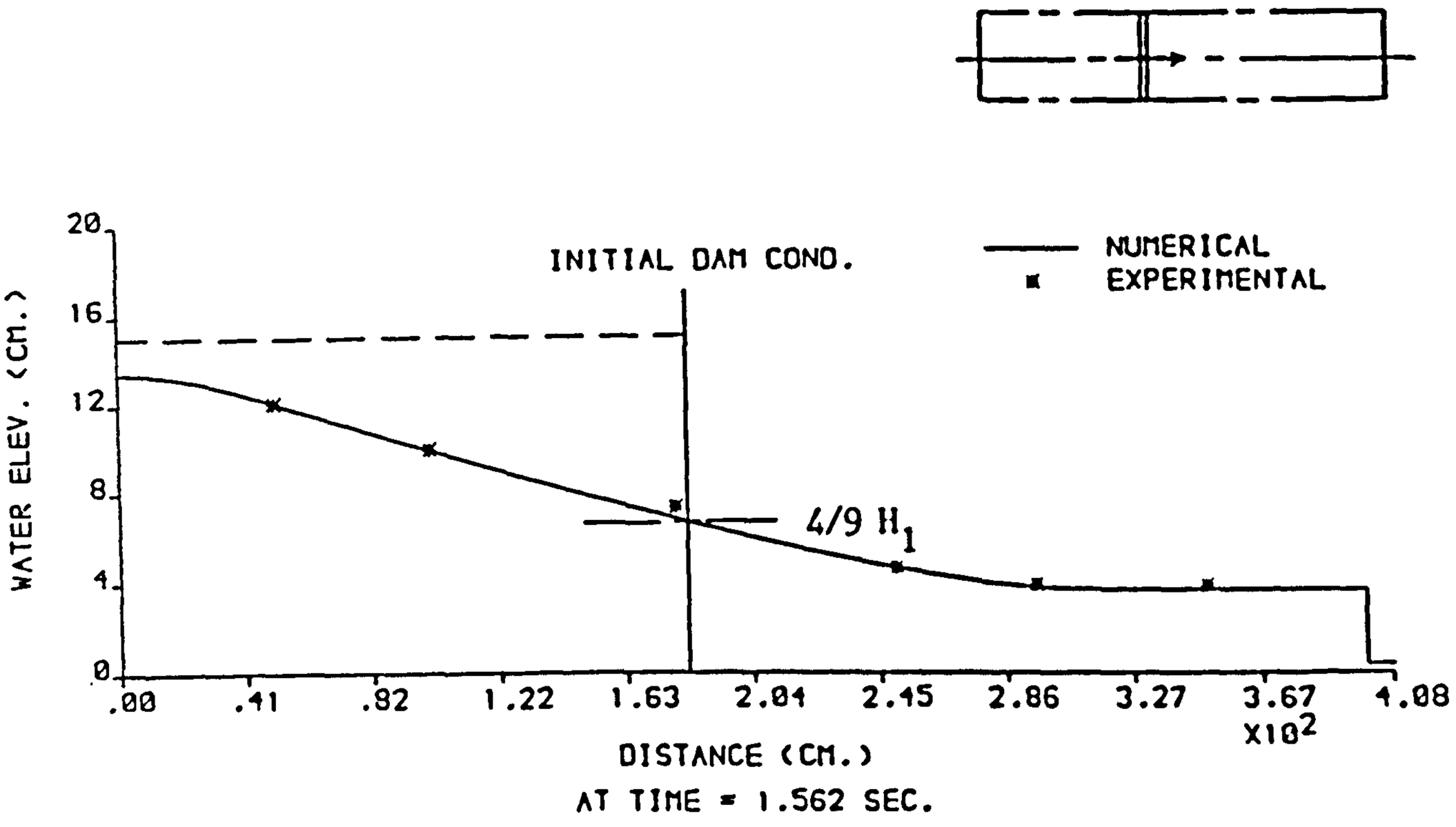

(A) The (X-T) Model

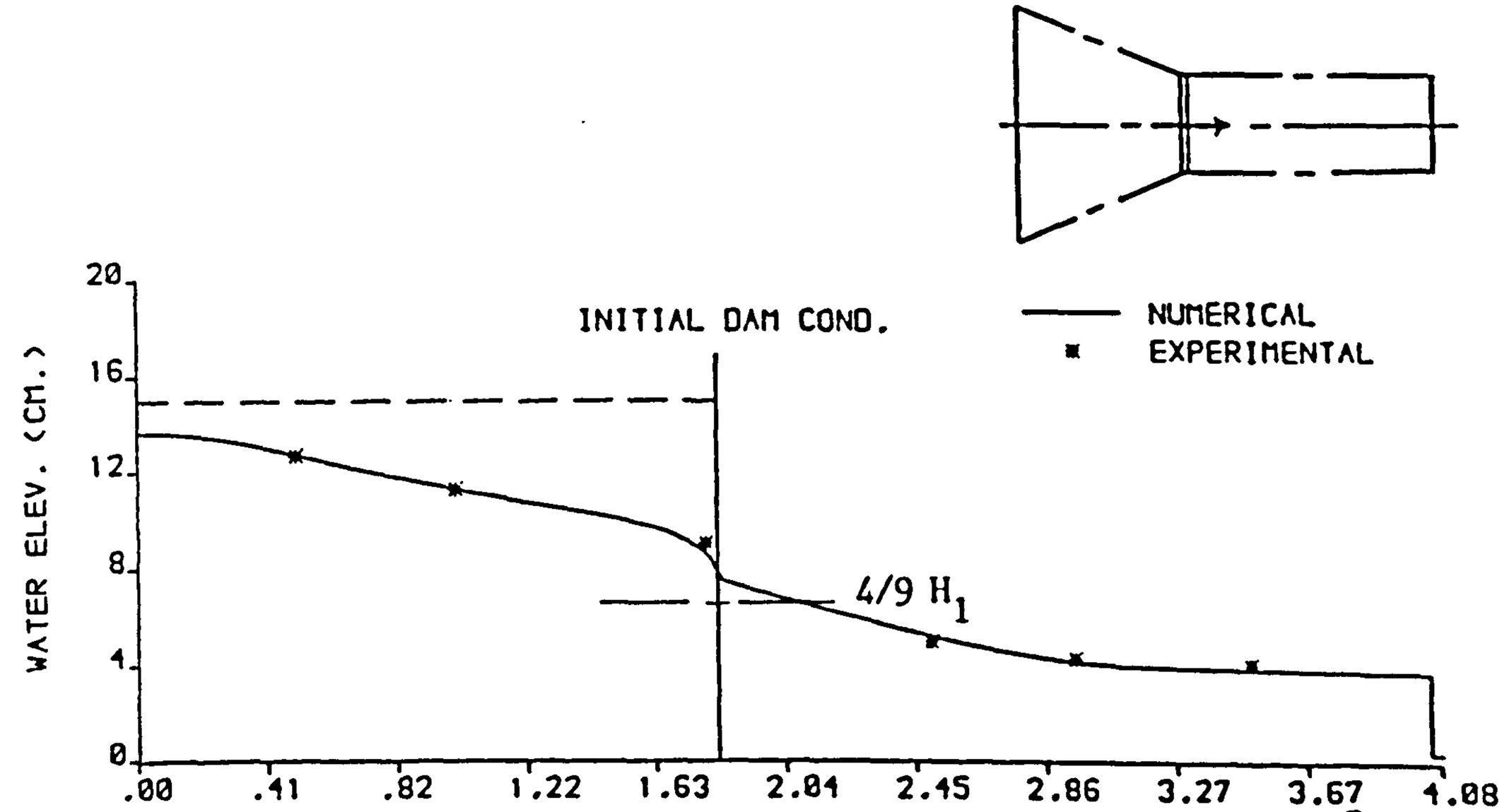

(B) The (RT-XT) Model

FIGURE 6.124 : COMPARISONS OF NUMERICAL AND EXPERIMENTAL PROFILES FROM THE FOUR MODELS , H_1 = 15 cm AND H_o = 0.375 cm, H_o / H_1 = 0.025 .

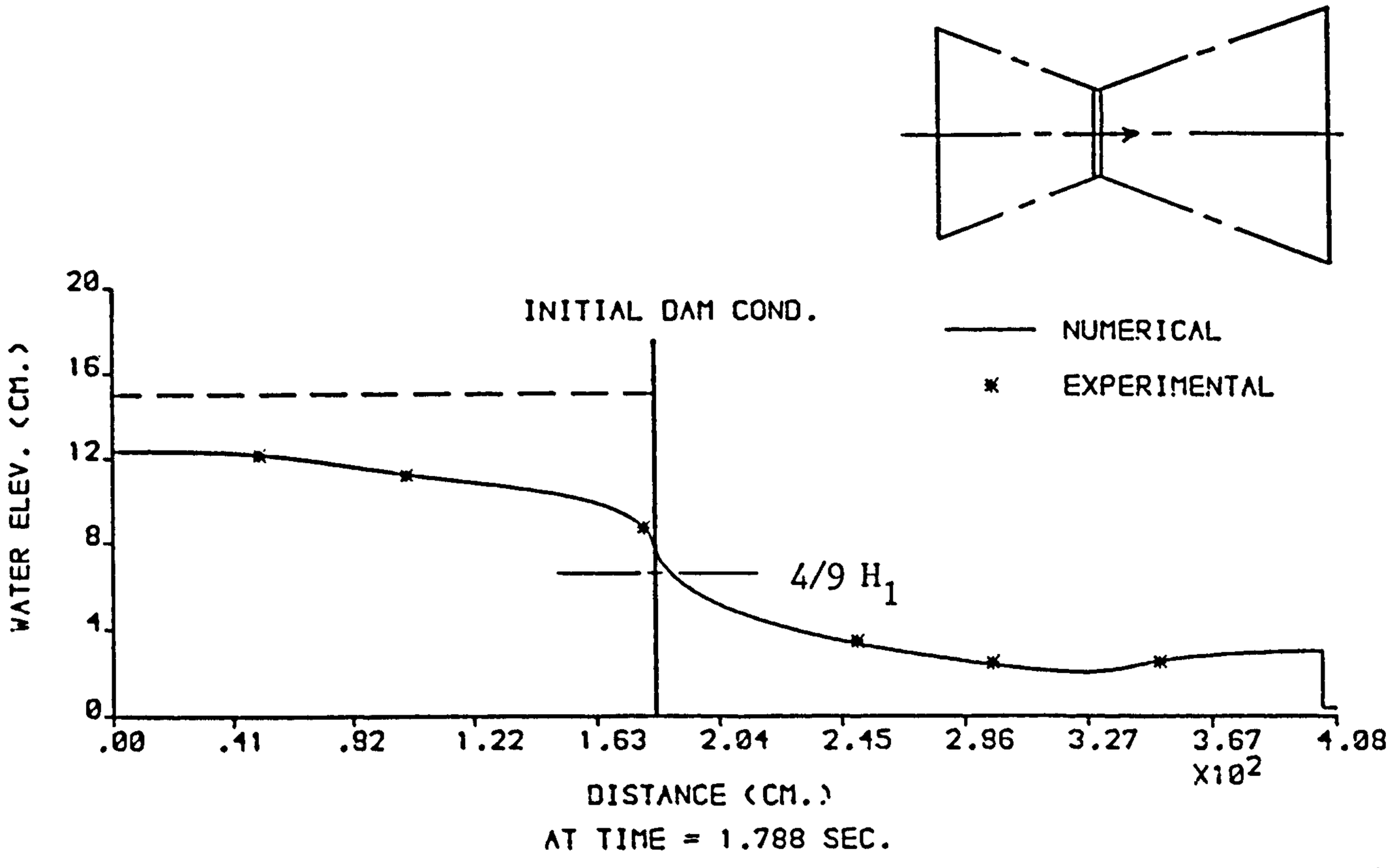

(C) The (RT-RT) Model

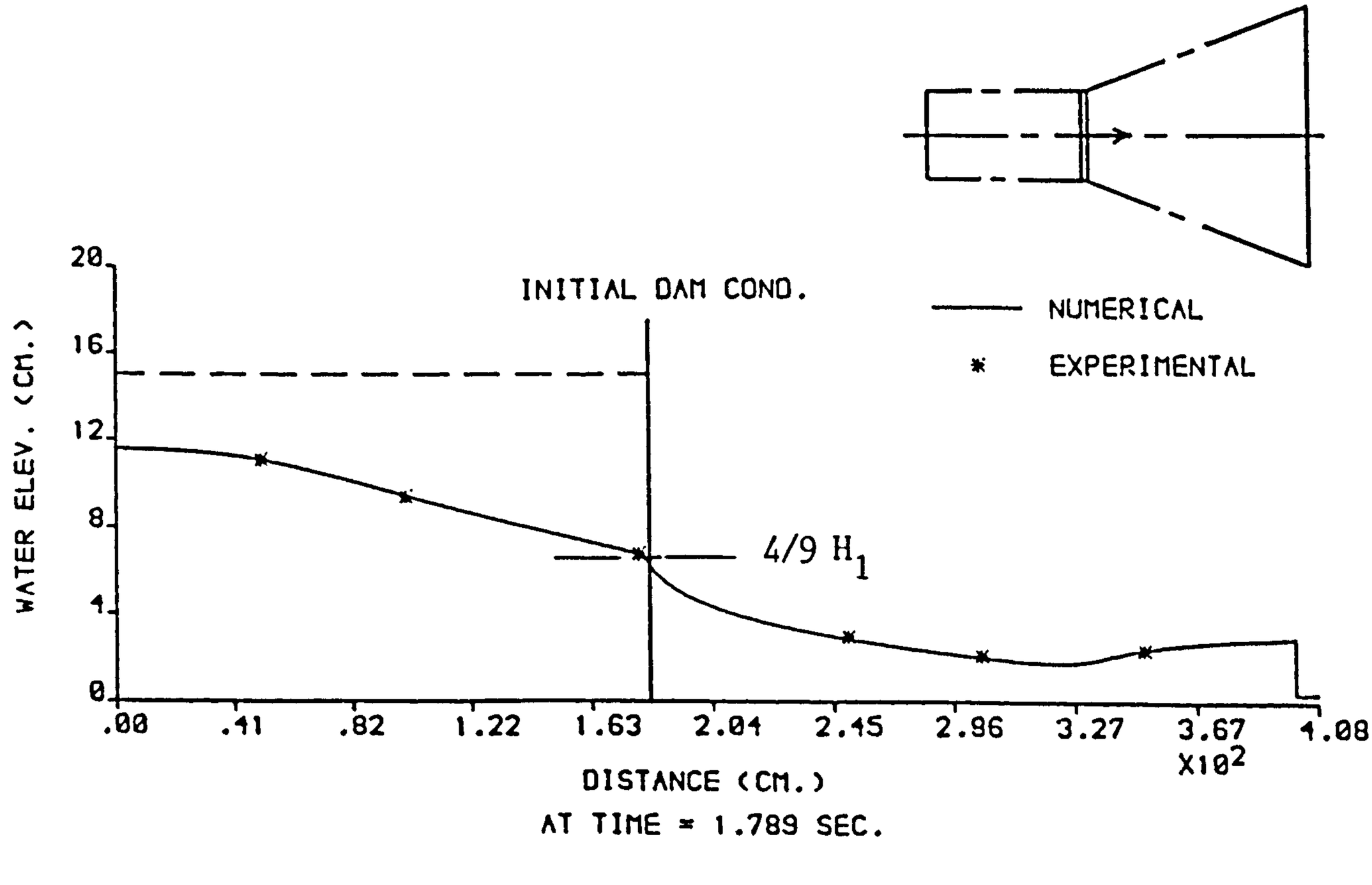

(D) The (XT-RT) Model

FIGURE 6.124 : CONT.

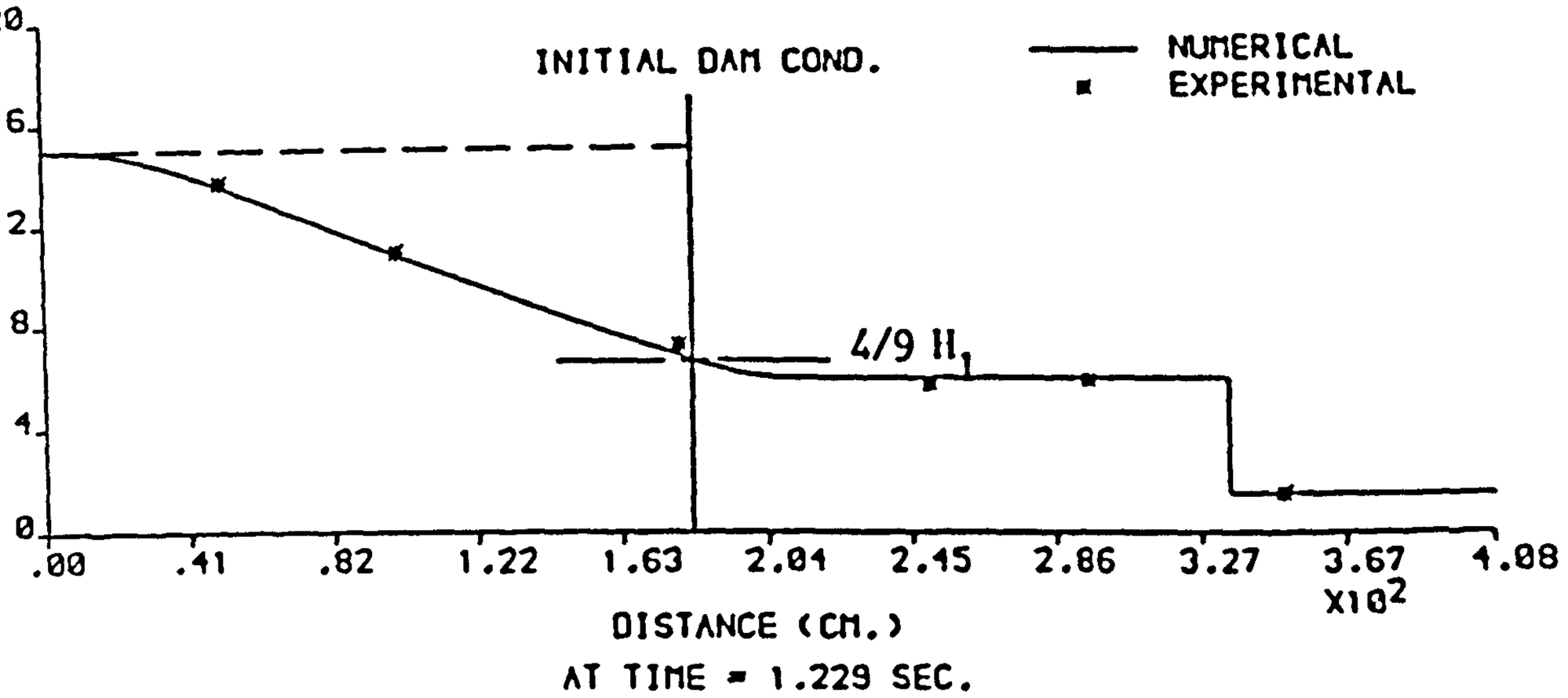

(A) The (X-T) Model

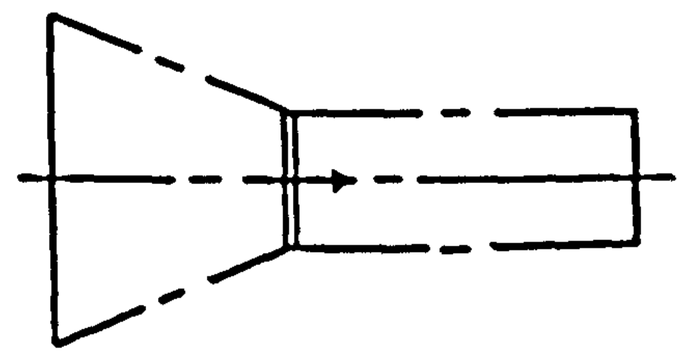

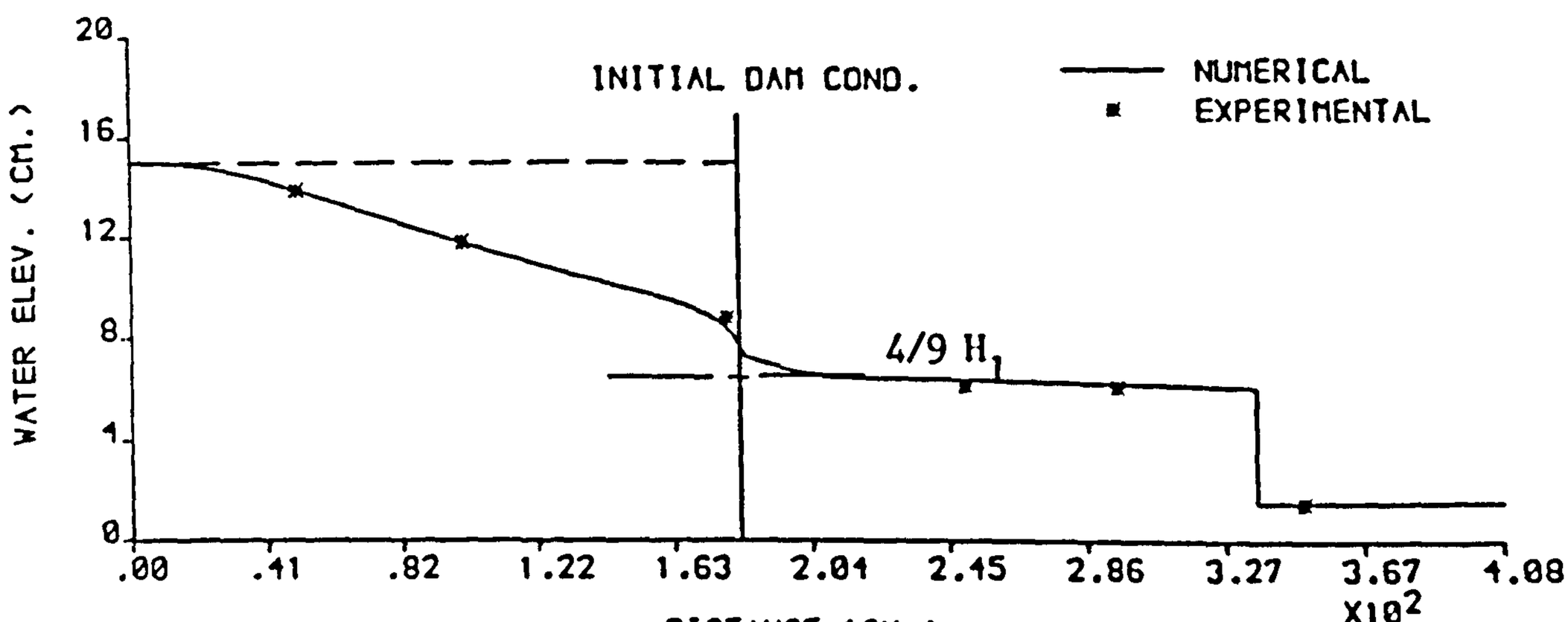

(B) The (RT-XT) Model

FIGURE 6.125 : COMPARISON OF NUMERICAL AND EXPERIMENTAL PROFILES FROM THE FOUR MODELS , H_1 = 15 cm AND H_o = 1.5 cm, $H_o / H_1 = 0.1$.

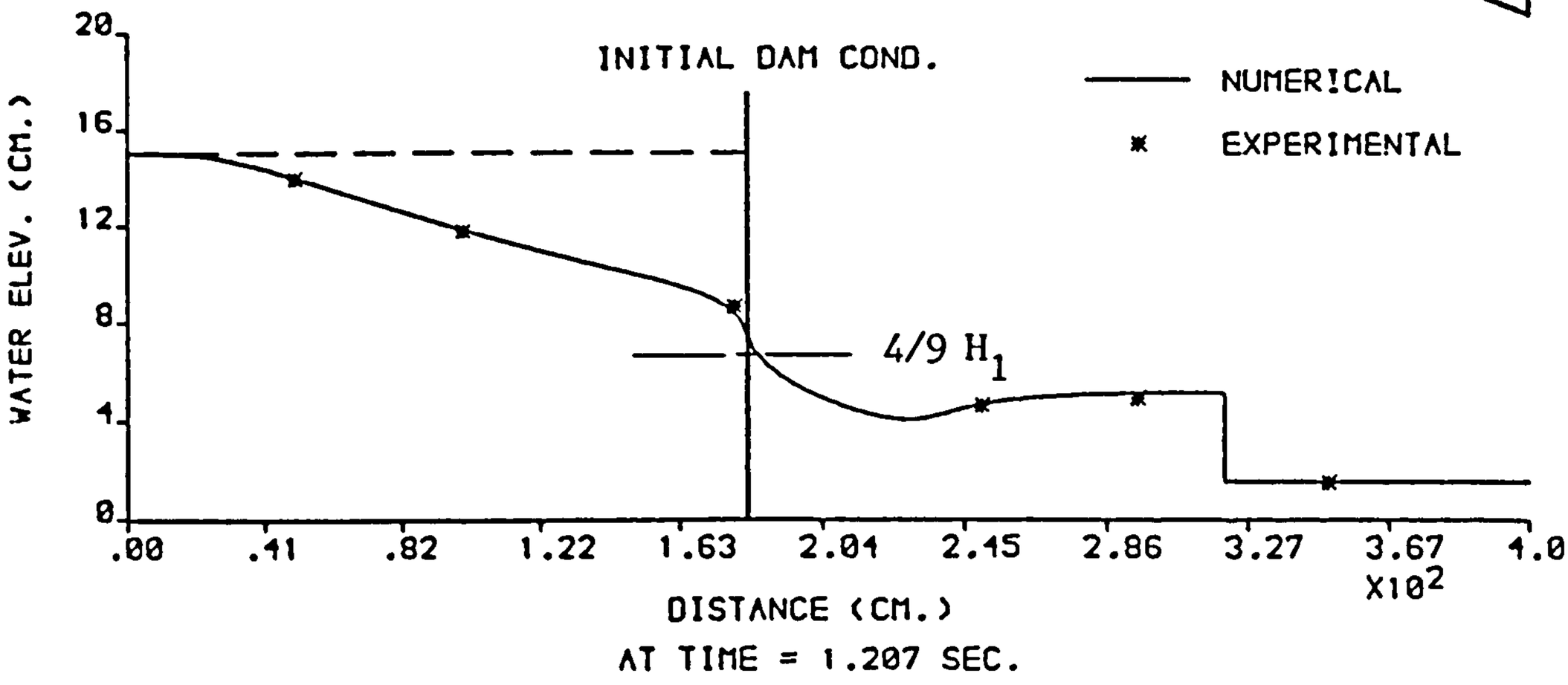

(C) The (RT-RT) Model

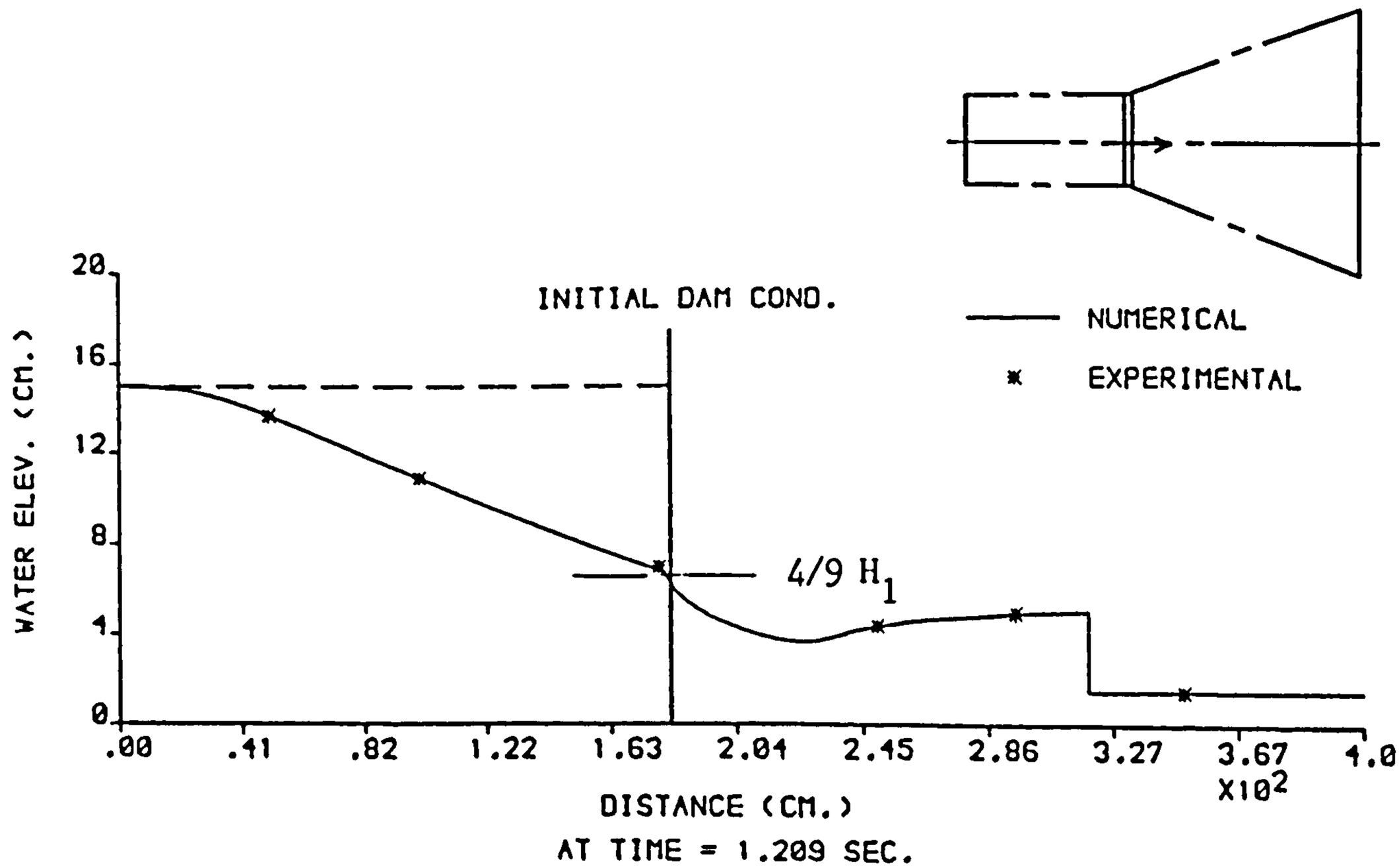

(D) The (XT-RT) Model

FIGURE 6.125 : CONT.

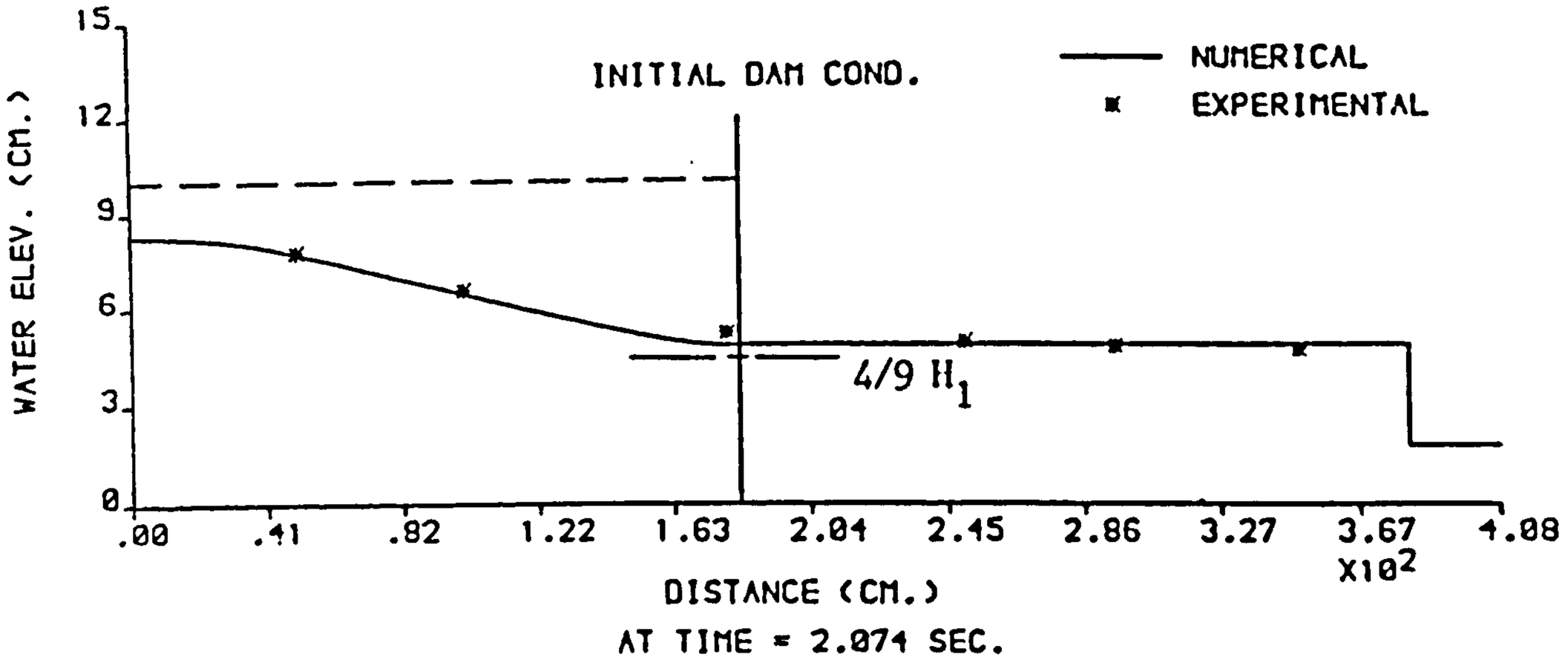

(A) The (X-T) Model

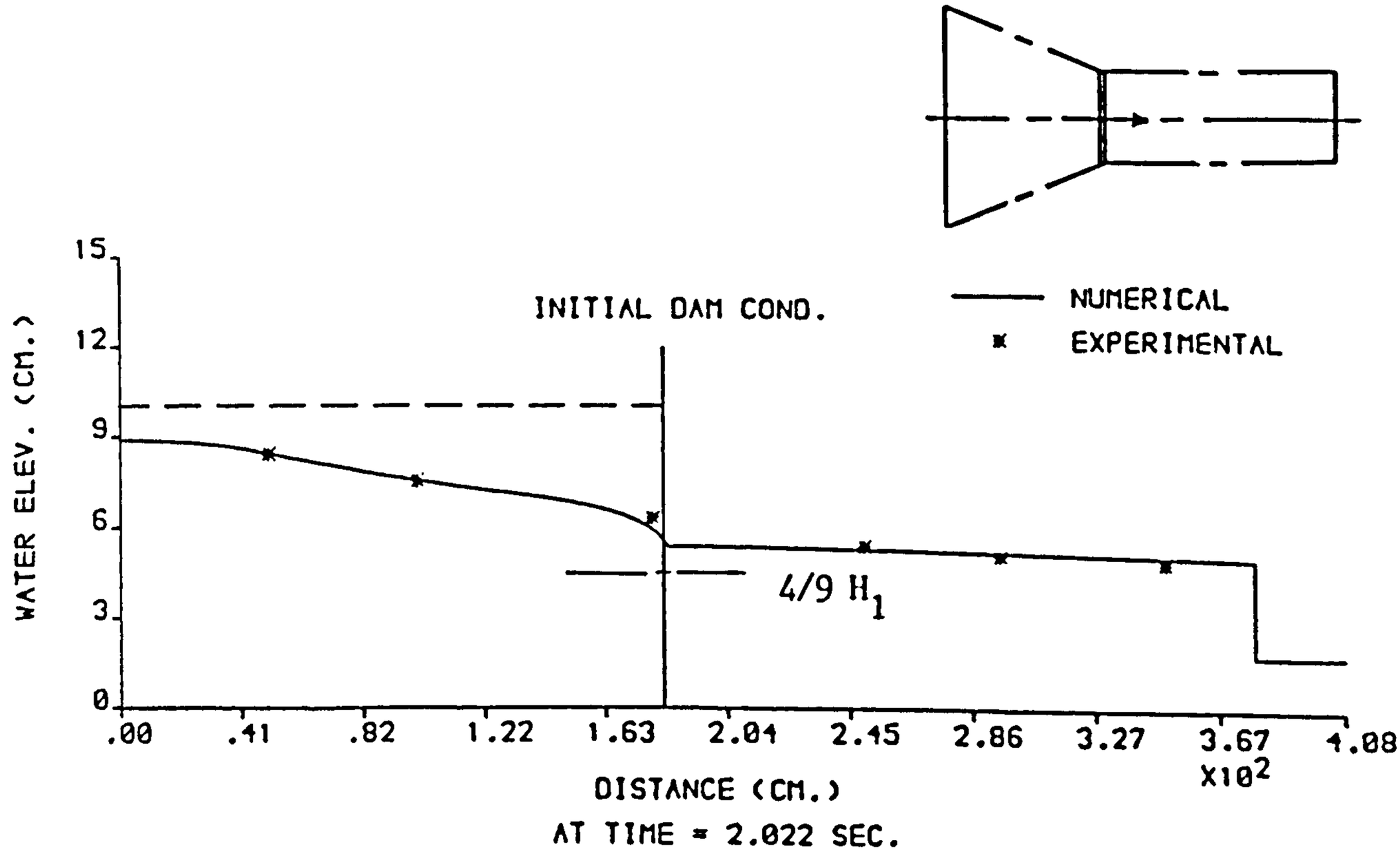

(B) The (RT-XT) Model

FIGURE 6.126 : COMPARISONS OF NUMERICAL AND EXPERIMENTAL PROFILES FROM THE FOUR MODELS , H_1 = 10 cm AND H_o = 1.76 cm, H_o / H_1 = 0.176 .

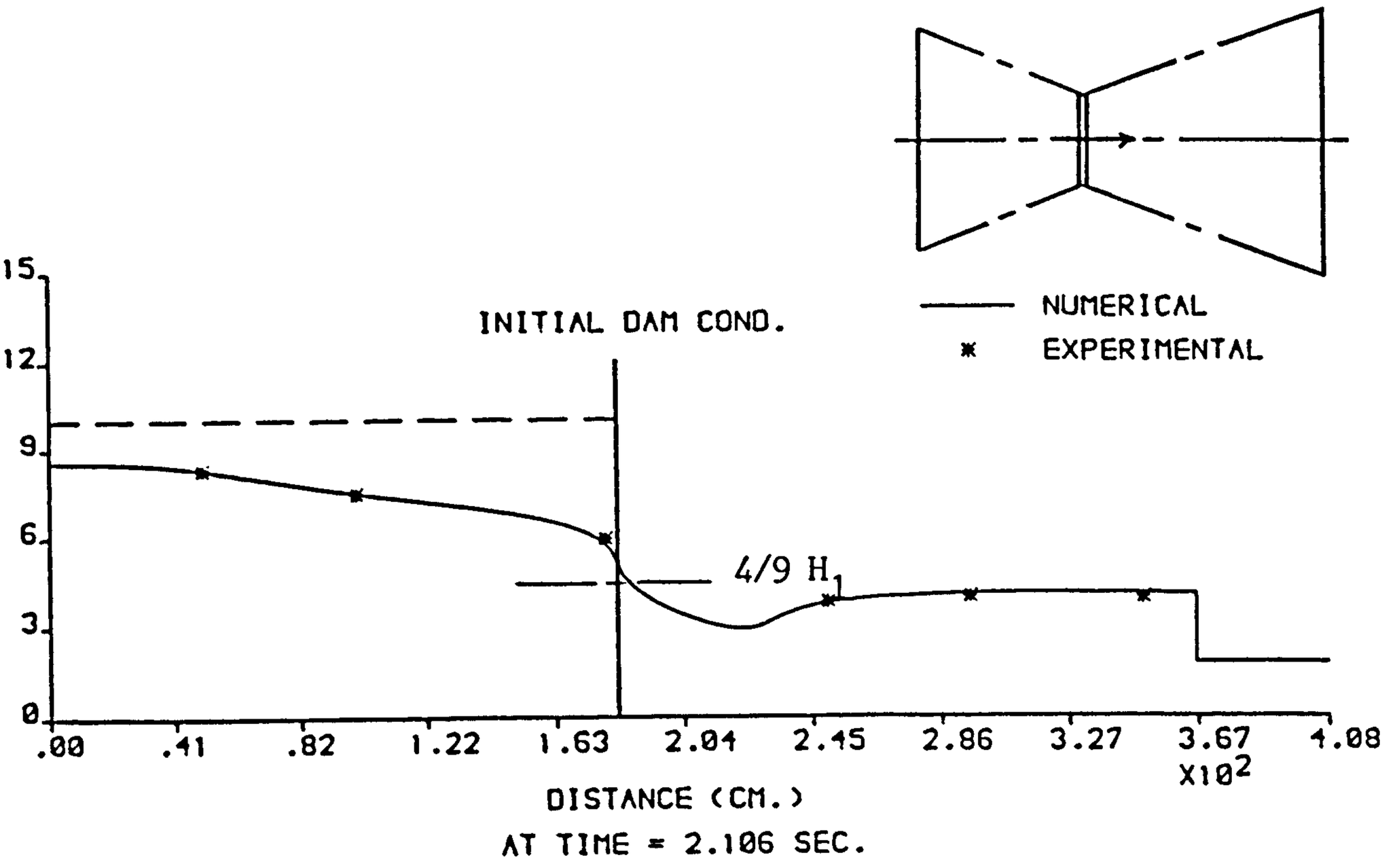

(C) The (RT-RT) Model

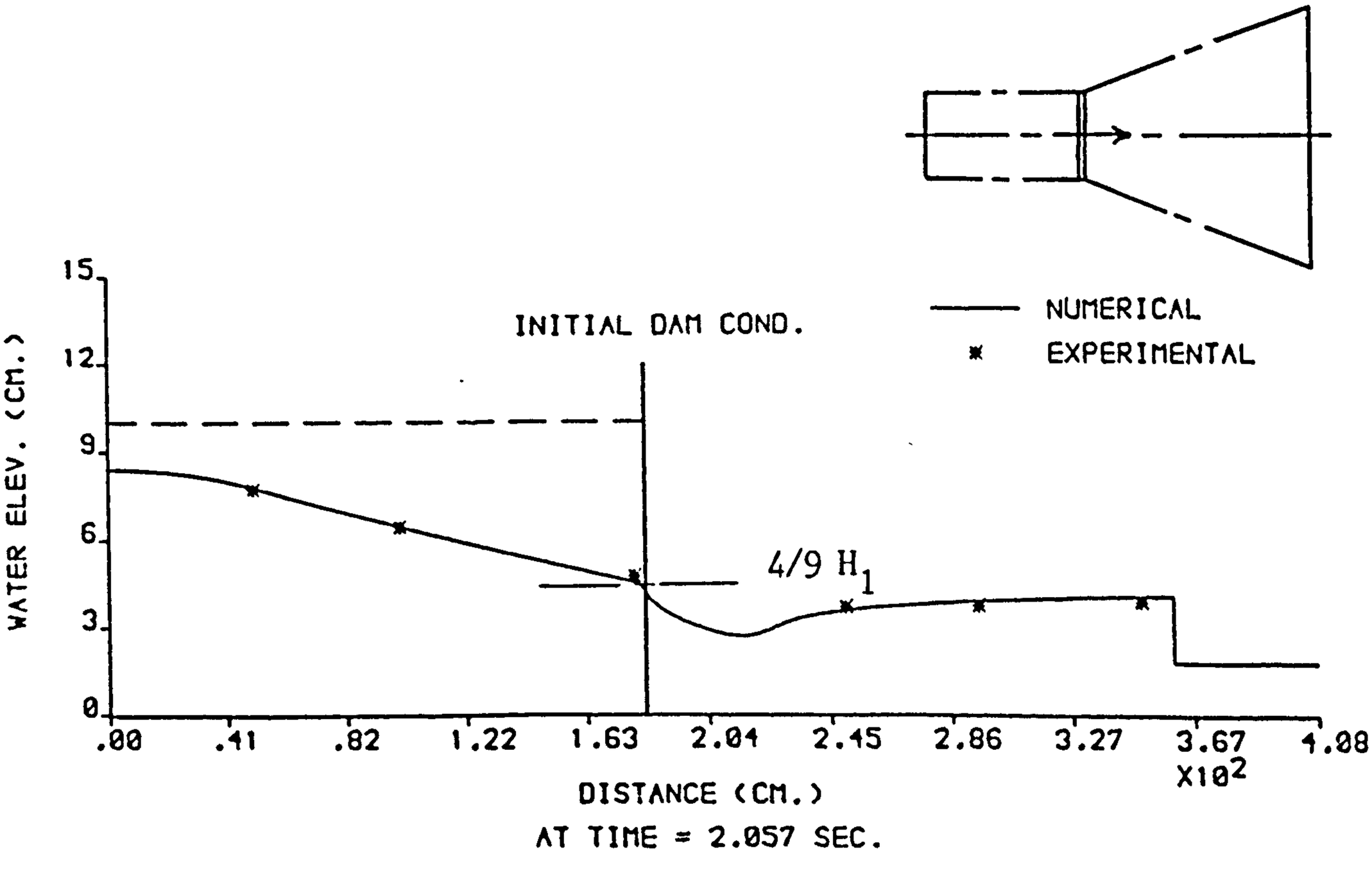

(D) The (XT-RT) Model

FIGURE 6.126 : CONT.

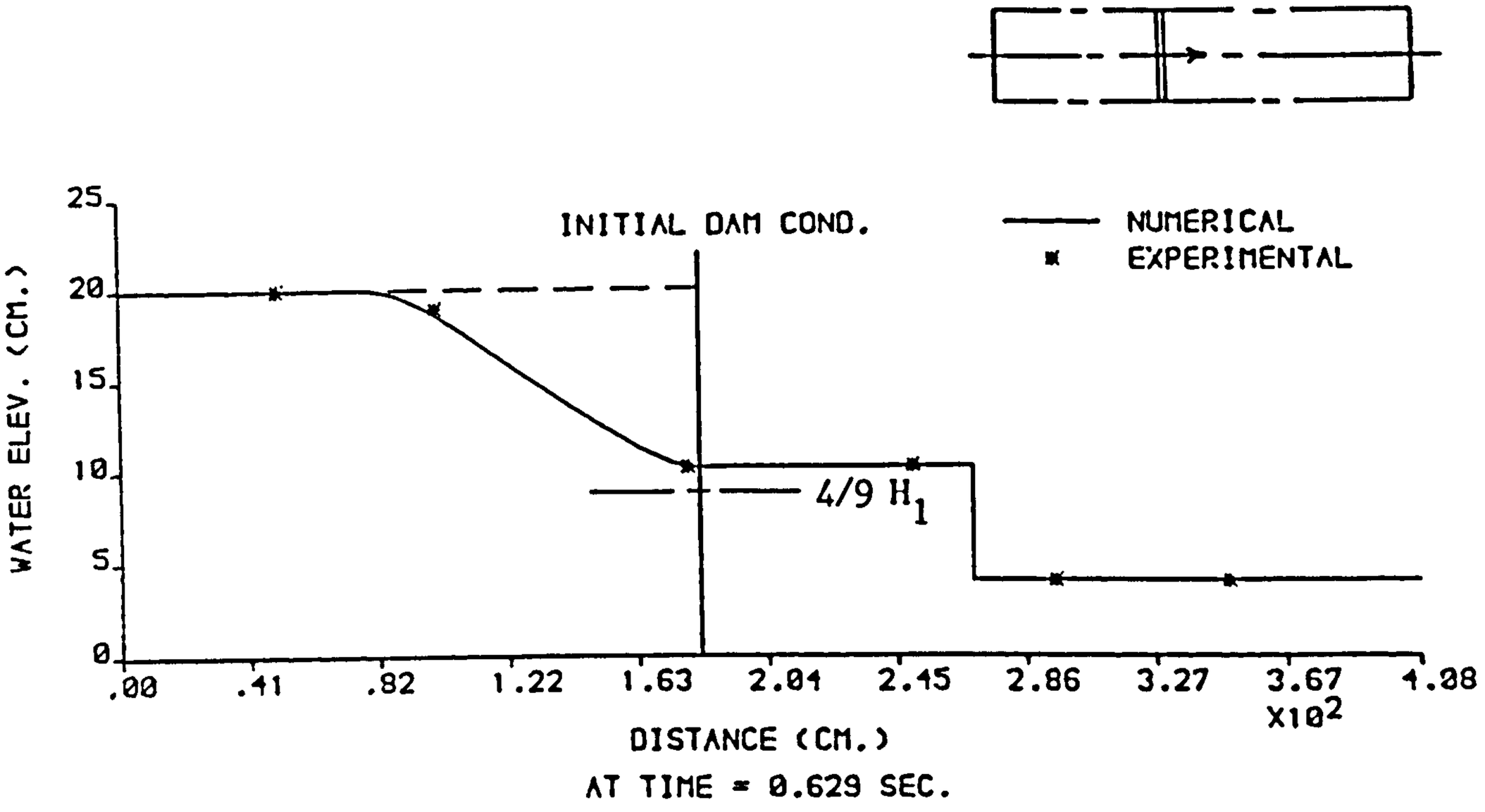

(A) The (X-T) Model

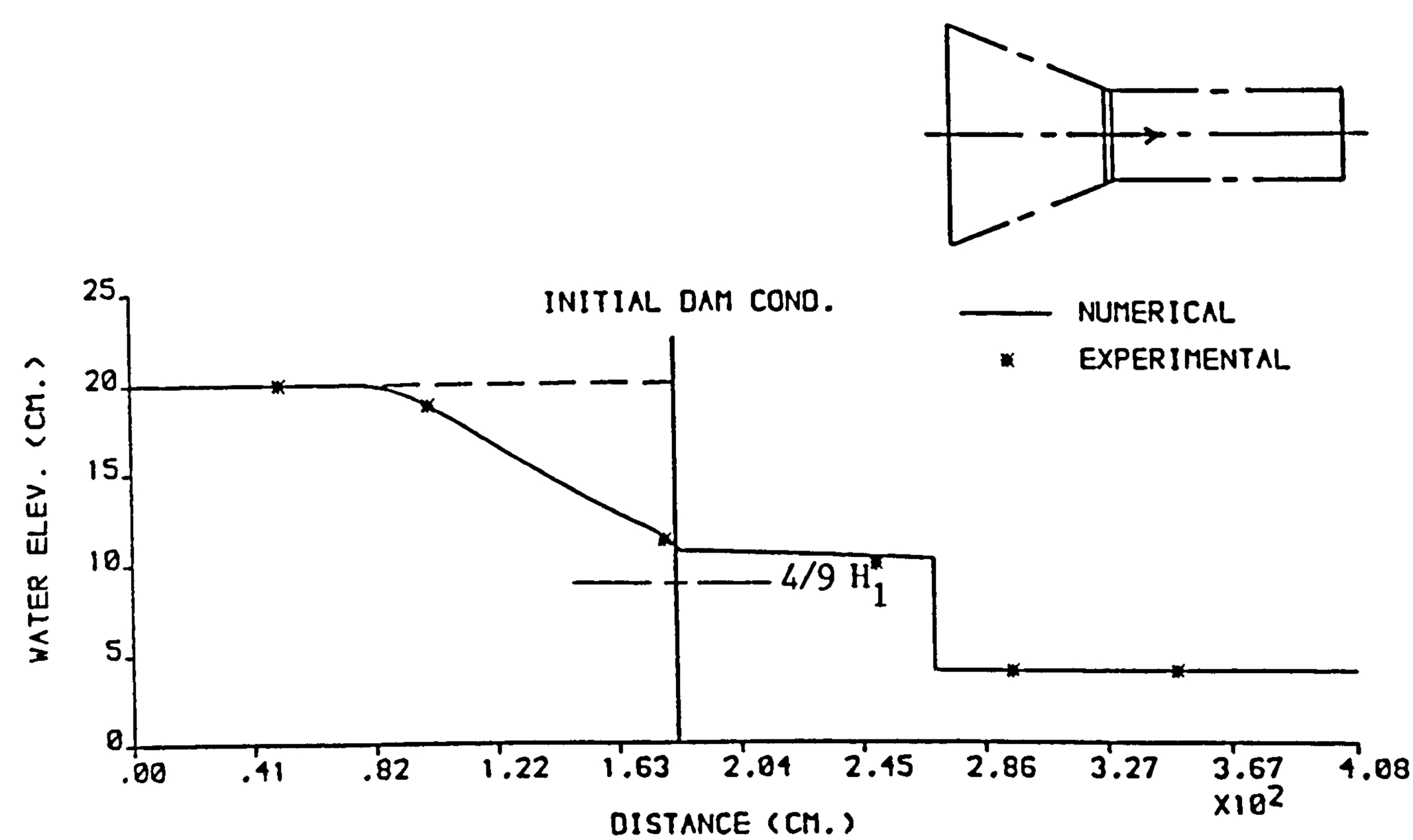

(B) The (RT-XT) Model

FIGURE 6.127 : COMPARISONS OF NUMERICAL AND EXPERIMENTAL PROFILES FROM THE FOUR MODELS , H_1 = 20 cm AND H_o = 4 cm , $H_o / H_1 = 0.2$.

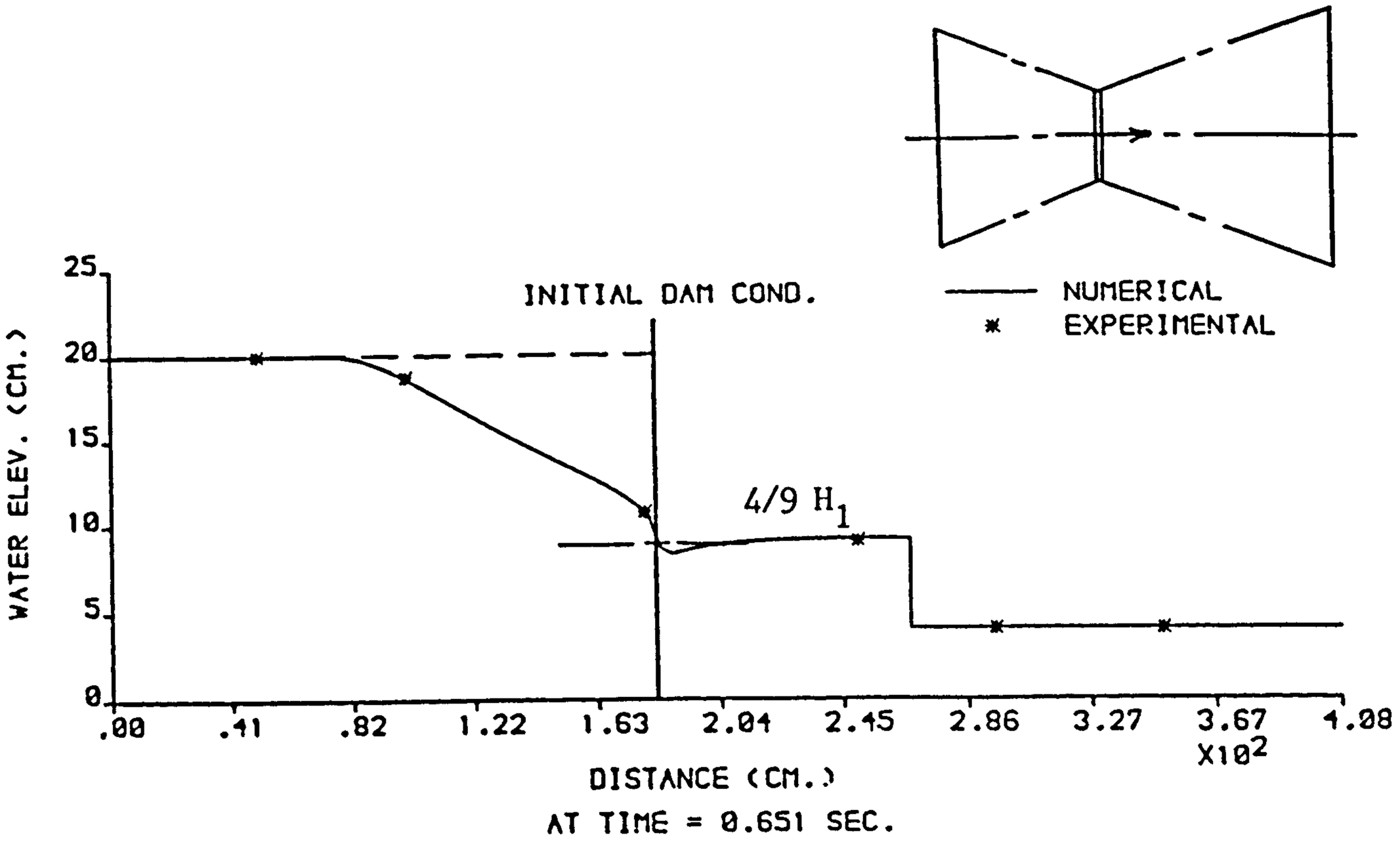

(C) The (RT-RT) Model

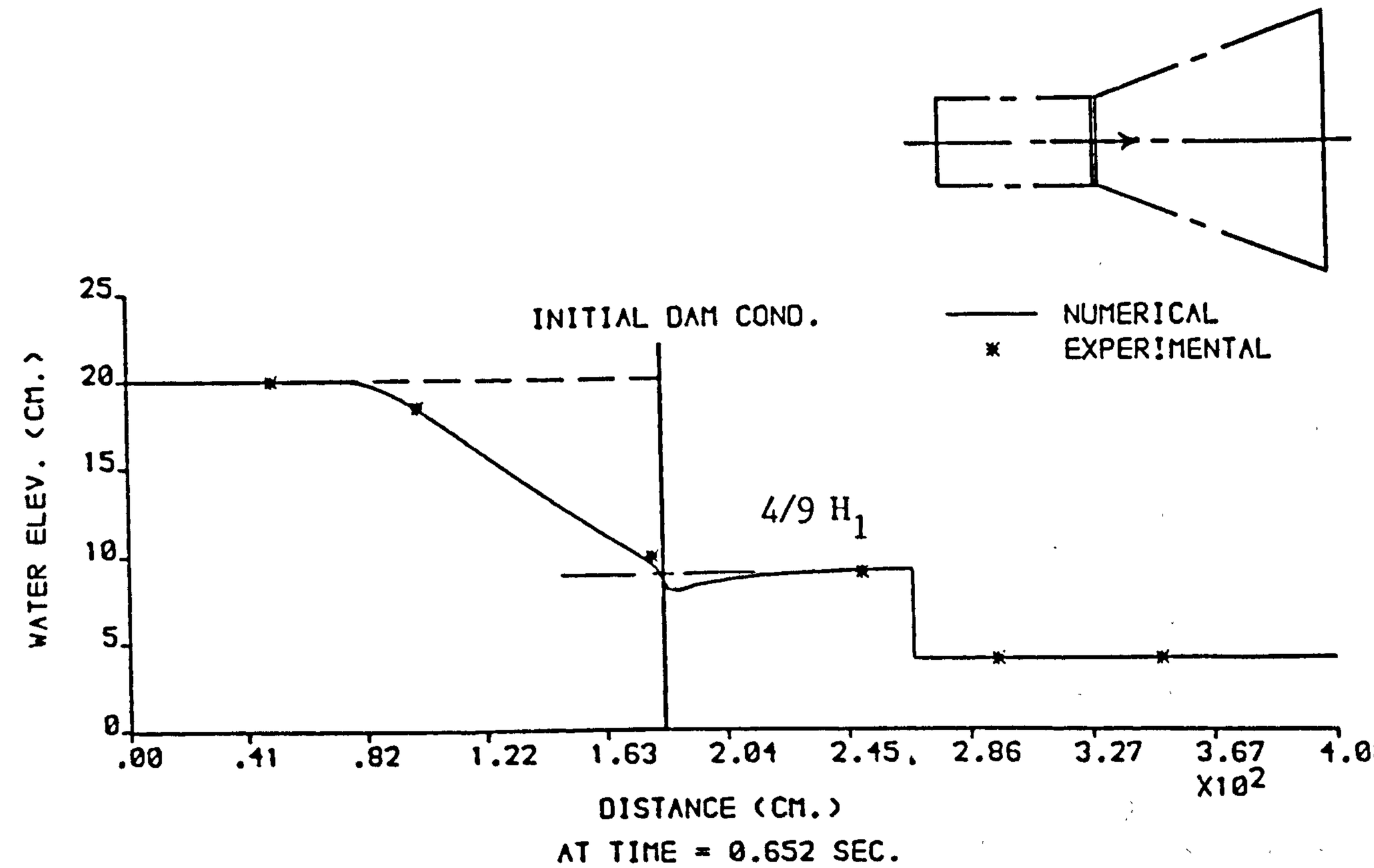

(D) The (XT-RT) Model

FIGURE 6.127 : CONT.

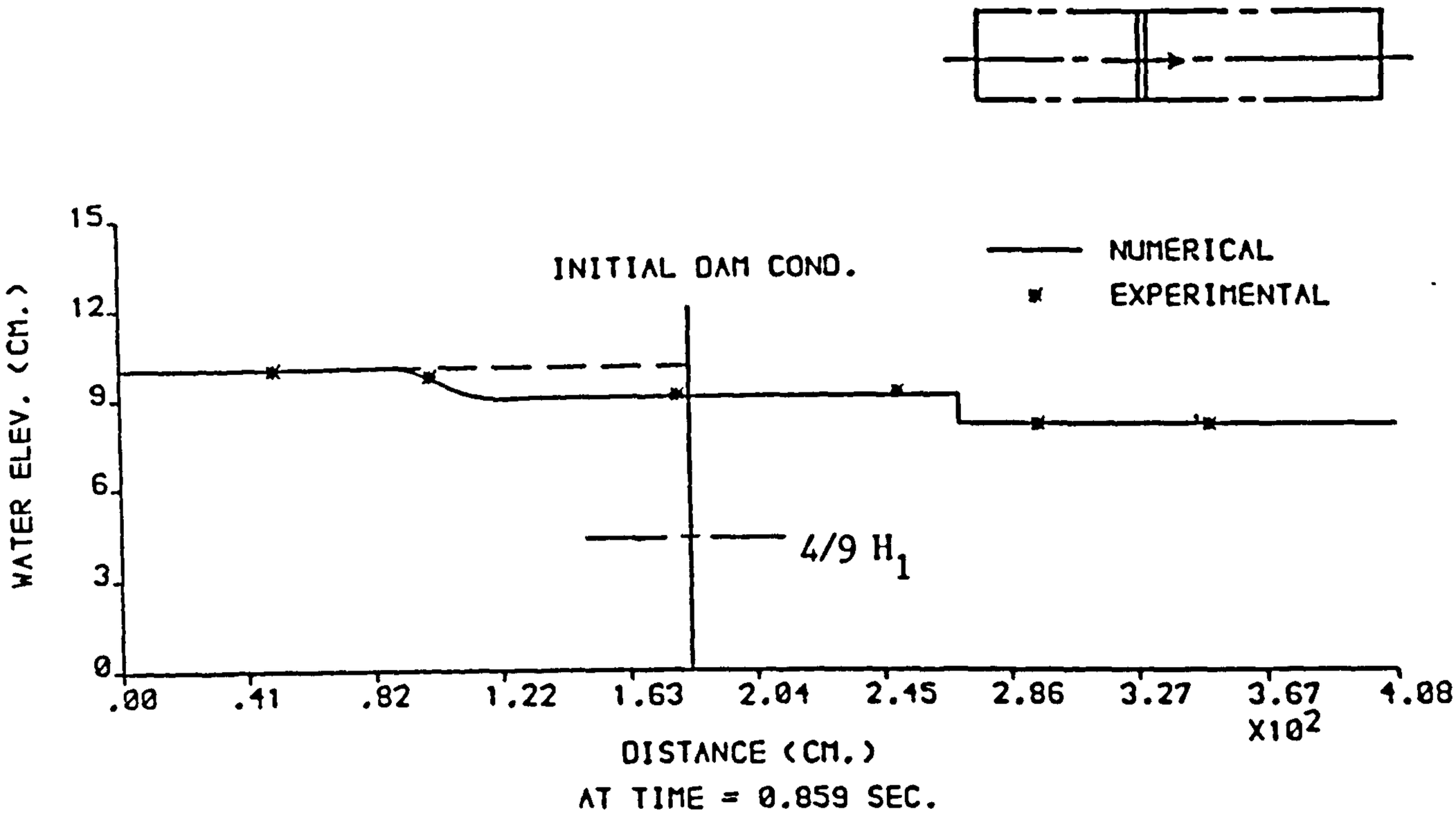

(A) The (X-T) Model

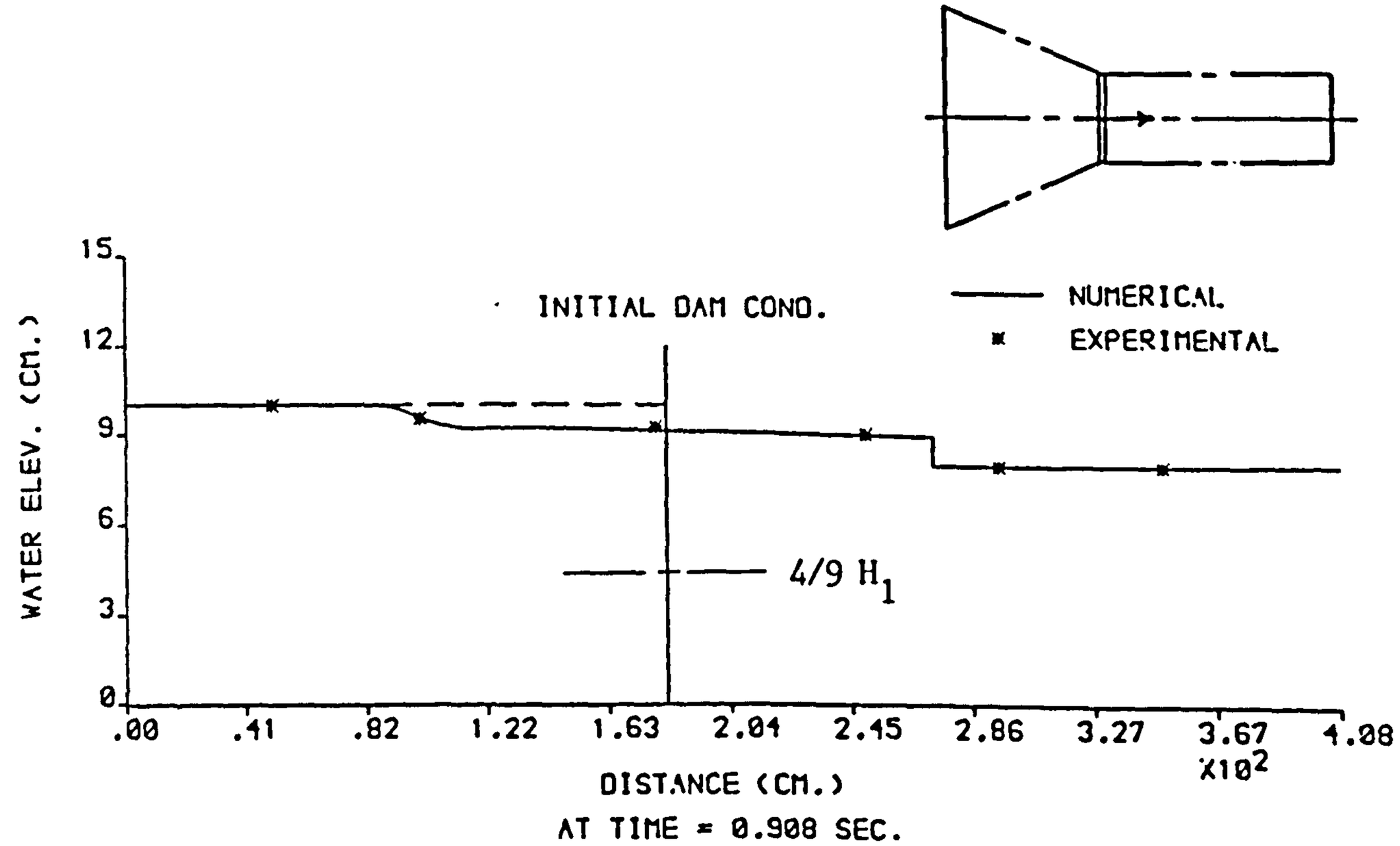

(B) The (RT-XT) Model

FIGURE 6.128 : COMPARISONS OF NUMERICAL AND EXPERIMENTAL PROFILES FROM THE FOUR MODELS , H_1 = 10 cm AND H_o = 8 cm , $H_o / H_1 = 0.8$.

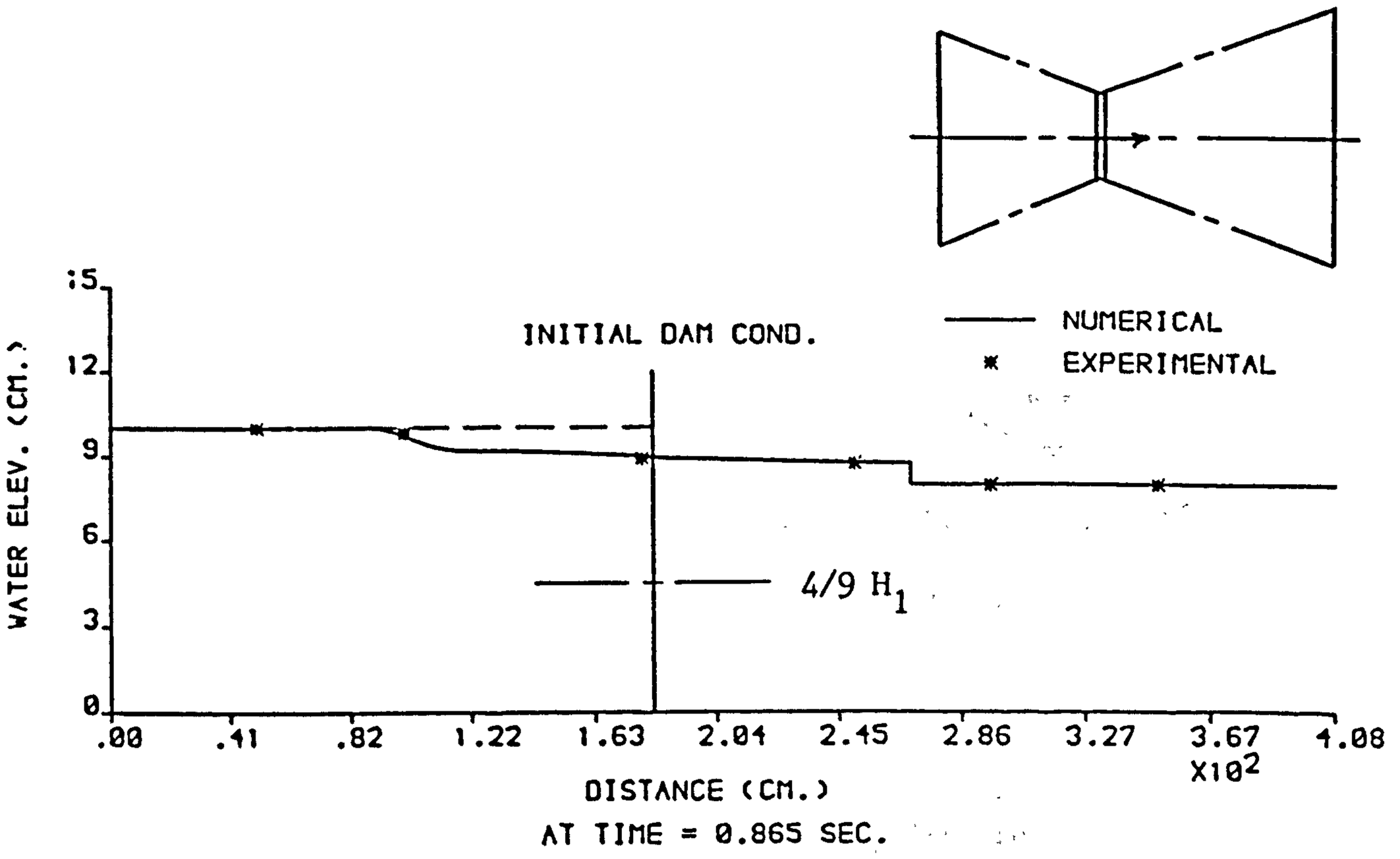

(C) The (RT-RT) Model

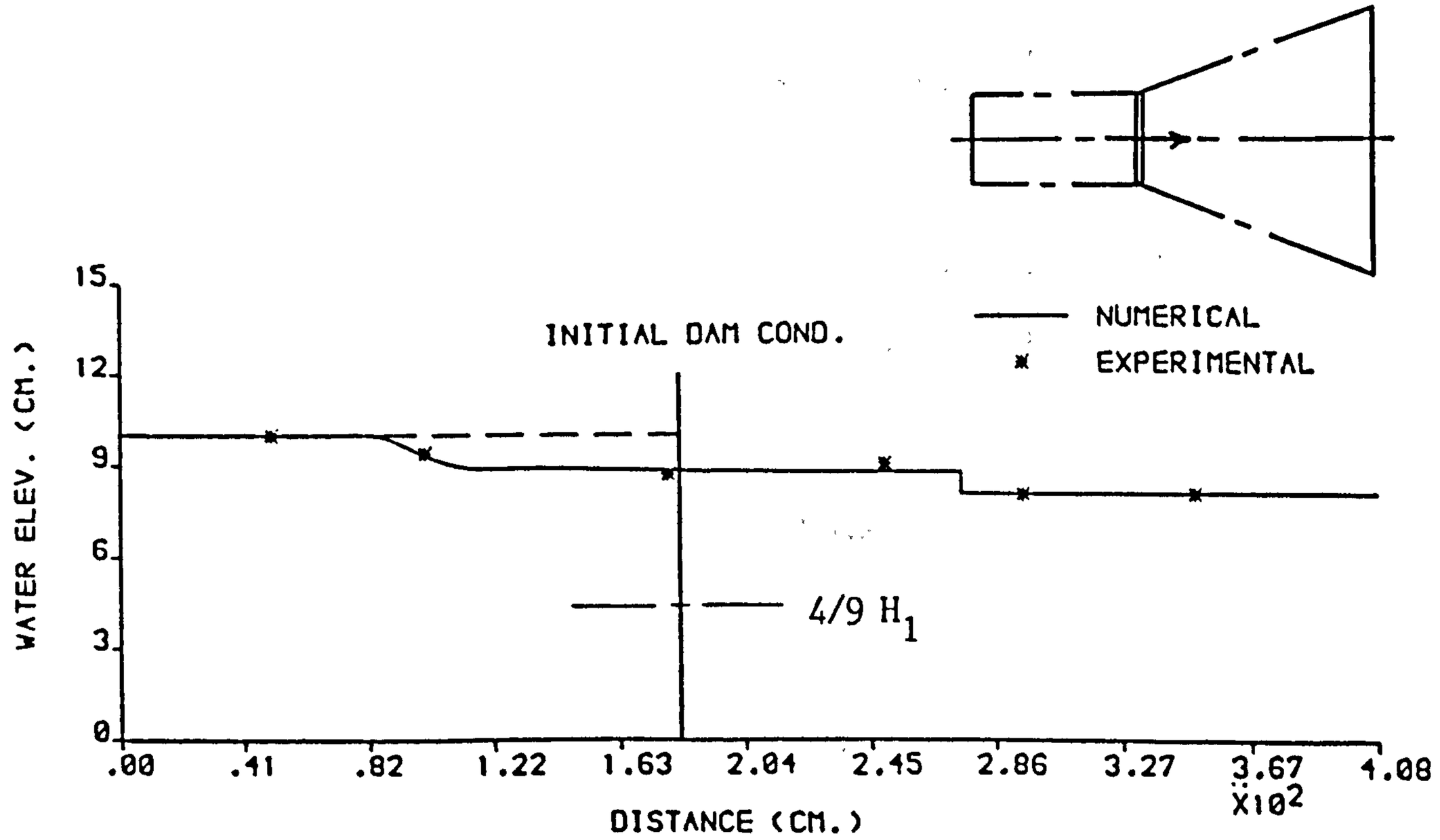

(D) The (XT-RT) Model

FIGURE 6.128 : CONT.

TABLE 6.1 : THE SUMMARY OF THE GENERAL DIFFERENCES .

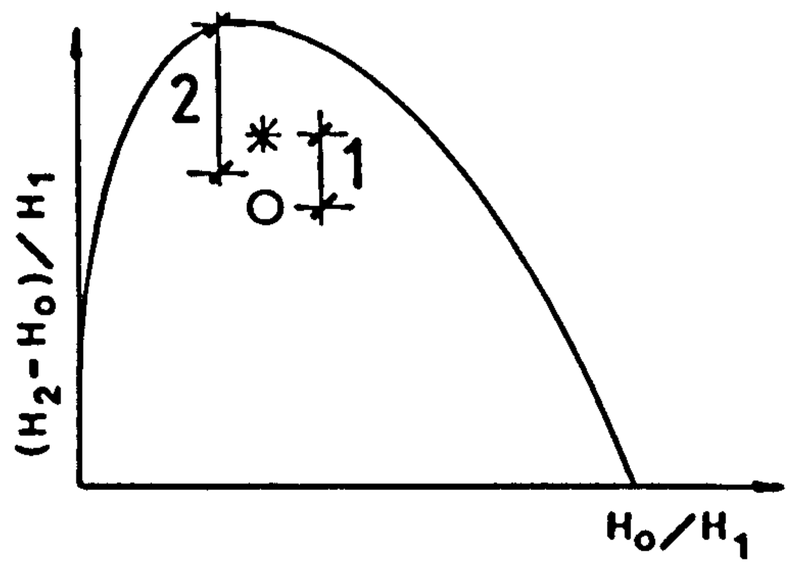

Front Height

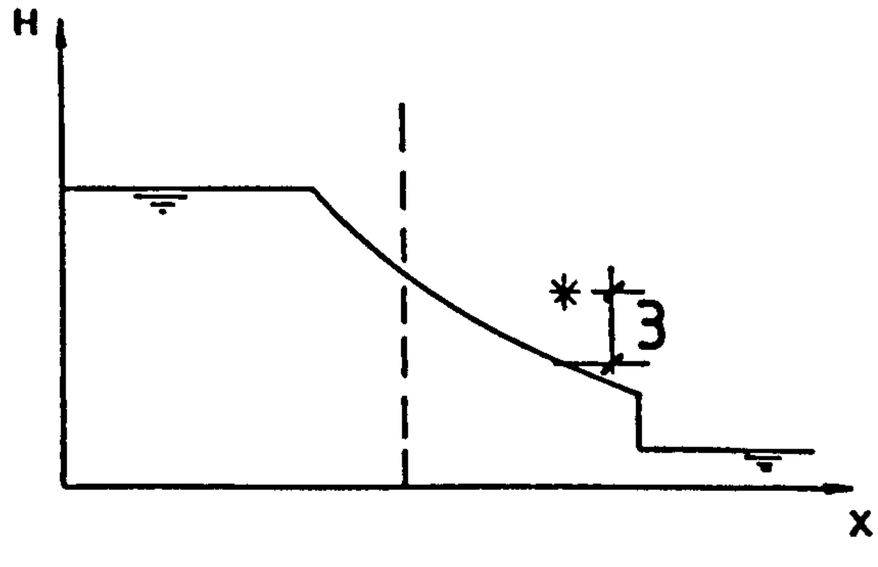

Depth Profile

The Difference (No.)	The Four Models (% Difference)			
	X - T	RT - XT	RT - RT	XT - RT
Difference between Experimental & Numerical Front Heights (1)	3 %	4 %	5 %	5 %
Difference between Stoker's Front Height and the Experimental & Numerical one (2)	4 %	3.5 %	20%	22%
General Difference between Experimental and Numerical Results (3)	6 %	6 %	5 %	5 %

Also ;

The Front Height in General for Model :

RT - XT Higher than X - T by 2 %

and

RT - RT Higher than XT - RT by 2 %

CHAPTER SEVEN
DISCUSSION, CONCLUSIONS AND RECOMMENDATIONS

7.1 Discussion and Conclusions

7.1.1 This study was aimed at numerical simulations of dam-break flood waves in prismatic channels with either a dry bed or finite water depth downstream. The theoretical basis behind such problem was established and followed by the development of numerical models. Both the well known X-T case and the less studied radial flow (R-T) situation were simulated. The X-T model not only reproduced the basic Ritter (1892) solution but also compared well with the numerical and physical models by Barr and Das (1980). The radial flow model reproduced the effects anticipated for convergent and divergent walls, namely:

a. Both surface heights and mean velocities increased in the convergent sections and decreased in the divergent ones.

b. The depth profiles intersected the dam at heights exceeding that from the ratio 4/9 in the convergent sections and lower in the divergent ones.

7.1.2 Combinations of the three basic models, namely the (X-T) with parallel sides and the (R-T) model with both convergent and divergent sides led to a further three composite numerical models; the contracted-plain (RT-XT), the contracted-expanded (RT-RT), and the plain-expanded (XT-RT) model. Physical models were built and tested in the laboratory in order to assess these numerical models. From the comparison of the numerical results and experimental data relating to front heights, surface profiles, front trajectories

and depth hydrographs, it is claimed that the composite numerical solution provides satisfactory simulation of the following phenomena, also observed on the physical models:

a. The converging R-T reservoir, of greater area than in X-T space, enhances the momentum supply per unit width and encourages a higher and faster downstream surge.

b. The R-T expansion downstream both encourages greater energy dissipation and also decreases the momentum supply (per unit width) - leading to lower and slower surges.

c. The water depth profiles of the (XT-RT) model cuts the dam site at a height of slightly less than given by the (4/9) ratio. Conversely, the water depth profiles of the (RT-XT) and (RT-RT) models are higher than this value.

d. The water depth in the (RT-RT) and (XT-RT) models falls suddenly at the transition section and a short reach exists with supercritical flow. The reach ends with an oblique hydraulic jump.

7.1.3 The explicit form of the characteristics method with specified time intervals also incorporated the Rankine-Hugoniot shock equations for computing the propagation of the shock front. The technique, which is often called the shock fitting method, gives a clear-cut front, but whose height closely matched the observed values in the physical models, confirming the useful nature of this particular technique.

7.1.4 Certain numerical difficulties, peculiar to this problem, were also resolved. These arose firstly where flow depths approached zero near the leading edge of the advancing flood wave (i.e. the dry

bed in the downstream channel) and secondly, near the upstream end of the finite-length reservoirs. Both cases were treated successfully by assuming a small fictitious depth of flow. A value of 10^{-4} times the initial water depth upstream the dam, of the order of the machine precision was found suitable.

7.1.5 The usual two-point interpolation process tended to cause the water surface to exhibit saw-toothed variations. This was corrected by interpolating between two adjacent grid points to find the intersection point. This situation was also found to occur by Liggett and Cunge (1975).

7.1.6 The numerical dissipation causes reductions in the water level on the reservoir side and arising from ignoring the negative wave computation can be reduced to an acceptable level if smaller time steps are used upstream of the dam. The nested-grid of ($\frac{1}{2}\Delta t$) upstream the dam gives a good improvement with low computer time consumption.

7.1.7 All the models were run for a sufficiently long time to allow the conservation of mass to be checked against the initial mass before the dam failure. The mass consumption was very small (less than 0.5%) as a computational error.

7.1.8 The (X-T) numerical model was also found to compare well with five mathematical models and experimental data [Katopodes and Schamber (1983)]. The (R-T) convergent sides model compared well with the numerical model of Marshall and Menendez (1981) in the negative wave region. A disagreement in the positive wave front seems to have been caused by the mass creation (3.66% of the initial mass) in Marshall and Menendez's model. The author's (R-T) model

consumed only very small mass (0.07% of the initial mass)..

7.2 Recommendations for Future Studies

7.2.1 In the negative wave calculation, the depth profiles approach the horizontal tangentially. This is physically reasonable but theoretically incorrect, since the negative wave front represents a discontinuity in the slope of forward characteristics emanating from the undisturbed zone in the reservoir. The depression wave front therefore also represents a discontinuity in the slope of the depth profiles, so that careful interpolation along it is suggested as a future refinement of the numerical model. The true flow position would require consideration of velocity variation in the vertical plane.

7.2.2 A small fictitious depth made possible simulation of the dam-break flood wave in a dry channel and near an upstream end of a finite-length reservoir with success. The generality of such fictitious initial and boundary conditions is questionable, although the models behaved well in such conditions. However, in the light of the method of the characteristics, satisfactory and more rigorous simulations of the movement of the liquid edge over dry bed have been obtained by Chowdhury (1982) - which may be relevant.

7.2.3 The (R-T) convergent sides model was compared only with Marshall and Menendez (1981) numerical model, and a good agreement in the negative wave region was observed, as stated before. In the author's physical models comparison was possible in the negative wave region, also with close results. No downstream convergence model was tested, so that for positive wave verification a physical

study seems to be essential in order to assess the complete range of the R-T numerical model.

7.2.4 The radial (R-T) models have been applied only to the rectangular channel with a smooth horizontal bed. A useful extension of this work may be made by studying the effects of different channel sections, bed slopes and resistance values.

REFERENCES

Abbott, M.B., (1966). An Introduction to the Method of Characteristics, Thames and Hudson, London.

Abbott, M.B., (1968). Unsteady Radial Flow of Oil Being Discharged from a Source on the Ocean, Coastal Engineering in Japan, Vol. 11, pp. 185-189.

Abbott, M.B., and E.W.Lindeyer, (1969). Two Transients for a Radial Nearly-Horizontal Flow, La Houille Blanche, No. 1, pp. 65-70.

Abbott, M.B., (1974). Continuous Flows, Discontinuous Flows and Numerical Analysis, Journal of Hydraulic Research, Vol. 12, No. 4, pp. 417-466.

Abbott, M.B., H.M. Petersen and O. Skovgaard, (1978). On the Numerical Modelling of Short Waves in Shallow Water, Journal of Hydraulic Research, Vol. 16, No. 3, pp. 173-204.

Abbott, M.B., (1979). Computational Hydraulics, Elements of the Theory of Free Surface Flows, Pitman Publishing Limited, London, pp. 283.

Amein, M., (1966a). Streamflow Routing on Computer by Characteristics, Water Resources Research, Vol. 2, No. 1, pp. 123-130.

Amein, M., (1966b). A Method for Determining the Behaviour of Long WavesClimbing a Sloping Beach, Journal of Geophysical Research, Vol. 71, No. 2, pp. 401-410.

Amein, M., (1977). The Dam-Break Wave and the Bore Collapse on a Beach, Proceedings of Dam Break Flood Routing Model Workshop, Water Resources Council, Washington, D.C., U.S.A., pp. 1-17.

Babb, A.O., and T.W. Mermel, (1968). Catalog of Dam Disasters, Failures and Accidents, U.S. Bureau of Reclamation, Washington, D.C., pp. 202, 63 and 48, U.S.A.

Balloffet, A., E. Cok, and A.F. Balloffet, (1974). Dam Collapse Wave in a River, J. Hydraulic Div., Proc. ASCE, Vol. 100, No. HY5, May, pp. 645-665.

Barr, D.I.H., (1973). Resistance Laws for Large Conduits, Water Power, August, pp.290-304.

Barr, D.I.H., (1976). Some Solution Procedures for the Colebrook-White Function, Water Power and Dam Construction, December, pp. 31-37.

Barr, D.I.H., and M.M. Das, (1980). Numerical Simulation of Dam-Burst and Reflections, with Verification Against Laboratory Data, Proc. Instn. Civil Engrs., Part 2, No. 69, June, pp. 359-373.

Chen, C.L., and L.A. Druffel, (1977). Dam-Break Flood Wave Computation by Method of Characteristics and Linearized Implicit Schemes, Proceedings of Dam Break Flood Routing Model Workshop, Water Resources Council, Washington, D.C., U.S.A., pp. 312-345.

Chen, C.L., (1980). Laboratory Verification of a Dam-Break Flood Model, J. Hydraulic Div., Proc. ASCE, Vol. 106, No. HY4, April, pp. 535-556.

Chen, C.L., and J.T. Armbruster, (1980). Dam-Break Wave Model : Formulation and Verification, J. Hydraulic Div., Proc. ASCE, Vol. 106, No. HY5, May, pp. 747-767.

Chen, C.L., (1982). Closure to Discussion (1981) on Laboratory Verification of a Dam-Break Flood Model, by C.L. Chen (1980), J. Hydraulic Div., Proc. ASCE, Vol. 108, No. HY2, February, pp. 275-283.

Chowdhury, J.U., (1982). Numerical Models for Shallow Water Tides in x-t River Networks and x-y-t Space, Ph.D. Thesis, Strathclyde University, Glasgow, U.K.

Courant, R.,and K.O. Friedrichs, (1948). Supersonic Flow and Shock Waves, Interscience Publishers, Inc., New York, U.S.A.

Craya, A., (1946). Calcul Graphique Regime Variables Dans les Canaux, La Houille Blanche, No. 1, pp. 19-38, No. 2, pp. 117-130.

Cunge, J.A., (1970). Calcul de Propagation des Ondes de Rupture de Barrage, La Houille Blanche, No. 1, pp. 25-33.

Cunge, J.A., (1975). Rapidly Varying Flow in Power and Pumping Canals, In Unsteady Flow in Open Channels, ed. K. Mahmood and V. Yevjevich, Water Resources Publications, Ft. Collins, Colorado, U.S.A., pp. 539-586.

Cunge, J.A., F.M. Holly, and A. Verwey, (1980). Practical Aspects of Computational River Hydraulics, Pitman Publishing Ltd., London.

Das, M.M., (1978). The Effect of Resistance on Steady and Unsteady Free Surface Profiles, Ph.D. Thesis, Strathclyde University, Glasgow, U.K.

Dressler, R.F., (1952). Hydraulic Resistance Effect Upon the Dam-Break Functions, Journal of Research of the U.S. National Bureau of Standards, Vol. 49, No.3, Sep., pp. 217-225.

Dressler, R.F., (1954). Comparison of Theories and Experiments for the Hydraulic Dam-Break Wave, International Assoc. of Scientific Hydrology, Publication No. 38, Vol. 3, pp. 319-328.

Dressler, R.F., (1958). Unsteady Non-Linear Waves in Sloping Channels, Proceedings of the Royal Society of London, Series A, Vol. 247, No. 1249, pp. 186-198.

Eguiazarov, J.B., (1935). Water-level Regulation in Pools of Regulated Rivers and Regulation of Water Discharge Below the Last Weir in Connection with the Utilization of the Hydraulic Power, Permanent Int'l Assoc. Navigation Congress - Reports, Int'l Congress of Navigation 16th, Brussels.

Escande, L.,F. Jougaro, L. Castex, and H. Barther, (1961). The Influence of Certain Parameters on a Sudden Flood Wave Downstream from a Dam, La Houille Blanche, No. 5, pp. 565-575.

Faure, J., and N. Nahas, (1961). A Numerical and Experimental Study of Steep-Fronted Solitary Waves, La Houille Blanche, No. 5, Oct., pp. 576-587.

Faure, J., and N. Nahas, (1961a). Two Problems of Unsteady Free Surface Flow Solved by Digital Computer, IAHR 9th Convention, Dubrovnik, Paper III 26, pp. 854-869.

France, P.W., (1981). Analysis of the Hydraulic Jump Within a Diverging Rectangular Channel, Proc. Instn. Civil Engrs., Part 2, Vol. 71, June, pp. 369-378.

Franz, D.D., (1977). Dam Break Flood Wave Analysis : Problems, Pitfalls, and Partial Solutions, Proceedings of Dam Break Flood Routing Model Workshop, Water Resources Council, Washington, D.C., U.S.A., pp. 354-383.

Fread, D.L., and T.E. Harbaugh, (1973). Transient Hydraulic Simulation of Breached Earth Dams, J. Hydraulic Div., Proc. ASCE , Vol. 99, No. HY1, January, pp. 139-154.

Gilmore, F.R., M.S. Plesset, and H.E. Crossley, (1950). The Analogy Between Hydraulic Jumps in Liquids and Shock Waves in Gases, Journal of Applied Physics, Vol. 21., March, pp. 243-249.

Hartree, D.R., (1953). Some Practical Methods of Using Characteristics in the Calculation of Non-Steady Compressible Flow, U.S. Atomic Energy Comm. Rep. No. AECU-2713.

Haws, E.T., (1954). Surges and Waves in Open Channels, Water Power, November, pp. 419-422.

Henderson, F.M., (1966). Open Channel Flow, Collier Macmillan Publishers, London.

Hunt, B., (1982) Asymptotic Solution for Dam-Break Problem, J. Hydraulic Div., Proc. ASCE, Vol. 108, No.HY1, January, pp. 115-126.

Hunt, B., (1983). Asymptotic Solution for Dam Break on Sloping Channel, J. Hydraulic Eng'g.,Proc.ASCE , Vol. 109, No. 12, December, pp. 1698-1706.

Hunt, B., (1984a). Dam-Break Soltuion, J. Hydraulic Eng'g.,Proc. ASCE, Vol. 110, No. 6, June, pp. 675-686.

Hunt, B., (1984b). Perturbation Solution for Dam-Break Floods, J. Hydraulic Eng'g.,Proc. ASCE, Vol. 110, No. 8, August, pp. 1058-1071.

Jovanovic, M., and M. Radojkovic, (1982). Numerical and Experimental Study of Two-Dimensional Dam Break Problems, Proceedings of the Symposium, Refined Modelling of Flows, Paris, 7-10 Sep., Vol. 2., pp. 491-497.

Katopodes, N., (1977). Unsteady Two-Dimensional Flow Through a Breached Dam by the Method of Characteristics, Ph.D. Thesis, University of California, Davis, U.S.A.

Katopodes, N., and T. Strelkoff, (1978). Computing Two-Dimensional Dam-Break Flood Waves, J. Hydraulic Div., Proc. ASCE , Vol. 104, No. HY9, September, pp. 1269-1288.

Katopodes, N., and T. Strelkoff, (1979). Two-Dimensional Shallow Water-Wave Models, J. Eng. Mech. Div., Proc. ASCE , Vol. 105, No. EM2, April, pp. 317-334.

Katopodes, N., (1980). Divergent Flow in the Vicinity of A Breached Dam, in Special Conference on Computer and Physical Modelling in Hydraulic Engineering, ed. G. Ashton, Proc. ASCE , 6-8 August, pp. 310-321.

Katopodes, N.D., and D.R. Schamber, (1981). Discussion on Laboratory Verification of a Dam-Break Flood Model, by C.L. Chen (1980), J. Hydraulic Div., Proc. ASCE, Vol. 107, No. HY2, February, pp. 246-249.

Katopodes, N.D., (1983). Discussion on Asymptotic Solution for Dam-Break Problem by B. Hunt, J. Hydraulic Eng'g., Proc. ASCE , Vol. 109, No. 4, April, pp. 634-637.

Katopodes, N.D., and D.R. Schamber, (1983). Applicability of Dam-Break Flood Wave Models, J. Hydraulic Eng'g., Proc. ASCE, Vol. 109, No. 5, May, pp. 702-721.

Katopodes, N.D., (1984). Two-Dimensional Surges and Shocks in Open Channels, J. Hydraulic Eng'g., Proc. ASCE , Vol. 110, No. 6, June, pp. 794-812.

Kaya, Y., (1985). Numerical and Physical Studies of the Water Motion Caused by Sudden Disturbances in Reservoirs, Etc., Ph.D. Thesis, Strathclyde University, Glasgow, U.K.

Keller, N.B., D.A. Levine, and G.B. Whitham, (1960). Motion of a Bore Over a Sloping Beach, J. Fluid Mech., Vol. 7, No. 2, pp. 302-316.

Khalifa, A.M., and J.A. McCorquodale, (1979). Radial Hydraulic Jump, J. Hydraulic Div., Proc. ASCE, Vol. 105, No. HY9, September, pp. 1065-1078.

Koloseus, H., and D. Ahmad, (1969). Circular Hydraulic Jump, J. Hydraulic Div., Proc. ASCE , Vol. 95, No. HY1, January, pp. 409-422.

Kordas, K., and H. Witkowska, (1976). Mathematical Model of a Dam-Break Wave, Proc. Int. Symp. on Unsteady Flow in Open Channels, BHRA Fluid Engineering, Cranfield, U.K., April, paper C2, pp. 19-28.

Kosorin, K., (1983). Hydraulic Characteristics of some Dam Break Wave Singularities, XX Congress of the International Association for Hydraulic Research, Proceedings, Subject A, Vol. 11, Sep. 5-9, pp. 520-528.

Lawson, J.D., and B.C. Phillips, (1983). Circular Hydraulic Jump, J. Hydraulic Eng'g.,Proc. ASCE, Vol. 109, No. 4, April, pp. 505-518.

Lax, P.D., (1954). Weak Solutions of Nonlinear Hyperbolic Equations and Their Numerical Computation, Comm. Pure. and Appl. Math., Vol. 7., No. 1., pp. 159-193.

Lax, P.D., and B. Wendroff, (1960). Systems of Conservation Laws, Communications on Pure and Applied Mathematics, Vol. XIII, pp. 217-237.

Lax, P.D., (1964). Development of Singularities of Solutions of Nonlinear Hyperbolic Partial Differential Equations, Journal of Mathematical Physics, Vol. 5, No. 5, May, pp. 611-613.

Lax, P.D., and B. Wendroff, (1964). Difference Schemes for Hyperbolic Equations with High Order of Accuracy, Communications on Pure and Applied Mathematics, Vol. XVII, pp. 381-398.

Levin, L., (1952). Mouvement Nonpermanent sur les Cours dEau a la Suite de Rupture de Barrage, Revue Generale de l'Hydraulique, No. 72, pp. 297-315

Liggett, J.A. and D.A. Woolhiser, (1967). Difference Solutions of the Shallow-Water Equation, J. Eng'g. Mech. Div., Proc. ASCE , Vol. 93, No. EM2, April, pp, 39-71.

Liggett, J.A., (1975). Basic Equations of Unsteady Flow, in Unsteady Flow in Open Channels, ed. K. Mahmood and V. Yevjevich, Water Resources Publications, Ft. Collins, Colorado, U.S.A., pp. 29-62.

Liggett, J.A. and J.A. Cunge, (1975). Numerical Methods of Solution of the Unsteady Flow Equations, in Unsteady Flow in Open Channels, ed. K. Mahmood and V. Yevjevich, Water Resources Publications, Ft. Collins, Colorado, U.S.A., pp. 89-182.

Lister, M., (1960). The Numerical Solution of Hyperbolic Partial Differential Equations by the Method of Characteristics, in Mathematical Methods for Digital Computers, ed. by A. Ralston and H.S. Wilf, John Wiley and Sons, Inc., New York, U.S.A., pp. 165-179.

MacDonald, T.C. and J. Langride-Monopolis,(1984). Breaching Characteristics of Dam Failures, J. Hydraulic Eng'g.,Proc. ASCE , Vol. 110, No. 5, May, pp. 567-586.

Marshall, G., and A.N. Menendez, (1981). Numerical Treatment of Nonconservation Forms of the Equations of Shallow Water Theory, Journal of Computational Physics, Vol. 44, pp. 167-188.

Martin, H., (1983). Dam-Break Wave in Horizontal Channels with Parallel and Divergent Side Walls, XX Congress of the International Association for Hydraulic Research, Proceedings, Subject A, Vol. 11, Sep. 5-9, pp. 494-505.

Martin, J.C., and W.J. Moyce, (1952). An Experimental Study of the Collapse of Liquid Columns on a Rigid Horizontal Plane, Philosophical Transactions of the Royal Society, (A), Vol. 244, pp. 312-324.

Massau, J., (1889). Lintegration Graphique, and Appendice au Memoire sur Lintegration Graphique, Assoc. des Ingenieurs Sortis des Ecoles Speciales de Gand, Belgium, Annales, Vol. 12, pp. 185-444.

Matsutomi, H., (1983). Numerical Computations of Two-Dimensional Inundation of Rapidly Varied Flows due to Breaking of Dams, XX Congress of the International Association for Hydraulic Research, Proceedings, Subject A, Vol. 11, Sep. 5-9, pp. 479-488.

McCalla, T.R., (1967). Introduction to Numerical Methods and Fortran Programming, John Wiley and Sons, New York, U.S.A.

Memos, C.D., A. Georgakakos, and S. Vomvoris, (1983). Some Experimental Results of the Two-Dimensional Dam-Break Problem, XX Congress of the International Association for Hydraulic Research, Proceedings, Subject A, Vol. 11, Sep. 5-9, pp. 555-563.

Montouri, C., (1965). Introduction d'un Debit Constant Dans un Canal Vide, XI Congress of the IAHR, Leningrad, Vol. 3, paper 55.

Nakagawa, H., S. Nakamura, and K. Ichihaschi, (1969). Generation and Development of a Hydraulic Bore due to the Breaking of a Dam, Bulletin of the Disaster Prevention Research Institute, Kyoto University, Japan, Vol. 19, Pt. 2, No. 154.

Outland, C.F. (1963). Man-made Disaster the Story of St. Francis Dam, The Arthur H. Clark Company , California, U.S.A.

Pickford, J., (1969). Analysis of Surges, Macmillan Civil Eng'g. Hydraulics, London, U.K.

Pohle, F.V., (1952). Motion of Water Due to Breaking of a Dam, and Related Problems, U.S. National Bureau of Standards, Gravity Waves, Circular 521, pp. 47-53.

Preissmann, A. and J.A. Cunge, (1961). Tidal Bore Calculation on an Electronic Computer, La Houille Blanche, No. 5, Oct.,pp. 588-596.

Price, R.K., (1974). Comparison of Four Numerical Methods for Flood Routing, J. Hydraulic Div., Proc. ASCE , Vol. 100, No. HY7, July, pp. 879-899.

Rajar, R., (1978). Mathematical Simulation of Dam-Break Flow, J. Hydraulic Div., Proc. ASCE , Vol. 104, No. HY7, July, pp. 1011-1025.

Re, R., (1946). A Study of Sudden Water Release from a Body of Water to a Canal by the Graphical Method, La Houille Blanche, No. 3, pp. 181-187.

Reynolds, G.M.,(1975). Liability of Consultants in Dam Investigations, Engineering Foundation Conference, Responsibility and Liability of Public and Private Interests on Dams, Asilomar Conference Grounds, Pacific Grove, California, Sep. 28-Oct. 3, Published by American Society of Civil Engineers.

Ritter, A., (1892). The Propagation of Water Waves, V.D.I. Zeitscher (Berlin), Vol. 36, Pt. 2, No. 33, pp. 947-954.

Sachdev, P.L., and P.L. Bhatnagar, (1969). Propagation of a Bore Produced by the Sudden Break of a Dam, Quart. Journ. Mech. and Applied Math., Vol. XXII, Pt. 4, pp. 501-512.

Sakkas, J.G. and T. Strelkoff, (1973). Dam-Break Flood in a Prismatic Dry Channel, J. Hydraulic Div., Proc. ASCE, Vol. 99, No. HY12, December, pp. 2195-2216.

Sakkas, J.G. and T. Strelkoff, (1976). Dimensionless Solution of Dam-Break Flood Waves, J. Hydraulic Div., Proc. ASCE , Vol. 102, No. HY2, February, pp. 171-184.

Sandover, J.A. and O.C. Zienkiewicz, (1957). Experiments on Surge Waves, Water Power, November, pp. 418-424.

Schamber, D.R. and N.D. Katopodes, (1984). One-Dimensional Models for Partially Breached Dams, J. Hydraulic Eng'g,Proc. ASCE , Vol. 110, No. 8, August, pp. 1086-1102.

Schoklitsch, A., (1917). On Waves Created by Dam Breaches, Akad. Wiss., Vienna, Austria, Proc.,Vol. 126, Pt. IIA, pp.1489-1514.

Sowers, G.F., (1974). Dam Safety Legislation: A solution or a problem, Engineering Foundation Conference Proceedings, Safety of small dams, New England College, Henniker, New Hampshire, August 4-9, Published by American Society of Civil Engineers.

Stoker, J.J., (1948). The Formation of Breakers and Bores, The theory of nonlinear wave propagation in shallow water and open channels, Communications on Applied Mathematics, New York Univeristy, Vol. 1, pp. 1-87.

Stoker, J.J., (1957). Water Waves, The Mathematical Theory with Applications, Interscience Publishers, Inc., New York, U.S.A.

Strelkoff, T., (1969). One-Dimensional Equations of Open-Channel Flow, J. Hydraulic Div., Proc. ASCE., Vol. 95, No. HY3, May, pp. 861-876.

Strelkoff, T., (1970). Numerical Solution of Saint-Venant Equations, J. Hydraulic Div., Proc. ASCE , Vol. 96, No. HY1, January, pp. 223-252.

Strelkoff, T., D. Schamber and N. Katopodes, (1977). Comparative Analysis of Routing Techniques for the Flood-wave from a Ruptured Dam, Proceedings of Dam-Break Routing Model Workshop, Bethesda, pp. 228-291.

Su, Shih-Tun, (1970). Dry-Bed Wave Due to Sudden Water Releases, PhD. Thesis presented to Colorado State University, Fort Collins, Colorado, U.S.A.

Su, Shih-Tun and A.H. Barnes ,(1970). Geometric and Frictional Effects on Sudden Releases, J. Hydraulic Div., Proc. ASCE , Vol. 96, No. HY11, Nov., pp. 2185-2200.

Su, Shih-Tun, (1977). Unsteady Flow Analysis of Dam-Break Waves, Proceedings of Dam Break Flood Routing Model Workshop, Water Resources Council, Washington D.C., U.S.A., pp. 18-46.

Terzidis, G. and T. Strelkoff, (1970). Computation of Open-Channel Surges and Shocks, J. Hydraulic Div., Proc. ASCE , Vol. 96, No. HY12, Dec., pp. 2581-2610.

Thomas, H.H., (1976). The Engineering of Large Dams, Part 1, A Wiley-Interscience Publication, John Wiley and Son, New York, pp. 53, 38 and 43, U.S.A.

Toran, J., (1973). Lessons from Dam Incidents, International Commission on Large Dams, Reduced edition, Imprimerie Louis-Jean.

U.S. Army,Corps of Engineers, (1960). Flood Resulting from Sudden Breached Dams, Miscellaneous paper no. 2-374, Report 1, Smooth Channel, Report 2, Rough Channel, (1961).

Vardy, A.E., (1976). On the Use of the Method of Characteristics for the Solution of Unsteady Flows in Networks, in Second International Conference on Pressure Surges, BHRA Fluid Engineering, 22-24 September, London, U.K., pp. H2-15 to H2-30.

Vasiliev, O.F., T.A. Temnoeva and S.M. Shugrin, (1965). Numerical Method for the Calculation of Unsteady Flows in Open Channels, Izv. Akad. Nauk SSSR, Mechanics, No. 2.

Vasiliev, O.F., (1970). Numerical Solution of the Non-Linear Problems of Unsteady Flows in Open Channels, Proceedings, International Conference on Numerical Methods in Fluid Dynamics, Berkeley, California, pp. 410-421.

Von Neumann, J. and R.D. Richtmyer, (1950). A Method for the Numerical Calculations of Hydrodynamic Shocks, J. Appl. Phys., Vol. 21, March, pp. 232-237.

Whitham, G.B., (1955). The Effects of Hydraulic Resistance in the Dam-Break Problem, Proceedings of the Royal Society of London, Series A, Vol. 227, pp. 399-407.

Whitham, G.B., (1958). On the Propagation of Shock Waves Through Regions of Non-Uniform Area or Flow, J. Fluid Mech., Vol. 4, pp. 337-360.

Wylie, E.B., (1980). Inaccuracies in the Characteristic Method , in Computer and Physical Modelling in Hydraulic Eng'g., ed. G. Ashton, Proc. ASCE , August, pp. 165-176.

Xanthopoulos, Th. and Ch. Koutitas, (1976). Numerical Simulation of a Two Dimensional Flood Wave Propagation Due to Dam Failure, Journal of Hydraulic Research, Vol. 14, No. 4, pp. 321-331.

Yevjevich, V., (1975). Sudden Water Release, in Unsteady Flow in Open Channels, ed. K. Mahmood and V. Yevjevich, Water Resources Publications, Ft. Collins, Colorado, U.S.A., pp. 587-668.